

Transactions of the ASME®

Technical Editor, T. H. OKIISHI (2003)

Associate Technical Editors

Gas Turbine (Review Chair)

R. NATOLE (2001)

Heat Transfer

R. BUNKER (2003)

Turbomachinery

R. ABHARI (2002)

R. DAVIS (2002)

C. KOCH (2002)

S. SJOLANDER (2002)

A. STRAZISAR (2000)

BOARD ON COMMUNICATIONS

Chairman and Vice-President

R. K. SHAH

OFFICERS OF THE ASME

President, JOHN R. PARKER

Executive Director, D. L. BELDEN

Treasurer, J. A. MASON

PUBLISHING STAFF

Managing Director, Engineering

CHARLES W. BEARDSLEY

Director, Technical Publishing

PHILIP DI VIETRO

Managing Editor, Technical Publishing

CYNTHIA B. CLARK

Managing Editor, Transactions

CORNELIA MONAHAN

Production Coordinator

VALERIE WINTERS

Production Assistant

MARISOL ANDINO

Transactions of the ASME, Journal of Turbomachinery

(ISSN 0889-504X) is published quarterly (Jan., Apr.,

July, Oct.) by The American Society of Mechanical

Engineers, Three Park Avenue, New York, NY

10016. Periodicals postage paid at New York, NY and

additional mailing offices. POSTMASTER: Send address

changes to Transactions of the ASME, Journal of

Turbomachinery, c/o THE AMERICAN SOCIETY

OF MECHANICAL ENGINEERS, 22 Law Drive,

Box 2300, Fairfield, NJ 07007-2300.

CHANGES OF ADDRESS must be received at Society

headquarters seven weeks before they are to be effective.

Please send old label and new address.

STATEMENT from By-Laws. The Society shall not be

responsible for statements or opinions advanced in papers

or ... printed in its publications (B7.1, Par. 3).

COPYRIGHT © 2000 by the American Society of Mechanical

Engineers. For authorization to photocopy material for

internal or personal use under those circumstances not falling

within the fair use provisions of the Copyright Act,

contact the Copyright Clearance Center (CCC), 222

Rosewood Drive, Danvers, MA 01923; tel: 978-750-8400,

www.copyright.com. Request for special permission

or bulk copying should be addressed to

Reprints/Permission Department.

INDEXED by Applied Mechanics Reviews and Engineering

Information, Inc. Canadian Goods & Services Tax

Registration #126148048

Journal of Turbomachinery

Published Quarterly by The American Society of Mechanical Engineers

VOLUME 122 • NUMBER 3 • JULY 2000

TECHNICAL PAPERS

- 397 1999 Turbomachinery Committee Best Paper Award: Development of Advanced Compressor Airfoils for Heavy-Duty Gas Turbines—Part 1: Design and Optimization (99-GT-95)
Ulf Köller, Reinhard Mönig, Bernhard Küsters, and Heinz-Adolf Schreiber
- 406 1999 Turbomachinery Committee Best Paper Award: Development of Advanced Compressor Airfoils for Heavy-Duty Gas Turbines— Part II: Experimental and Theoretical Analysis (99-GT-96)
Bernhard Küsters, Heinz-Adolf Schreiber, Ulf Köller, and Reinhard Mönig
- 416 The Influence of Technical Surface Roughness Caused by Precision Forging on the Flow Around a Highly Loaded Compressor Cascade (99-GT-366)
Robert Leipold, Matthias Boese, and Leonhard Fottner
- 426 A Correlation for Tip Leakage Blockage in Compressor Blade Passages (99-GT-388)
M. Hoeger, M. Lahmer, M. Dupslaff, and G. Fritsch
- 433 Variations in Upstream Vane Loading With Changes in Back Pressure in a Transonic Compressor (98-GT-344)
Douglas P. Probasco, Tim J. Leger, J. Mitch Wolff, William W. Copenhaver, and Randall M. Chriss
- 442 Boundary Layer Transition Induced by Periodic Wakes
Xiaohua Wu and Paul A. Durbin
- 450 Spectral Measurements in Transitional Boundary Layers on a Concave Wall Under High and Low Free-Stream Turbulence Conditions
Ralph J. Volino and Terrence W. Simon
- 458 Flowfield Measurements in the Endwall Region of a Stator Vane (99-GT-188)
M. B. Kang and K. A. Thole
- 467 A Time-Linearized Navier–Stokes Analysis of Stall Flutter (99-GT-383)
William S. Clark and Kenneth C. Hall
- 477 Influence of Compressor Deterioration on Engine Dynamic Behavior and Transient Stall-Margin (99-GT-439)
Z. S. Spakovszky, J. B. Gertz, O. P. Sharma, J. D. Paduano, A. H. Epstein, and E. M. Greitzer
- 485 Active Stabilization of Surge in an Axicentrifugal Turboshaft Engine (99-GT-438)
E. B. Nelson, J. D. Paduano, and A. H. Epstein
- 494 One-Dimensional Performance Prediction of Subsonic Vaned Diffusers (99-GT-433)
Beat Ribí and Peter Dalbert
- 505 On the Development and Application of the Fast-Response Aerodynamic Probe System in Turbomachines—Part 1: The Measurement System (99-GT-152)
Peter Kupferschmied, Pascal Köppel, Christian Roduner, and Georg Gyarmathy

(Contents continued on inside back cover)

This journal is printed on acid-free paper, which exceeds the ANSI Z39.48-1992 specification for permanence of paper and library materials. ©™

♻️ 85% recycled content, including 10% post-consumer fibers.

- 517 On the Development and Application of the Fast-Response Aerodynamic Probe System in Turbomachines—Part 2: Flow, Surge, and Stall in a Centrifugal Compressor (99-GT-153)
Christian Roduner, Peter Kupferschmied, Pascal Köppel, and Georg Gyarmathy
- 527 On the Development and Application of the Fast-Response Aerodynamic Probe System in Turbomachines—Part 3: Comparison of Averaging Methods Applied to Centrifugal Compressor Measurements (99-GT-154)
Pascal Köppel, Christian Roduner, Peter Kupferschmied, and Georg Gyarmathy
- 537 Impact of Film-Cooling Jets on Turbine Aerodynamic Losses (99-GT-421)
Dibbon K. Walters and James H. Leylek
- 546 Transient Heat Transfer Measurements Using a Single Wide-Band Liquid Crystal Test (99-GT-167)
Dragos N. Licu, Matthew J. Findlay, Ian S. Gartshore, and Martha Salcudean
- 553 Film Cooling Effectiveness for Short Film Cooling Holes Fed by a Narrow Plenum (99-GT-36)
C. A. Hale, M. W. Plesniak, and S. Ramadhyani
- 558 Predictions of a Film Coolant Jet in Crossflow With Different Turbulence Models (99-GT-124)
Asif Hoda and Sumanta Acharya
- 570 Continuous Monitoring of Binary Gas Mixture Concentration With Application to Turbine Blade Cooling Experiments (99-GT-365)
Tomas Strilka, Miklos Sajben, and Peter Nagy
- 579 Local Heat/Mass Transfer Measurements in a Rectangular Duct With Discrete Ribs (99-GT-121)
H. H. Cho, S. J. Wu, and H. J. Kwon

TECHNICAL BRIEF

- 587 On the Momentum Balance in Linear-Combination Models for the Transition Zone
J. Dey

ANNOUNCEMENTS

- 589 An Invitation to Review Article Authors for the New Era of Applied Mechanics Reviews
- 592 Information for Authors

Development of Advanced Compressor Airfoils for Heavy-Duty Gas Turbines— Part I: Design and Optimization

Ulf Köller

Reinhard Mönig

Siemens AG,
Power Generation (KWU)
D-45466 Mülheim a. d. Ruhr, Germany

Bernhard Küsters

Heinz-Adolf Schreiber

German Aerospace Center,
Institute of Propulsion Technology,
D-51170 Köln, Germany

A new family of subsonic compressor airfoils, which are characterized by low losses and wide operating ranges, has been designed for use in heavy-duty gas turbines. In particular the influence of the higher airfoil Reynolds numbers compared to aeroengine compressors and the impact of these differences on the location of transition are taken into account. The design process itself is carried out by the combination of a geometric code for the airfoil description, with a blade-to-blade solver and a numerical optimization algorithm. The optimization process includes the design-point losses for a specified Q3D flow problem and the off-design performance for the entire operating range. The family covers a wide range of inlet flow angle, Mach number, flow turning, blade thickness, solidity and AVDR in order to consider the entire range of flow conditions that occur in practical compressor design. The superior performance of the new airfoil family is demonstrated by a comparison with conventional controlled diffusion airfoils (CDA). The advantage in performance has been confirmed by detailed experimental investigations, which will be presented in Part II of the paper. This leads to the conclusion that CDA airfoils that have been primarily developed for aeroengine applications are not the optimum solution, if directly transferred to heavy-duty gas turbines. A significant improvement in compressor efficiency is possible, if the new profiles are used instead of conventional airfoils. [S0889-504X(00)02102-4]

Introduction

Modern heavy-duty gas turbine compressors used in combined cycle operation have to deal with a number of requirements. Due to economical and ecological demands, high efficiency as well as higher power output, based on both growing mass flows and increasing specific work, are desired. Gas turbines have to operate with sufficient surge margin in different climate conditions, at rotating speed variations due to frequency deviation in the power supply system, and at part-load conditions. These requirements can only be satisfied, if within the design process both the static and dynamic strength demands and the aerodynamic performance of the compressor blades are taken into account. The stacking of the profiles in the radial direction, as well as the profiles themselves, play an important role for the efficiency and the operational safety of the whole compressor.

Due to the high mass flow, the front compressor stages have to deal with transonic and supercritical velocity distributions, while in the middle and the rear stages subsonic flow is predominant. In this subsonic region it is very efficient to use profile families for blading in order to achieve a fast and reliable compressor design. The quality of an airfoil is mainly determined by the total pressure losses and the attainable operating range.

In the past, different airfoil families have been developed for use in subsonic compressor design. Based on extensive experimental studies, the NACA-65 airfoils [1] were implemented in many aeroengine and heavy-duty gas turbines. From the end of the seventies controlled-diffusion airfoils (CDA) made their way into modern compressor design, which were based on both experi-

mental and numerical research work [2]. For the design process itself, two different computer-aided methods are commonly in use: the direct and the inverse approach. In the direct method, the flow field is completely described by the specified cascade geometry and the flow conditions up- and downstream of the cascade. The inverse approach is based on the velocity distribution on the profile surfaces. Together with a given solidity and the inlet/exit flow conditions, the associated airfoil geometry can be defined [3,4]. However, this inverse design method requires multiple variations of the velocity distribution until an acceptable profile geometry is obtained. The first supercritical airfoil, which was designed by the inverse approach and validated by experimental results, was presented by Stephens [5]. In the following years many authors showed the superiority of the new design, both for supercritical and subsonic airfoils [6,7].

In the same way as gas turbines have to work at part-load, the compressor airfoils have to operate at off-design conditions, which means different inlet flow angles, Mach numbers, and axial velocity density ratios. By using an inverse approach, it is not possible to consider the cascade's performance at part-load conditions. Only the employment of a direct flow solver can provide information on the airfoil's off-design behavior.

A second reason for using the direct method is to enable the coupling of the flow solver with an optimization algorithm and a geometric code for the airfoil description in order to achieve an automated design tool. The variables needed as input to the geometric code can be used as independent variables for the optimization process. With the use of an automated approach, a large number of airfoil designs can be carried out, which is required to establish a new airfoil family. This idea of automated design has already been presented by Sanger [8] and used for optimizing the design of a controlled-diffusion stator blade row. With the increasing calculation capacity of modern computers, the employ-

Contributed by the International Gas Turbine Institute and presented at the 44th International Gas Turbine and Aeroengine Congress and Exhibition, Indianapolis, Indiana, June 7–10, 1999. Manuscript received by the International Gas Turbine Institute February 1999. Paper No. 99-GT-95. Review Chair: D. C. Wisler.

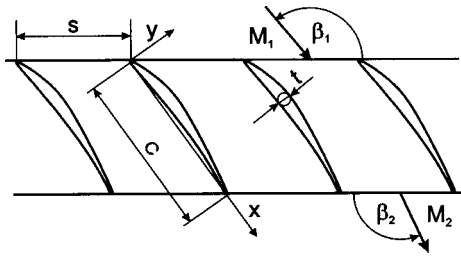


Fig. 1 Aerodynamic and geometric cascade parameters

ment of such coupled, automated design tools is still rising, Sanz [9] used an inverse hodograph method in conjunction with an optimization algorithm, Goel et al. [10] extended the use of this automated design to turbine airfoils and Pierret et al. [11] coupled a Navier–Stokes solver with an artificial neural network. Even algorithms based on genetic ideas made their way into airfoil design [12] and optimization is now used for solving different problems in turbomachinery [13]. But in all these airfoil design procedures, the off-design behavior is excluded.

Today in most heavy-duty gas turbines NACA-65 or CDA profiles are in use for designing the subsonic compressor stages. While the NACA-65 profiles were initially developed as airfoil profiles, the controlled-diffusion airfoils were originally designed for use in supersonic cascades. Hence, both families were not initially designed for use in subsonic heavy-duty gas turbine compressor stages. So the question must be raised: Do these airfoils represent an optimal solution to meet the requirements of such large compressors, where the profile loss and the airfoil's operating range are of utmost importance?

This paper deals with the development and experimental validation of a new compressor airfoil family under consideration of the special flow boundary conditions in a heavy-duty gas turbine compressor (Fig. 1). A direct approach is used because the design and the off-design behavior of the cascades need to be taken into account. As the profile geometry can be described by a number of geometric parameters, the search for an optimal airfoil geometry can be transferred to an optimum search in a multidimensional space and can be solved with a modern numerical optimization algorithm. Based on a variety of optimized profiles, a new airfoil family was created that covers the wide range of mechanical and aerodynamic properties of the multistage axial compressor. Detailed experimental investigations, carried out in the DLR transonic cascade wind tunnel, confirmed the superiority of the optimized profiles. The corresponding results are presented in Part II of this paper [14].

Analysis Methods

The airfoil design process used for the development of the new profile family is carried out automatically by the combination of a geometric code for the airfoil description with a blade-to-blade solver and a numerical optimization algorithm.

Profile Model. The geometry model implemented allows a direct description of the airfoil surfaces. As the suction side diffusion is mainly responsible for the profile losses at design conditions, the profile generation starts with the suction side construction and then attaches the pressure side.

Figure 2 gives an example of the airfoil geometry. For the construction of each surface two third-order spline functions are used. The leading edge geometry is described by an elliptical function, the trailing edge by a circular arc. In general a spline function definition requires the start and end point coordinates as well as the referring slopes. The leading edge enlargement shows the parameters used in this geometry model to define the coordinates and the slope at the suction side starting point S_1 : the leading edge radius r_{LE} , the inlet metal angle λ_1 , and the wedge

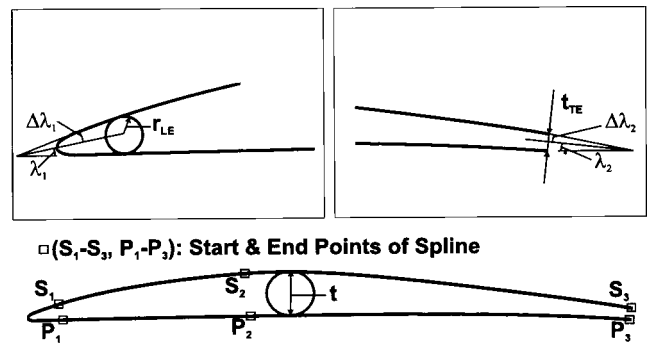


Fig. 2 Design parameters for airfoil generation

angle $\Delta\lambda_1$. Together with the x/y coordinates at location S_2 (the connection between the two suction side splines) and the corresponding data for the trailing edge, the two spline functions (from S_1 to S_2 and from S_2 to S_3) can be calculated. The pressure side is attached with the requirement that the maximum airfoil thickness matches the prescribed value of t . In a further step the circular leading edge is modified to an elliptical one.

The effectiveness and flexibility of this model is demonstrated in Fig. 3 by the reproduction of three given airfoil geometries. In the top diagram a controlled-diffusion airfoil of the V84.3A-Siemens gas turbine [15] is shown. The next airfoil was designed using the inverse approach for application in the first rotor hub section of an industrial compressor [16] and the third diagram shows an inverse designed high turning stator cross section [6]. All three reproductions are almost congruent with the original geometries. This underlines the flexibility of the geometry program to construct arbitrary profiles, which is necessary to allow a successful optimization process.

Blade-to-Blade Calculation Method. All calculations presented in Part I have been carried out with the inviscid/viscous flow solver MISES developed at MIT by Giles [17] and Drela [18]. A two-dimensional, steady-state and inviscid calculation of the flow field is coupled with an integral, compressible boundary layer calculation. The influence of the stream tube height is taken into account and for local supersonic regions the “artificial viscosity” formulation is implemented. The flow is discretized by a finite-volume approach, where two of the four element edges are identical to the streamlines. The corresponding computational grid topology and an enlargement of the leading edge region are shown in Fig. 4.

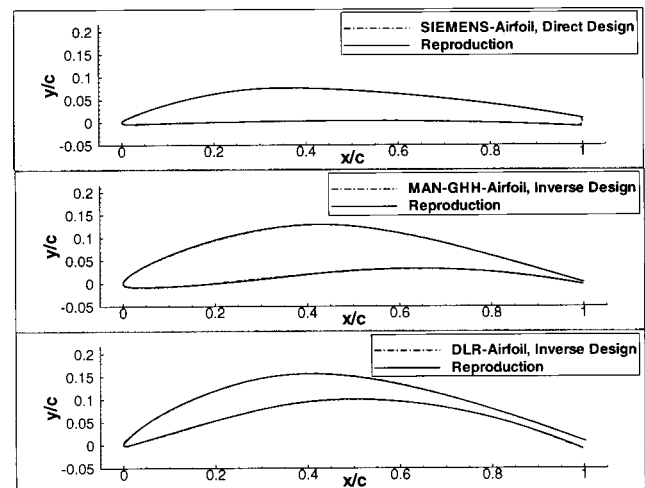


Fig. 3 Reproduction of three compressor profiles

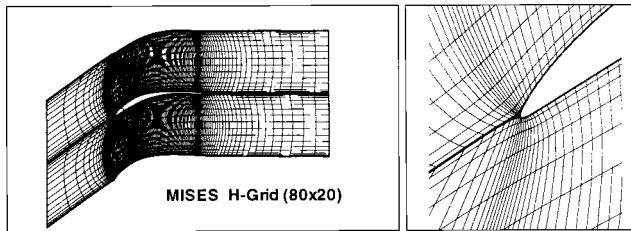


Fig. 4 Computational grid for subsonic compressor airfoil

Based on the inviscid flow results and the airfoil surface geometry, an integral calculation of the two-dimensional, compressible laminar and turbulent boundary layer equations is carried out during each iteration step of the flow solver. The laminar-turbulent transition can occur in three different modes depending on the free-stream turbulence level, the Reynolds number, and the pressure distribution: free, bypass, and transition in combination with a separation bubble [18,19]. Inviscid and viscous code elements are coupled by the displacement thickness. Contrary to most inviscid/viscous codes, MISES solves the boundary layer equations together with the flow field as a coupled system. After each iteration step, the computational grid node coordinates are adapted to the local flow conditions, so that in a converged solution the grid lines in the main flow direction coalesce with the streamlines. The exit flow angle and the total pressure loss are calculated by conservation of mass, momentum, and energy from the cascade exit to a specified mixing plane downstream.

For a first validation, experimental data and MISES calculations of the two inverse designed airfoils shown in Fig. 3 have been compared. Fig. 5 and Table 1 show the results for the MAN-GHH-Airfoil [16] at design point conditions with more than 38 deg of flow turning. The calculated Mach number distribution is in excellent agreement with the experimental data for both suction and pressure side. Static pressure rise, exit Mach number, and total pressure loss show a very good agreement and exit flow angle difference seems to be near the measurement accuracy. The MISES validation prior to the design of the new airfoil family was extended to the comparison of the complete operating range for both inverse designed airfoils. MISES showed satisfying agreement to the experimental data in all regarded conditions, so these first results confirmed the choice of MISES as the preferred flow solver for the intended airfoil design.

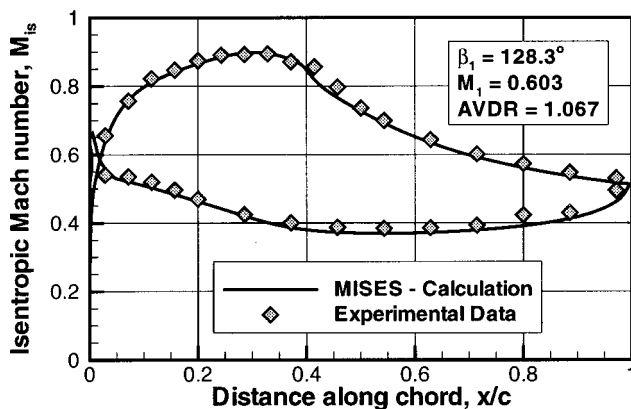


Fig. 5 MISES and experimental Mach number distribution

Table 1 Numerical and experimental exit data

| | β_2 | M_2 | ω | p_2/p_1 |
|------------|-----------|-------|----------|-----------|
| MISES | 89.7° | 0.466 | 1.51% | 1.098 |
| Experiment | 90.4° | 0.466 | 1.45% | 1.098 |

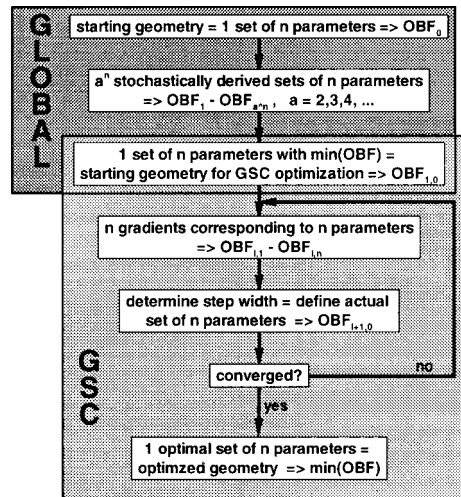


Fig. 6 Flowchart of optimization algorithm

Optimization Algorithm. The goal of each optimization process is the minimization or maximization of an objective function. Use of the geometric parameters ($\lambda_1, \Delta\lambda_1, r_{LE}, \lambda_2, \Delta\lambda_2, t_{TE}, \dots$) shown in Fig. 2 as optimization parameters for this process leads to an optimal airfoil design with respect to the given objective function. For each parameter lower and upper bounds have to be defined in order to avoid physically meaningless solutions. These definition ranges are also used for the normalization of each parameter. This allows comparison of parameter gradients based on different dimensions. The choice of which optimization algorithm should be adopted to solve a given problem depends strongly on the mathematical properties of the objective function. The higher the objective function's order of steadiness is, the more sophisticated the chosen optimization algorithm can be. But the question of whether the optimum reached is a global or local one cannot be answered.

For the optimization presented in this paper, a combination of two algorithms has been adopted: a normal-distributed random search code (GLOBAL) together with the deterministic Gauss-Seidel-Coordinate (GSC) strategy, which basically is a gradient method. A fundamental description of both is presented by Schwarz and Spiegel [13] and the corresponding flowchart is shown in Fig. 6. Each objective function call means blade-to-blade calculations for the stagger angle determination, the design and the off-design behavior for a given geometry (= set of n parameters) and is symbolized by “ \Rightarrow ” in the flowchart. Hence, for a certain airfoil the requested flow turning is achieved by the determination of the required stagger angle through preliminary blade-to-blade calculations in each objective function call.

At the beginning the user has to define one set of n parameters, which represent the initial (starting) geometry and the basis “ a ” for the random search code. Within the given definition ranges, a normal distribution of each parameter is generated with each starting parameter as an expected value and a preliminary user-specified standard deviation. For each of the so-derived “ a^n ” sets of parameters the objective function values are calculated. As the chosen objective function includes the calculation of the cascade's design and off-design behavior, the random search basis “ a ” was set to $a=2$. With a number of parameters “ n ” used in the optimization process between $n=6$ and $n=10$, “ a^n ” was in the range of 64 to 1024. That set of parameters, identified by the minimal objective function value, serves as input/starting geometry for the GSC strategy. Each GSC iteration cycle consists of three steps:

- search for the optimization direction in the n -dimensional space,

- determine the step width for the found optimization direction (leads to a new set of n parameters),
- check all defined convergence criteria.

The optimal set of n parameters defines the geometry, which with respect to the objective function, represents an optimal solution for the given problem. The higher the number a and the standard deviation in the random algorithm are, the more global the search is.

The combination of the three presented codes, the geometric profile model, the blade-to-blade flow solver, and the optimization algorithm together with a given objective function, enables the user to automatically design airfoils for a given vector diagram.

Airfoil Design

The prescribed tool for automated airfoil design has been used for a wide range of application. Based on a large number of optimizations, a new airfoil family has been developed.

Range of Application. Because an airfoil family used for the whole subsonic compressor has to cover flow turning problems for both the mid and the rear part of the compressor, for both the hub and the tip endwall blading, for both stators and rotors and for different reaction numbers, each considered variation parameter has to cover a wide range. In Table 2 the minimum and maximum values for each design parameter are given. One discrete value for each design parameter (β_1 , $\Delta\beta$, M_1 , t/c , s/c , and $AVDR$) is established in order to define one flow problem, which is to be solved by the automated design tool. Within these ranges only design relevant combinations of parameters have been adopted as a basis for the new airfoil family.

Objective Function. Apart from the flow solver the quality of optimization results depend mainly on the optimization algorithm itself and on the formulation of the objective function. If this formulation mathematically represents the desired physical behavior, a good design can be expected by using an optimization process. So the validation of a chosen objective function is one key to a successful automatic airfoil design.

As mentioned above, modern heavy-duty gas turbine compressors have to operate with high efficiency at varying conditions. This primarily means that the level of the total pressure loss at the design point and the entire incidence range of the cascade is essential for the compressor performance. Figure 7 illustrates all elements used for the objective function, which takes into account the complete airfoil's operating range. The corresponding formulation of the objective function is

$$\begin{aligned}
 OBF = & C_1 \cdot \frac{\omega_D}{\omega_{ref}} + C_2 \cdot \frac{\Delta\beta_1}{\Delta\beta_{1,ref}} \\
 & + C_3 \cdot \frac{|(\Delta\beta_{St}/\Delta\beta_1) - (\Delta\beta_{St}/\Delta\beta_1)_{ref}|}{(\Delta\beta_{St}/\Delta\beta_1)_{ref}} \\
 & + C_4 \cdot \frac{\omega_{80}}{\omega_{80,ref}} + C_5 \cdot \frac{\sigma_{80}}{\sigma_{80,ref}} + \Sigma PF. \quad (1)
 \end{aligned}$$

The total pressure loss at design conditions is called ω_D . The limits of the attainable operating range $\Delta\beta_1$ are defined by twice the value of ω_D . The relative stall margin is given by the expression $(\Delta\beta_{St}/\Delta\beta_1)$. To aspire to a "flat" loss curve, the mean value of the total pressure losses for the inner 80 percent of the operating range is called ω_{80} and the corresponding standard deviation σ_{80} . The abbreviation PF represents the penalty function

Table 2 Range of design parameters

| | β_1 | $\Delta\beta$ | M_1 | t/c | s/c | $AVDR$ |
|------------|-----------|---------------|-------|-------|-------|--------|
| Min | 130° | 4° | 0.35 | 0.04 | 0.7 | 0.9 |
| Max | 165° | 30° | 0.80 | 0.16 | 1.2 | 1.2 |

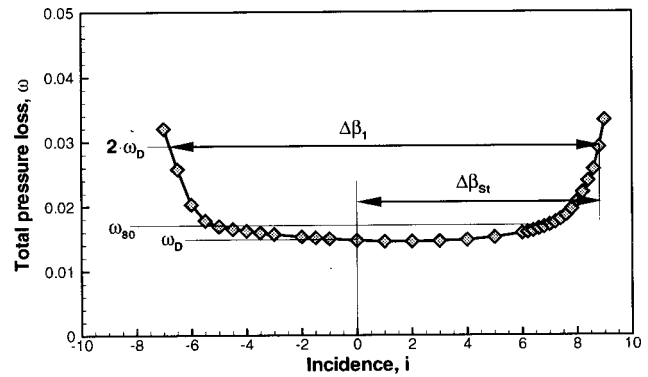


Fig. 7 Elements for objective function definition

terms, which introduce geometric restrictions for a mathematical formulation. For instance, due to static and dynamic strength requirements the cross section area of a rotor blade may not be less than a certain given value. If during the optimization process a geometry is generated that fails this criterion, a relating number PF will be added to the objective function value OBF . The reference values allow a normalization of the different objective function terms. The coefficients C are used for weighting each term against the others and must be specified by the user and validated by test runs of the design tool. The objective of the optimization process is to minimize this function.

With this type of objective function a design will be achieved, which is characterized by:

- low loss at design point condition;
- a wide operating range;
- a definite relative stall margin;
- a low and constant loss level within the inner 80 percent incidence range;
- no violation of any geometric restrictions.

This formulation represents a new approach in automated airfoil design, because the cascade's complete operating range is taken into account.

Airfoil Optimization. To give an impression of the presented tool's and objective function's efficiency, an optimization example will be presented and discussed in detail. Figures 8–10 show comparisons between the profile before and after the optimization. In the lower diagram of Fig. 8 the design point and cascade data (β_1 , $\Delta\beta$, M_1 , t/c , s/c , and $AVDR$) are noted. With a diffusion factor of $DF=0.42$, the loading of this cascade is

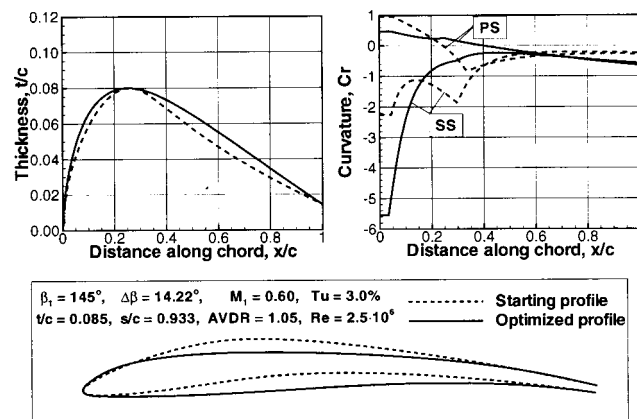


Fig. 8 Geometry of starting and optimized profiles

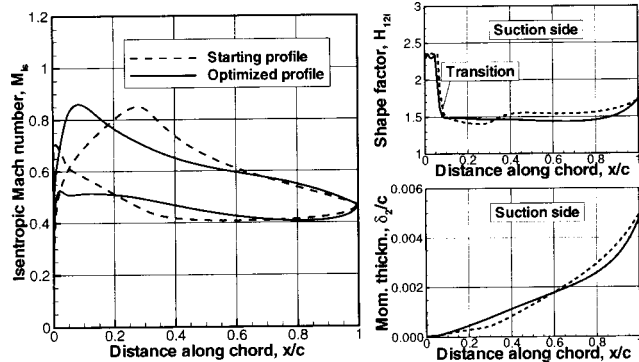


Fig. 9 Mach number distributions and boundary layer parameters for starting and optimized profiles

within an usual range for subsonic heavy-duty gas turbine compressor airfoils. The Reynolds number is set to 2.5×10^6 and the turbulence level to a value where bypass transition is predominant. That means that transition occurs at a location where the momentum thickness Reynolds number approaches a value of roughly 200.

As the upper left diagram shows, both geometries, the starting and the optimized design, have the same x/c value for the maximal thickness t/c at 25 percent. The thickness of the optimized profile in front of and behind the maximum is higher, because the starting airfoil's cross section area is too small and leads to a violation of the corresponding mechanical restriction. In the upper right diagram the curvature distributions of suction and pressure side are presented. The greatest differences appear on the front part of the suction side distribution, where the optimized airfoil has curvature values below -5 . This strong curvature leads to an almost flattened midpart of the suction side, as shown in the lower diagram of Fig. 8. The front wedge angle $\Delta\lambda_1$ has been considerably increased during the optimization process, which results in a thicker leading edge geometry. At the trailing edge both surfaces of the optimized airfoil are characterized by an increase in curvature and a higher rear wedge angle $\Delta\lambda_2$.

Comparing the Mach number distributions for design conditions in Fig. 9, the most significant difference is visible in the upstream propagation of the peak suction side Mach number for the optimized airfoil. As shown in the upper diagram on the right side, the laminar-turbulent transition on the suction side is located upstream of 10 percent chord. Suction side diffusion starts shortly after the transition location, when the turbulent boundary

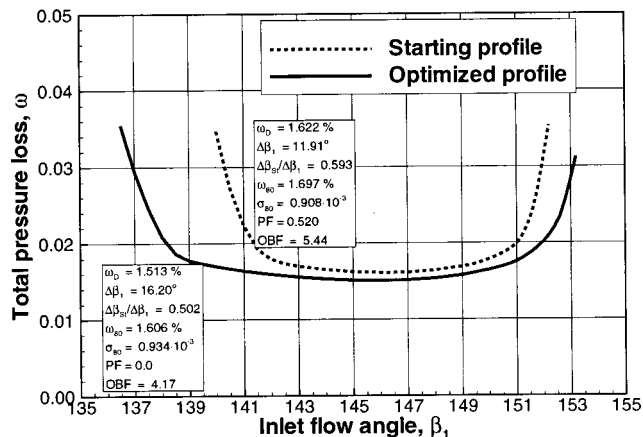


Fig. 10 Total pressure losses of starting and optimized profiles

layer is still thin. On the one hand this means that in the front accelerated part the boundary layer of the starting profile is already turbulent. On the other hand this leads to a smaller deceleration gradient for the optimized airfoil downstream of the peak Mach number. With incompressible shape factor values below 1.8, both airfoils show significant margin to suction side separation, which is assumed to occur at H_{12i} values between 2.5 and 3.0. The suction side boundary layer momentum thickness distributions are presented in the lower diagram on the right side. In conjunction with the Mach number distributions, the important role of the deceleration gradients can be clearly seen: The higher the local deceleration gradient is, the higher the local momentum thickness growth rate is. For instance, between 30 and 70 percent of chord, the diffusion on the starting geometry is significantly higher and the boundary layer momentum thickness grows with a higher gradient, as well. At the trailing edge of the starting profile the momentum thickness is slightly higher than for the optimized geometry.

The total pressure losses for both airfoils are presented in Fig. 10. In addition, the corresponding elements of the objective function are noted. With regard to the starting profile, the design losses have been reduced by more than 6 percent, the incidence range has been increased by more than 4 deg, including 1 deg larger stall margin, and the penalty function value has been reduced to zero. Correspondingly, the objective function value could be reduced from 5.44 to 4.17. The main cause of the increased operating range is the thicker leading edge geometry, which is less sensitive to any off-design inlet flow angle. The almost flattened midpart of the profile and the smaller trailing edge momentum thickness values lead to the reduced design point losses.

The considerable improvement in the design and the off-design behavior of the optimized profile proves the efficiency in airfoil design of both the optimization process and the objective function formulation. The starting profile's Mach number distribution with its acceleration until $x/c=30$ percent resembles closely a CDA-type distribution. For most of the CDA designs, apparently, it has been assumed that laminar flow is present on the suction side, at least partly up to 20–30 percent of chord. The new optimized airfoils, however, consider the effect of early transition at the high Reynolds number and turbomachinery turbulence level.

This optimization process has been carried out for approximately 400 airfoil designs in order to get enough optimal profiles as a basis for the new airfoil family. All design calculations have been carried out at a Reynolds number $Re=2.5 \times 10^6$, which represents an average for the blading in a real large-scale heavy-duty gas turbine compressor. Because the turbulence level is about 3 percent and higher in the mid- and rear-part compressor stages [20] and as further increase in turbulence level hardly affects the MISES-calculated transition location at Reynolds numbers higher than 2×10^6 (see also last section of this paper and Fig. 15), the turbulence level was set to a value of $Tu=3$ percent.

The optimization results have been used as a data basis to develop correlations for each geometric parameter as a function of the six varied flow and cascade parameters (β_1 , $\Delta\beta$, M_1 , t/c , s/c , and AVDR). Using these correlations in compressor design leads to an extremely fast and efficient blading design. In contrast to conventional airfoil families where geometric input like stagger, inlet, and outlet metal angles is needed, only the six flow and cascade parameters have to be defined. As a two-dimensional duct- or throughflow compressor design calculation results in the radial distributions of the flow properties in the axial gaps, all six parameters for each cross section in the flow path are given and the corresponding airfoil geometry is directly determined by the developed correlations. In order to validate these correlations and the corresponding airfoil family, a four-step process has been adopted:

- Check airfoil geometry within given ranges of application for violation of geometric restrictions.
- Check objective function curves/planes of the new airfoil

Table 3 Design parameters of test cascades A–D

| Cascade | A | B | C | D |
|---------------|--------|--------|--------|--------|
| M_1 | 0.715 | 0.607 | 0.556 | 0.438 |
| β_1 | 149.4° | 142.0° | 147.3° | 137.0° |
| $\Delta\beta$ | 10.3° | 14.7° | 12.8° | 18.0° |
| t/c | 5.0% | 7.0% | 7.4% | 9.3% |
| s/c | 0.855 | 0.888 | 0.953 | 0.874 |
| $AVDR$ | 1.06 | 1.05 | 1.05 | 0.99 |
| DF | 0.393 | 0.393 | 0.407 | 0.422 |

family for unusually high values in order to determine regions where the geometric correlations do not match the support points/results from the optimization process.

- Compare geometry and objective function values of an optimized airfoil with the corresponding representative of the new family for arbitrary combinations of the six flow and cascade parameters.
- Compare representatives of the new airfoil family with conventional controlled-diffusion airfoils.

Steps one and two were performed for more than 4000 geometries. In those parts of the range of application where these checks revealed unsatisfying results, the correlations have been corrected. In the third step for about ten combinations of the six flow and cascade parameters, new optimizations have been performed and their results have been compared to the representatives of the new airfoil family. All examples showed almost no changes in airfoil geometry and the decrease in the objective function value was negligible. As a part of the validation of this new approach, four examples for the step four comparisons are presented in the following section.

Comparison to Reference CDA Cascades. For the experimental investigation of the new airfoil family [14] four cascades have been selected, which are typical representatives for rotor and stator sections in the mid and rear part of a compressor [21]. The design parameters together with the diffusion factors are presented in Table 3. For these parameters, four profiles (A–D) have been adopted from the new airfoil family, where the inlet Mach number is decreased from cascade A to D. In order to demonstrate the superior behavior of the new design, four controlled-diffusion airfoils have been selected, which satisfy the same design requirements.

A comparison of the airfoil geometries is presented in Fig. 11. As the inlet Mach number decreases, the new (test) profiles show smaller stagger angles than the controlled-diffusion airfoils. Similar to the earlier example (Fig. 8), the new airfoils show more camber in the front and less camber in the midportion, and the leading edge geometries are thicker compared to the CDA shape.

The corresponding design point Mach number distributions are shown in Fig. 12. All test profiles are characterized by a front-loaded pressure distribution, boundary layer transition shortly before the velocity maximum at about 7–10 percent chord, and smaller deceleration gradients in the midpart of the airfoils. The differences between the new and the CDA design increase from

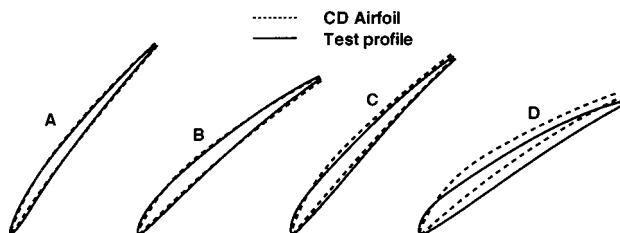


Fig. 11 Geometry of CDA and new airfoils

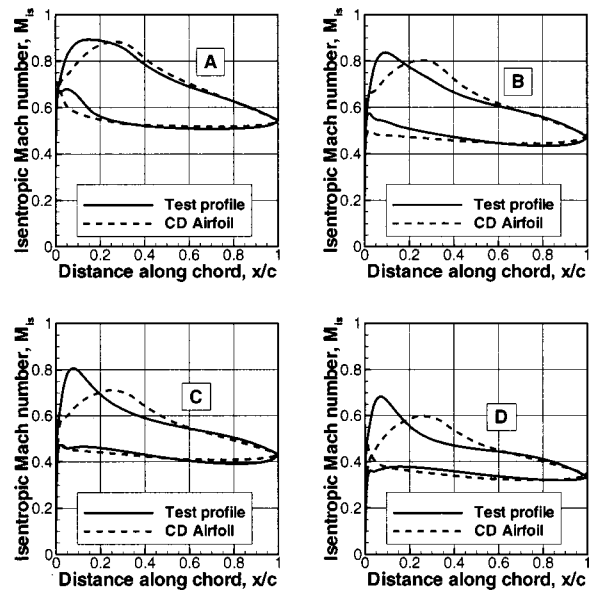


Fig. 12 Design Mach number distributions of CDA and new airfoils

cascade A to D (Fig. 11), which are characterized by decreasing inlet Mach numbers. As controlled diffusion airfoils were initially designed for use in supersonic and high subsonic applications and afterward transferred to use in mid and low subsonic stages, in particular the low subsonic airfoils show significant changes in design. In contrast, cascade A is quite similar for both designs, as a significantly increased front loading based on a thicker leading edge for the test profile would result in a local transonic flow region and lead to higher total pressure losses.

Figure 13 presents the total pressure losses for all four test profiles together with the corresponding controlled-diffusion airfoils. All representatives of the new airfoil family are characterized by increased operating ranges, including higher incidence range to stall. The highest growth can be seen for cascade B, where the stall margin rises from 5 deg for the CDA to 9 deg; all three other airfoils show an increase in stall margin of at least 1.5 deg. All four new profiles likewise show lower total pressure losses over the entire operating ranges.

In order to demonstrate the achievable benefit of this new airfoil family on the compressor efficiency and cost, additional loss curves (dash-dotted lines) are included in all four diagrams of Fig. 13. The five design parameters M_1 , β_1 , $\Delta\beta$, t/c , and $AVDR$ are kept at the same values already presented in Table 3, while the pitch-to-chord ratios are increased. For the test case D the same stall margin as for the controlled diffusion airfoil has been achieved by adopting a pitch-to-chord ratio of 1.05. Even with the maximum pitch-to-chord ratio covered in the range of application, the stall margins for the increased-pitch airfoils of test cases A–C are still higher than for the CD airfoils. Hence, for the presented comparisons (A–C) a s/c value of 1.2 has been adopted. As the stall margin (compared to CDA) does not decrease, the same compressor operation range can be guaranteed based on reduced numbers of blades and vanes. In all four cases a significant reduction in the total pressure losses for the entire operating ranges is visible. At design point conditions the losses are decreased by 20 percent. Based on this example a compressor efficiency rise of 1 percent and more can be expected.

In order to elucidate the reasons for the considerable increase in operating range the Mach number distributions at -5 deg and $+5$ deg incidence for cascade C are compared in Fig. 14. The corresponding incidence flow angles are marked in the total pressure loss diagram in Fig. 13. The importance of the thickened leading edge vicinity is demonstrated by the off-design behavior of test

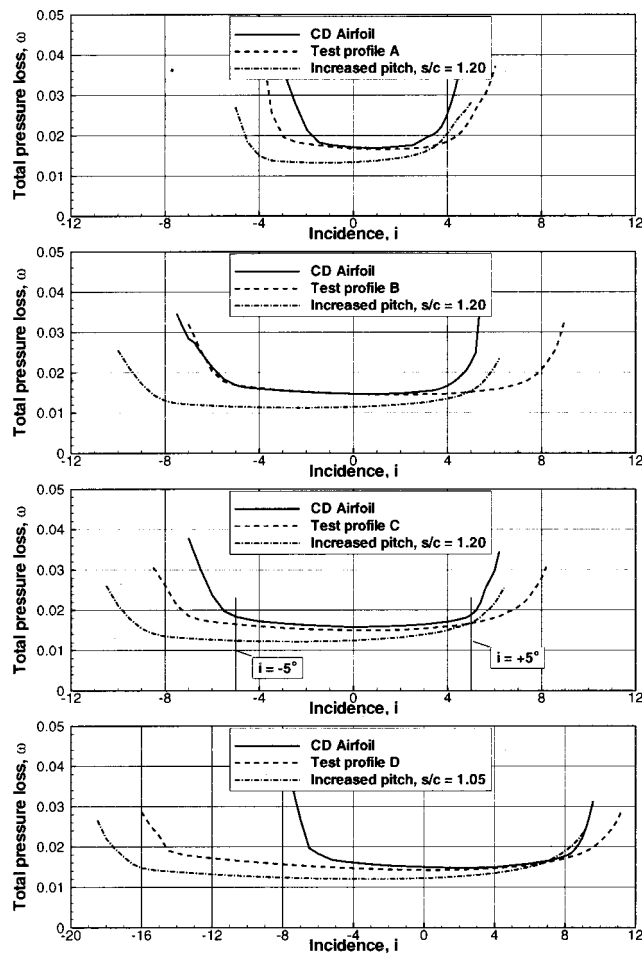


Fig. 13 Total pressure losses of CDA and new airfoils

profile C. While the CDA's peak Mach numbers are in the supersonic range, the new airfoil avoids these peaks at -5° and $+5^\circ$ deg incidence and stays at a moderate Mach number level. This peak reduction leads to a significant boundary layer unloading in the vicinity of the leading edge and finally results in an improvement of the separation behavior. In both diagrams in Fig. 14 downstream of $x/c=50$ percent on the suction side and downstream of $x/c=10$ percent on the pressure side, differences in the Mach number distributions can hardly be seen, so the cause for the increase in operating range has to be related to the change in the front part.

Summarizing, one can find that, compared to the reference airfoils, the new airfoil family is characterized by an increased leading edge thickness and a flattened midpart, a front-loaded Mach

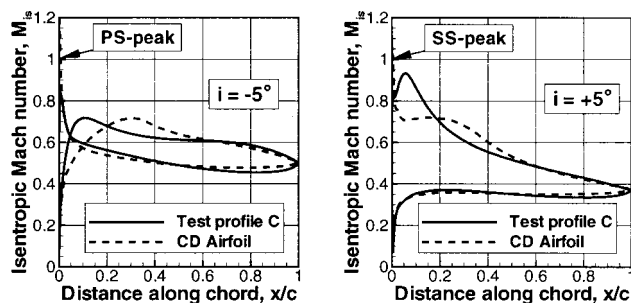


Fig. 14 Off-design Mach number distribution of CDA and new airfoils

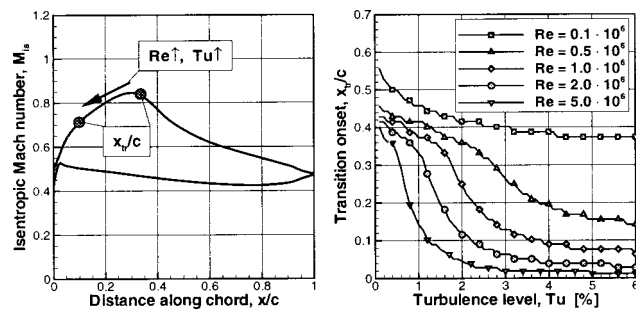


Fig. 15 Influence of Re and Tu on transition onset

number distribution, lower total pressure losses and considerably higher operating ranges including increased stall margin.

Influence of Reynolds Number. Compared to CDA, the new airfoil family is characterized by a front-loaded Mach number distribution. In order to emphasize that the upstream propagation of the boundary layer transition is caused by high Reynolds numbers, a corresponding numerical parameter study is presented in this chapter.

Due to the high mass flow and the resulting large dimensions in a heavy-duty gas turbine compressor, the rotor and stator chord lengths have to be considerably increased compared to aeroengine dimensions. Together with the higher inlet density at design point conditions, the profile Reynolds numbers are significantly higher ($Re=2-4 \times 10^6$). Together with the high turbulence levels in the mid and rear part of a multistage compressor, this leads to an early bypass transition of the blade boundary layer even at favorable pressure gradients [22].

In this context a numerical parameter study based on MISES calculations is presented in the right diagram in Fig. 15. Boundary layer transition is calculated for the suction side Mach number distribution shown on the left side of this figure ($M_1=0.6$). Both increasing Reynolds number and rising turbulence level result in an upstream propagation of the transition location. For low Reynolds numbers and small turbulence levels, the transition is insight a laminar separation bubble. For high Reynolds numbers and high turbulence levels the transition occurs in the bypass mode. The corresponding Mach number distribution is accelerated until $x/c=30$ percent. So, with turbulence levels $Tu \geq 3$ percent and Reynolds numbers $Re \geq 2 \times 10^6$ the onset of transition migrates upstream into the region with an accelerated boundary layer to a relative chord of $x/c=7$ percent. A further increase of the turbulence level does hardly affect this transition location. It is assumed that even unsteady effects like wake passing, described for example in the work of Halstead et al. [23], do not significantly influence this early transition location, because the Reynolds number is high.

An optimal airfoil design has to take into account the change in transition location and mode. Hence, compressor airfoils, which were initially designed for aeroengine flow conditions and then transferred to heavy-duty gas turbines, do not account for these effects and do not represent the optimal solution for the heavy-duty gas turbine compressor design.

To answer the opposite question, whether the new airfoil family would also show superior behavior in flow conditions where the transition onset is located further downstream, the results of a final optimization are presented in Fig. 16. As a basis for this design test profile C was selected. The corresponding design parameters are noted in Table 3. This test profile is used as starting geometry for an optimization carried out at $Re=0.8 \times 10^6$ and $Tu=1$ percent. The results and a comparison of both cascades are presented in Fig. 16. The top diagram shows the two geometries, the representative of the new airfoil family as a dotted line and the low-Reynolds-optimized profile as a solid line. In particular the

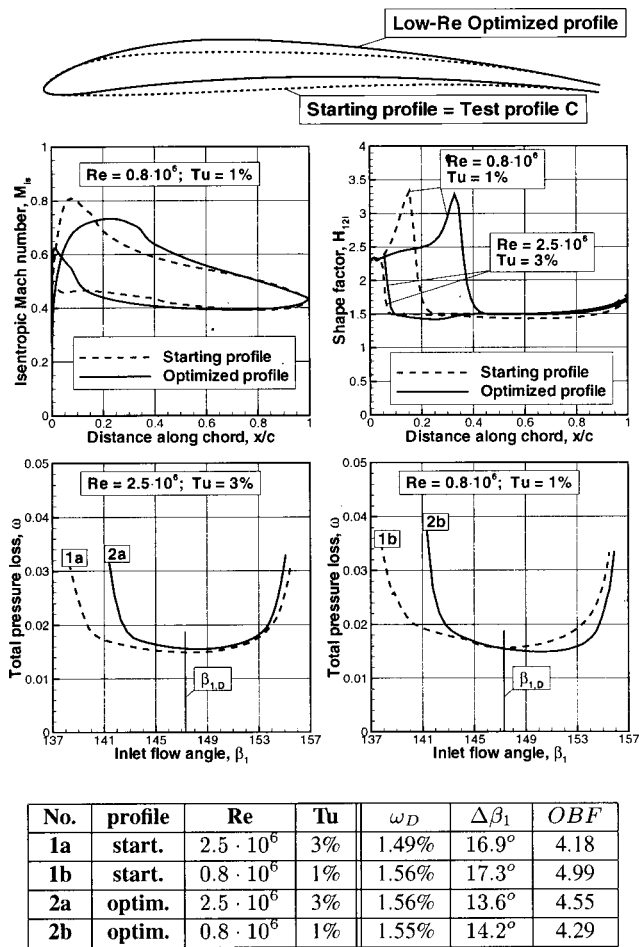


Fig. 16 Influence of Re and Tu on optimized profile geometry

midprofile region is characterized by an increase in camber. For the Mach number distribution at design point conditions (midleft diagram) the front-loaded suction side curve is changed to a “roof-top” or CDA-similar distribution with laminar suction surface flow up to 35 percent of chord. On the pressure side a deceleration in the first 20 percent of chord is visible for the optimized profile. In the rear parts of the suction and the pressure side the Mach number remained almost unaffected by the optimization. As the shape factor distributions for the low-Re numbers (midright diagram) indicate, the optimized airfoil’s transition has migrated further downstream. Lower losses on the suction side due to an extension of the laminar flow region are compensated by higher losses on the pressure side due to slightly increased deceleration in the front portion. Hence, both airfoils possess almost the same design point value: $\omega_D = 1.55$ percent \Leftrightarrow 1.56 percent (compare 2(b) \Leftrightarrow 1(b) in the attached table). The objective function value for the optimized airfoil has dropped from 4.99 to 4.29. In particular, the rise in stall margin is responsible for this improvement. So, for low-Re conditions the optimized, CDA-similar profile shows better design and off-design behavior, which confirms the use of such airfoils for these boundary conditions.

In order to demonstrate that the representative of the new airfoil family still possesses superior performance at high Reynolds numbers, the objective function values for both airfoils have been calculated at $Re = 2.5 \times 10^6$ and $Tu = 3$ percent. The corresponding total pressure losses are presented in the lower left diagram in Fig. 16. The test profile C (curve 1(a)) is characterized by lower losses and a wider operating range, which results in an objective function value of 4.18 compared to 4.55 for the low-Re-optimized airfoil (curve 2(a)).

Hence, for application in a heavy-duty gas turbine compressor with its specific boundary conditions, the new designed airfoil family has proved superior performance for design and off-design conditions. From this final low-Re optimization result, the transfer of this airfoil family to aeroengine application cannot be advised, as the controlled-diffusion airfoils in use until now seem to possess equal or even superior design and off-design behavior.

Conclusions

An important advantage is achieved by an automated design process, in which the blade geometry generation program and the flow solver are coupled to search for an aerodynamically optimized airfoil. Thereby, this process is not restricted to the “state of the art” experience of a design engineer. A further extension of the range of application can easily be achieved by integrating the results of additional optimizations/profile designs into the existing new airfoil family.

The superior performance of the new airfoil family for high Reynolds numbers, which is characterized by an increase in the attainable operating range and a decrease in the total pressure losses, confirms the efficiency of both the automated tool for optimized airfoil design and the formulation of the objective function. As the heavy-duty gas turbine compressor specific high Reynolds numbers lead to an upstream propagation of the boundary layer transition, an optimal velocity distribution has to account for these effects by a suction side maximum position in the front portion of the airfoil. Utilization of the newly developed airfoil family allows a reduction in blade and vane counts in comparison to conventional airfoils. For a given compressor operating range this leads to a further significant increase in efficiency.

As for each of the optimized airfoils the design and the off-design behavior is known, a complete database including the total pressure losses and the exit flow angles for different inlet flow angles, inlet Mach numbers, and AVDR values can easily be developed. Consequently, for the new airfoil family, such an extensive database has been generated in order to replace flow turning and total pressure loss correlations used in two dimensional duct- or throughflow streamline curvature codes. So, in the future, the risks in compressor development are significantly reduced by the knowledge of the exact off-design behavior during the first steps of the design process.

Nomenclature

- a = basis for number of random search points
- AVDR = axial velocity density ratio
- c = profile chord, m
- $C_1 - C_5$ = objective function coefficients
- Cr = curvature
- DF = diffusion factor
- H_{12i} = incompressible shape factor
- i = incidence = $\beta_1 - \beta_{1,D}$, deg
- M = Mach number
- OBF = objective function
- p = pressure, Pa
- $P_1 - P_3$ = spline points on pressure side
- PF = penalty function
- r = radius, m
- Re = Reynolds number = $(w_1 \cdot c) / \nu$
- s = pitch, blade spacing
- $S_1 - S_3$ = spline points on suction side
- t = maximum profile thickness, m
- Tu = turbulence level
- w = relative velocity, m/s
- x = coordinate in chordwise direction, m
- y = coordinate perpendicular to chordwise direction, m
- β = flow angle with respect to cascade front, deg
- $\Delta\beta$ = flow turning = $\beta_1 - \beta_2$, deg
- $\Delta\beta_1$ = incidence range from negative to positive stall, deg
- $\Delta\beta_{St}$ = incidence range from design to positive stall, deg

- δ_1 = boundary layer displacement thickness, m
 δ_2 = boundary layer momentum thickness, m
 λ = profile (metal) angle, deg
 $\Delta\lambda$ = profile wedge angle, deg
 ν = kinematic viscosity, m²/s
 σ = standard deviation
 ω = total pressure loss = $(p_{t1} - p_{t2}) / (p_{t1} - p_1)$

Subscripts

- 1 = inlet plane
2 = outlet plane
80 = inner 80 percent of incidence range
D = design value
LE = leading edge
is = isentropic entity
ref = reference value in objective function
t = total, stagnation value
tr = transition
TE = trailing edge

References

- [1] Johnsen, I., and Bullock, R., 1965, "Aerodynamical Design of Axial-Flow Compressors," NASA SP-36.
- [2] Hobbs, D., and Weingold, H., 1984, "Development of Controlled Diffusion Airfoils for Multistage Compressor Application," ASME J. Eng. Gas Turbines Power, **106**, pp. 271–278.
- [3] Korn, D., 1975, "Numerical Design of Transonic Cascades," ERDA Research and Development Report C00-3077-72.
- [4] Schmidt, E., 1979, "Computation of Supercritical Compressor and Turbine Cascades With a Design Method for Transonic Flows," ASME Paper No. 79-GT-30.
- [5] Stephens, H., 1979, "Application of Supercritical Airfoil Technology to Two-Dimensional Compressor Cascades: Comparison of Theoretical and Experimental Results," AIAA J., **17**, No. 6, pp. 594–600.
- [6] Rechter, H., Steinert, W., and Lehmann, K., 1985, "Comparison of Controlled Diffusion Airfoils With Conventional NACA 65 Airfoils Developed for Stator Blade Application in a Multistage Axial Compressor," ASME J. Eng. Gas Turbines Power, **107**, pp. 494–498.
- [7] Dunker, R., Rechter, H., Starken, H., and Weyer, H. B., 1984, "Redesign and Performance Analysis of a Transonic Axial Compressor Stator and Equivalent Plane Cascades With Subsonic Controlled Diffusion Blades," ASME J. Eng. Gas Turbines Power, **106**, pp. 279–287.
- [8] Sanger, N. L., 1983, "The Use of Optimization Techniques to Design Controlled Diffusion Compressor Blading," ASME J. Eng. Power, **105**, pp. 256–265.
- [9] Sanz, J., 1988, "Automated Design of Controlled Diffusion Blades," ASME J. Turbomach., **110**, pp. 540–544.
- [10] Goel, S., Cofer, J., and Hardev, S., 1996, "Turbine Airfoil Design Optimization," ASME Paper No. 96-GT-158.
- [11] Pierret, S., Van den Braembussche, R., 1997, "Turbomachinery Blade Design Using a Navier–Stokes Solver and Artificial Neural Network," Reprint from 4th National Congress of Theoretical and Applied Mechanics, May 22–23, Leuven, Belgium.
- [12] Lawerenz, M., 1995, "Aerodynamische Optimierung von Strömungsmaschinen unter Verwendung direkter numerischer Optimierungsverfahren," Abschlußbericht TURBOTECH-Verbundvorhaben 1.1.2.13.
- [13] Schwarz, R., and Spiegel, M., 1995, "Direkte Optimierungsverfahren zur Lösung aerodynamischer Problemstellungen bei Turbomaschinen," Abschlußbericht TURBOTECH-Verbundvorhaben 1.1.2.14.
- [14] Küsters, B., Schreiber, H. A., Köller, U., and Mönig, R., 1999, "Development of Advanced Compressor Airfoils for Heavy-Duty Gas Turbines: Part II—Experimental and Theoretical Analysis," ASME J. Turbomach., **122**, this issue, pp. 406–415.
- [15] Becker, B., Schulenberg, T., and Termuehlen, H., 1995, "The 3A-Series Gas Turbines With HBR Combustors," ASME Paper No. 95-GT-458.
- [16] Steinert, W., Eisenberg, B., and Starken, H., 1991, "Design and Testing of a Controlled Diffusion Airfoil Cascade for Industrial Axial Flow Compressor Application," ASME J. Turbomach., **113**, pp. 583–590.
- [17] Giles, M., 1985, "Newton Solution of Steady Two-Dimensional Transonic Flow," GTL Report No. 186, Oct.
- [18] Drela, M., 1986, "Two-Dimensional Transonic Aerodynamic Design and Analysis Using the Euler and Boundary Layer Equations," GTL Report No. 187, Feb.
- [19] Drela, M., 1995, "MISES Implementation of Modified Abu-Ghannam Shaw Transition Criterion," MISES User's Guide, MIT.
- [20] Pieper, S., and Schulte, J., 1995, "Verlustarme Verdichterauslegung (Experiment I und II)," FVV Forschungsbericht 581.
- [21] Schulenberg, T., and Zimmermann, H., 1995, "New Blade Design of Siemens Gas Turbines," POWER-GEN Europe, May 16–18, Amsterdam.
- [22] Mayle, E., 1991, "The Role of Laminar-Turbulent Transition in Gas Turbine Engines," ASME J. Turbomach., **113**, pp. 509–537.
- [23] Halstead, D. E., Wisler, D. C., Okiishi, T. H., Walker, G. J., Hodson, H. P., and Shin, H.-W., 1997, "Boundary Layer Development in Axial Compressors and Turbines: Part 1–4," ASME J. Turbomach., **119**, pp. 114–127, 426–444, 225–237, 128–139.

Development of Advanced Compressor Airfoils for Heavy-Duty Gas Turbines— Part II: Experimental and Theoretical Analysis

Bernhard Küsters¹

Heinz-Adolf Schreiber

German Aerospace Center,
Institute of Propulsion Technology,
D-51170 Köln, Germany

Ulf Köller

Reinhard Mönig

Siemens AG,
Power Generation (KWU),
D-45466 Mülheim a.d. Ruhr, Germany

In Part I of this paper a family of numerically optimized subsonic compressor airfoils for heavy-duty gas turbines, covering a wide range of flow properties, is presented. The objective of the optimization was to create profiles with a wide low loss incidence range. Therefore, design point and off-design performance had to be considered in an objective function. The special flow conditions in large-scale gas turbines have been taken into account by performing the numerical optimization procedure at high Reynolds numbers and high turbulence levels. The objective of Part II is to examine some of the characteristics describing the new airfoils, as well as to prove the reliability of the design process and the flow solver applied. Therefore, some characteristic members of the new airfoil series have been extensively investigated in the cascade wind tunnel of DLR Cologne. Experimental and numerical results show profile Mach number distributions, total pressure losses, flow turning, and static pressure rise for the entire incidence range. The design goal with low losses and especially a wide operating range could be confirmed, as well as a mild stall behavior. Boundary layer development, particularly near stall condition, is discussed using surface flow visualization and the results of boundary layer calculations. An additional experimental study, using liquid crystal coating, provides necessary information on suction surface boundary-layer transition at high Reynolds numbers. Finally, results of Navier–Stokes simulations are presented that enlighten the total pressure loss development and flow turning behavior, especially at high incidence in relation to the results of the design tool. [S0889-504X(00)02602-7]

Introduction

Efficiency improvements of axial flow compressors are directly linked to the aerodynamic quality and the performance characteristic of the blade elements. Also stable operating conditions at off-design depend on boundary layer separation behavior and flow turning characteristics of the cascades. Furthermore, a wide low-loss incidence range of the profiles allows some uncertainty in predicting the design point during the preliminary design without significant penalty in efficiency and enables a large stall margin.

In the past, a variety of numerical blade-to-blade methods have been successfully applied for tailoring the blade profiles. Thereby either direct or inverse methods were applied, both to analyze or define blade contours that satisfy the vector diagrams set by the preliminary throughflow design. Both inverse and direct methods basically have already been used as automated design tools and had been embedded in special numerical optimization algorithms which search, for example, for maximum efficiency at the design point or maximum loading.

Substantial improvements apart from the pure design point optimization, however, can be achieved only by employment of direct solvers, by which off-design performance can be analyzed and considered in the optimization process. Thereby, special aerodynamic features of the cascade, such as flow turning, minimum

loss, or special boundary layer behavior at off-design, can be asked for. This, however, involves considerable time-consuming blade-to-blade calculations and corresponding high computer performance. Using a fast and robust flow solver, the optimization process can nowadays be performed in a reasonable and acceptable time.

In Part I of this paper [1], the development of such an automated design system is described. This tool was then used to tailor a new family of subsonic airfoils suitable for heavy-duty gas turbine compressors. Design and optimization considered the specific boundary conditions of these large compressors, taking into account the effect of the high Reynolds number on boundary layer development and transition. The profile optimization process minimized an objective function that aimed for a low loss level in the entire operating range, a wide incidence range, and a certain stall margin. The blade-to-blade code used in this optimization process was the Q3D Euler solver MISES from Drela and Youngren [2–4] in its direct mode. It is a coupled inviscid/viscous interaction method that employs integral boundary layer equations for boundary layer and wake development. Boundary layer transition is predicted with the modified criterion of Abu-Ghannam/Shaw [5,6].

The objective of the present work was to validate the design process and to check whether the design goals like flow turning, loss level, incidence range, and stall margin were achieved. This involved the validation of the blade-to-blade solver, especially at off-design operating points.

For this reason four typical airfoil sections of the new family

¹Now with Siemens AG.

Contributed by the International Gas Turbine Institute and presented at the 44th International Gas Turbine and Aeroengine Congress and Exhibition, Indianapolis, Indiana, June 7–10, 1999. Manuscript received by the International Gas Turbine Institute February 1999. Paper No. 99-GT-96. Review Chair: D. C. Wisler.

have been tested in a wide range of inlet Mach numbers, inlet flow angles and at different AVDR values. Again, the blade-to-blade solver MISES was used to elucidate the boundary layer behavior and special features of the aerodynamic characteristics. Additionally, a modern Navier–Stokes solver has been applied to one of the cascades to give further information, especially on differences between experiment and MISES calculation.

Further emphasis was placed on a critical assessment of the boundary layer transition model, implemented in the MISES code. Therefore, an additional experiment was conducted to determine the impact of Reynolds number and turbulence level on the transition process. A validation of the transition model was of specific interest because at high Reynolds numbers and high turbulence levels, transition onset moved to the front portion of the blades. This had an essential impact on the optimized blade pressure distribution and the corresponding profile geometry.

Description of the Cascades

Design considerations for the optimized cascades focused on high aerodynamic efficiency and a stable wide operating range. In contrast to aeroengine compressors, an increase of blade loading and a drastic reduction of the number of blade rows is less important for an industrial large gas turbine.

Therefore, the Mach number level, flow turning, and gap-chord ratios of the developed profile family are moderate at the design point. For sample validation of the new profile family, four different cascades have been selected. These cascades are typical candidates for rotor or stator blade sections of the subsonic part of a multistage compressor [7].

After specifying the aerodynamic requirements for each cascade, such as inlet Mach number, inlet flow angle, flow turning, the AVDR, and gap-chord ratio as well as blade thickness, the geometry parameters prescribing the single blade shape are derived using the correlations of the complete profile systematic [8].

The design parameters of the four representative cascades are listed in Table 1, and Fig. 1 shows the corresponding geometry. Due to a moderate aerodynamic loading, with flow turning between 10 and 18 deg and gap/chord ratios from 0.89 to 0.95, the diffusion factors show values between 0.39 to 0.42.

As already described in Part I of this paper, the blades have been designed and optimized at a Reynolds number of 2.5×10^6 , which corresponds to the average Reynolds number of the blade elements in the real large gas turbine compressor [8]. Furthermore, the turbulence level was set to a relatively high value at which laminar-turbulent boundary layer transition on the blade surface occurs mostly in the so-called bypass mode [9]. Under the conditions of high turbulence level and high Reynolds number, transition starts at about 4–8 percent of chord on the blade suction side and 3–4 percent of chord on the pressure side. Transition onset on the suction side is relatively insensitive to the flow acceleration rate.

Table 1 Design parameters of the test cascades

| Cascade | A | B | C | D |
|---------------|--------|--------|--------|--------|
| M_1 | 0.715 | 0.607 | 0.556 | 0.438 |
| β_1 | 149.4° | 142.0° | 147.3° | 137.0° |
| $\Delta\beta$ | 10.3° | 14.7° | 12.8° | 18.0° |
| AVDR | 1.06 | 1.05 | 1.05 | 0.99 |
| s/c | 0.885 | 0.888 | 0.953 | 0.874 |
| DF | 0.393 | 0.393 | 0.407 | 0.422 |
| t/c | 5.0% | 7.0% | 7.4% | 9.3% |

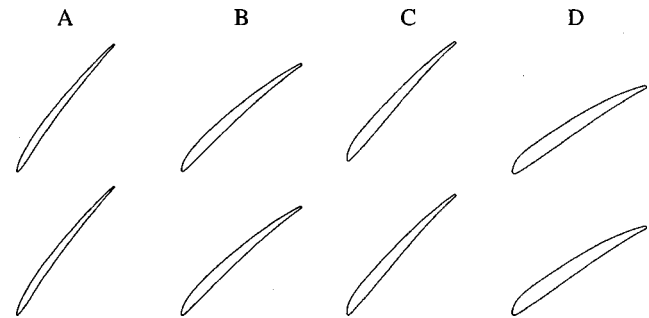


Fig. 1 Test cascades

Consequently, the blade design optimization finished with a forward loaded pressure distribution with a suction surface peak velocity near 8–12 percent of chord. This high peak, where the boundary layer is already turbulent, is immediately followed by a relatively high diffusion rate, which becomes progressively less severe farther downstream. Due to the forward-loaded pressure distribution typical for the whole profile family, all blades have a relatively thick front portion and a low overall camber. Also, the blade stagger angles are considerably lower than stagger angles of corresponding CDA blades with more camber in the rear.

Cascade A with an inlet Mach number of 0.715, a flow turning of 10.3 deg, and 5 percent maximum blade thickness was selected to be a typical candidate for a rotor section in one of the forward compressor stages. Furthermore, due to its relatively high inlet Mach number, it was of interest to validate the blade-to-blade code for supercritical flow conditions which are achieved at high positive and negative incidence angles. To limit surface Mach numbers that exceed sonic velocities, the optimization process flattened the velocity peak of blade A in the front portion. The corresponding design Mach number distribution of this cascade is plotted in Fig. 2, left.

The character of the profile velocity distribution of the cascades B, C, and D (Fig. 2), which are designed for lower inlet Mach

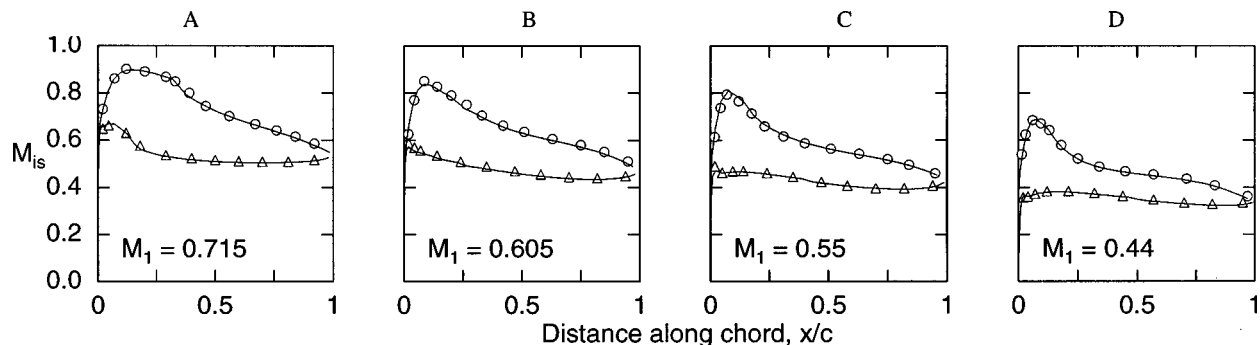


Fig. 2 Experimental and numerical design Mach number distributions of the four test cascades

Table 2 Experimental and MISES data of the four test cascades at design conditions with $Re=0.9-0.7 \times 10^6$

| Cascade | A | | B | | C | | D | |
|-----------|------------|--------|------------|--------|------------|--------|------------|--------|
| | Experiment | MISES | Experiment | MISES | Experiment | MISES | Experiment | MISES |
| M_1 | 0.715 | 0.715 | 0.606 | 0.607 | 0.555 | 0.556 | 0.441 | 0.440 |
| β_1 | 149.5° | 149.5° | 142.0° | 142.0° | 147.3° | 147.3° | 137.0° | 137.0° |
| β_2 | 139.1° | 139.2° | 127.7° | 127.3° | 134.4° | 134.6° | 119.7° | 119.3° |
| AVDR | 1.06 | 1.06 | 1.05 | 1.05 | 1.05 | 1.05 | 1.00 | 0.99 |
| ω | 0.0175 | 0.0161 | 0.0153 | 0.0152 | 0.0164 | 0.0152 | 0.0179 | 0.0155 |

numbers 0.6, 0.55, and 0.44, is more or less identical, although flow turning and profile thickness differ considerably (see Tables 1 and 2). It is worth mentioning that cascade *D*, with a blade thickness of 9.3 percent of chord and an inlet Mach number of 0.44, was optimized for an incidence angle range of 27 degrees. It could serve, for example, as a rotor hub section in one of the rear stages.

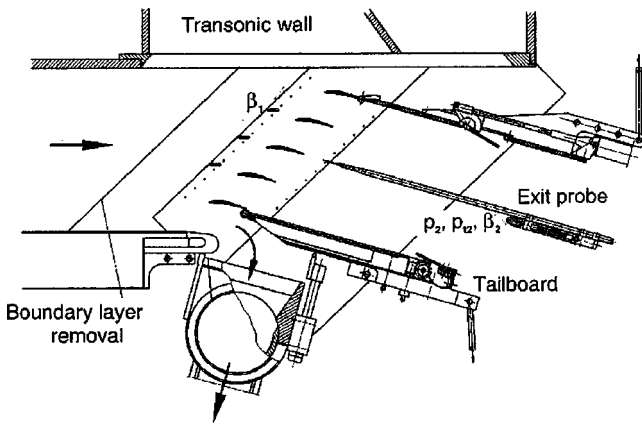


Fig. 3 Cross section of the DLR Transonic Cascade Tunnel



Fig. 4 Photograph of the test section

Table 3 Estimated uncertainties

| | |
|--------------------------------|----------------------|
| Upstream flow angle, β_1 | $\pm 0.2 - 0.4$ deg. |
| Exit flow angle, β_2 | $\pm 0.2 - 0.4$ deg. |
| Loss coefficient, ω | ± 0.0008 |
| AVDR | ± 0.01 |

Test Procedure

The four optimized cascades were extensively tested in the Transonic Cascade Tunnel of the DLR in Cologne. This tunnel is a closed loop, continuously running facility with a variable nozzle, an upper transonic wall, and a variable test section height. The air supply system enables an inlet Mach number range from 0.2 to 1.4 and a Mach number independent variation of the Reynolds number from about 1×10^5 to 3×10^6 . Tunnel sidewall boundary layers ahead of the cascade are removed through protruding slots. Tailboards combined with throttles are used to control inlet and exit boundary conditions and periodicity. Endwall boundary layers and the axial velocity density ratio, AVDR, are controlled using a suction system with suction slots located within the blade pack aft of the minimum pressure region (see Fig. 4).

A cross section and a photograph of the test section are shown in Figs. 3 and 4. For the present tests, 6 blades with 70 mm chord and an aspect ratio of 2.4 are installed. Tests were run with a total pressure of about 1.1 bar and a total temperature of 305 K, giving a Reynolds number of 0.7 to 1.1×10^6 for the investigated Mach number range from about 0.4 to 0.85.

The inlet flow angle is measured with probes at the same gap-wise locations for three consecutive blade channels. Furthermore, three center blades have been instrumented on the suction side to control flow periodicity and allow an additional flow angle determination [10,11]. The test procedure is to vary Mach number at each inlet angle for three different AVDR values. Prior to the tests, each individual test point has been precalculated using the blade-to-blade code MISES V2.4. The theoretical profile Mach number distribution, displayed real time together with the test data, served as a goal for the experimental distribution while adjusting the test conditions. By so doing, measurement accuracy, especially of the inlet flow angle and AVDR could be improved considerably. Table 3 provides some estimated uncertainties for key dependent variables, in which uncertainty is less near the design flow conditions and increases approaching the stalled flow conditions.

Test and Design Conditions

Before starting the entire test program, numerical blade-to-blade calculations have been performed to prove the usability of the experimental results for the assessment of the design. Especially, it was of interest to know whether the design flow turning, pressure ratio, and design incidence range, which have been calculated for the high Reynolds number and turbulence level, could be expected also from the experiments in the cascade wind tunnel.

All calculations for design and optimization were performed at a Reynolds number of 2.5×10^6 and a turbulence level of 3 percent, whereas the wind tunnel tests operated at a Reynolds number of $0.7 - 1.1 \times 10^6$ and a turbulence level between 0.5 and 1.0 percent. For cascade *C*, which has been designed for an inlet Mach number of 0.55 and a flow turning of 12.8 deg, blade performance was calculated in the entire operating range from negative to positive stall at both design and test conditions. Results in Fig. 5 show that the calculated total pressure losses have the same level and that the inlet flow angle range is practically identical. For all in-

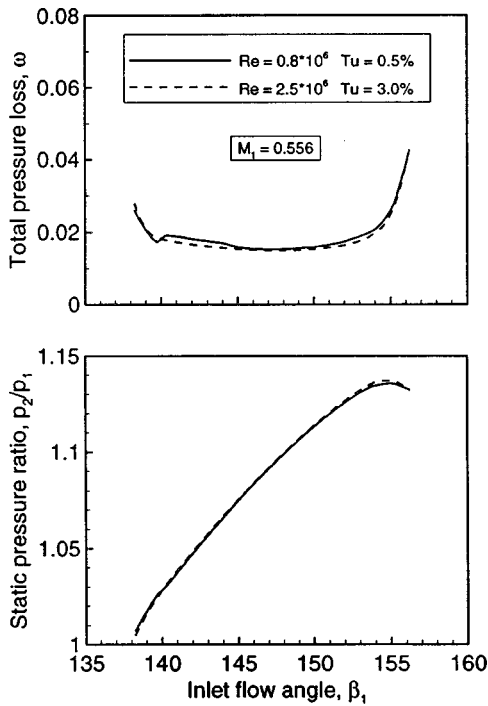


Fig. 5 Predicted performance at different Reynolds numbers, cascade C

cidences and especially at design condition ($\beta_1 = 147.3$ deg), the profile Mach number distributions shown in Fig. 6 are nearly identical.

Also, the static pressure ratio, which directly depends on flow turning and total pressure loss, is identical in the whole operating range. Marginally higher total pressure losses are normal for low Reynolds numbers, because at low Reynolds numbers boundary layers are slightly thicker. Furthermore, at negative incidences the pressure side shows a short laminar separation behind the leading edge, and at positive incidences the suction side has a small laminar bubble between 14–20 percent of chord. Both effects induce a further marginal increase in total pressure loss. Due to the different boundary layer transition behavior at low and high Reynolds numbers, the boundary layer development on the blade front portion is considerably different. However, for the overall blade per-

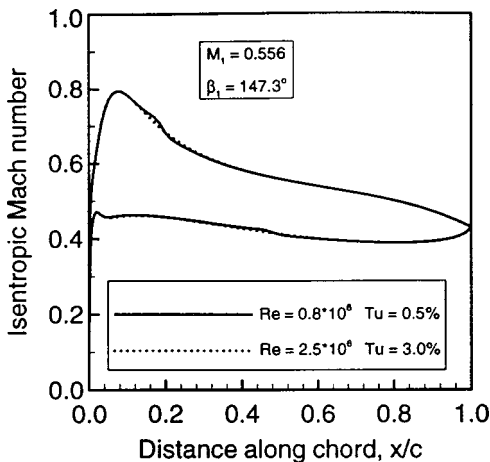


Fig. 6 Isentropic Mach number distribution at different Reynolds numbers, cascade C

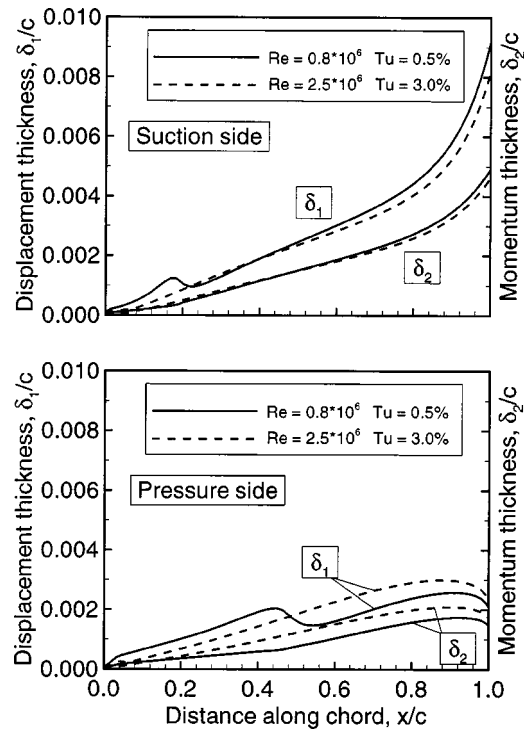


Fig. 7 Boundary layer thickness at different Reynolds numbers, cascade C, $M_1 = 0.556$, $\beta_1 = 147.3$ deg

formance and the boundary layer thickness at the blade trailing edge, this is of minor influence. The corresponding development of the displacement thickness δ_1 , and momentum thickness δ_2 , as well as the boundary layer form factor is shown in Figs. 7 and 8 for design and test conditions.

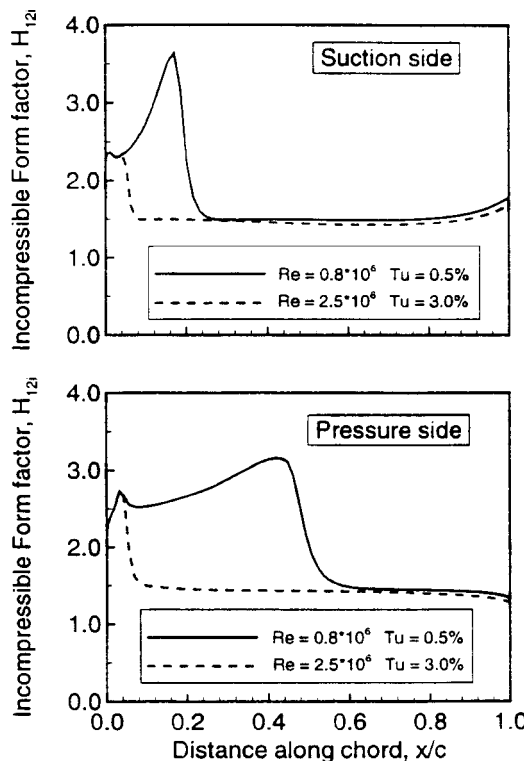


Fig. 8 Boundary layer form factor at different Reynolds numbers, cascade C, $M_1 = 0.556$, $\beta_1 = 147.3$ deg

Due to the forward-loaded pressure distribution, transition on the blade suction side occurs relatively early, either due to bypass transition at 7 percent of chord or in a laminar separation bubble at 18 percent of chord. Therefore, the essential decelerating part of the suction surface is turbulent and boundary layer thickness as well as the form factors achieve nearly identical values at the trailing edge. Furthermore, even the slightly thicker boundary layer on the suction side for the lower Reynolds number, is compensated by a somewhat smaller boundary layer thickness on the pressure side.

Validation of Design

The test program for each individual cascade covered the complete precalculated incidence range and a certain Mach number variation around design.

An excellent agreement between experiment and numerical analysis using MISES was achieved at the design point for all four cascades. The experimental profile Mach number distributions exactly fit the calculations (Fig. 2), and even exit flow angles agree within the experimental accuracy. A comparison of the design point data is given in Table 2 for wind tunnel flow conditions with $Re=0.7-0.9 \times 10^6$ and a turbulence level of $Tu \leq 1$ percent. Differences are observed only for the total pressure loss coefficients, where the experimental data are slightly higher than the numerical ones.

Because off-design performance and stall margin were two of the essential design goals during the optimization process, the experimental determination of the achievable flow angle range was of special interest. In particular, this validation was important because the optimization process provided profiles, which allow working ranges that are roughly 30 percent wider than ‘‘conventional’’ controlled diffusion blades designed for the same task. Such a theoretical comparison to a set of existing CDA profiles, using the four test cascades, is shown in Fig. 11 of the first part of this paper [1]. Happily, the present experiments using the four optimized test cascades confirmed each of the precalculated working ranges. Figure 9 provides the measured total pressure loss versus the incidence angle for cascade A, B, C, and D. For each cascade, the experimental working range $\Delta\beta_1$ is indicated and the corresponding design value is given in brackets. The working range hereby is defined in the conventional manner with $\Delta\beta_1 = \beta_{1max} - \beta_{1min}$, with β_{1min} and β_{1max} as the flow angles where the losses achieve twice of the design point losses ($\omega = 2 \times \omega_D$).

Even cascade D, with a design working range of 27 deg achieved an experimental range of nearly 25 deg. Also the possible flow angle increase until stall onset, $\Delta\beta_{Stall}$ at positive incidence, could be confirmed. Again, β_{1Stall} is achieved, when the losses become twice of the design point losses.

In addition to the experimental losses, Fig. 9 provides a comparison to theoretical losses from MISES with the Reynolds numbers and the turbulence level of the wind tunnel tests.

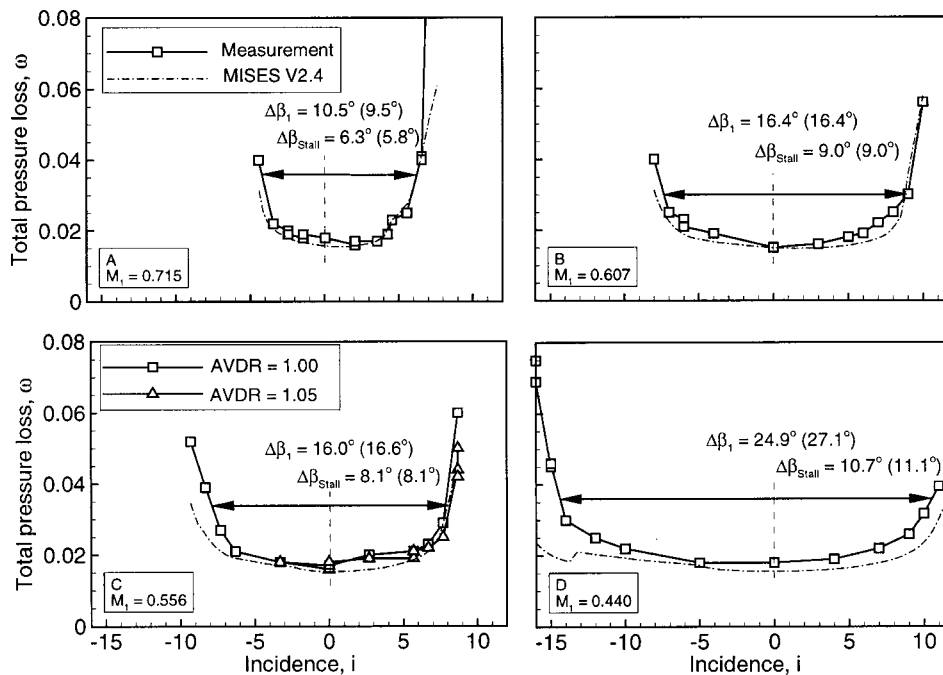


Fig. 9 Loss over incidence at design Mach number, experimental and MISES data, $Re = 0.9-0.7 \times 10^6$, $Tu \leq 1$ percent, experimental and design (in brackets) flow angle range

Table 4 Experimental and MISES data of test cascade D at $Re=0.7 \times 10^6$ and $Tu=1.0$ percent

| Incidence | -16° | | 0° | | +9° | | +11° | |
|-----------|------------|--------|------------|--------|------------|--------|------------|--------|
| | Experiment | MISES | Experiment | MISES | Experiment | MISES | Experiment | MISES |
| M_1 | 0.439 | 0.440 | 0.440 | 0.440 | 0.443 | 0.440 | 0.445 | 0.440 |
| β_1 | 121.0° | 121.0° | 137.0° | 137.0° | 146.0° | 146.0° | 148.0° | 148.0° |
| β_2 | 119.5° | 118.2° | 119.8° | 119.3° | 123.9° | 121.9° | 126.3° | 124.4° |
| AVDR | 0.99 | 0.99 | 1.00 | 0.99 | 1.00 | 0.99 | 0.99 | 0.99 |
| ω | 0.0695 | 0.0238 | 0.0179 | 0.0156 | 0.0262 | 0.0207 | 0.0395 | 0.0303 |

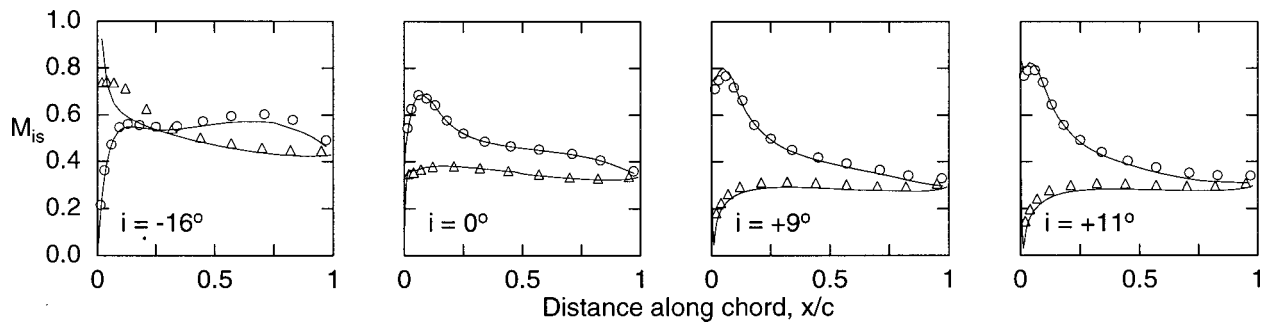


Fig. 10 Experimental and numerical Mach number distributions of test cascade *D*

Furthermore, representative for all cascades, Fig. 11 shows the dependency of the static pressure ratio and the exit flow angle on the inlet flow direction for both experiment and theoretical analysis. Noticeable is a gradual increase of the exit flow angle with positive incidences and a considerable deviation between experimental and theoretical values of up to 2 deg. This deviation, however, becomes less for very high incidences, when a strong boundary layer separation is simulated by the MISES code.

Profile Mach number distributions at off-design are discussed for cascade *D*, which has a wide incidence range of 25 degs, in Fig. 10 and the corresponding boundary conditions of the experiments and the simulation are provided in Table 4. Overall, the agreement to the MISES simulation was observed to be excellent in the entire working range. Only at an extreme negative incidence angle of -16 deg did MISES fail to calculate a severe separation at the pressure side leading edge. That also explains the relatively large discrepancy between measured and predicted losses in Fig. 9(*D*). At positive incidences, the small differences result from thicker experimental suction surface boundary layers and an increasing flow angle deviation. Overall, the off-design Mach number distributions shown in Fig. 10 are also representative for the other test cascades.

Navier–Stokes Analysis

It was of interest to know whether a Navier–Stokes solver would lead to even better agreement between experiment and simulation at positive incidences, where differences to the experimental exit flow angle (Fig. 11, top) were observed. Also, Navier–Stokes results can serve as an additional independent validation for the flow solver MISES applied during the design process.

Using cascade *B*, Navier–Stokes analyses have been performed on a computational domain extending from $-0.5c \leq x_{ax} \leq 1.9c$, where $x_{ax}=0$ corresponds to the blade leading edge. A multiblock grid with one *O*-block around the blade and four *I*-blocks was used with a total of 14,995 nodes. First grid spacing normal to the blade surface was chosen that yielded y^+ values between 2.0 and 3.0 within the boundary layer. The region near the leading edge has greater values, caused by the very thin boundary layer in this region. The DLR TRACE-U code [12,13], which has been developed to investigate steady and unsteady flow phenomena in turbomachines, has been used to perform the calculations. It allows multiblock grids and it is possible to perform two- or three-dimensional, steady or unsteady multistage calculations. Within the code, various numerical methods are implemented and can easily be exchanged. The essential ones used for the present Q3D steady-state calculations are as follows: The two-dimensional Reynolds-averaged Navier–Stokes equations are solved for a compressible ideal gas in conjunction with an eddy viscosity model. Convective fluxes are discretized using a second-order Roe-upwind TVD scheme and the viscous fluxes are discretized

using central differences. The turbulence model used for the calculations is the one-equation approach developed by Spalart and Allmaras [14] and modified by Eulitz [13].

The simulation was performed with laminar/turbulent boundary layers on both suction and pressure sides and start of transition was taken from the MISES calculations. Inlet and exit boundaries

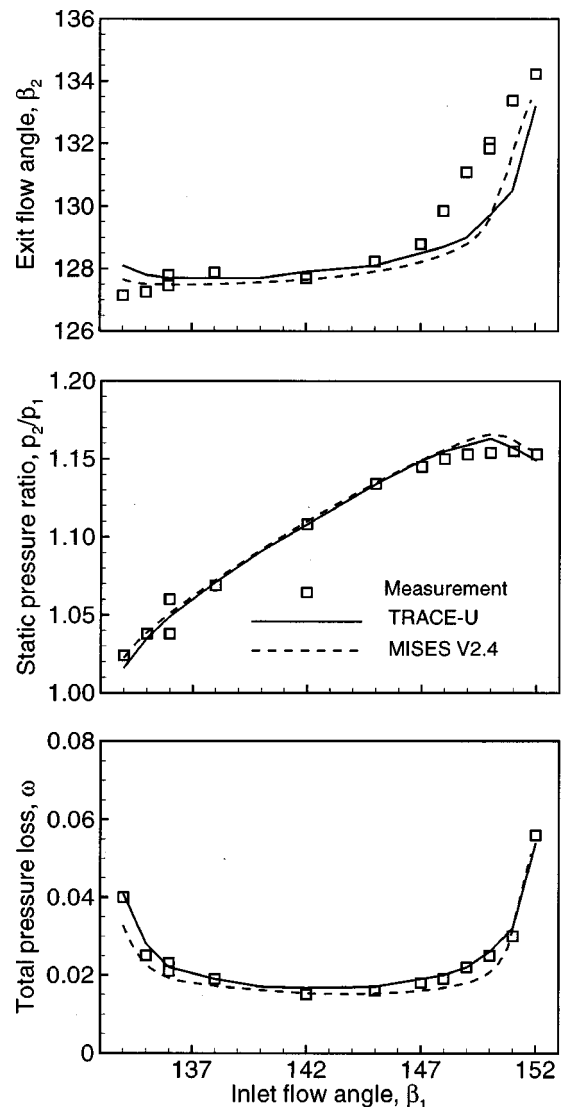


Fig. 11 Experimental performance data compared to MISES and Navier–Stokes calculations, cascade *B*, $M_1=0.607$, $AVDR=1.05$

are treated by nonreflecting boundary conditions according to Giles [15]. To simulate an axial stream tube variation, a linear stream tube thickness distribution from leading edge to trailing edge plane has been assumed. Spatial discretization is combined with a modified four-stage Runge–Kutta time stepping scheme. Implicit residual smoothing and local time stepping are used to accelerate convergence. The code has proven its reliability and high accuracy in cascade simulation even for highly loaded transonic flows [16].

Navier–Stokes calculations have been performed for the entire incidence range at the design Mach number of 0.607. The total pressure loss, static pressure ratio, and exit flow angle in Fig. 11 show good agreement between Navier–Stokes solution and experiment. Only the increasing exit flow angle at positive incidences could not be simulated accurately, although deviation to the experiments is something less in relation to MISES.

Even though the Navier–Stokes solver shows better agreement with all experimental data than MISES does, the differences from the MISES results are too marginal to justify its use in a design optimization process with extensive operating point calculations, due to an enormous increase in CPU time. On the other hand, it is a useful tool for validation after the design process and provides more information of critical flow conditions in addition to experimental investigations.

Boundary Layer Separation Behavior

Besides a wide inlet flow angle range, onset of boundary layer separation inside the blade rows is of specific interest for operation of a multistage compressor. The blade design optimization process, described in Part I of this paper, particularly asked for a wide margin between inlet flow angle at design and near stall ($\Delta\beta_{\text{Stall}}$). The final optimized blade and cascade geometries of the new profile family fortunately showed this wide incidence range

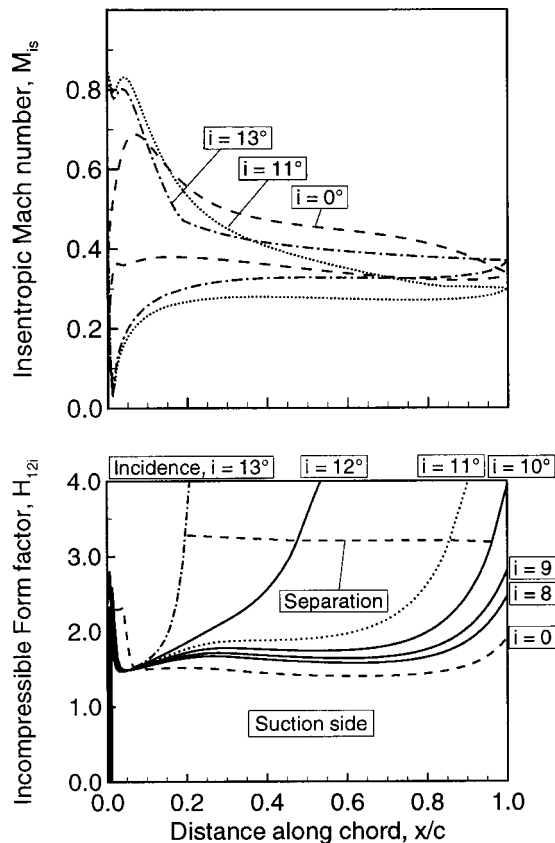


Fig. 12 Numerical separation behavior of cascade *D*, including MISES separation onset

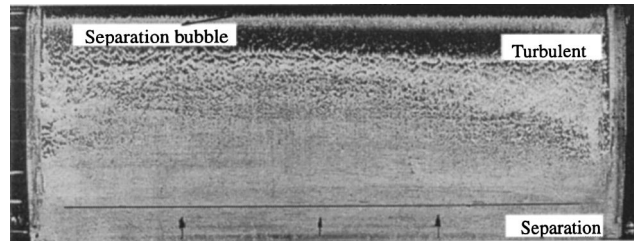


Fig. 13 Oil streak lines on the suction side of cascade *D*, $i = +9$ deg, flow direction from top to bottom

and especially a mild separation behavior. To discuss this behavior, profile Mach number distributions and the development of the suction surface form factor H_{12i} for design and high positive incidence angles are shown in Fig. 12. The distributions are calculated for cascade *D*, which showed a stall margin of about 11 deg. Qualitatively, these results are also typical for the other test cascades. At design ($i = 0$, $\beta_1 = 137$ deg) the form factor remains constant from transition location to about 85 percent of chord. Farther downstream, however, a slight increase of the form factor is calculated, caused by an increase of suction surface curvature and a resulting further deceleration in the rear part. Increasing the incidence angle, the shape of this form factor distribution remains; however, the steep increase of H_{12i} successively moves forward, until H_{12i} exceeds a value of 2.5 to 2.8, that is commonly used as a criterion for separation onset. The horizontal dashed line in the lower part of Fig. 12 indicates separation ($c_f = 0$) calculated with MISES. It corresponds to $H_{12i} = 3.0 + 400/\text{Re}_{22}$, implemented in MISES as the value for a change in boundary layer behavior.

Because the steep rise in H_{12i} is more or less concentrated on the rear part of the profile, boundary layer separation also remains concentrated on this rear blade portion. During a gradual rise in incidence from 8, 9, 10 to 11 deg, the separation line on the profile very slowly moves forward, but remains downstream of 85 percent of chord. Due to this, separation onset is very weak and no remarkable unsteady effects were observed in the experiment.

Surface flow visualization tests confirmed this observation. At an incidence angle of +9 deg (see Fig. 10) only little separation could be seen on the suction side of cascade *D*. The oil streak lines in Fig. 13 additionally visualize a small laminar separation bubble behind the velocity peak near the leading edge. Furthermore, nearly no secondary flow is observed on the blade surface, although blade loading with $i = +9$ deg is relatively high. This underlines the effectiveness of the end-wall boundary layer suction system.

Transition at High Reynolds Number

All calculations, using the modified Abu-Ghannam/Shaw criterion [5] with a high Reynolds number and turbulence level of 3 percent, showed transition within the accelerated front portion of the blade (see also results in Fig. 15, Part I of this paper). Therefore, the new high Reynolds number optimized profiles showed the characteristic front-loaded Mach number distribution. To ensure the design, it is of immense interest whether the transition location is predicted correctly or not. Most available experiments, either from stationary cascades or from real turbomachine blade rows, show that laminar flow is dominant on the accelerated part of the blade surface, even after a wake has passed the blade surface [17]. All these tests, however, have low Reynolds numbers ($\text{Re} \leq 0.8 \times 10^6$). There are not many data on transition location for the specific conditions, existing in large-scale heavy-duty gas turbines, such as high Reynolds numbers and high turbulence levels. One can find high Reynolds number tests for airplanes at low turbulence levels where boundary layers still remain laminar in an accelerated flow. There is a lack of data especially for favorable

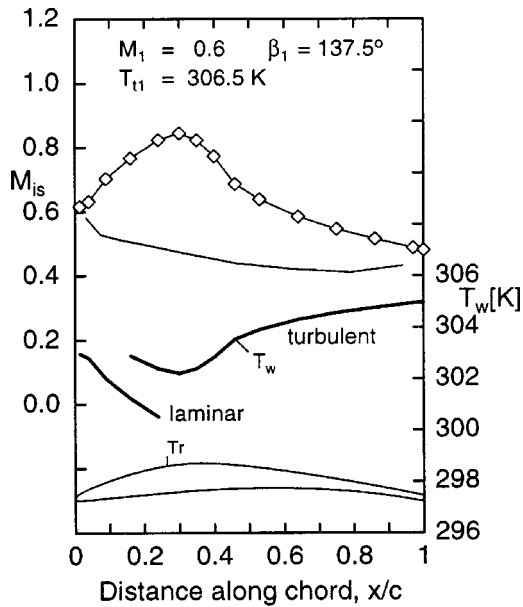


Fig. 14 Calculated adiabatic wall temperature on suction side and corresponding isentropic Mach number distribution

pressure gradients, high Reynolds numbers, and higher turbulence levels, so an additional experiment has been performed to ensure the existence of early transition onset. A test cascade, shown in Fig. 14, was chosen, with an inlet Mach number of 0.6 and a suction side acceleration up to 35 percent of chord. Tests were run with Reynolds numbers from 0.7 to 2.7×10^6 and turbulence levels from about 0.7 to 4 percent. Liquid crystal coatings were used to detect transition by visualizing the difference in adiabatic wall temperature between laminar and turbulent flow which is in the order of 1–2 K for this experiment. A more detailed description of this technique is given by Steinert and Starcken [18].

In Fig. 14 the adiabatic wall temperatures of the laminar and turbulent boundary layers are shown. The differences in temperature of the laminar and turbulent boundary layer is quite small (1–2 K), which made it necessary to have a very sensitive mixture of liquid crystals.

At usual wind tunnel test conditions without a turbulence screen and a low Reynolds number of about 0.8×10^6 , suction surface flow along the front portion is laminar and a strong laminar separation bubble develops with transition near 40 percent of chord. Increasing the Reynolds number to 2.0×10^6 , laminar flow in the front remains. Although the laminar separation bubble becomes less intensive, transition still occurs inside of the bubble (Fig. 15, left).

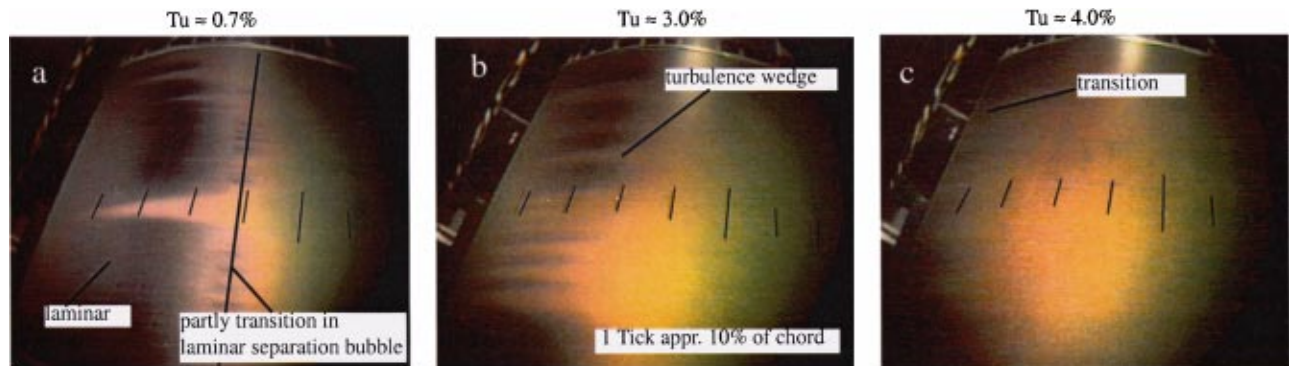


Fig. 15 Suction side transition visualized by liquid crystals, influence of turbulence level at $Re=2 \times 10^6$

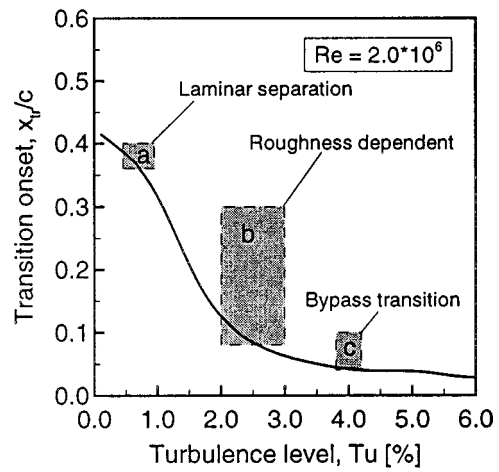


Fig. 16 Experimental (shaded area) and calculated (solid line) suction side transition onset for the profile shown in Fig. 14

Increasing the turbulence level to a value of about 3 percent, the separation bubble disappears and a line of fully turbulent boundary layer moves forward to about 30 percent. When raising the turbulence level at this high Reynolds number, the sensitivity of the boundary layer to surface roughness increases considerably [19,20], as can be seen in the center of Fig. 15. More turbulence wedges become visible downstream of distinct roughness particles.

At about 4 percent turbulence intensity, obviously the bypass mechanism becomes dominant, and transition moves forward and is observed upstream of 10 percent of chord along the entire blade (Fig. 15, right).

A comparison of the visualized transition location to the predicted onset using the criterion implemented in MISES [5] is shown in Fig. 16. Overall, the forward movement of transition onset with a rising turbulence level is, at least qualitatively, well predicted. Some uncertainty remains between $Tu=2-4$ percent where surface roughness seems to have an additional influence.

Conclusions

A series of new compressor airfoils has been developed for high Reynolds number subsonic axial flow compressor stages in heavy-duty gas turbines by making use of a modern optimization technique. The design objective was a wide low-loss operating range and a specific stall margin. The new profiles, which have been optimized for high Reynolds numbers, showed relatively thick leading edges and a front loaded pressure distribution. The present experimental and theoretical analysis has demonstrated

the ability of the design tool and the superior aerodynamic performance of the profiles developed. Besides a practically exact verification of the precalculated design point conditions, the design flow angle range and stall margin could be confirmed. To ensure the design philosophy, which is based on early boundary layer transition on the blade surface, an additional basic experiment was performed that enlightened the effect of the turbulence level at high Reynolds numbers and favorable pressure gradient on transition onset. The experimental results at least qualitatively confirmed the transition model used.

Additional analyses of the complete operating range from negative to positive stall using a sophisticated Navier–Stokes flow solver did show somewhat better agreement with the experiment, but an essential advantage in relation to the inviscid/viscous interaction method used for this subsonic cascade flow could not be proved. The designers, however, are curious to know whether a complex method that simulates the real unsteady flow effects in a turbomachinery environment could alter the design profile pressure distribution, which has been optimized under steady flow conditions.

Nomenclature

- AVDR = axial velocity density ratio = $(\rho_2 w_2 \sin \beta_2) / (\rho_1 w_1 \sin \beta_1)$
 DF = diffusion factor = $1 - w_2 / w_1 + (w_2 / w_1 \cos \beta_2 - \cos \beta_1) s / 2c$
 H_{12i} = incompressible boundary layer form factor = $\delta_{1i} / \delta_{2i}$
 M = Mach number
 Re = Reynolds number = $w_1 c / \nu_1$
 T = temperature
 Tu = turbulence level
 c = profile chord length
 i = incidence angle = $\beta_1 - \beta_{1\text{Design}}$
 p = pressure
 s = blade spacing, pitch
 t = maximum profile thickness
 w = velocity
 x = coordinate in chordwise direction
 x_{ax} = coordinate in axial direction
 $\Delta\beta$ = flow turning = $\beta_1 - \beta_2$
 $\Delta\beta_1$ = incidence range from negative to positive stall
 $\Delta\beta_{\text{stall}}$ = incidence range from design to positive stall
 β = flow angle with respect to cascade front
 δ_1 = boundary layer displacement thickness
 δ_2 = boundary layer momentum thickness
 ν = kinematic viscosity
 ρ = density
 ω = total pressure loss coefficient = $(p_{t1} - p_{t2}) / (p_{t1} - p_1)$

Subscripts

- 1 = inlet plane
 2 = exit plane
 is = isentropic entity
 t = total, stagnation value
 w = wall value

References

- [1] Köller, U., Mönig, R., Küsters, B., and Schreiber, H. A., 2000, "Development of Advanced Compressor Airfoils for Heavy-Duty Gas Turbines—Part I: Design and Optimization," ASME J. Turbomach., **122**, this issue, pp. 397–405.
- [2] Drela, M., and Youngren, H., 1991, "Viscous/Inviscid Method for Preliminary Design of Transonic Cascades," AIAA Paper No. 91-2364.
- [3] Youngren, H., 1991, "Analysis and Design of Transonic Cascades With Splitter Vanes," GTL Report No. 203, Mar., Cambridge, MA.
- [4] Drela, M., and Youngren, H., 1996, "A User's Guide to MISES 2.4," MIT Computational Aerospace Science Laboratory.
- [5] Drela, M., 1995, "Implementation of Modified Abu-Ghannam Shaw Transition Criterion," MISES User's Guide, MIT, Cambridge, MA.
- [6] Abu-Ghannam, B. J., and Shaw, R., 1980, "Natural transition of boundary layers—The effects of turbulence, pressure gradient and flow history," Journal of Mechanical Engineering Science, **22**, No. 5, pp. 213–228.
- [7] Schulenberg, Th., Zimmermann, H., 1995, "New Blade Design of Siemens

- Gas Turbines," presented at POWER-GEN Europe, May 16–18, Amsterdam.
- [8] Köller, U., 1999, "Entwicklung einer fortschrittlichen Profilsystematik für stationäre Gasturbinenverdichter," Dissertation, Ruhr Universität Bochum, Germany.
 - [9] Mayle, E., 1991, "The Role of Laminar–Turbulent Transition in Gas Turbine Engines," ASME J. Turbomach., **113**, pp. 509–537.
 - [10] Schreiber, H. A., Starke, H., and Steinert, W., 1993, "Transonic and Supersonic Cascades," AGARDograph "Advanced Methods for Cascade Testing," Ch. Hirsch, ed., AGARD AG 328, pp. 35–59.
 - [11] Steinert, W., Fuchs, R., and Starke, H., 1992, "Inlet Flow Angle Determination of Transonic Compressor Cascades," ASME J. Turbomach., **114**, No. 3, pp. 487–493.
 - [12] Eulitz, F., Engel, K., Pokorny, S., 1996, "Numerical Investigation of Inviscid and Viscous Interaction in a Transonic Compressor," *Loss Mechanisms and Unsteady Flows in Turbomachines*, AGARD-CP-571, Paper No. 38.
 - [13] Eulitz, F., Engel, K., Gebing, H., 1996, "Application of a one-equation eddy-viscosity model to unsteady turbomachinery flow," Engineering Turbulence Modeling and Experiments 3, W. Rodi and G. Bergeles, eds., Elsevier Science B.V. Amsterdam, pp. 741–751.
 - [14] Spalart, P. R., and Allmaras, S. R., 1992, "A One-Equation Turbulence Model for Aerodynamic Flows," Paper No. AIAA-92-0439.
 - [15] Giles M. B., 1990, "UNSFLO: A Numerical Method for the Calculation of the Unsteady Flow in Turbomachinery," GTL Rept. 205, Gas Turbine Laboratory, MIT, Cambridge, MA.
 - [16] Küsters, B., and Schreiber, H. A., 1998, "Compressor Cascade Flow With Strong Shock-Wave/Boundary-Layer Interaction," AIAA J., **36**, No. 11, pp. 2072–2078.
 - [17] Halstead, D. E., Wisler, D. C., Okiishi, T. H., Walker, G. J., Hodson, H. P., and Shin, H. W., 1997, "Boundary Layer Development in Axial Compressors and Turbines, Part 1–4," ASME J. Turbomach., **119**, pp. 114–127; 426–444; 225–237; 128–139.
 - [18] Steinert, W., and Starke, H., 1996, "Off-Design Transition and Separation Behavior of a CDA Cascade," ASME J. Turbomach., **118**, pp. 204–210.
 - [19] Koch, C. C., and Smith, L. H., 1976, "Loss Sources and Magnitudes in Axial-Flow Compressors," ASME J. Eng. Gas Turbines Power, **98**, pp. 411–424.
 - [20] Schäffler, A., 1980, "Experimental and Analytical Investigation of the Effects of Reynolds Number and Blade Surface Roughness on Multistage Axial Flow Compressors," ASME J. Eng. Power, **102**, pp. 5–12.

Discussion: "Development of Advanced Compressor Airfoils for Heavy-Duty Gas Turbines—Part II: Experimental and Theoretical Analysis" [ASME J. Turbomach., **122**, No. 3, pp. 406–414 (2000)]¹

N. A. Cumpsty

Whittle Laboratory, Cambridge University, Madingley Road, Cambridge, CB3 0DY, United Kingdom

My first aim in writing this discussion is to compliment the authors on two excellent papers. I found the results most interesting and the description and approach were a pleasure to read. The experimental confirmation was as near perfect as one has reason to hope for; as well as complimenting the authors my remarks also draw attention to the quality of the MISES code.

I have to admit that I had been skeptical of the benefits of automated optimization procedures. The results shown here, however, have arrived at a philosophy for optimum aerodynamic pressure distribution around the blades for very high Reynolds number, high free-stream turbulence, and modest inlet Mach number, which I would not have thought of. Because the explanation for the desirable features of the new blades is so clear, the successful solution seems in retrospect almost obvious; it clearly was not obvious and the authors are to be congratulated on their method

¹Küsters, Bernhard, 2000, "Development of Advanced Compressor Airfoils for Heavy-Duty Gas Turbines—Part II: Experimental and Theoretical Analysis," ASME Journal of Turbomachinery, Vol. 122, No. 3, pp. 406–414.

and their presentation. I am sure that this work will influence the blade profile shapes used in the future throughout the industry.

Figure 15 in the second paper, showing the surface flow visualization, is less clear than the pictures shown at the presentation in Indianapolis, which is a pity. What struck me at the conference is transition behavior which I had not seen before. As the turbulence level is raised at constant Reynolds number, the transition moves forward, but there is an intermediate range, around 3 percent free-stream turbulence, where the boundary layer turbulence starts near the leading edge as isolated wedges, presumably originating with small excrescences on the surface. In other words, the excrescences alone are not able to produce turbulence in the boundary layer because the local boundary layer Reynolds numbers is too low, but the interaction of free-stream turbulence of sufficient strength with the shear layer disturbance from these excrescences is able to initiate turbulence in the boundary layer.

Would the authors care to explain why their experiments were carried out at Reynolds numbers of about 10^6 and turbulence of about 1 percent, whereas the designs were at much higher values of both parameters? Surely the thrust of the design was that a different transition behavior is expected when the Reynolds number is higher than is common in aircraft engines and high free-stream turbulence is allowed for. (There is no reason to expect the turbulence levels to be significantly different for large land-based engines or aircraft engines.) If transition is going to occur in the region of flow acceleration on the suction surface, there is no benefit in having the peak suction well back on the chord. The optimum shape for the blades should therefore be different for the conditions of the design and the conditions of the tests. Given that the tests were carried out at Reynolds numbers much lower than design, in the range more typical of aircraft engines, and with relatively low free-stream turbulence, what does the agreement of measurements with calculations at high Reynolds number and turbulence intensity tell us? Does it say that at the comparatively low inlet Mach numbers used for these blades the exact nature of the blade shape and pressure distribution is not very important? Going back to NASA SP-36, Fig. 130 shows how loss is relatively insensitive to blade profile shape for inlet Mach numbers below about 0.8.

Closure to “Discussion of ‘Development of Advanced Compressor Airfoils for Heavy-Duty Gas Turbines—Part II: Experimental and Theoretical Analysis’” [ASME J. Turbomach., 122, No. 3, pp. 406–414 (2000)]

We would like to thank Professor Cumpsty for the encouraging and interesting comments on our contribution. During the course of the work we also have been pleased to see that by applying the automated design tool, the blade profiles and the blade pressure distribution followed the prescribed boundary conditions and the constraints that have been formulated in the objective function. Among other things, it became clear how the blade pressure dis-

tribution on the suction side reacts on boundary layer transition location and that early transition encourages a forward movement of the suction side maximum velocity.

He clearly recognized from our visualization experiment, which is presented in the second part of the paper, that boundary layer transition onset likewise depends on the free-stream turbulence level and surface roughness. This phenomenon has not been studied in detail so far, but we are aware that both the disturbances downstream of single roughness particles on the shear layer and the disturbances due to free-stream turbulence seem to interact in a complex mechanism. The clarification of this phenomenon, however, has not been the objective of the present paper. At this time, first of all, we wanted to supply evidence on upstream propagation of transition onset into the accelerated front portion of the blade with increasing free-stream turbulence *and* increasing Reynolds number. Further results and information on this Reynolds number and turbulence influence are discussed in an additional paper [1].

The extensive experiments to validate the new profile design and especially the MISES code employed were carried out at Reynolds numbers around 0.8×10^6 for two reasons: First, to limit energy consumption and blade loading, the total pressure was kept around 1.1 bar; second, short blade chord with an acceptable blade aspect ratio of 2.4 helped to limit endwall and secondary flow effects. Furthermore, no turbulence grids have been installed upstream of the test section, to ensure an undisturbed flow field with homogeneous inlet flow that allows highest measurement accuracy and periodicity.

The cascade performance results presented in the paper, from both experiment and simulation, show good agreement, although the tests had been performed at low Reynolds numbers and a low turbulence level and the design calculations were carried out at turbomachinery conditions when Reynolds number and turbulence level are high. The good agreement between measured low-Reynolds-number data and the calculated loss and flow turning values for higher Reynolds numbers and free-stream turbulence levels is based on the low shift in suction side transition location for these specific front-loaded profiles. While the calculated values show the suction side transition in the first 10 percent of chord, under the test conditions the velocity distributions of the airfoils encourage transition to occur a short distance after the suction side maximum, which is close to 10 percent of the chord length. Hence, in both cases, the suction side boundary layer, especially in the region of strong adverse pressure gradients, behaves similarly. This coincidence is responsible for the good accordance between test and calculation.

The answer to the last question is no. If one really looks in detail, it has been shown over the years that for subsonic Mach numbers up to 0.7 or 0.8, the total pressure loss level in the vicinity of the design point is not essentially dependent on the blade profile shape; presumably the data are compared for the same velocity triangles and cascade solidities. But for higher aerodynamic blade loading, and especially at off-design conditions, large differences are observed because the boundary layer behavior and resulting losses really depend on the blade and cascade geometry. Not solely optimizing at design point conditions, but reaching excellent off-design performance with large stall margin, is the advantage of the new design approach.

References

- [1] Schreiber, H. A., Steinert, W., and Küsters, B., 2000, “Effects of Reynolds Number and Free-Stream Turbulence on Boundary Layer Transition in a Compressor Cascade,” ASME Paper No. 2000-GT-263.

The Influence of Technical Surface Roughness Caused by Precision Forging on the Flow Around a Highly Loaded Compressor Cascade

Robert Leipold
Matthias Boese
Leonhard Fottner

Institut für Strahltriebwerke,
Universität der Bundeswehr München,
D-85577 Neubiberg, Germany

A highly loaded compressor cascade, which features a chord length ten times larger than in real turbomachinery, is used to perform an investigation of the influence of technical surface roughness. The surface structure of a precision forged blade was engraved in two 0.3-mm-thick sheets of copper with the above-mentioned enlarging factor (Leipold and Fottner, 1996). To avoid additional effects due to thickening of the blade contour, the sheets of copper are applied as inlays to the pressure and suction side. At the high-speed cascade wind tunnel, the profile pressure distribution and the total pressure distribution at the exit measurement plane were measured for the rough and the smooth blade for a variation of inlet flow angle and inlet Reynolds number. For some interesting flow conditions, the boundary layer development was investigated with laser-two-focus anemometry and one-dimensional hot-wire anemometry. At low Reynolds numbers and small inlet angles, a separation bubble is only slightly reduced due to surface roughness. The positive effect of a reduced separation bubble is overcompensated by a negative influence of surface roughness on the turbulent boundary layer downstream of the separation bubble. At high Reynolds numbers, the flow over the rough blade shows a turbulent separation leading to high total pressure loss coefficients. The laser-two-focus measurements indicate a velocity deficit close to the trailing edge, even at flow conditions where positive effects due to a reduction of the suction side separation have been expected. The turbulence intensity is reduced close downstream of the separation bubble but increased further downstream due to surface roughness. Thus the rear part of the blade but not the front part reacts sensitively on surface roughness. [S0889-504X(00)01302-7]

Introduction

The demand for increased cycle efficiencies leads to increased turbine inlet temperatures and to high pressure ratios in modern turbomachines. This trend to high pressures in the high pressure compressor requires very smooth blade surfaces to keep the profile boundary layer in the hydraulically smooth region. Thus, not only in terms of turbomachine performance but also in terms of cost reduction for the manufacturing process, surface roughness is a very interesting field to investigate.

The influence of surface roughness has been of interest for researchers for almost 100 years. One of the first and best-known investigations is that of Nikuradse [1], who did intensive research on pipe flows with sand grains of different size applied to the pipe walls. His measurements led to the so-called Nikuradse diagram, where the flow can be divided into three regions. The first region concerns the whole laminar region and a part of the turbulent region. It is marked by the fact that surface roughness has no influence on the flow. The second region shows an increase of the pressure drop coefficient when raising the Reynolds number. In the third region the pressure drop coefficient is independent of the Reynolds number. Nikuradse interpreted these regions with the relation of surface roughness height to the thickness of the laminar sublayer. In the first region the surface roughness is completely covered by the laminar sublayer, thus no influence of surface roughness can be found. In the second region the decrease of the

laminar sublayer thickness lets some roughness elements protrude through the sublayer, leading to an increase of the pressure drop coefficient. For the third region, the complete surface roughness protrudes through the sublayer, leading to no further increase of the pressure drop coefficient.

The influence of lateral surface roughness parameters was found to be important by Schlichting [2], who varied the density of roughness elements like hemispheres, cones, and rectangular dice of a plate flow. When increasing the density of roughness elements up to a critical value, the drag coefficient increased. A further increase of roughness density leads to a decrease in drag coefficient.

Even in turbomachines, the influence of surface roughness is subject of various investigations. Several investigations concern the influence of surface roughness on the performance of turbine or compressor rigs. An extensive investigation about the change of performance of turbine rigs is found in Bammert and Sandstedt [3–5]. They observed a performance degradation and a shift of the characteristic to smaller mass flow coefficients for the investigated turbine rigs that have been covered with sand grains of different sizes. Even for compressor rigs [6,7] an increased performance degradation was observed for an increased size of sand grains covering the compressor blades. A shift to smaller specific volumes is observed when increasing the size of adhered sand grains too. However, for all of these investigations the blades undergo a thickening of the profile contour when the sand grain is adhered to the blades. This effect has not been considered for the investigations described here. Suder et al. [8] took this effect into account and measured the characteristics of a transonic rotor where the blades have been covered with a rough and a smooth paint. The

Contributed by the International Gas Turbine Institute and presented at the 44th International Gas Turbine and Aeroengine Congress and Exhibition, Indianapolis, Indiana, June 7–10, 1999. Manuscript received by the International Gas Turbine Institute February 1999. Paper No. 99-GT-366. Review Chair: D. C. Wisler.

characteristics indicate that in the subsonic region the thickening of the blades is not negligible due to a shock system in the blade passage. When covering only parts of the blade, the front part of the suction and pressure side is found to react sensibly on applying surface roughness or thickness.

An investigation of boundary layer development along a rough turbine blade at a Reynolds number of 5.6×10^5 and a Mach number of 0.14 is given by Bammert and Sandstede [9]. The measurements inside the boundary layer have been performed with a small pitot tube. The blade is covered with sand grains of different size, causing the laminar to turbulent transition to move upstream when increasing the sand grain size. On the pressure surface the location of transition is almost not affected by surface roughness. But the laminar to turbulent transition is steeper for the rough blades than for the smooth ones. The boundary layer development along various compressor cascades [10] indicates only a small influence of the adhered sand grains on the laminar to turbulent transition. But the impulse deficit thickness, even of the laminar boundary layer, is increased due to surface roughness. For large sand grains covering the profile surface, a turbulent separation is detected on the suction side. A study of the performance of a compressor cascade covered with sand grains over varying lengths of surface is shown by Saxena et al. [11]. They found that a separation bubble on the suction side is likely to disappear due to surface roughness.

In spite of the fact that there are several investigations on the influence of surface roughness on flow fields, most of the investigations have been performed on complete rig setups or on cascades covered with sand grain. Thus, there is a need to investigate the influence of surface roughness caused by modern manufacturing methods. This is met by the present investigation.

Experimental Setup

High-Speed Cascade Wind Tunnel. The experiments were carried out in the high speed cascade wind tunnel (Fig. 1) of the "Universität der Bundeswehr München." This facility operates continuously in a large pressurized tank. Mach number and Reynolds number can be varied independently by setting the compressor delivery pressure and the pressure level inside the tank while the total temperature is kept constant. The turbulence intensity in the test section can be varied by using different turbulence generators in front of the nozzle. The following data were used in order to monitor the flow conditions of the cascade mainstream flow [12]: the total temperature in the settling chamber, the static pressure in the tank (downstream conditions), the static pressure, and the total pressure of the main stream flow upstream of the cascade.

Compressor Cascade. To investigate the influence of surface roughness on a flow around a compressor cascade, the chord length should be as large as possible in order to maximize the

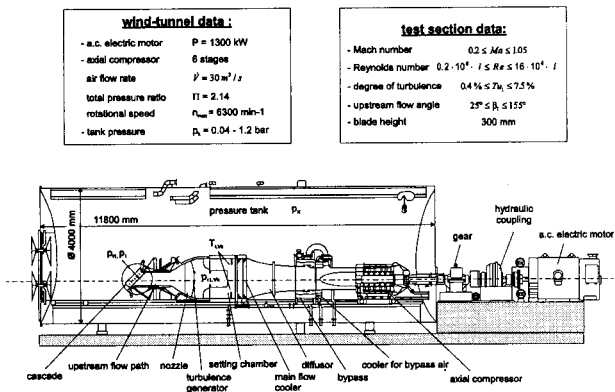
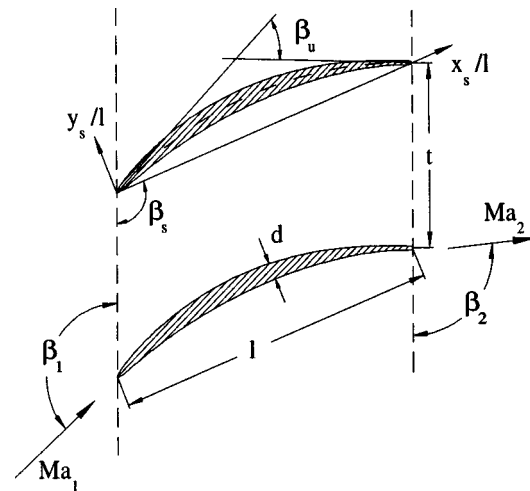


Fig. 1 High-speed cascade wind tunnel



| design conditions: NACA 65 K48, l=180mm | | | |
|---|----------|-----------|----------|
| t/l | = 0.55 | Ma_1 | = 0.67 |
| d_{max}/l | = 0.055 | Re_1 | = 450000 |
| β_u | = 48° | β_1 | = 132° |
| β_s | = 112.5° | β_2 | = 96° |

Fig. 2 NACA 65 K48 cascade

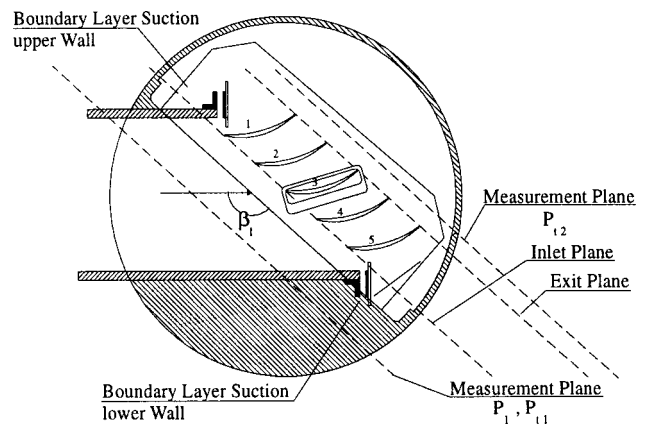


Fig. 3 NACA 65 K48 cascade mounted in test section

spatial resolution of the flow phenomena. On the other hand, the cascade should offer a large two-dimensional flow region at mid-span. As a compromise the cascade chosen consists of five blades featuring a chord length of 180 mm. The profile is a 48 deg circle bow with a superimposed NACA 65 thickness distribution. The main geometric parameters and design flow conditions are shown in Fig. 2. The cascade is mounted in the test section as shown in Fig. 3. The measurements concentrate on the center blade of the cascade. To ensure a homogenous inlet flow boundary layer suction is applied to the upper and lower walls. To monitor the main flow condition, the static inlet pressure, the total inlet pressure, and the total temperature in the settling chamber are measured. The local total pressure is measured at the exit measurement plane. A glass window is mounted to the sidewall of the cascade to deliver optical access to the center blade for the laser-two-focus measurements.

Transfer of Surface Roughness to the Airfoil. In order to simulate technical surface roughness correctly for the enlarged compressor model blades, a special technique has been developed [13]. The three-dimensional surface structure of a real blade is measured with a scanning white light interferometer obtaining an

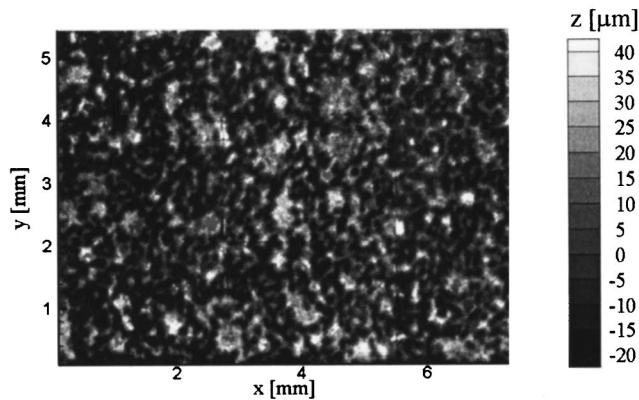


Fig. 4 Three-dimensional topology of applied sheet of copper

Table 1 Roughness parameters of real blade and applied sheet of copper

| | Ra | Rz | Rsk | S | Sm |
|---------------------|-------|------|-------|-------|-------|
| real blade | 0.70 | 7.27 | -1.28 | 0.017 | 0.035 |
| transferred surface | 11.15 | 69.3 | 0.47 | 0.168 | 0.335 |

ASCII data set that is used to create a bitmap used to control a laser micromachining process. With this process it is possible to engrave with a factor of ten an enlarged copy of the original blade surface roughness into a sheet of copper. For the present investigation the surface of a precision-forged airfoil is used as input for the laser machining process. Due to problems at the fabricator in creating an input bitmap out of the ASCII data file, only a qualitative reproduction of the original surface has been achieved. A scanning white light measurement of the sheet of copper with the enlarged surface roughness is displayed in Fig. 4. Some important roughness parameters of the real blades surface and the enlarged and transferred surface are given in Table 1. In order to perform the measurements at the large-scale compressor cascade, two sheets of copper are necessary, one for the suction side and one for the pressure side. Both sheets of copper are adhered to the center blade where the profile contour is changed to avoid an undesirable thickening of the blade contour.

Total Pressure Wake Traverse and Static Profile Pressure Measurement Technique. The total pressure loss of an airfoil can be estimated when traversing a total pressure probe through the wake caused by the airfoil. When investigating the influence of surface roughness, it is important to isolate the roughness influence from other parameters. This has been achieved by the use of two total pressure probes, which are traversed simultaneously over one pitch behind a blade divided into a rough and a smooth half. One probe is positioned behind the smooth blade, the other one behind the rough one. From these probes two pressure differences are recorded: the inlet total pressure versus the total pressure measured by the probe behind the smooth half of the airfoil and the total pressure difference between the two probes. This setup enables the use of accurate pressure transducers to measure the total pressure difference between the wake of the smooth and the rough blade. Each probe has a distance of 45 mm from midspan. It has been ensured by previous measurements of the secondary flow field with a five-hole probe [14] that neither probe is affected by secondary flow phenomena. In order to correct small total pressure inhomogeneities, each flow condition has been additionally measured with the center airfoil equipped with smooth sheets of copper. The wake traverse results have been corrected with the results of the wake traverse behind the smooth blade.

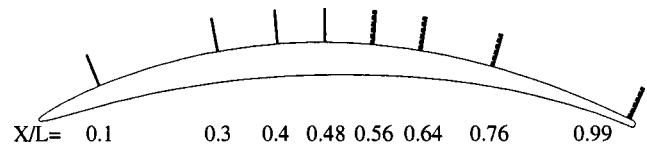


Fig. 5 Location of measurement planes

In order to determine the isentropic Mach number distribution over the blade, the center airfoil is equipped with 42 static pressure tappings. To enable a comparison of the isentropic Mach number distribution between the rough and the smooth half of the blade, each half is equipped with 8 pressure tappings on the pressure side and 13 pressure tappings on the suction side. The tappings are located at a distance of 40 mm from midspan. It has been ensured by oil-and-dye surface flow patterns that the measurement of profile pressures is not affected by secondary flow phenomena.

Investigation of Profile Boundary Layer. With the laser two-focus technique [15] the two-dimensional flow vector can be measured. This nonintrusive technique is able to measure the velocity and the direction of the flow very close to a wall. Thus, the velocities inside the profile boundary layer can be measured. The laser-two-focus technique is based on the principle of a light barrier. The light of a water-cooled argon-ion laser with an output power of 1.5 W is used to produce two parallel laser beams, which are focused to a size of $9 \mu\text{m}$ at a distance of $168 \mu\text{m}$, building the light barrier for particles made of an aerosol with an average diameter of $0.5 \mu\text{m}$. The back-scattered light of particles passing the focal volumes is received by two photodetectors. After amplification and signal processing, the time between the pulses of a particle passing the two foci is used to calculate the velocity with the known distance between the two foci. A statistical evaluation is necessary because the two pulses detected by the photodetectors are sometimes not of one particle. The flow angle can be detected by rotating the two foci. The measurement planes along the suction surface used to investigate the boundary layer development with the laser-two-focus anemometry are displayed in Fig. 5. Even though the statistical evaluation of velocity and angle are very accurate, the evaluation of turbulence is only qualitative. To minimize this lack of information the hot wire anemometry is used.

The hot-wire anemometry engaged at the HGK is based on the principle of constant temperature. A Wheatstone bridge is compensating the change of temperature of a wire applied to the flow. A change in flow velocities results in a changing thermal conduction at the wire. To keep the temperature of the wire constant, the electrical power has to be controlled. The control of the measurement chain and the data acquisition and evaluation is done with the Dantec streamware system. Different flow conditions require different types of probes. The measurement inside the profile boundary layer has been performed with the boundary layer probe 55P15 with a wire diameter of $5 \mu\text{m}$.

Results

Variation of Reynolds Number. The influence of the inlet Reynolds number at the design inlet angle $\beta_1 = 132 \text{ deg}$ and the design inlet Mach number $\text{Ma} = 0.67$ on the isentropic Mach number distribution of the rough and the smooth blade is displayed in Fig. 6. At the lowest Reynolds number, a laminar separation bubble is detected between $X/L = 0.43$ and $X/L = 0.66$ for the smooth and the rough blade. There is no reduction of separation length due to surface roughness. Only the thickness of the laminar separation bubble seems to be reduced indicated by slightly reduced isentropic Mach numbers at $X/L = 0.6$ for the rough blade. The rest of the distribution of isentropic Mach number is nearly identical for the rough and the smooth blade even on the pressure

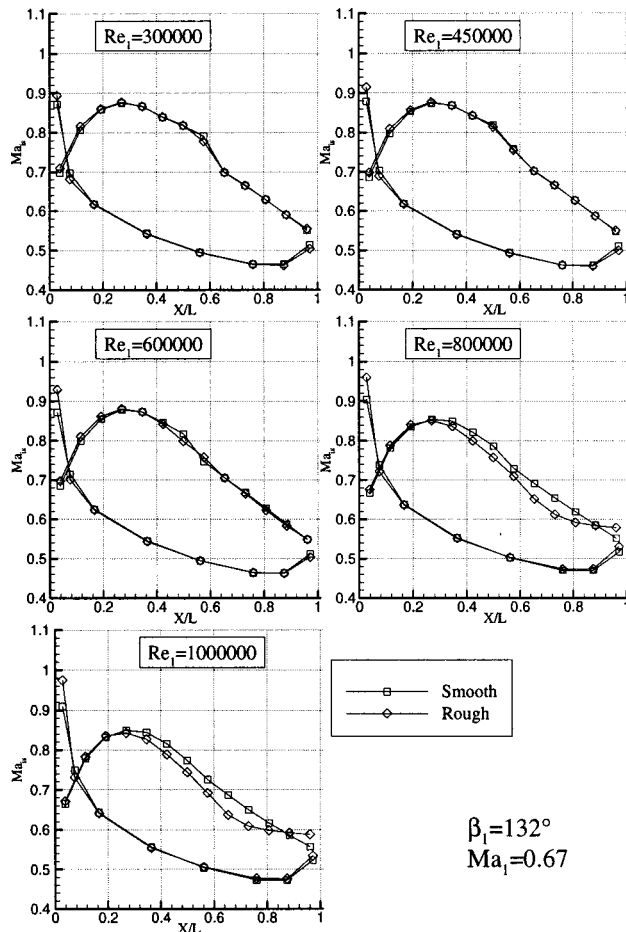


Fig. 6 Influence of Reynolds number on isentropic Mach number

side. At a design inlet Reynolds number of $Re_1=450,000$, the laminar separation bubble is reduced compared to the lower inlet Reynolds number. However, there is no difference in the extent of the bubble between the smooth and the rough blade ($X/L=0.43$ and $X/L=0.6$). A reduction of bubble height is imaginable for the rough blade but not clearly shown by the isentropic Mach number. For a further increase of inlet Reynolds number ($Re_1=600,000$) the separation bubble disappears on the rough blade. The isentropic Mach number of the smooth blade again indicates a laminar separation occurring between $X/L=0.43$ and $X/L=0.58$. At an inlet Reynolds number of $Re_1=800,000$ no laminar separation is detected for the smooth and the rough blade. But at $X/L=0.72$ a large turbulent separation can be observed for the rough blade that does not reattach. Even at the highest inlet Reynolds number of $Re_1=1,000,000$ a turbulent separation is shown by the isentropic Mach number distribution of the rough blade that is slightly shifted upstream to $X/L=0.65$. For all inlet Reynolds numbers no roughness effect on the isentropic Mach number of the pressure side could be observed.

The results of wake traverse with two total pressure probes are displayed in Fig. 7 for a variation of Reynolds number. The local total pressure loss and the local total pressure loss difference between the rough and the smooth blade is shown. Positive values of local total pressure loss difference between the rough and the smooth blade mean that there is additional total pressure loss due to surface roughness. At the lowest Reynolds number $Re_1=300,000$ a slight additional total pressure loss at the suction side can be observed, although a reduction of laminar separation bubble height in the distribution of isentropic Mach number is shown in Fig. 6. For higher inlet Reynolds numbers the local

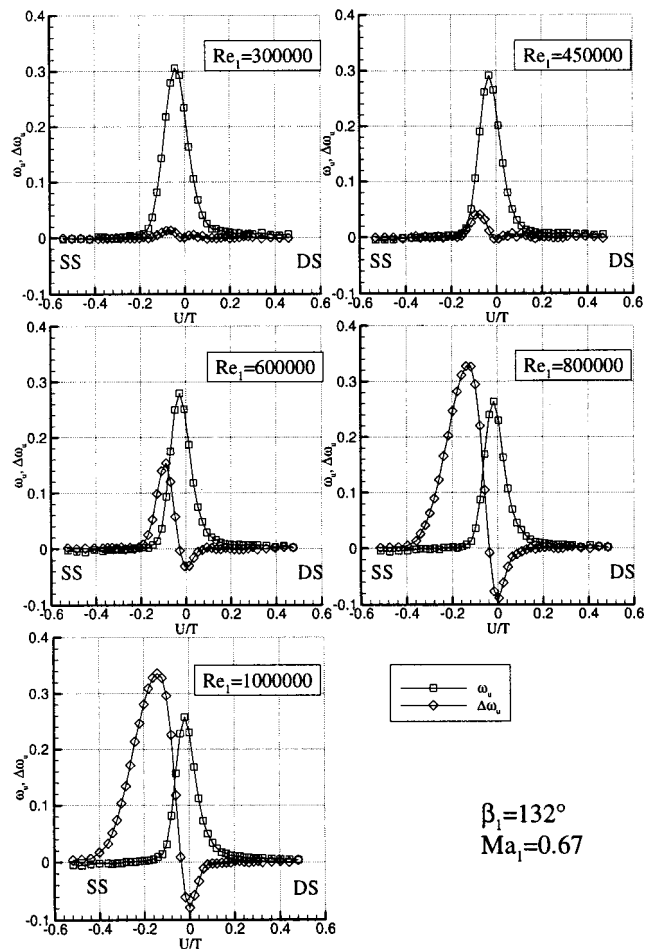


Fig. 7 Influence of Reynolds number on local total pressure loss

maximum of additional total pressure loss increased up to very high values, indicating high additional losses due to turbulent separation on the suction side caused by surface roughness.

The integral total pressure loss coefficient versus the inlet Reynolds number is displayed in Fig. 8. At an inlet Reynolds number of $Re_1=300,000$ the total pressure loss coefficients of the smooth and the rough blade are nearly identical. When increasing the inlet Reynolds number, the total pressure loss coefficient of the rough blade is always higher than that of the smooth blade. At $Re_1=600,000$ a sharp increase of total pressure loss coefficient for the rough blade indicates the beginning of turbulent separation on the suction side of the rough blade.

In order to obtain detailed information about the status of the boundary layer, laser-two-focus anemometry has been used. Due to the fact that this is a very time-consuming technique, only two inlet Reynolds numbers have been investigated ($Re_1=450,000$, $600,000$). A further reduction of measurement time has been achieved by reducing the number of chordwise measurements for $Re_1=600,000$. The results of the laser-two-focus anemometry are the velocities inside the boundary layer. A spline approximation is used to evaluate the boundary layer parameters displayed versus the dimensionless chordwise position in Fig. 9. At $Re_1=450,000$ the boundary layer thicknesses of the smooth and the rough blade are identical, whereas at $Re_1=600,000$ the boundary layer of the rough blade is always slightly thicker than the boundary layer of the smooth blade especially at $X/L=0.99$. The displacement thickness at $Re_1=450,000$ confirms that the laminar separation bubble is thicker for the smooth blade than for the rough blade (zoomed out). Even at $Re_1=600,000$ the displacement thickness

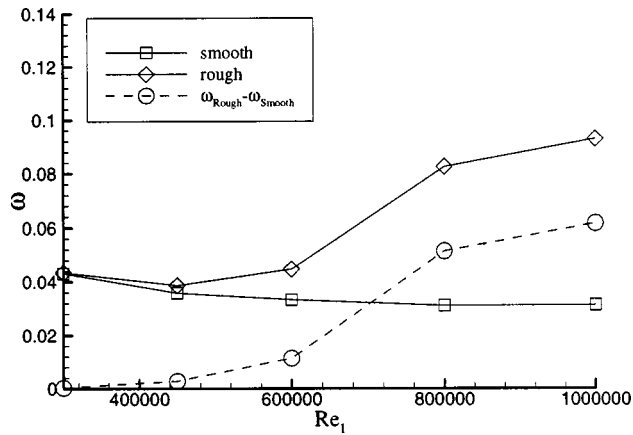


Fig. 8 Influence of Reynolds number on total pressure loss coefficient

indicates the laminar separation bubble for the smooth blade. Over the rough blade no laminar separation can be detected. The impulse deficit thickness shows no difference between the rough and the smooth blade at $Re_1=450,000$. At $Re_1=600,000$ the impulse deficit thickness of the rough blade is always slightly higher than that of the smooth blade even close to the trailing edge, indicating that the higher impulse deficit in the rough boundary layer is responsible for the observed higher total pressure loss coefficient. The comparison of shape factor H_{12} indicates the laminar separation at $Re_1=450,000$ due to very high values at $X/L=0.48$. The higher increase of shape factor close to the trailing edge for the rough blade is a hint that turbulent separation is likely to occur. At $Re_1=600,000$ the decrease of shape factor from a value of $H_{12}=4$ down to $H_{12}=1.8$ for the smooth blade is another indicator for a laminar separation over the smooth blade. The decrease of shape factor for the rough blade makes a transition without separation bubble likelier.

The steep increase at $X/L=0.99$ for the rough blade is again clearly indicating a beginning turbulent separation. The skin friction coefficient at $Re_1=450,000$ relieves the above discussion by a sharp decrease at $X/L=0.48$ also indicating the laminar separation. Very small skin friction coefficients at $X/L=0.99$ for the rough blade at both inlet Reynolds numbers confirm that there is a beginning turbulent separation.

The development of dimensionless root mean square of time-resolved velocity obtained by hot-wire anemometry is displayed in Fig. 10 for three inlet Reynolds numbers at the design inlet flow angle $\beta_1=132$ deg and the design inlet Mach number $Ma_1=0.67$. For each Reynolds number the measurements have been performed at four chordwise positions (Fig. 5). The distribution of turbulence at $X/L=0.64$ shows higher levels of turbulence for the smooth blade at an inlet Reynolds number of $Re_1=300,000$. Further downstream at $X/L=0.76$, the turbulence intensity of the rough blade is only slightly lower than for the smooth blade and at $X/L=0.99$ no difference is found between the rough and the smooth blade. This behavior indicates that the laminar separation is reduced for the rough blade, leading to lower levels of turbulence. But downstream of the laminar separation, surface roughness does increase the turbulence in the boundary layer of the rough blade. The decrease of turbulence short behind the laminar separation and the increase after the separation are of the same order resulting in an equal distribution of turbulence at the trailing edge. At the design inlet Reynolds number $Re_1=450,000$ higher levels of turbulence can be observed at $X/L=0.56$ and $X/L=0.64$ in the boundary layer of the smooth blade. This indicates a stronger laminar separation for the smooth blade than for the rough blade. At $X/L=0.76$ the surface roughness causes higher levels of turbulence only in the vicinity of the wall. Above a wall distance of 3 mm the degree of turbulence is higher for the smooth blade. The turbulence distribution close to the trailing edge shows higher turbulence up to the undisturbed flow for the rough blade. For the highest Reynolds number $Re_1=600,000$ only, at $X/L=0.56$ higher degrees of turbulence can be detected close to the

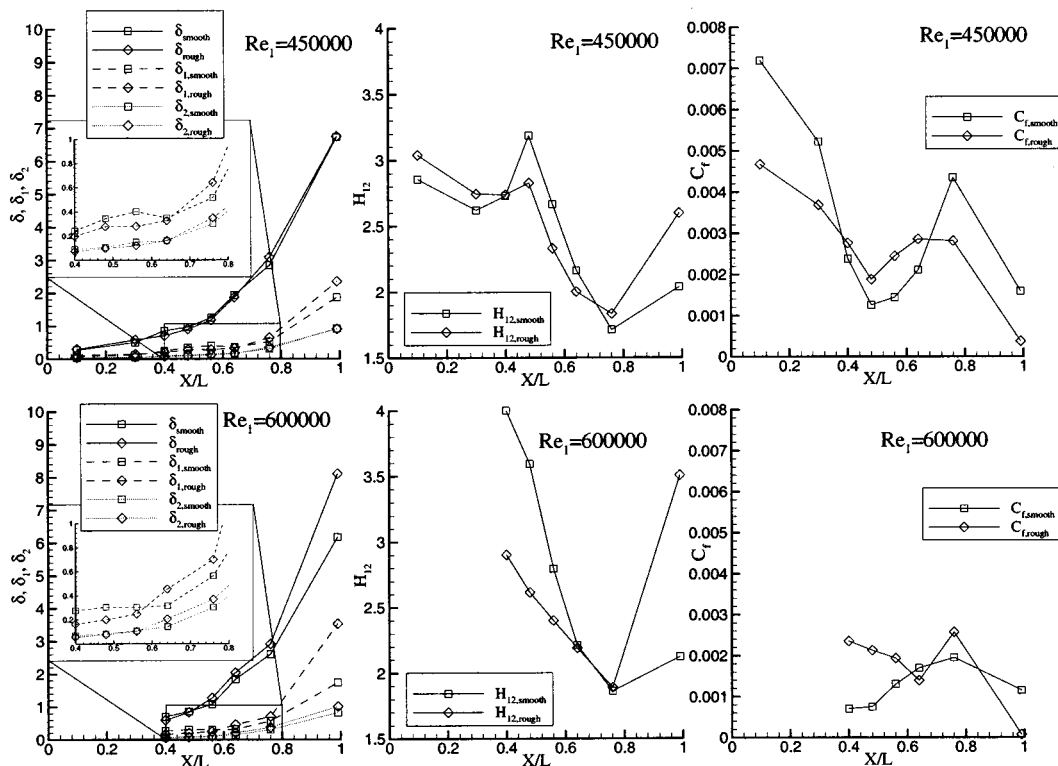


Fig. 9 Influence of Reynolds number on boundary layer parameters

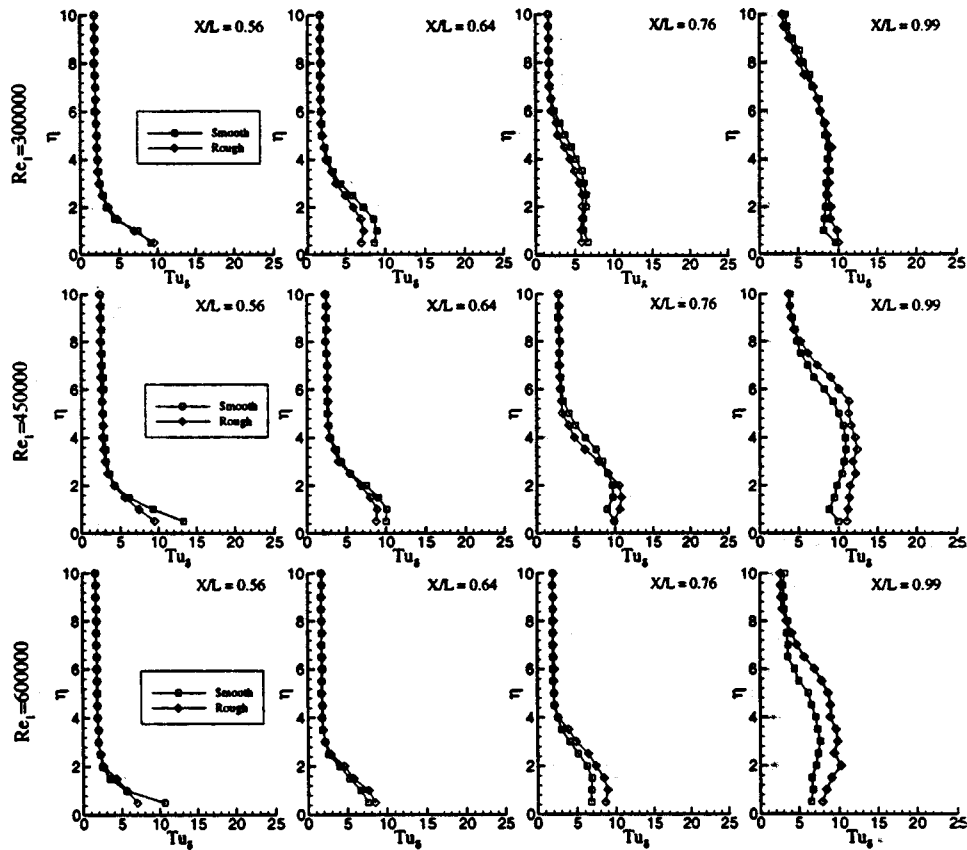


Fig. 10 Influence of Reynolds number on distribution of turbulence in boundary layer

wall for the smooth blade. At the three downstream positions, the turbulence level in the boundary layer on the rough blade is always higher than on the smooth blade.

The variation of Reynolds number shows an increased influence of surface roughness for an increased Reynolds number. The strength of a laminar separation occurring for the smooth blade up to a Reynolds number of $Re_1=600,000$ is decreased by surface roughness. The presence of a laminar separation leads to the assumption that the laminar boundary layer is not affected by surface roughness. The positive effect of decreasing strength of a laminar separation bubble due to surface roughness is compensated by negative effects of surface roughness on the turbulent boundary layer downstream of the laminar separation. For increasing Reynolds numbers even this negative effect is increasing leading to a turbulent separation.

Variation of Inlet Flow Angle. The influence of inlet flow angle on the isentropic Mach number distribution and the local total pressure loss at the design inlet Reynolds number $Re_1=450,000$ and the design inlet Mach number $Ma_1=0.67$ is shown in Fig. 11. At negative incidence ($\beta_1=129$ deg) and zero incidence ($\beta_1=132$ deg) the isentropic Mach number is not affected by surface roughness. A separation bubble is detected between $X/L=0.4$ and $X/L=0.65$. At positive incidence ($\beta_1=140$ deg) turbulent separation is detected. The turbulent separation is shifted slightly upstream for the rough blade. The local total pressure loss and the total pressure loss difference between the rough and the smooth blade show the same behavior for the inlet flow angles $\beta_1=129$ and $\beta_1=132$ deg. Only small additional total pressure losses due to surface roughness are observed. For the highest inlet flow angle $\beta_1=140$ deg surface roughness causes higher additional losses than for the two lower inlet flow angles. Here only a deceleration is observed on the suction side making a complete turbulent boundary layer possible.

The integral total pressure loss coefficient difference versus the inlet flow angle is shown in Fig. 12 for three different Reynolds numbers. For the lowest Reynolds number ($Re_1=300,000$) surface roughness causes slightly higher losses for $\beta_1=129$ deg. A Reynolds number of $Re_1=450,000$ gives higher loss coefficients for the rough blade. For $\beta_1=129$ and $\beta_1=132$ deg the difference between the loss coefficient of the smooth and the rough blade is nearly the same, whereas for $\beta_1=140$ deg the difference in loss coefficient is higher. This trend can clearly be identified for the Reynolds number $Re_1=600,000$. This leads to the presumption that the flow is more sensitive to surface roughness at high inlet flow angles.

The boundary layer investigated by the laser-two-focus anemometry is illustrated in Fig. 13. In order to reduce measurement time and due to the results of isentropic profile Mach number and wake traverse not showing any differences between $\beta_1=129$ deg and $\beta_1=132$ deg only at $\beta_1=132$ and $\beta_1=140$ deg and at $Re_1=450,000$, the boundary layer development has been investigated by means of laser-two-focus anemometry. The boundary layer parameters for an inlet flow condition $Re=450,000$ and $\beta_1=132$ deg have already been discussed above. The boundary layer thickness at $\beta_1=140$ deg is larger than for $\beta_1=132$ deg because of a complete turbulent boundary layer at the suction side. The turbulent separation at $X/L=0.7$ leads to a thick boundary layer. At an inlet flow angle $\beta_1=132$ deg surface roughness does not change the thickness of the boundary layer but at $\beta_1=140$ deg the boundary layer of the rough blade is thicker than of the smooth blade. The distribution of displacement thickness shows a steep increase at $X/L=0.7$ because of the turbulent separation. Higher values for the rough blade especially downstream of $X/L=0.7$ indicate a more distinct turbulent separation for the rough blade. The high gradient of the shape factor indicates a stronger turbulent separation. Even at $\beta_1=132$ deg the shape factor shows a steeper

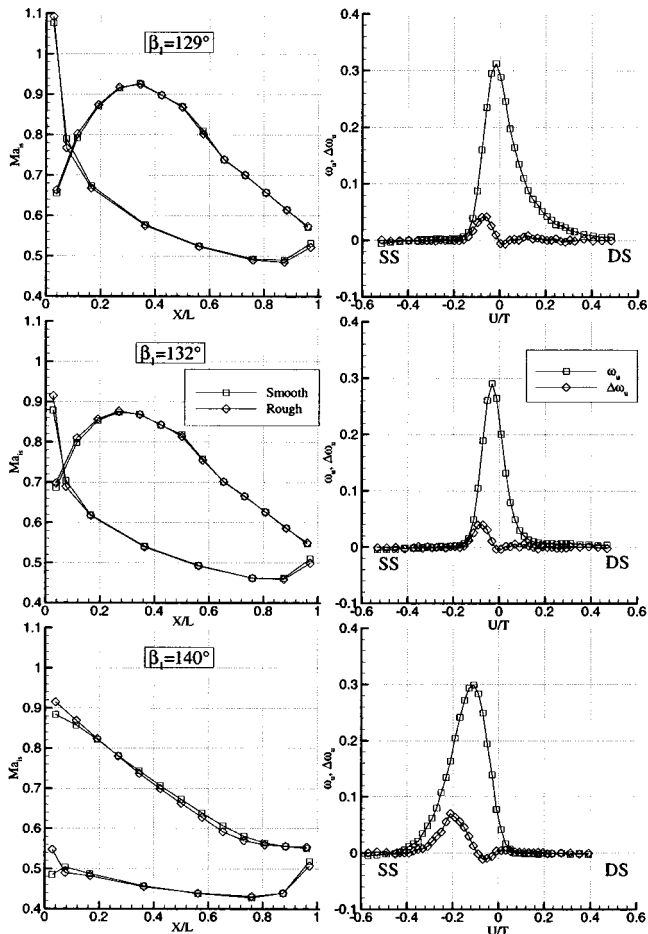


Fig. 11 Isentropic Mach number and wake traverse results for a variation of inlet angle

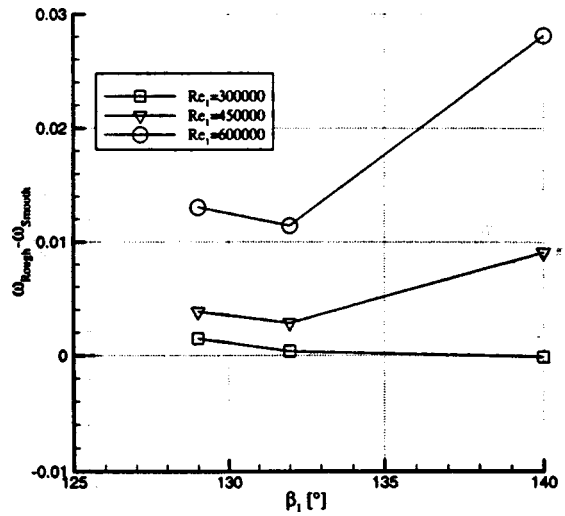


Fig. 12 Total pressure loss coefficient difference versus inlet flow angle

increase at the trailing edge for the rough blade, indicating the tendency to turbulent separation for the rough blade. The progression of skin friction coefficient at $\beta_1 = 140$ deg indicates a stronger turbulent separation due to lower values for the rough blade.

Figure 14 shows the root mean square of the time-resolved velocity measured by the one-dimensional hot wire anemometry for three inlet flow angles. A stronger laminar separation for the smooth blade is marked by higher levels of turbulence at the positions $X/L = 0.56$ and $X/L = 0.64$. Further downstream the surface roughness increases the turbulence intensity, leading to a compensation of turbulence reduction achieved in the laminar separation bubble. Even at an inlet flow angle $\beta_1 = 132$ deg the strength of laminar separation is reduced by surface roughness,

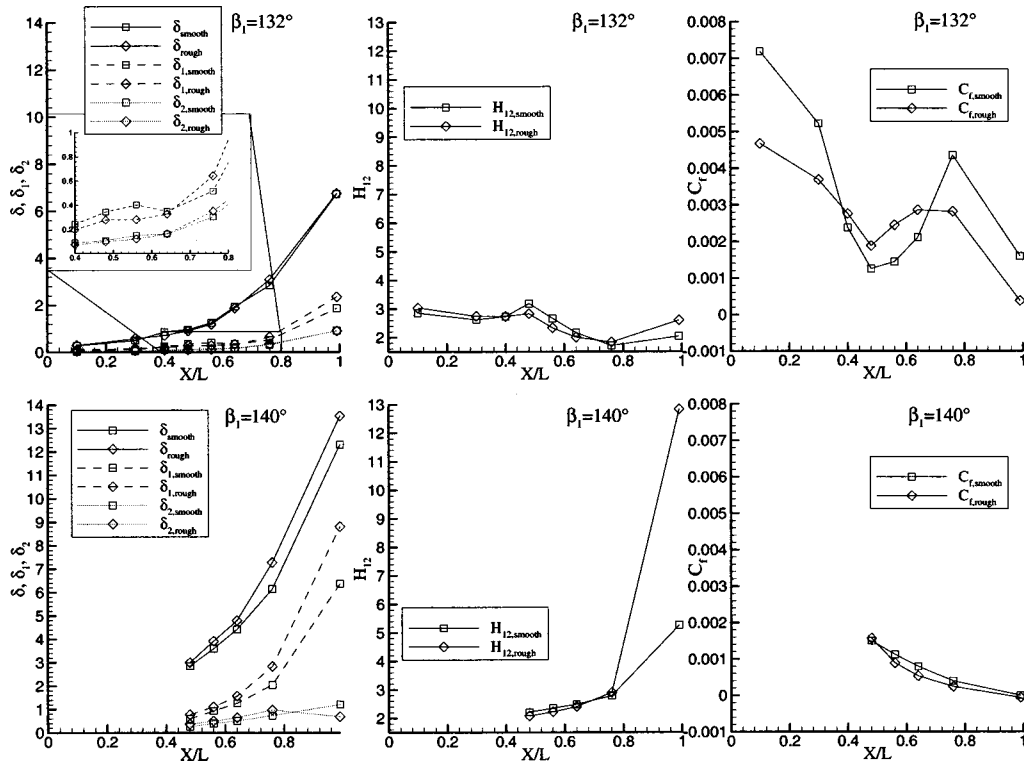


Fig. 13 Influence of inlet flow angle on boundary layer parameters

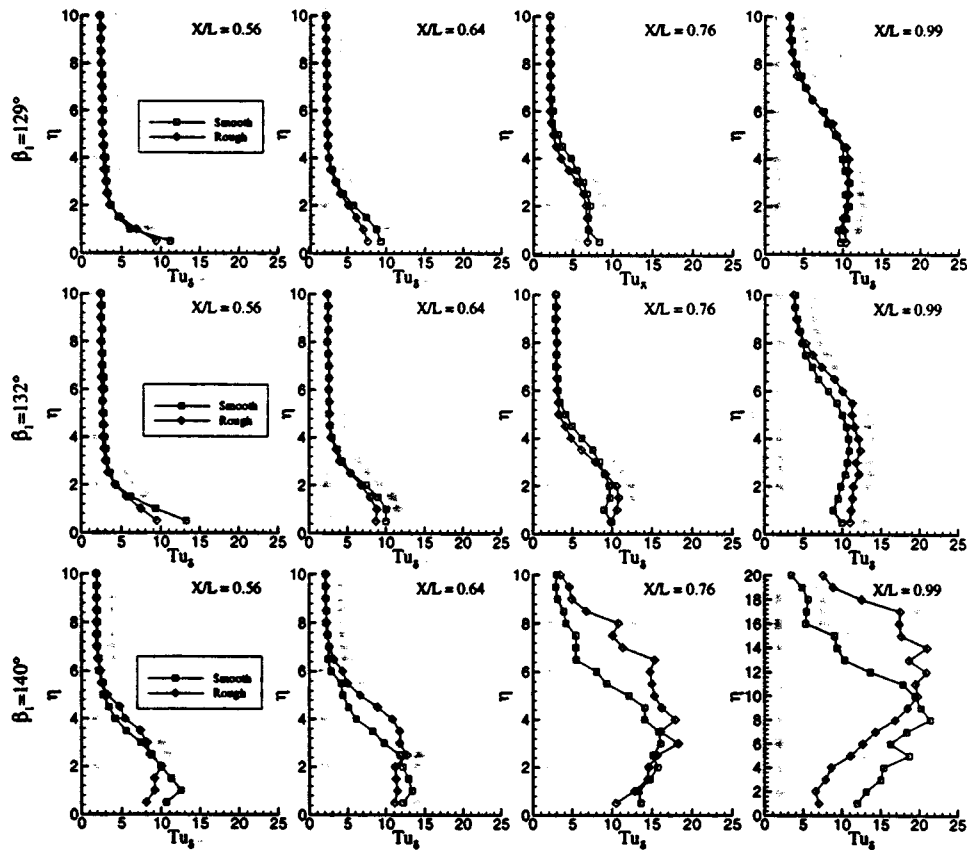


Fig. 14 Influence of inlet flow angle on distribution of turbulence in boundary layer

resulting in lower levels of turbulence. The production of turbulence after the laminar separation is now higher than the decrease of turbulence in the laminar separation bubble. Thus, the turbulence is higher for the rough blade close to the trailing edge. At $\beta_1 = 140$ deg the position of maximum turbulence is closer to the wall for the smooth blade for all positions marking the stronger turbulent separation of the boundary layer for the rough blade (at $X/L = 0.99$ the traverse length has been extended to 20 mm instead of 10 mm). A significant decrease or increase of turbulence due to surface roughness could not be observed.

The variation of inlet flow angles shows a similar influence of surface roughness for $\beta_1 = 129$ and $\beta_1 = 132$ deg. The reduction of the strength of the laminar separation is compensated by an increase of turbulence in the turbulent boundary layer. For an inlet flow angle of $\beta_1 = 140$ deg an increased influence of surface roughness is observed. The reason is a complete turbulent boundary layer at the suction side for the highest inlet flow angle without any laminar separation.

Conclusions

In order to investigate the influence of surface roughness on the flow around a highly loaded compressor cascade, measurements of the isentropic profile Mach number distributions and of the local total pressures at the exit measurement plane of a smooth and a rough blade have been performed. Furthermore, a detailed investigation of the suction side boundary layer has been done with laser-two-focus anemometry and one-dimensional hot-wire anemometry. The important results can be summarized as follows:

- Due to the presence of a laminar separation, even for the rough blade, the laminar boundary layer seems not to be affected by surface roughness.

- The beginning and end of a laminar separation at low inlet Reynolds numbers is not affected by surface roughness. Only at $Re_1 = 600,000$ is the laminar separation completely suppressed by roughness.

- The displacement thickness is larger in the region of a laminar separation bubble for the smooth blade. This leads to the assumption that the strength of a laminar separation is reduced by surface roughness.

- The positive effect on the laminar separation does not decrease the total pressure loss coefficient for the rough blade because the turbulent boundary layer is affected negatively by surface roughness.

- At high Reynolds numbers surface roughness causes the turbulent boundary layer to separate from the blade.

- At negative incidence and at design inlet flow angle the influence of surface roughness on the boundary layer and the total pressure losses is similar, but at positive incidence the boundary layer reacts more sensitively to surface roughness.

Acknowledgments

The reported investigations were performed in the scope of a project of the "Wehrtechnisches Technologieprogramm Luftfahrzeuge" and was funded by the "Bundesamt für Wehrtechnik und Beschaffung." Support and the permission for publication are gratefully acknowledged.

Nomenclature

- C_f = skin friction coefficient
- h = airfoil height, m
- H_{12} = shape factor = δ_1 / δ_2
- l, L = airfoil chord, m
- Ma = Mach number

p, p_t = static pressure, total (stagnation) pressure, Pa
 PS, SS = pressure side, suction side
 Ra = arithmetic average deviation from centerline, μm
 Re = Reynolds number
 Rz = ten point height parameter, μm
 Rsk = skewness
 S = average spacing between local peaks, mm
 Sm = average spacing of peaks over centerline, mm
 t = pitch, m
 T_t = total (stagnation) temperature, K
 Tu = local turbulence intensity, percent
 Tu_δ = turbulence intensity related to free-stream velocity, percent
 w = flow velocity, m/s
 x, u, z = axial, circumferential, spanwise coordinates, m
 x, y = lateral coordinates, mm
 z = surface height, μm
 β = circumferential (pitchwise) flow angle, deg
 β_s = stagger angle, deg
 δ = boundary layer thickness, m
 δ_1 = displacement thickness, m
 δ_2 = momentum thickness, m
 ω = loss coefficient = $(p_{t1} - p_t)/(p_{t1} - p_1)$

Subscripts and Superscripts

1,2 = cascade upstream and downstream conditions
 ax = axial
 is = isentropic
 u = at local circumferential position

References

- [1] Nikuradse, J., 1933, "Strömungsgesetze in rauhen Röhren," Beilage zu Forschung auf dem Gebiet des Ingenieurwesens, Forschungsheft 361 Ausgabe B Band 4.
- [2] Schlichting, H., 1936, "Experimentelle Untersuchungen zum Rauheitsproblem," Ingenieur-Archiv 7. Band, 1. Heft.
- [3] Bammert, K., and Sandstede, H., 1973, "Strömungsverluste durch die Oberflächenrauigkeit der Schaufeln einer Turbine," VDI-Berichte, No. 193.
- [4] Bammert, K., and Sandstede, H., 1972, "Measurements Concerning the Influence of Surface Roughness and Profile Changes on the Performance of Gas Turbines," ASME Paper No. 72-GT-34.
- [5] Bammert, K., and Sandstede, H., 1975, "Influences of Manufacturing Tolerances and Surface Roughness of Blades on the Performance of Turbines," ASME Paper No. 75-GT-35.
- [6] Bammert, K., and Woelk, G.-U., 1976, "Der Einfluß der Profilrauigkeit auf die Strömungsverluste von Axialverdichtern," VDI-Berichte No. 264.
- [7] Bammert, K., and Woelk, G.-U., 1979, "The Influence of Blading Surface Roughness on the Aerodynamic Behavior and Characteristic of an Axial Compressor," ASME Paper No. 79-GT-102.
- [8] Suder, K. L., Chima, R. V., Strazisar, A. J., and Roberts, W. B., 1995, "The Effect of Adding Roughness and Thickness to a Transonic Axial Compressor Rotor," ASME J. Turbomach., **117**, pp. 491–505.
- [9] Bammert, K., and Sandstede, H., 1980, "Measurements of the Boundary Layer Development Along a Turbine Blade With Rough Surfaces," ASME J. Eng. Power, **102**, No. 4, pp. 978–983.
- [10] Bammert, K., and Milsch, R., 1972, "Das Verhalten der Grenzschicht an rauhen Verdichterschaufeln," Sonderdruck Forschung im Ingenieurwesen, B. 38 No. 4.
- [11] Saxena, V. M., Shirvastava, K. D., and Agrawal, P. K., 1980, "Effect of Surface Roughness Over the Blade in Compressor Cascade," IE (I) **61**.
- [12] Sturm, W., and Fottner, L., 1985, "The High Speed Cascade Wind Tunnel of the German Armed Forces University Munich," 8th Symposium on Measuring Techniques for Transonic and Supersonic Flows in Cascades and Turbomachines, Genoa.
- [13] Leipold, R., and Fottner, L., 1998, "A Measurement Technique to Investigate the Influence of Surface Roughness on the Flow Around a Highly Loaded Compressor Cascade," 14th Symposium on Measuring Techniques in Transonic and Supersonic Flow in Cascades and Turbomachines, Limerick.
- [14] Hübner, J., 1996, "Experimentelle und theoretische Untersuchung der wesentlichen Einflußfaktoren auf die Spalt- und Sekundärströmung in Verdichtergittern," PhD Thesis, Universität der Bundeswehr München.
- [15] Schodl, R., 1978, "Entwicklung des Laser-Zwei-Fokus-Verfahrens für die berührungslose Messung der Strömungsvektoren, insbesondere in Turbomaschinen," Ph.D. Thesis, Technische Hochschule Aachen.

Discussion: "The Influence of Technical Surface Roughness Caused by Precision Forging on the Flow Around a Highly Loaded Compressor Cascade" [ASME J. Turbomach., **122**, No. 3, pp. 416–424 (2000)]¹

N. A. Cumpsty

University of Cambridge, Department of Engineering,
Whittle Laboratory, Madingley, Rd., Cambridge,
CB3 0DY, United Kingdom

I found this a very interesting paper, but one of the things I found so interesting the authors do not emphasize and it therefore seems appropriate to discuss it here.

It is conventional wisdom that loss from blades falls as the Reynolds number increases; likewise the efficiency of a given compressor tends to rise as the Reynolds number is increased. For cascades of compressor blades, it is normally assumed that the profile loss has fallen to a plateau for a Reynolds number (based on chord, inlet velocity, and viscosity upstream) of about 2×10^5 .

The present results show that on a rough blade (and rough here means a surface finish typical of many new blades entering service) the loss rises quite steeply with Reynolds number for values above about 6×10^5 , approximately doubling by the time the Reynolds number reaches 10^6 . This change occurs above the Reynolds number at which most cascade testing has taken place and would have been easy to miss in the past. Furthermore, most cascade testing has been on smooth blades and the rise in loss with increasing Reynolds number would have been missed even if the tests were carried out at Reynolds numbers above 6×10^5 .

For a large aircraft engine at cruise, the Reynolds numbers of the core compressor rotor blades are around 10^6 at entry and 2×10^6 at exit; at take-off the Reynolds numbers are a little over twice as large. The findings of this paper are therefore of great practical relevance to aviation as well as land-based engines and the authors are to be congratulated on providing us with some very useful information and insight.

A two-part paper presented at the same conference as this one drew attention to the importance of free-stream turbulence on the boundary layer behavior for blades [1,2]. The present paper gives the range of turbulence level achievable in the tunnel, but not the level used for the tests described. Could the authors provide this information?

References

- [1] Köller, U. D., Mönig, R., Küsters, B., and Schreiber, H.-A., 2000, "Development of Advanced Compressor Airfoils for Heavy-Duty Gas Turbines: Part I—Design and Optimization," ASME J. Turbomach., **122**, pp. 397–405.
- [2] Küsters, B., Schreiber, H.-A., Köller, U. D., and Mönig, R., 2000, "Development of Advanced Compressor Airfoils for Heavy-Duty Gas Turbines: Part II—Experimental and Theoretical Analysis," ASME J. Turbomach., **122**, pp. 406–415.

¹Leipold, R., Boese, M., and Fottner, L., 2000, "The Influence of Technical Surface Roughness Caused by Precision Forging on the Flow Around a Highly Loaded Compressor Cascade," ASME JOURNAL OF TURBOMACHINERY, Vol. 122, No. 3, pp. 416–424.

Closure to “Discussion of ‘The Influence of Technical Surface Roughness Caused by Precision Forging on the Flow Around a Highly Loaded Compressor Cascade’ ” [ASME J. Turbomach., 122, No. 3, p. 424 (2000)]

Robert Leipold, Matthias Boese, and Leonhard Fottner

First of all the authors would like to thank Prof. Cumpsty for pointing out the relevance of this work. The inlet turbulence level for the presented results vary with the inlet Reynolds number due to the use of passive turbulence generators. The inlet turbulence level was measured with a one-dimensional hot-film sensor, leading to an inlet turbulence level of $Tu_1 = 2$ percent at low Reynolds numbers and $Tu_1 = 3.5$ percent at high Reynolds numbers.

A Correlation for Tip Leakage Blockage in Compressor Blade Passages

M. Hoeger
M. Lahmer
M. Dupslaff
G. Fritsch

DaimlerChrysler Aerospace,
MTU Motoren- und Turbinen-Union München
GmbH, Dachauer Straße 665,
München, Germany 80995

Three-dimensional multistage Navier–Stokes simulations for compressor components, rigs, and cascades have been analyzed to gain insight into the tip leakage blockage evolution. From pitch-averaged flow quantities the local displacement caused by tip leakage is determined by means of a novel technique. Close to the throat an additional displacement of about 1–4 percent axial chord is observed for unchoked flow conditions. With tip gap height, stagger, and inlet Mach number as governing variables, a correlation for the tip leakage blockage transition function in blade passages is established, which may be used to improve the predictive capability of S1/S2 compressor aerodesign systems. [S0889-504X(00)00903-X]

Introduction

For a transonic compressor rotor, the highest efficiency penalty is observed close to the casing, where a three-dimensional shock system interacts with the secondary flow. With the introduction of modern three-dimensional Navier–Stokes methods, another valuable tool became available to analyze the nature of such complex flows in detail. The roll-up of a leakage vortex and its interaction with the passage shock were found to be the dominant phenomena causing additional blockage and high losses; see Adamczyk et al. [1] and Copenhaver et al. [2]. Numerous publications are concerned with the simulation of this type of flow. Although mostly standard turbulence models are used, all relevant phenomena are described correctly; see Jennions and Turner [3]. The theoretical findings in general compare well with experimental investigations employing advanced laser techniques; see, e.g., [4–6].

A thorough analysis of the three-dimensional data leads to an improved understanding of the physics, which in turn enables the engineer to describe the complex flow phenomena in an approximate manner with lower order models, which may then be used to optimize compressor blades methodically. Loss production in (subsonic) leakage flow, e.g., was best explained by the model of Storer and Cumpsty [7,8], in which the nonviscous mixing of an inhomogeneous tip region flow was identified as the most important mechanism. Chen et al. [9] show the leakage vortex trajectory to be independent of tip gap width and to be primarily governed by blade loading and convective phenomena. A wake-like behavior of the vortex core, with the static pressure rise generated by the shock to influence the vortex behavior as it traverses the shock, is assumed in the model of Puterbaugh and Brendel [10]. Khalid et al. [11] present a new methodology for quantifying end-wall blockage in compressors. Among other parameters the leakage flow total pressure is demonstrated to have a strong influence on end-wall blockage. This may become important for casing treatment considerations [12], for thick inlet boundary layers, and for flows where the leakage jet creates a reversed flow region, supplying the neighboring passage with low-energy material; see weak part of the tip leakage vortex in Fig. 1 (left).

Several authors reported the shock/leakage vortex interaction in the blade passage to be closely linked with the onset of stall, e.g., [1,4]. However, little information is available on the magnitude of the local displacement or blockage generated at the outer casing; see e.g., Khalid [13]. In this paper, a *tip leakage blockage transition function correlation* is presented that allows us to quantify approximately the end-wall blockage generated in the passage of a transonic compressor blade.

tion function correlation is presented that allows us to quantify approximately the end-wall blockage generated in the passage of a transonic compressor blade.

Background

The displacement by axially reversed flow originating from tip leakage vortex/shock interaction was discussed in Fritsch et al. [6]. The transformed rectangular blade passage in Fig. 1 (right) shows a three-dimensional displacement surface from axially reversed flow. The maximum displacement is found in the middle of the passage, where the shock (dark line in Fig. 1 (right)) intersects with the leakage vortex. Neglecting departures from rotational symmetry clearly seen in Fig. 1 (right), pitch-averaged displacement values are used as input into a throughflow calculation by Hoeger et al. [14]. The corresponding blade-to-blade predictions reproduced the tip-gap-dependent increase in inlet flow angle obtained in three-dimensional simulation with good accuracy. Since then three-dimensional Navier–Stokes simulations of many more compressors have been analyzed and the results encouraged the authors to attempt a correlation.

Multistage Navier–Stokes Simulations

Details of the Navier–Stokes solver TRACE_S, an explicit cell-centered second-order-accurate finite-volume scheme, are given in Fritsch et al. [6]. Its extension to multistage and to parallel architectures are found in Fritsch and Möhres [15].

Grid Topology and CPU-Time. Block-structured grids are employed to obtain high-quality grids and accurate convergent simulations for the complex geometry found in turbomachinery. All simulations utilized a composite **H/O**-grid with 155×33 nodes for the **H**-grid and 177×11 nodes for the **O**-grid in the S1 plane of the rotor; 65 nodes were used in the radial direction. A simple **H**-grid with $81 \times 9 \times 11$ nodes was used to grid the tip gap. A comparable resolution in the stator yielded a combined total of 896,231 nodes. Extensive grid studies, partly documented in Fritsch et al. [6], were performed to ensure that a comparison between experiment and simulation is not compromised by a lack of resolution. Execution time to convergence is approximately 6 CPU-hours on a SGI-Power Challenge using three R-8K processors with multigrid active for a single stage.

Turbulence Model. For economy a high Reynolds' $k-\varepsilon$ model, resulting in a mean wall distance of $y^+ = 25$ for rotor blade and casing and $y^+ = 75$ for the hub, was used; stator resolution was comparable with the exception of the casing, where the wall distance was increased to $y^+ = 75$. Wall distance for operating

Contributed by the International Gas Turbine Institute and presented at the 44th International Gas Turbine and Aeroengine Congress and Exhibition, Indianapolis, Indiana, June 7–10, 1999. Manuscript received by the International Gas Turbine Institute February 1999. Paper No. 99-GT-388. Review Chair: D. C. Wisler.

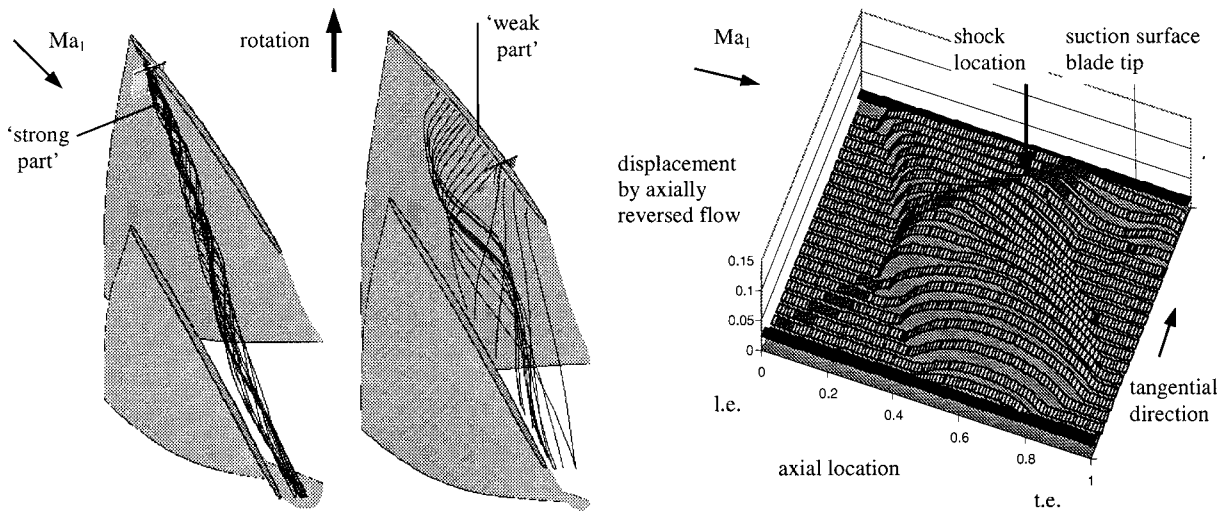


Fig. 1 Three-dimensional Navier-Stokes simulation of the tip leakage vortex for the TU-Darmstadt transonic compressor rig: strong and weak parts of the tip leakage vortex (left) and the resulting displacement by axial flow reversal (right); see [14]

points away from peak efficiency varies with the flow state. All simulations were run fully turbulent with wall functions applied to accurately represent the wall shear.

All simulations used a turbulence level of 4 percent at the entrance to the first blade passage. In subsequent blade passages, the mixing plane approach hands down the turbulence level from the upstream blade row.

Evaluation of the Displacement Thickness in Nonisoenergetic Flow

Meridional Average. The complex multiblock grid topology for a rotor passage (see [6]), is interpolated onto a standard H-grid. The conservative variables are flux-averaged for each radial plane to obtain the (blade to blade) pitch-average flow. Hereby the flow inside the tip gap is not taken into account.

The end-wall blockage phenomenon is discussed in terms of the displacement thickness at the outer casing normalized by the axial chord. The results for the displacement thickness may be transformed into nondimensional blockage values approximately by the simple algebraic operation

$$blk_{cas} = A_b/A = (\delta^*/c_{ax}) \cdot \Delta\theta \cdot (c_{ax}/A). \quad (1)$$

In Eq. (1) A_b and A are the blocked and the open area normal to the x axis and $\Delta\theta$ is the circumferential distance between the blades at a representative radial position close to the tip. In the following the two terms “blockage” and “displacement” are used interchangeably. A precise evaluation of the blockage in three-dimensional flow requires a two-dimensional integration; see [13].

End-Wall Boundary Layer Integration. From pitch-averaged results, four characteristic lines may be distinguished in the meridional plane; see Fig. 2:

- 1 the axially reversed flow limiting line $r(w_{ax}=0)$ with a maximum at the intersection of the shock and the vortex,
- 2 the displacement by axially reversed flow δ^*ar from the leakage vortex; see Hoeger et al. [14],
- 3 the inlet boundary layer displacement streamline δ^*s , entering the blade passage in a wall distance of δ_1^* ,
- 4 and the total displacement thickness δ^*

$$\delta^* = - \int_{r_{cas}}^{r_e} \left(1 - \frac{\overline{\rho w_{ax}}(r)}{(\rho w_{ax})_e} \right) dr \quad (2)$$

with $\overline{\rho w_{ax}}(r)$ as local pitch-averaged mass flow and the subscript “e” to indicate the edge of the boundary layer.

The inlet boundary layer displacement streamline may be understood as the locus of displacement of the inlet boundary layer profile undergoing convective changes in a nonviscous flow with compression shocks and reversed flow regions included, but without axial forces from work input and viscous entrainment into the boundary layer.

The total displacement streamline is based on a boundary layer approach, i.e., the assumption that for sufficiently high Reynolds numbers the flow at the end-wall may be split into a thin viscous layer, which displaces a main flow. The evaluation of $\delta^*(x)$ due to Eq. (2) was performed in two ways: (a) with the upper boundary r_e at a relative maximum in ρw_{ax} , and (b) for a fixed wall distance of about 40 percent passage height; see dashed lines in Fig. 2. At the rotor inlet no relative maximum in ρw_{ax} was found and integration (b) was used to determine δ_1^* throughout.

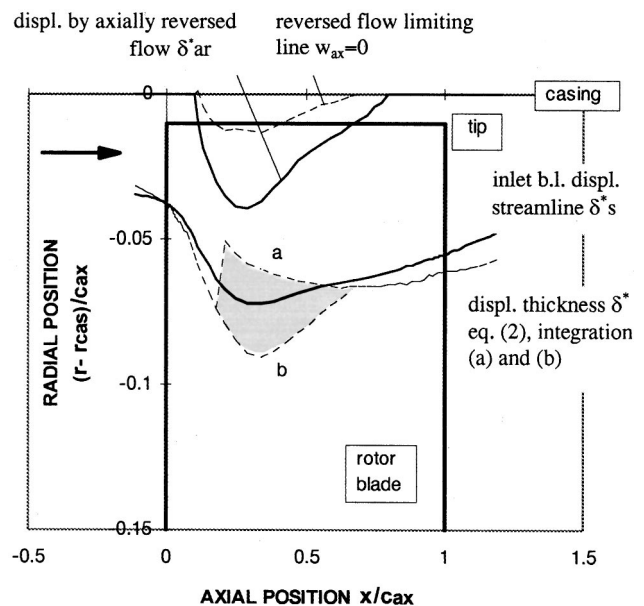


Fig. 2 Average displacement by leakage in the meridional plane (operating point close to stall)

Displacement Model. For boundary layer profiles in the reversed flow region, a relative maximum in w_{ax} is found; see Fig. 3, and it is not clear how to define the boundary layer edge for nonisoenergetic main flow. Some improvement in defining the upper integration boundary was reported in Khalid [13], by applying a velocity gradient criterion for locations at the blade in- and outlet. Inside the blade passage at about 30 percent chord, the actual displacement thickness may be expected to fall between the results of the two integration types (a) and (b); see Fig. 2. Here radial total pressure gradients from work input and compression shocks cannot be separated from the pure viscous changes. Downstream the shock region, below 75 percent chord both definitions converged for almost all cases investigated and the curve from the streamline integration δ^*s and those for δ^* are found to be similar in shape. We now assume the deviations from the convective changes, i.e., the influence of viscous entrainment and work input, to be small in comparison to δ^*s and to vary linearly with axial

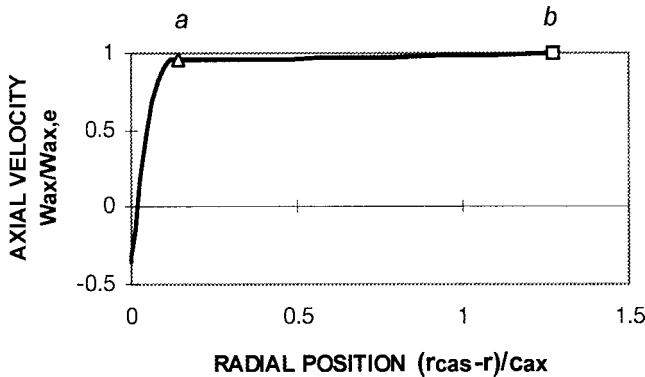


Fig. 3 Typical velocity profile in the reversed flow region with a relative maximum in w_{ax}

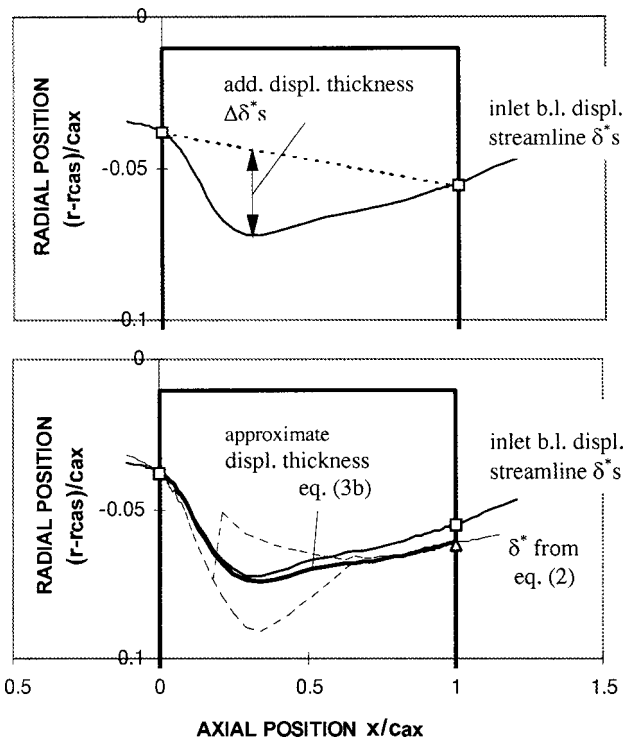


Fig. 4 Displacement definitions within the blade passage at the outer casing

distance. The difference between δ^*s and δ^* at the trailing edge may then be used to evaluate the displacement thickness δl in the blade passage, see Fig. 4 (bottom), by:

$$\delta^*(x) \approx \delta^*s(x) + (\delta^* - \delta^*s)_2 \cdot x/c_{ax} \quad (3)$$

Considering the departure of $\delta l s$ from a linear increase between in- and outlet, Eq. (3) may be recast in the form:

$$\delta^*(x) \approx \delta_1^* + \Delta \delta^*s(x) + (\delta_2^* - \delta_1^*) \cdot x/c_{ax} \quad (3b)$$

The problem of describing the end-wall boundary layer displacement in a nonisoenergetic flow is then split in a total displacement increase and an *additional displacement* from tip leakage. With Eq. (3b) we may write $\Delta \delta^*s \approx \Delta \delta^*$. The additional displacement $\Delta \delta^*s$ is obtained from a streamline-integration starting at the locus of the inlet boundary layer displacement thickness compared to a linear increase in δ^*s between the rotor in- and outlet; see Fig. 4 (top). An approximately linear increase in δ^*s was found for blades without tip gap.

Although the departure $\Delta \delta^*$ from a linear increase is a somewhat crude measure for operating points for which the leakage vortex is situated close to the blade inlet or exit plane (close to stall or near choke) this additional displacement creates diffusion in the rear part of the blade passage and is effective in describing the loading increase induced by the tip leakage vortex.

Analysis

Approach. Important parameters driving tip leakage flow are known to be tip gap height, inlet Mach number, profile section Mach number type, blade geometry, inlet boundary layer thickness and leakage jet total pressure; see Khalid et al. [11]. In the following the tip gap height, inlet Mach number, stagger angle, and a diffusion factor DR as loading parameter

$$DR = 1 - (w_2/w_1) + \Delta w_\theta / (2w_1) \cdot (s/c) \quad (4)$$

$$\Delta w_\theta = |w_1 \cos(\beta_1) - w_2 \cos(\beta_2)|$$

are used to establish a correlation for the additional displacement by tip leakage flow, i.e., the deviation of the displacement thickness from a linear increase between rotor in- and outlet plane; see Eq. (3b) and Fig. 4 (top). The correlation is based on a maximum value $\Delta \delta_m^*$, which controls a universal functional dependency, the tip leakage blockage or tip leakage displacement transition function. The correlation is established by introducing influence functions, which are used to correct the individual results for $\Delta \delta_m^*$. The influence functions are deduced either directly from the calculations (for the tip gap width) or by assuming functional dependencies (Mach number and stagger), with constants to be adapted to achieve a correlation for the additional displacement thickness as a function of the loading parameter.

Influence Functions.

Tip Gap Width. Rotor results for $\Delta \delta_m^*$ as well as those of predictions for a stator cascade¹ (normalized by the rotor values for 1 percent gap) are given in Fig. 5. A small additional displacement found for zero clearance is neglected and a linear dependency on gap/chord ratio (true chord) is assumed:

$$\Delta \delta_m^* \sim Fh = (h/c)/0.01 \quad (5)$$

Stagger. With the assumption of a nonviscous leakage flow [7], Bernoulli's equation may be applied to the flow at the tip gap. This assumption results in a leakage flow velocity equal to the inlet velocity $w_{t1} \approx w_1$. For low velocities at the pressure surface, the leakage jet is roughly normal to the blade chord. Figure 6 shows the average leakage flow vector, the circumferential component of which does not contribute to mass transport. The com-

¹Investigations were performed as part of a diploma thesis by A. Burgan, Univ. Valenciennes/MTU-DASA.

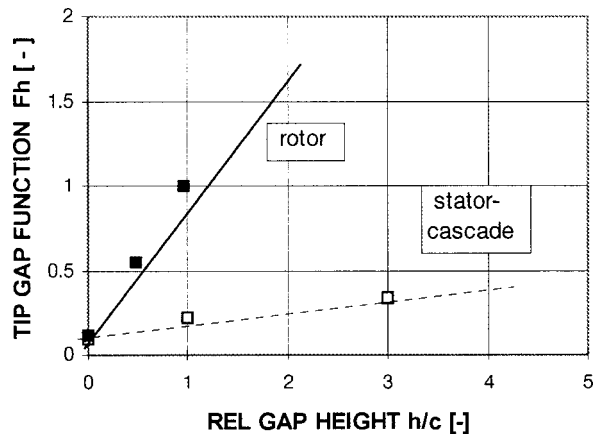


Fig. 5 Tip gap influence function F_h

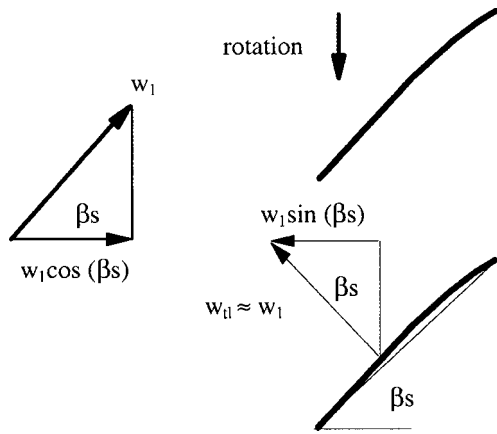


Fig. 6 Average tip leakage flow vector at the blade tip

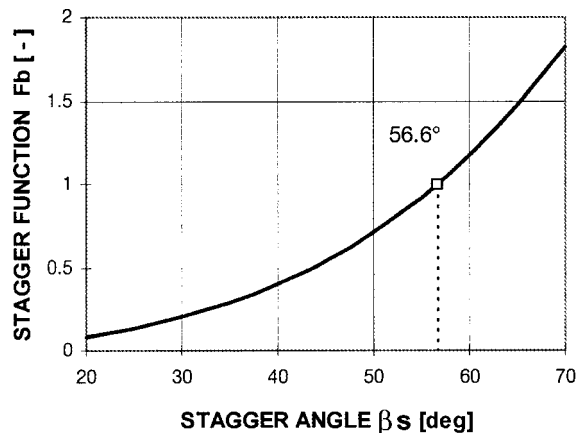


Fig. 7 Stagger angle influence function F_b

ponent $w_1 \sin(\beta_s)$, directed axially upstream, reduces the overall mass transport and increases the displacement at the casing. With the axial component $w_1 \cos(\beta_s)$ of the main flow directed opposite, the influence of the stagger angle on $\Delta \delta^*$ may be described by a functional dependency; see Fig. 7, of the type

$$\Delta \delta_m^* \sim F_b = t g^n(\beta_s) c_1 + c_2. \quad (6)$$

Best correlation was achieved (see following chapter) with the constants in Eq. (6) chosen to be $n=2$, $c_1=1.5$ and $c_2=0.35$.

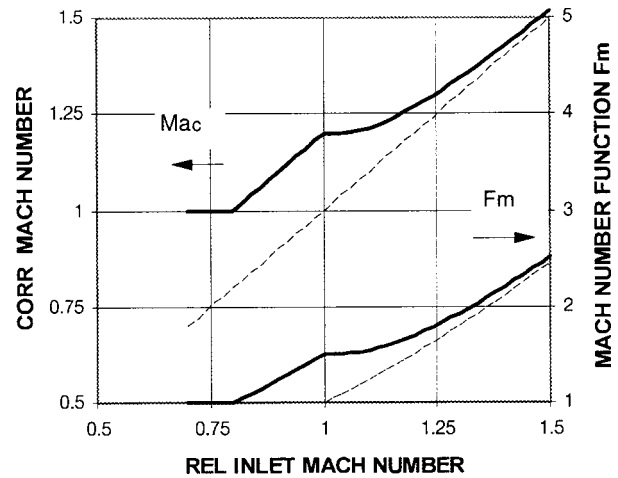


Fig. 8 Corrected preshock Mach number and normal shock pressure ratio

Mach Number. The blockage and loading parameter introduced by Khalid [13] was found to contain a Mach number dependence in an indirect manner; see predictions of Suder [16] for NASA rotor 37. Puterbaugh and Brendel [10] identified the shock-induced pressure rise as one of the prime variable for the local blockage. Similar to two-dimensional profile losses, the additional displacement generated by the shock/vortex interaction is supposed to be linked with the pressure ratio of a normal shock with a relative inlet Mach number Ma_{1c} .

$$\Delta \delta_m^* \sim F_m = (1 + 2\kappa/(\kappa + 1) \cdot (Ma_{1c}^2 - 1)) c_3 \quad (7)$$

with the constant $c_3 = 1$ to fit best for the correlation presented in the next section. For Mach numbers close to unity a correction is applied; see Fig. 8 and Schreiber [17]:

$$Ma_{1c} = \max(Ma_1; 0.8) + 0.2/\max(1; Ma_1^3). \quad (7b)$$

Reference Conditions. With the aid of Eqs. (5)–(7) all results are corrected for the reference conditions of a rotor with $Ma_1 = 0.8$, i.e., no shock losses, a stagger angle of 56.6 deg, and a tip gap of 1 percent chord (at these conditions we have $F_b = 1$, $F_h = 1$, $F_m = 1$) by

$$\Delta \delta_{m,corr}^* = \Delta \delta_m^* / (F_b F_h F_m) \quad (8)$$

with the constants in Eqs. (6) and (7) determined iteratively to establish a correlation for $\Delta \delta_{m,corr}^*$ as a function of the loading parameter. Although based on reasonable assumptions, this procedure is only justified by the correlation itself. Neither the Mach number nor the stagger dependence is based on a proven relationship.

Maximum Additional Displacement Correlation

Rotors. Simulations have been performed for a total of 15 rotors and two stator configurations. The design rotor parameters covered a range of stage number 1 to 4 with stagger angle $\beta_s = 47.4$ to 66.2 deg, inlet Mach number $Ma_1 = 0.81$ to 1.61, diffusion factors $DR = 0.28$ to 0.65, relative clearance $h/c = 0.1$ to 1.76, and inlet boundary layer thickness $\delta_{1c}^*/c_{ax} = 2$ to 14 percent.

Stators. A strong influence of the stagger on leakage flow behavior was already indicated in Fig. 5. In addition, radial migration of low-energy fluid due to spanwise pressure gradients and due to rotation may have a significant influence on block-age generation in highly loaded transonic rotors. For the stator cascade, as well as for a cantilevered stator (not presented here), the addi-

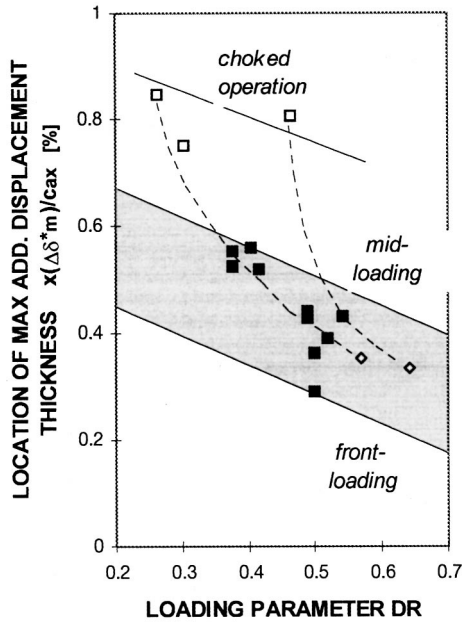


Fig. 9 Location x/c_{ax} of the maximum additional displacement thickness from tip leakage

tional displacement thickness was found to be one order smaller in magnitude than for the rotors. Only rotor results will therefore be presented on the following pages.

In Fig. 9, a strong dependence of the location of the displacement maximum on the loading is only found close to choked conditions, while in the remaining operation range the maximum is located between 55 and 35 percent chord.

A broad scatter for the original data reflects the influence of the different rotor designs, Fig. 10 (right). When corrected with the influence functions due to Eq. (8), the results for the corrected additional displacement thickness $\Delta\delta_{m,corr}^*$ fall on a small band and a weak correlation is obtained, Fig. 10 (left). Beginning at choked flow conditions $\Delta\delta_{m,corr}^*$ rises rapidly, see broken line in Fig. 10 (left), and is nearly independent of the loading at design conditions and close to stall. An opposite behavior was observed by Khalid et al. [11] for the total blockage increase, with his blockage parameter to grow rapidly when a critical value of the loading parameter is approached. Neglecting values at choked flow conditions, all data may be approximated by an error of ± 25

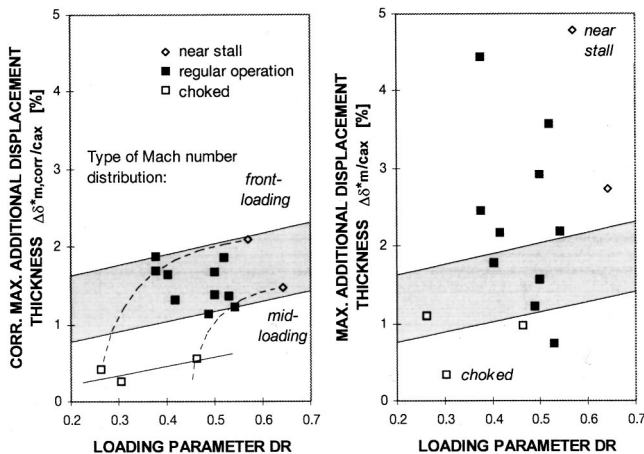


Fig. 10 Maximum additional displacement $\Delta\delta^*_s$ in percent c_{ax} : (right) original data; (left) correlation in Eq. (8)

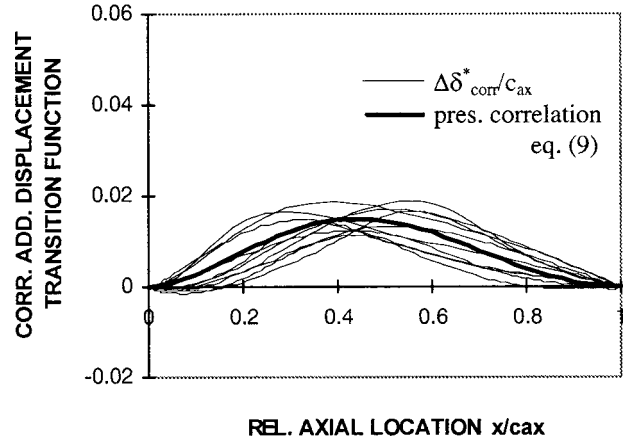


Fig. 11 Transition function for the corrected additional displacement thickness $\Delta\delta^*_s,corr(x)/c_{ax}$

percent by an average value of $\Delta\delta_{m,corr}^*/c_{ax} = 1.5$ percent for all loading levels. A maximum of $\Delta\delta_{m,corr}^*/c_{ax} = 2$ percent is not exceeded. Higher values are found only for an untypical rotor design, with an artificially increased pre-shock Mach number.

Displacement or Blockage Transition Function. With the aid of the maximum displacement correlation, Eq. (8), the variation of the additional displacement thickness within the blade passage may be corrected. The resulting curves in Fig. 11 show a common trend, but the influences of the type of blade section design and operating condition is still visible. A good estimate for the transition function is:

$$(\Delta\delta^*(x)/\Delta\delta_m^*)_{corr} = (\cos(x/c_{ax} \cdot c_4 - 1)\pi + 1)/2. \quad (9)$$

Within the two operation limits ‘‘close to stall’’ and ‘‘close to choke’’ average values of $\Delta\delta_{m,corr}^* = 0.015$ and $c_4 = 0.85$ are found to fit best. The type of loading distribution, which represents a basic design decision, may be taken into account more accurately by specifying $c_4 = 0.7$ and $c_4 = 1.1$ for designs with front loading or for those ‘‘close to choke,’’ respectively.

Stall Inception. The correlation given above indicates for the additional displacement generated by the leakage vortex an approximately constant maximum value with only little dependency on the blade loading. It can be seen for the TU-Darmstadt transonic rotor in Fig. 12 (top), that the displacement thickness at the rotor inlet first remains unchanged although the displacement at the throat increases with loading, while for higher loading levels a linear dependency is observed. For geometric details on the rotor see Fritsch et al. [6]. The opposite behavior is found for the additional displacement $\Delta\delta_m^*$, which first increases with blade loading and then keeps constant; see Fig. 12 (bottom). This behavior indicates that with sufficient blockage generated by the vortex/shock interaction, a deceleration of the flow already in front of the blocked region occurs. Hereby the streamlines are shifted inward from the casing and the displacement thickness now increases already in front of the rotor. Close to the throat, the additional displacement by the leakage vortex and the diffusion generated by it is allowed to remain constant or even decreases with blade loading until stall is reached.

In accordance with these findings, Bross et al. [18] for an axial pump with high stagger observed the position of a separation line on the casing first to travel upstream gradually with loading until it is found in a short distance upstream the rotor inlet plane. At stall the separation line was shifted to a location several axial chords upstream the rotor. Applying the stall criterion suggested by Smith [19] we find a displacement thickness critical for stall at

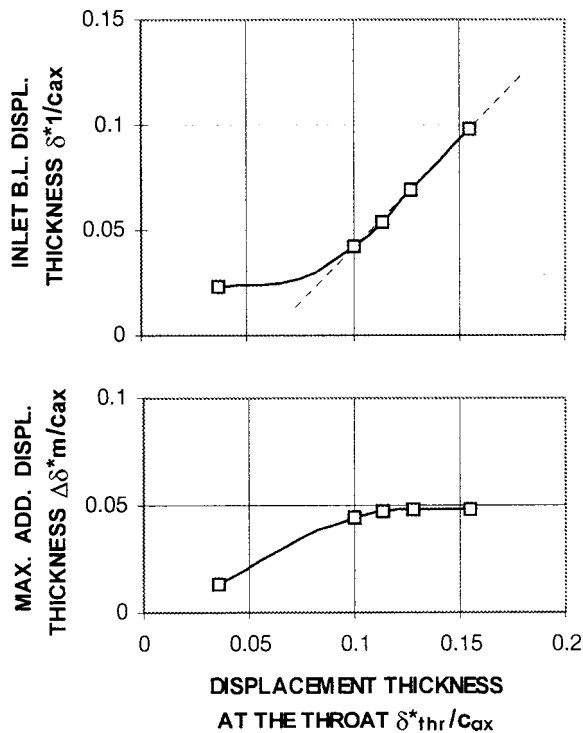


Fig. 12 Displacement thickness δ^*_1/c_{ax} at the rotor inlet (top) and additional displacement thickness $\Delta\delta^*_m/c_{ax}$ (bottom) as a function of the displacement thickness at the throat; TU-Darmstadt compressor rig

the rotor inlet of $\delta^*_1/c_{ax} = 0.181$. Actually the simulation yielded a value of 0.1 at stall, which may be explained by the higher blockage generated from shock/vortex interaction.

Application

Meridional Flowpath Boundary Layer Method. The end-wall boundary layer method of Hirsch (see [20]), is used to demonstrate the present approach. Pitch-averaged, boundary layer equations with blade force defect terms are solved. The variation of the blade loading in the boundary layer, the pressure gradient, and secondary flow effects are taken into account [21].

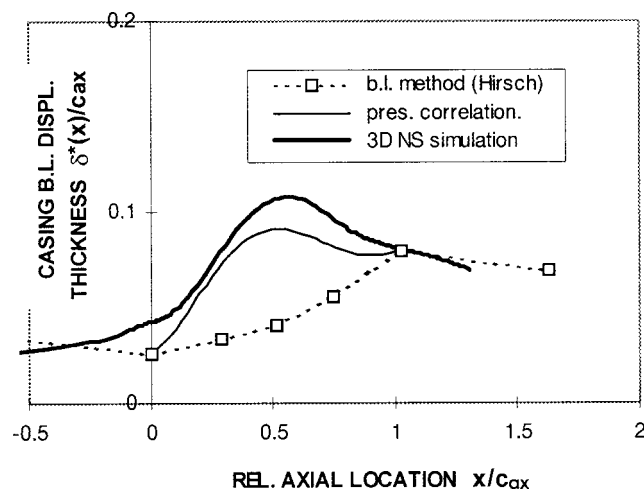


Fig. 13 Application of the present correlation to the TU-Darmstadt transonic compressor; design conditions

Improved Blockage Model. End-wall boundary layer predictions were performed with the pressure distribution from an S2-design calculation as input and the displacement thickness at the trailing edge prescribed (in an iterative manner). Although somewhat too low values are found in front of the rotor compared to the three-dimensional results, the total increase in displacement between in- and outlet is predicted with good accuracy, Fig. 13, but inside the blade passage the boundary layer method underestimates the results of the three-dimensional Navier–Stokes simulations by far.

An improved prediction is obtained by combining the displacement thickness predicted by the boundary layer code at the rotor in- and outlet stations with the present correlation, Eq. (3b). From Eq. (9) the universal transition function is obtained for the additional displacement thickness. The actual values for an individual blade are then calculated, applying the influence functions due to Eq. (8). With the present approach the predictions from the boundary layer method are improved by up to 100 percent within the blade passage and the modified results are in closer agreement with the Navier–Stokes result in Fig. 13.

Conclusions

Simulations are performed with a steady three-dimensional multistage Navier–Stokes code TRACE_S for several transonic compressor rotors. From pitch-averaged results, the displacement at the casing generated by the tip leakage vortex is evaluated by a new technique. The problem in defining an end-wall boundary layer displacement thickness inside the blade passage is split into a total linear displacement increase between rotor in- and outlet approximately found for zero tip gap width and an additional displacement from tip leakage flow. A linear variation of the displacement thickness due to viscous entrainment and work input with the axial distance is assumed. The additional displacement in the blade passage may now be evaluated even in nonisoenergetic flow by a streamline integration.

The results reveal a region with axially reversed flow induced by the leakage vortex, generating an additional displacement or blockage. Based on stagger angle, inlet Mach number, clearance height, and the diffusion factor as loading parameter, a correlation for the additional displacement by tip leakage flow is established. For unchoked operation and the reference conditions of a rotor with a stagger angle of 56.6 deg, 1 percent chord tip gap width and zero shock strength, a maximum additional displacement of about 1.5 percent axial chord is predicted with only a weak dependence on the loading parameter. A transition function of sinus shape is found to fit best with the average data.

Starting at choked conditions, the additional displacement from tip leakage flow increases with loading and the location of its maximum travels upstream until the throat area is decreased. Now streamlines are forced to travel radially inward from the casing in front of the rotor. A downstream influence stems from the fact that the additional displacement creates diffusion and thereby increases the blockage at the rotor exit plane. Close to stall, a further increase in loading is demonstrated mainly to increase displacement and deceleration in front of the rotor, while the additional displacement in the blade passage is allowed to remain approximately constant.

Acknowledgments

Support for code development and validation through the German Ministry of Education and Research under contract numbers 20T9402 of the E3E program and 0327040J of the AG Turbo program is gratefully acknowledged. The authors would also like to thank Dr. G. Ramm MTU München GmbH for his assistance in post-processing the numerical data.

The code was jointly developed by MTU München GmbH and the Institute for Propulsion Technology of the German Aerospace Research Establishment (DLR).

Nomenclature

| | |
|------------------|---|
| c, c_{ax} | = chord, axial chord |
| F_m, F_b, F_h | = influence functions, Eqs. (5)–(7) |
| h | = tip gap width |
| s | = spacing |
| Ma_1 | = inlet Mach number (relative frame) |
| DR | = diffusion factor, Eq. (4) |
| x, r, θ | = cylindrical coordinates |
| w | = velocity (relative frame) |
| δ^*_{ar} | = displacement from axial flow reversal |
| δ^* | = displacement thickness, Eq. (2) |
| δ^*_s | = displacement by inlet casing b.l. streamline |
| $\Delta\delta^*$ | = additional displ. by tip leakage flow, Eq. (3b) |
| βs | = stagger angle, deg |

Subscripts

| | |
|------|--|
| 1, 2 | = rotor in- and outlet plane |
| corr | = corrected for a reference rotor, Eq. (8) |
| cas | = location at the outer casing |
| tl | = tip leakage flow |

References

- [1] Adamczyk, J. J., Celestina, M. L., and Greitzer, E. M., 1993, "The Role of Tip Clearance in High-Speed Fan Stall," *ASME J. Turbomach.*, **115**, pp. 28–39.
- [2] Copenhaver, W. W., Hah, C., Mayhew, E., and Wadia, A. R., 1996, "The Effect of Tip Clearance on a Swept Transonic Compressor Rotor," *ASME J. Turbomach.*, **118**, pp. 230–239.
- [3] Jennions, I. K., and Turner, M. G., 1993, "Three-Dimensional Navier–Stokes Computations of Transonic Fan Flow Using an Explicit Flow Solver and an Implicit $k-\epsilon$ Solver," *ASME J. Turbomach.*, **115**, pp. 261–272.
- [4] Suder, K. L., and Celestina, M. L., 1996, "Experimental and Computational Investigation of the Tip Clearance Flow in a Transonic Axial Compressor Rotor," *ASME J. Turbomach.*, **118**, pp. 218–230.
- [5] Blaha, C., Hennecke, D. K., Fritsch, G., Hoeger, M., and Beversdorff, M., 1997, "Laser-2-Focus Measurements in a Transonic Compressor Blisk-Rotor and Comparison With 3D Numerical Simulations," ISABE Paper No. 97-7069.
- [6] Fritsch, G., Hoeger, M., Blaha, C., and Bauer, D., 1997, "Viscous 3D Compressor Simulation on Parallel Architectures," AIAA Paper No. 97-2876.
- [7] Storer, J. A., and Cumpsty, N. A., 1991, "Tip Leakage Flow in Axial Compressors," *ASME J. Turbomach.*, **113**, pp. 252–259.
- [8] Storer, J. A., and Cumpsty, N. A., 1994, "An Approximate Analysis and Prediction Method for Tip Clearance Loss in Axial Compressors," *ASME J. Turbomach.*, **116**, pp. 648–656.
- [9] Chen, G. T., Greitzer, E. M., Tan, C. S., and Marble, F. E., 1991, "Similarity Analysis of Compressor Tip Clearance Flow Structure," *ASME J. Turbomach.*, **113**, pp. 260–271.
- [10] Puterbaugh, S. L., and Brendel, M., 1997, "Tip Clearance Flow-Shock Interaction in a Transonic Compressor Rotor," *J. Propul. Power*, **13**, No. 1, pp. 24–30.
- [11] Khalid, S. A., Khalsa, A., Waitz, I., Tan, C., Greitzer, E., Cumpsty, N., Adamczyk, J., and Marble, F., 1999, "Endwall Blockage in Axial Compressors," *ASME J. Turbomach.*, **121**, pp. 499–509.
- [12] Khalsa, A. S., 1996, "Endwall Blockage in Axial Compressors," Ph.D. Thesis, Department of Aeronautics and Astronautics, Massachusetts Institute of Technology.
- [13] Khalid, S. A., 1995, "The Effects of Tip Clearance on Axial Compressor Pressure Rise," Ph.D. Dissertation, Massachusetts Institute of Technology.
- [14] Hoeger, M., Fritsch, G., and Bauer, D., 1999, "Numerical Simulation of the Shock-Tip Leakage Vortex Interaction in a HPC Front Stage," *ASME J. Turbomach.*, **121**, pp. 456–468.
- [15] Fritsch, G., and Möhres, W., 1997, "Multistage Simulations for Turbomachinery Design on Parallel Architectures," Proc. 9th Parallel CFD Conf., Manchester, UK.
- [16] Suder, K., 1998, "Blockage Development in a Transonic, Axial Compressor Rotor," *ASME J. Turbomach.*, **120**, pp. 465–477.
- [17] Schreiber, H. A., 1988, "Shock Losses in Transonic and Supersonic Compressor Cascades," VKI Lecture Series LS 88-03 "Transonic Compressor," Brussels/Belgium, Feb. 1–5.
- [18] Bross, S., Brodersen, S., Saathoff, H., and Stark, U., 1997, "Experimental and Theoretical Investigation of the Tip Clearance Flow in an Axial Flow," 2nd European Conference on Turbomachinery Fluid Dynamics and Thermodynamics, Antwerp, Belgium.
- [19] Smith, L. H., 1970, "Casing Boundary Layers in Multistage Axial-Flow Compressors," *Flow Research in Blading*, L. S. Dzung, ed., Elsevier, Amsterdam.
- [20] De Ruyck, J., Hirsch, C., and Kool, P., 1979, "Investigations on Axial Compressor End-Wall Boundary Layer Calculations," Proc. Int. Joint Gas Turbine Congress and Exhibition, Israel.
- [21] De Ruyck, J., and Hirsch, C., 1981, "Investigations of an Axial Compressor End-Wall Boundary Layer Prediction Method," *ASME J. Eng. Power*, **103**, No. 2.

Douglas P. Probasco

Tim J. Leger

J. Mitch Wolff

Department of Mechanical & Materials
Engineering,
Wright State University,
Dayton, OH 45435

William W. Copenhaver

Air Force Research Laboratory,
Wright-Patterson Air Force Base, OH 44135

Randall M. Chriss

NASA Glenn Research Center,
Cleveland, OH 43210

Variations in Upstream Vane Loading With Changes in Back Pressure in a Transonic Compressor

Dynamic loading of an inlet guide vane (IGV) in a transonic compressor is characterized by unsteady IGV surface pressures. These pressure data were acquired for two spanwise locations at a 105 percent speed operating condition, which produces supersonic relative Mach numbers over the majority of the rotor blade span. The back pressure of the compressor was varied to determine the effects from such changes. Strong bow shock interaction was evident in both experimental and computational results. Variations in the back pressure have significant influence on the magnitude and phase of the upstream pressure fluctuations. The largest unsteady surface pressure magnitude, 40 kPa, was obtained for the near-stall mass flow condition at 75 percent span and 95 percent chord. Radial variation effects caused by the spanwise variation in relative Mach number were measured. Comparisons to a two-dimensional nonlinear unsteady blade/vane Navier–Stokes analysis show good agreement for the 50 percent span results in terms of IGV unsteady surface pressure. The results of the study indicate that significant nonlinear bow shock influences exist on the IGV trailing edge due to the downstream rotor shock system. [S0889-504X(00)00303-2]

Introduction

Gas turbine engines are a vital energy source for both industrial and military applications. Recent research has focused on identifying the flow mechanisms that produce high cycle fatigue (HCF) failures in these engines. There is a need for an improved understanding of the flow physics that drive failures in engine components. This greater understanding will lead to the ability of manufacturers to achieve higher levels of performance and, in general, a more efficient and reliable system. There are continually increasing demands on gas turbine engines for greater durability, reduced noise levels, reduced size, and greater thrust. Durability has become a major parameter in component design. Designing compression system components resistant to HCF failure is critical to capitalize on technology improvements. A considerable portion of recent research involves the unsteady interaction between adjacent blade rows, which drives HCF in both the compressor and turbine sections.

The two principal types of blade row interaction are usually referred to as potential flow and wake interactions [1]. Potential flow interaction results from the variations in the velocity potential or pressure fields associated with the blades of a neighboring row and their effect upon the blades of a given row moving at a different rotational speed. This type of interaction is of serious concern when the axial spacing between adjacent blade rows is small or the flow Mach number is high. Wake interaction is the effect upon the flow through a downstream blade row of the vortical and entropic wakes shed by one or more upstream rows.

Recently, computational work has been initiated to develop nonlinear, time-accurate, inviscid (Euler) and viscous (Navier–Stokes) solution techniques for unsteady flows through isolated and aerodynamically coupled blade rows (see Verdon [1] for a review). For coupled systems of rotating and stationary blade rows, the relative motions between adjacent rows give rise to

unsteady aerodynamic excitations, which can initiate blade vibrations, generate discrete-tone noise, and degrade aerodynamic efficiency.

Some experimental investigations for compression systems have been made into vane/blade interactions. For compressors, initial research was accomplished using low-speed rigs [2] or annular cascades [3]. The low speed and large scale of these experimental rigs simplifies the measurements, but transonic flow phenomena, i.e., shock interaction, cannot be modeled. Recently, high-speed axial compressor research has been initiated. These facilities are beneficial for testing actual hardware components with research issues including miniature measurement techniques and data reduction methods. In particular, Johnston and Fleeter [4–6] have used a transonic compressor facility to investigate rotor wake phenomena, IGV/rotor potential fields, and rotor surface pressures using pressure sensitive paints. These research studies have provided an important initial step toward understanding the basic physics of the unsteady aerodynamic flow interactions in a compression system, but additional research is required.

The objective of this research is to investigate and quantify the fundamental vane/blade interaction phenomena relevant to the upstream bow shock forcing function of a downstream rotor in a transonic compression system. This is accomplished by performing a series of experiments in the Compressor Aero Research Lab (CARL), a high-speed, highly loaded compressor facility. IGV unsteady surface pressures are experimentally determined for different back pressures for a transonic operating point. In addition, a nonlinear, unsteady, fully viscous multiblade row computational fluid dynamics (CFD) analysis is compared with the experimental data. The CFD code utilized is entitled Vane/Blade Interaction (VBI), which solves the full Navier–Stokes equations through the use of a Runge–Kutta scheme along with the Baldwin–Lomax model for turbulence [7]. The study presented here will show: (1) Bow shock influences from a downstream transonic stage are significant; (2) the bow shock influence grows with increased stage back pressure; (3) the influence can be adequately modeled with an unsteady, nonlinear Navier–Stokes analysis; (4) the bow shock influence of a transonic rotor varies with span and must be mod-

Contributed by the International Gas Turbine Institute and presented at the 43rd International Gas Turbine and Aeroengine Congress and Exhibition, Stockholm, Sweden, June 2–5, 1998. Manuscript received by the International Gas Turbine Institute February 1998. Paper No. 98-GT-344. Associate Technical Editor: R. E. Kielb.

eled accordingly, and (5) higher-order harmonic content of unsteady surface pressures is significant and important for transonic vane/blade analyses.

Research Facility

Compressor Aero Research Lab (CARL). The experiments for this study were conducted in the Air Force Research Laboratory's Compressor Aero Research Lab facility at Wright-Patterson Air Force Base. The research compressor is a high-speed, highly loaded 1 1/2 stage compression system. The compressor facility consists of an open or closed-loop (currently open) tunnel system with an upstream venturi flow meter to measure the mass flow rate. The compressor is driven by a 1490 kW electric motor with a variable speed range of 6000 to 21,500 rpm.

The research compressor, Fig. 1, was designed to simulate the second stage of a highly loaded military core compressor. Wakes from a first stage are simulated by an upstream blade row. The primary intent for this research compressor is to investigate the influence of an upstream stage on the flow swallowing capability of a downstream transonic stage. Details on the compressor design are defined by Law [8] and are summarized in Table 1.

To study the effect of different upstream stages, an IGV assembly is placed upstream of the rotor section. The IGV's were designed to create a wake consistent with a modern technology, highly loaded, low aspect ratio stage. Therefore, they have a wide trailing edge, as shown in Fig. 2. The IGV's do not turn the flow as would a normal IGV assembly. They have a constant solidity

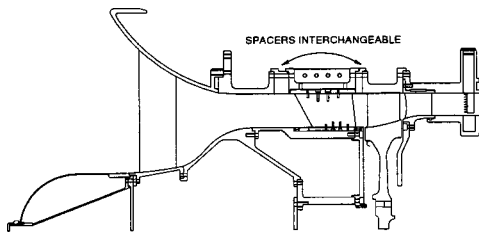


Fig. 1 Schematic of SMI compressor rig

Table 1 Compressor design parameters

| PARAMETER | ROTOR | STATOR |
|---------------------------------------|--------|--------|
| Number of Airfoils | 33 | 49 |
| Aspect Ratio - Average | 0.961 | 0.892 |
| Inlet Hub/Tip Ratio | 0.750 | 0.816 |
| Flow/Annulus Area, kg/sec | 18.14 | -- |
| Flow/Unit Area, kg/sed/m ² | 0.738 | -- |
| Flow rate, kg/sec | 15.63 | -- |
| Tip Speed, Corrected m/sec | 341.4 | -- |
| M _{REL} LE Hub | 0.963 | 0.820 |
| M _{REL} LE Tip | 1.191 | 0.690 |
| PR Rotor | 1.880 | -- |
| η_{iso} Rotor, % | 93.5 | -- |
| PR Stage | -- | 1.840 |
| η_{iso} Stage, % | -- | 90.2 |
| D Factor Hub | 0.545 | 0.502 |
| D Factor Tip | 0.530 | 0.491 |
| LE Tip Dia., m | 0.4826 | 0.4826 |
| LE Hub Dia., m | 0.3620 | 0.3928 |
| TE Tip Dia., m | 0.4826 | 0.4826 |
| TE Hub Dia., m | 0.3872 | 0.4038 |

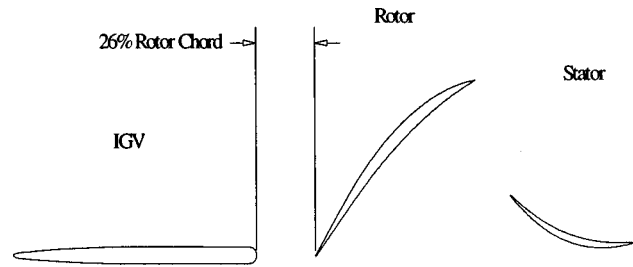


Fig. 2 Flow path through SMI compressor rig

(spacing to chord ratio) along the span and have no steady aerodynamic loading in order to achieve a uniform two-dimensional wake. There are 24 IGV's in the upstream passage. The axial spacing between the IGV blades trailing edge and the rotor leading edge is 26 percent of the IGV chord.

IGV Surface Pressure Instrumentation. The IGV's are instrumented with miniature Kulite pressure transducers. Figure 3 shows the locations of these pressure transducers. Two different blades are instrumented with ten pressure transducers each. To investigate spanwise effects, two different spanwise locations are instrumented, 50 and 75 percent as shown measured from the hub. A picture of the actual mounted transducers for one blade is shown in Fig. 4. The blade surface is machined to allow the pressure transducers to be mounted flush. To protect the pressure sensor, a thin layer of RTV was placed over the diaphragm. Grooves for the lead wires were also machined to ensure no disturbance to the flow. The lead wires are bundled and fed out of the casing.

Two adjacent IGV's are instrumented, giving data for one flow passage. Flow periodicity is assumed with one blade's data phase shifted to the other blade for analysis.

LQ-125 miniature pressure transducers from Kulite are used for the surface pressure measurements. These transducers were designed to measure absolute pressure up to 172.4 kPa. The pressure transducers are manufactured directly on the blades with a pressure sensing element 0.1524 cm in diameter. It has an internally compensated temperature range of -1.1 to 54.44°C . The natural frequency of the pressure transducer is specified as 300 kHz, giving a usable frequency range of 100 kHz.

Calibration of the transducers for sensitivity and offset was achieved through bench tests. Before installation of the instrumented IGV, the transducers were subjected to variable pressures at a nominal temperature of 21.1°C and an elevated temperature of 43.3°C . The results of this study indicated, for this range of temperature variation, a transducer sensitivity of 0.02 percent per

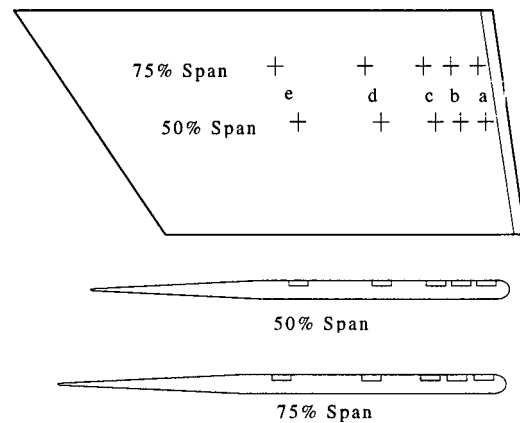


Fig. 3 Transducer locations on IGV: (a) 95, (b) 89, (c) 83, (d) 70, (e) 50 percent IGV chord

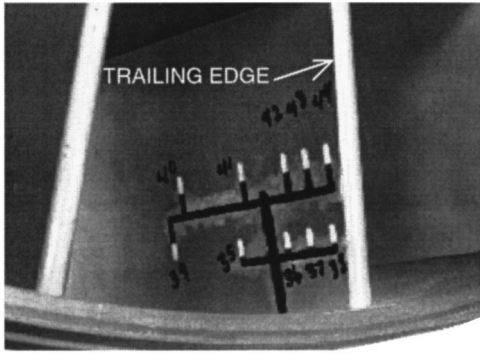


Fig. 4 Actual transducer application on IGV

degree C. However, the offset was influenced by temperature variation and the magnitude of the shift varied from a high of 0.2516 kPa/°C to a low of 0.0148 kPa/°C.

Based on this bench calibration, no special procedures were established to control sensitivity with inlet air temperature shifts. However, to control transducer offset variation, the transducers' amplifiers were rebalanced at atmospheric conditions for any inlet temperature shift of 1.4°C or greater.

From these bench procedures, offset and precision errors were established as ± 0.414 kPa and ± 0.276 kPa, respectively. In addition, during the experiment, a zero response data set was recorded. The data were then processed in the same manner as the actual test data. This signal is representative of the static pressure uncertainty due to system noise influences. Based on all of the above-described calibration and operating procedures, the measured random uncertainty was ± 0.689 kPa. This value includes all errors due to random noise and temperature changes.

Computational Analysis

A nonlinear unsteady Euler/Navier–Stokes vane blade interaction model, VBI 2D, was developed by Rao and Delaney [9], under sponsorship of the Air Force, for turbine configurations. This model analyzes the relative motion of adjacent blade rows by allowing one row to move with respect to the other. The VBI code is utilized for the IGV/rotor interaction in the compressor by modeling both the IGV and rotor. A brief overview of the VBI code will now be given.

Grid Generation. Two separate grids are generated, and **H** and **O** grid, for each blade row. The two grids are then embedded to form a composite grid by a chimera method called PEGSUS [10]. PEGSUS creates the appropriate hole boundaries and interpolation stencils involved in the communication of embedded grids. The embedding process eliminates problems with cell skewness near the leading and trailing edges of the airfoils. The transition from the inflow and outflow boundaries to the airfoil leading and trailing edges causes this problem. The PEGSUS results are read directly into the VBI code.

Numerical Method. The VBI code solves the Euler/Navier–Stokes equations using an explicit Runge–Kutta scheme in quasi-three-dimensional space. Figure 5 represents the coordinate system used in the formulation [7]. The Baldwin–Lomax [11] model for turbulence and transition is utilized within the code. The governing equations for flow on a blade-to-blade surface of revolution will now be given [7]:

$$\frac{\partial Q}{\partial t} + \frac{\partial E}{\partial m} + \frac{\partial F}{\partial \theta} = H \quad (1)$$

where:

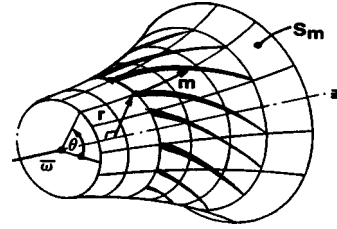


Fig. 5 Coordinate system used in VBI formulation

$$H = H_i - H_v + \frac{\partial E_v}{\partial m} + \frac{\partial F_v}{\partial \theta}$$

$$Q = rb \begin{bmatrix} \rho \\ \rho u \\ \rho v \\ \rho e \end{bmatrix} \quad E = rb \begin{bmatrix} \rho u \\ \rho u^2 + p \\ \rho uv \\ u(\rho e + p) \end{bmatrix}$$

$$F = b \begin{bmatrix} \rho v \\ \rho uv \\ \rho v^2 + p \\ v(\rho e + p) \end{bmatrix} \quad E_v = \frac{rb}{\text{Re}} \begin{bmatrix} 0 \\ \sigma_{11} \\ \sigma_{12} \\ E_4 \end{bmatrix}$$

$$F_v = \frac{b}{\text{Re}} \begin{bmatrix} 0 \\ \sigma_{12} \\ \sigma_{22} \\ F_4 \end{bmatrix} \quad H_i = rb \begin{bmatrix} 0 \\ (\rho v^2 + p) \frac{1}{r} \frac{dr}{dm} + p \frac{1}{b} \frac{db}{dm} \\ -\rho uv \frac{1}{r} \frac{dr}{dm} \\ 0 \end{bmatrix}$$

$$H_v = \frac{rb}{\text{Re}} \begin{bmatrix} 0 \\ \sigma_{22} \frac{1}{r} \frac{dr}{dm} + \sigma_{33} \frac{1}{b} \frac{db}{dm} \\ -\sigma_{12} \frac{1}{r} \frac{dr}{dm} \\ 0 \end{bmatrix}$$

The following equations represent the energy components:

$$e = \frac{p}{\rho(\gamma-1)} + \frac{1}{2}(u^2 + v^2) \quad (2)$$

$$E_4 = u\sigma_{11} + v\sigma_{12} + \frac{1}{\gamma-1} \frac{\mu}{\text{Pr}} \frac{\partial a^2}{\partial m} \quad (3)$$

$$F_4 = u\sigma_{12} + v\sigma_{22} + \frac{1}{\gamma-1} \frac{\mu}{\text{Pr}} \frac{1}{r} \frac{\partial a^2}{\partial \theta} \quad (4)$$

where E_4 and F_4 are the viscous terms from the energy equation. It is now necessary to represent the shear stress equations:

$$\sigma_{11} = 2\mu \frac{\partial u}{\partial m} + \lambda \nabla \cdot V \quad (5)$$

$$\sigma_{12} = \mu \left(\frac{\partial v}{\partial m} - \frac{v}{r} \frac{dr}{dm} + \frac{1}{r} \frac{\partial u}{\partial \theta} \right) \quad (6)$$

$$\sigma_{22} = 2\mu \left(\frac{1}{r} \frac{\partial v}{\partial \theta} + \frac{u}{r} \frac{dr}{dm} \right) + \lambda \nabla \cdot V \quad (7)$$

$$\sigma_{33} = 2\mu \frac{u}{b} \frac{db}{dm} + \lambda \nabla \cdot V \quad (8)$$

For this analysis, it is assumed that Stokes' hypothesis is true. For turbulent results, the viscosity is represented in an appropriate form. The laminar and turbulent viscosities are accounted for with the turbulent viscosity found from the Baldwin-Lomax eddy-viscosity model.

Boundary Conditions. Nonreflective inflow and outflow boundary conditions are utilized for the **H**-grids with a reference plane method of characteristics scheme. For the **O**-grids, the reference planes are inherently nonparallel due to the fact that they are conforming to the airfoil shapes. It is then necessary for the VBI code to set the reference planes parallel to each other and perpendicular to the inflow boundary. This allows for the reference plane method of characteristics scheme to be utilized successfully at these boundary points. As the blade moves relative to the vane with the progression of a time step, the information from the previous time step is used to define the necessary vane outflow or blade inflow boundaries.

A phase-lagged technique is utilized for the blade to blade periodic boundary conditions. The computation is performed on one vane or blade from each row at a time. The solution fields for adjacent vanes or blades are stored for the use in the phase-lagging procedure [7].

An overlapping of the **H**-grids at the vane outlet and blade inlet allows for information to be passed from one row to another. At least three cells must overlap for accurate information exchange. A bilinear interpolation method is used to transfer the data from the IGV **H**-grid to the rotor **H**-grid to find the necessary boundary conditions.

Results

A series of experiments were performed to investigate the IGV unsteady surface pressure response due to the upstream traveling pressure field generated by the downstream rotor. The stage back pressure was varied by exit area changes and the IGV response measured at two spanwise positions. A computational study was then completed utilizing the VBI code with comparisons made to the experimental data.

Experimental. The experimental data were recorded on a 28 channel analog tape recorder with a flat response up to 80 kHz. The data were digitized off-line at an effective sample rate of 500 kHz by reducing the tape playback speed by one quarter and sampling at 125 kHz. Anti-aliasing was achieved using a Precision Filters TD6B Linear Phase Time Delay Filter. An effective cutoff frequency of 132 kHz was used for the data reduction. This gives a 1 percent attenuation of the signal at 77 kHz. The blade pass frequency is 7.8 kHz. Therefore, the first 11 blade pass harmonics are resolved without aliasing or attenuation. Data were digitized for a time record of 68 ms, as was dictated by storage limitations, which gives approximately 11 rotor revolutions. Ensemble averaging was performed on the data in order to average out any inconsistencies that may exist from one rotor blade to the next. The ensemble averaging was accomplished based on the rotor blade pass frequency; since the rotor has 33 blades, about 363 records were ensemble averaged. To assist in discussion of the results, the data are presented as two blade passages from the same averaged single passage record.

For an analysis of the effects of back pressure on the surface pressure variations on the IGV's the 105 percent corrected rotor speed was used with a 26 percent rotor chord spacing. This spacing is very representative of typical compressor designs. At 105 percent corrected rotor speed, the relative Mach number at 75 percent span is 1.22 and at 50 percent span it is 1.14. A nondimensionalized difference of the pressure values across the blade was determined from the measured absolute pressure data as defined by:

$$p_n = \frac{p_1 - p_2}{p_s} \quad (9)$$

Back Pressure Influence. Five different back pressures were used defining a complete speed line, as detailed in Fig. 6. They were open throttle (point *a*), peak efficiency (point *c*), near stall (point *e*) and two other points in between (points *b* and *d*). The experimental results from all five back pressures are shown on the same plot for comparison at each chordwise location. Averaged time-resolved results from both spanwise locations are presented in Figs. 7 and 8 with only four chordwise measurements shown due to a lost transducer at 75 percent span and 50 percent chord.

Figure 7(*d*) represents the data at the 50 percent span, 95 percent chord location. At this chord location, the near-stall back pressure is where the unsteady pressure loading is the highest. The overall magnitude of this unsteady loading is a normalized pressure of approximately 0.32. This translates into a pressure variation of 29.65 kPa, which is quite substantial within a compressor from a structural point of view. The results presented in Fig. 7(*d*) are consistent with the governing flow physics concerning transonic compressor operation and variations in back pressure [12]. As the back pressure is increased, the mass flow rate is decreased. Once on the horizontal portion of the characteristic (points *b*–*e*), the downstream back pressure increase will push the compressor bow shock farther upstream from the blade leading edge resulting in a stronger bow shock and also a phase lead, relative to the rotor blade, in sensing the shock influence on the IGV. This concept is demonstrated in Fig. 9. Therefore, the bow shock will move forward and be sensed earlier on the IGV as the back pressure is increased with a maximum value found at the near stall location. As will be demonstrated in all the results presented, this trend is consistently found experimentally.

Even though the bow shock wave is weaker at the open throttle position, a substantial unsteady pressure fluctuation is shown. Its normalized value is 0.12 (11.03 kPa). The change in phase, with respect to the rotor leading edge, of the unsteady pressure loadings with variations in back pressure is clearly shown in Fig. 7(*d*). As the flow rate is increased from the near-stall condition to the open throttle condition, Fig. 7(*d*) shows a continually increasing phase lag in the unsteady surface pressure values. This result is consistent with the previous description of the bow shock movement with an increase in back pressure, as described in Fig. 9. The farther the shock's position is upstream of the rotor leading edge, the earlier it will reach the IGV's. This effect is also shown by considering the phase information from a first harmonic Fast Fourier Transform analysis of the data. Figure 10 shows the first harmonic phase results for the five different back pressures. As the flow rate is decreased the phase plots are continually shifted forward.

Figure 7(*c*) shows the results at 89 percent chord. Again, the near stall back pressure has the largest overall pressure fluctuation, 0.16 or 14.48 kPa. In comparison with Fig. 7(*d*), the unsteady pressure magnitudes have decreased due to viscous dissipation as the pressure wave moves upstream. The bow shock's strength weakens the farther upstream it travels, but the shock is definitely present at the 89 percent chord location for the near-stall

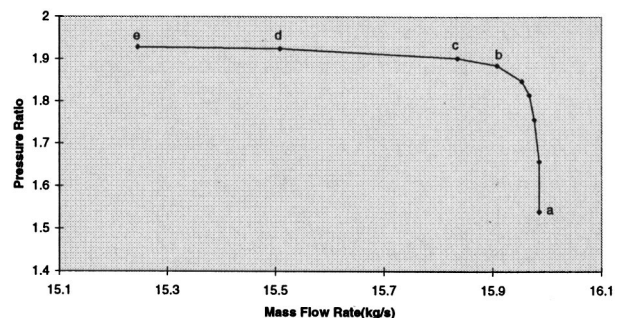


Fig. 6 Compressor performance map for: (a) open throttle; (b) above design; (c) peak efficiency; (d) below design; (e) near-stall

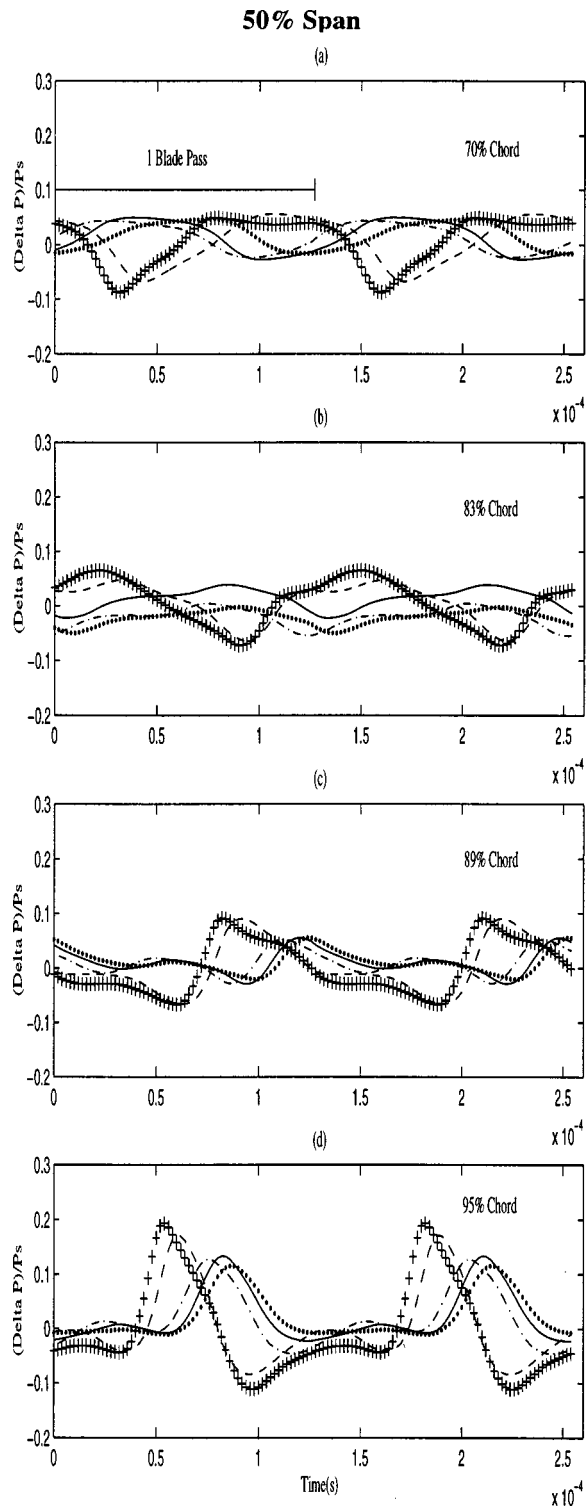


Fig. 7 Differenced nondimensionalized pressure time traces for various back pressures at 50 percent span and different chordwise positions on IGV: (a) 70, (b) 83, (c) 89, (d) 95 percent

back pressure. Similar trends are found at the 83 percent and 70 percent chord locations, Figs. 7(b) and 7(a), as the 95 percent and 89 percent chord results just discussed.

In review of the 50 percent spanwise results, several statements can be made. Back pressure plays a significant role in the magnitude of the unsteady surface pressure fluctuations measured on the IGV by the downstream transonic rotor. The higher the back pres-

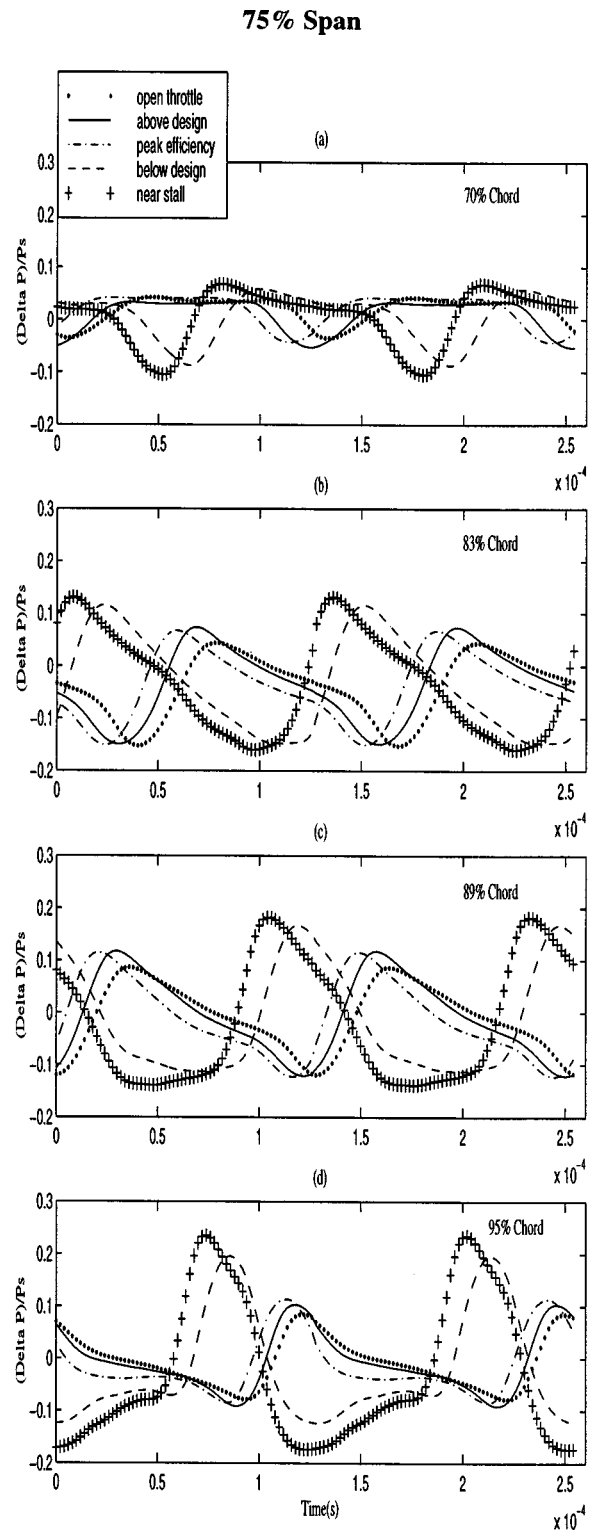


Fig. 8 Differenced nondimensionalized pressure time traces for various back pressures at 75 percent span and different chordwise positions on IGV: (a) 70, (b) 83, (c) 89, (d) 95 percent

sure, the farther the bow shock's location moves upstream. Therefore, stronger unsteady surface pressures are experienced by the IGV's. As the back pressure was increased, the unsteady pressure histories show a continually increasing phase shift in the results. This trend holds for all chordwise locations, as shown in Fig. 10. Finally, the farther upstream on the IGV's, the weaker the pressure fluctuations measured on the IGV surface.

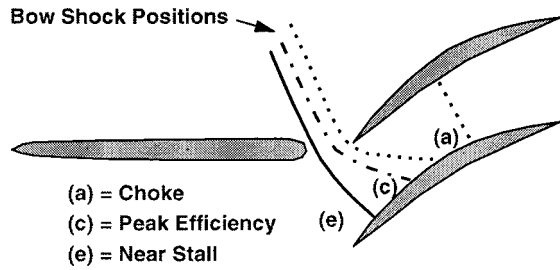


Fig. 9 Sketch of various shock positions

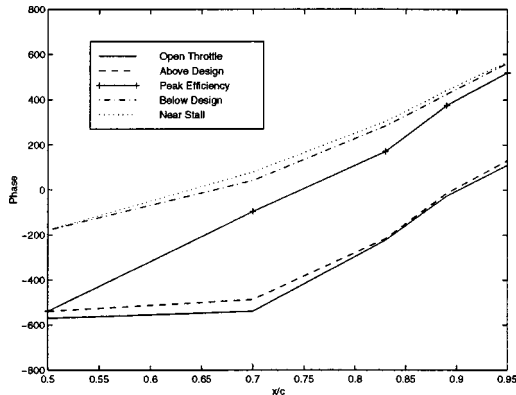


Fig. 10 First harmonic unsteady delta pressure phase results: 50 percent span

Spanwise Variations. To investigate three-dimensional effects, instrumentation was applied at the 75 percent spanwise location at the same chordwise locations as the 50 percent. Figure 8 shows the results from the 75 percent span transducers for 105 percent speed. Due to the increased radial distance at 75 percent span, the rotor blade speed is higher resulting in a higher relative Mach number (1.22 versus 1.14). It is expected this higher Mach number will result in a stronger bow shock and increased unsteady IGV surface pressure measurements over those at 50 percent span.

The near-stall back pressure results in Fig. 8(d) show the greatest unsteady pressure fluctuation of 0.43 normalized or 40 kPa. This is a significant increase over the 29.65 kPa at the 50 percent span, 95 percent chord location. The pressure data from the peak efficiency back pressure have a maximum magnitude of approximately 0.19 or 17.24 kPa. All trends seen at the 50 percent spanwise location are duplicated at 75 percent span; however, the magnitude changes are more pronounced. Figure 11 shows the first harmonic unsteady phase distribution with IGV chord. As the back pressure is decreased, the phase distribution shifts ahead. At 75 percent span, the effect of the bow shock at the 95 percent chord location is quite evident at all flow rates. When compared to the 50 percent span results, the 75 percent span results show the increased bow shock strength of the transonic rotor downstream of the IGV's. The trends for the remainder of the chord locations upstream (Fig. 8(a) and 8(b)) are the same as the 95 percent chord data, which was true at the 50 percent span as well.

As was shown, all of the trends at the 50 percent spanwise location were true at the 75 percent span. Therefore, the unsteady pressure magnitude decreases with decreasing back pressure, the phase relationship moves forward with decreasing back pressure, and the pressure magnitude increases in moving closer to the trailing edge. In addition, when compared to the 50 percent span results, significant spanwise variations are evident. These effects are caused by the change in rotor relative Mach number with radial location. The first harmonic unsteady pressure magnitudes, Fig. 12, show a spanwise location effect as well as the fact that the pressure magnitude increases in moving towards the IGV trailing

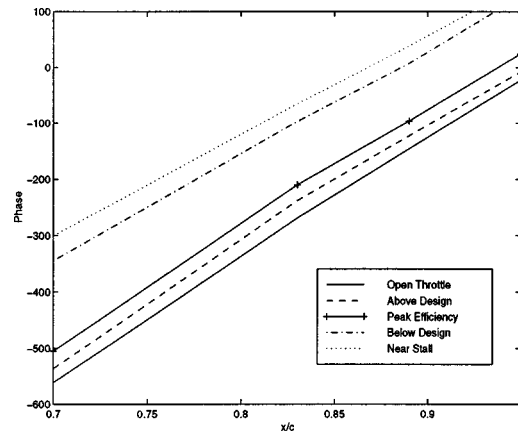


Fig. 11 First harmonic unsteady delta pressure phase results 75 percent span

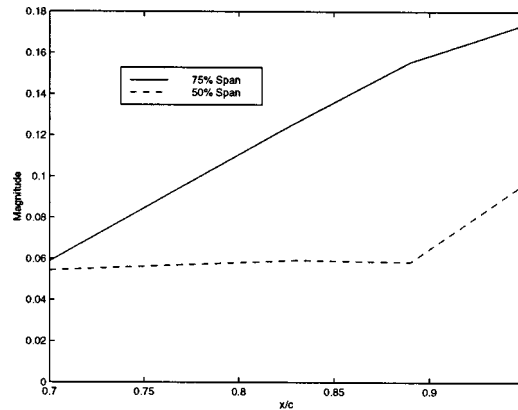


Fig. 12 Comparison of first harmonic magnitude for 50 percent span and 75 percent span near-stall

edge. The first harmonic magnitude of the 75 percent span is significantly larger than that of the 50 percent span and the magnitudes at the 95 percent chord location are dominant with the values then dropping off with movement upstream along the IGV surface.

Harmonic Content. Another important discovery is significant higher-order harmonic content within the unsteady pressure signals. Figure 13 demonstrates this fact for both the 50 and 75

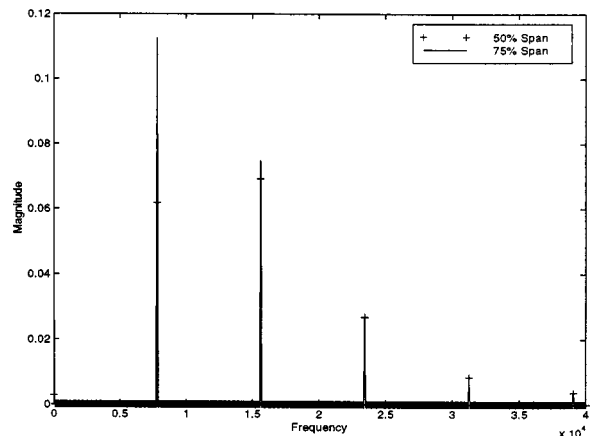


Fig. 13 FFT of near-stall 95 percent chord experimental data

percent span data through a Fast Fourier Transform analysis. The blade pass frequency is dominant for the 75 percent span data but the second harmonic is significant in magnitude. The 50 percent span data show that the second harmonic is actually dominant. The power of the higher-order harmonics for both spanwise positions decrease significantly past the second. In order to model or analyze vane/blade interactions properly, it is necessary to take the higher-order harmonic content into account. The magnitude at the blade pass frequency is generally dominant, but the fluctuations that occur above this frequency can be important as well, thereby creating a necessity to perform a nonlinear analysis.

Computational. A comparison of computational results and experimental data will be shown. The operating point used for this comparison is the 105 percent corrected speed, below design back pressure. This operating point is shown in Fig. 6. A grid independence check was done for the computational work and the number of grid points for both the **H** and **O**-grids for each row will now be given. For the IGV row, the **O**-grid contains 281×27 points and the **H**-grid, 273×93 . The rotor **O**-grid needed 351×27 points and the **H**-grid, 293×93 , for grid independence. A total of 4896 time steps were used per rotor blade pass with 171,360 time steps needed for convergence. Figure 14 represents a pressure-time history for a node between the IGV trailing edge and the rotor leading edge for the below-design operating point. A total of 35 rotor blade passes were analyzed to reach a nearly periodic solution as shown in Fig. 14. The rotor passage has a 30 percent stream tube contraction, so this value was input into the VBI code to account for the spanwise component of the quasi-three-dimensional analysis. An algebraic turbulence model is utilized to model viscous effects in the computational results presented. This turbulence model is turned on after one complete unsteady blade pass. Finally, in modeling the current configuration, 24 IGV's and 33 rotor blades, it was possible to reduce the numbers to 8 IGV's and 11 blades due to periodicity. A phase-lagged boundary condition is then utilized, making it necessary to perform the computations on only one vane or blade of each row at a time through the use of storage of data from previous blade positions with respect to the IGV. The analysis using the reduced 8 IGV's and 11 rotor blades can be seen in Fig. 15.

Figure 15 represents the computational Mach contour lines for 11 rotor blades and 8 inlet guide vanes for this below design back pressure at 50 percent span. For this operating point, a bow shock at the leading edge of the rotor is known to exist. The back pressure needed to operate at this low flow rate forces the bow shock upstream of the rotor leading edge. In the computational analysis, the bow shock is clearly evident and is upstream of the rotor

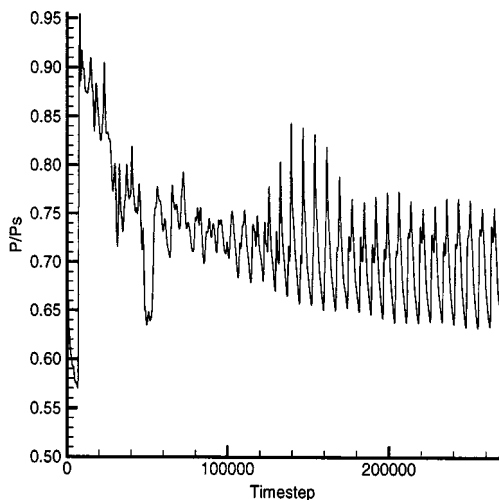


Fig. 14 Pressure time history for convergence check

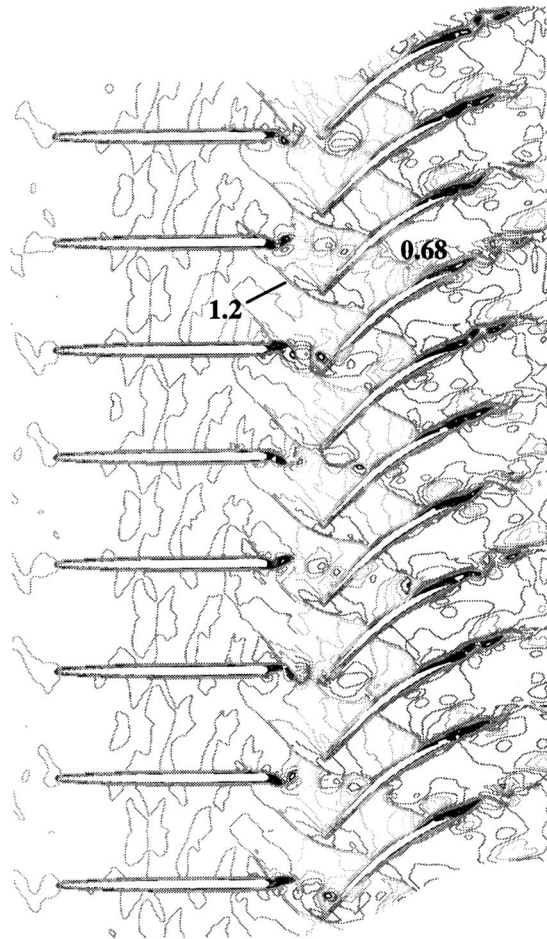


Fig. 15 105 percent speed: below design Mach number contours; 50 percent span

leading edge. The Mach numbers before and after the shock match experimental values reasonably, an indication of the solution accuracy. The upstream shock interaction causes a significant unsteady pressure force on the IGV's.

The rotor trailing edge separation noted in Fig. 15 is thought to be due to the two-dimensional analysis (lack of three-dimensional relief) as well as a low-Reynolds-number limitation in the turbulence model so that the physics may not be completely captured in part of the blade boundary layer, leading to separation. However, this is thought to have little effect on the upstream solution and the bow shock considered in the present work.

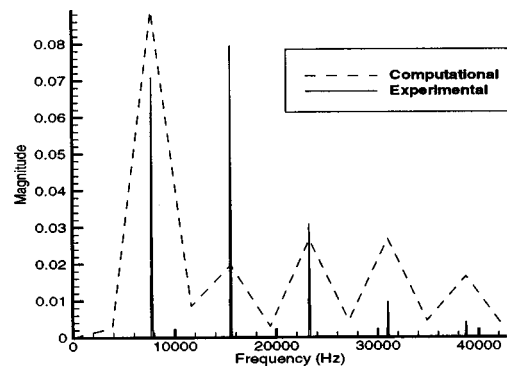


Fig. 16 Frequency response comparison: 95 percent chord 50 percent span

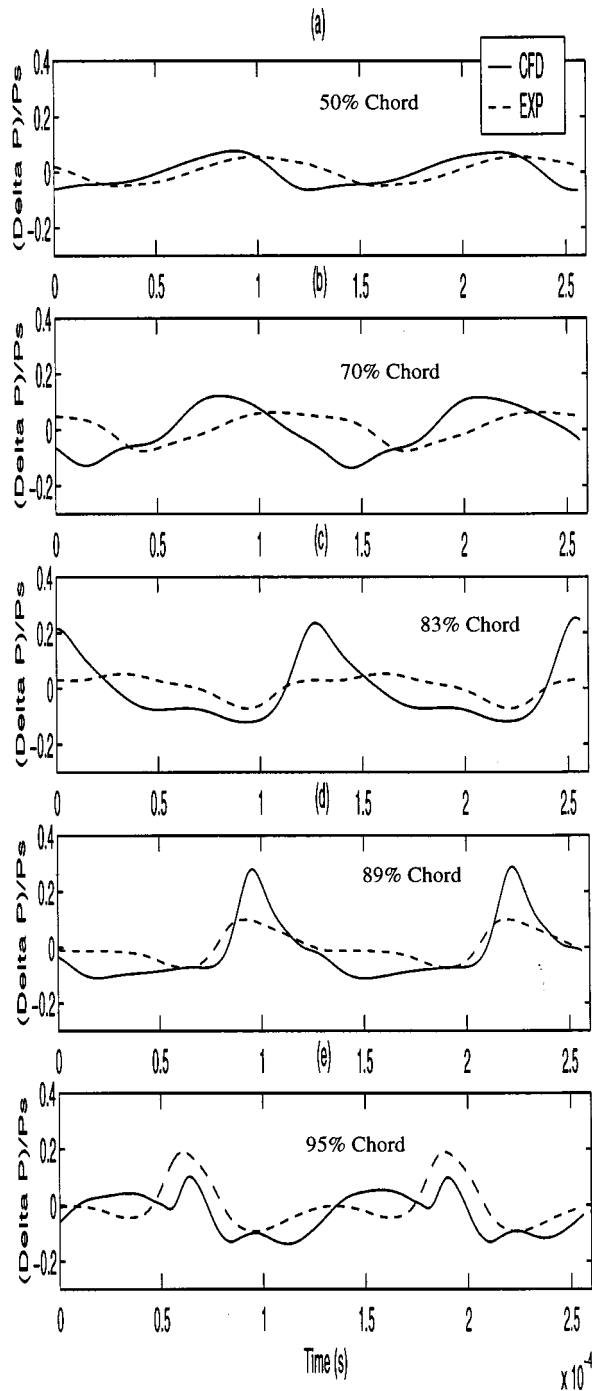


Fig. 17 Comparison of computational and experimental pressure for below design (a) 50, (b) 70, (c) 83, (d) 89, (e) 95 percent chord location on IGV

A comparison of the frequency response between the experimental data and computational results is shown in Fig. 16. The 95 percent chord location data were used for this analysis. Figure 16 demonstrates excellent agreement in frequency. The higher-order harmonic magnitudes are in general captured by the computational analysis with the second harmonic being under predicted.

A comparison of the local blade loading on the IGV's is shown in Fig. 17. The computational results shown are for the last two blade passes of the 35 total. As can be seen in the figure, the interaction weakens from the trailing edge to the leading edge. At the 95 percent chord location, both the experiment and computa-

tions show the steep pressure rise due to the bow shock, with the results showing reasonable agreement in magnitude and phase. For the 89 percent chord location, Fig. 17(d), the shock structure is still the dominating physical phenomenon. The computational analysis slightly overpredicts the unsteady magnitude response with the phase in excellent agreement. At 83 percent chord, the results show that the shock has dissipated somewhat and that this dissipation is underpredicted in the simulation. However, the results still show good phase agreement. The comparisons for 70 and 50 percent chord show relatively poor agreement. Although in reasonable agreement in magnitude, the simulation shows phase agreement.

The computational model predicted the magnitude and phase of the unsteady pressure on the IGV surface very well for the operating point used for this study. The computation demonstrates the complex character of the unsteady loading as was seen in the experiment, thereby capturing the higher harmonic content that is present in this interaction. The code, however, did tend to underpredict the shock dissipation in moving upstream along the IGV. From our study, the code predicted the unsteady loading accurately enough to potentially be useful for HCF analyses on blade rows upstream of a rotor row.

Summary and Conclusions

This study quantifies the potential influence of a compressor rotor on an upstream IGV. The rotor's influence on the unsteady IGV surface pressure distribution was established experimentally and simulated computationally.

This study reports results from a transonic core compressor stage typical of current military in-service flight hardware. The IGV/rotor spacing is also typical of current in-service hardware.

The rotor's influence on the unsteady IGV surface pressure distribution was quantified at two spanwise locations (50 and 75 percent) experimentally. In addition, a two-dimensional unsteady Navier-Stokes solver was used to predict the unsteady surface pressure distribution at 50 percent span.

The unsteady surface pressure measurements show a higher than expected influence on the IGV, which is due solely to the influence of the downstream rotor. The peak instantaneous local loading was found to be 40 kPa. The bow shock influence increased as the compressor was throttled, i.e., as the stage exit back pressure was increased.

The experiment showed a steep pressure gradient induced by the rotor bow shock wave. Spectral analysis of the time-resolved pressure history contained significant harmonic content, which suggests that the bow shock is the dominant influence on the IGV pressure field. In addition, the spectral analysis showed that the second harmonic is of the same order of magnitude as the first, indicating that first-order models of this type of bow shock interaction may not adequately predict this flow phenomena.

In addition, the experiment showed a significant difference in the upstream influence (IGV unsteady surface pressures) with span, indicating that spanwise effects are deemed to be important in transonic compressor analysis.

The numerical simulation showed that a two-dimensional computation may be quite useful in predicting upstream potential forcing functions due to downstream blade rows. The code was better able to predict the bow shock interaction near the IGV trailing edge, while the results farther upstream show that the code overpredicts the strength of the bow shock wave.

The computation also demonstrated the capability to predict the complex nature of the forcing function by showing similar harmonic content as was shown in the experimental results. These results show that two-dimensional unsteady computations show promise in forecasting unsteady blade surface pressure distributions which may be useful in the study of forced blade response.

Acknowledgments

The authors would like to thank Dr. Herb Law, Mr. Steve Gorrill, Mr. Ron Berger, Mr. Bob Wirrig, Mr. Bill Uhlman, and Mr. Terry Norris at CARL for their excellent support in obtaining the experimental data. The data quality is a true testament to their dedication to excellence. The authors would also like to thank Dr. Rolf Sondergaard and Mr. Charles Stevens from AFRL/PRTT for help with the computational results. In addition, the authors acknowledge the Air Force Office of Scientific Research for their financial support in this effort through the summer research program and an extension grant. Finally, this work was supported in part by a grant of HPC time from the DoD HPC Center, MSRC at Wright Patterson Air Force Base through the use of the HPC03 and CFS01 machines.

Nomenclature

a = speed of sound
 b = stream tube thickness
 c = chord length
 e = internal energy
 E = flux vector in m direction
 F = flux vector in θ direction
 H = source term vector
 m = meridional coordinate
 M = Mach number
 p = pressure
 Pr = Prandtl number
 Q = vector of dependent variables
 Re = Reynolds number
 r = radial coordinate
 S_m = stream tube surface
 t = time
 u = velocity component in m direction
 v = velocity component in θ direction
 V = contravariant velocity component
 x = distance along vane or blade
 z = axial coordinate
 γ = ratio of specific heats
 θ = circumferential coordinate

λ = second coefficient of viscosity = $-2/3\mu$

μ = coefficient of viscosity

ρ = density

σ = shear stress

ω = angular velocity

Subscripts

i = inviscid term

n = normalized

s = IGV inlet

v = viscous term

1 = IGV upper surface

2 = IGV lower surface

References

- [1] Verdon, J. M., 1992, "Unsteady Aerodynamic Methods for Turbomachinery Aeroelastic and Aeroacoustic Applications," AIAA Paper No. 92-0011.
- [2] Kim, K. H., and Fleeter, S., 1992, "Compressor Blade Row Unsteady Aerodynamic Response to Attached and Separated Flow Forcing Functions," AIAA Paper No. 92-0147.
- [3] Henderson, G. H., and Fleeter, S., 1992, "Airfoil Wake and Linear Theory Gust Response Including Sub and Super-resonant Flow Conditions," AIAA Paper No. 92-3074.
- [4] Johnston, R. T., Feiereisen, J. M., and Fleeter, S., 1994, "Rotor Wake and Potential Forcing Functions, Including Blade Row Interactions," AIAA Paper No. 94-2975.
- [5] Johnston, R. T., and Fleeter, S., 1996, "Time-Resolved Variations of an IGV Flow Field in the Presence of a Rotor Potential Field," AIAA Paper No. 96-2670.
- [6] Johnston, R. T., and Fleeter, S., 1997, "Rotor Blade Pressure Measurement in a High Speed Axial Compressor Using Pressure and Temperature Sensitive Paints," AIAA Paper No. 97-0162.
- [7] Rao, K. V., Delaney, R. A., and Topp, D. A., 1992, "Turbine Vane-Blade Interaction," Interim Report WL-RT-92-2002.
- [8] Law, C. H., 1989, "Two Axial Compressor Designs for a Stage Matching Investigation," AFWAL-TR-89-2005.
- [9] Rao, K., and Delaney, R., 1990, "Investigation of Unsteady Flow Through Transonic Turbine Stage; Part 1: Analysis," AIAA Paper No. 90-2408.
- [10] Benek, J. A., Donegan, T. L., and Suhs, N. E., 1987, "Extended Chimera Grid Embedding Scheme With Application to Viscous Flows," AIAA Paper No. 87-1126-CP.
- [11] Baldwin, B., and Lomax, H., 1978, "Thin Layer Approximation and Algebraic Model for Separated Turbulent Flows," AIAA Paper No. 78-257.
- [12] Pierzga, M. J., and Wood, J. R., 1985, "Investigation of the Three-Dimensional Flow Field Within a Transonic Fan Rotor: Experiment and Analysis," ASME J. Eng. Gas Turbines Power, **107**, No. 2, pp. 436-449.

Xiaohua Wu
e-mail: wu@transition.stanford.edu

Paul A. Durbin
e-mail: durbin@vonkarman.stanford.edu

Center for Integrated Turbulence Simulation and
Department of Mechanical Engineering,
Stanford University,
Building 500,
Stanford, CA 94305-3030

Boundary Layer Transition Induced by Periodic Wakes

Turbulent wakes swept across a flat plate boundary layer simulate the phenomenon of wake-induced bypass transition. Benchmark data from a direct numerical simulation of this process are presented and compared to Reynolds-averaged predictions. The data are phase-averaged skin friction and mean velocities. The predictions and data are found to agree in many important respects. One discrepancy is a failure to reproduce the skin friction overshoot following transition. [S0889-504X(00)00503-1]

1 Introduction

Compressor and turbine blades operate in highly perturbed external flows. Their flow conditions are such that substantial regions of laminar flow exist, even though the laminar boundary layers are highly buffeted [1]. Transition to turbulence often occurs after midchord.

The desire to apply advances in Computational Fluid Dynamics to prediction of flow in turbomachinery blade rows has led to efforts to predict transitional flows with turbulence models [2]. Reynolds-averaged Navier–Stokes computations of wake-induced transition on a compressor blade have been carried out recently by Kang and Lakshminarayana [3]. They concluded that qualitative agreement with experiment suggests this to be a promising approach. A review of research on transition in turbines was prepared by Simon and Ashpis [4].

Although turbulence closure models are developed and calibrated for turbulent flow prediction, there is a fervent hope that they will suffice for prediction of bypass transition. The basis for such hope might be stated as follows: Transition from laminar to turbulent flow can be described as a bifurcation between solution branches. If a turbulence model admits a laminar solution at low Reynolds number and a turbulent solution at high Reynolds number, then the model will bifurcate at a critical Reynolds number. The critical Reynolds number might be representative of that for fluid dynamic transition. This bifurcation of steady solution branches with increasing Reynolds number occurs in computations of plane channel flow [5]. The bifurcation point is a function of the model and its empirical coefficients. In a boundary layer, transition occurs as the flow evolves downstream and the description in terms of laminar and turbulent branches of the model is less clear. This picture is further clouded by the fact that most turbulence models are ill defined in the limit of zero turbulence: An exception is the $k-\omega$ model, for which ω is determined by the mean rate of strain, even in the absence of turbulent energy [6]. One should not be too sanguine about the ability of turbulence models to predict bypass transition. They are certainly not meant for this purpose.

A comprehensive test of low-Reynolds-number $k-\varepsilon$ models in bypass transition has been conducted by Savill [2]. Experimental data in the ERCOFTAC database on boundary layers under moderate levels of free-stream turbulence provided the benchmark data. The results of these tests show promise; turbulence models may be a suitable engineering tool in some transitional turbomachinery applications. The particular route to turbulence depends somewhat on the source of perturbation: Grid turbulence provides a free-stream disturbance that convects uniformly above the boundary layer; turbomachine blades are subjected to impinging turbulent wakes.

An idealized benchmark case for the turbomachinery application would be flat plate boundary layer transition induced by periodically passing wakes. The use of a flat plate mimics many important features of turbomachines without the complexities of pressure gradients and surface curvature [1,7–9]. Admittedly stagnation point distortion of wakes at blade leading edge is omitted in the wake passing flow over a flat plate, as are other features of the turbomachine cascade environment. However, the basic flat plate case is a time-honored, productive starting point. Attempts to obtain quantitative experimental data in the wake–flat plate configuration have been difficult; there are many technical issues that confound experimenters. For instance, Liu and Rodi [10] employed the configuration shown in Fig. 1(a). The squirrel cage of cylinders produced an extra wake on its upstream side. This is one of many impediments to designing a benchmark experiment. In addition to the technical difficulties is the sheer quantity of data required to obtain space–time, phase-averaged statistics. Essentially one wants $\langle C_f \rangle(x, 2\pi\phi)$ and $\langle U \rangle(x, y, 2\pi\phi)$. Here the

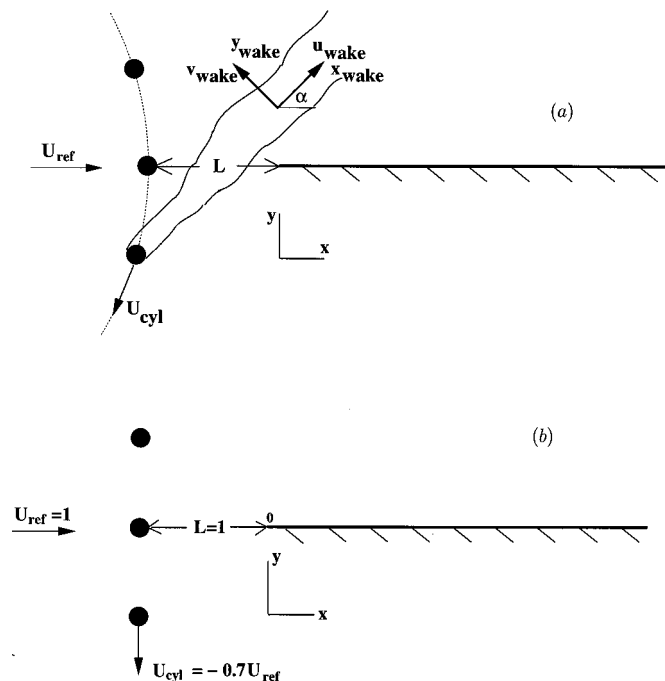


Fig. 1 (a) Layout in the experiments of Liu and Rodi [10]; (b) layout in the present numerical simulation; the computational domain is defined as $0.1 \leq x/L \leq 3.5$, $0.0 \leq y/L \leq 0.8$, $0.0 \leq z/L \leq 0.2$

Contributed by the International Gas Turbine Institute for publication in the JOURNAL OF TURBOMACHINERY. Manuscript received by the International Gas Turbine Institute November 1998. Associate Technical Editor: T. H. Okiishi.

angle brackets denote a phase average and ϕ is the phase of the wake passing. ϕ varies between 0 and 1 as wakes sweep periodically across the plate.

The obstacles to physical experimentation can be overcome by Direct Numerical Simulation (DNS). Computer power is now at the stage where, in a small number of selected cases, reliable benchmark data may be produced by accurate computation of the Navier–Stokes equations. The relatively low Reynolds numbers involved in transitional flow make DNS feasible. Years of experience in turbulence simulation have led to guidelines on grid resolution and domain size requirements. These have been combined with further resolution studies in Wu et al. [11]. It was concluded therein that a $1024 \times 401 \times 128$ grid sufficed for the present problem of wake-induced bypass transition. The total of 52.5×10^6 points is one of the largest that has been used for transition simulation. A wealth of data have been generated. A small subset of those data will be presented herein.

2 Simulation of Wake-Induced Transition

Figure 1(b) is a schematic of the flow domain of these simulations. This is a rectangular box, $0.1 \leq x \leq 3.5$, $0 \leq y \leq 0.8$ in nondimensional units. The Reynolds number $Re = U_{ref} L / \nu$ is 1.5×10^5 , where $U_{ref} = 1$ is the inlet reference velocity. The grid spacing was uniform in x and z , and stretched in y . A Blasius boundary layer with $Re_\theta = 80$ was imposed at the inlet, where θ is the boundary layer momentum thickness. Self-similar wakes were swept periodically across the entrance to the flow domain. Their half-width was 0.1 and the velocity deficit was 0.14, scaled on the inlet reference velocity. The translational velocity of the wakes was 0.7. These inlet conditions are analogous to those of the experiment by Liu and Rodi ([10]; Fig. 1(a)). Further details can be found in Wu et al. [11] and Wu and Durbin [12].

Two wake passing periods have been simulated: $T = 1.67$ and $T = 0.42$. In the first case the distance between wake centers is $1.67 \times 0.7 = 1.17$, which is 11.7 times their initial half width. The wakes remain well separated. In the second case the wakes start

with a centerline separation of about 2.9 times their width, but merge inside the domain. This high-frequency simulation is meant to produce sustained high intensity free-stream turbulence in the transitional region.

The present paper provides relevant phase-averaged data. We will also present Reynolds-Averaged Navier–Stokes (RANS) simulations of wake induced transition using turbulence models. These consist of two-dimensional, unsteady RANS computations. The RANS computations were performed on a 201×101 grid. The spacing was uniform in x and stretched in y . The models used in this paper are S–A [13] and v^2-f [14]. These both use an eddy viscosity formula for mean flow prediction. The models are stated in the appendix. The details of the RANS computations are essentially the same as in Durbin [14].

Self-similar wakes were swept across the inlet in correspondence with the DNS. The wakes were generated by a separate computation and imposed as the inlet boundary condition. Figure 2 compares the inlet wakes predicted by the v^2-f model to those used in the DNS. The agreement is quite good. A virtue of the present test case is that one can closely match the inlet conditions of the RANS simulation to those of the DNS.

The S–A model solves an equation for a pseudo eddy viscosity, then invokes a nonlinear transformation to obtain the actual eddy viscosity (see the appendix). This procedure was introduced by Baldwin and Barth [15] in the interest of formulating a computationally amenable turbulent transport model. S–A has become a popular model in external aerodynamics: Indeed, it is computationally amenable.

The v^2-f model originated as an attempt to represent the non-local and anisotropic effects of a wall on a proximate field of turbulence with a lesser level of complexity than full second-moment closure. This model has proved effective in predictions of complex flows and of surface heat transfer [16]. Both models have been used without any modification for transition prediction, per se.

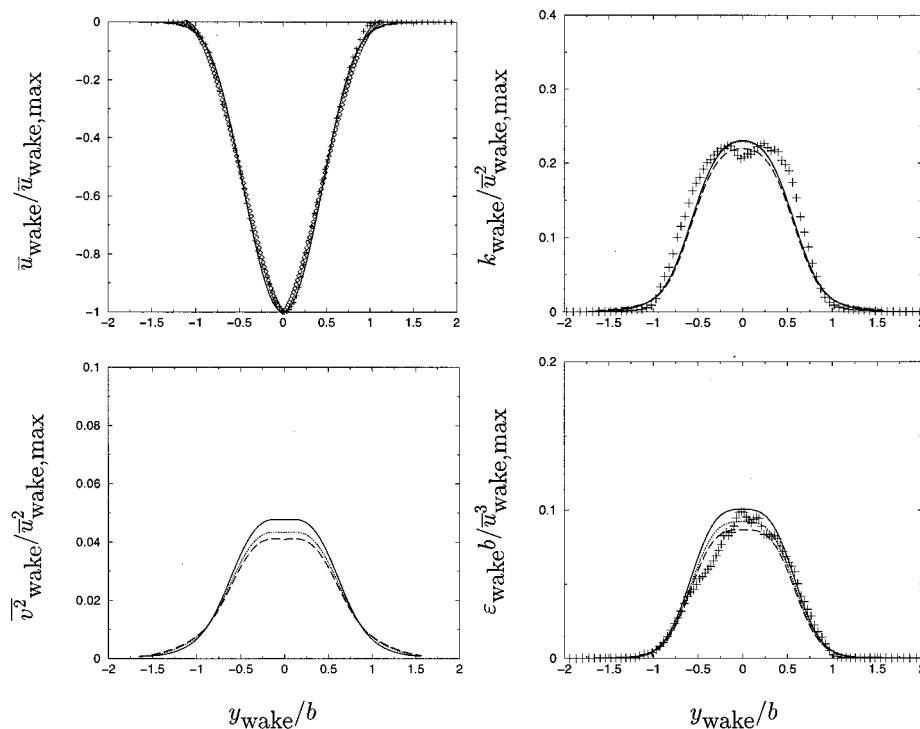


Fig. 2 Characteristics of the temporarily developing planewake used for generation of inflow profiles; lines: v^2-f model at three instants; \diamond plane cylinder wake of Schlichting [18]; + Wu et al. [11] at one instant.

3 Phase-Averaged Fields

The DNS fields were averaged at a fixed phase over 50 cycles of the wake passing, and over the spanwise direction. Data on the mean velocity and surface skin friction as functions of x , y , ϕ will be presented here. These are representative of a phase-averaged and time-averaged database that has been created from the numerical simulations.

Figure 3 contains three sets of contours: the instantaneous u -velocity; the phase-averaged DNS data; and a v^2-f simulation. These are for the low-frequency case. The instantaneous contours (Fig. 3(a)) show that the boundary layer is laminar for $x < 1$ and turbulent for $x > 1.5$. The transition to turbulence is less clear in the phase-averaged cases (Figs. 3(b,c)). However, the boundary layer is observed to thicken downstream of $x = 1.5$, indicating that this region has become turbulent. Some thickening is also observed beneath the wake, both in the data and in the RANS computation. The thickening beneath the wake is the forced response of the buffeted laminar boundary layer to the passing wake. At this frequency the wakes remain well separated across the entire computational domain.

Time-averaged data were obtained by further averaging over all phases; i.e.,

$$\bar{C}_f = \int_0^1 \langle C_f \rangle d\phi$$

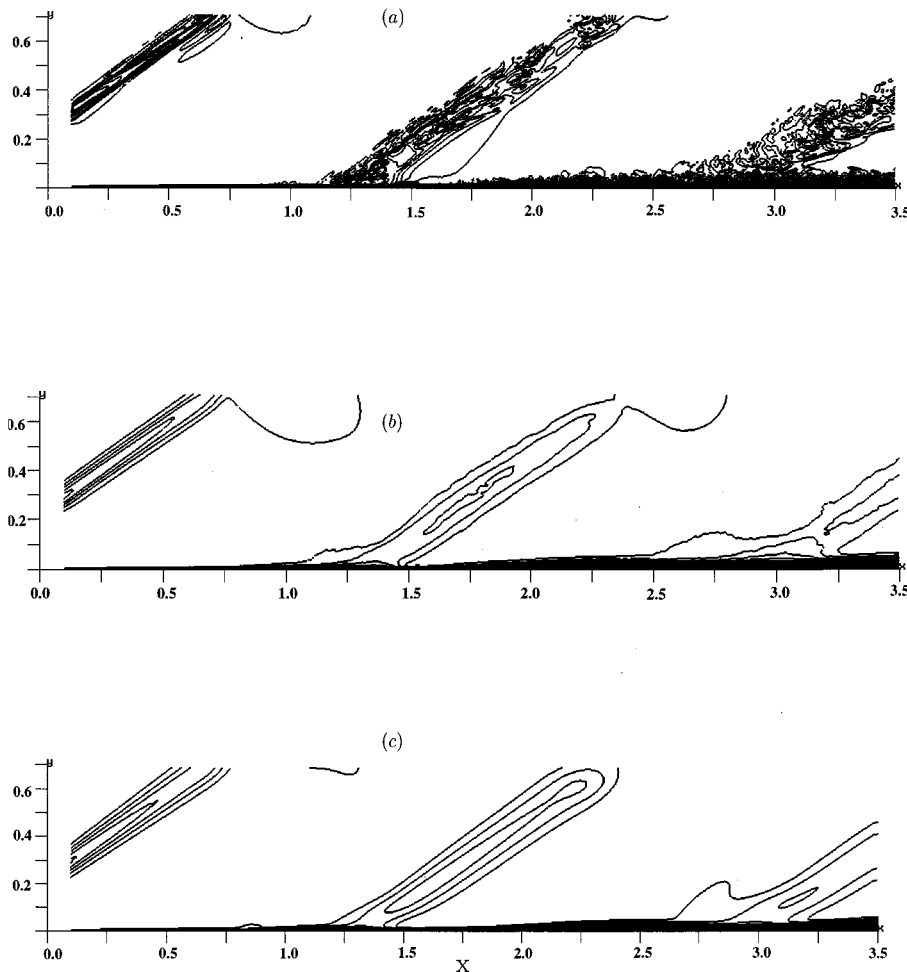


Fig. 3 (a) Instantaneous u over one x - y plane at $t=32.5T$ in the DNS of Wu et al. [11]; (b) phase-averaged $\langle u \rangle$ at $\phi=0.5$ from the DNS of Wu et al. [11]; (c) phase-averaged $\langle u \rangle$ at $\phi=0.5$ from the present unsteady RANS using v^2-f model

where the overbar indicates a time-average. These data give an average onset of transition at about $x=0.7$ in the low-frequency case and about $x=0.5$ at high frequency. At the transition location the average Re_θ is about 200, which happens to approximate the linear critical Reynolds number. Figure 4 contains time-averaged mean skin friction coefficient \bar{C}_f as a function of x for the two different passing frequencies. Computations with v^2-f are included for comparison. Computations with S-A are included as well in Fig. 4(a).

S-A undergoes an early transition. This is not unexpected since the user-specified trip function was not used for these computations: That trip function requires the transition to be specified, which would defeat the purpose of the present testing. The destruction terms in the S-A model (appendix, Eq. (1)) are quadratic in the eddy viscosity, while production is linear. In the limit $\nu_t \rightarrow 0$ production is balanced only by diffusion and transition occurs at very low Reynolds number. An analysis of instability in plane channel flow is described in the appendix. The inclusion of a dissipation equation permits a balancing of production and destruction that controls transition in that type of model [6]. The v^2-f model includes a dissipation equation (see the appendix).

The v^2-f computation shows better transitional behavior. It follows the laminar branch to a reasonable distance before \bar{C}_f begins to increase toward turbulent levels. It is known from experiments that, following transition, C_f overshoots the turbulent

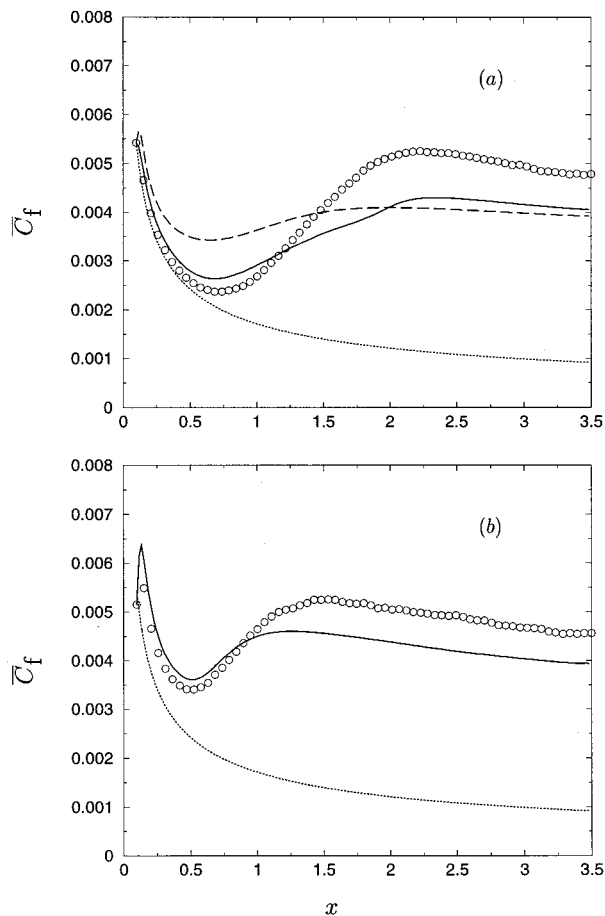


Fig. 4 Time-averaged mean skin-friction coefficient; ○ DNS of Wu et al. [11]; — unsteady RANS using v^2-f model; - - - unsteady RANS using S-A model; · · · Blasius solution without wake; (a) $T=1.67$; (b) $T=0.4175$

level and then relaxes to the flat-plate correlation. Both RANS models fail to reproduce the overshoot. This is simply because the models were calibrated for flat-plate skin friction. At the exit of the flow domain $Re_\theta=1100$ in the DNS. The boundary layer statistics have assumed turbulent profiles at this point, but the skin friction is still influenced by the path of transition and the free-stream wake.

Space-time fields, $\langle C_f \rangle(x, \phi)$, are displayed in Fig. 5 for the low-frequency case. The transition region moves periodically as wakes pass across the inlet. The location and movement of transition is mimicked reasonably well by the v^2-f computation. S-A again suffers from early transition.

The contour levels downstream of transition are underpredicted by the models because of the lack of overshoot, as was already seen in Fig. 4. The contour plots in Fig. 5(b) give further hope that turbomachinery rows can be computed by unsteady RANS methods with little, if any, modification by special purpose transition models. But if highly accurate prediction of the transition region is needed, such as the C_f overshoot, then special models would still be required.

A notable feature of Fig. 5 is the large perturbation near $x=0$ produced by the impacting wake. This perturbation decays rapidly from the inlet and is not the cause of transition. Wu et al. [11] have examined this inlet disturbance in the instantaneous DNS fields and also concluded that it decays rapidly downstream. In the direct simulations, the transition to turbulence is effected through the generation of turbulent spots, which first appear in the vicinity of $x=0.7$, at this frequency.

Figures 5(a, b) show tongues of low $\langle C_f \rangle$ (blue color) that protrude between the lobes of the undulating line of transition (yellow contour in 5(a)). These are areas in which the laminar skin friction is highly disturbed by the wake. Curves of skin friction along the plate at an instant are horizontal sections through the contour plot. One can imagine that a slice showing $\langle C_f \rangle(x)$ at constant phase would reveal a complex form, cutting across the buffeted laminar region, into the turbulent region, possibly intersecting a patch of perturbed laminar flow, and finally traversing the downstream turbulent region.

Figure 6 contains six such slices, at $\phi=0, 0.2, 0.4$ in part: (a) and at $\phi=0.5, 0.7, 0.9$ in part (b). These are the same data as in Fig. 5, but displayed in the form of line plots, $\langle C_f \rangle(x)$, at the various ϕ . Bell-shaped protrusions upstream of $x=1.5$ are the footprint of the passing wake. They enter the domain just before $\phi=0$ in Fig. 6(a) and progress downstream, becoming increasingly pronounced. Both the DNS and RANS simulations contain this feature. It appears that this peak grows due to prolonged forcing of the laminar layer, in a frame of reference moving with wake, and is distinct from the bifurcation to turbulence. Downstream of $x=2.0$ the flow is always turbulent, although perturbations by the external wake are still seen.

Where the onset of self-sustained turbulence occurs is not entirely clear in these line plots. In fact, the DNS data for $\phi=0$ seem to pass into and out of the turbulent region. The ambiguity is resolved by Fig. 5(a), which shows the undulation form of the transition. Indeed, at $\phi=0$ in that figure a laminar patch around $x=1.75$ is protruding between the turbulent regions. The RANS simulation in Fig. 5(b) also has this patch, but it is narrower and is present at a later phase.

The high-frequency case was chosen to simulate sustained, high-intensity free-stream turbulence; it is less relevant to the problem of transition induced by discrete wakes. The transition line shows only faint undulations, as seen in Fig. 7. The slight raggedness of the DNS contours is due to finite sample size. They suggest that the free stream is persistently turbulent. This case shows even more definitively that the large perturbations at $x=0$, created by impingement of the wake on the surface, do not trigger transition. The agreement between the model and data is similar to the low-frequency case: The transition location is quite reasonably predicted, but the overshoot following transition is not reproduced.

The remaining figures provide DNS data and RANS results for the flow field. Figure 8 shows the development of time-averaged integral parameters of the boundary layer. Decline of the form factor provides a gross indicator of transition from a laminar to a turbulent velocity profile. As seen previously, Fig. 8(a) shows a premature drop in the form factor predicted by the S-A model. The v^2-f results are in better agreement with the data. However, the form factor lies above and the displacement thickness below the data after transition.

Figure 9 displays log-linear mean flow profiles at four phases $\phi=0., 0.25, 0.5, 0.75$. The free-stream region shows the location of the turbulent wake at each of these instances. The x -location is $x=1.0$, which is in the region of large oscillations of the skin friction, but is primarily a buffeted laminar layer (see Fig. 5).

Figure 10 displays mean flow profiles at the same four phases but now the x location is $x=1.5$, which is in the region that is intermittently laminar or turbulent. Examination of Fig. 5(a) shows that $x=1.5$ the flow is on the laminar side of the transition line for $\phi=0.5, 0.75$ ($\Delta, +$) and on the turbulent side for $\phi=0., 0.25$ (\circ, \diamond). The RANS simulation in 5(b) is on the laminar side of the transition line for $\phi=0.5$ and on the turbulent side for $\phi=0$, but both $\phi=0.25$ and 0.75 are on the border of transition. So there is a slight difference in phase between the DNS and RANS results. This shows up in the profiles of Fig. 10: The DNS profiles at $\phi=0.5, 0.75$ ($\Delta, +$) are quite similar near the wall, being of

laminar form. The RANS profile at $\phi=0.5$ (Δ) is of the laminar form, but at $\phi=0.75$ (+) it has already started to shift toward the turbulent profiles.

4 Conclusion

In aggregate, the results presented in this paper show a promise for applying turbulence models to predict the gross features of transitional flow over turbomachinery blades. The direct simulation data provided here can be used to benchmark models specifically intended to predict transition.

Acknowledgments

We are grateful to Dr. David Asphis of NASA-Glenn research center for discussions on transition in turbines. This work is supported by the Academic Strategic Alliance Program of the U.S. Department of Energy Accelerated Strategic Computing Initiative.

Appendix

Spalart-Allmaras. The equation for the pseudo-eddy viscosity $\tilde{\nu}$ is

$$D_t \tilde{\nu} = c_{b1} \tilde{S} \tilde{\nu} - c_{w1} f_w \left[\frac{\tilde{\nu}}{d} \right]^2 + \frac{1}{\sigma} [\nabla \cdot (\nu + \tilde{\nu}) \nabla \tilde{\nu} + c_{b2} |\nabla \tilde{\nu}|^2] \quad (1)$$

The actual eddy viscosity is obtained through the nonlinear relation

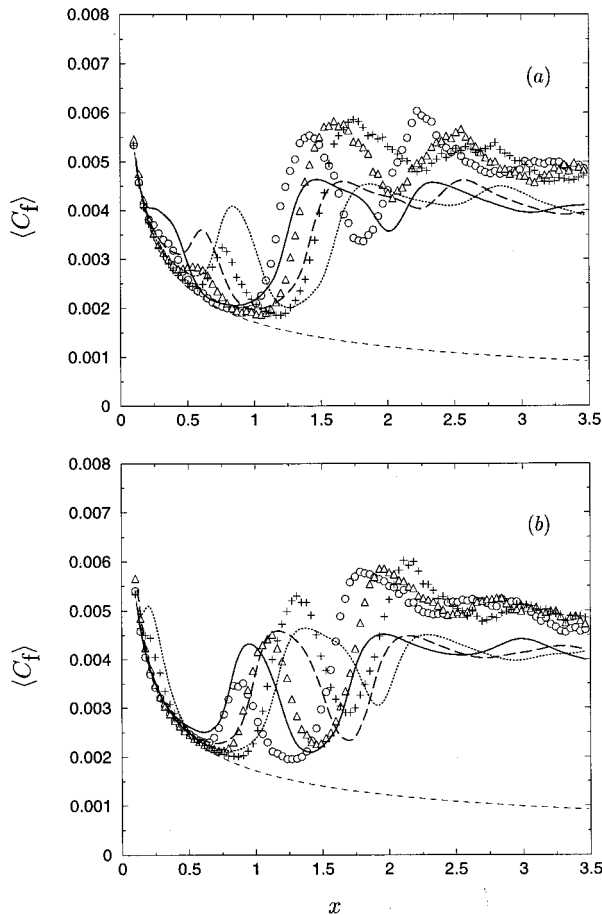


Fig. 6 Phase-averaged mean skin-friction coefficient for $\mathcal{T} = 1.67$; symbols: DNS of Wu et al. [11]; lines: present unsteady RANS using v^2-f model; (a) \circ — $0.0\mathcal{T}$, \triangle — $0.2\mathcal{T}$, $+$ \cdots $0.4\mathcal{T}$; (b) \circ — $0.5\mathcal{T}$, \triangle — $0.7\mathcal{T}$, $+$ \cdots $0.9\mathcal{T}$; — — — Blasius solution

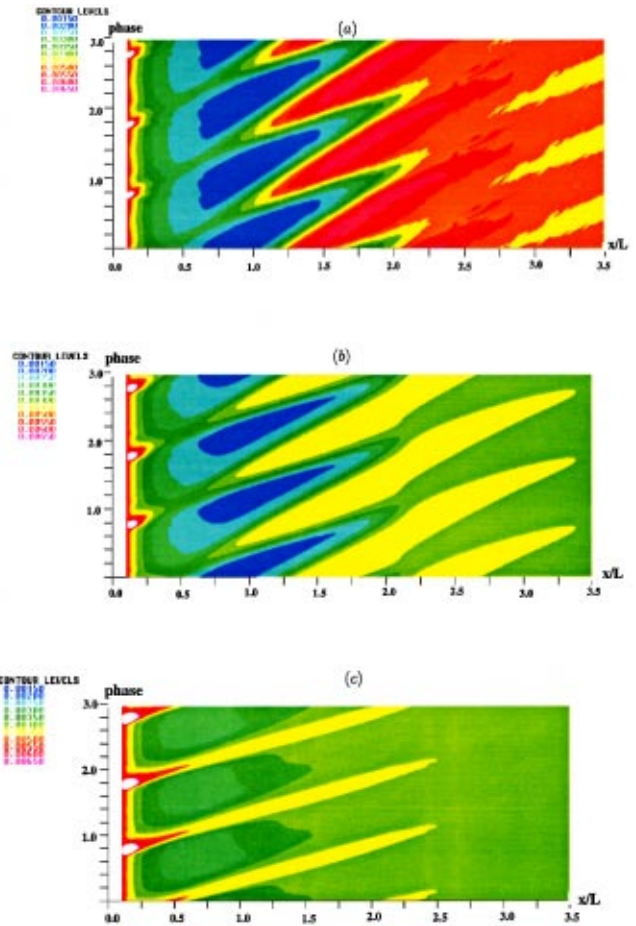


Fig. 5 $X-t$ diagram of the phase-averaged skin-friction coefficient $\langle C_f \rangle$ for $\mathcal{T} = 1.67$; (a) DNS of Wu et al. [11]; (b) unsteady RANS using v^2-f model; (c) unsteady RANS using S-A model

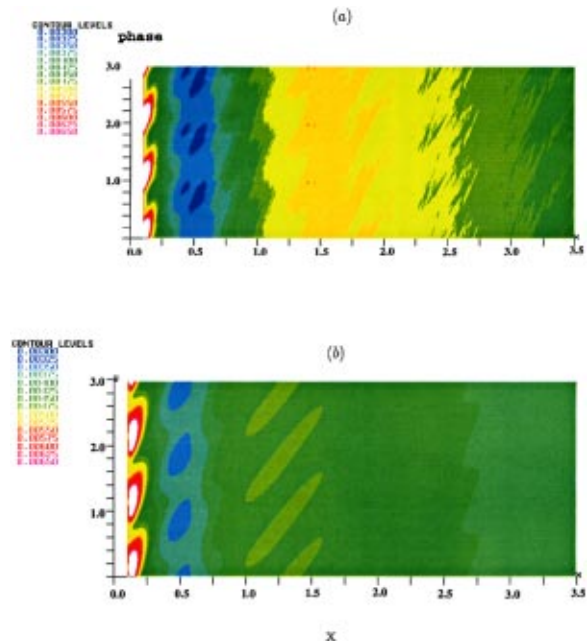


Fig. 7 $X-t$ diagram of the phase-averaged skin-friction coefficient $\langle C_f \rangle$ for $\mathcal{T} = 0.4175$; (a) DNS of Wu et al. [11]; (b) unsteady RANS using v^2-f model

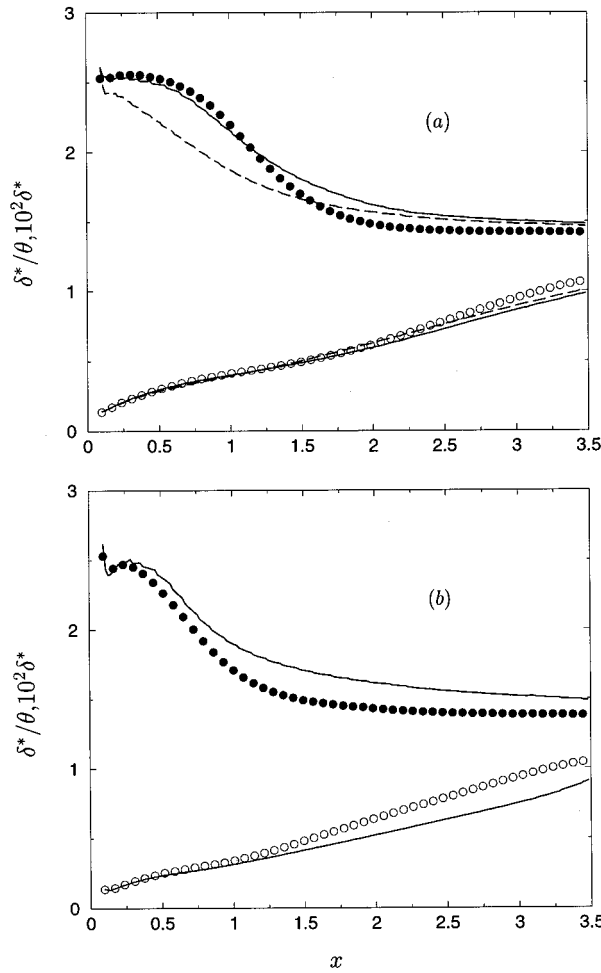


Fig. 8 Time-averaged mean integral parameters; symbols DNS of Wu et al. [11]; — unsteady RANS using v^2-f model; - - unsteady RANS using S-A model; ● δ^*/θ ; ○ $10^2\delta^*$; (a) $T=1.67$; (b) $T=0.4175$

$$\frac{v_t}{\nu} = \frac{\chi^4}{\chi^3 + 7.1^3}; \quad \chi = \bar{v}/\nu$$

In the production term \tilde{S} is a transformed mean vorticity:

$$\tilde{S} = S + \left[\frac{\bar{v}}{\kappa^2 d^2} \right] \frac{\nu + v_t - \bar{v}}{\nu + v_t}$$

where S is the magnitude of the vorticity. The modified production term is designed to produce a linear variation of \bar{v} from the wall through the log-layer in an equilibrium, flat plate boundary layer. The wall distance term $(\bar{v}/d)^2$ is modulated by the function

$$f_w = g \left[\frac{65}{g^6 + 64} \right]; \quad g = r + 0.3(r^6 - r) \quad r = \bar{v}/\tilde{S}\kappa^2 d^2$$

Numerical values of some constants have been inserted; the remaining constants are $c_{b1}=0.1355$, $c_{b2}=0.622$, $\sigma=2/3$, $c_{w1}=c_{b1}/\kappa^2+(1+c_{b2})/\sigma$.

When Eq. (1) is applied to parallel flow, \bar{v} is a function of (y, t) . A crude stability analysis can be performed for plane channel flow to understand why this model bifurcates early. For small amplitude perturbations to laminar flow, $\bar{v} \ll \nu$, and Eq. (1) assumes the nondimensional, linearized form

$$\sigma \partial_t \bar{v} - \text{Re} \sigma c_{b1} S \bar{v} = \partial_y^2 \bar{v} \quad (2)$$

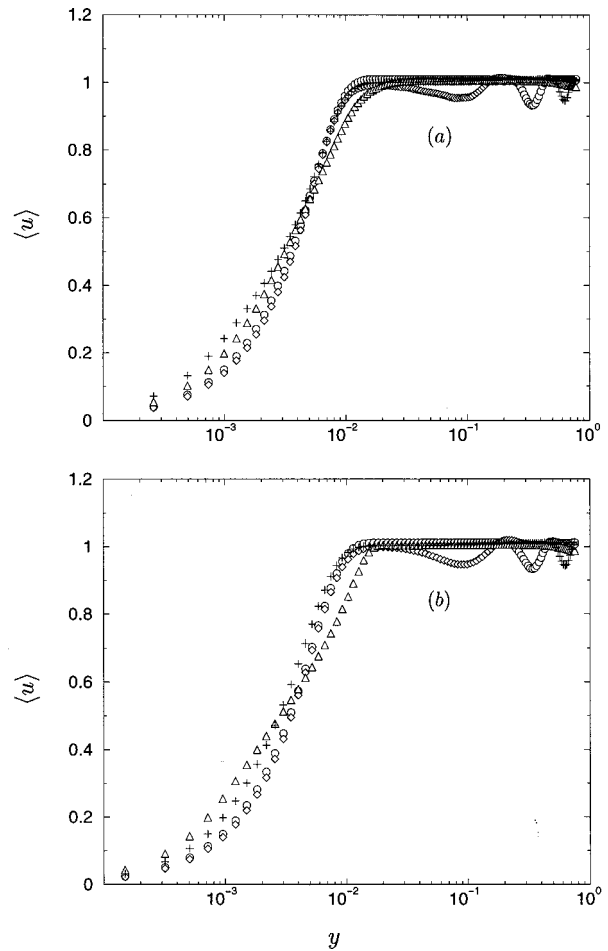


Fig. 9 Phase-averaged mean streamwise velocity at $x/L=1.0$ for $T=1.67$; (a) DNS of Wu et al. [11]; (b) unsteady RANS using v^2-f model; ○ $0.0T$, ◇ $0.25T$, △ $0.50T$, + $0.75T$

where Re is the Reynolds number. For plane Poiseuille flow $U=1-y^2$ and $S=2|y|$, for the flow domain $-1 < y < 1$. Let $\mathcal{R} = 2 \text{Re} \sigma c_{b1}$. Then the equation determining neutral stability is

$$\partial_y^2 \bar{v} + \mathcal{R}|y| \bar{v} = 0$$

Since $\bar{v} > 0$, a symmetric solution is sought: $\partial_y \bar{v}(0) = 0$, $\bar{v}(1) = 0$. A closed-form solution is readily written in terms of Airy functions. These give the neutral stability condition $\mathcal{R} \approx 4$. Then

$$\text{Re} \approx 2/\sigma c_{b1} \approx 22$$

This is well below experimental determinations of the global critical Reynolds number (≈ 900).

v^2-f . This model is based on the standard $k-\varepsilon$ model and on second-moment closures. One can think of kf as an analogy to the redistribution term in second-moment closure. The transport and Helmholtz equations for this model are:

$$\left. \begin{aligned} D_t k &= P - \varepsilon + \nabla \cdot [(\nu + \nu_t) \nabla k] \\ D_t \varepsilon &= \frac{C'_{\varepsilon 1} P - C_{\varepsilon 2} \varepsilon}{T} + \nabla \cdot \left[\left(\nu + \frac{\nu_t}{\sigma_\varepsilon} \right) \nabla \varepsilon \right] \\ D_t \overline{v^2} &= kf - N \frac{\overline{v^2}}{k} \varepsilon + \nabla \cdot [(\nu + \nu_t) \nabla \overline{v^2}] \\ f - L^2 \nabla^2 f &= C_1 \frac{(2/3 - \overline{v^2}/k)}{T} + C_2 \frac{P}{k} + \frac{(N-1)\overline{v^2}/k}{T} \end{aligned} \right\} \quad (3)$$

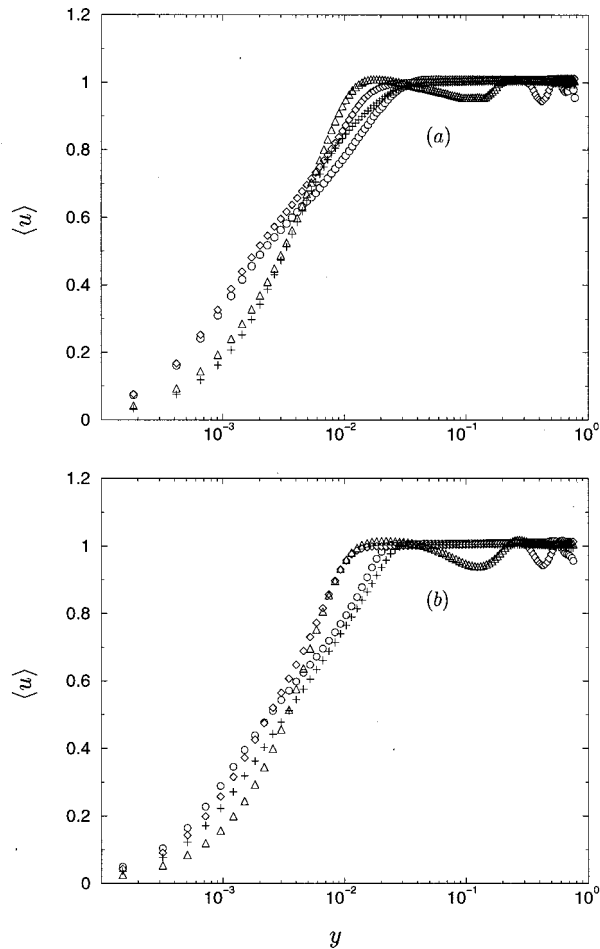


Fig. 10 Phase-averaged mean streamwise velocity at $x/L = 1.5$ for $T = 1.67$; (a) DNS of Wu et al. [11]; (b) unsteady RANS using ν^2-f model; \circ $0.0T$; \diamond $0.25T$; \triangle $0.50T$; $+$ $0.75T$

The rate of turbulent kinetic energy production has the usual definition

$$P = 2\nu_t S^2; \quad S^2 = (\partial_j U_i + \partial_i U_j)(\partial_j U_i + \partial_i U_j)/4$$

The following boundary conditions apply on no-slip walls:

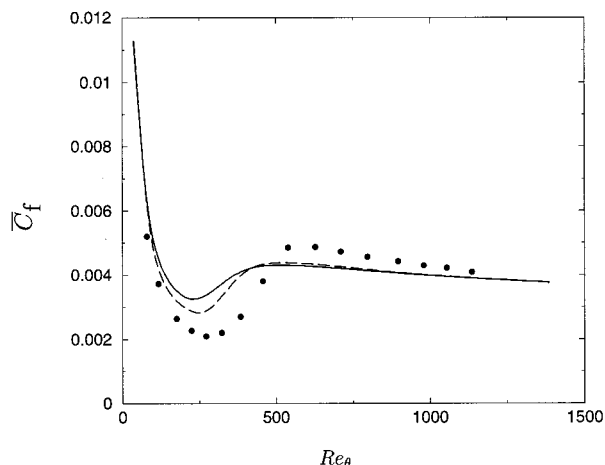


Fig. 11 Skin friction coefficient for the T3A case; \bullet ERCOFTAC database; — ν^2-f ($n=1$); - - ν^2-f ($n=6$)

$$k=0; \quad \overline{v^2}=0; \quad \varepsilon = 2\nu \lim_{y \rightarrow 0} k/y^2;$$

$$f = -(24 - 4N)\nu^2 \lim_{y \rightarrow 0} \overline{v^2}/\varepsilon y^4$$

The integer N defines a set of models [17]. The choice $N=6$ gives the simple boundary condition $f=0$. That is the value used here.

The length and time scales are

$$\left. \begin{aligned} C'_{\varepsilon_1} &= C_{\varepsilon_1} (1 + 0.045 \sqrt{k/\nu^2}) \\ T &= \max \left[\frac{k}{\varepsilon}; 6 \left(\frac{\nu}{\varepsilon} \right)^{1/2} \right]; \quad L = \max \left[\frac{k^{3/2}}{\varepsilon}, C_\eta \left(\frac{\nu^3}{\varepsilon} \right)^{1/4} \right] \end{aligned} \right\} \quad (4)$$

The model constants are

$$C_{\varepsilon_1} = 1.4; \quad C_{\varepsilon_2} = 1.9; \quad C_\mu = 0.22; \quad C_1 = 0.4; \quad C_2 = 0.3 \quad (5)$$

A calibration for two values of N is

$$N=1: \quad C_L = 0.25; \quad C_\eta = 85.0; \quad \sigma_\varepsilon = 1.3$$

$$N=6: \quad C_L = 0.23; \quad C_\eta = 70.0; \quad \sigma_\varepsilon = 1.0$$

These two calibrations give quite similar predictions in turbulent flow. Figure 11 shows they also yield similar transition predictions for the ERCOFTAC T3A case.

Nomenclature

- b = inlet wake half-width
- C_f = skin friction
- k = turbulence kinetic energy
- L = characteristic length scale
- Re = Reynolds number $-U_{ref}L/\nu$
- Re_θ = momentum thickness Reynolds number
- t = time
- u = instantaneous streamwise velocity component
- U_{ref} = characteristic velocity scale
- U_{cyl} = cylinder velocity, inlet wake traversing velocity
- x, y, z = Cartesian coordinates
- α = wake angle $\tan^{-1} U_{cyl}/U_{ref}$
- ϕ = phase of wake passing
- ν, ν_t = molecular and turbulent eddy viscosity
- T = wake passing period
- δ^* = displacement thickness
- ε = viscous dissipation rate of k
- θ = momentum thickness

Subscripts

- blasius = laminar Blasius solution
- ref = upstream reference value
- max = maximum wake deficit
- wake = in wake coordinate system

Superscripts

- = time-averaging

Other symbols

- $\langle \rangle$ = phase-averaging

References

- [1] Halstead, D. E., Wisler, D. C., Okiishi, T. H., Walker, G. J., Hodson, H. P., and Shin, H. W., 1997, "Boundary Layer Development in Axial Compressors and Turbines—Part 1: Composite Picture; Part 2—Compressors; Part 3—LP turbines; Part 4—Computations and Analysis," *ASME J. Turbomach.*, **119**, pp. 114–127, 128–138, 225–237, 426–443.
- [2] Savill, M., 1996, "One Point Closures Applied to Transition," in: *Turbulence and Transition*, Hallback et al., eds., Kluwer Press.
- [3] Kang, D. J., and Lakshminarayana, B., 1997, "Numerical Prediction for Unsteady Transitional Boundary Layer Flow Due to Rotor–Stator Interaction," *AIAA Paper No. 97-2752*.
- [4] Simon, F. F., and Ashpis, D. E., 1996, "Progress in Modeling of Laminar to

- Turbulent Transition on Turbine Vanes and Blades," NASA TM-107180.
- [5] Durbin, P. A., and Laurence, K., 1996, "Nonlocal Effects in Single Point Closure," in: *Advances in Turbulence Research—1996*, Korea University, Seoul, Korea, pp. 109–120.
- [6] Wilcox, D. G., 1993, *Turbulence Modeling for CFD*, DCW Industries, Inc.
- [7] Dong, Y., and Cumpsty, N. A., 1990, "Compressor Blade Boundary Layers, Part 1: Test Facility and Measurements With No Incident Wakes; Part 2: Measurements With Incident Wakes," *ASME J. Turbomach.*, **112**, pp. 222–240.
- [8] Orth, U., 1993, "Unsteady Boundary Layer Transition in Flow Periodically Disturbed by Wakes," *ASME J. Turbomach.*, **115**, pp. 707–713.
- [9] Hodson, H. P., 1998, "Blade Row Interactions in Low Pressure Turbines," in: *Blade Row Interference Effects in Axial Turbomachinery Stages*, C. H. Sieverding and H. P. Hodson, eds., von Karman Institute for Fluid Dynamics Lecture Series 1998–02.
- [10] Liu, X., and Rodi, W., 1991, "Experiments on Transitional Boundary Layers With Wake Induced Unsteadiness," *J. Fluid Mech.*, **231**, pp. 229–256.
- [11] Wu, X., Jacobs, R. G., Hunt, J. C. R., and Durbin, P. A., 1999, "Simulation of Boundary Layer Transition Induced by Periodically Passing Wakes," *J. Fluid Mech.*, **398**, pp. 109–153.
- [12] Wu, X., and Durbin, P. A., 2000, "Numerical Simulation of Heat Transfer in a Transitional Boundary Layer With Passing Wakes," *ASME J. Heat Transfer*, in press.
- [13] Spalart, P. R., and Allmaras, S. R., 1994, "A One-Equation Turbulence Model for Aerodynamic Flows," *La Recherche Aerospaciale*, **1**, pp. 5–21.
- [14] Durbin, P. A., 1995, "Separated Flow Computation With the v^2-f Model," *AIAA J.*, **33**, pp. 659–664.
- [15] Baldwin, B. S., and Barth, T. J., 1991, "A One-Equation Turbulent Transport Model for High-Reynolds Number Wall Bounded Flows," *AIAA Paper No. 91-0610*.
- [16] Parneix, S., Behnia, M., and Durbin, P. A., 1998, "Computation of 3-D Turbulent Boundary Layers Using the v^2-f Model," *Flow, Turbulence and Combustion*, **60**, pp. 19–46.
- [17] Lien, F. S., Kalitzin, G., and Durbin, P. A., 1998, "RANS Modeling for Compressible and Transitional Flows," *Proc. Summer Program*, Center for Turbulence Research, pp. 267–286.
- [18] Schlichting, H., 1979, *Boundary Layer Theory*, McGraw-Hill, New York.

Spectral Measurements in Transitional Boundary Layers on a Concave Wall Under High and Low Free-Stream Turbulence Conditions

Ralph J. Volino

Department of Mechanical Engineering,
United States Naval Academy,
Annapolis, MD 21402

Terrence W. Simon

Heat Transfer Laboratory,
Department of Mechanical Engineering,
University of Minnesota,
Minneapolis, MN 55455

The relationship between free-stream turbulence and boundary layer behavior has been investigated using spectral measurements. The power spectral densities of turbulence quantities in transitional and fully turbulent boundary layers were computed and compared to the power spectra of the same quantities measured in the free stream. Comparisons were made using the "transfer function." The transfer function is the ratio of two spectra at each frequency in the spectra. Comparisons were done in flows with low (0.6 percent) and high (8 percent) free-stream turbulence intensities. Evidence was gathered that suggests that relatively low-frequency, large-scale eddies in the free stream buffet the boundary layer, causing boundary layer unsteadiness at the same low frequencies. These fluctuations are present in both transitional and fully turbulent boundary layers. They are seen under both high and low free-stream turbulence conditions, although they are stronger in the high-turbulence case. Examination of the turbulent shear stress suggests that the low-frequency fluctuations enhance transport in the boundary layer but they are not so effective in promoting eddy transport as are turbulent eddies produced and residing within the boundary layer. In the fully-turbulent boundary layer, higher-frequency fluctuations are added to the low-frequency unsteadiness. These higher-frequency fluctuations, not seen in the transitional boundary layer, are associated with turbulence production in the boundary layer and appear not to be directly related to free-stream unsteadiness. [S0889-504X(00)00403-7]

Introduction

Free-stream turbulence has a strong effect on the behavior of boundary layers. Elevated free-stream disturbance levels tend to cause early transition from laminar to turbulent flow, can lead to higher skin friction and heat transfer coefficients, and can affect boundary layer separation. High free-stream turbulence tends to cause rapid (bypass) transition, but when stabilizing effects such as acceleration are present, the transition zones can be extended.

Highly disturbed flows are found in many applications, including gas turbine engines where free-stream turbulence levels as high as 20 percent are possible. It is generally accepted [1] that a significant fraction of the boundary layer on a gas turbine blade can be transitional as a result of concurrent, strong acceleration. Accurate prediction of heat transfer and fluid mechanics, necessary for improved turbine design, depends therefore on an ability to predict the effects of high turbulence intensity and strong acceleration on transition. While transitional flows can, in principle, be calculated through direct numerical simulation (DNS) of the Navier–Stokes equations, this is not practical and will not be practical for design purposes for perhaps the next decade. Designers must therefore depend on transition models.

Existing transition models are not robust and tend to perform poorly when applied to high-disturbance environments [1]. Presently lacking is the good understanding of the interaction between the free-stream and boundary layer needed for accurate prediction of transition in high-disturbance environments. This "receptivity" of the boundary layer to free-stream disturbances has been under investigation for some time, as documented by Reshotko

[2]. While it is clear that the free-stream influences the boundary layer, the mechanism by which this happens is not entirely clear, particularly under high-free-stream-disturbance conditions [3]. Most turbulence models assume that turbulence enters the boundary layer from the free stream by a diffusion process. Recent studies such as Johnson and Ercan [4], Mayle et al. [5,6], and Voke and Yang [7], however, suggest that pressure fluctuations, not diffusion, are the primary mechanism by which turbulence enters the boundary layer.

In an effort to understand bypass transition better, experiments have been conducted by several investigators to document flow behavior at high free-stream turbulence levels. Volino and Simon [8] provide a review of transition work. Most of the work has focused on mean quantities such as local heat transfer coefficients, mean velocity and temperature profiles, and statistical quantities, such as the turbulent kinetic energy, turbulent shear stress, and turbulent heat flux. Other studies have considered the structure of the boundary layer turbulence using techniques such as quadrant analysis [9]. Documentation of this type has been valuable for building an understanding of the flow and testing models, but it has not provided the necessary information for relating the boundary layer behavior to the free-stream conditions.

The present study attempts to address the boundary layer–free-stream relationship by examining the power spectral density (PSD) of boundary layer and free-stream turbulence. Spectra, unlike mean and statistical quantities, provide some information about the range of eddy scales and the distribution of turbulence kinetic energy among these scales in a flow. By comparing the boundary layer and free-stream spectra, one may learn characteristics of the relationship between the two. Spectral analysis will

Contributed by the International Gas Turbine Institute for publication in the JOURNAL OF TURBOMACHINERY. Manuscript received by the International Gas Turbine Institute August 1997. Associate Technical Editor: T. H. Okiishi.

not reveal all the secrets associated with the receptivity mechanism, but it does provide another perspective of this complex flow.

The method of comparison of spectra used here is the "transfer function." The transfer function, commonly used in controls or vibration analyses, is a ratio of an output function PSD to an input function PSD. The ratio is taken at each represented frequency over the full range of frequencies in the signals. In this paper, a transfer function is calculated by dividing the PSD from the boundary layer (considered to be the output or dependent function) by the PSD of the free stream (the input or independent function). The boundary layer can be considered to be the system. When a system has a single input and a single output, the transfer function gives a clear indication of which frequencies in the input are amplified by the system and, thus, are present in the output signal. The relationship between the free-stream and boundary layer turbulence spectra is not so simple. Certainly, the free-stream turbulent kinetic energy has an influence on the boundary layer, but boundary layer turbulence is also generated by other mechanisms, such as near-wall bursting, during which translational kinetic energy in the external flow is converted to turbulence energy in the boundary layer. The transfer function can show evidence of free-stream influences on the boundary layer. Also, energy in the boundary layer spectra that is not visible in the free stream indicates a direct origin from sources other than the free stream. The transfer function between the spectra of the turbulent shear stress, $-\overline{u'v'}$, and the turbulent kinetic energy, $\overline{u'^2}$, will tell how turbulent transport is related to the overall fluctuation level in the boundary layer.

Blair and Anderson [10] and Sohn and Reshotko [11] present boundary layer spectra from flows with free-stream turbulence intensities (FSTI) below about 2 percent. Their focus was mainly on Tollmein-Schlichting wave frequencies during the early part of transition. At higher FSTI, Thole and Bogard [12] and Moss and Oldfield [13] acquired data for spectral analysis in fully turbulent boundary layers. Both studies showed two distinct frequencies in the boundary layer. At low wavenumbers, fluctuations in the boundary layer could be tied directly to fluctuations in the free stream at the same frequencies, supporting the work of Mayle et al. [5,6], Johnson and Ercan [4], and Voke and Yang [7] noted above. At higher wavenumbers, turbulence appeared to be generated in the near wall region and was not directly linked to the free stream. In the present study, boundary layer spectra were obtained in an unaccelerated, low-free-stream-turbulence-intensity (FSTI <0.6 percent), transitional flow along a concave wall and in high FSTI (8 percent), accelerated, transitional flows along a concave wall. To the authors' knowledge, this is the first such detailed documentation of such high FSTI transition.

Data Acquisition

Experiments were conducted in a wind tunnel facility described in detail by Kim and Simon [14] and more recently by Volino and Simon [15,16]. All data were acquired in a boundary layer along a test wall with concave streamwise curvature. The test wall was 68 cm wide, and measurements were made near the spanwise center-

line. The test wall had a constant radius of curvature, R , of 97 cm. The strength of curvature, δ/R , ranged from about 0.5 to 2 percent, depending on flow conditions. A suction slot at the leading edge of the test wall insured that a new boundary layer began at the leading edge. A flexible convex wall formed the opposite side of the test section. This wall could be moved to provide the desired streamwise pressure gradient on the test wall. The spacing between the walls was 11.4 cm at the inlet to the test section, decreasing in the streamwise direction when the flow was to be accelerated. In the low-FSTI configuration, air at STP entered the test section with a streamwise unsteadiness of about 0.6 percent. High (8 percent) FSTI was provided with a two-dimensional passive grid consisting of 4.22 cm diameter PVC pipes with 60 percent blockage, as described by Kim et al. [17]. A 1-m-long settling chamber between the grid and the beginning of the test section provided uniform flow to within 3 percent in mean velocity and 6 percent in turbulence level at the entrance to the test section. The turbulence is nearly isotropic. Streamwise decay of the free-stream turbulence in the test section is low and is quantified in Table 1.

Data were acquired using hot-wire anemometry. For u' spectra, a single-wire boundary layer probe (TSI model 1218) was used. For v' and $u'v'$ spectra, a cross-wire boundary layer probe (TSI Model 1243) was used. Single-wire data were acquired in the viscous sublayer at $y^+ = 5$, near the position of maximum turbulence intensity ($y^+ = 17$), and in the free stream. Because the cross-wire probe could not be positioned so close to the wall, data were acquired at y^+ between 50 and 100 and in the free stream.

Data were acquired from the hot-wires using a 12 bit digital oscilloscope. For each spectrum, data were acquired in four sections at sampling rates of 100 Hz, 1 kHz, 10 kHz, and 100 kHz. The data were low-pass filtered at 1/10th the sampling rate (10 Hz, 100 Hz, 1 kHz and 10 kHz for the four sections, respectively). Twenty sets of 4096 data points were acquired for each of the four sections. A Fast Fourier Transform (FFT) was performed on each set of 4096 points to compute each PSD. After the sections of a spectrum were averaged for smoothing, they were pieced together. The data obtained with the 100 Hz sampling rate were used to provide the section of the PSD from 0 to 5 Hz, the 1 kHz sampled data provided the section from 5 to 50 Hz, the 10 kHz sampled data provided the section from 50 to 500 Hz, and the 100 kHz sampled data provided the final section of the PSD from 500 to 5000 Hz. Acquiring the spectra in sections allowed better resolution of the lower frequencies. In the most recent work, after it was recognized that very little energy resided in the 0 to 5 Hz band, the 100 Hz sampled data were not acquired. For these spectra, the 1 kHz sampled data provided to 0 to 50 Hz section of the PSD. The choices of sampling rates, filters, sample size, etc., were primarily functions of the equipment used in the measurements (e.g., a digitizer with 4096 point buffer) and the flow in question. Under different conditions, other choices might be more appropriate.

The uncertainty in the time-averaged quantities $\overline{u'^2}$, $\overline{v'^2}$, and $-\overline{u'v'}$ are 5, 10, and 10 percent, respectively. The uncertainty introduced in the smoothed spectral decomposition is consistent with the above-mentioned quantities. At each frequency in the

Table 1 Conditions for low (1L–3L) and high (1H–7H) FSTI cases

| Station | x [m] | U_∞ [m/s] | $Re_x \times 10^{-5}$ | Re_θ | γ [%] | $K \times 10^{-6}$ | FSTI [%] | u_∞' [m/s] | $\Lambda_{u'}$ [cm] | v_∞' [m/s] | $\Lambda_{v'}$ [cm] | $U_\infty/\Lambda_{v'}$ [Hz] |
|---------|--------|------------------|-----------------------|-------------|--------------|--------------------|----------|-------------------|---------------------|-------------------|---------------------|------------------------------|
| 1L | 0.11 | 17.2 | 1.08 | 220 | ~0 | 0 | 0.63 | 0.10 | 6700 | 0.022 | 10.3 | 167 |
| 2L | 0.36 | 17.2 | 3.76 | 170 | 20-60 | 0 | 0.62 | 0.10 | 6700 | 0.024 | 11.5 | 149 |
| 3L | 1.13 | 17.2 | 11.7 | 2040 | ~100 | 0 | 0.60 | 0.10 | 6700 | -0.022 | ~11 | ~150 |
| 1H | 0.1003 | 6.23 | 0.39 | 260 | 6 | 5.56 | 5.3 | 0.35 | 4.37 | 0.34 | 1.5 | 420 |
| 2H | 0.1895 | 7.32 | 0.87 | 197 | 7 | 4.03 | 4.2 | 0.30 | 3.34 | 0.32 | 1.9 | 397 |
| 3H | 0.2607 | 8.30 | 1.37 | 227 | 12 | 3.13 | 3.5 | 0.29 | 4.18 | 0.32 | 2.2 | 403 |
| 4H | 0.3449 | 9.74 | 2.11 | 209 | 17 | 2.29 | 2.9 | 0.26 | 3.91 | 0.32 | 2.7 | 376 |
| 5H | 0.4231 | 11.00 | 2.92 | 246 | 26 | 1.80 | 2.6 | 0.25 | 4.72 | 0.32 | 3.2 | 351 |
| 6H | 0.5805 | 12.92 | 4.71 | 389 | 72 | 1.30 | 2.1 | 0.23 | 3.42 | 0.30 | 3.6 | 372 |
| 7H | 0.7353 | 14.63 | 6.79 | 495 | 93 | 1.01 | 1.8 | 0.23 | 3.79 | 0.31 | 3.5 | 436 |

spectra, 60 points (30 to each side of the point in question) are curve fit with a power law. The value at each frequency is presented as the value of the curve fit at that frequency.

Transfer functions were calculated by dividing the PSD of one spectrum by the PSD of another at each frequency in the spectra. The uncertainties in the transfer functions, taken as the combined error in the two spectra used to compute them, range from ~10 percent for transfer functions involving only $\overline{u'^2}$ spectra, to 15 percent for transfer functions involving $\overline{v'^2}$ and $-\overline{u'v'}$ spectra.

Experimental Conditions

Under low-FSTI conditions, the free-stream velocity was set to a constant 17.2 m/s and spectral measurements were taken at three streamwise positions; Re_x of 1.08×10^5 , 3.76×10^5 , and 11.7×10^5 . A stable streamwise (Görtler) vortex pattern was observed downstream of the first measurement station. Spectral measurements were taken at spanwise positions corresponding to the upwash and downwash locations of the Görtler vortices. The spectra appeared similar at the two locations, so results are presented below for only the downwash location measurements. At the first station, the boundary layer was laminar or in the early stages of transition. At the second station the boundary layer was transitional, and at the third station it was fully turbulent. Transition was augmented by the Görtler instability as documented in Volino and Simon [18]. Flow parameters for this case are provided in Table 1. Further details of the case are available in Kim et al. [17] and Volino and Simon [15,18].

In the high-FSTI configuration, two cases were considered, one of which is presented here. Both were done in accelerated flow, and results were qualitatively similar for the two cases. Stable Görtler vortices were not observed. Acceleration stabilized the flow and extended the transition zone in spite of the high FSTI. In cases done without acceleration at 8 percent FSTI, transition occurred very near the leading edge. The flow entered the test section with a velocity of 4.9 m/s and FSTI of about 8 percent. The flow was accelerated through the test section with a constant velocity gradient, dU_∞/dx , of 13.7 s^{-1} . The acceleration parameter, K , decreased from a maximum of 9×10^{-6} at the leading edge to 1×10^{-6} at the last measurement station, as shown in Table 1. The Reynolds number and K ranges were chosen for this case to simulate roughly the conditions on the downstream half of the pressure side of a gas turbine blade. The FSTI decreased with streamwise distance, mainly due to the increase in the free-stream velocity. At the last measurement station, the FSTI was 1.8 percent. Spectra were acquired at seven streamwise stations. The boundary layer was transitional at the first six stations, becoming almost fully turbulent (although not yet a mature turbulent boundary layer) by the seventh station. Flow parameters for this case are presented in Table 1. Figure 1 shows a time trace of velocity taken in the boundary layer at the sixth measurement station. Note the two distinct zones in the transitional flow. One zone is characterized by high-frequency, high-amplitude fluctuations. This zone is considered turbulent. The second zone is characterized by lower-frequency, high-amplitude fluctuations. The flow in this zone is not turbulent, but is badly disturbed. The intermittency, γ , is the fraction of the time that the flow appears turbulent. This value was determined using the instantaneous turbulent shear stress. The signals from a cross-wire probe were digitized at a 100 kHz sampling rate and used to calculate the first time derivative of the instantaneous $u'v'$. The square of this derivative was then compared to a threshold value given as $0.00585 U_\infty^4$, where U_∞ is the local time-averaged free-stream velocity. The flow was declared turbulent whenever the threshold was exceeded. The threshold level was set so that the flow declared turbulent corresponded to those zones that appeared turbulent in visual inspection of traces such as that in Fig. 1. The intermittency varies with distance from the wall, but reaches a maximum at a plateau between $y^+ \approx 30$ and $y^+ \approx 80$. The intermittencies listed in Table 1 are based on data taken at

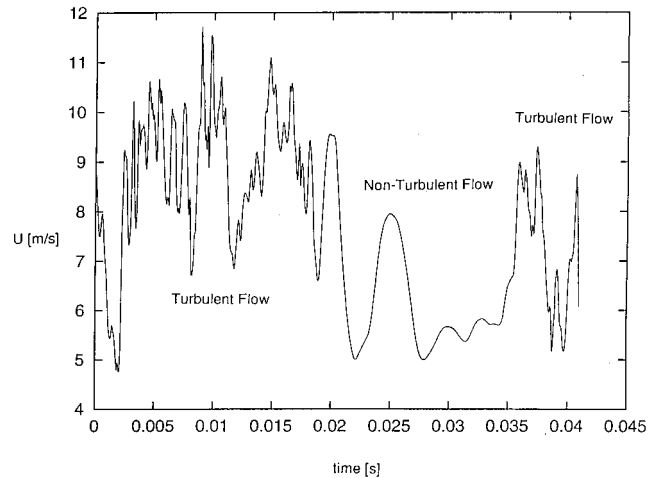


Fig. 1 Velocity time trace showing intermittent flow: high-FSTI case, Station 6, $y^+ = 17$

$y^+ = 50$. The uncertainty in γ is 10 percent. This represents an improvement over intermittencies determined by Volino and Simon [15,16] in the same flow using an analog circuit. The intermittency values remained nearly the same for the first three measurement stations. The beginning of the rise in γ corresponds to the point where K dropped below about 3×10^{-6} . Values of K above 3×10^{-6} are associated with relaminarization [19], so the relationship between γ and K for this flow is consistent with previous researchers' results. More details of this case are available in Volino and Simon [15,16].

Results

Low-FSTI, Unaccelerated Flow. The free-stream u' spectra for the low-FSTI case are shown in Fig. 2. The spectra are left in dimensional coordinates for lack of a clear choice of nondimensionalizing parameter. The spectra do not change greatly in the streamwise direction. The integral length scale in the free stream is $\Lambda_{u'} = 6.7 \text{ m}$, found according to Hinze [20]. The spectra are plotted as $f \times \overline{u'^2(f, df)}/df$ versus $\log f$. In these coordinates, the area under any section of the spectrum is proportional to the energy in that section of the spectrum. In this case, the energy is centered around 0.8 Hz. Fluctuations at these low frequencies are associated with streamwise unsteadiness, and are not due to eddy motion. Nearly all of the energy in $\overline{u'^2}$ lies below 20 Hz.

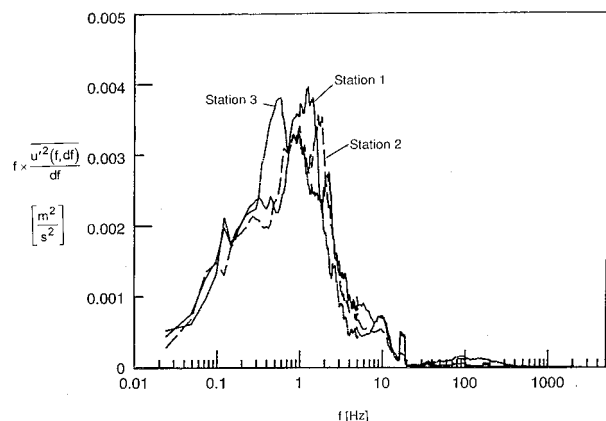


Fig. 2 Free-stream u' spectra: low-FSTI case

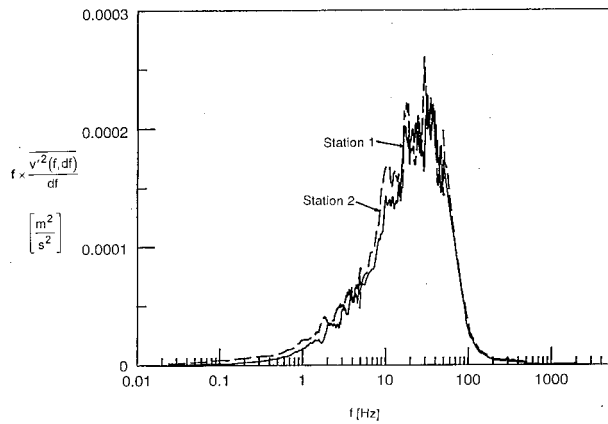


Fig. 3 Free-stream v' spectra: low-FSTI case

Figure 3 shows the free-stream v' spectra at the first and second measurement stations. Below 10 Hz, there is much less energy in $\overline{v'^2}$ than in $\overline{u'^2}$. Above 90 Hz, u' and v' are fairly isotropic (visible in an expanded plot). The integral length scale associated with v' , $\Lambda_{v'}$, is 11 cm. The frequency associated with this length scale, $U_\infty/\Lambda_{v'}$, is 150 Hz (local values of U_∞ are used throughout the results to compute frequencies and length scales). This length scale could be associated with the largest eddies in the flow. The energy in $\overline{v'^2}$ is centered around 20 Hz, in contrast to the $\overline{u'^2}$ PSD. The component $\overline{v'^2}$ appears to be a better descriptor of eddy motion in this case.

Figure 4 shows the transfer function of u' between the boundary layer at $y^+ = 6$ and the free stream at the three streamwise measurement stations. At the first measurement station, the boundary layer contains more energy than does the free-stream in the frequency range 13 to 150 Hz. The low-frequency, $f < 13$ Hz, streamwise unsteadiness is “damped” by the boundary layer, as are the higher frequencies, $f > 150$ Hz. The boundary layer is apparently amplifying the free-stream turbulence for $13 < f < 150$ Hz. This is the range containing most of the energy associated with eddy motion in the free stream (Fig. 3). A possible explanation for the amplification follows: Large-scale, free-stream eddies buffet the boundary layer, causing a displacement of fluid in the y direction (normal to the wall). This displacement causes v' fluctuations in the boundary layer at the frequency associated with the free-stream eddies. It also causes u' fluctuations within the boundary layer at the same frequency due to the normal gra-

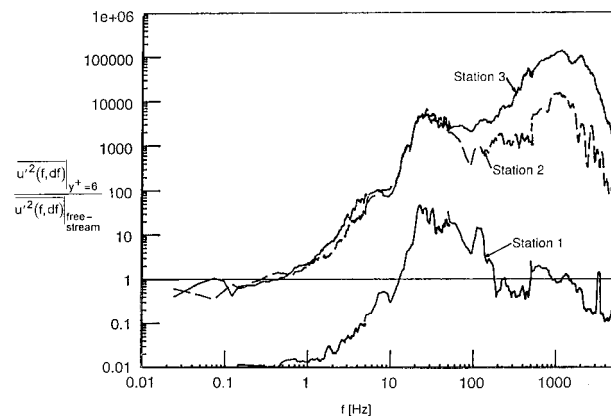


Fig. 4 Transfer function of u' between $y^+ = 6$ and free stream: low-FSTI case

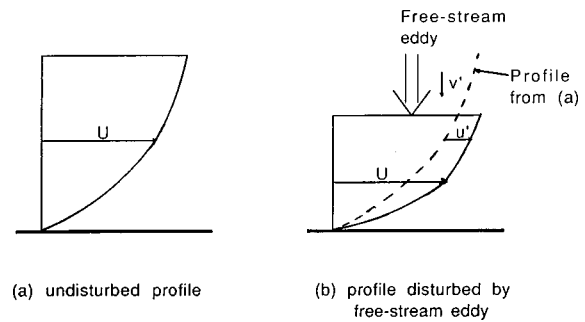


Fig. 5 Depiction of u' caused by large-scale free-stream eddies buffeting the boundary layer: (a) undisturbed profile, (b) profile disturbed by free-stream eddy

dient of streamwise velocity, $\partial U/\partial y$, as depicted by Fig. 5. Amplification occurs because $\partial U/\partial y$ is much larger in the boundary layer than in the free stream. Bradshaw [21] used the terms “inactive motion” and “splat mechanism” to describe this effect. The low-frequency unsteadiness discussed with the u' spectra, which is a streamwise unsteadiness, would not produce this effect because it would not cause a displacement of fluid in the y direction. Voke and Yang [7] provide a very similar description of the free-stream effect on the boundary layer based on a Large Eddy Simulation of a high-FSTI boundary layer. They state that the wall-normal free-stream fluctuations are most significant, and provide further information on how the free-stream disturbance may eventually lead to transition.

At the downstream measurement stations (Fig. 4) where the boundary layer has become turbulent, the broad-band peak of station 1 has grown, and a new broad-band peak centered almost two decades higher has emerged. The higher frequencies are probably associated with boundary layer turbulence, originating from near-wall turbulence production, rather than amplification of anything present in the free stream. The very high values of the transfer function support this conclusion. The transfer functions at the two downstream stations are very similar to each other, although there is some growth at the higher frequencies between the two stations.

Figure 6 shows the transfer function of u'^2 between the boundary layer at $y^+ = 35$ and the free stream at the first and third measurement stations. At the upstream station, the boundary layer and free stream have approximately equal energies (transfer function = 1) below 2 Hz and above 800 Hz. At the intermediate frequencies, centered around 20 Hz, the boundary layer has more energy than the free stream. The transfer function is qualitatively similar to that at $y^+ = 6$ (Fig. 4), but with less “damping” of the

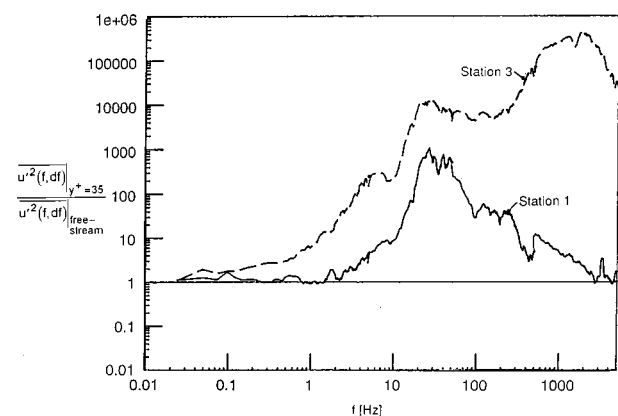


Fig. 6 Transfer function of u' between $y^+ = 35$ and free-stream: low-FSTI case

high and low frequencies and higher values at the intermediate frequencies. If the low transfer function values are due to near-wall viscous effects, the lower values at $y^+ = 6$ compared to those at $y^+ = 35$ should be expected.

At the low FSTI, linear stability theory can be applied to predict unstable frequencies in the boundary layer. Based on stability plots from Schlichting [22], the unstable frequencies for Tollmien-Schlichting (T-S) waves are between 1200 and 2000 Hz at station 1, and between 400 and 1500 Hz at station 2. The boundary layer is unstable for Görtler instability at all frequencies. The low frequency peak at 30 Hz is below the unstable T-S wave band. Free-stream buffeting, as described above, may therefore provide a better explanation for this peak. The higher frequency peak appearing at station 2 may be attributable to a T-S instability. Another possible explanation is that the higher frequency peak is indicative of turbulence as opposed to pretransitional fluctuations. This is supported by the persistence of the peak at station 3, where the boundary layer is fully turbulent.

Mayle et al. [6] provide a theory for predicting the most effective frequency for promoting pretransitional boundary layer fluctuations based on the free-stream spectra and length scales. Applying this theory to the present case, a most effective frequency of 330 Hz is predicted. This frequency is between the peaks in the transfer functions of Figs. 4 and 6. If one examines the boundary layer u' spectra (not shown, but available in Volino and Simon, [15]) 330 Hz is not a significant frequency at stations 1 or 2, but the turbulence is centered around this frequency in the fully turbulent boundary layer at station 3.

High-FSTI, Accelerated Flow. The free-stream u' spectra for the high-FSTI case are shown in Fig. 7. Unlike the low-FSTI case, there is considerable evolution in the streamwise direction. At the first streamwise station, the energy is centered around a peak at 20 Hz. This peak decays rapidly, as do all frequencies below about 400 Hz. Above 400 Hz there is some increase in magnitude with streamwise distance. The overall energy in the free stream drops at first before settling out to a more constant value at the downstream stations. The growth at higher frequencies may be due to a cascading of energy from the low frequencies to the high frequencies (large scales to small); however, some of what appears to be growth is just a slight shift toward higher frequencies due to the accelerating free-stream velocity. The integral length scale, $\Lambda_{u'}$, associated with the u' fluctuations is 4.4 cm at the first measurement station, and remains in the 3.4 cm to 4.4 cm range as the flow moves downstream. The frequency associated with these fluctuations, $U_\infty/\Lambda_{u'}$, rises from 150 Hz at the first station to 420 Hz at the most downstream station. These $\Lambda_{u'}$ values could be associated with large-scale eddy motion. Fig-

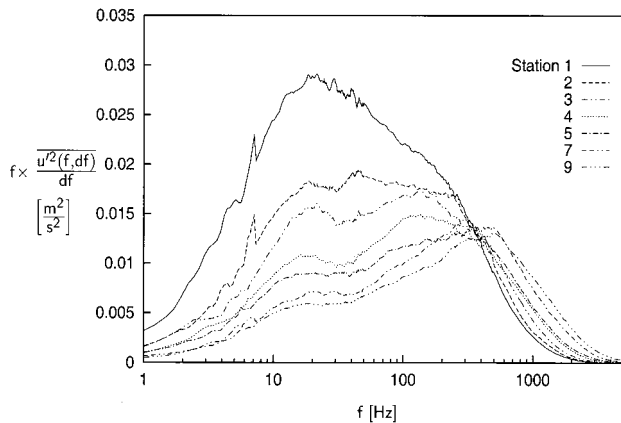


Fig. 7 Free-stream u' spectra: high-FSTI case with streamwise acceleration

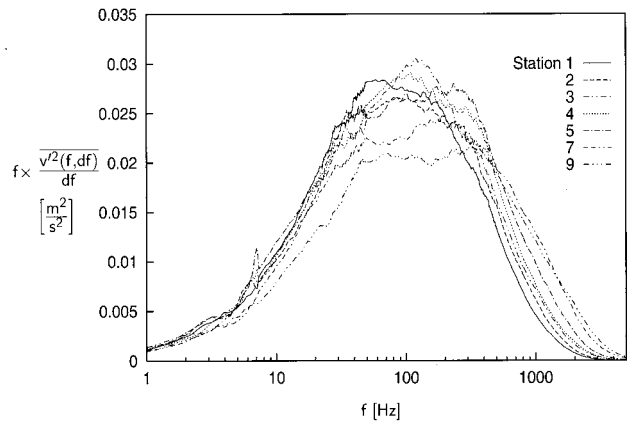


Fig. 8 Free-stream v' spectra: high-FSTI case with streamwise acceleration

ure 8 shows v' spectra in the free stream. The energy is centered around 100 Hz, and there is less evolution in the streamwise direction than was observed in u' . The integral length scale, $\Lambda_{v'}$, associated with the v' spectra is 1.6 cm at the first station, increasing to 3.7 cm at the downstream stations. The associated frequency, $U_\infty/\Lambda_{v'}$, remains fairly constant at about 400 Hz. The u' and v' components, although different, are more comparable in this case than in the low-FSTI case, particularly at the low frequencies. This indicates that the free-stream disturbance in the high-FSTI case is more associated with large scale eddy motion, whereas in the low-FSTI case it was associated more with streamwise unsteadiness.

Figure 9 shows the transfer function of u' between the boundary layer at $y^+ = 5$ and the free stream. At the first streamwise position, the boundary layer and free stream have about the same energy between 0 and 10 Hz. Between 10 and 400 Hz there is more energy in the boundary layer. This peak in the transfer function is centered around 100 Hz, which corresponds to the peak in the free-stream v' spectra in Fig. 8. This correlation between the transfer function and the free-stream v' spectrum at the upstream stations was also seen in the low-FSTI case in Figs. 3, 4, and 6. Above 400 Hz there is much less energy in the boundary layer than in the free stream. The boundary layer appears to damp out the high-frequency fluctuations, acting as a low-pass filter. This behavior also agrees with the low-FSTI case. At the downstream stations, the transfer function remains above 1.0 for all frequencies. The peak at 100 Hz remains, but the most significant growth

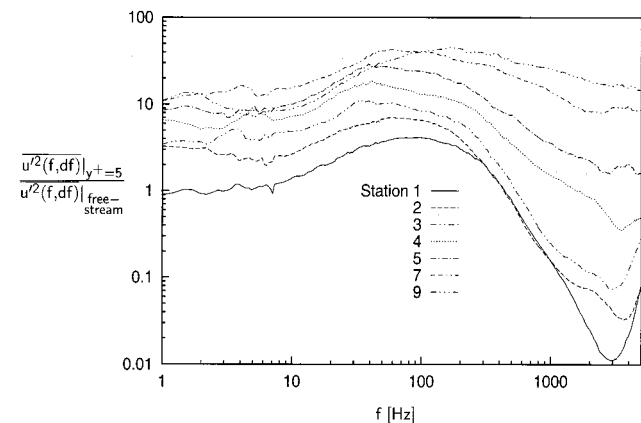


Fig. 9 Transfer function of u' between $y^+ = 5$ and free-stream: high-FSTI case with streamwise acceleration

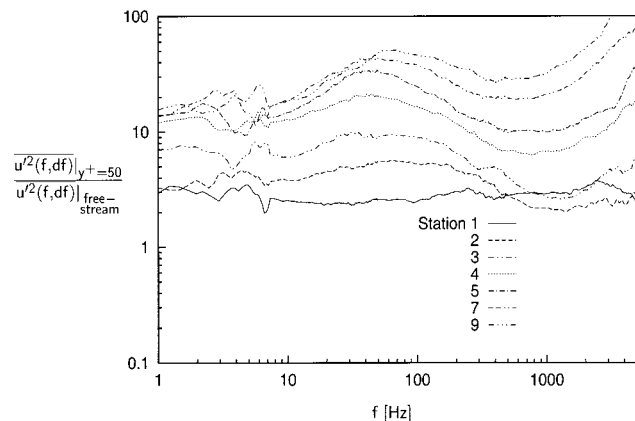


Fig. 10 Transfer function of u' between $y^+=50$ and free-stream: high-FSTI case with streamwise acceleration

occurs above 400 Hz. This again agrees with the low-FSTI case, although the actual values of the transfer functions are lower in the high-FSTI case due to the higher levels of free-stream u' in this case.

Figure 10 shows the u' transfer function between the boundary layer at $y^+=50$ and the free stream. The level of the transfer function is higher at this location than at $y^+=5$ (Fig. 9), but the trends are the same in both figures. Similar results are observed at $y^+=17$ (not shown). Figure 11 shows the v' transfer function between $y^+=50$ and the free stream. The transfer function increases with frequency at all streamwise positions and increases across the entire spectrum with streamwise position. Above 400 Hz, the u' and v' transfer functions of Figs. 10 and 11 are similar. Below 400 Hz they are quite different. The v' transfer function is lower and does not exhibit the 100 Hz peak seen in the u' transfer function.

The results presented in Figs. 10 and 11 are consistent with the explanations proposed above for the low-FSTI case. Free-stream eddies buffet the boundary layer causing a displacement of fluid in the y direction. As depicted in Fig. 5, this displacement, combined with the normal gradient of streamwise velocity, $\partial U/\partial y$, leads to an amplification of u' fluctuations at a frequency associated with the free-stream eddies. This explains the 100 Hz peak in Fig. 10. One would not expect a similar amplification of v' , since the gradient $\partial V/\partial y$ is small. As expected, there is no 100 Hz peak in

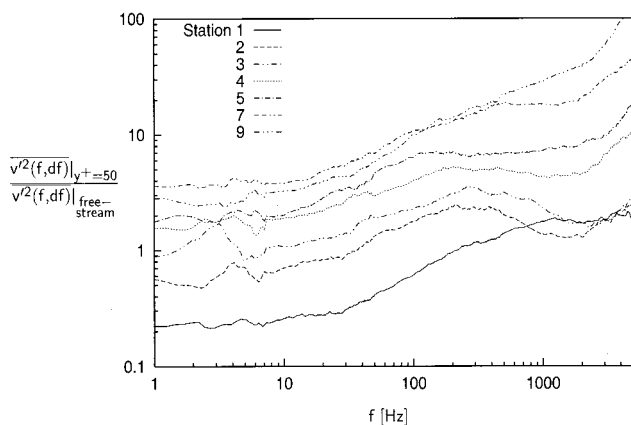


Fig. 11 Transfer function of v' between $y^+=50$ and free-stream: high-FSTI case with streamwise acceleration

Fig. 11. The highest frequencies in the boundary layer are associated with turbulence produced in the near-wall region. At these frequencies, u' and v' are similar.

Bypass transition occurs in the high-FSTI case, but unstable frequency ranges may still be estimated. The accelerating boundary layer is stable according to linear stability theory through the first five stations, then becomes unstable in the 700–1200 Hz band at the two downstream stations. The peaks in the spectra and transfer functions are at lower frequencies than the unstable band, indicating, as expected, that Tollmien–Schlichting type instabilities do not play a significant role in this case.

The Mayle et al. [6] theory predicts a most effective frequency of about 1500 Hz for producing pretransitional fluctuations in the boundary layer. This frequency does not correspond directly with the peaks in the boundary layer spectra or the transfer functions. Possibly the free-stream turbulence, which has its peak at a much lower frequency of 100 Hz (Figs. 7 and 8) is not particularly effective at promoting the type of disturbance described by Mayle et al. [6] in this case.

Mayle et al. [6] also predict the most important frequency for promoting laminar heat transfer in a boundary layer subject to free-stream turbulence. This frequency, which is based on the boundary layer thickness, is about 30 Hz for the present case. This frequency is close to the peak in the free-stream disturbance and the lower frequency peak in the transfer function. This suggests that the free stream in the present case, while not so effective in directly promoting fluctuations that lead to transition, does promote fluctuations that lead to enhanced heat transfer. This is supported by the results of Volino and Simon [16], who document significantly higher heat transfer in this case than would be expected for low disturbance conditions. The lower frequency fluctuations may also play an indirect role, though changes in the mean velocity profile, in promoting transition, as proposed by Volino [23].

Turbulent Shear Stress. The turbulent shear stress, $-\overline{u'v'}$, is the important turbulence quantity for transport of momentum. Figure 12 shows the spectra of $-\overline{u'v'}$ for the high-FSTI case, measured at $y^+=50$. At the first streamwise station, there is relatively little energy in $-\overline{u'v'}$ and the peak is around 100 Hz. At the next station there is little change. Moving to the third, fourth, and fifth stations, there is some growth in $-\overline{u'v'}$, particularly at the higher frequencies, but the overall levels remain relatively low compared to downstream levels. The correlation $-\overline{u'v'}$ rises sharply as the flow moves to the last two measurement stations, and the peak in $-\overline{u'v'}$ shifts to 600 Hz. These stations correspond to the end of transition, where near-wall turbulence produc-

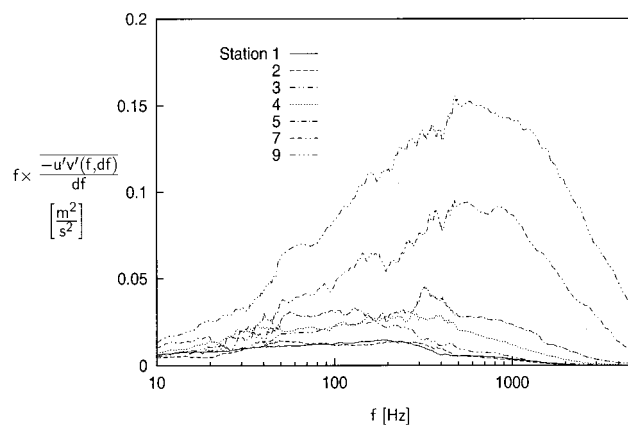


Fig. 12 Boundary layer turbulent shear stress spectra at $y^+=50$: high-FSTI case with streamwise acceleration

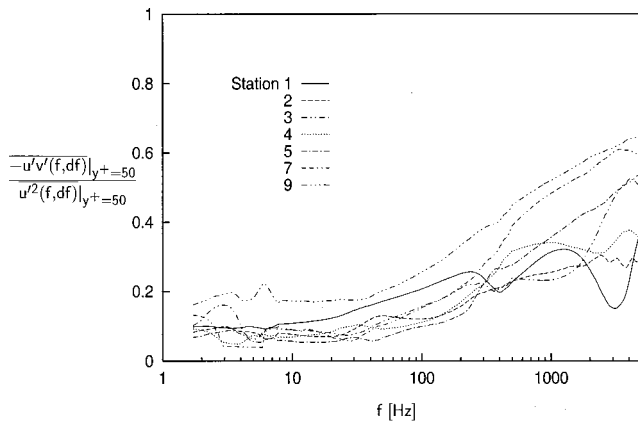


Fig. 13 Transfer function between $-\overline{u'v'}$ and $\overline{u'^2}$ at $y^+=50$: high-FSTI case with streamwise acceleration

tion at higher frequencies is believed to be important. At the last station, the flow is fully turbulent, although not mature.

The transfer function can be used to relate the turbulent shear stress to the fluctuation levels of u' or v' . Figure 13 shows the transfer function between $-\overline{u'v'}$ at $y^+=50$ and u' at the same position. The transfer function is about 0.1 for frequencies below 50 Hz and rises to between 0.4 and 0.7 at 5000 Hz. The high-frequency values tend to rise with increasing streamwise distance, reaching an asymptotic position at downstream stations. Similar measurements, taken in a flow with lower acceleration and more fully turbulent stations, showed the same asymptotic values [15].

The 100 Hz peak in $-\overline{u'v'}$ for the upstream stations, shown in Fig. 12, suggests that the free stream does have an effect in enhancing the momentum transport in the boundary layer. Free-stream eddies buffeting the boundary layer could enhance mixing in the boundary layer, but they would not be so effective as would be the turbulent eddies produced and residing within the boundary layer. This speculation is supported by the lower correlation between $-\overline{u'v'}$ and u' at the lower frequencies than at the high frequencies, as shown in Fig. 13. In agreement with this, Hancock and Bradshaw [24] reported a stronger effect of the free-stream turbulence on $\overline{u'^2}$ than on $-\overline{u'v'}$.

These results are complemented and supported by the results of Volino and Simon [25], where the structure of transitional and fully turbulent boundary layers was documented using octant analysis, an extension of quadrant analysis. Based on the octant distribution, they concluded that the lower correlation in the transitional flow is due to a lack of small-scale eddies.

Conclusions

Spectral analysis has been shown to be useful for comparing the boundary layer turbulence to that of the free stream. The following conclusions are somewhat speculative in nature, but are supported by the results presented above.

1 Low-frequency unsteadiness of the streamwise velocity, u' , which is the predominant unsteadiness in the low free-stream turbulence flow, does not penetrate to very near the wall, as shown by a very low transfer function at $y^+=6$.

2 Large-scale, free-stream eddies are believed to buffet the boundary layer and enhance transport. This is true in both low and high free-stream turbulence flows. With low FSTI the enhancement is small, but with high FSTI, it may be significant. Even at high FSTI, however, the transport is not so effective as observed downstream in the fully turbulent boundary layer, where near-wall turbulence production and smaller-scale eddies are present within

the boundary layer. This conclusion regarding transitional and fully turbulent boundary layers is consistent with that reached using octant analysis.

3 The highest frequencies in the free stream appear to be damped by the boundary layer.

4 The relationship between near-wall turbulence production and the boundary layer unsteadiness caused by the free stream is still not entirely clear, but some light has been shed on it. Based on the Mayle et al. [6] theory, the free-stream fluctuations in the present experiments do not appear to have much of a direct role in producing near wall turbulence and transition. It is possible that the boundary layer unsteadiness induced by the free stream may tend to destabilize the boundary layer, which could have an indirect role in promoting near-wall turbulence production. Considering the free-stream unsteadiness separately from the near-wall production may aid in the development of transition models. Volino [23] has proposed such a model.

Acknowledgments

This work was sponsored by the NASA Lewis Research Center under grant NASA/NAG3-881. The grant monitor was Fred Simon.

Nomenclature

- FSTI = free-stream turbulence
intensity = $\sqrt{(\overline{u'^2} + 2\overline{v'^2})}/3/U_\infty$
 f = frequency
 K = acceleration parameter = $(v/U_\infty^2)(dU_\infty/dx)$
PSD = power spectral density = $\overline{u'^2(f,df)}/df$,
 $\overline{v'^2(f,df)}/df$, or $-\overline{u'v'(f,df)}/df$
 R = radius of curvature
 Re_x = Reynolds number based on distance from leading edge and local free-stream velocity
 Re_θ = momentum thickness Reynolds number
 U = mean streamwise component of velocity
 u' = fluctuating component of streamwise velocity
 $\overline{u'^2}$ = mean square of fluctuating streamwise velocity, based on full spectrum
 $\overline{u'^2(f,df)}$ = contribution to $\overline{u'^2}$ from a frequency band of width df , centered at
 $f = \lim_{\Delta f \rightarrow df} \int_f^{f+\Delta f} \overline{u'^2(f)} df$
 u_τ = friction velocity, $\sqrt{\tau_0/\rho}$
 $-\overline{u'v'}$ = turbulent shear stress
 $-\overline{u'v'(f,df)}$ = contribution to $-\overline{u'v'}$ from a frequency band of width df , centered at
 $f = \lim_{\Delta f \rightarrow df} \int_f^{f+\Delta f} -\overline{u'v'(f)} df$
 V = mean normal component of velocity
 v' = fluctuating normal component of velocity
 $\overline{v'^2}$ = mean square of fluctuating normal velocity, based on full spectrum
 $\overline{v'^2(f,df)}$ = contribution to $\overline{v'^2}$ from a frequency band of width df , centered at
 $f = \lim_{\Delta f \rightarrow df} \int_f^{f+\Delta f} \overline{v'^2(f)} df$
 x = streamwise coordinate
 y = coordinate normal to wall
 y^+ = distance from wall in wall coordinates = yu_τ/ν
 δ = boundary layer thickness
 γ = intermittency
 $\Lambda_{u'}$ = integral length
scale = $(U/4u'^2)(\overline{u'^2(f=0,df)}/df)$, where U is the local free-stream velocity

$\Lambda_{\nu'}$ = integral length
 scale = $(U/4\nu'^2)(\nu'^2(f=0,df)/df)$, where U
 is the local free-stream velocity
 ν = kinematic viscosity
 ρ = density
 τ_0 = wall shear stress

Subscript

∞ = in the free stream

References

- [1] Mayle, R. E., 1991, "The Role of Laminar-Turbulent Transition in Gas Turbine Engines," *ASME J. Turbomach.*, **113**, pp. 509-537.
- [2] Reshotko, E., 1976, "Boundary-Layer Stability and Transition," *Annu. Rev. Fluid Mech.*, **8**, pp. 311-349.
- [3] Morkovin, M. V., and Reshotko, E., 1990, "Dialogue on Progress and Issues in Stability and Transition Research," *Laminar Turbulent Transition* R. Michel and D. Arnal, eds., Springer-Verlag, Berlin.
- [4] Johnson, M. W., and Ercan, A. H., 1997, "Predicting Bypass Transition: A Physical Model Versus Empirical Correlations," ASME Paper No. 97-GT-475.
- [5] Mayle, R. E., and Schultz, A., 1997, "The Path to Predicting Bypass Transition," *ASME J. Turbomach.*, **119**, pp. 405-411.
- [6] Mayle, R. E., Dullenkopf, K., and Schultz, A., 1998, "The Turbulence That Matters," *ASME J. Turbomach.*, **120**, pp. 402-409.
- [7] Voke, P. R., and Yang, Z., 1995, "Numerical Study of Bypass Transition," *Phys. Fluids*, **7**, pp. 2256-2264.
- [8] Volino, R. J., and Simon, T. W., 1995, "Bypass Transition in Boundary Layers Including Curvature and Favorable Pressure Gradient Effects," *ASME J. Turbomach.*, **117**, pp. 166-174.
- [9] Willmarth, W. W., and Lu, S. S., 1972, "Structure of the Reynolds Stress Near the Wall," *J. Fluid Mech.*, **55**, Part 1, pp. 65-92.
- [10] Blair, M. F., and Anderson, O. L., 1987, "Study of the Structure of Turbulence in Accelerating Transitional Boundary Layers," United Technologies Research Center report R87-956900-1.
- [11] Sohn, K. H., and Reshotko, E., 1991, "Experimental Study of Boundary Layer Transition With Elevated Freestream Turbulence on a Heated Flat Plate," NASA CR 187068.
- [12] Thole, K. A., and Bogard, D. G., 1996, "High Freestream Turbulence Effects on Turbulent Boundary Layers," *ASME J. Fluids Eng.*, **118**, pp. 276-284.
- [13] Moss, R. W., and Oldfield, M. L. G., 1996, "Effect of Free-Stream Turbulence on Flat-Plate Heat Flux Signals: Spectra and Eddy Transport Velocities," *ASME J. Turbomach.*, **118**, pp. 461-467.
- [14] Kim, J., and Simon, T. W., 1991, "Free-Stream Turbulence and Concave Curvature Effects on Heated Transitional Boundary Layer, Vol. I—Final Report," NASA CR 187150.
- [15] Volino, R. J., and Simon, T. W., 1995, "Measurements in Transitional Boundary Layers Under High Free-Stream Turbulence and Strong Acceleration Conditions," NASA CR 198413.
- [16] Volino, R. J., and Simon, T. W., 1997, "Boundary Layer Transition Under High Free-Stream Turbulence and Strong Acceleration Conditions: Part 1—Mean Flow Results; Part 2—Turbulent Transport Results," *ASME J. Heat Transfer*, **119**, pp. 420-432.
- [17] Kim, J., Simon, T. W., and Russ, S. G., 1992, "Free-Stream Turbulence and Concave Curvature Effects on Heated, Transitional Boundary Layers," *ASME J. Heat Transfer*, **114**, pp. 338-347.
- [18] Volino, R. J., and Simon, T. W., 1997, "Measurements in a Transitional Boundary Layer With Görtler Vortices," *ASME J. Fluids Eng.*, **119**, pp. 562-568.
- [19] Jones, W. P., and Launder, B. E., 1972, "Some Properties of Sink-Flow Turbulent Boundary Layers," *J. Fluid Mech.*, **56**, pp. 337-351.
- [20] Hinze, J. O., 1975, *Turbulence*, 2nd ed., McGraw-Hill, New York.
- [21] Bradshaw, P., 1994, "Turbulence: the Chief Outstanding Difficulty of our Subject," *Exp. Fluids*, **16**, pp. 203-216.
- [22] Schlichting, H., 1979, *Boundary Layer Theory*, 7th ed., McGraw-Hill, New York.
- [23] Volino, R. J., 1998, "A New Model for Free-Stream Turbulence Effects on Boundary Layers," *ASME J. Turbomach.*, **120**, pp. 613-620.
- [24] Hancock, P. E., and Bradshaw, P., 1989, "Turbulence Structure of a Boundary Layer Beneath a Turbulent Free Stream," *J. Fluid Mech.*, **205**, pp. 45-76.
- [25] Volino, R. J., and Simon, T. W., 1994, "An Application of Octant Analysis to Turbulent and Transitional Flow Data," *ASME J. Turbomach.*, **116**, pp. 752-758.

Flowfield Measurements in the Endwall Region of a Stator Vane

M. B. Kang¹

K. A. Thole²

Mechanical Engineering Department,
Virginia Polytechnic Institute
and State University,
Blacksburg, VA 24061

A first-stage stator vane experiences high heat transfer rates, particularly near the end-wall, where strong secondary flows occur. In order to improve numerical predictions of the complex endwall flow at low-speed conditions, benchmark quality experimental data are required. This study documents the flowfield in the endwall region of a stator vane that has been scaled up by a factor of nine while matching an engine exit Reynolds number of $Re_{ex} = 1.2 \times 10^6$. Laser Doppler velocimeter (LDV) measurements of all three components of the mean and fluctuating velocities are presented for several flow planes normal to the turbine vane. Measurements indicate that downstream of the minimum static pressure location on the suction surface of the vane, an attenuated suction side leg of the horseshoe vortex still exists. At this location, the peak turbulent kinetic energy coincides with the center of the passage vortex location. These flowfield measurements were also related to previously reported convective heat transfer coefficients on the end-wall showing that high Stanton numbers occur where the passage vortex brings mainstream fluid toward the vane surface. [S0889-504X(00)00803-5]

Introduction

Today's gas turbine designs have the aim of increasing turbine vane heat loads while improving the durability. To accommodate these demands, an understanding of the relevant flow mechanisms affecting the turbine vane heat transfer and aerodynamic losses is needed to insure peak performance. One region that can impact turbine vane durability is the endwall or platform area where the flow is quite complex.

As the endwall boundary layer approaches the stagnation location of the protruding airfoil, it experiences an increase in pressure causing a stronger deceleration for the higher speed fluid than the lower speed fluid in the boundary layer. The differences in the deceleration gives rise to a transverse pressure gradient along the vane causing the higher speed fluid to turn toward the endwall. Subsequently, the formation of a horseshoe vortex occurs just upstream of the turbine vane. One leg of the horseshoe vortex wraps around the pressure side of the vane. While the pressure side leg joins into what is known as the passage vortex, there is more uncertainty as to how the suction side leg develops through the passage. The suction side leg of the horseshoe vortex moves along the suction side of the vane and has the opposite sense of rotation as the passage vortex.

Although there have been a number of endwall flowfield studies, many of those studies have been for rotor blades as compared to stator vanes where stators generally have smaller turning angles and higher flow accelerations. The flowfield measurements presented in this paper are for a stator vane geometry. This work is also important because there has been a rather limited number of studies with reported turbulence measurements and because this study relates the measured surface heat transfer to the measured flowfields.

Past Studies

Throughout the literature there have been a number of proposed endwall flowfield models. Sieverding [1] presents a summary of these models including one of the first given by Langston et al.

¹Present address: Boeing Defense & Space Group, 6633 Canoga Ave., P.O. Box 7922, Canoga Park, CA 91309-7922.

²Present address: Mechanical Engineering Department, Virginia Polytechnic Institute and State University, Blacksburg, VA 24061.

Contributed by the International Gas Turbine Institute and presented at the 44th International Gas Turbine and Aeroengine Congress and Exhibition, Indianapolis, Indiana, June 7–10, 1999. Manuscript received by the International Gas Turbine Institute February 1999. Paper No. 99-GT-188. Review Chair: D. C. Wisler.

[2]. Sharma and Butler [3], Goldstein and Spores [4], and Wang et al. [5] have proposed other models. All of these studies include a horseshoe vortex at the leading edge-endwall intersection with pressure-side and suction-side legs. The differences between these models have been on the role of the leading edge vortex that wraps around the suction side. While Sharma and Butler [3] suggest that the suction side leg is entwined with the passage vortex, Goldstein and Spores [4] show a distinct vortex rising along the span of the turbine blade above the passage vortex. Wang et al. [5] indicated a number of additional vortices occurred in the end-wall region for their low Reynolds number study. Gregory-Smith and Cleak [6] indicated the existence of the suction side leg of the horseshoe vortex only at a position close to the suction-endwall corner very near to the leading edge of their rotor blade. Gregory-Smith and Cleak [6] had a relatively large aspect ratio of 2.1 for their rotor blade study. The fact that they reported the suction side vortex only near the vane-endwall corner may have been influenced, however, by the fact that they had a laminar separation bubble on the suction side of the rotor. Alternatively, Moore et al. [7], who had an aspect ratio of 1, reported fluid from the suction side leg of the horseshoe vortex had convected to the outside of the passage vortex away from the suction surface. Moore et al. [7], however, had placed a boundary layer trip on the blade itself, which may have also influenced the endwall flow.

While several investigators have reported some turbulence measurements, for example Bailey [8] and Moore et al. [7], the majority of these measurements have reported measurements at a location downstream of the passage exit. The most detailed turbulence field measurements inside the passage have been those reported by Gregory-Smith et al. [9] for a rotor blade endwall region. Gregory-Smith et al. [9] reported turbulence levels as high as 29 percent in the vortex core where these high turbulence levels were associated with large aerodynamic losses. In a later study, Gregory-Smith et al. [9] used a grid having an inlet turbulence level of 5 percent to remove the boundary layer separation on the blade. In this study they reported high turbulent Reynolds stresses in the vortex.

Boyle and Russell [10] performed surface heat transfer experiments over a large Reynolds number range for a stator vane geometry. At low Reynolds numbers, they found that Stanton number contours closely followed the inviscid streamlines from the pressure side to the suction side of the airfoil. At higher Reynolds numbers the surface heat transfer correlated closely with the free-stream velocity and thereby appeared more similar to the static

pressure contours. In relating information from the flow visualization to the heat transfer data, Gaugler and Russell [11] combined two studies, their own and that of York et al. [12], for a large-scale turbine vane in which they found that the peak Stanton number coincided with the region having the most intense vortex action.

Based on past studies, there is a clear need to investigate further the heat transfer characteristics of the endwall of a modern day stator vane. Although there has been a link between flowfield visualization and surface heat transfer measurements, a link between measured secondary flows and measured heat transfer is still needed. In addition, benchmark quality flowfield data, including both mean and turbulent velocities, are still needed for comparisons with computational predictions for a vane.

Experimental Design and Measurements

A stator vane, scaled up by a factor of nine, was placed in a wind tunnel facility for this study. The experiment was designed to have a large scaling factor to allow for good measurement resolution in an existing wind tunnel. The construction and the development of the scaled-up stator turbine vane and the test section have been previously documented by Kang et al. [13]. The wind tunnel used in this study is recirculating with a corner test section, shown in Fig. 1(a). This test section contains a scaled-up central turbine vane with two adjacent vanes. The outside adjacent vane was constructed by attaching a leading edge to a plexiglass sidewall allowing for optical access. The placement of this flexible wall exactly matches that surface of an adjacent vane. At the point where an adjacent vane geometry stops, the flexible wall was positioned such that the central vane matched the two-dimensional, inviscid pressure distribution computationally predicted for periodic vanes at low-speed conditions. Pressure measurements on the central vane were made to insure that the flexible wall and stagnation point were positioned correctly. For

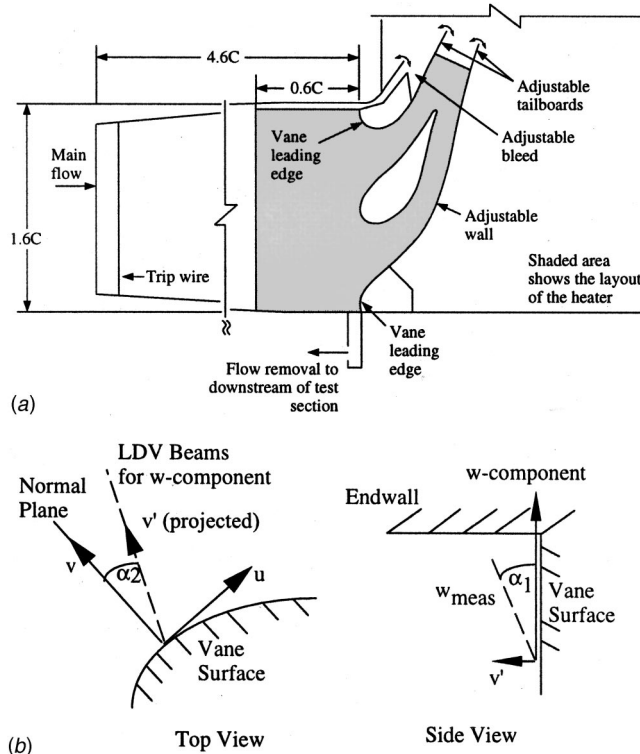


Fig. 1 (a) Top view of the corner test section; (b) velocity correction scheme for the w component

Table 1 Geometric and flow conditions for the stator vane

| | |
|------------------------------|--------------------------|
| Scale factor | 9 |
| Scaled-up true chord length | 59.4 cm |
| Pitch / true chord | 0.77 |
| Span / true chord | 0.93 |
| Re_{ex} | 1.2×10^6 |
| Inlet and exit angles | 0° and 78° |
| Approach length / true chord | 4.6 |

Table 2 Boundary layer parameters one chord upstream

| | |
|--------------------|-------------------|
| δ_{99} (cm) | 5.0 |
| δ^* (cm) | 1.06 |
| θ (mm) | 7.1 |
| H | 1.50 |
| Re_θ | 3340 |
| U_∞ (m/s) | 7.33 |
| Re_{ex} | 1.2×10^6 |

the data presented in this paper, flowfield measurements were taken at locations only upstream of where an actual adjacent vane would geometrically end for the passage.

The upstream side wall boundary layers were removed by adjustable bleeds while tailboards on the outer vanes insured that periodic flow occurred in both passages around the central airfoil (Radomsky and Thole, [14]). The flow was prevented in going from the pressure to the suction sides under the vane by applying a sealant at the base of the vane. A description of the turbine vane itself is given by Table 1.

Inlet boundary layer measurements were made one chord upstream of the stator vane test section on the top and bottom endwalls (Kang et al. [13]). The inlet boundary layer parameters are listed in Table 2. Note that the incident turbulence level upstream of the vane was 0.6 percent. The ratio of boundary layer thickness-to-span is $\delta_{99}/S = 0.09$ for $Re_{ex} = 1.2 \times 10^6$.

Flowfield Measurements

The two-component back-scatter fiber optic LDV system used in this study consisted of a 5 W laser and a TSI model 9201 Colorburst beam separator. Velocity data were processed using a TSI model IFA 755 Digital Burst Correlator controlled using the TSI FIND software. Two different focusing lenses were used for these measurements. The 350 mm focusing lens without a beam expander was used to make measurements of the streamwise (u) and pitchwise (v) components through the top endwall. The spanwise component (w) was measured from the side using the 750 mm focusing lens with a beam expander, as indicated in Fig. 1(b). The probe volume length and diameter for the 350 mm lens were 1.3 mm and $90 \mu\text{m}$ whereas the probe volume length and diameter for the 750 mm lens with the beam expander were 0.85 mm and $46 \mu\text{m}$. For each component of velocity, 10,000 data points were measured to compute mean and turbulence quantities. The LDV data were corrected for biasing using residence time weighting.

To allow measurements to be made close to the endwall–vane surface, the LDV fiber optic probe needed to be slightly tilted off of the vane spanwise axis by an angle of α_1 . For the pressure side planes, the probe needed to be tilted slightly off the axis normal to the vane surface by an angle of α_2 to insure that measurements along the pressure side of the vane were not blocked by the inside adjacent vane. Because of these tilts, the measured spanwise velocity component (w_{meas}) needed to be corrected to get the true spanwise velocity component (w). This correction was possible since the true streamwise and pitchwise velocity components

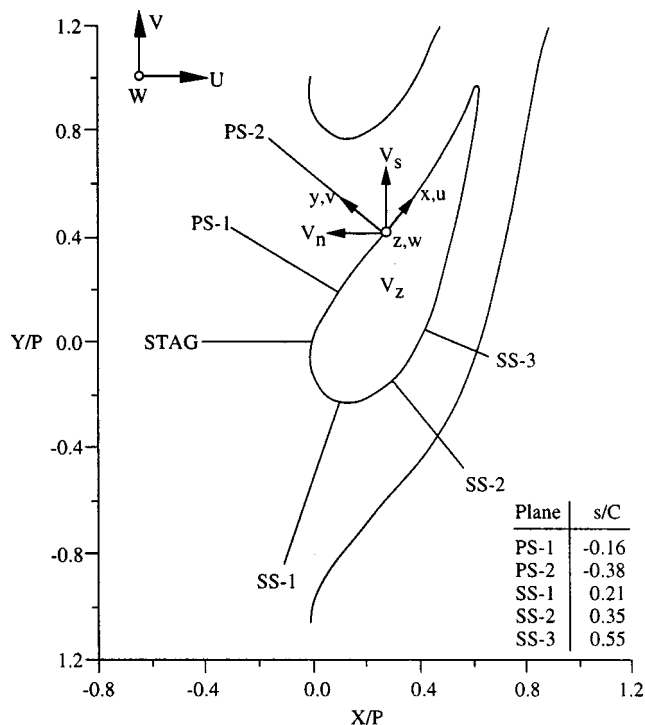


Fig. 2 Locations of the flowfield measurement planes

(with respect to the vane surface) were also measured. The correction scheme that was applied is illustrated in Fig. 1(b) and given by the following relation:

$$w = [w_{\text{meas}} \cos \alpha_1 - v' \sin \alpha_1] \quad (1)$$

where v' is the velocity component projected normal to the measurement plane calculated from the relation,

$$v' = v \cos \alpha_2 + u \sin \alpha_2 \quad (2)$$

The spanwise tilt for all of the planes was $\alpha_1 = 4.8$ deg. The normal axis tilt was $\alpha_2 = 30$ deg and 17 deg for the PS-1 and PS-2 planes, respectively. There was no normal axis tilt for the suction side planes. The largest corrections occurred at the vane midspan due to the high streamwise velocity component, u . Near the wall the correction was much smaller.

Flowfields were measured for two pressure side planes (PS-1 and PS-2) and three suction side planes (SS-1, SS-2, and SS-3) where those planes were orthogonal to the vane surface, as shown in Fig. 2. Note that Kang et al. [13] previously presented flowfield results for the stagnation plane (STAG). The measured local velocity components (u , v , and w) are also shown in Fig. 2. These velocities were then transformed into the streamwise, normal, and spanwise components (V_s , V_n , and V_z) as discussed later in the text.

Endwall Heat Transfer Measurements

Previously reported heat transfer results will be used in this study to relate the secondary flows to the surface heat transfer. A full description of the heat transfer experiments and data is given by Kang et al. [13] and will be briefly described here. The heat transfer results were obtained with a constant heat flux plate that was placed on the bottom endwall surrounding the Styrofoam stator vane. A calibrated infrared camera was used to collect the surface temperature information from the constant heat flux plate on the bottom endwall. The input heat flux was corrected for radiation losses, which amounted to between 4–23 percent of the input power, and conduction losses, which amounted to 1.7–3.5 percent of the input power. No correction was necessary regarding

Table 3 Uncertainty estimates

| Value | Uncertainties |
|--------|--|
| St | 4.5% for $St = 3 \times 10^{-3}$ ($\Delta T = 5^\circ\text{C}$) |
| V_s | 1% near vane-endwall |
| V_n | 7.5% near vane-endwall |
| V_z | 1.5% near vane-endwall |
| k | 2.4% near vane-endwall |
| SKE | 3.5% near vane-endwall |
| ψ | 1.5% near vane-endwall |
| ϕ | 1% near vane-endwall |

heat losses from conduction to the turbine vane itself because the vane was constructed using Styrofoam. Using the measured temperatures and the remaining convective heat flux, the heat transfer coefficients were computed.

Uncertainty Estimates

Uncertainties were calculated based on a 95 percent confidence interval. The partial derivative and sequential perturbation methods, described by Moffat [16], were used to estimate the uncertainties of the measured values. The estimates of uncertainties on each of the values presented in this paper are given in Table 3. Note that the uncertainty estimates were made for the near-endwall region where the highest uncertainties arise. The uncertainty in the Stanton number was quoted for the lowest temperature difference measured which dominated the total uncertainty. The uncertainty for the normal velocity (V_n) was significantly higher than the other velocity components and primarily arose from the uncertainty in the flow angle at the midspan location. For V_n , both u and v velocity components contributed with neither dominating. In comparison for V_s , the term $u \cos \psi_{ms}$ is quite large with the u component dominating. While for V_s the uncertainty was dictated by the uncertainty in the u component, the uncertainty for V_n was dictated by the uncertainty in ψ_{ms} .

Flowfield Analysis

The primary interest of this study was to discern the horseshoe vortex legs and the passage vortex convecting through the turbine vane passage. The velocity vectors of these vortices, which will be referred to as the secondary flow vectors, were determined by transforming the measured local velocities (u , v , and w in Fig. 2) into the mean flow direction based on that occurring at the midspan (V_s , V_n , and V_z). For this transformation the inviscid turning angle was calculated based on the measured velocities at the vane midspan (u_{ms} and v_{ms}) from the following relation:

$$\psi_{ms} = \tan^{-1}(v_{ms}/u_{ms}) \quad (3)$$

The local transformed velocities were calculated using the following:

$$V_s = u \cos \psi_{ms} + v \sin \psi_{ms} \quad (4)$$

$$V_n = -u \sin \psi_{ms} + v \cos \psi_{ms} \quad (5)$$

$$V_z = w \quad (6)$$

The secondary flow vectors are plotted using the components normal to the mean flow direction (V_n , V_z).

In addition to the transformed velocities, contours of the secondary kinetic energy, turbulent kinetic energy, pitch and yaw flow angles are also presented. The normalized secondary kinetic energy is calculated from the following relation:

$$\text{SKE} = (V_n^2 + V_z^2) / \int_0^S \frac{1}{S} U_{in}^2 dz \quad (7)$$

Note that the denominator for the SKE is the inlet kinetic energy calculated across the entire span including the endwall boundary layers. The turbulent kinetic energy (k) and the pitch (ϕ) and yaw (ψ) flow angles were calculated using the relations given in the nomenclature.

Results

The results presented in this paper are for several planes orthogonal to the scaled-up turbine vane on the suction and pressure sides. Prior to making measurements of the flowfield along the endwall pressure and suction surfaces, measurements were made at the vane midspan to compare with those predicted. These measurements were made to insure that the flowrates in each of the two passages were matched and good inlet conditions were achieved. The prediction was made using the two-dimensional, inviscid solver RAMPANT [15]. The computational domain included one passage with periodic boundary conditions.

Figure 3(a) shows a comparison of the measured static pressure distribution and the predicted static pressure distribution from the two-dimensional, inviscid, low-speed calculation. Figure 3(b) compares the velocity components for the inside and outside vane passages as compared with that predicted by RAMPANT for a measurement location at the vane geometric stagnation location. These measurements indicate good periodic flow conditions on the inside and outside passages around the central turbine vane.

Figures 4(a) and 4(b) compare the measured and predicted streamwise velocities and flow angles for each of the flow planes measured at the vane midspan. Note that $y/P=0$ is always measured normal to and outward from the vane surface. Again, the measured values are compared with that predicted using

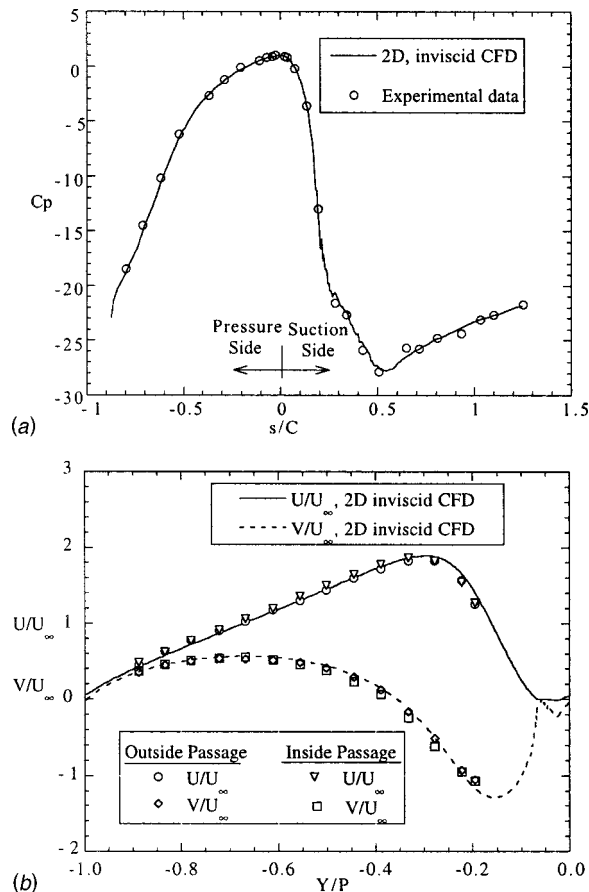


Fig. 3 (a) Static pressure distribution for vane geometry; (b) velocity measurements for inside and outside passages around the central vane compared with CFD

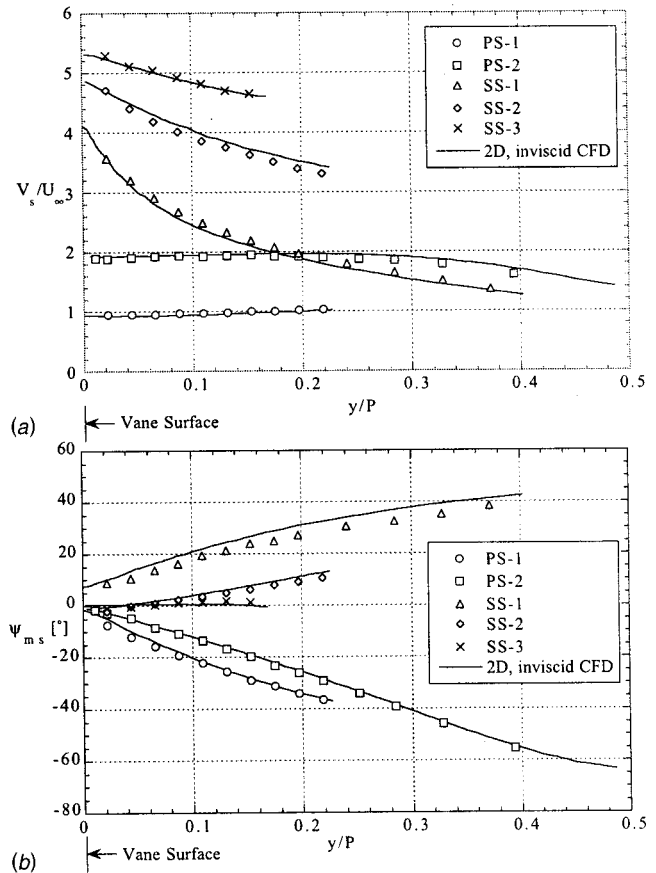


Fig. 4 Comparison of measured and predicted: (a) V_s/U_∞ , and (b) Ψ_{ms} , at the vane midspan

RAMPANT. These results indicate good agreement between that predicted and measured. Across the pressure side planes there is a fairly uniform streamwise velocity while, as expected, there is a large variation across the suction side planes. The flow angles show large turning for the first locations on the pressure and suction sides. Farther downstream, the flow angles are such that the flow is parallel with the surface on the suction side.

Pressure Side Flowfield. Figure 5(a) shows contours of the mean streamwise velocity (V_s) superimposed on the secondary flow vectors for the PS-1 plane for an exit Reynolds number of $Re_{ex} = 1.2 \times 10^6$. Note that the velocity components are normalized by the upstream inlet velocity and the vector scale above the plot shows a unit vector. The location $y/P=0$ is where the surface of the pressure side of the vane is located. At this location, only the passage vortex is detected, which means that the pressure side leg of the horseshoe vortex has already merged with the passage vortex. As expected from past studies, the passage vortex is turning in the clockwise direction. The center of the vortex is located off the vane at $y/P=0.125$ at a spanwise position of $z/S=0.04$, which is slightly below the edge of the boundary layer. It is clear that the vortex has skewed the streamwise velocity contours such that high-speed fluid has been brought down close to the endwall at the location where there is a downward vortex motion. Previously Kang et al. [13] presented surface streakline visualization on the endwall showing that the separation line for PS-1 occurred at $y/P=0.15$, which coincides with the slight positive w component measured on the outside of the vortex. Mainstream fluid is being pulled down by the vortex toward the endwall at a spanwise position as high as $z/S \sim 0.22$. Contours of the secondary kinetic energy (Eq. (7)) normalized by the inlet kinetic energy are shown

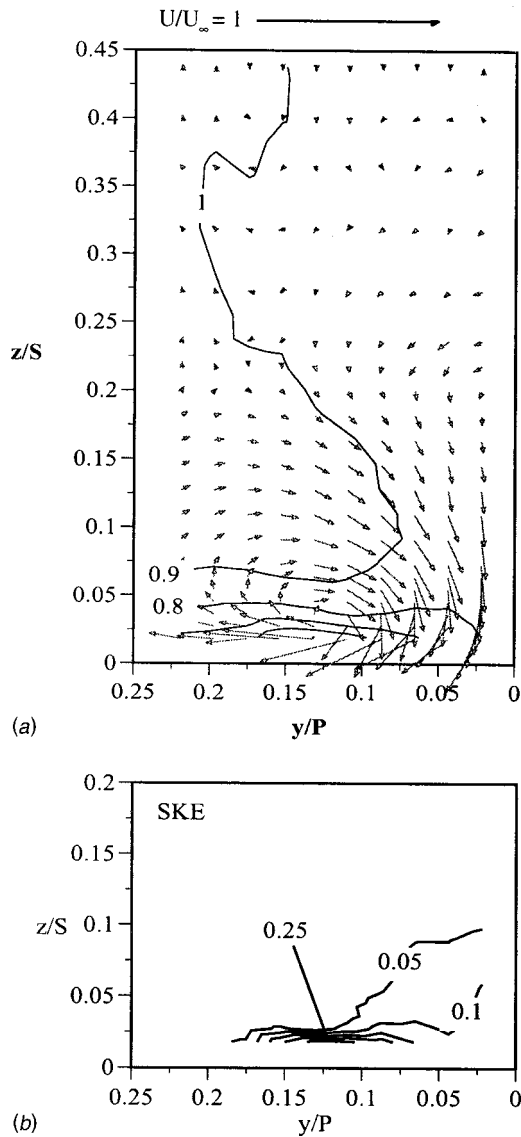


Fig. 5 Measurements of: (a) V_s/U_∞ and secondary velocity vectors, and (b) secondary kinetic energy contours for PS-1

in Fig. 5(b). Contours of the secondary kinetic energy show that the peak value occurs near the endwall surface at a pitch location corresponding to the center of the vortex.

Figure 6(a-d) presents the turbulent velocity fluctuations at PS-1 of all three velocity components along with the combined fluctuations in terms of a turbulent kinetic energy. The peak streamwise velocity fluctuation (u_{rms}) is significantly lower than the other fluctuating velocities with the peak for the spanwise velocity fluctuation (w_{rms}) being the highest. These trends in the relative levels of the streamwise and spanwise velocity fluctuations are the same for all of the other flow planes that have been measured, and are consistent with the measurements presented by Gregory-Smith and Cleak [6]. The peak rms levels for PS-1 all occur at a pitch position that corresponds to the center of the vortex but are at a spanwise position nearer to the endwall at $z/S=0.03$. The peak in turbulent kinetic energy level also occurs at the same pitch position, but slightly closer to the endwall than the center of the vortex. In converting the turbulent kinetic energy to a turbulence intensity, the peak corresponds to a turbulence intensity of 26 percent based on the inlet velocity. The k/U_∞^2 contours are somewhat asymmetric in that closest to the pressure

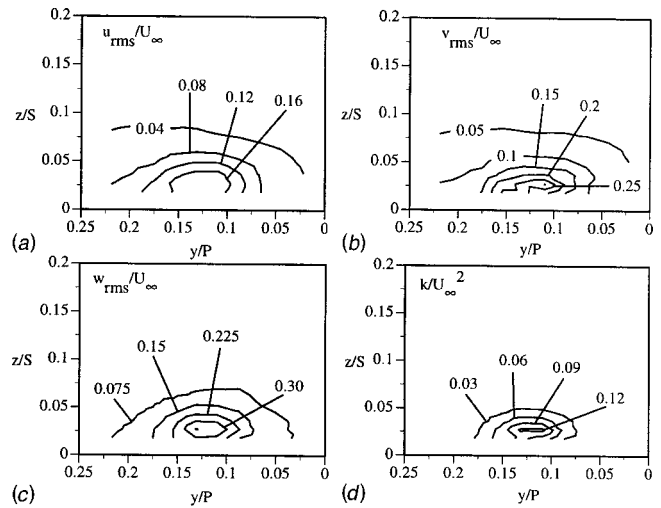


Fig. 6 Normalized contours of measured: (a) u_{rms}/U_∞ , (b) v_{rms}/U_∞ , (c) w_{rms}/U_∞ , and (d) k/U_∞^2 for the PS-1 plane

side vane surface the contours are wrapped under, while away from the vane surface the contours indicate little spanwise gradient.

The yaw angle contours shown in Fig. 7(a) for PS-1 are levels where the midspan value have been subtracted off for that given pitch location ($\psi - \psi_{ms}$). The ψ_{ms} values used for each given pitch location were taken from Fig. 4(b). The pitch flow angle (ϕ) at the midspan location was zero. The yaw contour levels for PS-1 are large positive values near the endwall surface, indicating that close to the endwall the boundary layer fluid is turning much less than at the midspan location. The lower velocity boundary layer fluid does not react to the upcoming vane surface and has a tendency to continue flowing in the same direction as at the inlet. Above the vortex center, which is located near the edge of the boundary layer, the contour levels are negative, indicating the flow is turning slightly more than at the midspan location. These negative values occur because of the streamwise vorticity that the flow experiences as it progresses through the passage. Clearly, the flow in the endwall region is quite skewed. The pitch flow angles, shown in Fig. 7(b), indicate very strong negative values near the endwall-vane corner on the downward side of the vortex leg. The magnitude of the pitch angles on the upward side of the vortex leg indicate that there is only a slight upward curling of the vortex. The cross-pitch pressure gradient drives the flow along the endwall from the pressure surface to the suction surface.

Figure 8(a) shows the secondary velocity vectors superimposed with the streamwise velocity contours for PS-2. The center of the vortex is located at approximately the same position off the vane and endwall as it was for PS-1 at $y/P=0.125$ and $z/S=0.04$. The

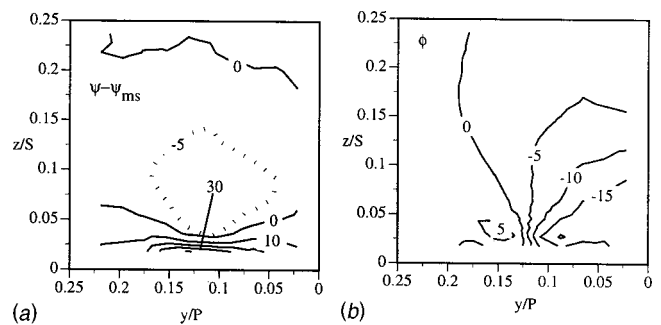


Fig. 7 Contours of measured: (a) yaw ($\Psi - \Psi_{ms}$) and (b) pitch (ϕ) angles for the PS-1 plane

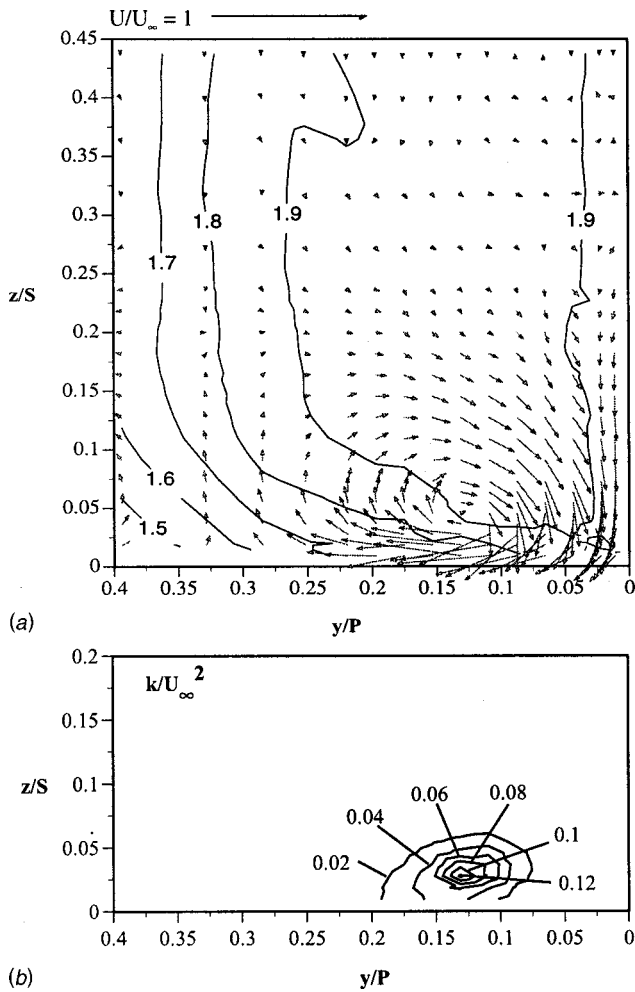


Fig. 8 Measurements of: (a) V_s/U_∞ contours and secondary velocity vectors, and (b) turbulent kinetic energy contours for PS-2

size of the vortex, however, at this location is much larger. Mainstream fluid is being pulled down along the pressure surface toward the endwall starting at a spanwise position of $z/S=0.275$, which is higher than occurred for PS-1. At this location the flow has accelerated such that the streamwise velocity component is as much as 1.9 times faster than the inlet velocity. It is clear that again the vortex has caused some skewing of the streamwise velocity profiles near the endwall at $z/S=0.05$. The turbulent kinetic energy contours for PS-2, given in Fig. 8(b), are quite similar to those for PS-1 with the only difference being a slightly larger peak region for PS-1. The peak level corresponds to the same pitch position ($y/P=0.12$) as the center of the vortex, but slightly closer to the endwall ($z/S=0.03$ for k/U_∞^2 and $z/S=0.05$ for the center of the vortex).

Suction Side Flowfield. Three planes normal to the vane were measured along the suction side of the vane. Figure 9(a) shows the secondary velocity vectors superimposed on the streamwise velocity contours for SS-1. Note that $y/P=0$ now represents the suction surface of the vane. The secondary velocity vectors show both the suction side leg of the horseshoe vortex and the passage vortex from the neighboring vane with the two vortices having opposite rotation directions. The suction leg of the horseshoe vortex is located very close to the vane surface with the center being at $y/P=0.05$. At this location, the mainstream flow has already been highly accelerated. The streamwise velocity contours near the endwall have been skewed due to the passage vor-

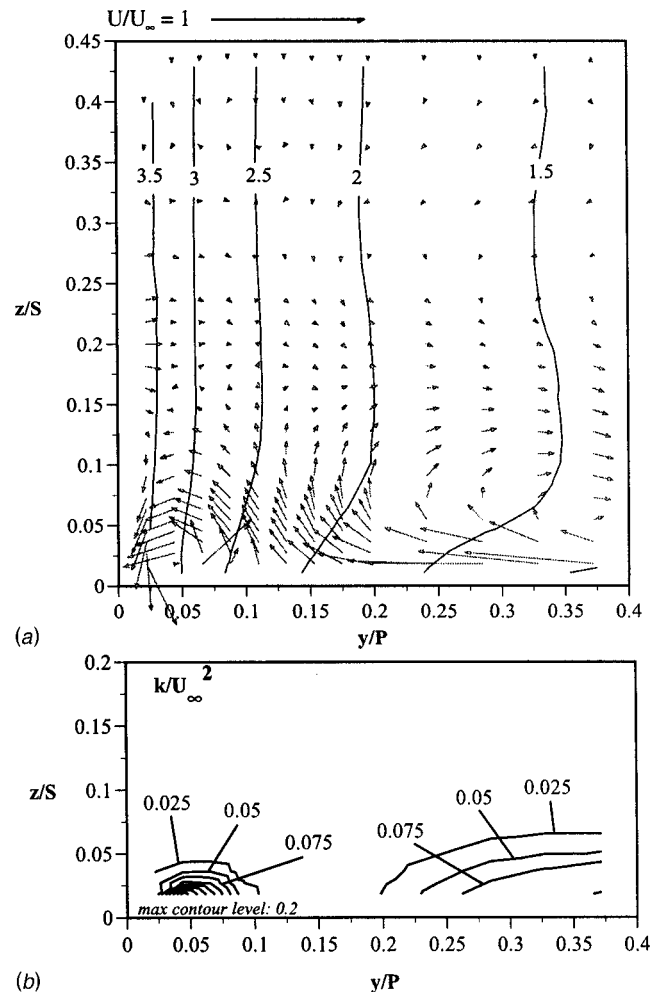


Fig. 9 Measurements of: (a) V_s/U_∞ contours and secondary velocity vectors, and (b) turbulent kinetic energy contours for SS-1

tex. Close to the vane—endwall corner, the streamwise velocity contours show no variation, indicating that the endwall boundary layer is very thin. The suction side leg of the vortex has only a slight effect on the streamwise velocity component near the vane—endwall corner.

The turbulent kinetic energy contours for SS-1, shown in Fig. 9(b), indicate two distinct contour regions for the suction side leg of the horseshoe vortex and the passage vortex. The primary difference in the turbulent kinetic energy levels are that the suction side leg of the horseshoe vortex has higher levels as compared with the passage vortex. The suction side leg of the horseshoe vortex covers a much smaller region of the endwall relative to the passage vortex. The region between the two contour levels has very low turbulence levels. The turbulent kinetic energy levels of the passage vortex shown for SS-1 are very similar to the levels that occurred for PS-1.

The secondary flow vectors and streamwise velocity contours for SS-2 are shown in Fig. 10(a) while the turbulent kinetic energy contours are given in Fig. 10(b). The measurement plane SS-2 is at a surface distance from the stagnation position along the suction surface at $s/C=0.4$, which is still in the acceleration region and just slightly before the minimum static pressure on the vane surface. At this location the suction side leg of the vortex still exists, with the size of the suction leg vortex being much smaller than the passage vortex. The passage vortex has moved significantly closer to the vane surface as compared with SS-1. The streamwise velocity contours show that at this location the

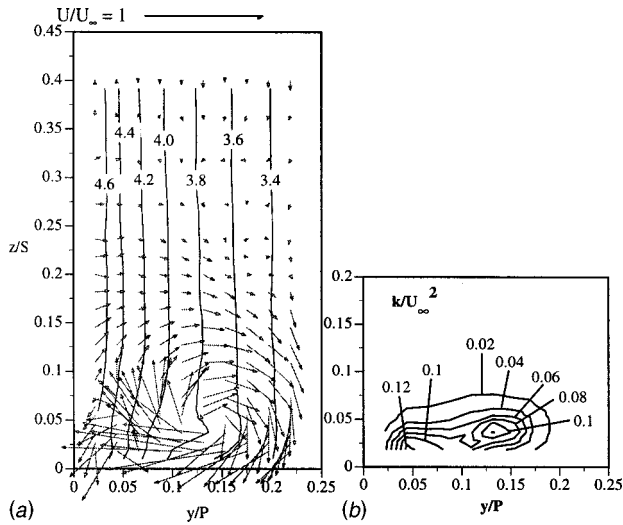


Fig. 10 Measurements of: (a) V_s/U_∞ contours and secondary velocity vectors, and (b) turbulent kinetic energy contours for SS-2

velocity has accelerated to between three and four times the inlet velocity.

The turbulent kinetic energy contours for SS-2 in Fig. 10(b) still show two distinct peak regions from the two vortices but with some overlapping. The one difference between these two high turbulence regions is that the peak turbulence region for the passage vortex is somewhat farther off the endwall than for the suction side vortex. The turbulent kinetic energy contours also show similar contour levels for the two vortex regions with the peaks occurring at the vortex centers. The passage vortex is slightly higher off the endwall than the suction side vortex.

The measurement plane SS-3 is at a surface distance from the stagnation location of $s/C=0.56$, which is approximately the position where the minimum static pressure on the vane occurs. At this location, Fig. 11(a) shows that the passage vortex is quite strong and affecting the mean streamwise velocity components. A suction side leg of the horseshoe vortex very near to the vane surface is still evident, but is very small for the SS-3 plane. The center of the passage vortex is located at a pitch distance even closer to the vane surface at $y/P=0.12$ as compared with the SS-2 where the passage vortex center is located at $y/P=0.14$. The center of the passage vortex is also located slightly higher in the span direction for SS-3 as compared with SS-2. It is clear from the measurements shown in SS-3 that the suction side leg of the horseshoe vortex is being attenuated by the passage vortex at the vane-endwall junction. At this location, the measurements do not agree with the model proposed by Goldstein and Spores [4], who suggested that the suction leg remains distinct rising along the span of the turbine blade above the passage vortex beginning downstream of the boundary layer separation line. The SS-3 plane, shown in Fig. 11(a), is downstream of the separation line. It should be pointed out, however, that the Goldstein and Spores results were for a rotor blade.

The peak turbulent kinetic energy level for SS-3, shown in Fig. 11(b), is much higher than any of the other flow plane locations. Another difference for this plane is that the peak turbulent kinetic energy level is at a pitch and span position that correspond to the center of the vortex. This is distinctly different from the other planes in that the peak level has typically occurred at a spanwise position just below the center of the vortex. The presence of the highly turbulent fluid farther off the endwall is due to the lift induced by the passage vortex.

Contours of the secondary kinetic energy Eq. (7), which has been normalized by the inlet kinetic energy, for SS-3 are shown in

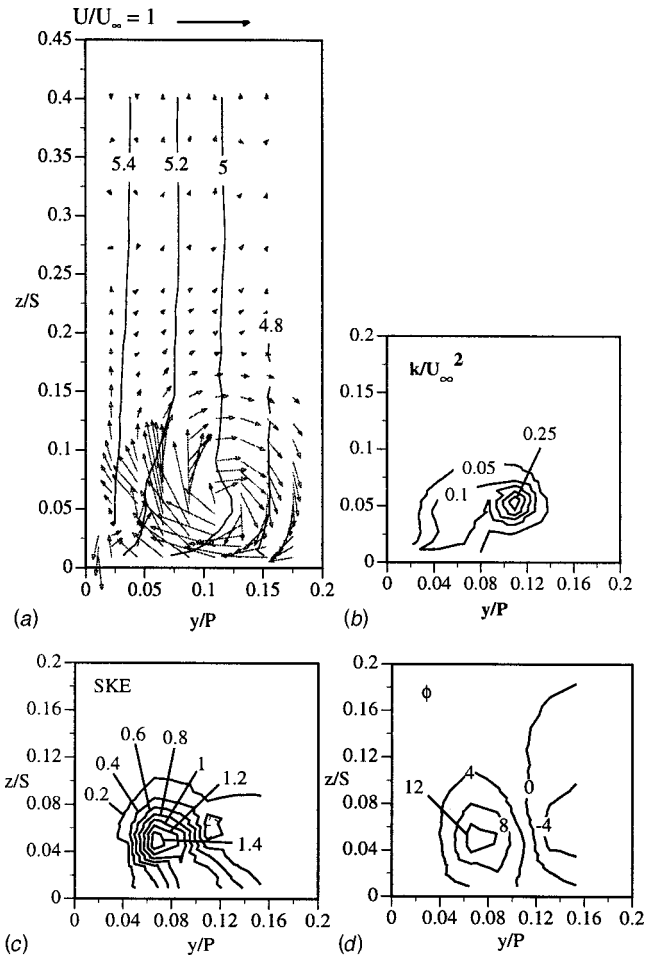


Fig. 11 Measurements of: (a) V_s/U_∞ contours and secondary velocity vectors; (b) turbulent kinetic energy contours for SS-3. Contours of measured: (c) secondary kinetic energy, and (d) pitch (ϕ) angles for the SS-3 plane.

Fig. 11(c). Compared with PS-1, the secondary kinetic energy levels are much higher. Another large difference between PS-1 and SS-3 is that for SS-3 the peak level occurs much off the endwall surface at $z/S=0.05$. The yaw angles relative to that at the midspan for SS-3 indicate much smaller values as compared with PS-1. While there are higher negative pitch values for PS-1, there are much higher positive pitch values for SS-3, shown in Fig. 11(d). The higher positive pitch values for SS-3 indicate that the passage vortex is lifting off the endwall surface. This has been previously reported through endwall visualization studies indicated by the ink climbing onto the suction surface.

Convective Heat Transfer Coefficients for Measured Flow-field Planes.

The local heat transfer coefficients on the endwall for each of the flow plane locations were obtained from the previously reported Stanton number contours by Kang et al. [13]. Note that the Stanton numbers presented by Kang et al. used the upstream inlet velocity for scaling the local heat transfer coefficients. The Stanton numbers shown in Fig. 12 for each of the flow planes are based on the local streamwise velocity (V_s) at the vane midspan. By using the local midspan streamwise velocity as the normalizing scale, the effect of the secondary flows on the surface heat transfer can be addressed. The farthest y/P location where the Stanton numbers are plotted in Fig. 12 corresponds to the last measurement location in that flow plane.

For both the stagnation region and the pressure side of the vane, the highest Stanton number values occur nearest to the vane sur-

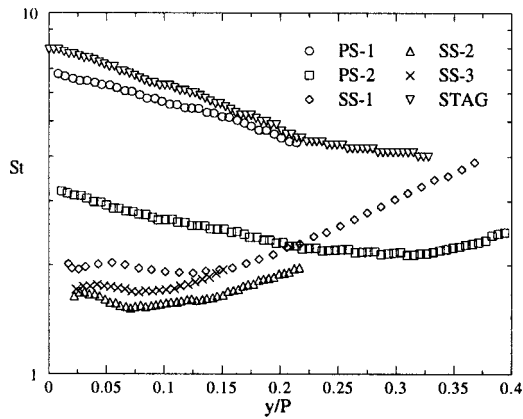


Fig. 12 Stanton number based on V_s for all the planes (based on measured heat transfer coefficients from Kang et al. [13])

face. These peak values occur where the secondary flows are bringing the high-speed mainstream fluid down toward the end-wall thereby thinning the boundary layer. Where the secondary flow is turning upward, the Stanton numbers remain relatively constant. Further away from the vane surface at PS-2, the Stanton numbers again increase at $y/P=0.3$. This increase occurs due to the influence of the horseshoe vortex from the adjacent vane. Although V_s has increased for PS-2 and has been taken into account, the flow condition on the pressure side significantly decreased St for PS-2 relative to PS-1.

For the suction side, moving away from the vane there is first a slight increase in the Stanton number, between $y/P=0.03$ and 0.05 , due to the downward motion of the suction side leg vortex. This increase is then followed by a decrease, with the minimum Stanton number occurring near where the suction side leg of the horseshoe vortex and passage vortex meet. Beyond this point, where the passage vortex is turning upward, there is a rapid increase in the Stanton number. This increase is caused by the upward turning of the passage vortex. Progressing from SS-1 to SS-2, there is a decrease in the overall Stanton number levels. The Stanton numbers for SS-2 and SS-3 are the same close to the vane with only slight differences further away from the vane. Surface heat transfer measurements on the vane midspan indicate that the transition to turbulent flow occurs near the SS-3 vane position (Radomsky and Thole, [14]).

Conclusions

This paper has presented detailed mean and turbulent statistics for the endwall region of a stator vane geometry. The flowfield measurements along the pressure side of the vane indicated that at a position fairly close to the flow stagnation location, only the passage vortex was present, and any remnants of the pressure side leg of the horseshoe vortex were no longer evident. The rms levels of the turbulent fluctuations indicated that the spanwise velocity fluctuations were typically higher than either the streamwise or cross-span fluctuations. The peak turbulent kinetic energy coincided with the same pitch location as the center of the passage vortex region, but at a span position slightly closer to the vane endwall for most of the flow planes measured. The only flow plane where this differed was at the minimum static pressure location on the suction side of the vane. At this location the peak turbulent kinetic energy coincided with the center of the vortex. For this flow plane, high positive pitch values were deduced indicating a lift from the endwall.

The suction side flow planes showed evidence of both the passage and suction side leg of the horseshoe vortex at the farthest downstream position measured, which, again, coincided with the minimum static pressure location along the vane midspan. The

suction side vortex at this location was, however, being attenuated by the passage vortex, which filled almost the entire passage.

The heat transfer measurements showed high Stanton numbers occurred where the mainstream fluid was being brought down to the endwall surface due to the downward leg of the vortices. This happened for both the remnants of the leading edge vortex as well as the passage vortex. As the passage vortex turned upward, there was a decrease in the Stanton numbers across the passage.

Acknowledgments

The authors would like to thank William Kvasnak and Fred Soechting at Pratt & Whitney, W. Palm Beach, Florida, for their support of this work. Thanks for partial support from the DOE-Advanced Gas Turbine Systems Research Program and to Dan Fant for being the contract monitor.

Nomenclature

| | |
|---------------|---|
| C | = true chord of stator vane |
| C_p | = pressure coefficient = $1 - (P_{0,in} - P_s) / (0.5\rho U_{in}^2)$ |
| H | = shape factor = δ^*/θ |
| k | = turbulent kinetic energy = $1/2(u_{rms}^2 + v_{rms}^2 + w_{rms}^2)$ |
| P_0, p_s | = total inlet and local static pressures |
| P | = vane pitch |
| Re_{ex} | = Reynolds number, defined as $Re_{ex} = CU_{ex}/\nu$ |
| Re_θ | = Reynolds number, defined as $Re_\theta = U_{in}\theta/\nu$ |
| s | = vane surface distance from flow stagnation |
| S | = span of stator vane |
| SKE | = secondary kinetic energy |
| St | = Stanton number, defined as $St = h/\rho C_p V_s$ |
| U, u | = reference and local mean velocities; see Fig. 2 |
| v' | = projected velocity component, see Fig. 1(b) |
| V, v | = reference and local mean velocities; see Fig. 2 |
| V_n | = transformed mean normal velocity |
| V_s | = transformed mean streamwise velocity |
| V_z | = transformed mean spanwise velocity |
| W, w | = reference and local mean spanwise velocities; see Fig. 2 |
| X, x | = reference and local streamwise coordinate; see Fig. 2 |
| Y, y | = reference and local normal coordinate; see Fig. 2 |
| Z, z | = reference and local spanwise coordinate; see Fig. 2 |
| α | = LDV tilt angle; see Fig. 1(b) |
| δ_{99} | = boundary layer thickness |
| δ^* | = displacement thickness |
| θ | = momentum thickness |
| ϕ | = pitch angle = $\tan^{-1}(w/u)$ |
| ρ | = density |
| ν | = viscosity |
| ψ | = yaw angle = $\tan^{-1}(v/u)$ |

Subscripts

| | |
|--------|---|
| 1, 2 | = spanwise and normal tilt angles for LDV |
| avg | = average |
| in, ex | = inlet and exit |
| meas | = measured values |
| ms | = midspan values |
| rms | = root mean square |

References

- [1] Sieverding, C. H., 1985, "Recent Progress in the Understanding of Basic Aspects of Secondary Flows in Turbine Blade Passages," *ASME J. Eng. Gas Turbines Power*, **107**, pp. 248–257.
- [2] Langston, L. S., Nice, M. L., and Hooper, R. M., 1977, "Three-Dimensional Flow Within a Turbine Cascade Passage," *ASME J. Eng. Power*, **99**, pp. 21–28.
- [3] Sharma, O. P., and Butler, T. L., 1987, "Predictions of Endwall Losses and Secondary Flows in Axial Flow Turbine Cascades," *ASME J. Turbomach.*, **109**, pp. 229–236.

- [4] Goldstein, R. J., and Spores, R. A., 1988, "Turbulent Transport on the Endwall in the Region Between Adjacent Turbine Blades," *ASME J. Heat Transfer*, **110**, pp. 862–869.
- [5] Wang, H. P., Olson, S. J., Goldstein, R. J., and Eckert, E. R. G., 1997, "Flow Visualization in a Linear Turbine Cascade of High Performance Turbine Blades," *ASME J. Turbomach.*, **119**, pp. 1–8.
- [6] Gregory-Smith, D. G., and Cleak, J. G. E., 1992, "Secondary Flow Measurements in a Turbine Cascade With High Inlet Turbulence," *ASME J. Turbomach.*, **110**, pp. 1–8.
- [7] Moore, J., Schaffer, D. M., and Moore, J. G., 1987, "Reynolds Stresses and Dissipation Mechanisms Downstream of a Turbine Cascade," *ASME J. Turbomach.*, **109**, pp. 258–267.
- [8] Bailey, D. A., 1980, "Study of Mean- and Turbulent-Velocity Fields in a Large-Scale Turbine-Vane Passage," *ASME J. Eng. Power*, **102**, pp. 88–95.
- [9] Gregory-Smith, D. G., Graves, C. P., and Walsh, J. A., 1988, "Growth of Secondary Losses and Vorticity in an Axial Turbine Cascade," *ASME J. Turbomach.*, **114**, pp. 173–183.
- [10] Boyle, R. J., and Russell, L. M., 1990, "Experimental Determination of Stator Endwall Heat Transfer," *ASME J. Turbomach.*, **112**, pp. 547–558.
- [11] Gaugler, R. E., and Russell, L. M., 1984, "Comparison of Visualized Turbine Endwall Secondary Flows and Measured Heat Transfer Patterns," *ASME J. Eng. Gas Turbines Power*, **106**, pp. 168–172.
- [12] York, R. E., Hylton, L. D., and Mihelc, M. S., 1984, "An Experimental Investigation of Endwall Heat Transfer and Aerodynamics in a Linear Vane Cascade," *ASME J. Turbomach.*, **106**, pp. 159–167.
- [13] Kang, M., Kohli, A., and Thole, K. A., 1999, "Heat Transfer and Flowfield Measurements in the Leading Edge Region of a Stator Vane Endwall," *ASME J. Turbomach.*, **121**, pp. 558–568.
- [14] Radomsky, R. W., and Thole, K. A., 2000, "Flowfield Measurements for a Highly Turbulent Flow Around a Stator Vane," *ASME J. Turbomach.*, **122**, pp. 255–262.
- [15] FLUENT/UNS User's Guide, Vers. 4.2, Fluent, Inc., Lebanon, NH.
- [16] Moffat, R. J., 1988, "Describing the Uncertainties in Experimental Results," *Exp. Therm. Fluid Sci.*, **1**, pp. 3–17.

A Time-Linearized Navier–Stokes Analysis of Stall Flutter

William S. Clark
Assistant Research Professor

Kenneth C. Hall
Associate Professor,
Fellow ASME

Department of Mechanical Engineering
and Materials Science,
Duke University,
Durham, NC 27708

A computational method for predicting unsteady viscous flow through two-dimensional cascades accurately and efficiently is presented. The method is intended to predict the onset of the aeroelastic phenomenon of stall flutter. In stall flutter, viscous effects significantly impact the aeroelastic stability of a cascade. In the present effort, the unsteady flow is modeled using a time-linearized Navier–Stokes analysis. Thus, the unsteady flow field is decomposed into a nonlinear spatially varying mean flow plus a small-perturbation harmonically varying unsteady flow. The resulting equations that govern the perturbation flow are linear, variable coefficient partial differential equations. These equations are discretized on a deforming, multiblock, computational mesh and solved using a finite-volume Lax–Wendroff integration scheme. Numerical modeling issues relevant to the development of the unsteady aerodynamic analysis, including turbulence modeling, are discussed. Results from the present method are compared to experimental stall flutter data, and to a nonlinear time-domain Navier–Stokes analysis. The results presented demonstrate the ability of the present time-linearized analysis to model accurately the unsteady aerodynamics associated with turbomachinery stall flutter.

[S0889-504X(00)00203-8]

1 Introduction

Turbomachinery stall flutter is an aeroelastic instability of compressor and fan blades that often occurs near the stall or choke lines on the operating map. Stall flutter usually appears at part speeds where blades are subjected to high mean flow incidences. The vibratory frequencies associated with stall flutter generally coincide with one of the blade's lowest natural frequencies. Frequently, the mode of blade vibration corresponds to the first torsional mode. However, stall flutter can sometimes occur in the first bending mode as well.

A flutter model is composed of two parts: a structural dynamic model of the bladed-disk to predict the mode shapes and natural frequencies of the airfoil vibratory modes, and an unsteady aerodynamic model to predict the aerodynamic forces induced by airfoil vibration. While current finite element models of the structural dynamic behavior of bladed disks are quite acceptable for this application (at least for structurally tuned rotors), unsteady aerodynamic models of separated viscous flows that are both physically accurate and computationally efficient have heretofore been unavailable. Instead, designers have had to rely on empirical correlations.

In conventional stall flutter, the blade vibration is the primary fluid dynamic driver (see Sisto [1] and Chi and Srinivasan [2]). While significant progress has been made in the computational modeling of inviscid unsteady flows over the past 40 years, little headway has been made in modeling unsteady viscous flows, other than through direct simulation using nonlinear time-marching techniques. Unfortunately, these methods are computationally very expensive, and thus of limited use for routine design.

A number of investigators have developed time-linearized models of unsteady inviscid flows in turbomachinery. In the time-linearized approach, the flow is decomposed into a nonlinear steady flow plus a small-perturbation harmonic unsteady flow. The resulting time-linearized equations are linear variable coefficient equations that can be solved very efficiently. Verdon and Caspar [3], Verdon [4], Whitehead and Grant [5], and later Hall [6] developed time-linearized models of two-dimensional poten-

tial flow in cascades. Hall and Crawley [7], Hall and Clark [8], and Holmes and Chuang [9] developed two-dimensional time-linearized Euler solvers. Hall and Lorence [10] have developed a three-dimensional linearized Euler solver and showed that three-dimensional effects have a strong influence on unsteady flows in turbomachinery. All of these analyses are inviscid, however, and thus are not capable of predicting unsteady flows with flow separations, an important feature of stall flutter.

Recently, Clark and Hall [11] developed a time-linearized Navier–Stokes analysis of unsteady viscous flows in cascades. They were able to predict unsteady laminar flows, including laminar separated flows, within a time-linearized framework. Furthermore, their results clearly demonstrated the destabilizing influence of viscosity (flow separation) on the aeroelastic stability of cascades, especially for torsional vibrations of the blades. However, this initial work was limited to laminar flows, and thus neglected the important role of turbulence on the unsteady flow field. More recently, Holmes and Lorence [12] have presented a three-dimensional time-linearized Navier–Stokes analysis with a $k-\omega$ turbulence model. Their computational results, however, were limited to flows with thin attached boundary layers.

In this paper, we apply the time-linearization technique to the two-dimensional Reynolds-averaged Navier–Stokes equations. The one-equation turbulence model due to Spalart and Allmaras [13] provides the necessary closure for the Reynolds stress terms. We present computational predictions of unsteady, viscous flows resulting from torsional blade vibrations of a cascade of fan blades. The computational results from the present time-linearized Navier–Stokes method are compared to experimental data, and also to a nonlinear time-domain Navier–Stokes analysis. Two operating conditions are considered. The first condition presented corresponds to a design point on the operating line of the fan, that is, the steady flow is attached and the blades are subjected to relatively low incidence angles. The second condition corresponds to off-design operation. In this case, the blades are subjected to high incidence angles, and the steady flow separates from the blade over much of the suction surface. In both cases, numerical predictions are found to be in good agreement with the available experimental data.

Contributed by the International Gas Turbine Institute and presented at the 44th International Gas Turbine and Aeroengine Congress and Exhibition, Indianapolis, Indiana, June 7–10, 1999. Manuscript received by the International Gas Turbine Institute February 1999. Paper No. 99-GT-383. Review Chair: D. C. Wisler.

2 Theory

2.1 Governing Equations. In strong conservation law form, the two-dimensional Reynolds-averaged Navier–Stokes equations are given by

$$\begin{aligned} \frac{d}{dt} \int \int_D \mathbf{U} dx dy + \oint_{\partial D} \left(\mathbf{F} - \mathbf{U} \frac{\partial f}{\partial t} \right) dy - \oint_{\partial D} \left(\mathbf{G} - \mathbf{U} \frac{\partial g}{\partial t} \right) dx \\ = \int \int_D \mathbf{S} dx dy \end{aligned} \quad (1)$$

where D is a deforming control volume bounded by the control surface ∂D . The quantities $\partial f/\partial t$ and $\partial g/\partial t$ are the x and y components of the velocity of the control surface ∂D . The vector of conservation variables \mathbf{U} , the flux vectors \mathbf{F} and \mathbf{G} , and the source vector \mathbf{S} are given by

$$\begin{aligned} \mathbf{U} = \begin{bmatrix} \rho \\ \rho u \\ \rho v \\ \rho e \\ \rho \bar{v} \end{bmatrix}, \quad \mathbf{F} = \begin{bmatrix} \rho u \\ \rho u^2 + p - \tau_{xx} \\ \rho uv - \tau_{xy} \\ \rho uH - \tau_{hx} \\ \rho u\bar{v} - \tau_{vx} \end{bmatrix}, \\ \mathbf{G} = \begin{bmatrix} \rho v \\ \rho uv - \tau_{xy} \\ \rho v^2 + p - \tau_{yy} \\ \rho vH - \tau_{hy} \\ \rho v\bar{v} - \tau_{vy} \end{bmatrix}, \quad \mathbf{S} = \begin{bmatrix} 0 \\ 0 \\ 0 \\ 0 \\ S_t \end{bmatrix} \end{aligned} \quad (2)$$

The first four equations are the conservation of mass, x and y components of conservation of momentum, and conservation of energy, respectively. The fifth equation is the Spalart–Allmaras turbulence model written in strong conservation form.

In these equations, ρ is the density, u and v are the velocity components in the x and y directions respectively, e is the total internal energy, H is the total enthalpy, and p is the static pressure. The fluid is assumed to be a perfect gas, so that the total energy e is related to the total enthalpy H by

$$H = e + \frac{p}{\rho} = \frac{\gamma}{\gamma-1} \frac{p}{\rho} + \frac{1}{2} (u^2 + v^2) \quad (3)$$

The shear stresses τ_{xx} , τ_{xy} , and τ_{yy} are given by

$$\tau_{xx} = (\mu + \mu_t) \left(\frac{4}{3} \frac{\partial u}{\partial x} - \frac{2}{3} \frac{\partial v}{\partial y} \right) \quad (4)$$

$$\tau_{xy} = (\mu + \mu_t) \left(\frac{\partial u}{\partial y} + \frac{\partial v}{\partial x} \right) \quad (5)$$

$$\tau_{yy} = (\mu + \mu_t) \left(\frac{4}{3} \frac{\partial v}{\partial y} - \frac{2}{3} \frac{\partial u}{\partial x} \right) \quad (6)$$

where μ , μ_t , and ν are the molecular viscosity, the turbulent viscosity, and the kinematic viscosity, respectively. The terms τ_{hx} and τ_{hy} in the energy equation are given by

$$\tau_{hx} = u \tau_{xx} + v \tau_{xy} - q_x \quad (7)$$

$$\tau_{hy} = u \tau_{xy} + v \tau_{yy} - q_y \quad (8)$$

where q_x and q_y are the x and y components of the heat flux, respectively, and can be written as

$$q_x = - \left(\frac{\mu c_p}{\text{Pr}} + \frac{\mu_t c_p}{\text{Pr}_t} \right) \frac{\partial T}{\partial x} \quad (9)$$

$$q_y = - \left(\frac{\mu c_p}{\text{Pr}} + \frac{\mu_t c_p}{\text{Pr}_t} \right) \frac{\partial T}{\partial y} \quad (10)$$

where c_p is the specific heat at constant pressure, T is the temperature, and Pr and Pr_t are the laminar and turbulent Prandtl numbers, respectively.

In the present study, the laminar coefficient of viscosity is determined using Sutherland's law. The turbulent viscosity is modeled using the one-equation turbulence model due to Spalart and Allmaras [13]. The turbulence model describes the convection, production, and destruction of the turbulent viscosity μ_t in terms of \bar{v} , the working "conservation" variable, i.e.,

$$\mu_t = \rho \bar{v} f_{v1}(\chi) \quad (11)$$

where

$$\chi = \frac{\bar{v}}{\nu}, \quad f_{v1} = \frac{\chi^3}{\chi^3 + 7.1^3} \quad (12)$$

The working variable \bar{v} is used in lieu of the turbulent viscosity μ_t because \bar{v} , by construction, varies nearly linearly near the airfoil surface. The turbulent viscosity, on the other hand, varies rapidly near the airfoil surface, requiring very fine grids to resolve the laminar sublayer. Compared to some other turbulence models, e.g., $k-\epsilon$ models, which require very tight grid spacing near the airfoil surface, the Spalart–Allmaras turbulence model grid requirements are quite modest. Indeed, a computational grid with a grid spacing $\Delta y^+ = 5.0$ near the airfoil surface is acceptable.

The remaining viscous "shear" terms in the turbulence equation are given by

$$\tau_{vx} = \frac{1}{\lambda} \rho (\nu + \bar{v}) \frac{\partial \bar{v}}{\partial x} \quad (13)$$

$$\tau_{vy} = \frac{1}{\lambda} \rho (\nu + \bar{v}) \frac{\partial \bar{v}}{\partial y} \quad (14)$$

where λ is a constant equal to $2/3$.

Finally, the nonzero entry in the source vector S_t in Eq. (2) models the diffusion, production, and destruction of turbulence, and is a function of the local density, viscosity, the working variable \bar{v} , as well as the gradients of these quantities, and the distance from the fluid particle to the surface of the airfoil. (For a complete description of the turbulence model, the reader is referred to the paper by Spalart and Allmaras [13].) Note that other than the dependence on the distance d from a fluid element to the surface of the airfoil, the turbulence model is entirely local; no global boundary layer quantities, such as the momentum thickness or displacement thickness, are required. Furthermore, as implemented in the present effort, the turbulence model is similar in form to the other conservation equations, and is simply and elegantly solved as an additional conservation equation using an explicit computational fluid dynamic flow solver (see Section 3).

We note that in the present study the flow is assumed to be fully turbulent, i.e., no transition model is used.

2.2 Linearization of Governing Equations. Next, we assume that the unsteadiness in the flow is induced by a small harmonic motion of the airfoils with frequency ω and interblade phase angle σ . Therefore, the unsteadiness in the flow will be a small harmonic perturbation about a mean, but nonuniform, background flow, and the Navier–Stokes equations can be linearized. Hall and Clark [8] have shown that to improve the accuracy of a time-linearized flow solver, one should make use of strained coordinates. Thus, we make the coordinate transformation given by

$$x(\xi, \eta, \tau) = \xi + f(\xi, \eta) e^{j\omega\tau} \quad (15)$$

$$y(\xi, \eta, \tau) = \eta + g(\xi, \eta) e^{j\omega\tau} \quad (16)$$

$$t(\xi, \eta, \tau) = \tau \quad (17)$$

Here, f and g are small perturbation functions chosen in such a way that in the strained coordinate system, the airfoils appear to be stationary. Said another way, the coordinates ξ, η are attached

to the moving airfoil. Within the blade passage, we require that the unsteady grid motion functions f and g vary smoothly.

Next, we decompose the unsteady solution into a steady part, plus a small-perturbation harmonic part, i.e.

$$\mathbf{U}(\xi, \eta, \tau) = \bar{\mathbf{U}}(\xi, \eta) + \mathbf{u}(\xi, \eta)e^{j\omega\tau} \quad (18)$$

Note that the flow decomposition is defined in the strained coordinate system. Substitution of Eq. (18) into the expression for the flux vector \mathbf{F} , and expansion in a first-order perturbation series, gives

$$\mathbf{F} = \bar{\mathbf{F}} + \frac{\partial \bar{\mathbf{F}}}{\partial \bar{\mathbf{U}}} \mathbf{u}e^{j\omega\tau} + \mathbf{f} \cdot \nabla \bar{\mathbf{F}}e^{j\omega\tau} + \mathcal{F}e^{j\omega\tau} \quad (19)$$

where $\bar{\mathbf{F}} \equiv \mathbf{F}(\bar{\mathbf{U}}, \xi, \eta)$. Also, $\nabla = \{\partial/\partial \xi, \partial/\partial \eta\}^T$ and $\mathbf{f} = \{f, g\}^T$. The first term on the right-hand side of Eq. (19), $\bar{\mathbf{F}}$, represents the mean flux vector. In general $\bar{\mathbf{F}}$ is a function of the spatial coordinates ξ and η , the mean values of conservation variables $\bar{\mathbf{U}}$, and gradients of the mean conservation variables. The second term on the right-hand side of Eq. (19), $[\partial \bar{\mathbf{F}}/\partial \bar{\mathbf{U}}]\mathbf{u}e^{j\omega\tau}$, represents a perturbation in the flux vector due to perturbations in the conservation variables themselves. This term will have contributions from both the viscous and inviscid elements of the flux vector. The third term on the right-hand side of Eq. (19), $\mathbf{f} \cdot \nabla \bar{\mathbf{F}}e^{j\omega\tau}$, represents the perturbation in the flux vector due to perturbations in the spatial location of the computational node. The flux vectors in the two-dimensional form of the Navier–Stokes equations do not depend explicitly on ξ and η and, therefore, this term is zero. (However, when using the quasi-three-dimensional form of the governing equations, the flux terms *do* depend explicitly on ξ and η , and this term would be nonzero.) Finally, the fourth term on the right-hand side of Eq. (19), $\mathcal{F}e^{j\omega\tau}$, represents the perturbation in the flux vector due to the straining of the computational grid that occurs when df or dg is nonzero. Because the mean solution is attached to the computational grid, straining the computational mesh coordinates induces stresses in the fluid. Only elements of the flux vector that depend on flow gradients (i.e., shear stress, heat conduction, and turbulence model source terms) will contribute to this term. This last term may be neglected if the grid motion is rigid body translation and/or rotation in the vicinity of boundary layers, separated regions, and wakes (Clark and Hall [11]).

The remaining flux and source vectors are similarly expanded in perturbation series, so that

$$\mathbf{G} = \bar{\mathbf{G}} + \frac{\partial \bar{\mathbf{G}}}{\partial \bar{\mathbf{U}}} \mathbf{u}e^{j\omega\tau} + \mathbf{f} \cdot \nabla \bar{\mathbf{G}}e^{j\omega\tau} + \mathcal{G}e^{j\omega\tau} \quad (20)$$

$$\mathbf{S} = \bar{\mathbf{S}} + \frac{\partial \bar{\mathbf{S}}}{\partial \bar{\mathbf{U}}} \mathbf{u}e^{j\omega\tau} + \mathbf{f} \cdot \nabla \bar{\mathbf{S}}e^{j\omega\tau} + \mathcal{S}e^{j\omega\tau} \quad (21)$$

Substitution of these perturbation series into the conservation equations described by Eqs. (1) and (2) and grouping terms of equal order in the perturbation quantities yields the zeroth-order mean flow equations,

$$\oint_{\partial \mathcal{D}} (\bar{\mathbf{F}}d\eta - \bar{\mathbf{G}}d\xi) - \int \int_{\mathcal{D}} \bar{\mathbf{S}}d\xi d\eta = 0 \quad (22)$$

and the first-order time-linearized unsteady flow equations,

$$\begin{aligned} & \int \int_{\mathcal{D}} \left(j\omega \mathbf{I} - \frac{\partial \bar{\mathbf{S}}}{\partial \bar{\mathbf{U}}} \right) \mathbf{u}d\xi d\eta + \oint_{\partial \mathcal{D}} \left(\frac{\partial \bar{\mathbf{F}}}{\partial \bar{\mathbf{U}}} \mathbf{u}d\eta - \frac{\partial \bar{\mathbf{G}}}{\partial \bar{\mathbf{U}}} \mathbf{u}d\xi \right) \\ & = - \int \int_{\mathcal{D}} (j\omega \bar{\mathbf{U}} - \bar{\mathbf{S}})(d\xi dg + d\eta df) + \int \int_{\mathcal{D}} \mathbf{f} \cdot \nabla \bar{\mathbf{S}}d\xi d\eta \\ & + \oint_{\partial \mathcal{D}} [(j\omega f \bar{\mathbf{U}} - \mathbf{f} \cdot \nabla \bar{\mathbf{F}} - \mathcal{F})d\eta - (j\omega g \bar{\mathbf{U}} - \mathbf{f} \cdot \nabla \bar{\mathbf{G}} - \mathcal{G})d\xi] \\ & - \oint_{\partial \mathcal{D}} [\bar{\mathbf{f}}dg - \bar{\mathbf{G}}df] \end{aligned} \quad (23)$$

where \mathbf{I} is the identity matrix. Equation (23) has been arranged so that terms that are homogeneous in \mathbf{u} appear on the left-hand side, and inhomogeneous source terms appear on the right-hand side.

From Eq. (22), it is apparent that the mean flow is independent of the unsteady perturbation flow and grid motion. The perturbation flow, on the other hand, depends on the steady flow in two ways. First, the time-linearized Navier–Stokes equations are linear, inhomogeneous, variable coefficient differential equations. The variable coefficients (mean flow Jacobians) are a function of the mean flow field. Second, the inhomogeneous terms of Eq. (23) are also functions of the mean flow field as well as the prescribed grid motion. Thus, the general solution procedure is to first compute the mean flow. Then, with the mean flow solution known, one forms the Jacobians appearing on the left-hand side, and the inhomogeneous terms on the right-hand side of Eq. (23), and solves the resulting time-linearized Navier–Stokes equations.

Finally, we note that we fully linearize *all* terms in the governing equations, including Sutherland’s viscosity law, the Spalart–Allmaras turbulence model, and the artificial viscosity model used to capture shocks (see Section 3.2). Our experience indicates that simply “freezing” the turbulence model, that is using the steady value of the eddy viscosity in the unsteady analysis with no unsteady perturbation in the viscosity due to the unsteady solution, produces physically incorrect solutions.

2.3 Boundary Conditions. For the steady flow problem, the total pressure, total density, and tangential velocity are prescribed at the upstream far-field boundary; the static pressure is prescribed at the downstream far-field boundary. On the airfoil surface, the no-slip condition requires that the velocity be zero. We also require boundary conditions for the turbulence model. At the upstream far-field boundary, the mean flow turbulence $\bar{\nu}$ is prescribed to be a small but nonzero number, just large enough to “seed” the flow with a small amount of turbulence. On the airfoil surface, we require that $\bar{\nu}$ be zero, because the turbulent viscosity must go to zero at the surface. Finally, the flow is required to satisfy periodicity, i.e.,

$$\bar{\mathbf{U}}(\xi, \eta + G) = \bar{\mathbf{U}}(\xi, \eta) \quad (24)$$

where G is the blade-to-blade gap.

Similarly, for the unsteady time-linearized flow solution, we require that the flow be periodic with interblade phase angle σ , i.e.,

$$\mathbf{u}(\xi, \eta + G) = \mathbf{u}(\xi, \eta)e^{j\sigma} \quad (25)$$

An unsteady no-slip condition must also be specified on the airfoil surface. Toward that end, let the vector $\mathbf{R}(s, \tau)$ describe the position of the airfoil surface where s is the distance along the airfoil surface. Because the motion of the airfoil is small and harmonic, we may write that

$$\mathbf{R}(s, \tau) = \bar{\mathbf{R}}(s) + \mathbf{r}(s)e^{j\omega\tau} \quad (26)$$

Substitution of Eq. (26) into the no-slip condition and collection of first-order terms gives the unsteady no-slip equation

$$\mathbf{v}(s) = j\omega \mathbf{r}(s) \quad (27)$$

where \mathbf{v} is the perturbation velocity on the airfoil surface.

Finally, for the unsteady flow, we require that outgoing acoustic, vortical, and entropic waves pass through the far-field boundary without reflection. This is equivalent to requiring that there be no incoming waves at the far-field boundary.

3 Numerical Implementation

3.1 Computational Grid. For the present investigation, we use a block-structured grid topology (see Fig. 1). An O-grid is generated around the airfoil so that grid nodes can be concentrated in viscous regions near the airfoil without wasted grid resolution in the far-field region. In the far-field, an H-grid is used because, in this region, one would like a nearly uniform grid to resolve acoustic waves. The grid is generated numerically using the elliptic grid generation technique of Thomas and Middlecoff [14] with modifications to generate grids with periodic boundaries required for modeling turbomachinery cascades. Inhomogeneous “source” functions are used to cluster grid points near the airfoil surface

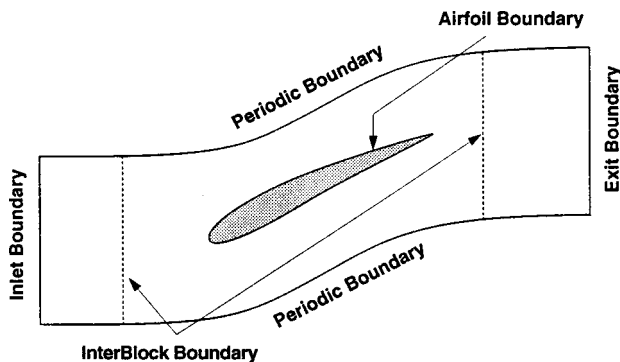


Fig. 1 Identification and location of numerical boundary types in computational domain

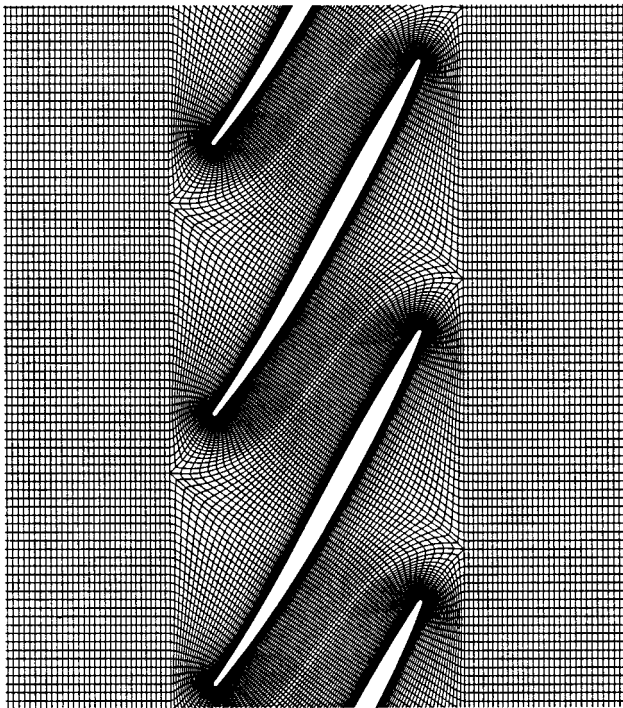


Fig. 2 Typical computational grid generated for experimental fan blade (Buffum et al. [23]); multiple passages are shown for clarity

and provide control over grid orthogonality. A typical computational grid generated using this technique is shown in Fig. 2.

Similarly, a linearized elliptic grid generation technique has been developed to generate the unsteady grid motion functions f and g required for flutter calculations. The boundary conditions on f and g are that the motion of the grid be equal to the displacement of the airfoil at the surface of the airfoil, and that the motion of the grid be equal to zero on the periodic and far-field boundaries.

3.2 Numerical Integration Scheme. For numerical integration of Eqs. (22) and (23), we add a pseudo-time term to the nonlinear mean and time-linearized unsteady Navier–Stokes equations, as suggested by Ni and Sisto [15], so that

$$\frac{d}{d\tau} \int_{\mathcal{D}} \mathbf{U} d\xi d\eta + \oint_{\partial\mathcal{D}} (\mathbf{F}d\eta - \mathbf{G}d\xi) = \int_{\mathcal{D}} \mathbf{S} d\xi d\eta \quad (28)$$

and

$$\begin{aligned} \frac{d}{d\tau} \int_{\mathcal{D}} \mathbf{u} d\xi d\eta + \int_{\mathcal{D}} \left(j\omega \mathbf{I} - \frac{\partial \mathbf{S}}{\partial \mathbf{U}} \right) \mathbf{u} d\xi d\eta \\ + \oint_{\partial\mathcal{D}} \left(\frac{\partial \mathbf{F}}{\partial \mathbf{U}} \mathbf{u} d\eta - \frac{\partial \mathbf{G}}{\partial \mathbf{U}} \mathbf{u} d\xi \right) = \mathbf{b} \end{aligned} \quad (29)$$

where \mathbf{b} represents the right-hand side of Eq. (23). The addition of the time-dependent terms, the first term on the left of Eqs. (28) and (29), enables us to solve these equations using conventional time-marching algorithms. The equations are advanced in pseudo-time until the conservation variables reach their steady state values. Hence, the time derivative terms introduced into Eqs. (28) and (29) are driven to zero, and the original steady nonlinear and unsteady linearized Navier–Stokes equations are recovered.

To solve Eqs. (28) and (29), we have implemented a modified version of an explicit finite-volume Lax–Wendroff scheme (Ni [16]; Saxer [17]; Davis et al. [18]; Clark [19]). All spatial derivatives used to evaluate the viscous shear stresses, heat fluxes, etc., are centered differences and are second-order accurate in space. A combination of second and fourth-order smoothing is used to capture shocks (for transonic flows) and eliminate spurious sawtooth modes from the solution (Holmes and Connell [20]). Because only the steady-state values of the mean and perturbation flow are required, there is no need to advance the equations time accurately. Thus, we accelerate convergence using local time stepping and multiple grid acceleration techniques.

3.3 Unsteady Far-Field Boundary Conditions. Because the computational domain must be finite in extent, nonreflecting far-field boundary conditions are applied at the inflow and outflow boundaries to prevent spurious reflections of outgoing pressure, entropy, and vorticity waves. The development of highly accurate nonreflecting boundary conditions continues to receive much attention in the literature. In the present study, we use the Fourier mode decomposition technique developed for time-linearized Euler equations (Hall and Crawley [7]; Giles [21]; Hall et al. [22]). If the far-field steady flow is uniform and inviscid, then the unsteady pressure, vorticity, and entropy waves (eigenmodes) will be Fourier modes in the circumferential direction. Each wave (eigenmode) will have a corresponding wavenumber (eigenvalue). The direction of propagation of a given wave is determined by the wavenumber and the corresponding dispersion relation. Thus, at each iteration of the flow unsteady flow solver, the time-linearized solution is Fourier transformed in the circumferential direction to determine the amount of each incoming and outgoing wave present in the solution. For flutter problems, all waves should originate inside the domain. Therefore, the incoming waves are set to zero. The remaining waves are converted back to conservation variables, and inverse Fourier transformed to obtain the solution along the far-field boundary.

To apply the Fourier decomposition technique, two simplifying assumptions are implicitly made. First, we assume that unsteady

viscous forces may be neglected. This assumption is valid since the waves that persist over long distances are long wavelength disturbances for which spatial derivatives, and hence viscous forces, are small. Second, we assume that the mean flow in the far field is uniform. This is clearly not true in the downstream region where a substantial velocity defect exists in the steady viscous wake. In fact, small reflections do occur, especially in the vicinity of the wake. However, these reflections tend to have short wavelengths, and thus are acoustically cut off. Any reflections tend to decay rapidly as they propagate upstream and, therefore, have little effect on the solution in the vicinity of the airfoil.

4 Computational Results

This section presents a flutter stability analysis for a tip section of a low aspect ratio fan blade. The influence of frequency, incidence, and flow separation on the aeroelastic stability of the cascade is investigated. Numerical solutions from the present method are compared to experimental data and numerical results obtained from a nonlinear, time-accurate time-marching analysis.

4.1 Benchmark Flutter Data. In this paper, we compare the results of our unsteady time-linearized Navier–Stokes analysis to a set of data recently obtained in the NASA Oscillating Cascade Facility [22]. The NASA Lewis Oscillating Cascade Facility (see Fig. 3) is a linear cascade wind tunnel capable of inlet flow speeds approaching Mach 1.0. The tunnel has a high-speed airfoil drive system capable of oscillating the cascaded airfoils in a torsional motion at prescribed interblade phase angles with realistic values of reduced frequency.

The airfoils used in the experiment have a cross section similar to that found in the tip region of modern low aspect ratio fan blades. The airfoil section was designed using the Pratt & Whitney compressor aerodynamic design system. Loading levels, losses, solidity, and stagger angle are representative of current design practices, although Mach numbers are somewhat smaller. The aerodynamic chord of the airfoil c is 8.90 cm. The airfoils have a maximum thickness of 4.8 percent of the chord, with the maximum thickness located at 62.5 percent of the chord. The linear cascade has nine airfoils set at a stagger angle γ of 60 deg and a solidity of 1.52. Pressure taps are distributed on several of the airfoil surfaces to measure both steady and unsteady pressure distributions.

Buffum et al. [23] measured the unsteady aerodynamic response of the airfoils pitching about their midchords for several combinations of steady Mach number and incidence, and unsteady reduced frequency and interblade phase angle. In this paper, we compare the present time-linearized Navier–Stokes analysis to data obtained at two operating conditions, a low-speed low-incidence case, and a low-speed high-incidence case. The later case is representative of operating conditions conducive to stall flutter.

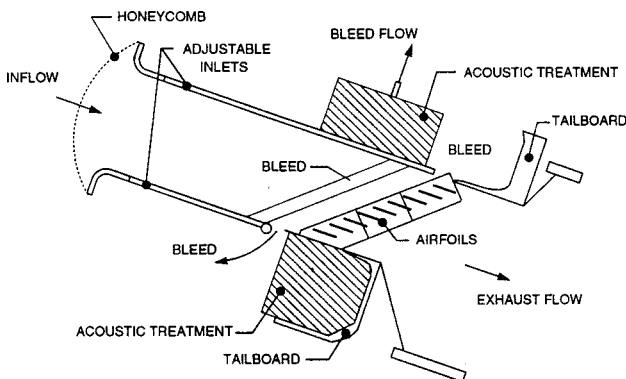


Fig. 3 NASA Lewis oscillating cascade facility

4.2 Low-Speed, Low-Incidence Flutter. The first operating condition considered corresponds to an inlet Mach number M_∞ of 0.2, an inflow angle β_1 of 60 deg (0 deg of incidence measured with respect to the chord line), and a Reynolds number Re based on chord of 380,000. At this low-incidence flow condition, viscous effects are thought to be insignificant because the flow remains attached over most of the airfoil and the boundary layers are thin. Figure 4 shows the experimentally measured steady surface pressure data for this case along with the numerical results obtained using the present method ($C_p = (p - p_\infty) / (\rho_\infty U_\infty^2)$). The computational grid used here and throughout the paper unless otherwise noted contained 129×33 nodes in the O-grid region, and 33×33 nodes in the upstream and downstream H-grid regions. The different symbol types in Fig. 4 correspond to data acquired from different airfoils in the cascade. All three instrumented blades are in fair agreement with one another, indicating that reasonable steady passage-to-passage periodicity has been obtained in the experiment. The dashed line corresponds to the steady solution computed using the present method for an inflow angle of 60 deg. The predicted surface pressure distribution has a similar shape to the data, but the pressure levels are not well predicted. By adjusting the inflow angle β_1 to 62 deg, the surface pressure distribution, denoted now by the solid line, agrees more closely with the experimental results. As errors in the measurement of the cascade stagger angle and/or inflow angle may occur that can substantially alter the steady pressure distribution, it is not unreasonable to adjust the numerically prescribed inflow angle to obtain a closer match to the steady experimental data. Note that with the 2 deg adjustment, the overall agreement between the present method and the experimental data is quite good.

Also shown in Fig. 4 is the steady pressure distribution computed by Capece [24] using NPHASE, a fully nonlinear time-accurate time-marching computational model for predicting two-dimensional, nonlinear, unsteady flows through vibrating cascades. NPHASE uses an implicit, cell-centered, finite-volume algorithm based on Roe's approximate Riemann solver. The Baldwin–Lomax [25] turbulence model is used to compute the eddy viscosity. A detailed description of the NPHASE algorithm is given by Ayre and Verdon [26]. Capece found that the best match to the experimental data was obtained by NPHASE with a prescribed inflow angle of 61.5 deg. While the overall agreement is good, the pressure on the suction surface of the airfoil is slightly underpredicted by NPHASE.

Figure 5 shows the steady Mach number contours for this low-speed low-incidence case computed using the present steady

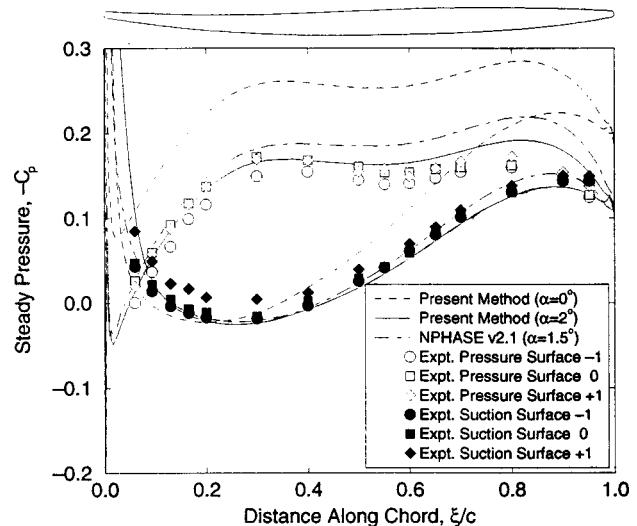


Fig. 4 Steady pressure distribution on airfoil sources of Buffum cascade; $M=0.2$, $\beta_1=60$ deg, $Re=380,000$

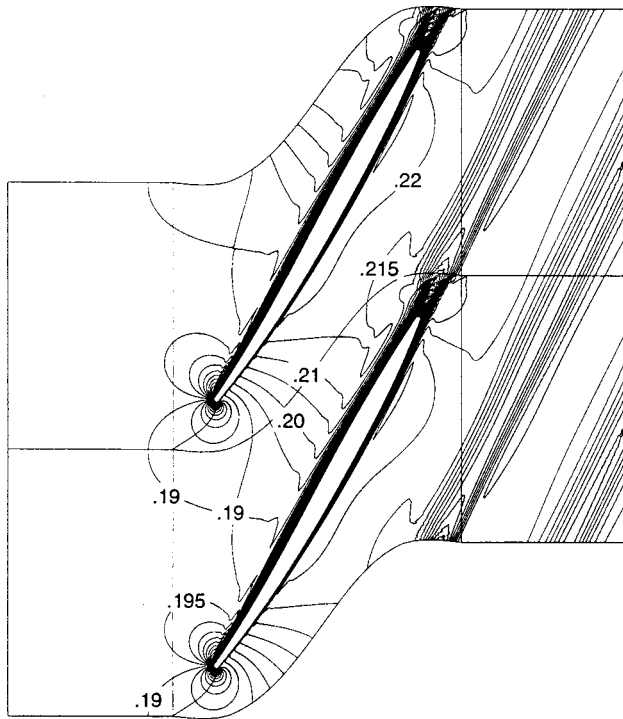


Fig. 5 Steady Mach contours in blade passages of Buffum cascade; $M=0.2$, $\beta_1=62$ deg, $Re=380,000$

Navier–Stokes analysis. The boundary layers are seen to be relatively thin, although on the suction surface there is a small separation bubble near the leading edge—the flow re-attaches approximately 5 percent of the chord downstream of the leading edge—that causes an immediate thickening of the suction surface boundary layer.

Having computed the steady flow, we next consider the unsteady flow arising from torsional vibrations of the airfoils in cascade. For this example, the airfoils in the cascade pitch about their midchords with an interblade phase angle σ of 180 deg and a reduced frequency $k \equiv \omega c/U_\infty$ of 1.2. The amplitude of torsional vibration α is 1.2 deg, an amplitude typical of that observed in actual flutter. As with the steady flow calculations, the unsteady flow computations were performed using a single blade passage regardless of interblade phase angle.

Shown in Fig. 6 is the computed unsteady real (in-phase) and imaginary (out-of-phase) parts of the unsteady surface pressure predicted using the present time-linearized Navier–Stokes analysis. Also shown for comparison are the experimental data, together with the results of the NPHASE computational model. (The unsteady pressures have been nondimensionalized by $\rho_\infty V_\infty^2 \alpha$.) Unsteady pressure levels predicted by the present time-linearized method are in reasonably good agreement with the experimental data of Buffum et al. [22], as are the NPHASE results. The largest differences between the two computational solution solutions are near the leading edge of the suction surface.

Next, for this steady operating condition and reduced frequency of torsional vibration, the unsteady aerodynamic moment and work per cycle were computed for a range of interblade phase angles σ and reduced frequencies k . Results for three different reduced frequencies are shown in Fig. 7 for interblade phase angles σ ranging from -180 to $+180$ deg. Shown is the aerodynamic work done on the blade per vibration cycle Ξ as a function of interblade phase angle σ . As defined in the present effort, if the work per cycle is positive, then the unsteady aerodynamic loads (in the absence of any mechanical damping) result in the aeroelastic instability of flutter. From this figure, we conclude that over a

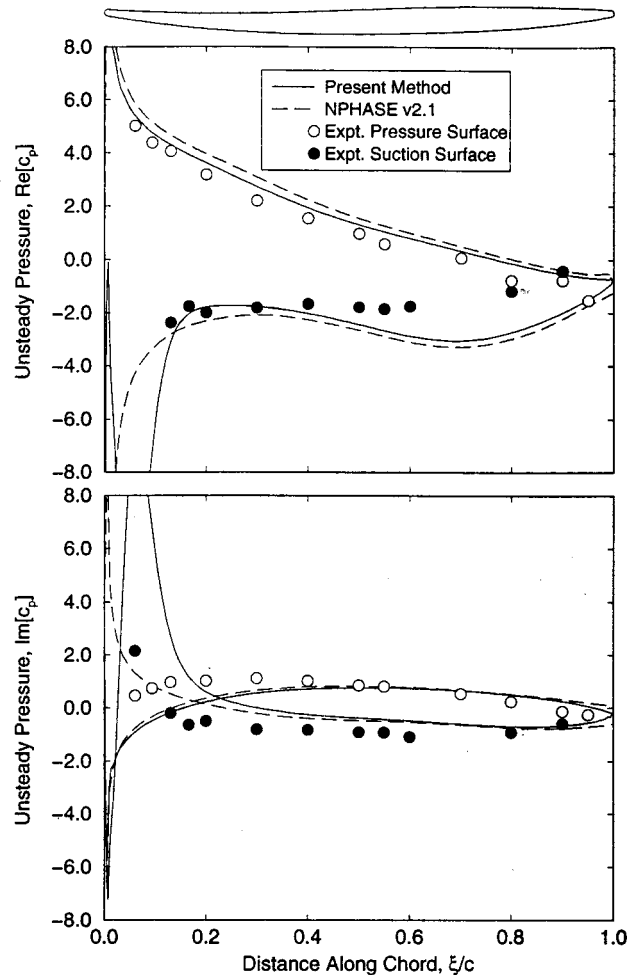


Fig. 6 Unsteady pressure distribution on pitching airfoil surfaces of Buffum cascade; $M=0.2$, $\beta_1=62$ deg, $Re=380,000$, $k=1.2$, $\sigma=180$ deg

range of interblade phase angles σ from 0 to 165 deg the system is aeroelastically unstable. Note, however, that increasing the reduced frequency k has a stabilizing influence on the system in two ways. First, as the frequency is increased, the range of unstable interblade phase angle decreases. Second, the maximum work per

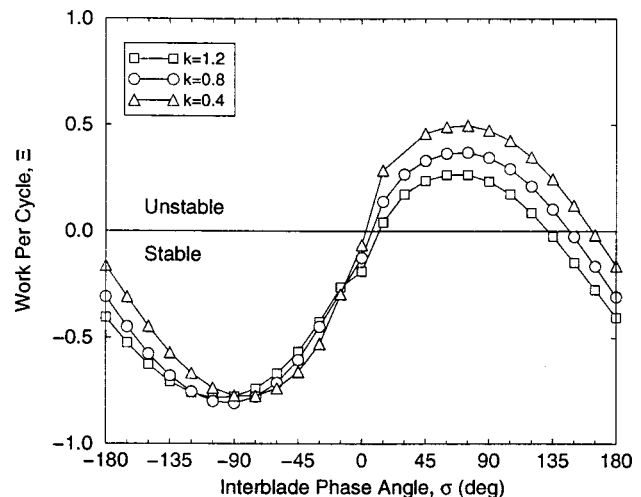


Fig. 7 Aerodynamic work per cycle due to pitching motion of airfoils for three reduced frequencies; $M=0.2$, $\beta_1=62$ deg, $Re=380,000$

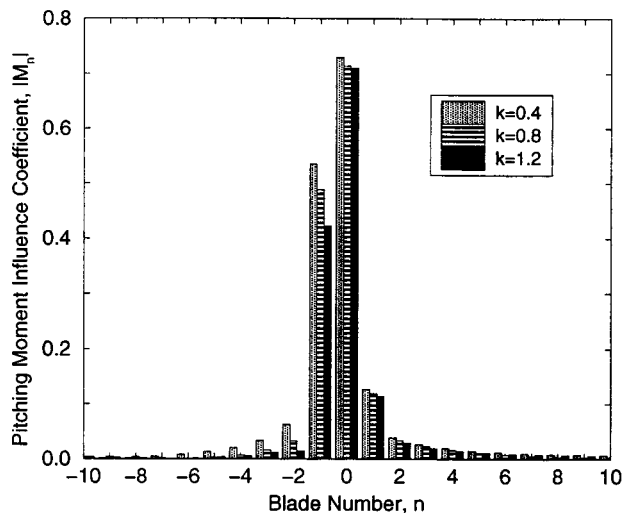


Fig. 8 Magnitude of pitching moment influence coefficients for three reduced frequencies; $M=0.2$, $\beta_1=62$ deg, $Re=380,000$

cycle for each reduced frequency is reduced. This is consistent with industrial design experience with unstalled flutter, i.e., that increasing the reduced frequency generally has a stabilizing influence on unstalled torsional flutter.

Shown in Fig. 8 is the magnitude of the (complex) unsteady aerodynamic moment in influence coefficient form. The influence coefficients are obtained by performing a discrete Fourier transform on the unsteady moment as a function of interblade phase angle. The result is a measure of the influence of the individual blades on a reference blade. Thus, the blade index corresponding to $n=0$ describes the moment produced on the reference blade due to vibration of the reference blade itself. The $n=1$ coefficient indicates the moment produced on the reference blade due to a unit vibration of the neighboring blade on the suction side of the reference airfoil, and so on. For this example, we note that the $n \geq 2$ coefficients are relatively small. Physically, this means that only the reference blade and its two nearest neighbors significantly influence the reference blade. Experimentally, this implies that good unsteady passage-to-passage periodicity can be obtained using the nine-bladed NASA Lewis oscillating cascade facility.

4.3 Low-Speed, High-Incidence Flutter. Next, we consider the case where the inlet Mach number M_∞ is 0.2 and the Reynolds number Re is 380,000 as before, but the experimentally reported inflow angle β_1 is now 70 deg. Figure 9 shows the computed steady surface pressure distribution computed using the present method along with the experimental data for this case. As before, all three instrumented blades are in good agreement with one another, indicating that steady passage-to-passage periodicity has been maintained in the experiment. The solid line corresponds to the steady solution obtained using the present method for an inflow angle of 69 deg. Again, the inflow angle has been adjusted slightly to obtain a mean flow solution more closely in agreement with the experimental data. The one area where the present method does not match the data very well is in the leading edge region of the suction surface. A nearly constant pressure region is experimentally observed over the first 20 percent of the chord. The present method, however, shows a monotonically increasing pressure rise. This minor disagreement between the data and the present method arises because we assume that the flow is fully turbulent, whereas the actual flow is likely laminar, transitioning to turbulent in this region. This hypothesis has been verified in numerical studies with a potential/boundary layer interaction code [27]. Finally, the dashed line shown in Fig. 9 shows the steady

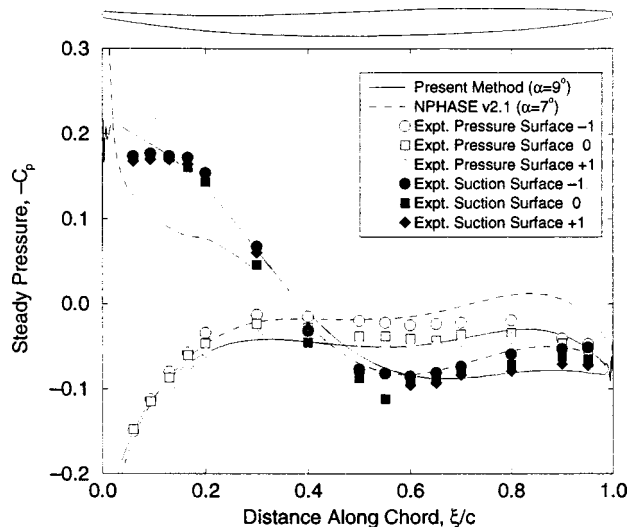


Fig. 9 Steady pressure distribution on airfoil surfaces of Buffum cascade; $M=0.2$, $\beta_1=70$ deg, $Re=380,000$

surface pressures distribution computed using NPHASE. The best data match by NPHASE occurred when the inflow angle was 67 deg.

Figure 10 shows the predicted steady Mach contours for this high incidence case. Note the large separated region that extends from the suction surface leading edge to approximately the airfoil's midchord. Also note that the airfoil wakes are much thicker than those predicted for the low incidence configuration (see Fig. 5). To visualize experimentally this high incidence flow, Buffum coated an airfoil's surface with an oil-pigment mixture. At 10 deg incidence, separation from the suction surface was observed. The largest separated region was found to exist at the midspan where the flow was observed to separate from the leading edge and re-

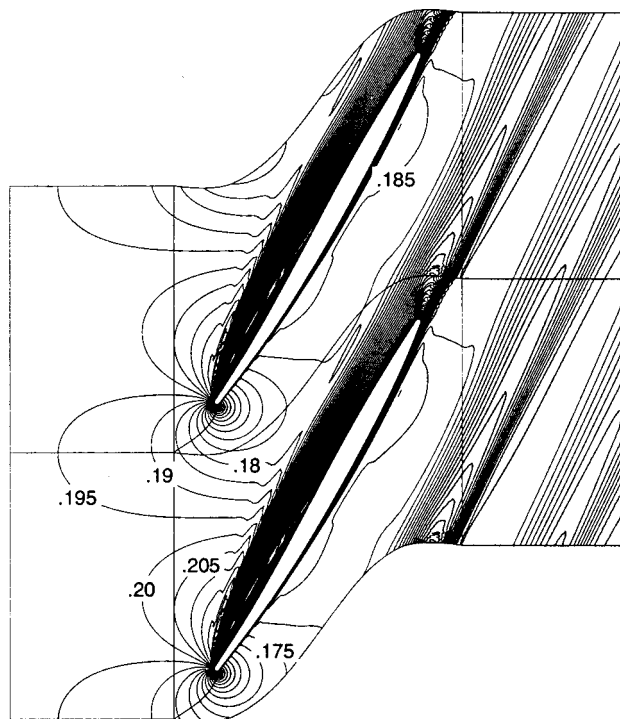


Fig. 10 Steady Mach contours in blade passages of Buffum cascade; $M=0.2$, $\beta_1=69$ deg, $Re=380,000$

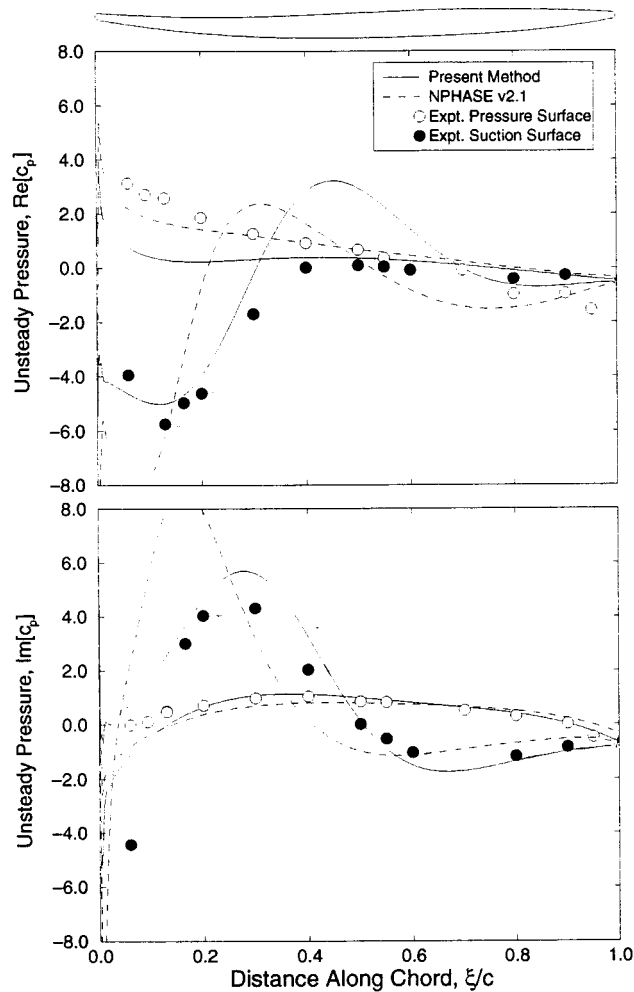


Fig. 11 Unsteady pressure distribution on pitching airfoil surfaces of Buffum cascade; $M=0.2$, $\beta_1=69$ deg, $Re=380,000$, $k=1.2$, $\sigma=180$ deg

attach at 40 percent chord. The separated region predicted by the present method is slightly larger, extending over approximately 50 percent of the chord.

Figure 11 shows a comparison between the predicted unsteady surface pressures using both numerical algorithms and experimental data. As before, the unsteady pressures have been nondimensionalized with $\rho_\infty V_\infty^2 \alpha$. The computed imaginary part of the unsteady surface pressure predicted by the present linearized Navier–Stokes method is in excellent agreement with the experimental data. The computed real part does not agree as well, but is qualitatively in agreement with the experiment. Surface pressure predictions provided by NPHASE, on the other hand, agree with the experimental data on the pressure surface, but large differences in the unsteady surface pressure are observed between NPHASE. It may be that the Baldwin–Lomax turbulence model used by NPHASE is not well suited for massively separated flows.

Figure 12 shows the steady and unsteady pressure distributions computed using the present method using three different computational grids, a coarse grid (65×17 nodes in the O-grid region), a medium resolution grid (129×33 nodes), and a fine grid (257×65 nodes). Although some differences in the solutions are observed, especially on the suction surface, the medium and fine grid solutions are in very good agreement indicating the solution is nearly grid converged.

Finally, as before, unsteady flow calculations were performed over a range of frequencies and interblade phase angles. Figure 13

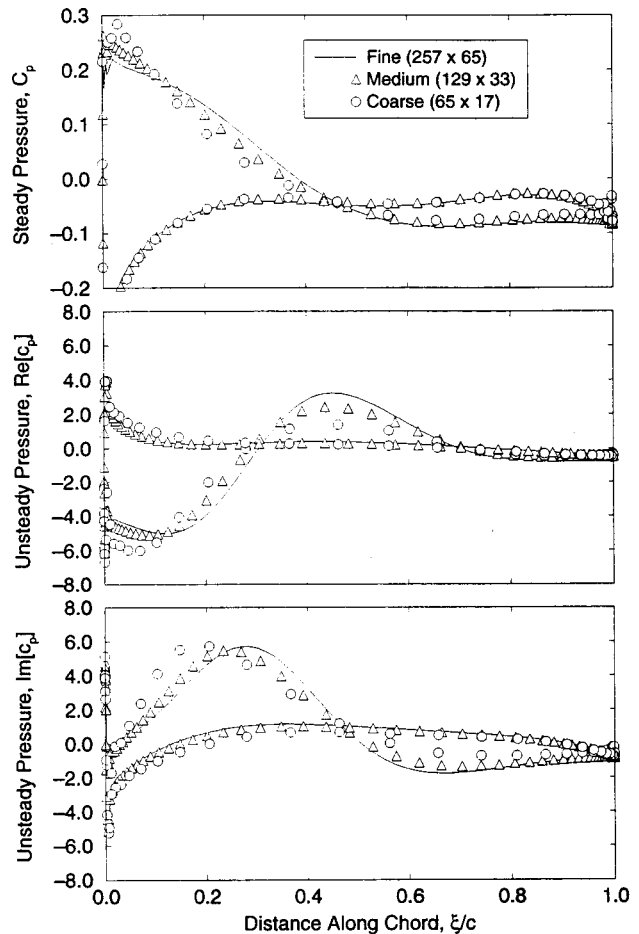


Fig. 12 Steady and unsteady pressure distribution on airfoil surfaces of Buffum cascade for various grid resolutions; $M=0.2$, $\beta_1=69$ deg, $Re=380,000$, $k=1.2$, $\sigma=180$ deg

shows the aerodynamic work per cycle Ξ as a function of interblade phase angle σ . From this figure, we conclude that over a range of interblade phase angles ranging from 0 to 165 deg the system is aeroelastically unstable. Note the strong effect of increased frequency on the system's stability. As before, increasing

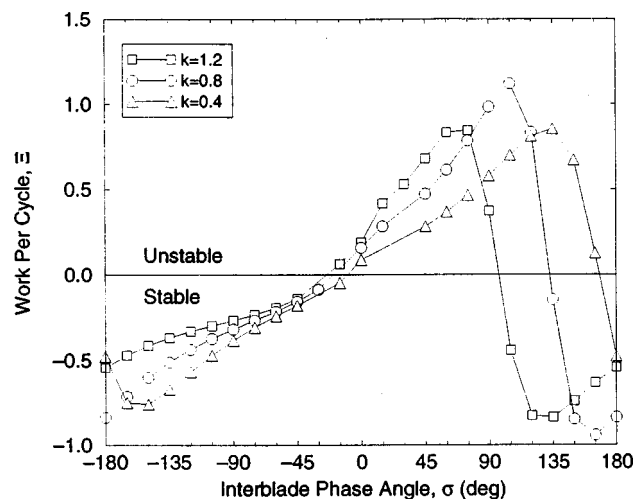


Fig. 13 Aerodynamic work per cycle due to pitching motion of airfoils for three reduced frequencies; $M=0.2$, $\beta_1=69$ deg, $Re=380,000$

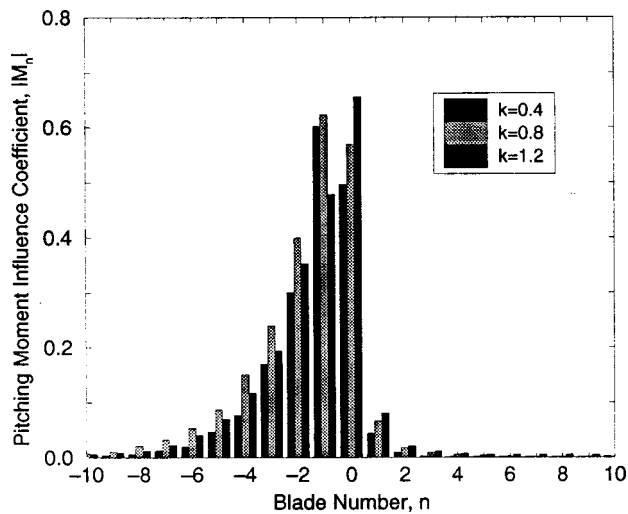


Fig. 14 Magnitude of pitching moment influence coefficient for three reduced frequencies; $M=0.2$, $\beta_1=69$ deg, $Re=380,000$

the reduced frequency has a stabilizing influence on the aeroelastic system in that the range of unstable interblade phase angles diminishes as the frequency of vibration increases. However, the peak work per cycle actually increases as the frequency of vibration increases from $k=0.4$ to $k=0.8$. This result may explain in part why increasing blade stiffness has not always been an effective strategy for eliminating observed stall flutter.

Finally, Fig. 14 shows an estimate of the cascade influence coefficients. Interestingly, there is much more participation by distant neighboring blades in this high incidence configuration than in the low-incidence case. The influence coefficient corresponding to blade indices ± 4 are still large when compared to the blade's self influence coefficient. This may indicate that the mechanisms of stall flutter are fundamentally different than those of unstalled flutter. Furthermore, the NASA Lewis oscillating cascade facility, which has just nine fan blades, may not have enough airfoils to ensure unsteady passage-to-passage periodicity.

4.4 Computational Efficiency. One advantage of a time-linearized analysis, often cited by proponents of this modeling strategy, is its computational efficiency compared to conventional time-accurate, time-marching algorithms. Because the governing equations are solved in the frequency domain, conventional steady-state acceleration techniques may be used to speed convergence. In addition, the use of complex periodicity conditions allows one to compute the unsteady flow using a computational grid spanning a single blade passage, regardless of the interblade phase angle, greatly reducing the number of computational grid points required.

For example, for the low-speed high-incidence example reported in Section 4.3, the computations were performed on a single processor Silicon Graphics workstation equipped with an R10000 processor operating at 195 MHz. The steady code required 4341 iterations to converge six orders of magnitude, and 42 minutes of CPU time, the unsteady analysis for $k=1.2$ and $\sigma=180$ deg required 8378 iterations to converge, and 161 minutes of CPU time. These times are, of course, only representative, and will vary with Mach number, reduced frequency, interblade phase angle, Reynolds number, etc. Nevertheless, a single unsteady calculation requires on the order of just 3.8 times as much computational time as the corresponding steady flow calculation. Thus, the present linearized analysis requires one to two orders of magnitude less computational time to converge than conventional time-accurate, time-marching algorithms. (We would also note that the unsteady calculations are performed using complex arithmetic,

which simplifies code development, but also degrades computational performance. It is possible to write the unsteady code using only real arithmetic, improving somewhat the computational efficiency.)

5 Concluding Remarks

In this paper, we have presented a novel time-linearized Navier–Stokes computational analysis of stall flutter in cascades. Based on the results obtained to date, we make the following observations:

1 The time-linearized Navier–Stokes analysis is able to model the complex steady and unsteady flow associated with stall flutter, including large separated flow regions. Results of this analysis compare quite well with experimental data of high-incidence stall flutter.

2 The method is computationally efficient, making it useful for routine use in aeroelastic design; the computational time required to compute the unsteady flow due to a single mode shape of blade motion at a single frequency and interblade phase angle is of the same order as the time required to compute the background steady flow. Furthermore, results obtained with the present time-linearized Navier–Stokes analysis agree with experimental data as well as predictions obtained using a conventional (and computationally expensive) nonlinear time-domain analysis.

3 Numerical results from the low-speed, incidence–incidence example are consistent with industrial design experience, i.e., that increasing the reduced frequency generally increases aerodynamic damping. The high-incidence results, on the other hand, seem contradictory to standard design practices, as the range of unstable interblade phase angles is reduced by increasing the reduced frequency, but the aerodynamic damping of the least stable interblade phase angle becomes more unstable with increasing reduced frequency. Additional numerical and experimental studies need to be performed to understand this phenomenon.

4 While the present method is two-dimensional, stall flutter in actual turbomachines is likely to be highly three-dimensional with the extent of the separated region varying significantly from hub to tip. Nevertheless, the results presented in this paper demonstrate the feasibility of using a time-linearized Navier–Stokes model to predict stall flutter, and the method should be readily extendable to three dimensions, albeit with an attendant increase in computational requirements.

Before gas turbine engine designers can consistently avoid stall flutter, the underlying mechanisms must be understood. Computationally efficient and experimentally validated models, such as the present time-linearized Navier–Stokes code, are an invaluable tool for studying the aerodynamics of stall flutter.

Acknowledgments

This work was supported by a research contract from General Electric Aircraft Engines with Dr. Robert Kielb serving as technical monitor.

References

- [1] Sisto, F., 1987, "Stall Flutter," in: *AGARD Manual on Aeroelasticity in Axial-Flow Turbomachines, Vol. 1, Unsteady Turbomachinery Aerodynamics*, M. F. Platzer and F. O. Carta, eds., AGARD-AG-298, Ch. 7.
- [2] Chi, R. M., and Srinivasan, A. V., 1985, "Some Recent Advances in the Understanding of Turbomachine Subsonic Stall Flutter," *ASME J. Eng. Gas Turbines Power*, **107**, pp. 408–417.
- [3] Verdon, J. M., and Caspar, J. R., 1982, "Development of a Linear Unsteady Aerodynamic Analysis for Finite-Deflection Subsonic Cascades," *AIAA J.*, **20**, No. 9, pp. 1259–1267.
- [4] Verdon, J. M., 1987, "Linearized Unsteady Aerodynamic Theory," in: *AGARD Manual on Aeroelasticity in Axial Flow Turbomachines, Vol. 1, Unsteady Turbomachinery Aerodynamics (AGARD-AG-298)*, M. F. Platzer and F. O. Carta, eds., Neuilly sur Seine, France, Ch. 2.
- [5] Whitehead, D. S., and Grant, R. J., 1981, "Force and Moment Coefficients of High Deflection Cascades," in: *Proc. 2nd International Symposium on Aeroelasticity in Turbomachines*, P. Suter, ed., Juris-Verlag, Zurich, pp. 85–127.

- [6] Hall, K. C., 1993, "Deforming Grid Variational Principle for Unsteady Small Disturbance Flows in Cascades," *AIAA J.*, **31**, No. 5, pp. 891–900.
- [7] Hall, K. C., and Crawley, E. F., 1989, "Calculation of Unsteady Flows in Turbomachinery Using the Linearized Euler Equations," *AIAA J.*, **27**, No. 6, pp. 777–787.
- [8] Hall, K. C., and Clark, W. S., 1993, "Linearized Euler Predictions of Unsteady Aerodynamic Loads in Cascades," *AIAA J.*, **31**, No. 3, pp. 540–550.
- [9] Holmes, D. G., and Chuang, H. A., 1993, "2D Linearized Harmonic Euler Flow Analysis for Flutter and Forced Response," in: *Unsteady Aerodynamics, Aeroacoustics, and Aeroelasticity of Turbomachines and Propellers*, H. M. Atassi, ed., Springer-Verlag, New York, pp. 213–230.
- [10] Hall, K. C., and Lorence, C. B., 1993, "Calculation of Three-Dimensional Unsteady Flows in Turbomachinery Using the Linearized Harmonic Euler Equations," *ASME J. Turbomach.*, **115**, pp. 800–809.
- [11] Clark, W. S., and Hall, K. C., 1995, "A Numerical Model of the Onset of Stall Flutter in Cascades," *ASME Paper No. 95-GT-377*.
- [12] Holmes, D. G., and Lorence, C. B., 1998, "Three-Dimensional Linearized Navier–Stokes Calculations for Flutter and Forced Response," in: *Unsteady Aerodynamics and Aeroelasticity of Turbomachines: Proc. 8th International Symposium held in Stockholm, Sweden, 14–18 Sept. 1997*, T. H. Fransson, ed., Kluwer Academic Publishers, Dordrecht, pp. 211–224.
- [13] Spalart, P. R., and Allmaras, S. R., 1992, "A One Equation Turbulence Model for Aerodynamic Flows," *AIAA Paper No. 92-0439*.
- [14] Thomas, P. D., and Middlecoff, J. F., 1980, "Direct Control of the Grid Distribution in Meshes Generated by Elliptic Equations," *AIAA J.*, **18**, No. 6, pp. 652–656.
- [15] Ni, R. H., and Sisto, F., 1976, "Numerical Computation of Nonstationary Aerodynamics of Flat Plate Cascades in Compressible Flow," *ASME J. Eng. Power*, **98**, pp. 165–170.
- [16] Ni, R. H., 1982, "A Multiple-Grid Scheme for Solving the Euler Equations," *AIAA J.*, **20**, No. 11, pp. 1565–1571.
- [17] Saxer, A. P., 1992, "A Numerical Analysis of 3-D Inviscid Stator/Rotor Interactions Using Non-reflecting Boundary Conditions," Ph.D. Thesis, Department of Aeronautics and Astronautics, Massachusetts Institute of Technology, Cambridge, Massachusetts.
- [18] Davis, R. L., Ni, R. H., and Carter, J. E., 1987, "Cascade Viscous Flow Analysis Using the Navier–Stokes Equations," *J. Propulsion*, **3**, No. 5, pp. 406–414.
- [19] Clark, W. S., 1998, "Investigation of Unsteady Viscous Flows in Turbomachinery Using a Linearized Navier–Stokes Analysis," Ph.D. Thesis, Duke University.
- [20] Holmes, D. G., and Connell, S. D., 1989, "Solution of the 2-D Navier–Stokes Equations on Unstructured Adaptive Grids," *AIAA Paper No. 89-1943-CP*.
- [21] Giles, M. B., 1990, "Nonreflecting Boundary Conditions for Euler Equation Calculations," *AIAA J.*, **28**, No. 12, pp. 2050–2058.
- [22] Hall, K. C., Lorence, C. B., and Clark, W. S., 1993, "Nonreflecting Boundary Conditions for Linearized Aerodynamic Calculations," *AIAA Paper No. 93-0882*.
- [23] Buffum, D. H., Capece, V. R., King, A. J., and EL-Aini, Y. M., 1996, "Experimental Investigation of Unsteady Flows at Large Incidence Angles in a Linear Oscillating Cascade," *AIAA Paper No. 96-2823*.
- [24] Capece, V., 1998, "Numerical Investigation of Oscillating Cascade Aerodynamics at Large Mean Incidence," presented at the 3rd National High Cycle Fatigue (HCF) Conference, San Antonio, TX, Feb. 2–5.
- [25] Baldwin, B. S., and Lomax, H., 1978, "Thin Layer Approximation and Algebraic Model for Separated Turbulent Flows," *AIAA Paper No. 78-257*.
- [26] Ayre, T. C., and Verdon, J. M., 1994, "Numerical Unsteady Aerodynamic Simulation for Blade Forced Response Phenomena," Wright Laboratory Technical Report, WL-TR-95-2011.
- [27] Epureanu, B., Hall, K. C., and Dowell, E. H., 1999, "Reduced Order Model of Unsteady Viscous Flows in Turbomachinery Using Viscous–Inviscid Coupling," submitted to *Journal of Fluids and Structures*.

Z. S. Spakovszky

Gas Turbine Laboratory,
Department of Aeronautics and Astronautics,
Massachusetts Institute of Technology,
Cambridge, MA 02139

J. B. Gertz

O. P. Sharma

Pratt & Whitney,
East Hartford, CT 06108

J. D. Paduano

A. H. Epstein

E. M. Greitzer

Gas Turbine Laboratory,
Department of Aeronautics and Astronautics,
Massachusetts Institute of Technology,
Cambridge, MA 02139

Influence of Compressor Deterioration on Engine Dynamic Behavior and Transient Stall-Margin

This paper presents an experimental and analytical investigation of compressor stability assessment during engine transient operation. A two-dimensional, linear, compressible, state-space analysis of stall-inception (Feulner et al., 1996, ASME J. Turbomach., 118, pp. 1–10) was modified to account for engine transients and deterioration, with the latter modeled as increased tip-clearance and flow blockage. Experiments were performed on large commercial aircraft engines in both undeteriorated and deteriorated states. Unsteady measurements of pressure in these test engines during rapid accelerations revealed the growth of pre-stall disturbances, which rotate at rotor speed and at approximately half rotor speed. These disturbances are stronger in deteriorated engines. The model showed that the signal at shaft speed was the first compressible system mode, whose frequency is near shaft speed, excited by geometric nonuniformities. The computed behavior of this mode during throttle transients closely matched engine data. The signal increased in strength as stall was approached and as the engine deteriorated. This work firmly establishes the connection between observed signals in these engines and first principles stability models. [S0889-504X(00)01603-2]

1 Introduction

There have been a number of theoretical studies of the rotating stall inception process in multistage axial flow compressors. Early flow models by Emmons et al. [1], who first detected modal perturbations of long wavelength prior to stall, were extended by Moore [2] and Moore and Greitzer [3] for incompressible flow.

A compressible analysis for multistage compressors was developed by Bonnaure [4], who showed that compressibility has a major effect on compressor stability behavior. Feulner et al. [5] formulated an input-output state-space version of this model suitable for control studies. Tryfonidis et al. [6] compared the model's predictions to experimental data from several compressors. The present paper adapts this model to study the effect of compressor deterioration on transient pre-stall behavior.

An engine loses performance over its life due to deterioration. One cause is increased blade tip-clearances. We have found that deteriorated compressors show larger amplitudes of "pre-stall waves" during acceleration transients than do undeteriorated compressors. These pre-stall waves can be seen from unsteady static pressure measurements during a transient.

This paper presents experimental data taken during acceleration transients in the core compressor of an undeteriorated and a deteriorated commercial aircraft engine. The goals are to establish a physical explanation for the experimentally observed pre-stall phenomena and to link the behavior to changes in the transient stall-margin between the deteriorated and undeteriorated engines. In addition, dynamic behavior of the high-speed compressor during transient operation is simulated for the first time. The analytical approach is based on an existing linearized, two-dimensional, compressible, state-space model.

2 Engine Experiments

Experiments were performed on two test engines: an undeteriorated engine with tight and uniform tip-clearances, and a deteriorated engine with enlarged tip-clearances and poor stability. The

measurements were conducted during rapid accelerations of the engines from idle to take-off power. A single fast-response wall static pressure measurement was made during acceleration transients in a stator passage near the center of the core compressor. In addition, compressor performance measurements such as corrected rotor speed and total pressure ratio were taken during the same event to construct the transient engine operating line. Figure 1 depicts the corrected rotor speed measurement normalized by the corrected design speed during the acceleration transient. Time is in rotor revolutions and the beginning of the acceleration is indicated as zero rotor revolutions.

The fast response static pressure data taken in the test engines was analyzed by computing the evolution of the power spectral density during the transient event. The measured, instantaneous

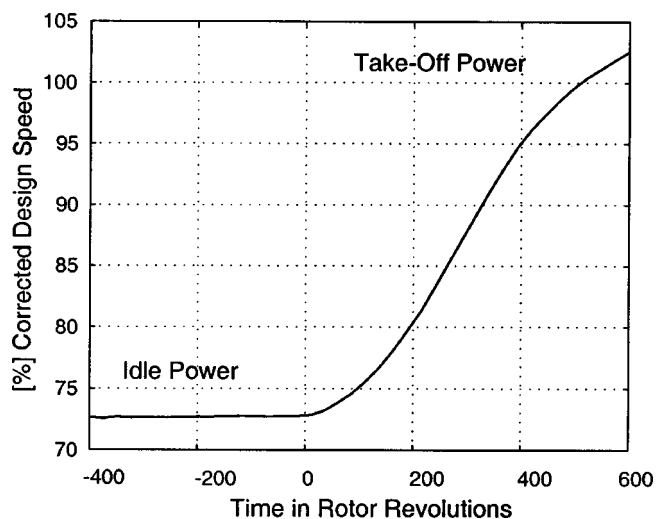


Fig. 1 Measured compressor rotor speed during acceleration transient

Contributed by the International Gas Turbine Institute and presented at the 44th International Gas Turbine and Aeroengine Congress and Exhibition, Indianapolis, Indiana, June 7–10, 1999. Manuscript received by the International Gas Turbine Institute February 1999. Paper No. 99-GT-439. Review Chair: D. C. Wisler.

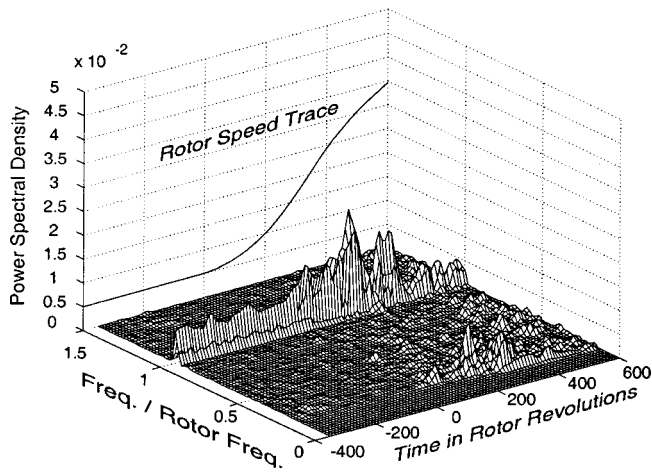


Fig. 2 Spectrogram of measured unsteady static pressure signal of undeteriorated engine during the transient

midcompressor static pressure signal of the undeteriorated engine was normalized by the quasi-steady static pressure at the same location.

A spectrogram of the pressure signal is plotted in Fig. 2. The time axis is in rotor revolutions and the frequency axis is normalized by rotor frequency. The measured transient rotor speed is projected in the background to provide a reference to the acceleration transient.

The spectrogram reveals a pronounced pressure perturbation traveling at rotor frequency. This pressure perturbation starts to increase when the engine is accelerated (time=0), reaches a dominant peak at a time of roughly 200 rotor revolutions and decreases at higher operating speeds.

The same measurements were taken in the deteriorated engine and processed as described above. Figure 3 depicts the spectrogram of the normalized unsteady static pressure signal obtained from the deteriorated engine during the acceleration transient. The pressure perturbations traveling at rotor frequency show the same trend as in Fig. 2; however, the pressure signal measured in the deteriorated engine exhibits a much larger peak during the acceleration transient. The spectrogram also shows a spike at about half the rotor frequency. This spike is conjectured to be a rotating stall precursor, as will be discussed later.

In summary, the experiments reveal the growth of pressure perturbations that travel at both rotor frequency and about half rotor

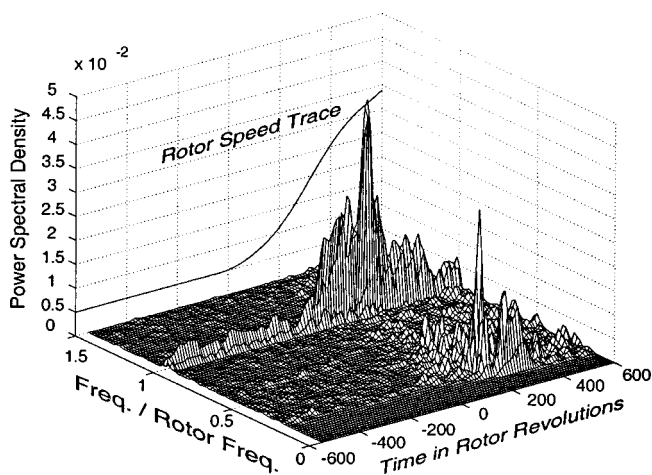


Fig. 3 Spectrogram of measured unsteady static pressure signal of deteriorated engine during the transient

frequency, with the former being stronger. These observations are more pronounced in the deteriorated engine with poor stability. The following research questions are of interest:

- How do these observations relate to engine deterioration and its effect on stability during the acceleration transient?
- What are the physical mechanisms responsible for the observed unsteady phenomena in the experiments?
- What level of analytical modeling is needed to capture this behavior?

3 Compressor Model for Transient Engine Acceleration Simulation

3.1 Basic Formulation. The basic formulation of the compressible, two-dimensional compressor model originates from Bonnaure [4]. An input-output formulation was derived by Feulner et al. [5] and modified by Fr chet te [7] and Weigl et al. [8]. The overall analysis consists of models of the inlet and exit ducts, the blade rows, and the interblade row gaps, as depicted in Fig. 4. These various models are stacked up axially through the compressor, linked through boundary conditions at each interface, and closed by end conditions at the inlet and exit of the compressor ducts.

The hub-to-tip ratio is assumed high enough to neglect radial variations of the flow quantities. Thus the model is two-dimensional with axial and circumferential unsteady flow field variations. Effects of viscosity and heat transfer outside of the blade rows are also neglected. The flow perturbations are taken small enough to allow the flow field equations to be linearized around a steady, uniform state. Each variable is then considered to be the sum of a mean value and a small perturbation, as shown below for the static pressure:

$$p = \bar{p} + \delta p. \quad (1)$$

The resulting linearized flow field equations are solved using a spatial Fourier expansion in terms of the circumferential coordinate θ for the pressure perturbations

$$\delta p(x, \theta, t) = \sum_{n=-\infty}^{\infty} \tilde{\delta p}_n(x, t) e^{jn\theta}, \quad (2)$$

where $\tilde{\delta p}_n(x, t)$ denotes the n th spatial Fourier coefficient of the pressure perturbations, x is the axial coordinate, and t is time. Feulner et al. [5] added external forcing (inputs) and sensing (outputs) to the model and identified states in the resulting dynamic equations. This yields a state-space formulation of the compressor model for each spatial harmonic number n at a specified operating point of the engine.

3.2 Modifications to Address Engine Transients. The analysis of Feulner et al. [5] was modified to include unsteady pressure fluctuation forcing in the blade passages (for a detailed description see Spakovszky [9]). These can originate from pressure fluctuations and disturbances in the compressor gas path (i.e.,

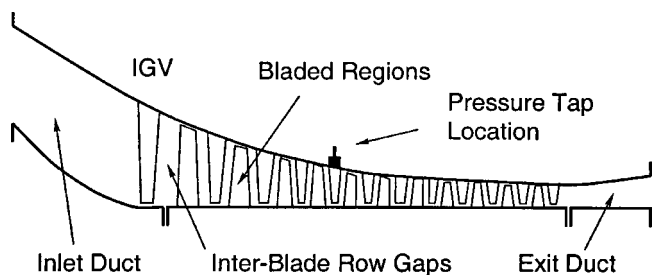


Fig. 4 Modeled regions of the multistage high-speed compressor

effects from nonuniform tip-clearances, a deteriorated casing, unsteady flow phenomena on the blade scale, etc.). The other major modification is the consideration of transient engine operation. Since the compressor dynamics depend inherently on the engine operating point, the dynamics will in general vary as the engine is accelerated.

The modified system dynamics can be written for each spatial harmonic number n as a *linear-time-varying* (LTV) state-space system [9]

$$\begin{aligned}\dot{\mathbf{x}}(t) &= \mathbf{A}_n(t)\mathbf{x}(t) + \mathbf{B}_n\mathbf{u}(t) \\ \widetilde{\delta p}_n(t) &= \mathbf{c}_n\mathbf{x}(t),\end{aligned}\quad (3)$$

where $\mathbf{x}(t)$ is the state vector and $\mathbf{u}(t)$ is the forcing (input) vector. The $\mathbf{A}_n(t)$ matrix contains the dynamics of the compressor and is constructed from compressor geometry and performance information that can vary in time (note that the $\mathbf{A}_n(t)$ matrix is time dependent). The \mathbf{B}_n matrix models the unsteady pressure fluctuation forcing in the blade passages and sets up a forcing signal $\mathbf{u}(t)$ as an input to the system. The vector \mathbf{c}_n selects the right states to reconstruct the sensed n th spatial Fourier coefficient of the pressure perturbations $\widetilde{\delta p}_n(t)$ at the midcompressor stator location depicted in Fig. 4.

A mean-line compressor performance code was used to generate performance correlations of the engine test data (viscous losses, deviation and incidence effects, air-bleed, guide vane schedule, etc.), which are needed to build the \mathbf{A}_n matrix. The correlations were computed for a discrete set of operating points defined by the inlet Mach number M_{inlet} and the rotor speed Ω . A set of hyper-surfaces was fitted to the performance correlations to obtain a continuous and analytical description of the variable compressor performance over the map [9]. The speed lines computed from the fitted analytical performance model agreed well with data. The resulting speed lines for the undeteriorated engine are plotted in Fig. 5. The total pressure ratio, the inlet Mach number, and the rotor speed are normalized by the corresponding design values.

The experiments included measurements of total pressure ratio and rotor speed during the acceleration transient (as depicted in Fig. 1). These are displayed as a transient operating line on the compressor map in Fig. 5 (solid line). To simulate the transient acceleration of the engine, the measured transient operating line was discretized in time. The transient operating line was computed using the data-matched analytical compressor performance solution for a specified series of quasi-steady operating points

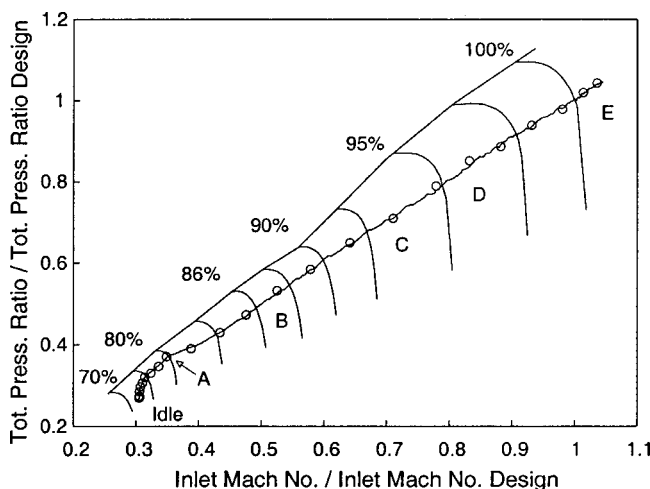


Fig. 5 Undeteriorated engine compressor map and transient operating line: solid line=experiment, circles=matched computation

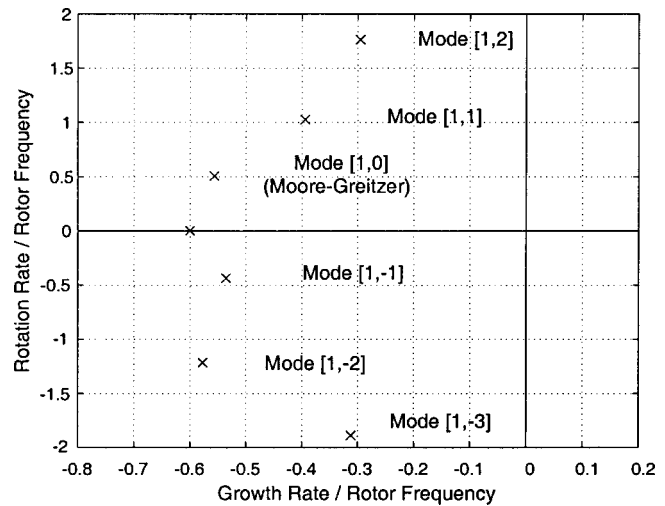


Fig. 6 Compressor system pre-stall modes with first spatial harmonic content ($n=1$) at a part-power operating point

(circles in Fig. 5), defined using the measured rotor speed and the data-matched inlet Mach number during the acceleration transient. The computed points compare well to the measured transient operating line and give confidence in the use of this model to calculate the \mathbf{A}_n matrix. The state-space compressor model yields two results: a solution in the frequency domain and a solution in the time domain.

3.3 Frequency Domain Solution. The state-space equations have an unforced (homogeneous) solution in the frequency domain, found by solving an eigenvalue problem. Each complex eigenvalue and its corresponding eigenvector of \mathbf{A}_n represents an n th spatial harmonic pre-stall wave. These waves rotate around the annulus (the rotation rate is ω , the imaginary part of the eigenvalue) and can grow or decay in time (the growth rate is σ , the real part of the eigenvalue). The stability of the compression system depends on the least stable eigenvalue of \mathbf{A}_n for any n . Analysis shows that first circumferential spatial harmonic ($n=1$) modes are the least stable ones. Modes with higher harmonic content are well damped and do not contribute much to the system response. Therefore we will carry out the analysis for $n=1$ only, dropping the subscript n .

Figure 6 depicts the first harmonic modes when the compressor is at a part-power condition far from stall ($M_{\text{inlet}}=0.356 \cdot M_{\text{design}}$ and $\Omega=0.8 \cdot \Omega_{\text{design}}$). The pre-stall modes are labeled $[n, m]$, n denoting the circumferential spatial harmonic number (here $n=1$) and m indicating essentially the axial wave number. Higher values of m indicate more nodes within the compressor as well as higher rotation frequency. The sign reflects the direction of rotation. Mode $[1, 0]$ is similar to that seen in incompressible flow (the mode shape of the mass flow perturbation is approximately uniform along the axial direction through the compressor) and will be referred to as the classical Moore–Greitzer mode. At the operating point shown the Moore–Greitzer mode is well damped. Experiments show that this mode grows into a finite rotating stall cell when the compressor is throttled into instability. Other modes are compressible [6] and travel in both directions. Note that the first compressible mode $[1, 1]$ rotates at a rate very close to rotor speed. The $[1, 0]$ and $[1, 1]$ modes will be of special interest in further analysis.

3.4 Time Domain Solution. To obtain the response of the compression system to forcing, the random forcing input to the linear, time varying system described in Eq. (3) must be specified. The random forcing was chosen as white noise, augmented with rotor frequency noise in each blade row, thus modeling geometric

nonuniformities. The white noise and rotor frequency noise levels were set at the level seen in the experiments [9].

The time step between the discrete operating points (*global* time step) is chosen to be 25 rotor revolutions to yield good resolution of the discrete transient operating line and to be on the order of the time it takes for the compressor dynamics to change during the acceleration transient (the compressor dynamics are assumed to be constant during the global time step). For every operating point corresponding to a discrete time i , a set of constant \mathbf{A}^i , \mathbf{B}^i , and \mathbf{c}^i matrices is computed and the linear system defined in Eq. (3) is excited with random forcing and integrated over the global time step. The *local* time step in the integration process is set to 0.1 rotor revolutions to resolve the output signal at an affordable computation time. This integration process is performed for each discrete operating point along the transient operating line (circles in Fig. 5), simulating the compressor dynamic response during the acceleration transient [9]. For each global time step the initial conditions are reset to zero. The initial settling time is so short (a fraction of a rotor revolution), that the initial conditions have no influence on the system response.

The simulated dynamic response at the midcompressor pressure perturbation sensor $\delta p_{\text{sens}}(t)$ is then reconstructed as

$$\delta p_{\text{sens}}(t) = \text{Re} \left\{ \sum_{n=0}^{\infty} \widetilde{\delta p}_n(t) e^{jn\theta_{\text{sens}}} \right\} \approx \text{Re} \left\{ \widetilde{\delta p}_1(t) e^{j\theta_{\text{sens}}} \right\}, \quad (4)$$

where θ_{sens} is the circumferential angle of the pressure sensor location. The infinite Fourier series is approximated by the first spatial harmonic alone, based on the observations that higher harmonics are well damped.

The formulated LTV state-space compressor model can be employed to simulate compressor dynamic behavior during transient engine operation. In the following, the model will be used to explain the observed phenomena in the test engines.

4 Simulation of the Undeteriorated Engine

The compressor performance data and matched transient operating line of the undeteriorated engine in Fig. 5 were used in simulating the compressor dynamic behavior during the acceleration transient with the LTV system defined in Eq. (3). The spectrogram of the simulated midcompressor sensor signal is depicted in Fig. 7. Comparison with Fig. 2 shows that the simulation matches the measurement well.

Another view of the simulation is provided in Fig. 8 in which the power spectral density in Figs. 2 and 7 are integrated between normalized frequencies of 0.9 and 1.1, with the result denoted as the [1, 1] signal. In both cases the integrated power reaches the

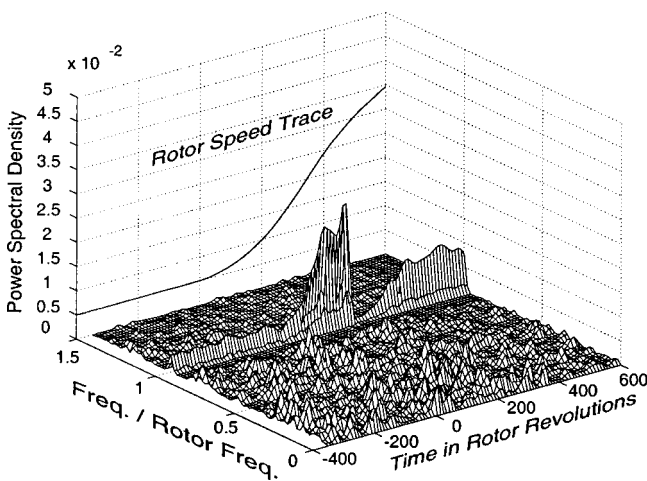


Fig. 7 Spectrogram of simulated unsteady static pressure signal of undeteriorated engine during the transient

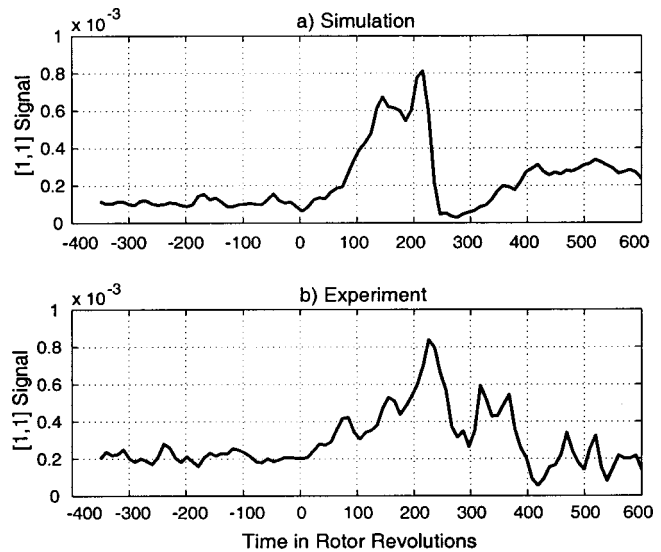


Fig. 8 Integrated [1, 1] signal during the acceleration transient: (a) simulation, (b) experiment

peak value about 200 rotor revolutions into the acceleration. This period of time (0 to 200 rotor revolutions, corresponding to 73 percent to 83 percent corrected design speed) corresponds to the time that the transient operating line has departed from the steady-state operating line. The [1, 1] signal decays abruptly after this time to a roughly constant level as seen in Fig. 8.

A major question arising from the observations is what physical mechanism is responsible for the amplification of the [1, 1] signal during the transient acceleration phase? This is discussed in the following section.

4.1 Discussion of Undeteriorated Engine Simulation Results.

The dynamics of the compressor described by the \mathbf{A} matrix change during the transient event, and it is of interest to analyze the eigenvalue migration during the acceleration transient. The first few pre-stall modes having a first circumferential spatial harmonic content are plotted in Fig. 9 as a function of time in the transient acceleration phase. All modes are in the stable region with negative growth rates. The incompressible, rotating stall-like mode [1, 0] travels at about half of the rotor frequency. Measure-

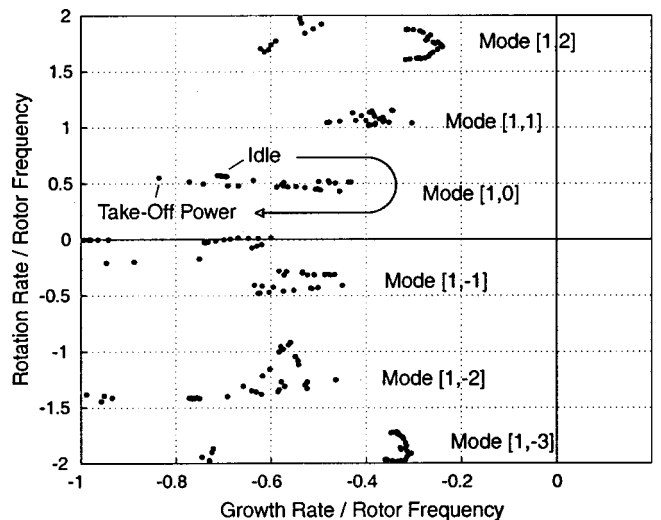


Fig. 9 Compressor system pre-stall modes with first harmonic content during the acceleration transient

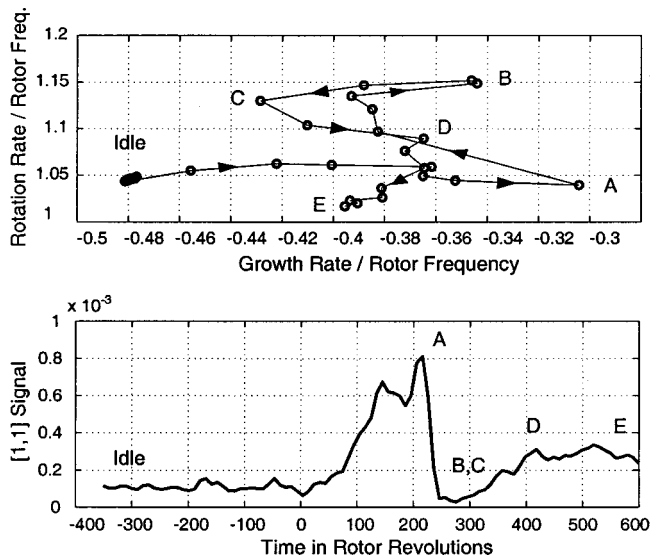


Fig. 10 Motion of [1, 1] mode (top) and simulated [1, 1] signal (bottom) during the acceleration transient

ments at stalled conditions in these engines show rotating stall traveling at about 50 percent rotor speed. Mode [1, 0] has the largest variation in growth rate but varies little in rotation rate. This is explained by the Moore and Greitzer [3] formulation for incompressible flow, where the growth rate σ and the rotation rate ω of this mode can be related to fluid inertia in the rotors λ , in rotors and stators μ , and to the slope of the total-to-static pressure rise map Ψ^{ts} with respect to the flow coefficient ϕ :

$$\sigma = \frac{\partial \Psi^{ts} / \partial \phi}{(2 + \mu)} \quad \text{and} \quad \omega = \frac{\lambda}{(2 + \mu)}. \quad (5)$$

The growth rate σ depends dominantly on the slope of Ψ^{ts} since the nondimensional blade row inertias change only slightly with the vane schedule. The latter circumstance also implies that the rotation rate ω will be approximately constant with the operating point as seen. The speed line in Fig. 5 is steep near idle, then lessens to a lower slope and increases again to steeper slopes over the remainder of the operating range. Thus the growth rate of mode [1, 0] changes rapidly off idle and then returns to lower values (see Fig. 9).

The upper plot in Fig. 10 gives a more detailed look at the motion of the [1, 1] eigenvalue. Several points are labeled on this figure to correspond to the lower plot which shows the evolution of the magnitude of this signal. The purpose is to explain how motion of the [1, 1] eigenvalue affects the [1, 1] signal.

There are three basic effects of eigenvalue motion: (1) Eigenvalue growth rate (equivalently damping) indicates the amplitude of the mode's resonant peak and the stability. (2) eigenvalue rotation rate (equivalently frequency) determines proximity of the resonance peak to forcing at multiples of the rotor frequency. When the rotation rate of the [1, 1] mode is near rotor rotation (unity), a large response is expected. (3) Eigenvalue natural frequency ($\omega_N = \sqrt{\sigma^2 + \omega^2}$) reflects the compliance of the mode, and thus its susceptibility to forcing. Based on these three factors, eigenvalue locations with imaginary parts near one and real parts near zero will yield highest response to rotor frequency forcing.

Returning to Fig. 10, one can see that at idle the [1, 1] mode is far to the left (well damped and with a natural frequency furthest from unity). Thus this idle response is low, and remains that way until zero rotor revolutions, when the acceleration transient begins (refer to Fig. 1). At this point the eigenvalue shifts dramatically to the right, and at 200 rotor revolutions (point A) all three of the properties described above are conducive to large amplitude re-

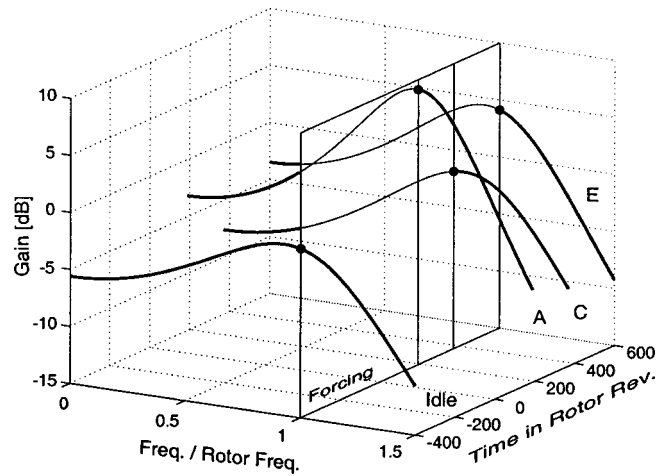


Fig. 11 Simple model of analogy: gain curves of mass-spring-damper system during acceleration transient

sponse of the [1, 1] mode. After this peak amplitude point, the mode moves vertically and to the left, away from rotor frequency excitation, and to a higher natural frequency (implying lower compliance, points B and C). At these points the response is small. After this the eigenvalue wanders toward the excitation frequency, but remains far enough left that the response is small (points D and E).

These effects can be further elucidated by considering a mass-spring-damper, as a mechanical analogy for the resonant [1, 1] mode. The mass-spring-damper system response is described by

$$\ddot{y}(t) + 2\zeta\omega_0\dot{y}(t) + \omega_0^2y(t) = F(t)/m, \quad (6)$$

where $y(t)$ is the displacement (analogous to modal amplitude) and $F(t)/m$ is the forcing divided by mass. ω_0 is given by $\omega_0^2 = k/m$ (where k is the spring constant) and ζ is given by $2\zeta\omega_0 = d/m$ (where d is the damping constant). The effects of eigenvalue motion can be better understood using this model. For instance, if the mass is held constant (analogously, the inertia within the compressor remains unchanged), and ω_0 is allowed to vary while holding ζ constant, two of the three effects described above are felt. First, the frequency of the resonant peak approaches one. Second, the overall compliance k of the system is reduced so the forced response amplitude increases because at steady state $y_{\text{steady-state}} = F/k$.

To apply this analogy to the experimental data, we substitute σ and ω of the [1, 1] mode (Fig. 10) into Eq. (6). This yields a model that ignores all dynamics except those near the rotor frequency. The gain curves (y/F) for the resulting system at four representative points (Idle, A, C, and E) are shown in Fig. 11. Rotor frequency forcing is indicated by a plane at the rotor frequency and the intersection points on each of the curves. At ground idle, the response curve is low and flat. At point A (during acceleration), a larger resonant response is seen due to low damping ratio ζ (higher growth rate σ), with frequency coinciding closely with the forcing. At point C the damping ratio increases and the natural frequency rises; therefore the resonance peak is flatter and no longer coincident with the forcing. At the final point, E, the [1, 1] eigenvalue is closer to the rotor frequency, has slightly lower damping, and more compliance, yielding the increased output amplitude seen in Fig. 11. Because the [1, 1] signal depends on the square of the gain curve, the variations in Fig. 10 are more pronounced than those shown in Fig. 11.

The analysis can be summarized as follows. During the transient the compressor dynamics change. Depending on the eigenvalue locations, more or less energy originating from the rotor noise forcing is fed into the [1, 1] mode and this effect is reflected in the amplification of the [1, 1] signal.

5 Simulation of the Deteriorated Engine

Engine deterioration was assumed to result from an increase in tip-clearance and was modeled as an increase in blockage, with local blockage factors (the ratio of effective through-flow area versus geometric through-flow area) being reduced. The tip-clearances were also assumed to change with rotor speed due to centrifugal and thermal effects as tabulated in Table 1. These estimates were based on experience rather than measurements. The maps and the measured transient operating lines of the undeteriorated engine (solid lines) and the deteriorated engine (dashed lines) are plotted in Fig. 12. The peak pressure ratios drop due to the tip-clearance deterioration, and the increased blockage lowers the mass flows.

The deteriorated compressor performance and the measured transient operating line of the deteriorated compressor were used to simulate the dynamic behavior of the compressor during the acceleration transient. The simulation results obtained from the time domain solution were processed in the same manner as for the undeteriorated compressor.

The integral power of the simulated pressure signal at rotor frequency during the acceleration transient is shown in Fig. 13(a) (dashed line) together with the result for the undeteriorated compressor (solid line). The initial level of the [1, 1] signal is higher in the deteriorated case but both signals converge to the same value after the peak. The ratio of the peak values (between deteriorated and undeteriorated compressors) is also roughly a factor of two in both data and simulations (Fig. 13(b)). A(u) denote the instant of peak power shown in Fig. 13 for the undeteriorated engine and the deteriorated engine respectively.

Figure 14 compares the eigenvalue locations of the deteriorated compressor (analyzed at peak point A(d) in Fig. 13) to those of the undeteriorated compressor (analyzed at peak point A(u) in Fig. 13). Only those eigenvalues with frequencies less than 2 are shown. Mode rotation rates are not affected by deterioration; however, all of the eigenvalues are shifted to lower damping ratios, causing the system response to forcing to increase. The large shift of the Moore-Greitzer [1, 0] mode, together with the shift of the

Table 1 Modeled engine deterioration over the range of operating speeds

| % corr. design speed | TC/chord [%] | blockage [%] |
|----------------------|--------------|--------------|
| 70 - 85 | +0.62 | -1 |
| 85 - 105 | +0.32 | -1 |

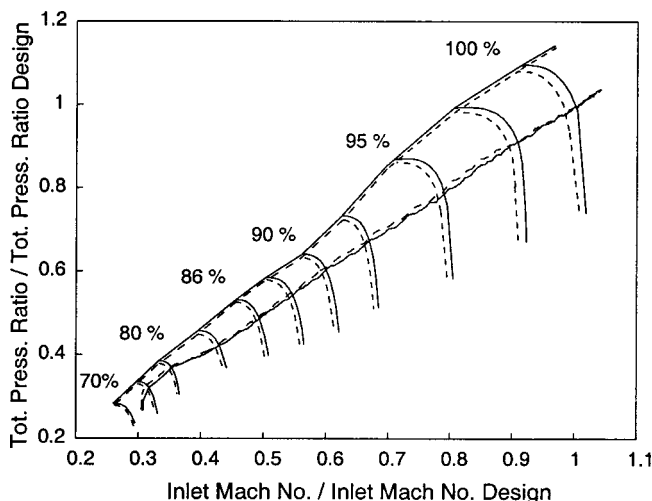


Fig. 12 Deteriorated (dashed) and undeteriorated (solid) compressor maps and measured transient operating lines

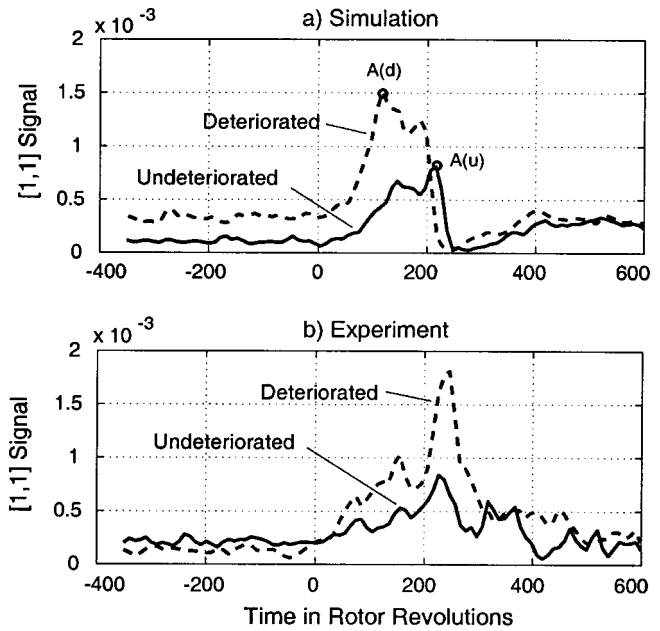


Fig. 13 (a) Simulation, and (b) experimental results of the [1, 1] signal during the acceleration (solid=undeteriorated engine, dashed=deteriorated engine)

[1, 1] mode, is primarily responsible for the increased amplitude of the response to rotor frequency excitation shown in Fig. 13. As mass flow is further reduced, the model predicts that the [1, 0] mode will overtake the [1, 1] mode and become unstable first. However, because of the strong forcing at rotor frequency, the [1, 1] signal is the most easily measured indicator of deterioration in stability.

This discussion suggests that there is a connection between the disturbances seen rotating at rotor frequency and those seen at roughly 50 percent of rotor frequency, although this cannot be captured in the present linearized analysis. As mentioned, the rotating stall frequency is near 50 percent rotor frequency, and the linearized stability theory predicts the mode with that rotation rate to go unstable first. However, a *nonlinear* form of interaction between the [1, 1] and the [1, 0] mode may also exist, by which strong rotor frequency disturbances cause the incompressible-like modes to become unstable prior to the point of linear instability.

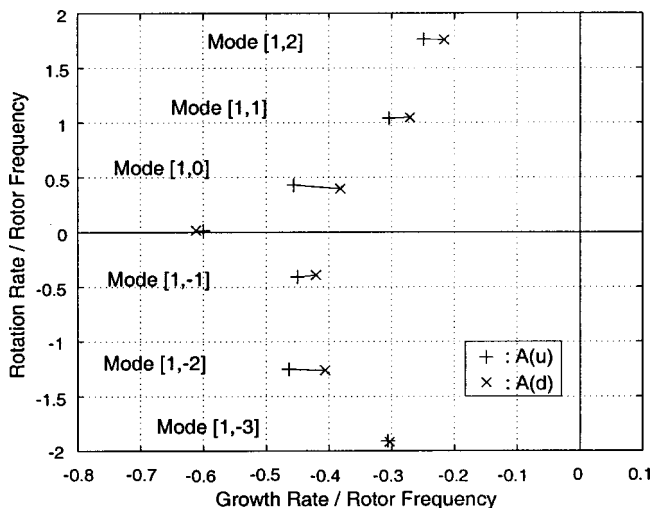


Fig. 14 Deteriorated (X) and undeteriorated (+) compressor system pre-stall modes at peak points A(d) and A(u)

For instance, rotor frequency disturbance may set up a ‘‘background flow’’ in which the [1, 0] mode becomes unstable. It would be useful to examine the impact of compressible mode stability on overall compressor stability using a nonlinear analysis, such as that described by Hendricks et al. [10].

6 Deterioration Effect on Transient Stall-Margin

An enlarged view of the measured transient operating lines of the undeteriorated (solid) and the deteriorated engine (dashed) is plotted in Fig. 15. The calculated stall lines are also plotted. The stall point was calculated as the point when the least stable mode (the rotating stall-like mode [1, 0]) reached neutral stability (zero growth rate). We will define the stall-margin SM at each operating point as the distance between the operating point and the corresponding stall point at the same inlet corrected flow:

$$SM = \left\{ \frac{\pi_{\text{stall}} - \pi_{\text{oper.}}}{\pi_{\text{oper.}}} \right\}_{\text{const. inlet corr. flow}}, \quad (7)$$

where the total-to-total pressure ratio is denoted by π . Measurements of the steady-state stall-margin in the two test engines showed a loss in stall-margin of about 5 percent due to deterioration. Using Eq. (7) the steady-state stall-margin at ground idle is 30 percent for the undeteriorated engine and 26 percent for the deteriorated engine. The deterioration (modeled as an increase of 0.62 percent in tip-clearance to chord ratio) reduced the steady-state stall-margin by 4 percent, in good agreement with the measured results.

The *transient* stall-margin is defined as the minimum stall-margin along the transient operating line

$$SM_{\text{trans}} = \min_{\text{inlet corr. flow}} \{SM\}, \quad (8)$$

yielding 12 percent for the undeteriorated engine and 7 percent for the deteriorated engine. Thus the transient stall-margin is more than 18 points lower than the steady-state stall-margin in both the undeteriorated and the deteriorated case. This is because during acceleration transients the operating lines depart from the steady-state level toward the stall line, reducing the instantaneous stall-margin.

The simulation shows that the [1, 1] modes with the largest growth rates correspond to operating points along the transient operating line with the smallest stall-margins (points A(u) and A(d)). In other words, the peaks in the [1, 1] signals correspond to operating points with the smallest stall-margins during the acceleration transient. This suggests that the [1, 1] signal can be used as

a measure of transient stall-margin and that changes in the [1, 1] signal during the life of an engine can be related to the change in stall-margin.

7 Conclusions and Summary

This paper is a combined experimental and analytical approach to the assessment of stability in a multistage compressor of a commercial aircraft engine during engine transients. The mechanism of the experimentally observed phenomena in the pre-stall flow field and the effect of deterioration on the engine dynamic behavior are investigated using a modified version of a two-dimensional, linear, compressible, modal, state-space model of stall-inception [5]. From the applications of this new time-varying version of this model to engine data during a transient, the following conclusions can be drawn:

- The effect of engine deterioration on the compressor dynamic behavior, observed in the measurements as well as in the simulations, is an enhanced pressure perturbation rotating at rotor frequency during an acceleration transient. The model, based on the idea of compression system resonant response, captures the measured dynamics of the compression system and is therefore an appropriate tool for understanding the experimental observations.
- Amplification of the pressure perturbations traveling at rotor frequency can be related to the quasi-steady variation in compressor dynamics during the acceleration transient. Pre-stall compressor modes change in both frequency and damping during the transient so as to alter the response of the [1, 1] mode to forcing by rotor frequency noise.
- Experiments on deteriorated compressors showed a larger growth in the [1, 1] signal during acceleration transients. Modeling the engine deterioration as increased tip-clearances resulted in good agreement with the experimental data.
- Deterioration (a maximum increase of 0.62 percent in tip-clearance to chord ratio) decreased the steady-state stall-margin by 4 percent. During off idle acceleration transients, the instantaneous stall-margin was reduced by over 18 points from the steady-state value. The difference between the steady-state and transient stall-margins were roughly the same for both the undeteriorated (18 out of 30 percent) and the deteriorated engines (19 out of 26 percent). In both cases, the [1, 1] signal was the strongest at the point of minimum stall-margin. This suggests therefore that this signal can be used as a measure of stall-margin.

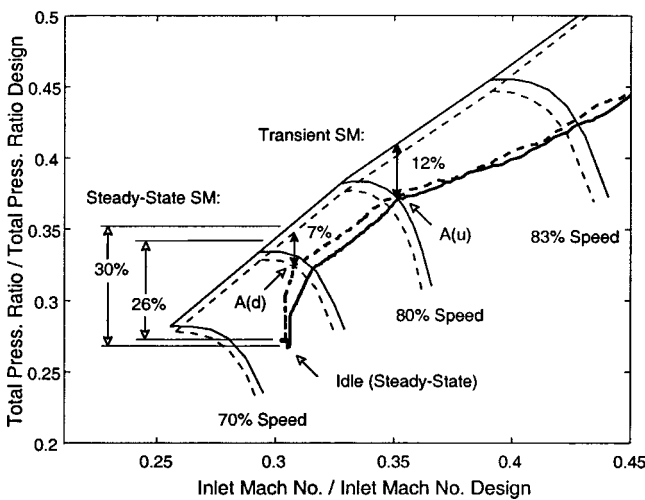


Fig. 15 Deteriorated (dashed) and undeteriorated compressor (solid) stall lines and transient operating lines at low speeds

Acknowledgments

The authors would like to thank S. Chowdhury and M. Feulner at Pratt & Whitney for the very useful comments and insightful discussions and for the help in engine testing. This work was supported by the US Air Force Office of Scientific Research, Dr. James McMichael, technical manager.

References

- [1] Emmons, H., Pearson, C., and Grant, H., 1955, ‘‘Compressor Surge and Stall Propagation,’’ *Trans. ASME*, **79**, pp. 455–469.
- [2] Moore, F., 1984, ‘‘A Theory of Rotating Stall of Multistage Axial Compressors: Part I—Small Disturbances,’’ *ASME J. Eng. Gas Turbines Power*, **106**, pp. 313–320.
- [3] Moore, F., and Greitzer, E., 1986, ‘‘A Theory of Post-Stall Transients in Axial Compressors: Part I—Development of the Equations,’’ *ASME J. Eng. Gas Turbines Power*, **108**, pp. 68–76.
- [4] Bonnaure, L., 1991, ‘‘Modelling High Speed Multistage Compressor Stability,’’ Master’s thesis, Department of Aeronautics and Astronautics, MIT.
- [5] Feulner, M., Hendricks, G., and Paduano, J., 1996, ‘‘Modeling for Control of Rotating Stall in High Speed Multi-Stage Axial Compressors,’’ *ASME J. Turbomach.*, **118**, pp. 1–10.
- [6] Tryfonidis, M., Etchevers, O., Paduano, J., Epstein, A., and Hendricks, G., 1995, ‘‘Pre-stall Behavior of Several High-Speed Compressors,’’ *ASME J. Turbomach.*, **117**, pp. 62–80.

- [7] Fréchette, L. G., 1997, "Implications of Stability Modeling for High-Speed Axial Compressor Design," Master's thesis, Department of Aeronautics and Astronautics, MIT.
- [8] Weigl, H., Paduano, J., Fréchette, L., Epstein, A., and Greitzer, E., 1998, "Active Stabilization of Rotating Stall and Surge in a Transonic Single Stage Axial Compressor," *ASME J. Turbomach.*, **120**, pp. 625–636.
- [9] Spakovszky, Z., 1997, "Simulation of Engine Clearances Effects on Compressor Dynamic Behaviour During Acceleration Transients," Master's thesis, Swiss Federal Institute of Technology, ETH Zürich.
- [10] Hendricks, G., Sabnis, J., and Feulner, M., 1997, "Analysis of Instability Inception in High-Speed Multistage Axial-Flow Compressors," *ASME J. Turbomach.*, **119**, pp. 714–722.

Active Stabilization of Surge in an Axicentrifugal Turbo shaft Engine

E. B. Nelson

J. D. Paduano

A. H. Epstein

Gas Turbine Laboratory,
Department of Aeronautics and Astronautics,
Massachusetts Institute of Technology,
Cambridge, MA 02139

Active stabilization of surge was implemented on an Allied Signal LTS-101 axicentrifugal gas producer, reducing the surging mass flow by 1 percent, for an operating range increase of 11 percent. Control was achieved using high-response sensors in the inlet and diffuser throat, coupled to actuators that injected air near the diffuser throat. System identification and modeling indicate that a classical surge-type eigenmode and an eigenmode associated with engine duct acoustics dominate the engine's input-output properties. The surge eigenmode's stability determines the open-loop surge mass flow. A robust linear controller with three inputs and one output stabilized this eigenmode without destabilizing the acoustic mode. The controller facilitated a 1 percent reduction in surging mass flow at 95 percent NI corrected; this increases the engine's choke to surge stable operating range by 11 percent. This paper elucidates the measured unsteady presurge behavior of the engine, and outlines a systematic procedure for surge control law development. [S0889-504X(00)01803-1]

I Introduction

In aircraft engines, the compression system instability known as surge is currently avoided using steady state means. This includes vane scheduling and system matching to insure that the surge line is sufficiently far from the operating line. Recent research considers unsteady means, such as active control, to prevent surge. Performance and/or operability benefits can be realized from an extension of the stable operating range, that is, a reduction of the engine mass flow at which surge occurs.

In the research of Fink [1], Huang and Ffowcs Williams [2], Pinsley et al. [3], Gysling et al. [4], and Simon et al. [5], active control of surge was studied on laboratory turbocharger rigs. These studies showed that surge is the result of instability of small perturbations at specific frequencies. Furthermore, this work demonstrated that by stabilizing the small-perturbation dynamics, the large-amplitude surge event can be prevented. These initial studies not only demonstrated active control, but also provided an analytical framework for applying the concept to more complex compression systems.

This work has motivated surge control experiments in engines and engine components. Notable examples include Ffowcs-Williams et al. [23], Freeman et al. [6], Eveker et al. [7], and Bae [20]. These studies shared the notion of preventing surge using unsteady measurements that feed back to high-response actuators. The goal of the work reported herein was to demonstrate techniques that reduce the surging mass flow of an engine through stabilization.

An Allied Signal LTS-101 turboshaft helicopter engine was used for this research. By studying the perturbations prior to surge and characterizing the engine's input-output dynamics, we show that the small perturbation properties observed in laboratory scale rigs are present in this engine. We discuss how these perturbations are modeled by incorporating one-dimensional acoustic ducts into a system model similar to that suggested by Greitzer [8]. Finally, we describe the control law development and implementation, and the range extension that was achieved. At each stage, fundamental concepts developed in previous work are applied, and modified as needed for the engine environment.

The paper traces the control system development process. The first step is to measure frequency responses from the actuator to all of the available sensors. The second step is to select a set of

sensors for feedback. Next, a state-space model is fit to the frequency response data between the input and the selected outputs. This model is then used for control law design. The closed-loop behavior measured by all the available sensors motivates changes to both the feedback sensor configuration and the control law design. Implementation issues and control system strategies also influence compensator design and redesign. We present only the ultimate results of this process, emphasizing the system features that have the greatest impact on the success of the stabilizing controller.

II Test Apparatus and Open Loop Tests

The tests presented here were conducted on an Allied Signal LTS-101 600A-2 600 horsepower class turboshaft helicopter engine,¹ modified specifically for active control research. The LTS-101 has a single axial stage and a centrifugal stage with vaned diffuser. Figure 1 shows a side view of the engine. The design pressure ratio is about 8:1, and the design corrected weight flow is about 5 lb/s.

The gas producer installed at MIT was modified for these experiments. First, the diffuser throat area was slightly enlarged to ensure that the centrifugal stage limited the stable operating range. Second, the turbine nozzle guide vane area was reduced to move the operating line closer to the surge line and thus reduce the

¹Among the many vehicles powered by the LTS-101 are the Kawasaki BK117 "Eurocopter," the Aerospaziale AS350D "Astar" & HH-65 "Dolphin," and the Bell 222.

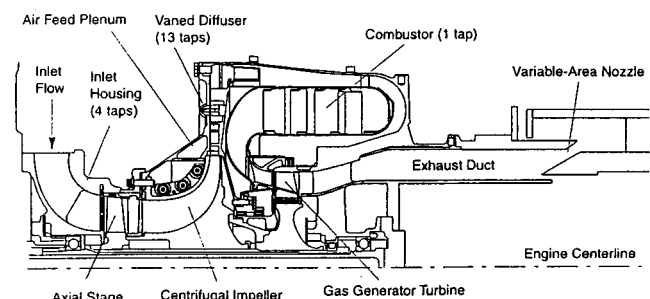


Fig. 1 LTS-101 gas producer: note plenum above impeller shroud

Contributed by the International Gas Turbine Institute and presented at the 44th International Gas Turbine and Aeroengine Congress and Exhibition, Indianapolis, Indiana, June 7–10, 1999. Manuscript received by the International Gas Turbine Institute February 1999. Paper No. 99-GT-438. Review Chair: D. C. Wisler.

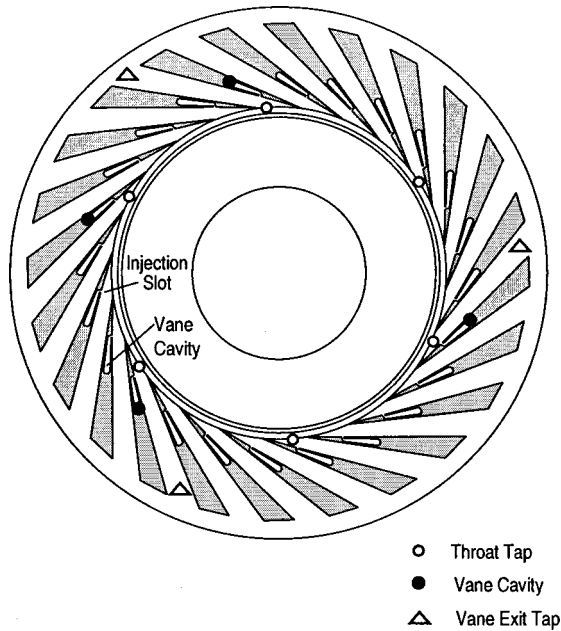


Fig. 2 Circumferential tap locations within diffuser

turbine inlet temperature while operating near surge. Third, the power turbine and shaft were removed [9] and replaced with a variable area exit nozzle.

The engine mounting and nozzle arrangement are unusual in that the engine is mounted on linear bearings and translated axially to change the nozzle area (Fig. 1). To accomplish this, the nozzle consists of two concentric cones, one mounted to the engine, the other to the stationary exhaust system. This arrangement also facilitates measurement of engine thrust.

Three separate desktop PC computers were used. One recorded steady-state engine performance, controlled engine operation, and monitored diagnostic parameters. The second acquired high-speed dynamic data from pressure transducers at five axial stations, which are shown in Figs. 1 and 2. The third implemented the feedback control law and sent commands to the actuator.

Actuation Using Air Injection. The centrifugal compressor of this engine employs a vaned diffuser. Actuation is implemented by injecting laboratory air into the throats of the diffuser passages, at about the diffuser discharge pressure [24]. This approach was chosen both because it was expedient and because this form of actuation is “close-coupled” to the compressor, a desirable feature for effective surge control as discussed by Simon et al. [5]. Close-coupled means that the actuation is located near or in the compressor. Such actuators have a nearly instantaneous effect on the energy source of the surge instability (the compressor), without long delays or intermediate dynamics.

The standard engine configuration includes slots at the throat of each vaned diffuser passage which communicate through a circumferential plenum above the impeller shroud (the slots can be seen in Fig. 2, and the plenum is shown in Fig. 1). This approach is used in many high-pressure-ratio centrifugal compressors to increase their surge margin. For these experiments, the orifices connecting the throat slots and the plenum were enlarged to improve the speed of response, and a control valve was mounted external to the plenum. The valve, adapted from a Moog linear force motor, can modulate the injectant from 2 to 5 percent of the engine air flow at a full signal bandwidth of 330 Hz [21].

All tests were conducted at a mean injection level of 3.8 percent. Thus we “baseline” performance with mean injection, and judge controller performance against this baseline. All compressor characteristics are given in terms of flow downstream of the com-

pressor (inlet flow+ injected flow); range extension results based on upstream mass flow are nearly identical, since the mean blowing case is taken as the baseline. All data and analysis presented herein are at 95 percent corrected speed. Time-resolved presurge measurements show that a surge mode similar to that seen in laboratory-scale rigs is present, and that when this mode is unstable (or nearly so) the system enters surge. However, unlike the laboratory scale rigs, the engine also exhibits acoustic modes.

Steady Injection Tests. The influence of steady injection on the speed line shape is shown in Fig. 3. Without injection, the stable region of the characteristic slopes negatively, and flattens to a peak over a short range of corrected mass flow [10,11]. With steady injection, the characteristic is flatter, with a larger region of shallow slope. Injection also causes surge inception to be more gradual, exhibiting a longer evolution of a dynamic instability. Finally, steady injection stabilizes the compressor to lower corrected mass flows, at the expense of a reduced engine pressure ratio.

Unsteady data were taken at surge inception with steady injection while closing the exhaust nozzle in small, discrete steps near the surge line. Figure 4 shows static pressure traces, taken at two axial stations, during the last 230 rotor revolutions prior to surge.

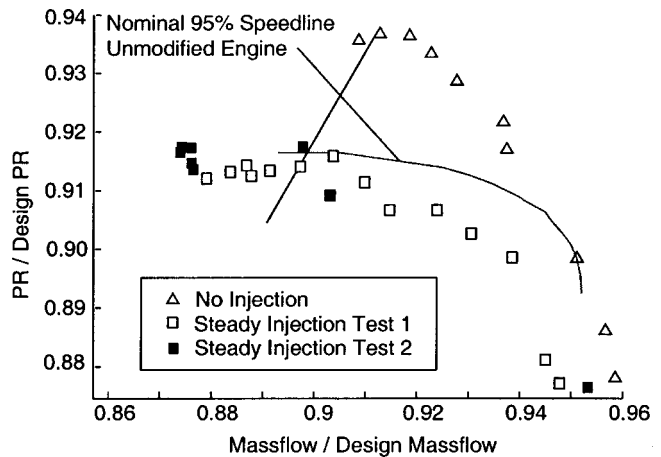


Fig. 3 Speed lines at 95 percent corrected speed

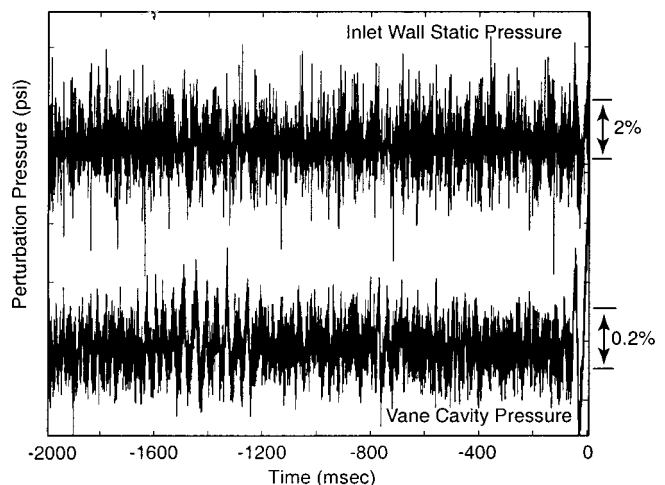


Fig. 4 Open-loop unsteady pressure traces 2 s prior to surge. See Fig. 2 for location of vane cavity pressure taps. Perturbation magnitudes given in percent compressor exit pressure.

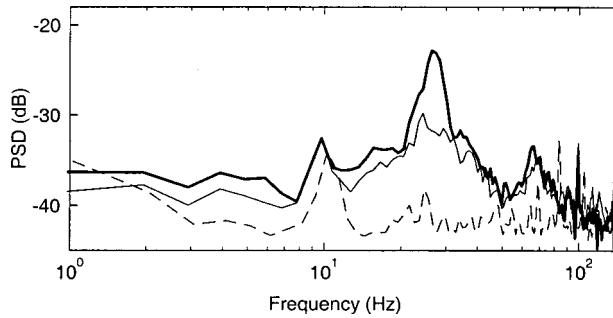


Fig. 5 Power spectral density of vane cavity pressure. Bold=immediately prior to surge; solid=0.34 percent in mass flow from surge; dashed=4.7 percent in mass flow from surge.

Note that although the data are quite noisy, a high-frequency resonance is visible, as well as a lower frequency resonant transient immediately prior to surge.

Figure 5 shows the power spectrum of static pressure in the small diffuser-vane cavity that feeds into the throat slot (see Fig. 2). Spectra were taken at three operating points: one at +4.7 percent mass flow from surge, one at +0.3 percent mass flow, and one immediately prior to surge. Two peaks are apparent immediately prior to surge, at 28 and 68 Hz. As the compressor is throttled toward the surge line, these two peaks grow dramatically.

Based on these observations, the time-resolved pressure data were low-pass and band-pass filtered at 30 and 70 Hz, respectively. The 70 Hz band-pass filtered time history (Fig. 6) shows a resonance for hundreds of revolutions prior to surge. Examination of the relative phases measured at the inlet, vane cavity, diffuser exit, and combustor stations suggest that this is an acoustic mode; it has a standing-wave-like, spatially varying pressure. Acoustic modes at other frequencies were also observed. Because they do not appear to play a role in surge inception, they will not be discussed in detail here.

The low-pass filtered time history shows a 28 Hz signal with different characteristics than the 68 Hz signal. First, the phase is similar at all axial locations, indicative of a “slug flow” type oscillation, like the surge mode described in the model of Greitzer [8]. Second, the 28 Hz signal grows rapidly just prior to surge,

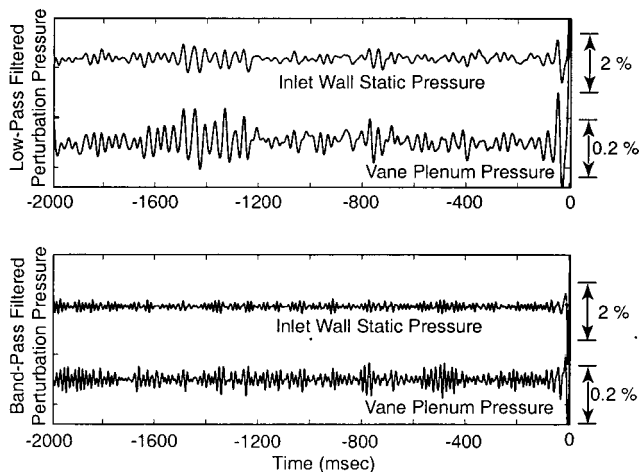


Fig. 6 Static pressure data from Fig. 4, low-pass filtered at 30 Hz to highlight the surge mode (top), and band-pass filtered with a center frequency of 70 Hz to highlight the acoustic mode (bottom)

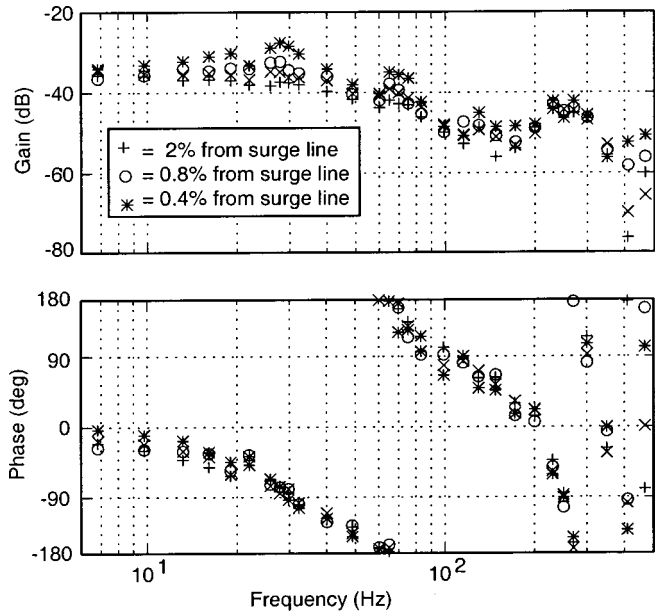


Fig. 7 Transfer functions from valve command to inlet static pressure

suggesting that this mode leads to surge inception. This conjecture is strengthened by system identification results below; thus we identify this eigenmode as the “surge mode.”

Forced Response Tests. Forced response testing was used to obtain transfer functions of the engine dynamics. These transfer functions provide an input–output characterization for control law design, and give a quantitative description of the frequency and stability properties of the system. The input is the command to the injection valve, while the outputs are the pressure signals. These transfer functions include the dynamics of the valve, pressure taps, and anti-aliasing filters in addition to the engine dynamics.

Because the noise levels in the engine are high and frequency sweeps have not proven effective, a series of tests at discrete frequencies was required for system identification. Figure 7 shows transfer functions at three mass flows. Each symbol on this figure represents 45 seconds of data, taken as the valve is modulated at a fixed frequency and ± 0.25 percent mass flow. The peak at 28 Hz becomes sharper as mass flow is reduced, and the phase drop becomes more sudden, indicating that the stability of the 28 Hz “surge mode” decreases as the mass flow is reduced. Numerical fits to the data in Fig. 7 confirm these observations; the fitted eigenvalues become less stable as mass flow is reduced. The 68 Hz “acoustic” mode does not change as much.

Empirical Model for Control Law Design. To obtain a mathematical model for control law design, the frequency response data in Fig. 7 are “fit” with a state-space model, i.e., a set of ordinary differential equations of the form

$$\dot{x} = Ax + Bu$$

$$y = Cx + Du,$$

where x , y , and u are vectors, and A , B , C , and D are matrices. The goal of this fit is to obtain a dynamic model with input–output properties similar to those found experimentally near surge.

Fitting input–output data in this way is more difficult when there are several outputs that must be fit simultaneously (i.e., when the vector y has more than one element). We used the procedure developed by Jacques [12]. The number of outputs was limited to three by the throughput of the real time control computer. For various choices of three sensors, a state-space model

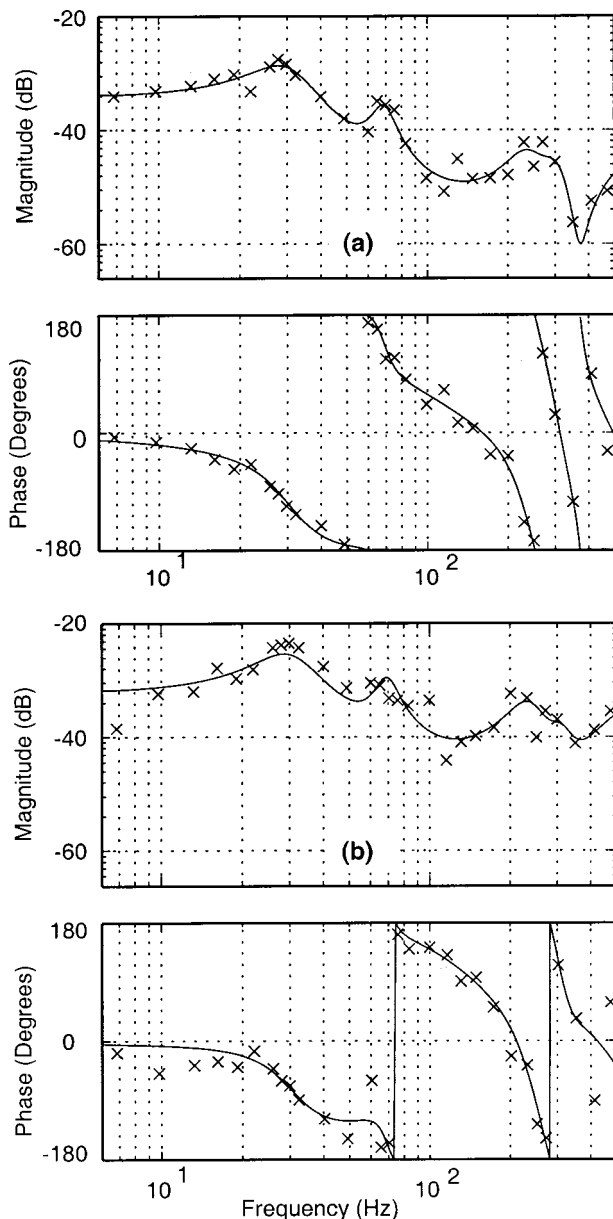


Fig. 8 SIMO transfer function fit for best compensator designs: (a) valve command to compressor inlet static pressure; (b) valve command to diffuser throat static pressure

was fit to the data and control laws were designed. Figure 8 shows the transfer functions of the state-space model which yielded controllers with the largest range extension. The outputs are one diffuser throat and two inlet sensors (the transfer function to only one of the two inlet sensors is shown). We use this fit to estimate the eigenvalues of the system in the next section.

Comparisons With Theoretical Predictions. To validate our physical understanding of the measured behavior, two models were constructed. The first is based on the lumped parameter model of Greitzer [8]. This model has only one eigenmode, which goes unstable when the compressor begins to pump energy into the unsteady oscillations of a Helmholtz-like resonance. The second model uses one-dimensional acoustic duct elements rather than lumped ducts. See Appendix A for details.

Table 1 shows the measured eigenvalue frequencies (from the fits in Fig. 7) and the predicted eigenvalues. The lumped-parameter surge model correctly predicts the existence of a system

Table 1 Predicted and actual surge eigenvalues

| | Surge Mode | 1st Acoustic Mode |
|------------------------|------------|-------------------|
| Experiment | 27 Hz | 68 Hz |
| Lumped Parameter Model | 24 Hz | None |
| Acoustic Duct Model | 32 Hz | 101 Hz |

eigenmode that becomes unstable near the peak of the map. This result reinforces numerous experimental studies showing that this model describes the basic physics involved in surge inception [1,3,13]. However, the eigenvalue at 68 Hz is not predicted by this model.

The acoustic surge model predicts the existence of an infinite number of eigenvalues, at progressively higher frequencies, associated with acoustic modes in the ducts. The lowest of these modes is close to the measured acoustic mode in frequency. An eigenvalue near the surge frequency is also predicted by this model. Note that compressibility in the ducts has a strong effect on the predicted surge frequency, even though its fundamental behavior can be understood by considering incompressible (lumped) ducts. Although further refinement is necessary, the results support our explanation of the physics involved.

III Control Law Design

The goal of the feedback controller is to stabilize the dynamic system at flow rates below the open-loop surge line. Experiments and modeling indicate that there is one unstable eigenmode (at 28 Hz) that must be stabilized while operating the engine below the surge line. However, we have shown that another mode participates in the input-output dynamics. Although the acoustic mode need not be explicitly stabilized, it must be accounted for in the controller design. In fact, we found that simple feedback controllers tended to destabilize the 68 Hz acoustic mode and therefore achieved no range extension. Other controllers, designed without the benefit of several sensors and/or without explicit consideration of modeling errors, were also unsuccessful.

Based on this experience, we adopted a robust multi-input control design method. This method was successfully used for rotating stall control in a compressor that had resonant acoustic modes [13,14]. The details of the technique and its application to the surge control problem are given in Appendix B. The procedure creates a compensator that stabilizes the surge mode without destabilizing the acoustic mode, and directly accounts for uncertainty in the locations of the system eigenvalues. The following additional features are also important to mention:

- 1 The method is widely available and proven effective for control law design. The design algorithms are easily understood and used by a control engineer.
- 2 It automatically accounts for multiple inputs and multiple outputs.
- 3 Robustness constraints, such as models of uncertainty and noise in the system, are included to improve the resulting design.

For details on the design procedure, see Weigl et al. [13] and Weigl and Paduano [14]. Appendix B discusses some of the properties of the compensator that was used to achieve the results in the next section.

IV Experimental Stabilization of Surge

The robust multi-input controller was experimentally tested on the LTS-101 using the following procedure: The engine was

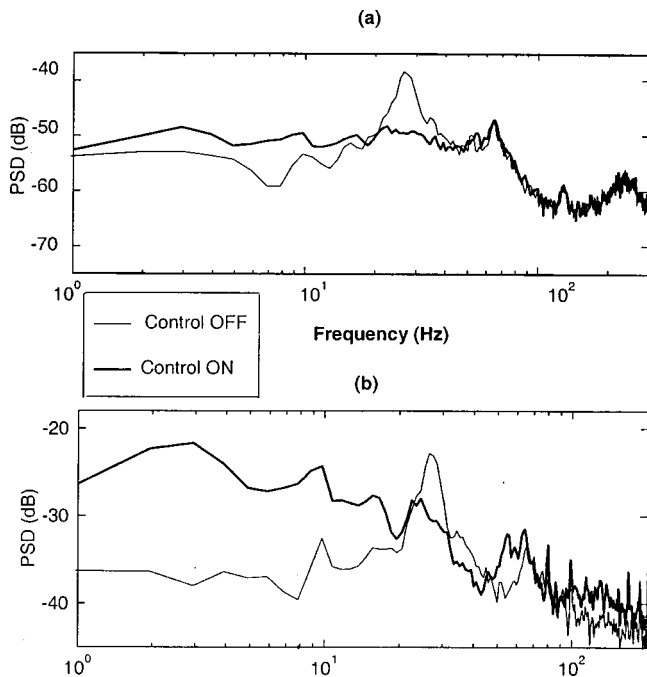


Fig. 9 Control effectiveness in suppressing surge mode, at open-loop surge mass flow: (a) inlet static pressure; (b) vane cavity static pressure

brought to a point near the surge line while operating open loop. Then, the control loop was closed. The nozzle exit area was then reduced in discrete steps, eventually driving the system below the open loop surge line. The engine operated for at least 45 seconds between steps. The closed-loop surge point was then recorded for comparison with open-loop results.

Figure 9 shows the power spectra of pressure in the diffuser vane cavity and at the compressor inlet with and without control, near the open-loop surge line. Feedback reduces the 28 Hz resonance peak by about 10 dB. The vane cavity sensor shows a small closed-loop excitation of the acoustic resonance. This was found to be an acceptable level of relative stability for this mode.

Figure 10 shows the compressor map with and without control. At the same level of average air injection into the diffuser, the closed-loop stabilized machine surges at a mass flow 1.0 percent less than the engine without control. This is an 11 percent increase in the operating range of the baseline engine without injection,

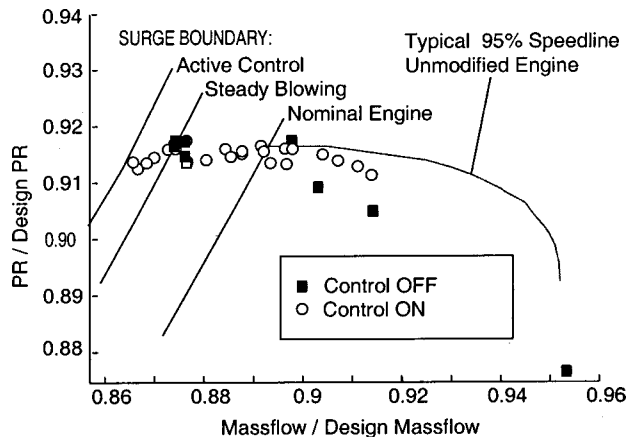


Fig. 10 Compressor range extension with active stabilization of surge

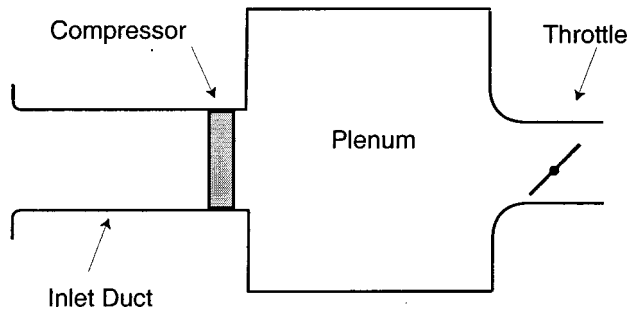


Fig. 11 Compression system geometry for lumped-parameter surge model

from choke to surge. The stabilized engine produces about 3.7 percent more thrust than the baseline, as measured on the test stand. Recall that all quantities are respect to the steady blowing baseline case described in Section II.

V Summary and Conclusions

Active surge control experiments have been performed on a turboshaft engine gas producer. By sensing static pressure in the engine inlet and compressor diffuser, and injecting air into the diffuser, systematic identification and control studies were conducted, and the following conclusions were drawn:

- (i) Surge without control results from instability of a lumped parameter type oscillation mode.
- (ii) As originally conjectured by Epstein et al. [22], by feeding back small amplitude perturbations, the mode associated with surge can be stabilized, allowing operation in previously unstable and inaccessible regimes. A useful range extension results.
- (iii) Acoustic modes also exist in the engine's unsteady behavior. A model incorporating one-dimensional duct acoustics gives good agreement with measured resonance frequencies.
- (iv) Acoustic modes in the engine can be excited by feedback. Therefore control laws designed to stabilize surge must account for the existence of these modes. A systematic procedure for such control law design has been demonstrated.

At the 95 percent N1 corrected speed line, the mass flow range from choke to surge was increased by 11 percent with active control. Furthermore, the test stand thrust of the gas producer increased by 3.7 percent with control. The mass flow range and thrust with and without control were compared at the same nominal injection level of 3.8 percent corrected engine mass flow.

Although these results represent a full-scale validation of the concept of surge stabilization, much work remains. No attempt has been made to assess the trade-offs that exist associated with the actuation; only range extension with respect to a baseline is given. The actuator configuration was chosen mainly for its ease of implementation; clearly the pressure drop associated with injection into the diffuser must be weighed against the benefits of range extension, to determine the impact on overall engine performance. This calculation is somewhat premature for this experiment; more realistic actuators (which either bleed or recirculate engine mass flow) should be tested before benefits are analyzed. Finally, one must devise stabilization methods that actuate only when necessary (see Freeman et al. [6] for a discussion). We have successfully tested such methods, but thorough quantification of the behavior of these control laws is still needed. Based on these comments, we reiterate that the main goal here has been to validate our understanding of surge inception, and to illustrate a systematic procedure for applying this understanding. By stabilizing the dynamics presumed to lead to surge, we are able to delay surge onset; thus our dynamic model is corroborated.

Acknowledgments

This research was funded by AFOSR Grant #F49620-95-1-0409, Marc Jacobs, technical monitor, by AFOSR Grant #F49620-96-1-0407, Mark Glauser, technical monitor, and by the Allied Signal Engine Company. Moog provided the high-speed control actuator and Kulite Semiconductor provided high-frequency-response pressure transducers. Harald Weigl provided the initial H^∞ design codes. Jin-Woo Bae, Jim Lentendre, and Bill Ames assisted in running the tests, and Brian Corn aided in the engine set up and operation. Brandon Gordon assisted in engine modeling. Lt. Nelson was partially supported by AFIT, and by the Air Force Research Laboratory (AFRL/VAAD).

Appendix A

Surge Model Development. In this appendix, a classic lumped-parameter surge model is first reviewed. Although the essence of presurge oscillations is captured by this model, the existence of acoustic modes is not predicted by the model. Therefore, the model is modified to include duct acoustics. Both models are compared to experimental results in Section II.

Lumped-Parameter Surge Model. To obtain a simple model that captures the physics governing surge, Greitzer [8] divided the compression system into four lumped components (see Fig. 11): (1) a duct to account for all the kinetic energy of the unsteady flow in the system, (2) a plenum to represent the potential energy of expansion and compression of fluid, (3) a throttle, which dissipates energy, and (4) the compressor, which can either dissipate energy or add energy to oscillations, depending on the slope of the compressor map. Using mass and momentum conservation, and assuming isentropic compression in the plenum, the following second-order model can be developed:

$$\dot{\phi} = \frac{1}{\ell} (\Psi_c(\phi) - \psi)$$

$$\dot{\psi} = \frac{1}{B^2 \ell} \left(\frac{\alpha_{pi}}{\rho^*} \phi - \alpha_{pe} \Phi_t(\psi) \right)$$

where $\psi = P/\rho U_{ref}^2$ is the nondimensional pressure in the plenum, $\phi = u/U_{ref}$ is the flow velocity in the duct, $\Psi_c(\phi)$ is the compressor total-to-static pressure rise map, and $\Phi_t(\psi)$ is the inverse of the throttle map, i.e., $\Phi_t = \sqrt{2\psi/K_t}$, K_t being the throttle coefficient. The rest of the parameters depend on the systems dimensions. B is Greitzer's nondimensional parameter governing surge behavior, $B = U_{ref}/a_p \sqrt{V/LA_{ref}}$, where a_p is the speed of sound in the plenum and U_{ref} , A_{ref} , V , and L are a reference velocity, a reference area, the plenum volume, and the duct length respectively. Finally, α_{pi} and α_{pe} are the plenum inlet and exit areas nondimensionalized by A_{ref} , and ρ^* is the plenum fluid density nondimensionalized by some reference density. This model differs from Greitzer's formulation only in the details of the nondimensionalization. For instance, here we have taken L_{ref}/U_{ref} as the reference time, instead of one over the Helmholtz frequency, to simplify the acoustic expressions below.

We can use this model to understand the behavior of compressors as they approach and enter surge, the influence of the compliance-to-inertia ratio B [8], or (if additional dynamics are added, as in Moore and Greitzer, [15]), to elucidate the interaction between rotating stall and surge. Thus as a basic model, this representation is valuable. In the context of the current research, we are interested in understanding the physics that govern the frequency of the presurge oscillations in engines, and in understanding the source of the second peak in the spectra and frequency responses. This second eigenvalue was conjectured to arise due to longitudinal variations in velocity and pressure in the ductwork of the engine. To check this conjecture, an acoustically coupled model is developed in the next section.

Modified Surge Model: Acoustic Ducts. To introduce acoustics into the surge model, we use a transmission matrix approach [16] applied to the system representation shown in Fig. 12. Each of the seven segments in this model is represented by a 2×2 transmission matrix. These matrices relate the Laplace transforms of the nondimensional perturbation pressure and axial velocity at the inlet to those at the exit [17]. The general form for the transmission properties of a duct is:

$$\begin{bmatrix} \psi_{out}(s) \\ \phi_{out}(s) \end{bmatrix} = \begin{bmatrix} T_{11}(s) & T_{12}(s) \\ T_{21}(s) & T_{22}(s) \end{bmatrix} \begin{bmatrix} \psi_{in}(s) \\ \phi_{in}(s) \end{bmatrix},$$

where perturbation pressure and velocity are nondimensionalized as in the previous surge model. By stacking transmission matrices from inlet to exit and applying the boundary conditions, an eigenvalue problem can be derived. Alternatively, one can develop an input-output relationship between any two variables. We choose the latter approach, using velocity into the injector as the input, and inlet static pressure at station 2 as the output.

The model in Fig. 12 consists of three acoustic ducts, one lumped duct, a compressor, and two lumped segments representing expansion and contraction. One can derive a transmission matrix for each segment using continuity, momentum and, for the acoustic ducts, Euler's equation and perfect gas relations. The results are summarized below.

Acoustic Duct:

$$T_{Ac} = \begin{bmatrix} \cos(\ell\omega/c^*) & -i \cdot c^* \cdot \rho^* \sin(\ell\omega/c^*) \\ -\frac{i}{c^* \cdot \rho^*} \sin(\ell\omega/c^*) & \cos(\ell\omega/c^*) \end{bmatrix},$$

$$\ell = (\text{duct length})/L_{ref},$$

$$c^* = (\text{duct sound speed})/U_{ref},$$

$$\rho^* = (\text{duct fluid density})/\rho_{ref}.$$

Lumped Duct:

$$T_{Duct} = \begin{bmatrix} 1 & -\rho^* i \omega \\ 0 & 1 \end{bmatrix}$$

Compressor and Throttle:

$$T_C = \begin{bmatrix} 1 & \rho_{in}^* m_c \\ 0 & \rho_{in}/\rho_{out} \end{bmatrix}, \quad T_{Th} = \begin{bmatrix} 1 & \rho_{in}^* m_t \\ 0 & \rho_{in}/\rho_{out} \end{bmatrix},$$

$$\text{where } m_i = \frac{\partial \Psi_i}{\partial \phi}$$

Sudden Expansion:

$$T_{Ex} = \begin{bmatrix} 1 & 2\rho^* \Phi_o(1 - \alpha_r) \\ 0 & \alpha_r \end{bmatrix}$$

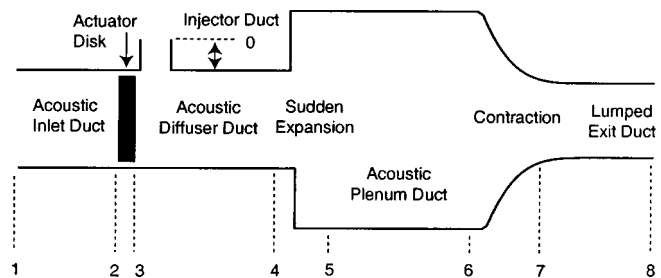


Fig. 12 Acoustic model of LTS-101 with acoustic ducts and plenum

Smooth Contraction:

$$T_{\text{Con}} = \begin{bmatrix} 1 & 2\rho^* \Phi_o (1 - \alpha_r^2) \\ 0 & \alpha_r \end{bmatrix},$$

where in the last two equations α_r is the ratio of inlet to outlet area, and Φ_o is the mean flow through the component.

To derive a transfer function for the system, we start by writing continuity at station 4 in terms of pressure and velocity:

$$\begin{bmatrix} \psi_4 \\ \phi_4 \end{bmatrix} = \begin{bmatrix} \psi_3 \\ \phi_3 \end{bmatrix} + \begin{bmatrix} 0 \\ \alpha_o \end{bmatrix} \phi_0$$

where ϕ_0 is the velocity at the exit of the injector. Since the injector valve is choked, station 0 is assumed to have infinite impedance; thus, this boundary is assumed to be a pure velocity source independent of the pressure at station 0. Next, we substitute this equation into the transmission matrix relation between stations 3 and 8, writing the conditions at station 3 in terms of those at station 1 using the upstream transmission matrices:

$$\begin{bmatrix} \psi_8 \\ \phi_8 \end{bmatrix} = T_{\text{Duct}}^{78} \cdot T_{\text{Con}}^{67} \cdot T_{\text{Ac}}^{56} \cdot T_{\text{EX}}^{45} \cdot T_{\text{Ac}}^{34} \left(T_C^{23} \cdot T_{\text{Ac}}^{12} \begin{bmatrix} \psi_1 \\ \phi_1 \end{bmatrix} + \begin{bmatrix} 0 \\ \alpha_o \end{bmatrix} \phi_0 \right)$$

Each matrix in this equation is evaluated as a function of frequency ω , the matrices are multiplied out, and variables are defined for the results as follows:

$$\begin{bmatrix} \psi_8 \\ \phi_8 \end{bmatrix} = \begin{bmatrix} T_1(i\omega) & T_2(i\omega) \\ T_3(i\omega) & T_4(i\omega) \end{bmatrix} \cdot \begin{bmatrix} \psi_1 \\ \phi_1 \end{bmatrix} + \begin{bmatrix} U_1(i\omega) \\ U_2(i\omega) \end{bmatrix} \phi_0.$$

The boundary conditions are then applied. The inlet and exit are assumed to be "pressure release" boundaries to atmosphere (i.e., $\psi_1 = \psi_8 = 0$). Rearranging yields the relation

$$\phi_1(i\omega) = - \frac{U_1(i\omega)}{T_2(i\omega)} \phi_0(i\omega).$$

Finally, we obtain the transfer function from the injector to the static pressure measurement station (2) by applying the appropriate transmission matrix:

$$\begin{bmatrix} \psi_2 \\ \phi_2 \end{bmatrix} = T_{\text{Ac}}^{12} \begin{bmatrix} \psi_1 \\ \phi_1 \end{bmatrix} = \begin{bmatrix} V_1(\omega) & V_2(\omega) \\ V_3(\omega) & V_4(\omega) \end{bmatrix} \cdot \begin{bmatrix} 0 \\ \phi_1 \end{bmatrix},$$

where the boundary condition at station 1 has already been introduced. The desired transfer function is thus obtained as:

$$\frac{\psi_2}{\phi_0}(i\omega) = - V_2(i\omega) \frac{U_1(i\omega)}{T_2(i\omega)}.$$

Our modified version of the surge model appears to be much different than the basic surge model; but if the acoustic ducts are replaced by lumped ducts and plenums, the model is essentially the same. Acoustics introduces transcendental relationships in the transfer function, making eigenvalue computation difficult. Rather than solve for eigenvalues directly, fits to the derived transfer function are performed to deduce the eigenvalue locations.

Appendix B

Control Law Design. Modern robust control design procedures use models that take into account modeling and/or system identification errors. Consider a linear system, with multiple inputs and multiple outputs, of the form:

$$\begin{aligned} \dot{x} &= A_{\text{true}}x + B_{\text{true}}u \\ y &= C_{\text{true}}x + D_{\text{true}}u \end{aligned}$$

The subscript "true" indicates that this dynamic system is the actual system to be controlled. We can develop a model for this system using either theoretical or experimental methods, but neither will yield an exact replica of the true system. To represent the inaccuracy of our model, we develop a "family" of models that is

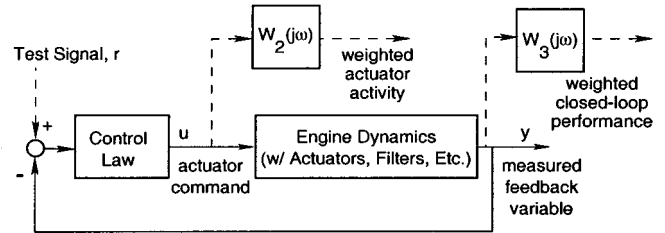


Fig. 13 Block diagram of control system used for specification of design constraints

sufficiently general to include the true system as one of its members. We have found that for rotating stall and surge problems, a useful family of models is of the following form [18,14]:

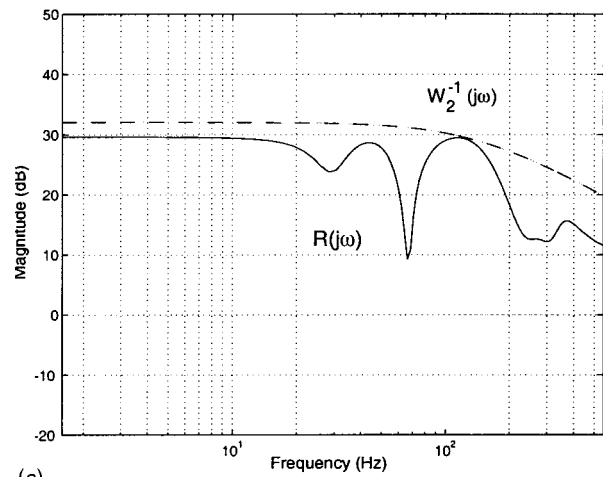
$$\dot{x} = T^{-1} \Lambda T x + \hat{B} u$$

$$y = \hat{C} x + \hat{D} u,$$

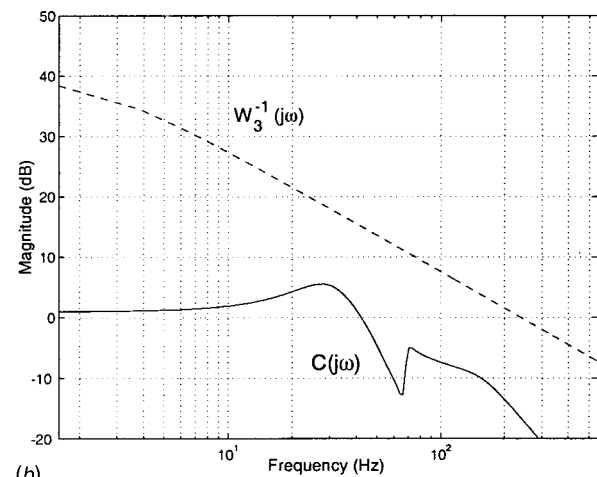
where

$$\Lambda = \text{diag}(\lambda_1, \lambda_2, \dots, \lambda_N),$$

$$\lambda_n = \lambda_{n_o} + \Delta \omega_n e^{i\phi}, \quad 0 < \phi < 2\pi$$



(a)



(b)

Fig. 14 (a) Closed-loop transfer function from r to u (solid); shaped by W_2^{-1} (dashed); (b) closed-loop transfer function from r to y (solid); shaped by W_3^{-1} (dashed)

and

$$\lambda_{n_o} = \text{eigenvalues of } \hat{A}.$$

In this family of models, most of the structure of the input-output system is assumed to be well known (that is, $\hat{B} \cong B_{\text{true}}$, $\hat{C} \cong C_{\text{true}}$, and $\hat{D} \cong D_{\text{true}}$), but each eigenvalue is allowed to exist anywhere inside a disk of radius $\Delta\omega_n$, centered at the nominal location λ_{n_o} .

The control law design requirements are completed by imposing the following two requirements:

$$\sigma_{\max} \left(\frac{u}{r}(j\omega) \right) < |W_2^{-1}(j\omega)|$$

$$\sigma_{\max} \left(\frac{y}{r}(j\omega) \right) < |W_3^{-1}(j\omega)|$$

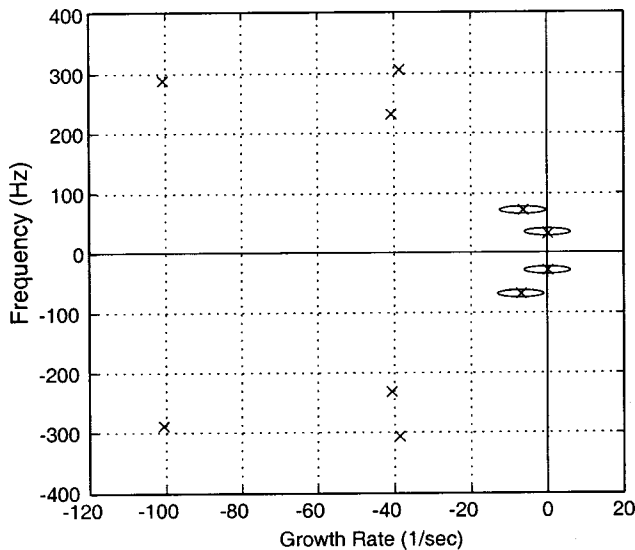


Fig. 15 Design plant model showing eigenvalue perturbation circles; note that surge eigenvalues are neutrally stable

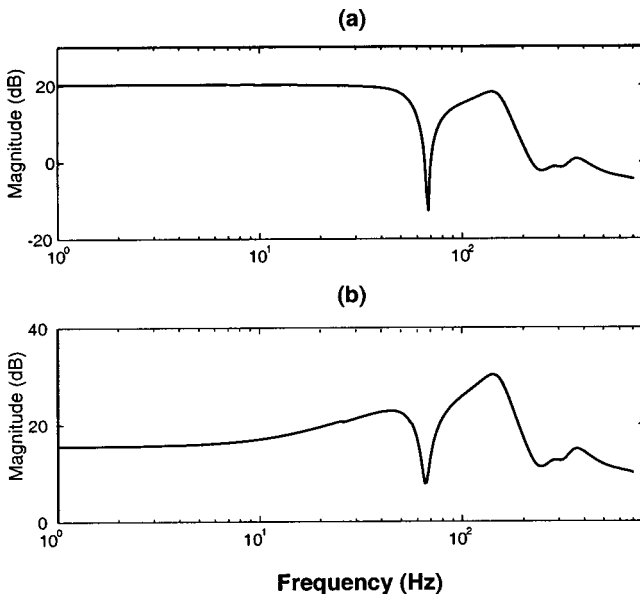


Fig. 16 Compensator transfer functions: (a) compressor inlet static pressure to valve command (one of two similar transfer functions); (b) diffuser throat static pressure to valve command

where u , r , and y are defined above and shown in Fig. 13, and σ_{\max} denotes the maximum value of the multivariable transfer function. The magnitudes of the diagonal transfer functions $W_2^{-1}(s)$ and $W_3^{-1}(s)$ are plotted in Fig. 14. These are standard robust design constraints that are adjusted to limit both the controller bandwidth (W_2^{-1}) and the closed-loop frequency response magnitude (W_3^{-1}); see Kwaakernaak [19] for more details. The control law design procedure creates a compensator that is guaranteed to stabilize any linear system that is a member of the family defined above, and to meet the above robustness constraints.

Design Results. The identification results in Section II are used as the nominal model for control law design, with one modification. To create a stabilizing controller, the eigenvalue associated with surge is moved (using the diagonalized formulation in the previous section) to the neutral stability axis. Then the design uncertainty of the eigenvalues is modeled, as shown in Fig. 15. Note that the identified eigenvalue location for the surge mode is a member of the family defined by this figure; thus the system is required to remain stable for the identified system as well as the unstable one beyond the surge line. Note also that the uncertainty disks are stable for all modes except the surge mode. In other words, for every model in this family, only the surge mode can be unstable. This reflects our conjecture that acoustic modes remain stable over the operating range of interest.

Recall that the sensors chosen for control are one diffuser throat and two inlet sensors. These choices are the result of an iterative process of control law design, experimental testing, data analysis, and redesign. The automated nature of the control law design procedure makes this iteration possible. In all, 15 compensators were created and available for testing.

The compensator that solves the control design problem defined here consists of three scalar transfer functions, one from each sensor to the actuator. Two of these three transfer functions are shown in Fig. 16 (since two of the sensors chosen are in the same place axially, two of the compensator transfer functions are almost identical). Note that both transfer functions contain a zero at ~ 70 Hz, to avoid destabilization of the 68 Hz acoustic mode. The design procedure has optimally placed this notch to avoid destabilization even if the acoustic mode should be different in frequency or damping than the identified model states. Note also that the throat tap transfer function has a 20 dB/decade upward slope in the 30 Hz region (surge frequency). Apparently the design procedure has automatically chosen to introduce Proportional-Derivative (PD) type action into the compensation, consistent with a lead-lag compensator design.

References

- [1] Fink, D. A., 1988, "Surge Dynamics and Unsteady Flow Phenomena in Centrifugal Compressors," MIT Gas Turbine Laboratory Report No. 193.
- [2] Huang, X. Y., and Ffowes Williams, J. E., 1989, "Active Stabilization of Compressor Surge," *J. Fluid Mech.*, **204**, pp. 245–262.
- [3] Pinsley, J. E., Guenette, G. R., Greitzer, E. M., and Epstein, A. H., 1991, "Dynamic Control of Centrifugal Compressor Surge Using Tailored Structures," *ASME J. Turbomach.*, **113**, pp. 723–732.
- [4] Gysling, D. L., Dugundji, J., Greitzer, E. M., and Epstein, A. H., 1991, "Dynamic Control of Centrifugal Compressor Surge Using Tailored Structures," *ASME J. Turbomach.*, **113**, pp. 710–722.
- [5] Simon, J. S., Valavani, L., Epstein, A. H., and Greitzer, E. M., 1993, "Evaluation of Approaches to Active Compressor Surge Stabilization," *ASME J. Turbomach.*, **115**, pp. 57–67.
- [6] Freeman, C., Wilson, A. G., Day, I. J., and Swinbanks, M. A., 1998, "Experiments in Active Control of Stall on an Aeroengine Gas Turbine," *ASME J. Turbomach.*, **120**, pp. 637–647.
- [7] Eveker, K., Nett, C. N., Sharma, O. P., and Gysling, D. L., 1998, "Integrated Control of Rotating Stall and Surge in High-Speed Multistage Compression Systems," *ASME J. Turbomach.*, **120**, pp. 440–445.
- [8] Greitzer, E. M., 1976, "Surge and Rotating Stall in Axial Flow Compressors, Part I: Theoretical Compression System Model, and Part II: Experimental Results and Comparison with Theory," *ASME J. Eng. Power*, **98**, pp. 190–217.
- [9] Borrer, S. L., 1994, "Natural and Forced Response Measurements of Hydrodynamic Stability in an Aircraft Gas Turbine Engine," M. S. thesis, Dept. of Aeronautics and Astronautics, Massachusetts Institute of Technology.

- [10] Corn, B. A., 1998, "Surge Dynamics of a Helicopter Engine Gas Generator," M.S. thesis, Dept. of Aeronautics and Astronautics, Massachusetts Institute of Technology.
- [11] Corn, B. A., 1998, "LTS-101 Gas Generator Data Archive," Run 80, 6 Aug., created by Eric B. Nelson.
- [12] Jacques, R., 1994, "FORSE Transfer Function ID," Space Engineering Research Center, Massachusetts Institute of Technology.
- [13] Weigl, H. J., Paduano, J. D., Frechette, L. G., Epstein, A. H., Greitzer, E. M., Bright, M. M., and Strazisar, A. J., 1998, "Active Stabilization of Rotating Stall and Surge in Transonic Single Axial Compressor," *ASME J. Turbomach.*, **120**, pp. 625–636.
- [14] Weigl, H. J., and Paduano, J. D., 1997, "Application of H-infinity Control With Eigenvalue Perturbations to Stabilize a Transonic Compressor," presented at the IEEE International Conference on Control Applications, Hartford, Oct. 5–7.
- [15] Moore, F. K., and Greitzer, E. M., 1986, "A Theory of Post-Stall Transients in Axial Compression Systems, Part I—Development of Equations, and Part II—Application," *ASME J. Eng. Gas Turbines Power*, **108**, pp. 68–97.
- [16] Nelson, E. B., 1998, "An Experimental Study of Surge Control in the Allied Signal LTS-101 Helicopter Turboshaft Engine," M.S. thesis, Department of Aeronautics and Astronautics, Massachusetts Institute of Technology.
- [17] Takahashi, Y., Rabins, M. J., and Auslander, D. M., 1972, *Control of Dynamic Systems*, Addison-Wesley.
- [18] Smith, R. S., Chu, C. C., and Fanson, J. L., 1994, "The Design of H^∞ Controllers for an Experimental Non-collected Flexible Structure Problem," *IEEE Trans. Control Syst. Technol.*, **2**, No. 2.
- [19] Kwakernaak, H., 1993, "Robust Control and H-Infinity Optimization: Tutorial Paper," *Automatica*, **29**, No. 2, pp. 255–273.
- [20] Bae, J. W., 1998, "An Experimental Study of Surge Control in a Helicopter Gas Turbine Engine," M.S. thesis, Dept. of Aeronautics and Astronautics, Massachusetts Institute of Technology.
- [21] Berndt, R. G., 1995, "Actuation for Rotating Stall Control of High Speed Axial Compressors," M.S. thesis, Dept. of Aeronautics and Astronautics, Massachusetts Institute of Technology.
- [22] Epstein, A. H., Ffowcs-Williams, J. E., and Greitzer, E. M., 1989, "Active Suppression of Aerodynamic Instabilities in Turbomachines," *J. Propulsion*, **5**, No. 2, pp. 204–211.
- [23] Ffowcs Williams, J. E., Harper, M. F. L., and Allwright, D. J., 1993, "Active Stabilization of Compressor Instability and Surge in a Working Engine," *ASME J. Turbomach.*, **115**, pp. 68–75.
- [24] McNulty, G. S., 1993, "A Study of Dynamic Compressor Surge Control Strategies for a Gas Turbine Engine," M.S. thesis, Dept. of Aeronautics and Astronautics, Mass. Institute of Technology.

One-Dimensional Performance Prediction of Subsonic Vaned Diffusers

Beat Ribi
Peter Dalbert

Sulzer Turbo Ltd.,
Zurich, Switzerland

A simple one-dimensional theory to predict the performance of a diffuser using as few empirical factors as possible is presented. The prediction method uses two empirical functions to assess both the pressure recovery and the losses. The functions have been calibrated from experimental data from the company's standard diffusers. The method is, however, adaptable for any type of subsonic vaned diffusers, provided that the empirical functions can be calibrated from measurements. The pressure rise in the diffuser is calculated from the continuity equation, taking into account the blockage, while the losses are determined by means of displacement and momentum thickness. These values are calculated at design point from an integral boundary layer calculation. To take into account the influence of flow separation at off-design, the calculated displacement and momentum thickness are increased according to empirical functions. When designing a new impeller, the method provides a simple way to evaluate the diffuser, resulting in the best combination in terms of efficiency and range. It further provides a simple means of estimating the change to be expected in a known stage performance characteristic due to a modification of the diffuser geometry. [S0889-504X(00)01703-7]

Introduction

Despite the progress in accuracy and speed of CFD codes, there are still large areas where simple one-dimensional prediction methods are indispensable. The need for such prediction tools is stressed by recent publications (e.g., [1,2]).

A compressor manufacturer needs a one-dimensional calculation method for the performance prediction of diffusers of standardized geometry for the following reasons:

First, when designing a new impeller, a fast tool is needed to evaluate the diffuser that results in the best stage performance. This includes

- the matching of impeller and diffuser, and
- the limit of dynamic stability which can be expected.

However, finding the best matching with respect to efficiency is a task that only can be achieved if the losses are accurately predicted.

As shown in this paper, it is possible to design a stage that is dynamically stable at a given minimum flow rate, provided that the slope of the impeller pressure rise as well as the characteristics with their slopes of dynamic head and diffuser pressure recovery are known. According to this, the most suitable diffuser for a new impeller (whose characteristics have already been predicted by means of CFD calculation) can be evaluated by checking several diffusers based on the present one-dimensional calculation.

Second, such a one-dimensional calculation provides a simple means of estimating the change to be expected in a known stage performance characteristic, due to a modification of the diffuser geometry. This is relevant in extending a database of measured stage characteristics to include diffuser configurations that have not been tested. Possible changes may refer to

- the diffuser vane angle α_{3D} ,
- the ratio of diffuser height to impeller exit height b_{2D}/b_2 ,

- the number of diffuser vanes z'^1 and
- the radial extent of the vaned diffuser.²

Basic Ideas

The goal is, therefore, to provide a tool that is able to predict the characteristic of any diffuser geometry by means of a simple straightforward one-dimensional theory using as few empirical factors as possible. In the literature, an almost uncountable number of different one-dimensional calculations can be found. All of them present several factors or empirical correlations mostly gained from measurements in order to match the pressure recovery and the efficiency correctly. Such empirical methods incorporate, e.g., a pressure recovery expressed as a function of inlet blockage (see [3]), or losses related to incidence or wall friction (see [4]). These predictions generally only apply to the family of diffusers from which the correlations are derived. The prediction method shown here is not any better in this respect. It also includes empirical functions trimmed to match the company's standard diffusers. However, two such functions suffice to predict both the pressure recovery and the losses. In addition, these functions can be easily adapted to match alternative diffuser configurations, particularly because one function is assumed to be applicable to a broader range of diffuser geometries.

The basic ideas are as follows:

- At design point, the thermodynamic state and velocity in several calculation stations along the diffuser are calculated assuming an inviscid core flow and a velocity profile in the boundary layer. The required displacement thickness δ^* and momentum thickness θ result from an integral boundary layer calculation as proposed by Stratford/Beavers [5].³
- At off-design the calculated displacement thickness is increased to take into account a further restriction of the flow area due to separated flow, resulting in δ_{sep}^* . The increase in displace-

¹Provided that the change in solidity is within certain limits.

²Provided that there are correlations to assess the impact on downstream components such as scrolls or return channels.

³According to Herbert [6], the idea of using a theoretical boundary layer method for assessing the pressure recovery in a diffuser channel was already proposed by Pinot [7]. Unfortunately this work is not published in the open literature.

Contributed by the International Gas Turbine Institute and presented at the 44th International Gas Turbine and Aeroengine Congress and Exhibition, Indianapolis, Indiana, June 7–10, 1999. Manuscript received by the International Gas Turbine Institute February 1999. Paper No. 99-GT-433. Review Chair: D. C. Wisler.

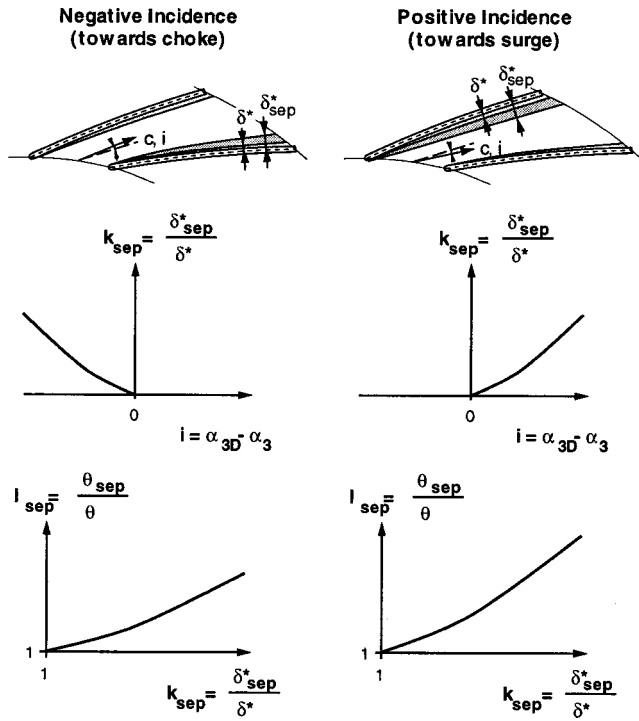


Fig. 1 Increased displacement and momentum thickness due to separated flow

ment thickness, $k_{sep} \delta^*$, is a function of incidence and local Mach number. The function contains experimental constants that apply only to the current standardized diffusers. Knowing the factor by which the displacement thickness has been increased, a similar but more moderate increase, $l_{sep} \theta$, is provided for the increase of the momentum thickness θ_{sep} . This function accounts for the reduction of momentum within the boundary layer due to flow separation.

A sketch of the situation at off-design (negative as well as positive incidence), showing that the empirical factors increase the calculated displacement and momentum thickness, is given in Fig. 1.

By assuming an inviscid core flow, the prediction does not take into account any other dissipation processes, such as shock losses or dissipation due to secondary flows other than the region of separated flow.

Detailed Description of the Calculation Procedure

Calculation Stations in the Vaned Diffuser. The calculation stations used in this procedure are marked in Fig. 2, where a typical vaned diffuser of the present diffuser family is shown. While the vanes themselves remain unchanged with respect to position and shape of the leading edge, curvature and thickness,

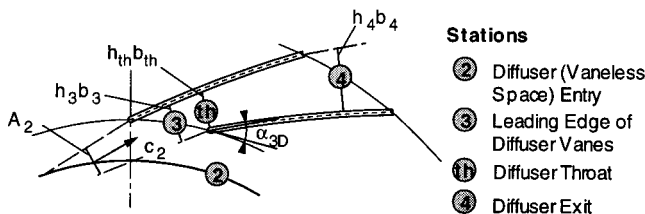


Fig. 2 Calculation stations of the vaned standardized diffuser

all the following may be varied within certain limits: vane angle α_{3D} , diffuser height b_{2D} , radial extent r_4/r_2 and number of vanes z' .

Sections Between Calculation Stations

Impeller Exit to Diffuser Vane Leading Edge. Unlike other one-dimensional predictions reported in literature (see [4,6]) the vaneless space is not treated as a purely vaneless diffuser calculation.⁴ The section from impeller exit (Station 2) to diffuser vane leading edge (Station 3) is rather considered as a converging channel (towards choke) or diverging channel (towards surge) as, for example, depicted in Japikse [8]. Its inlet area, A_2 , is determined by the diffuser inlet flow angle α_2 and the circumferential extent of a diffuser segment:

$$A_2 = 2 \pi r_2 b_2 \sin(\alpha_2) \frac{1}{z'} \quad (1)$$

The equivalent exit area A_3 is assumed to be perpendicular to α_3 . According to Fig. 3, the flow-through area A_3 then is given as follows:

(a) for values of α_3 larger than the vane angle α_{3D} :

$$A_3 = b_3 h_3 = b_3 \left[2 \pi r_3 \sin(\alpha_{3D}) \frac{1}{z'} + \frac{2 \pi r_3 \sin(\alpha_{3D}) \frac{1}{z'} - d_D}{\cos(\alpha_3 - \alpha_{3D})} \right] \quad (2a)$$

and (b) for values of α_3 smaller than α_{3D} :

$$A_3 = b_3 h_3 = b_3 \left[\begin{array}{l} 2 \pi r_3 \sin(\alpha_3) \frac{1}{z'} \\ + 2 \pi r_3 \cos(\alpha_3) \frac{1}{z'} \tan(\alpha_{3D} - \alpha_3) \\ - \frac{d_D/2}{\cos(\alpha_{3D} - \alpha_3)} \end{array} \right] \quad (2b)$$

It is further assumed that the boundary layer thickness on the diffuser end walls (front and rear) is zero at the inlet and grows up to Station 3 according to the relations given by Stratford and Beavers [5]. The angle, α_3 , at Station 3 can then be expressed by a function of the known inlet angle, α_2 , and the iteratively calculated values for the density, ρ_3 , and the displacement thickness at the two end walls, δ_{2-3}^* , (assumed to be equal for both walls):⁵

$$\alpha_3 = \tan \left(\arctan \alpha_2 \frac{b_2 \rho_2}{(b_3 - 2 \delta_{2-3}^*) \rho_3} \right) \quad (3)$$

Diffuser Vane Leading Edge to Diffuser Throat. The diffuser throat is given by the smallest width h_{th} between the adjacent

⁴That is, by stepwise determination of the state at any radius from impeller exit to the leading edge of the diffuser vanes.

⁵Note: In the analysis presented here, a simplification is made when the influence of compressibility, blockage and losses is taken into account to calculate the velocity and the thermodynamic state only, but not to a readjust α_3 .

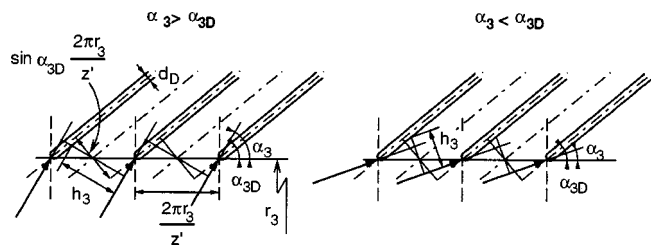


Fig. 3 Geometric considerations to determine the through-flow area A_3

diffuser vanes. From the diffuser leading edge to the throat, an additional boundary layer is developed on the suction side of the vane. The resulting displacement and momentum thickness at the throat (Station *th*) are considered to be increased because of flow separation at flow angles with a positive incidence (toward surge). The additional thicknesses due to the separation are treated in one of the following sections.

Diffuser Throat to the Diffuser Trailing Edge. Since all through-flow areas are perpendicular to the mainstream direction, Station 4 is actually a plane at the radius of the trailing edge r_4 perpendicular to the centerline of the channel.⁶ The area is given by the diffuser outlet width h_4 and the height b_4 .

From the diffuser throat to the trailing edge, there are four walls along which a boundary layer develops: the two end walls and the walls on the pressure and suction side of the vane. Although the suction side does not extend to this plane (see Fig. 2) the length from the throat to 4 is used to calculate the boundary layer for both pressure and suction side. Separation can occur on one of the two sides: on the pressure side for negative incidence and on the suction side for positive incidence. An increase of the displacement and momentum thickness is foreseen for both cases.

Inclusion of Zones of Separated Flow. There are several methods described in the literature to calculate the boundary layer in an integral form. If the stepwise development of the boundary layer around the curved surface is known, it might even be possible to predict the location of separation. There is, however, no simple way to calculate the state and growth of a zone of separated flow. Instead of using a more sophisticated calculation, it is assumed that the extent of the separated flow can be indicated for a given profile by first calculating the displacement and momentum thickness without separation and then by increasing these values by empirical factors. The required factors are, therefore, defined as follows:

$$k_{\text{sep}} = \frac{\delta_{\text{sep}}^*}{\delta^*} \quad (4)$$

$$l_{\text{sep}} = \frac{\theta_{\text{sep}}}{\theta} \quad (5)$$

It is obvious that k_{sep} and l_{sep} are arbitrary and have to be evaluated for each given profile (and may even need to be changed for a considerably different solidity).

Function Describing the Increase of Displacement Thickness due to Separation. The empirical factor k_{sep} is based mainly on engineering judgment and simple axial compressor performance correlation methods. Hence, it is assumed to be a function of incidence i and local Mach number M .

From the available data that have been collected during the last two decades, the characteristic for the pressure recovery is known for a variety of diffusers combined with several impellers. After some suitable geometries are selected from this bulk of measured stages, the pressure recovery is calculated for each measurement point using the dynamic head delivered by the impeller as input. In the next step, the factor k_{sep} to increase the displacement thickness as a function of the two parameters i and M has been successively changed until the best match between calculated and measured pressure recovery is found for all investigated configurations. The geometries selected for trimming k_{sep} cover the whole range of possible geometric variations of the company's standardized diffusers. Hence, the selection comprises eight sufficiently different impeller/diffuser combinations. The diffuser vane angle, α_{3D} , was set to 14, 18, or 26 deg, the relative height, b_{2D}/D_2 , varies from 2 to 8 percent, and the radial extent of the diffuser, r_4/r_2 , from 1.33 to 1.50. All diffusers have 24 vanes. Due to

⁶Later, when comparing the one-dimensional-calculation with measurements, the radius where the pressure taps are located is taken as r_4 .

Table 1 Stage configurations selected to determine the separation function k_{sep} (the values refer to the stage Mach numbers Mu_2 for which the function was adjusted)

| | | | Diffuser | | | |
|---------------|-------|--------------|---------------|---------------|---------------|---------------|
| α_{3D} | | | 14° | 22° | 22° | 26° |
| r_4/r_2 | | | 1.33 | 1.33 | 1.50 | 1.50 |
| Impeller | | | | | | |
| β_{2S} | z'' | b_{2D}/D_2 | | | | |
| 35° | 14 | 2.4% | 0.5, 0.8, 1.0 | | | |
| 35° | 14 | 4.8% | 0.5, 0.8, 1.0 | | | |
| 48° | 16 | 2.0% | | 0.4, 0.8, 1.0 | | |
| 48° | 16 | 4.0% | | 0.4, 0.8, 1.0 | | |
| 42° | 9 + 9 | 3.1% | | | | 0.5, 0.8, 1.0 |
| 42° | 9 + 9 | 5.6% | | | | 0.5, 0.8, 1.0 |
| 48° | 16 | 6.0% | | | 0.5, 0.8, 1.0 | |
| 48° | 16 | 8.0% | | | 0.5, 0.8, 1.0 | |

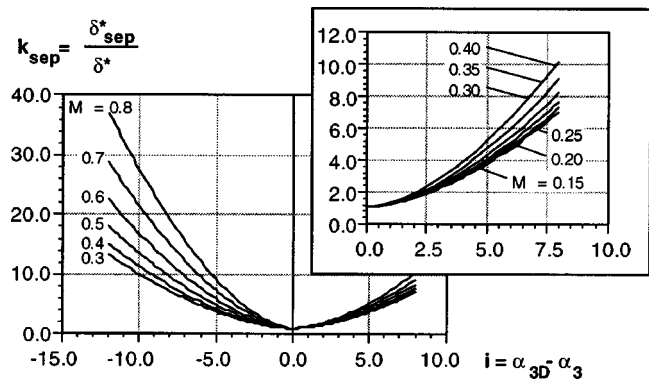


Fig. 4 Factor k_{sep} to increase the calculated displacement thickness in order to account for separation

different blade exit angles β_{2S} and number of blades z'' (with and without splitters) of the selected impellers, a considerable difference in the velocity profile at diffuser inlet is guaranteed. Table 1 gives an overview of the selected configurations and the stage Mach numbers Mu_2 for which the k_{sep} has been adjusted. The result, i.e., the function yielding the best agreement between measurement and calculation for these configurations, is shown in Fig. 4.

This fit was achieved by a power function for both the angle of incidence i and the local Mach number M and is given by the following equations:

(a) negative incidence ($i < 0$):

$$k_{\text{sep}} = (i + 0.16i^2)(1.80M^3 + 1) + 1 \quad (6a)$$

(b) positive incidence ($i > 0$):

$$k_{\text{sep}} = (i + 0.16i^{1.4})(8.00M^3 + 1) + 1 \quad (6b)$$

Function Describing the Increase of Momentum Thickness Due to Separation. Once the flow has separated, the deficiency of momentum within the boundary layer has to be taken into account. This is done by introducing an additional factor l_{sep} by which the calculated momentum thickness for attached flow is increased. It is, however, assumed that the degree of separation is already captured by the increase of displacement thickness, i.e., by k_{sep} . The analogue factor l_{sep} is, therefore, only a function of k_{sep} ; even so, it may be different for positive and negative incidence.

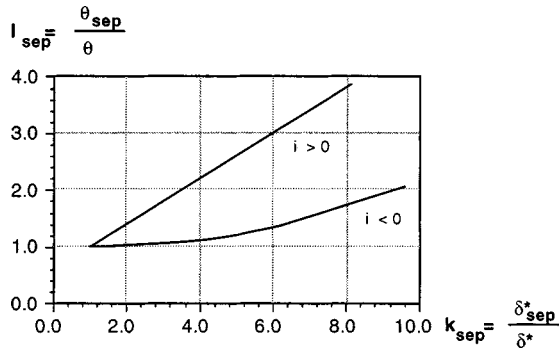


Fig. 5 Factor l_{sep} to increase the calculated momentum thickness in order to account for separation

It is worth noting that expressing θ_{sep}/θ as a factor of δ_{sep}^*/δ^* is the same as providing a factor for increasing the form factor H_{12} , because with $H_{12} \equiv \delta^*/\theta$ and Eqs. (4) and (5), the following relation is found:

$$H_{12_{sep}} \equiv \frac{\delta_{sep}^*}{\theta_{sep}} = \frac{k_{sep} \delta^*}{l_{sep} \theta} = \frac{k_{sep}}{l_{sep}} H_{12}$$

Since k_{sep} is always larger than l_{sep} , an increase of the form factor for separated flow is guaranteed.

Assuming that the velocity profiles along a wall with a given adverse pressure gradient evolve in a similar manner, the function describing l_{sep} is of more general validity. As a result, to find a suitable relation for l_{sep} only two of the above-mentioned configurations have been selected (one with impeller with $\beta_{2S} = 35$ deg and 14 deg diffuser and one with impeller with $\beta_{2S} = 48$ deg combined with 22 deg diffuser). The resulting relation is shown in Fig. 5.

The function l_{sep} can then be described by the following equations:

(a) negative incidence ($i < 0$):

$$l_{sep} = 0.03e^{(0.5(k_{sep}-1))} + 0.97 \text{ when } k_{sep} \leq 6.18 \quad (7a')$$

$$l_{sep} = 0.2(k_{sep} - 1) + 0.334 \text{ when } k_{sep} > 6.18 \quad (7a'')$$

(b) positive incidence ($i > 0$):

$$l_{sep} = 0.4(k_{sep} - 1) + 1 \quad (7b)$$

Some Examples and Test of Accuracy

Measured and Predicted Characteristics. From the remaining impeller/diffuser combinations, which have not been used to calibrate the empirical functions, two examples have been chosen to give an idea of the capability of the prediction method. For that purpose the measured and predicted pressure rise coefficient C_p and loss coefficient ω are plotted against the diffuser inlet flow angle α_2 at different stage Mach numbers Mu_2 . Figure 6 shows the results found for an impeller with $\beta_{2S} = 35$ deg, $z'' = 14$,⁷ combined with a diffuser with $\alpha_{3D} = 18$ deg, $z' = 24$ and radial extent $r_4/r_2 = 1.33$. In Fig. 7 the same comparison is given for another impeller ($\beta_{2S} = 45$ deg, $z'' = 15$) with a 24-vane diffuser with $\alpha_{3D} = 26$ deg, $r_4/r_2 = 1.50$. Each impeller/diffuser combination was investigated for two different exit heights b_2/D_2 , while the impeller exit and the diffuser inlet height were identical ($b_{2imp} = b_{2diff}$).

The region where instability—mild surge or rotating stall—has been detected during the measurement are marked with a shaded area. Within this area, an accurate prediction is no longer possible due to erroneous input data. Beyond this region, the C_p characteristics are generally fairly well predicted, but in some cases the values are rather too high. In the latter example (Fig. 7), an ex-

⁷Although β_{2S} and z'' are identical to the listed values for one of the impellers in Table 1, the impeller used here is significantly different from the one used there.

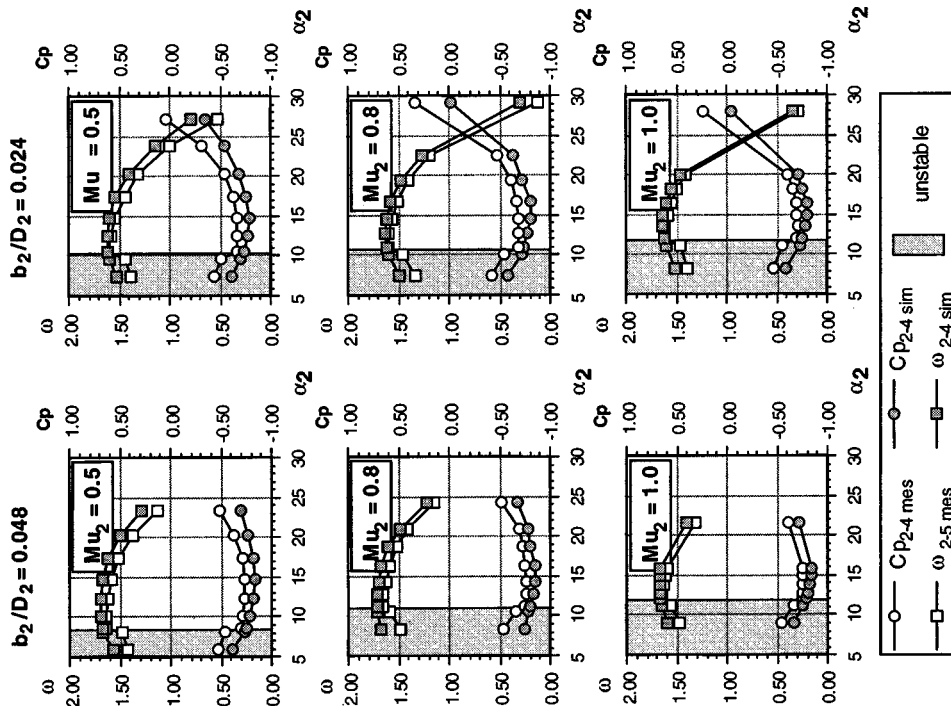


Fig. 6 Measured and predicted characteristics for an 18 deg diffuser with $z' = 24$, $r_4/r_2 = 1.33$, in combination with an impeller with $\beta_{2S} = 35$ deg, $z'' = 14$

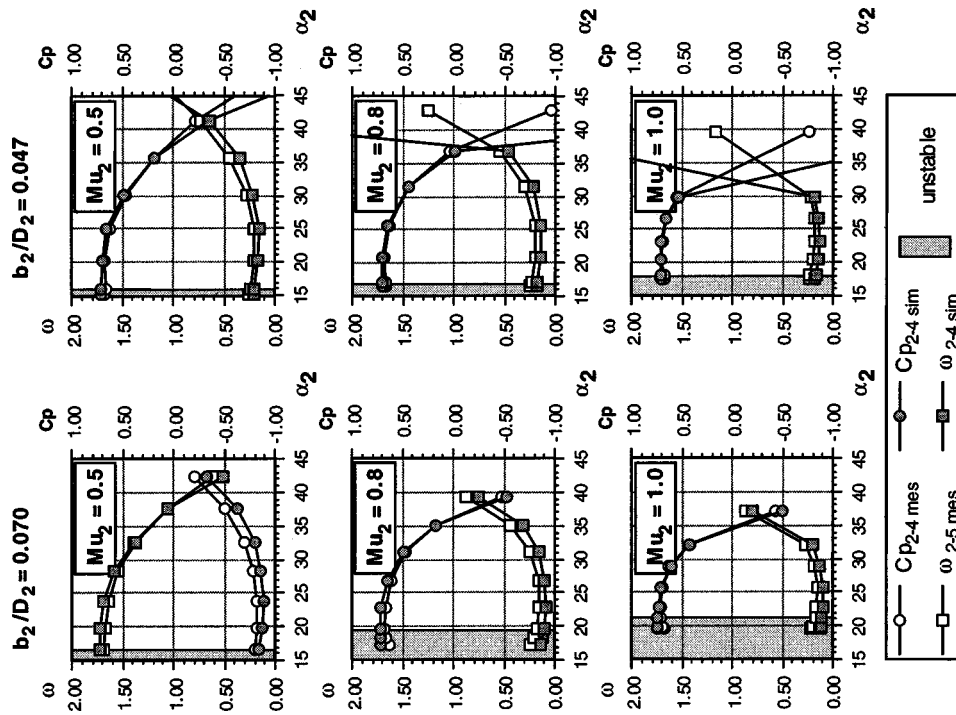


Fig. 7 Measured and predicted characteristics for a 26 deg diffuser with $z' = 24$, $r_4/r_2 = 1.50$, in combination with an impeller with $\beta_{2s} = 45$ deg, $z'' = 15$

tre discrepancy is found for the highest flow angle at high stage Mach number ($Mu_2 = 0.8$ and 1.0) and small diffuser height ($b_2/D_2 = 0.047$). According to the prediction method there is excessive separation leading to premature choke. For the loss coefficients, unfortunately no direct comparison between measurement and prediction is possible, since the measured losses include the losses in the return channel while the predicted ones do not.⁸ As a consequence, the measured values for ω should always be higher than the predicted ones. Furthermore, the difference between the two loss coefficients should increase with increasing incidence to the de-swirl vanes in the return channel and with the increase of the remaining kinetic energy at the exit of the diffuser. The latter goes along with mass flow and increases, therefore, with increasing diffuser inlet flow angle α_2 . Considering these effects, the trend shown by the predicted loss coefficient seems to be reasonable.

Slopes of Measured and Predicted Characteristics Near-Choke and Surge. During the design procedure, apart from efficiency, two other questions are of utmost importance: Where does the stage choke and where is the limit of dynamic stability for a given impeller/diffuser configuration? The answer to these questions can only be given provided that the prediction is accurate enough at flow conditions close to surge and choke.

To verify the accuracy of the given one-dimensional prediction, a comparison with measurements is performed. For the majority of the measured stages, the maximum flow rate is given by the intersection of compressor characteristic and flow resistance curve of the test rig ducting, rather than a real choke condition in either the impeller or the diffuser throat. Therefore, the accuracy of the prediction method has to be assessed by comparing the slopes of measured and predicted diffuser characteristics at maximum flow rate.

It is reasonable to do the same for flow conditions in the vicinity of surge. This is outlined as follows: The onset of dynamic

instability is related to the pressure rise characteristic of the stage. It is common knowledge (e.g., [9]) that a compressor is potentially dynamically stable in any duct work as long as the slope of its pressure rise characteristic is negative:

$$\frac{\partial Dp_{\text{comp}}}{\partial \alpha_2} \leq 0 \quad (8)$$

where Dp_{comp} , the normalized pressure rise, is defined as

$$Dp_{\text{comp}} = \frac{\Delta p_{\text{comp}}}{\rho_1^* u_2^2 / 2} \quad (9)$$

As shown by Hunziker [10], this argument can be extended to the individual stage components when subdividing the pressure rise of the whole stage, Dp_{comp} , into the contributions of each component (impeller, diffuser, and scroll or return channel). Thus, in order to assess the contribution of the diffuser to the onset of dynamic instability, it is necessary to consider the slope of the diffuser, $\partial Dp_{\text{diff}} / \partial \alpha_2$.

With a given pressure coefficient, Cp_{diff} , and a given dynamic head, $p_2^* - p_2$, the normalized pressure rise, Dp_{diff} , of the diffuser is provided by:

$$Dp_{\text{diff}} = Cp_{\text{diff}} \frac{p_2^* - p_2}{\rho_1^* u_2^2 / 2} \quad (10)$$

Hence, the slope, $\partial Dp_{\text{diff}} / \partial \alpha_2$, can be easily determined.⁹

The comparisons have been performed for a series of impellers, which have been combined with the company's standard diffusers of short ($r_4/r_2 = 1.33$) or full length ($r_4/r_2 = 1.50$). The diffuser vane angle α_{3D} varied between 10 deg to 34 deg in steps of 4 deg. The impellers cover a design flow rate $\phi_{1\text{design}}^*$ from 0.01 up to

⁸While the static pressure at diffuser exit has been measured, the total pressure only can be derived where the flow angle is known. This is not the case for the flow leaving the diffuser, but for the flow after the return channel.

⁹It has to be stressed that it is not sufficient to consider the slope of the pressure recovery characteristic, $\partial Cp_{\text{diff}} / \partial \alpha_2$, since $\partial Dp_{\text{diff}} / \partial \alpha_2$ depends on both the characteristic of pressure recovery and dynamic head (see later).

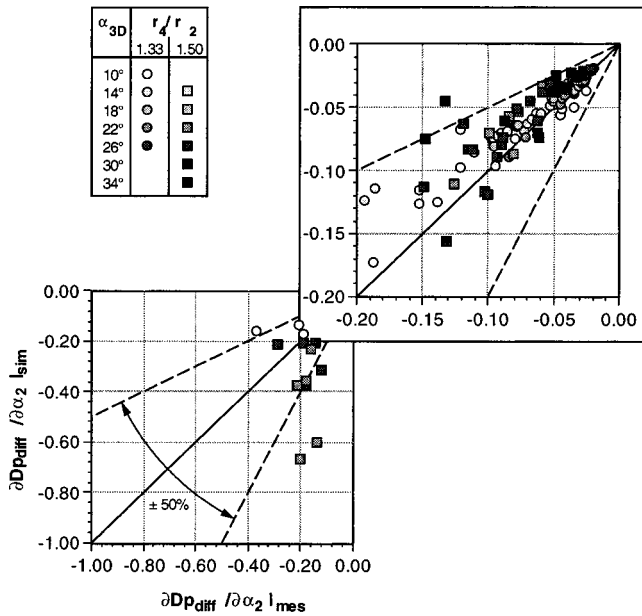


Fig. 8 Comparison of measured and predicted slopes $\partial Dp_{diff}/\partial\alpha_2$ at maximum flow rate

0.11, with blade exit angles β_{2S} ranging from 15 to 60 deg. The stage Mach number Mu_2 was between 0.4 and 1.0, with air as working fluid.

Near Choke. The comparison between measured and predicted slope for maximum flow rate is shown in Fig. 8.¹⁰ This figure shows a clear trend where the agreement is improved toward small negative values of the slope. This behavior is already expected due to the introduction of the empirical method. Relatively small amounts of (negative) slope at maximum flow correspond to operating points with low negative incidence. As a consequence, any uncertainty due to the incidence-dependent increase of blockage does not yet influence the pressure rise noticeably. In contrast, operating points with steep pressure rise characteristics, i.e., large negative slopes, go along with large negative incidence values and thus with poorer accuracy. However, for slopes smaller than -0.5 , the characteristic is already considerably steep and even an error of about 50 percent (boundary marked by dotted line) has no bearing.

Near Surge. Figure 9 shows the comparison of predicted versus measured slope for operating points close to the instability line. While the slopes at choke are strongly negative, those at surge exhibit much smaller values and may even be above zero in the case of a rather ‘‘open’’ diffuser (i.e., large values of α_{3D}) that has been combined with an impeller designed for lower flow rates. As a consequence, for the slopes at surge a different scale has to be applied than for those at maximum flow rate. Therefore, for Fig. 9 the same scale as for the enlarged part of Fig. 8 is chosen.

Figure 9 seems to lack the trend found for the slopes near choke, i.e., an improved agreement with increasing values of the slope. This is also expected from the prediction method. The slope $\partial Dp_{diff}/\partial\alpha_2$ is determined by both the characteristics of the pressure recovery and dynamic head, which is given by the impeller and not by the diffuser. For a given dynamic head characteristic, strongly negative values of $\partial Dp_{diff}/\partial\alpha_2$ correspond to operating points which are further away from the incidence free condition.

The question arising now is how much an ill-predicted slope influences the prediction of the instability line. At the stability

¹⁰For this comparison, those operating points where the one-dimensional prediction indicated choked flow or merged displacement thicknesses δ^* in any calculation stations have been omitted.

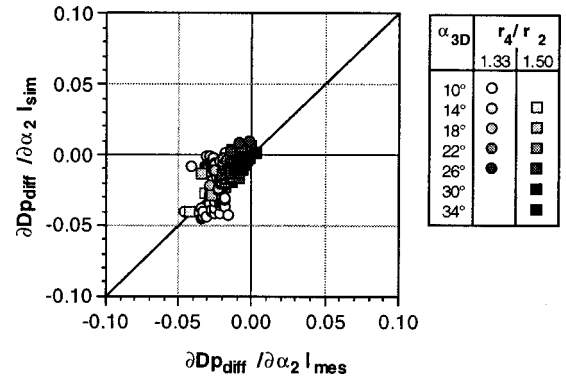


Fig. 9 Comparison between measured and predicted slopes $\partial Dp_{diff}/\partial\alpha_2$ at surge

limit, given by $\alpha_{2\text{ mes}}$, a certain slope $\partial Dp_{diff}/\partial\alpha_2|_{mes}$ was measured. An incorrectly predicted slope, $\partial Dp_{diff}/\partial\alpha_2|_{sim}$, then shows a wrong position on the $Dp_{diff}-\alpha_2$ characteristic, resulting in a difference to $\alpha_{2\text{ mes}}$. Given the shape of the $Dp_{diff}-\alpha_2$ characteristic in the vicinity of $\alpha_{2\text{ mes}}$, the error $\Delta\alpha_{2\text{ err}}$ due to the ill prediction can be assessed. In Appendix A1, an expression for $\Delta\alpha_{2\text{ err}}$ is given assuming a parabolic shape of the $Dp_{diff}-\alpha_2$ characteristic, $Dp_{diff}=a\alpha_2^2+b\alpha_2+c$, in the vicinity of the stability line:

$$\Delta\alpha_{2\text{ err}} = \frac{1}{2a} \left(\frac{\partial Dp_{diff}}{\partial\alpha_2} \Big|_{sim} - \frac{\partial Dp_{diff}}{\partial\alpha_2} \Big|_{mes} \right) \quad (11)$$

This assessment, however, requires the knowledge of the shape of the characteristic, at least of the term a . Therefore, a much simpler and more convenient approach has been chosen, where the error due to a wrong prediction for the pressure rise Dp_{diff} is taken into account. Referring to Fig. 10, assume that at operating point 1 the pressure rise $Dp_{diff}(1)$ and the angle $\alpha_2(1)$ are known. With the measured slope $\partial Dp_{diff}/\partial\alpha_2|_{mes}$ the pressure rise $Dp_{diff}(2)$ is reached at $\alpha_{2\text{ mes}}(2)$, whereas with the predicted $\partial Dp_{diff}/\partial\alpha_2|_{sim}$, $\alpha_{2\text{ sim}}(2)$ is found for the same Dp_{diff} . The corresponding difference $\alpha_{2\text{ sim}}(2) - \alpha_{2\text{ mes}}(2)$, i.e., the error $\Delta\alpha_{2\text{ err}}$, then can be given by:

$$\Delta\alpha_{2\text{ err}} = \Delta\alpha_{2\text{ mes}} \left(1 - \frac{\partial Dp_{diff}/\partial\alpha_2|_{mes}}{\partial Dp_{diff}/\partial\alpha_2|_{sim}} \right) \quad (12)$$

The relative error E_{rel} is simply this amount divided by the angle found at the stability limit:

$$E_{rel} = \Delta\alpha_{2\text{ err}} / \alpha_{2\text{ sim}} \quad (13)$$

The result of this assessment is shown in Fig. 11, where the distribution of the relative error against the diffuser vane angle

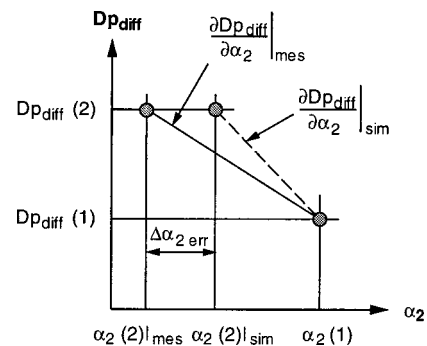


Fig. 10 Parameters required for the assessment of the influence of an ill-predicted slope

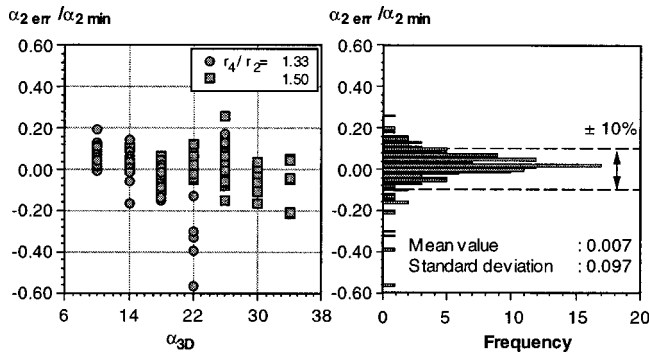


Fig. 11 Distribution and frequency of the relative error $\Delta\alpha_{2\text{err}}/\alpha_{2\text{min}}$

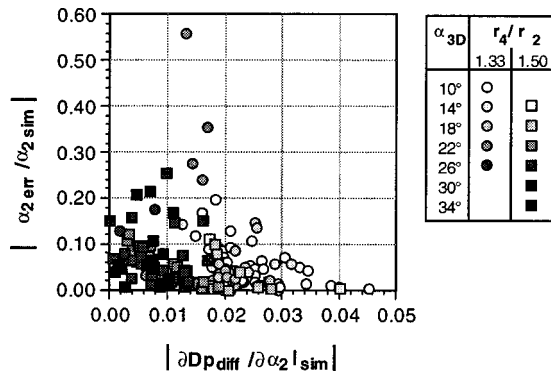


Fig. 12 Relation between relative error $\Delta\alpha_{2\text{err}}/\alpha_{2\text{min}}$ and predicted slope $\partial Dp_{\text{diff}}/\partial\alpha_2|_{\text{sim}}$

α_{3D} is shown on the left and a histogram on the right. Out of a series of 164 data points, there are three points with relative errors that exceed the 100 percent margin. These points have been omitted.

The bulk of the remaining data lies within a ± 10 percent range. For a customer's compressor generally a surge margin within ± 5 percent is guaranteed. The result found herein is probably not quite that good, but it still qualifies the involved one-dimensional prediction as a useful tool.

In all three data points where the relative error exceeds the 100 percent margin, the predicted slope is almost zero. Equation (12) indicates that the relative error tends toward $\pm\infty$ when $\partial Dp_{\text{diff}}/\partial\alpha_2|_{\text{sim}}$ approaches zero. This trend is proven by Fig. 12.

Application

Design for Given Minimum Flow Rate. Matching of impeller and diffuser is not only aimed at finding the combination yielding the best stage efficiency. In some applications it might be useful to guarantee a certain minimum flow rate. As shown below it is possible to design a stage that is dynamically stable at a given minimum flow rate, provided that the slope of the impeller pressure rise characteristic and the values and slopes of dynamic head and diffuser pressure recovery are known. As already stated, a compressor stage is dynamically stable as long as the sum of the slopes of its components is negative (e.g., [10]). Neglecting the influence of a scroll or a return channel, at the given minimum flow rate, the following inequality has to be satisfied:

$$\frac{\partial Dp_{\text{imp}}}{\partial\alpha_2} + \frac{\partial Dp_{\text{diff}}}{\partial\alpha_2} \leq 0 \quad (14)$$

or with Dp_{diff} expressed similar to Eq. (9), and derived:

$$\frac{\partial Dp_{\text{diff}}}{\partial\alpha_2} = Cp_{\text{diff}} \frac{\partial}{\partial\alpha_2} \left(\frac{p_2^* - p_2}{\rho_1^* u_2^2/2} \right) + \left(\frac{p_2^* - p_2}{\rho_1^* u_2^2/2} \right) \frac{\partial Cp_{\text{diff}}}{\partial\alpha_2} \quad (15)$$

Equation (14) can be written as:

$$\frac{\partial Dp_{\text{imp}}}{\partial\alpha_2} + Cp_{\text{diff}} \frac{\partial}{\partial\alpha_2} \left(\frac{p_2^* - p_2}{\rho_1^* u_2^2/2} \right) + \left(\frac{p_2^* - p_2}{\rho_1^* u_2^2/2} \right) \frac{\partial Cp_{\text{diff}}}{\partial\alpha_2} \leq 0 \quad (16)$$

To solve these equations, the following characteristics are required, for a new impeller:

- $Dp_{\text{imp}} - \alpha_2$ characteristic,
- $2(p_2^* - p_2)/\rho_1^* u_2^2$ characteristic,

and for the diffuser:

- $Cp_{\text{diff}} - \alpha_2$ characteristic

Assume that a newly designed impeller has to be combined with one of the standardized diffusers and that the minimum flow rate, expressed by $\alpha_{2\text{min}}$, that has to be met is given. For the quantities at $\alpha_{2\text{min}}$ the following abbreviations are used:

$$D' \equiv \left. \frac{\partial Dp_{\text{imp}}}{\partial\alpha_2} \right|_{\alpha_{2\text{min}}} \quad (17)$$

$$C \equiv Cp_{\text{diff}}|_{\alpha_{2\text{min}}} \quad (18)$$

$$C' \equiv \left. \frac{\partial Cp_{\text{diff}}}{\partial\alpha_2} \right|_{\alpha_{2\text{min}}} \quad (19)$$

$$S \equiv \left. \frac{p_2^* - p_2}{\rho_1^* u_2^2/2} \right|_{\alpha_{2\text{min}}} \quad (20)$$

$$S' \equiv \left. \frac{\partial}{\partial\alpha_2} \left(\frac{p_2^* - p_2}{\rho_1^* u_2^2/2} \right) \right|_{\alpha_{2\text{min}}} \quad (21)$$

Therefore, of the impeller at $\alpha_{2\text{min}}$, the following variables need to be known:

- D' ,
- S , and
- S'

and of the diffuser (at $\alpha_{2\text{min}}$):

- C and
- C'

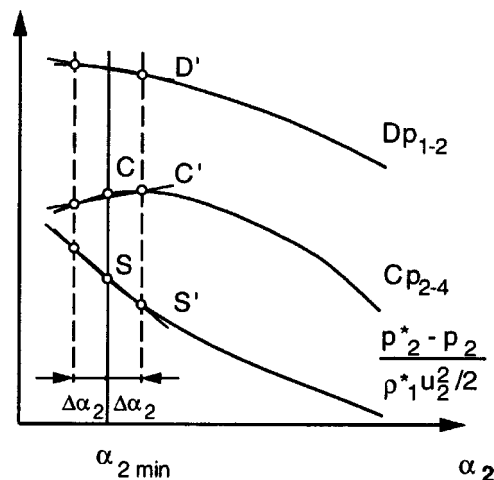


Fig. 13 Sketch of the characteristics and values needed to fulfill the criteria for dynamically stable operation at $\alpha_{2\text{min}}$

Simplifying Eq. (16) via Eqs. (16)–(21) yields:

$$D' + CS' + C'S \leq 0 \quad (22)$$

The characteristics and values required for Eq. (22) (or Eq. (16)) are shown in Fig. 13.

From the impeller, apart from S , only the slopes have to be known (D' and S'). When designing the impeller by means of CFD, at least two calculations are required: one at a flow rate higher than that associated with $\alpha_{2\min}$ and one at a flow rate below this value ($\pm \Delta \alpha_2$). It is further argued that the prediction of a slope with CFD might be more accurate than the prediction of an absolute value. Knowing the impeller quantities (D' , S , and S') with the present one-dimensional prediction method, a rapid evaluation of the suitable diffuser yielding the required slope at $\alpha_{2\min}$ then is possible.

Estimation of the Influence of a Modified Diffuser Geometry on a Measured Performance Characteristic

Possible Modifications. The use of the present one-dimensional prediction method provides the opportunity to handle diffuser geometries other than the ones that are measured. As long as the diffuser vanes themselves still follow the specified geometry with respect to the shape of the leading edge, curvature, and thickness, it is possible to predict the effects of:

- change of diffuser vane angle α_{3D} ,
- change of diffuser height b_{2D}/b_{2I} (i.e., a pinched diffuser),
- change of diffuser vane number z' and
- change of diffuser radius ratio r_4/r_2 .¹¹

The change of the diffuser vane number is probably more hazardous because of the considerable change in solidity.

“Subtracting-and-Adding” Procedure. The idea is to “subtract” the characteristic (i.e., efficiency) of the diffuser with which the stage characteristic was originally measured and then “add” the characteristic of the new diffuser. It is argued that this “subtracting-and-adding” procedure guarantees the best achievable accuracy because the contribution of any influence not covered in the one-dimensional prediction (e.g., skewness of the incoming velocity profile and the resulting secondary flows) is almost ruled out.

Application of the one-dimensional prediction requires knowledge of the thermodynamic state at impeller exit (p_2, T_2), the stagnation pressure p_2^* (or velocity c_2), and the discharge angle of the impeller α_2 . Setting the static pressure p_2 arbitrarily to unity and using the pressure ratio p_2^*/p_2 in combination with static temperature T_2 and flow angle α_2 is, however, still sufficient. Unfortunately often not all of these variables are known when measuring a compressor stage as an entirety. Therefore, to get the required input data a certain procedure (depending on the available data) has to be carried out for each measurement point. In Appendix A2 such a procedure is outlined for the data set stored in the in-house stage stacking method.

Once the required input data at diffuser inlet are known, the diffuser performance can be assessed for both the original and the changed diffuser, yielding p_4^* (or p_4^*/p_2) and T_4^* for each diffuser. As outlined in Appendix A3, the change in stage efficiency then can be assessed by:

¹¹Note: Considering a stage with a return channel or scroll following the diffuser, it does not suffice to take into account the change in diffuser loss alone. The one-dimensional prediction for the diffuser would predict a lower loss coefficient ω_{2-4} for the shorter diffuser because of the reduced build-up of separation along the walls. However, in the shorter diffuser the flow is less diffused and therefore, the dynamic head at the inlet of the following return channel or scroll is increased. As a consequence, the losses in this stage element increase too and lead to a lower efficiency of the combination diffuser plus return channel or diffuser plus scroll. Therefore the change of losses in the return channel or scroll, ω_{4-5} , have to be assessed also.

$$\Delta \eta_{\text{stage}} = (1 - \gamma_0) \frac{\kappa - 1}{\kappa} \frac{\ln(p_4^{*\text{orig}}/p_2/p_4^{*\text{new}}/p_2)}{\ln(T_4^*/T_2)} \quad (23)$$

for all measured ϕ_1^* values. The change in stability (i.e., the resulting shift in $\phi_{1\text{stab}}^*$), however, is not as easy to predict as the change in efficiency. The stability limit can be dictated by the impeller alone. An example of this circumstance is when the impeller undergoes severe rotating stall, resulting in a sharp drop of the impeller’s pressure rise characteristic. In such instances the stability line is likely to be unchanged even with an other diffuser. However, in case $\phi_{1\text{stab}}^*$ is not determined by such phenomena, a prediction procedure is conceivable. It is fair to assume that the instability occurs at the same slope of the stage’s $\mu_y - \phi_1^*$ characteristic as in the original stage:

$$\left. \frac{\partial \mu_y}{\partial \phi_1^*} \right|_{\text{new}}^{\text{stab}} = \left. \frac{\partial \mu_y}{\partial \phi_1^*} \right|_{\text{orig}}^{\text{stab}} \quad (24)$$

The locus on the new characteristic, where the same slope is reached, then is found by the same procedure, as proposed in Appendix A1 to find the error due to an ill-predicted slope. The new characteristic, therefore, has to be approximated by at least a second-order polynomial to indicate the ϕ_1^* value with the same slope, which then is $\phi_{1\text{stab}}^*$.¹²

Some Examples. Shown below are three examples where, based on a known stage characteristic, the new characteristic for a changed diffuser has been predicted by applying the “subtracting-and-adding” method. For the first two examples, a data set as used by the in-house stage-stacking program (RADAX) has been used, i.e., η_p , μ_0 , and γ_0 at ten ϕ_1^* -values. For these examples the original stage was the same (impeller: $\beta_{2S} = 45$ deg, $z'' = 15$; diffuser: $\alpha_{3D} = 22$ deg, $z' = 24$, $r_4/r_2 = 1.50$, at $Mu_2 = 0.8$ while $b_{2I}/D_2 = b_{2D}/D_2 = 0.071$). For the last example another base was chosen (impeller: $\beta_{2S} = 50$ deg, $z'' = 18$; diffuser: $\alpha_{3D} = 22$ deg, $z' = 12$, $r_4/r_2 = 1.35$, at $Mu_2 = 0.8$ while $b_{2I}/D_2 = b_{2D}/D_2 = 0.038$). Here the values for η_p , μ_0 , and γ_0 were taken directly from the measurement.

Change of Diffuser Vane Angle. From the stored data of the first stage, i.e., with regular 22 deg diffuser (base characteristic),

¹²It has to be emphasized that the influence of any change in diffuser geometry on the stability line might be predicted with more accuracy as long as the change leads to a shift of the stability line to the right (higher flow rates), i.e., when the specified slope of the new diffuser characteristic is reached at a higher flow angle. Some additional difficulties are encountered when this slope lies to the left of the original one, since the impeller variables (discharge flow angle and dynamic head at impeller exit) have to be extrapolated.

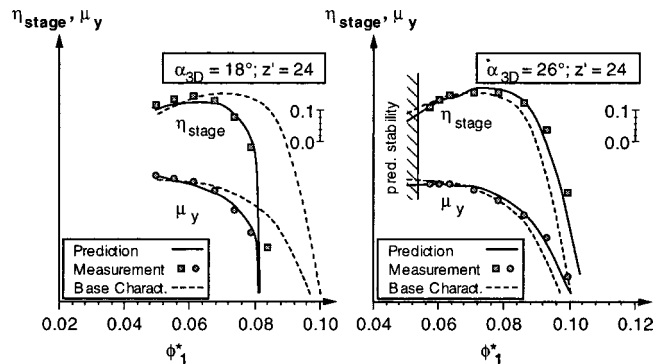


Fig. 14 Predicted influence of diffuser vane angle change based on data prepared for the stage stacking program (RADAX). Original stage ($Mu_2 = 0.8$); impeller: $\beta_{2S} = 45$ deg, $z'' = 15$, $b_{2I}/D_2 = 0.071$; diffuser: $\alpha_{3D} = 22$ deg, $z' = 24$, $r_4/r_2 = 1.50$, $b_{2D}/D_2 = 0.071$.

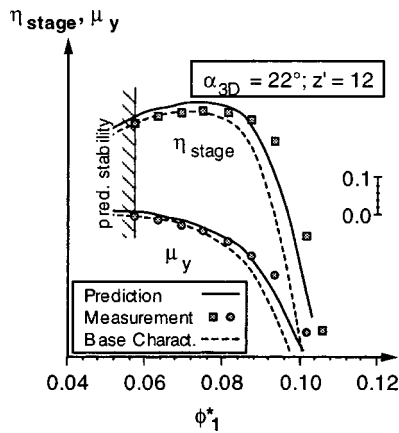


Fig. 15 Predicted influence of diffuser vane number based on data prepared for the stage stacking program (RADAX): original stage ($\mu_2=0.8$): impeller: $\beta_{2S}=45$ deg, $z''=15$, $b_{21}/D_2=0.71$; diffuser: $\alpha_{3D}=22$ deg, $z'=24$, $r_4/r_2=1.50$, $b_{2D}/D_2=0.071$

the characteristics for a diffuser with the same radial extent ($r_4/r_2=1.50$), but with $\alpha_{3D}=18$ deg and 26 deg, are calculated. The results are shown in Fig. 14, together with the measured characteristics and the base characteristic.

The quality of agreement between prediction and measurement is about the same for the 18 deg and the 26 deg diffuser; however, the peak efficiency has been underestimated (about 1.5 points) for the former and overestimated (about 1 point) for the latter. The predicted stability limit was far too low for the 18 deg diffuser compared to measurement (the predicted slope of μ_y at the lowest flow rate is much steeper than the measured one). For the 26 deg diffuser the predicted stability line is 7.3 percent too low.

Change of Diffuser Vane Number. The same impeller and diffuser were chosen to check the performance of the prediction method in terms of a reduced vane number. z' was set to 12 instead of 24 and then compared with the measured characteristic (see Fig. 15).

Compared to the measurement, the efficiency is overestimated by about 2 points at low flow rates and then drops too fast toward choke. The stability line is fairly well predicted, being 0.7 percent too high. This example shows that even with the functions for the separation (k_{sep} and l_{sep}) being gained from diffusers with rather

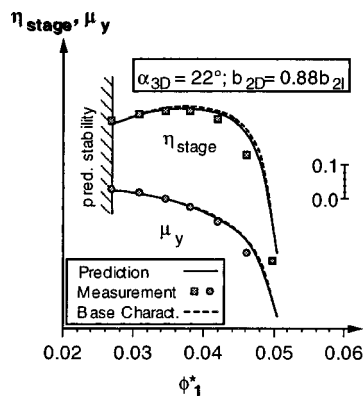


Fig. 16 Predicted influence of reduced diffuser height, based on measurements: original stage ($\mu_2=0.8$): impeller: $\beta_{2S}=50$ deg, $z''=18$, $b_{21}/D_2=0.038$; diffuser: $\alpha_{3D}=22$ deg, $z'=12$, $r_4/r_2=1.35$, $b_{2D}/D_2=0.038$

high solidity (i.e., 24 vanes) the influence of a change in diffuser geometry is well predictable for diffusers with considerable lower solidity ($z'=12$).

Change of Diffuser Height. The capability of the method to predict the characteristics of a pinched diffuser is shown in Fig. 16. Toward choke, the measured characteristic falls off earlier than predicted. The predicted peak efficiency is slightly too high and the stability limit is about 0.4 percent lower than measured.

Summary and Conclusions

In the present paper the following topics were covered:

- A simple straightforward one-dimensional theory for the prediction of the performance of vaned diffusers is presented. The method mainly relies on two empirical functions, by which the increase of displacement and momentum thickness due to separation on the suction (toward surge) or the pressure side (toward choke) is taken into account. The static pressure and the mean velocity in any calculation station are calculated assuming an inviscid core flow and a boundary layer of known displacement and momentum thickness at each diffuser wall. Due to the calibration of the functions with the company's standard diffusers, they apply only to this type of diffusers, although the method itself is adaptable for any type of subsonic vaned diffusers.

- The accuracy of the method was examined by comparing measured and predicted characteristics. Special interest was focused on the slope near choke and surge. The results have shown that surge prediction seems to be possible within ± 10 percent.

- It is shown how the present method provides a useful tool during the design process of a new stage when the best matching between a new impeller and a standardized diffuser has to be found. The "best" matching may refer to the efficiency as well as operating range. Therefore, it was further outlined how to design a stage that is dynamically stable at a given minimum flow rate. It was assumed that the slope of the impeller pressure rise characteristic as well as the values and slopes of dynamic head were known from CFD calculations, while the pressure recovery of the diffuser and its slope were assessed by means of the present one-dimensional prediction method.

- It was also shown how the one-dimensional prediction method can be used to estimate the change to be expected in a known stage performance characteristic when modifying the diffuser geometry. Examples were shown for the change of diffuser vane angle, diffuser vane number, and height ratio between impeller exit and diffuser entry.

The results are encouraging, although in some cases an improvement is required.

Acknowledgments

The authors would like to thank Sulzer Turbo, Ltd., for permission to publish this paper, and all the colleagues who assisted in this work.

Nomenclature

- A = area
- b = height
- c = absolute velocity
- Cp = pressure recovery = $(p_{i+1} - p_i) / (p_i^* - p_i)$
- D = diameter
- Dp = nondimensional pressure rise (see Eq. (9))
- h = width, enthalpy
- H_{12} = form factor = δ^* / θ
- i = incidence angle = $\alpha_{3D} - \alpha_3$
- k_{sep} = empirical factor for increase of displacement thickness (see Eq. (4))
- l_{sep} = empirical factor for increase of momentum thickness (see Eq. (5))

- \dot{m} = flow rate
- M = local Mach number
- Mu_2 = stage Mach number = $u_2 / \sqrt{\kappa RT_E^*}$
- p = pressure
- r = radius
- R = gas constant
- T = temperature
- u = velocity
- u_2 = impeller tip speed
- z' = number of diffuser vanes
- z'' = number of impeller blades
- α = flow angle of absolute velocity
- α_{3D} = diffuser vane angle setting
- β_{2S} = impeller exit blade angle
- γ_0 = degree of reaction = $\Delta h_{imp} / \Delta h^* = \Delta h_{imp} / \mu_0 u_2^2$
- δ^* = displacement thickness
- η_p = polytropic efficiency
- θ = momentum thickness
- κ = isentropic coefficient
- μ_0 = work coefficient
- μ_y = polytropic head
- ρ = density
- ϕ = flow coefficient = $\dot{m} / \rho_E u_2 D_2^2$
- ω = loss coefficient = $(p_i^* - p_{i+1}^*) / (p_i^* - p_i)$

Subscripts

- comp = referring to compressor
- diff = referring to diffuser
- err = error
- E = stage entry
- i = referring to segment i
- imp = referring to impeller
- mes = measurement
- sep = referring to separation
- sim = simulation
- stage = referring to stage
- th = diffuser throat
- u = circumferential
- 1 = Station 1
- 2 = Station 2, diffuser (vaneless space) entry
- 3 = diffuser channel leading edge
- 4 = diffuser exit
- 5 = return channel exit

Superscripts

- new = referring to modified characteristic
- orig = referring to original characteristic
- stab = at stability line
- * = referring to stagnation condition

Appendix A1

Influence of an Ill-Predicted Slope on the Stability Limit.

For accurate prediction of the dynamic instability, the slope is the important quantity that has to be correctly predicted. At the stability limit, the measured data points in $\alpha_{2\text{mes}}(1)$ and $\alpha_{2\text{mes}}(2)$ result in a certain slope, $\partial Dp_{\text{diff}} / \partial \alpha_2|_{\text{mes}}$. Based on the predicted pressure rise, a different slope would be calculated, $\partial Dp_{\text{diff}} / \partial \alpha_2|_{\text{sim}}$. As shown in Fig. A1-1, an incorrectly predicted slope, $\partial Dp_{\text{diff}} / \partial \alpha_2|_{\text{sim}}$, shows a wrong position on the $Dp_{\text{diff}} - \alpha_2$ characteristic, resulting in a difference to $\alpha_{2\text{mes}}$. The difference to $\alpha_{2\text{mes}}$, the error $\Delta \alpha_{2\text{err}}$, can be assessed provided that the shape of the $Dp_{\text{diff}} - \alpha_2$ characteristic is known in the vicinity of $\alpha_{2\text{mes}}$.

If the $Dp_{\text{diff}} - \alpha_2$ characteristic be approximated by second-order polynomial:

$$Dp_{\text{diff}} = a\alpha_2^2 + b\alpha_2 + c \quad (\text{A1-1})$$

the two known slopes then have to satisfy:

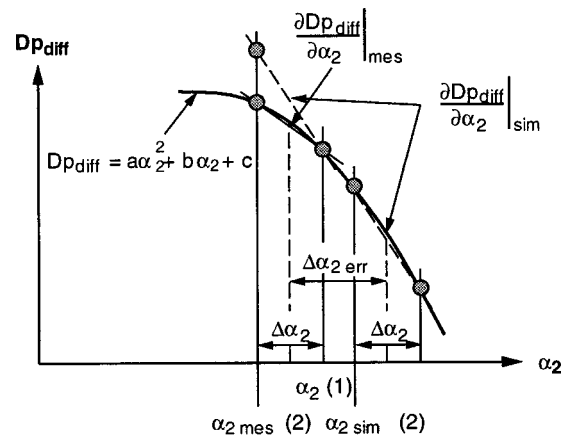


Fig. A1-1 Parameters to assess the influence of an ill-predicted slope on the instability line

$$\left. \frac{\partial Dp_{\text{diff}}}{\partial \alpha_2} \right|_{\text{mes}} = 2a \left(\alpha_{2\text{mes}} + \frac{1}{2} \Delta \alpha_2 \right) + b \quad (\text{A1-2a})$$

$$\left. \frac{\partial Dp_{\text{diff}}}{\partial \alpha_2} \right|_{\text{sim}} = 2a \left(\alpha_{2\text{sim}} + \frac{1}{2} \Delta \alpha_2 \right) + b \quad (\text{A1-2b})$$

and so the difference, $\Delta \alpha_{2\text{err}} = \alpha_{2\text{sim}} - \alpha_{2\text{mes}}$, can be assessed by:

$$\Delta \alpha_{2\text{err}} = \frac{1}{2a} \left(\left. \frac{\partial Dp_{\text{diff}}}{\partial \alpha_2} \right|_{\text{sim}} - \left. \frac{\partial Dp_{\text{diff}}}{\partial \alpha_2} \right|_{\text{mes}} \right) \quad (\text{A1-3})$$

Appendix A2

Calculation of Required Data for the One-Dimensional Prediction Using the Degree of Reaction. For a measured stage the characteristic of efficiency, η_{stage} , and work coefficient, μ_0 , are stored in the in-house stage stacking program (RADAX). In addition the degree of reaction, γ_0 , is known. It is assumed that γ_0 and μ_0 do not change noticeably when using another diffuser.¹³ The velocity c_2 at impeller exit then can be assessed:

$$\frac{c_2^2}{2} = \Delta h^* - \Delta h_{\text{imp}} = \mu_0 (1 - \gamma_0) u_2^2 \quad (\text{A2-1})$$

The circumferential component c_{u2} is known due to the measured μ_0 value (provided that there is no pre-swirl, i.e., $c_{u1} = 0$):

$$c_{u2} = \mu_0 u_2 \quad (\text{A2-2})$$

With c_2 and c_{u2} , the flow angle can be calculated:

$$\alpha_2 = \arccos \left(\frac{c_{u2}}{c_2} \right) \quad (\text{A2-3})$$

With the knowledge or with an arbitrary set of pressure and temperature at stage inlet (p_1^*, T_1^*), valid for the original characteristic, the static temperature at impeller exit is found:

$$T_2 = T_1^* + \frac{\gamma_0 \mu_0 u_2^2}{c_p} \quad (\text{A2-5})$$

The ratio of stagnation pressure and static pressure is then:

¹³With the definition of γ_0 as the ratio of total-to-static enthalpy rise of the impeller and total enthalpy rise of the stage, this value does not change appreciably when different diffusers of approximately similar efficiency are combined with the same impeller.

$$\frac{p_2^*}{p_2} = \left[\frac{\kappa-1}{2} \frac{c_2^2}{\kappa RT_2} + 1 \right]^{\kappa/\kappa-1} = \left[(\kappa-1) \frac{\mu_0(1-\gamma_0)u_2^2}{\kappa RT_2} + 1 \right]^{\kappa/\kappa-1} \quad (A2-6)$$

Hence all the quantities required as input for the one-dimensional prediction are known.

Appendix A3

Assessment of the Influence on the Stage Efficiency Due to a Modified Diffuser. Provided that the efficiency of the impeller, η_{imp} , is unchanged, the change in stage efficiency, which is to be expected due to the different diffusers, can be evaluated as follows:

$$\Delta \eta_{\text{stage}} = \eta_{\text{stage}}^{\text{orig}} - \eta_{\text{stage}}^{\text{new}} = \gamma_0(\eta_{\text{imp}}^{\text{orig}} - \eta_{\text{imp}}^{\text{new}}) + (1-\gamma_0)(\eta_{\text{diff}}^{\text{orig}} - \eta_{\text{diff}}^{\text{new}}) \approx 0 + (1-\gamma_0)(\eta_{\text{diff}}^{\text{orig}} - \eta_{\text{diff}}^{\text{new}}) \quad (A3-1)$$

where the static-to-total efficiencies of the diffusers are defined as:

$$\eta_{\text{diff}}^{\text{orig}} = \frac{\kappa-1}{\kappa} \frac{\ln(p_4^{*\text{orig}}/p_2)}{\ln(T_4^{*\text{orig}}/T_2)} \quad (A3-2)$$

$$\eta_{\text{diff}}^{\text{new}} = \frac{\kappa-1}{\kappa} \frac{\ln(p_4^{*\text{new}}/p_2)}{\ln(T_4^{*\text{new}}/T_2)} \quad (A3-3)$$

Considering adiabatic conditions, $T_4^{*\text{new}} = T_4^{*\text{orig}} = T_4^*$, Eq. (A3-1) can be written as:

$$\Delta \eta_{\text{stage}} = (1-\gamma_0) \frac{\kappa-1}{\kappa} \frac{\ln(p_4^{*\text{orig}}/p_4^{*\text{new}})}{\ln(T_4^*/T_2)} \quad (A3-4)$$

or when using the ratio P_2^*/p_2 as input and yielding p_4^*/p_2 as output:

$$\Delta \eta_{\text{stage}} = (1-\gamma_0) \frac{\kappa-1}{\kappa} \frac{\ln(p_4^{*\text{orig}}/p_2/p_4^{*\text{new}}/p_2)}{\ln(T_4^*/T_2)} \quad (A3-5)$$

References

- [1] Oh, H. W., Yoon, E. S., and Chun, M. K., 1997, "An Optimum Set of Loss Models for Performance Prediction of Centrifugal Compressors," Proc. Inst. Mech. Eng., Part C: J. Mech. Eng. Sci., **211**, Part A.
- [2] Hammoud, J. A., et al., 1996, "A Method of Performance Prediction for Turbocharging Centrifugal Compressors," presented at the ASME International Congress on Fluid Dynamics & Propulsion, Cairo, Egypt, Dec.
- [3] Reneau, L. R., Johnston, J. P., and Kline, S. J., 1967, "Performance and Design of a Straight, Two-Dimensional Diffuser," ASME J. Basic Engineering, **89**.
- [4] Traupel, W., 1977, *Thermische Turbomaschinen*, Band I, Auflage 3, Springer-Verlag.
- [5] Stratford, B. S., and Beavers, G. S., 1959, "The Calculation of the Compressible Turbulent Boundary Layer in an Arbitrary Pressure Gradient—A Correlation of Certain Previous Methods," Aeronautical Research Council, R&M No. 3207, Sept.
- [6] Herbert, M. V., 1980, "A Method of Performance Prediction for Centrifugal Compressors," Aeronautical Research Council, R&M No. 3843, Feb.
- [7] Pinot, P., 1977, "Diffuser Performance at Low Area Ratio and Length/Width Ratio," Rolls-Royce Technical Note LTN 72395, Jan.
- [8] Japikse, D., 1996, "Centrifugal Compressor Design and Performance," Concepts ETI, Wilder, VT, pp. 3–42.
- [9] Greitzer, E. M., 1981, "The Stability of Pumping Systems—The Freeman Scholar Lecture," ASME J. Fluids Eng., **103**, pp. 193–242.
- [10] Hunziker, R., 1993, "Einfluss der Diffusorgeometrie auf die Instabilitätsgrenze des Radialverdichters," Dissertation ETH Zürich.

On the Development and Application of the Fast-Response Aerodynamic Probe System in Turbomachines—Part 1: The Measurement System

Peter Kupferschmied

Pascal Köppel

Christian Roduner

Georg Gyarmathy

Turbomachinery Laboratory,
Institute of Energy Technology,
ETH—Swiss Federal Institute of Technology,
8092 Zurich, Switzerland
<http://www.lsm.ethz.ch>

This contribution gives an overview of the current state, performance, and limitations of the fast-response aerodynamic probe measurement system developed at the Turbomachinery Lab of the ETH Zurich. In particular, the following topics are addressed:

- **Probe technology:** *Miniature probes with tip diameter ranging from 0.84 to 1.80 mm (one-sensor and three-sensor probes, respectively) have been developed. New technologies derived from microelectronics and micromechanics have been used to achieve an adequate packaging of the microsensor chips used. Both the sensor packaging and the sensor calibration (time-independent and time-dependent) are crucial issues for the DC accuracy of any measurement.*

- **Aerodynamic probe calibration:** *The methods used for the sensor calibration and the aerodynamic probe calibration, the pertinent automated test facilities, and the processing of the output data are briefly presented. Since these miniature probes are also capable of measuring the mean flow temperature, aspects related to the effective recovery factor and the self-heating of the probe tip are treated and some recommendations related to sensor selection are given.*

- **Measurement system and data evaluation:** *The early measurement chain described in Gossweiler et al. (1995) has evolved into the fast-response aerodynamic probe system. This automatic system incorporates dedicated measurement concepts for a higher accuracy and a more efficient operation in terms of time and failures. An overview of the data evaluation process is given.*

The fast-response aerodynamic probe system has been tested in real-sized turbomachines under industrial conditions within the temperature limits of 140°C imposed by the sensor technology (axial-flow turbofan compressor, axial-flow turbine, centrifugal compressor). These applications confirmed the potential of the system and encouraged its further development. Now, the system is routinely used in the facilities of the Turbomachinery Lab and in occasional measurement campaigns in other laboratories.

Part 2 of this contribution (Roduner et al.) will focus on the application of the fast-response aerodynamic probe system in a transonic centrifugal compressor of the ETH Turbomachinery Laboratory, while Part 3 (Köppel et al.) treats more sophisticated data analysis methods. [S0889-504X(00)01003-5]

Introduction

A better understanding of the unsteady flow phenomena such as secondary flow or rotor–stator interactions is a key to further improvements in turbomachinery. In addition to complex CFD methods, modern measurement techniques with time-resolving capabilities are necessary to determine the instantaneous flow quantities. Such systems have to satisfy numerous requirements like bandwidth (high above the blade-passing frequency of typically 5 to 12 kHz), high spatial resolution, large Mach number range (from 0.1 up to transonic), high measurement accuracy of the flow quantities, good access to the test section, and low disturbances in the investigated flow section. Furthermore, resistance to higher temperatures and large pressure ranges is of great advantage.

In this context, fast-response aerodynamic probes are a promising alternative to other time-resolved measurement techniques,

such as, hot-wire anemometry [1] or laser techniques [2]. Besides the flow angles, the Mach number, and the velocity (and unlike these complementary techniques), fast-response pressure probes can also measure both time-resolved total and static pressures. All these flow quantities are determined from the pressure levels and fluctuations at different points of the probe tip measured with miniature piezoresistive pressure sensor chips [3–8]. Another advantage of fast-response pressure probes compared to hot-wires is the probe robustness and the insensitivity of the calibration to dirt contamination. The easier access to the test section compared to optical methods is an additional asset for fast-response pressure probes.

In the last decade, a fast-response probe measurement system has been developed for turbomachinery at ETH Zurich [9], with the emphasis on a thorough characterization and optimization of all its components. The system has been successfully used in several applications under industrial conditions, e.g., in an axial-flow jet engine compressor, in a centrifugal compressor [10], and in an axial-flow turbine. Thanks to the probe design, the sensor technology, and adequate measurement concepts used, the present gen-

Contributed by the International Gas Turbine Institute and presented at the 44th International Gas Turbine and Aeroengine Congress and Exhibition, Indianapolis, Indiana, June 7–10, 1999. Manuscript received by the International Gas Turbine Institute February 1999. Paper No. 99-GT-152. Review Chair: D. C. Wisler.

eration of fast-response aerodynamic probe systems allows us to determine both the AC and DC signal parts with a good accuracy (i.e., velocity uncertainty below 1 percent).

Overview of the Measurement System

The development of a fast-response aerodynamic probe measurement technique at the ETH Turbomachinery Laboratory over the past ten years comprised on the one hand generic research on sensors, on miniature probe technology, and probe aerodynamics. On the other hand, applied research targeted the development of a complete system for time-resolved flow measurements dedicated to turbomachinery.

Joint efforts on both research paths have lead to the present generation of fast-response aerodynamic probe system. To achieve the main goals, i.e., the accurate measurement of both AC and DC parts of the flow quantities, the system was divided into three parts:

- *Hardware components*, consisting of sensors, miniature probes, calibration facilities, probe traversing systems, data acquisition electronics, probe monitoring computer system, and data evaluation and analysis computers.
- *Software components*, consisting of calibration software, probe monitoring and measurement software, and data evaluation and analysis software.
- *Methods and concepts*, which include all procedures necessary to prepare and operate the measurement system in an optimized way, to achieve accurate and reliable measurements. These methods are based on a thorough characterization of the properties of all system elements, the objectives of the measurement campaigns, and the experience gained during measurements in turbomachines.

The benefits of experience have been consistently used to improve the software and hardware elements listed above. A main objective was to facilitate the use of the system by means of software implementations, making it suitable for routine measurements.

Pressure and Temperature Measurement With Miniature Sensor Chips

Miniature-Pressure Sensor Chips. The requirements in terms of size, pressure sensitivity, and the objective of measuring not only the AC but also the DC part of the pressure signal reduce the choice to piezoresistive and capacitive pressure sensors. Preference is given to the piezoresistive, because it does not require, in contrast to the capacitive principle, any signal conditioning in the close proximity of the sensor.

However, commercially available packaged pressure sensors are too large to fit into really miniature probes. An alternative is offered by raw sensor chips derived from biomedical applications (Fig. 1). This avoids the size increase due to a double packaging. An overview of pressure sensor chip types used in fast-response aerodynamic probes is given in Table 1.

Sensor Chip Characteristics. Assuming a constant excitation current I_e in the Wheatstone bridge (Fig. 1, right), the output signal voltage depends strongly on the pressure applied on the

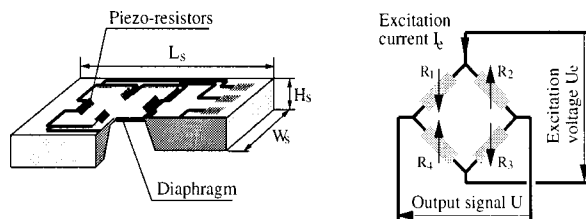


Fig. 1 Piezoresistive miniature pressure sensor chip

Table 1 Typical data of miniature differential pressure sensor chips used in fast-response aerodynamic probes (monocrystalline silicon at $T \approx 30^\circ\text{C}$)

| | Keller 1026 | Sensym P788 | NovaSensor NPD240 |
|--|-----------------|-----------------|-------------------|
| Size (L_s, W_s, H_s) [mm] | 2.0, 1.0, 0.5 | 1.7, 0.6, 0.15 | 1.0, 0.7, 0.2 |
| Surface $L_s \times W_s$ [mm ²] | 2.00 | 1.02 | 0.70 |
| Resistors on diaphragm | 4 | 4 | 2 |
| Bridge resistance R_e | 4.7 k Ω | 5.2 k Ω | 0.8 k Ω |
| Pressure sensitivity S_I ($I_e = 1$ mA) [mV/mA bar] | typ. 55 | typ. 70 | typ. 10 |
| Pressure sensitiv. S_{5mW} ($P_D = 5$ mW) [mV/bar] | typ. 58 | typ. 67 | typ. 62 |
| Spec. pressure range (linearity range) [mbar] | n.a. | 400 | -65 ... + 400 |
| Excitation voltage U_{e5mW} ($P_D = 5$ mW) [V] | ≈ 4.8 V | ≈ 5.1 V | ≈ 2.0 V |
| Dissip. power density ξ_{D5mW} [mW/mm ²] | 2.5 | 4.9 | 7.1 |

diaphragm, and weakly on temperature. On the other hand, the excitation voltage U_e is weakly dependent on the pressure, but strongly on temperature (Fig. 2). This enables the pressure sensor to measure also the diaphragm temperature.

Sensor Chip Selection Criteria. The following basic criteria are used to select the appropriate chip type and chip individuals for an application in aerodynamic probes:

- *Sensor geometry and size* in accordance with the general shape and size of the probe tip (see ‘‘Optimization of the probe geometry’’). Due to its small size, the sensor diaphragm shows a mechanical eigenfrequency between 500 and 900 kHz. The limiting frequency for turbomachinery measurements (blade-passing frequencies typically 5 to 12 kHz) may be given by the pneumatic cavity if the sensor is mounted in the probe interior (see ‘‘Dynamic sensor calibration’’).
- *Pressure sensitivity*, normalized with a given excitation current:

$$S_I = \frac{U(\Delta p, T_{\text{Ref}}) - U(0, T_{\text{Ref}})}{\Delta p \cdot I_e} \left[\frac{\text{mV}}{\text{bar mA}} \right] \quad (1)$$

This definition addresses a possible overheating of the sensor diaphragm, which would strongly reduce the pressure signal stability (DC) and increase the error on the measured flow temperature.

- *Total bridge resistance R_e* (cf. Fig. 1, right):

$$R_e = \frac{U_e}{I_e} = \frac{(R_1 + R_4) \cdot (R_2 + R_3)}{R_1 + R_2 + R_3 + R_4} \quad (2)$$

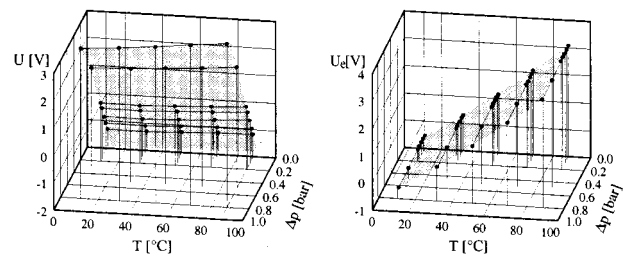


Fig. 2 Typical excitation and output signals of a piezoresistive pressure sensor chip (Sensym P788, $I_e = 1$ mA)

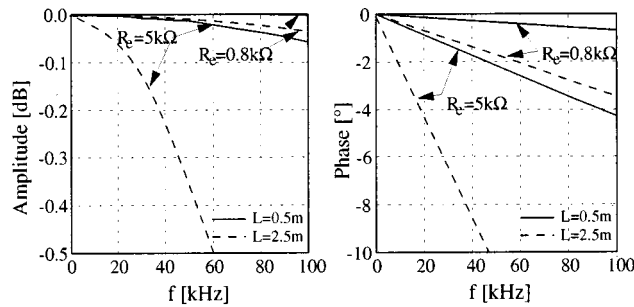


Fig. 3 Alteration of the amplitude and phase response due to bridge resistance R_e and cable length L [17]

For high-performance applications, it should be noted that higher bridge resistance R_e and long electric connections to the amplifiers affect the amplitude and phase response of the system (Fig. 3).

- *Temperature sensitivity:* The temperature dependency can be described by the temperature coefficient of the resistance TCR_e

$$TCR_e(T_m) = \frac{1}{R_e(T_m)} \frac{R_e(T_2) - R_e(T_1)}{T_2 - T_1}, \quad (3)$$

with $T_m = (T_1 + T_2)/2$. A higher coefficient provides a higher resolution of the diaphragm temperature measurement.

- *Stability of the signals:* The accurate measurement of both the AC and DC part of the pressure signal relies on stable sensor signals. The remaining errors can be corrected to some extent by applying appropriate concepts during the measurement.

- *Dissipation power density:* This parameter describes roughly the transfer of the sensor's dissipated heat to the hosting probe tip:

$$\xi_{diss} = \frac{P_{diss}}{L_s \cdot W_s}. \quad (4)$$

ξ_{diss} should be kept low to avoid an overheating of the sensor diaphragm, which would decrease the sensor stability and the accuracy of the temperature measurement.

- *Pressure limitation:* Although some preferred sensor chips are designed for differential pressures up to 350 mbar only, they can be used up to several bar. All nonlinearities occurring in this case are taken into account in the sensor calibration process. In the following, a full-scale (FS) value of 1 bar is assumed for operating the sensor types presented in Table 1.

- *Temperature limitation:* Most pressure sensor chips mounted in fast-response aerodynamic probe are machined from monocrystalline silicon. Due to the resistor noise (p - n -junction), this material sets an upper limit to the operating temperature at 120°C to 140°C, depending on the doping level. However, the materials used to build the probe (metals, ceramics, adhesives, and polymers) withstand more than 200°C.

Development Trends. Higher temperature applications require other micromachining techniques for the sensor manufacturing. For example, the commercial availability of a chip based on silicon-on-insulator (SOI) technology with comparable size and properties would allow operating temperatures up to 240°C [11].

Probe Technology

Design Process. Miniature fast-response probes are designed in an iterative process, which takes aspects from various fields into account. A general flow chart of this process and its interdependencies is shown in Fig. 4. In order to obtain optimal probe characteristics, various development objectives and design criteria have to be carefully balanced:

Mechanical Optimization of the Probe with respect to the measurement task: Straight shaft geometries are preferentially used in

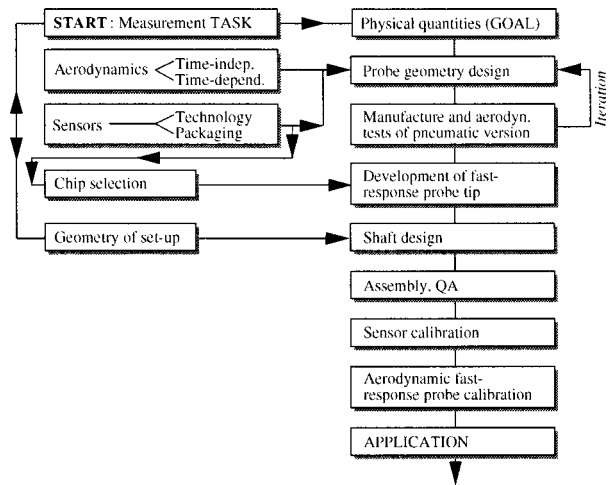


Fig. 4 Fast-response probe design and development steps

turbomachinery to facilitate access to the flow region. Mechanical design is also an issue to estimate the deflection and to prevent the probe from breaking. The following cases are considered: Aerodynamic load, flutter, excitation due to Kármán vortex street, and mechanical excitation induced by the turbomachine (e.g., components, blade passing). A structural analysis has been performed with a finite element program (NASTRAN) for each type of fast-response aerodynamic probe in order to determine the eigenfrequencies, the modes, and the expected bending. This analysis and the experience gained from applications did not reveal any significant vibrations or perturbations of the pressure measurement.

Optimization of the Probe Geometry. Over the last years, different probe geometries such as cylinders [3] wedges [5], or pyramids [12] have been used for fast-response measurements. The choice of the geometry should not only be dictated by static design considerations derived from pneumatic probes [13] but also by the time-dependent characteristics [14]: Investigations by Humm et al. [15,16] have demonstrated the strong influence of both geometry and size on the accuracy of the measured time-dependent flow quantities in highly fluctuating flow fields. Therefore, a cylindrical geometry was chosen, this being the best compromise for the fast-response aerodynamic probe for fast-response measurements in fluctuating flows.

- The lower angular sensitivity of a cylinder as compared to wedge probes does not affect this decision, assuming that a good overall resolution of the pressure measurement is provided. For example, measurements at only $M=0.2$ with a cylindrical probe (fast-response aerodynamic probe C1S18) under industrial conditions showed an angular uncertainty due to the noise over the whole measurement system below 0.04 deg.

- However, the angular range of the probe, i.e., the range over which measurements can still be correctly evaluated, is of great importance. The typically highly fluctuating flows encountered behind rotating turbomachine stages require large yaw angle tolerance ranges for radially traversed probes: Even if yaw angle fluctuations $\Delta\varphi_{max}$ of ± 20 deg seem to be a typical upper limit for ensemble-average of fluctuations, the required angular range $\Delta\varphi_{max}$ may be far larger if multisensor probe data are processed as real time series (see ‘‘Concepts of Application’’ and [17]).

- In the typical operating range ($Re=10^3 \dots 10^5$), the Reynolds dependency of cylindrical probes remains low for small probe diameters. Corrections might be necessary if the probes are operated under low pressure conditions such as encountered in blow down facilities.

- The maximum Mach number considered for past and present

applications of the fast-response aerodynamic probe was 0.8. The Mach number effect is taken into account with aerodynamic calibrations.

Miniaturization of the Probe Size. Due to the intrusion of the probes into the flow, a small size generally helps to reduce time-dependent and time-independent interactions with the flow. Experiments by Humm [16] have clearly demonstrated that the severe measurement errors due to time-dependent effects are directly proportional to probe size. Thus, the size reduction becomes of crucial importance. Furthermore, the spatial resolution of the probe increases when the distance between the pressure taps is smaller.

Optimization of Sensor Properties. This objective is a compromise between the basic sensor properties, the sensor packaging technique, and the concepts applied during the measurements. All these elements, and in particular the impact of the minimum probe size on the sensor properties, have been thoroughly investigated. As a consequence, the prototype probes, such as the four-sensor probe Z4LS25 with an outer diameter of 2.50 mm [9] have evolved toward a second probe generation, designated fast-response aerodynamic probe.

Development of Fast-Response Aerodynamic Probe. New concepts allowing the manufacturing of small series of probes were necessary for the further miniaturization of these multisensor probes. Thus, two types of cylindrical probe with an outer diameter of 1.80 mm have been developed, accommodating one and three sensors, respectively (Fig. 6, left). A fourth sensor can be implemented into the latter probe type in the future, enabling three-dimensional flow measurements.

The sensor chips are located inside the probe, with the chip diaphragm turned towards the interior (Fig. 5). This avoids damages due to particle impacts on the chip's active side. Thus fast-response aerodynamic probe were successfully operated over several hundred hours without damages.

Alternative methods for the manufacturing and the sensor packaging derived from micromechanics and microelectronics were required to scale the diameter of three-sensor probes down to 1.8 mm. For example, the geometry of the complex miniature probe parts has to be manufactured within 0.01 mm. Reliable electrical connections of the sensor chips are also important issues considering the complexity of the probe interior.

As shown later ("Measurement concepts"), the probes are operated in the differential pressure mode. By supplying the probe interior with a reference pressure close to the common pressure level of the turbomachine, sensors with per se small pressure ranges can be utilized (typically 350 mbar). This mode not only enhances the pressure sensitivity of the sensors, but also allows readjustment of the sensor's gain and zero during the application. This is of great advantage for accurate measurement of the DC signal part, considering the limited stability of microsensors due to hysteresis drift effects.

For this reason, all fast-response aerodynamic probe types are equipped with a controlled pressure supply. The smallest fast-response probe using this philosophy is the Pitot with a tip diameter of 0.84 mm (Fig. 6, right). With this design and the type of microsensor used, a sensitivity of typically 90 mV/bar (at 5 mW excitation power) before amplification can be achieved.

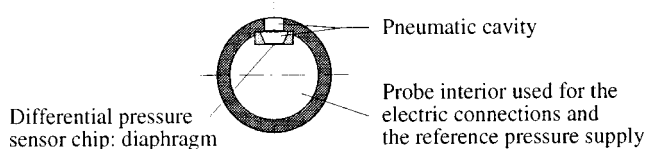


Fig. 5 Schematic view of the sensor chip location in a cylindrical fast-response probe

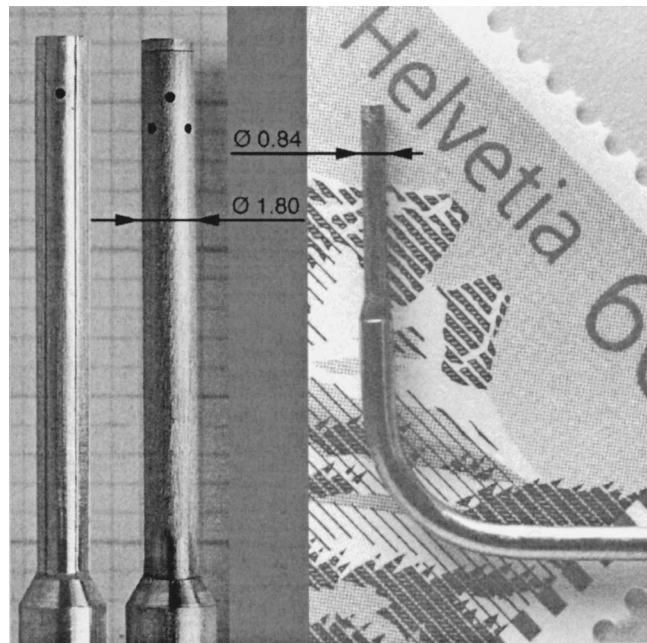


Fig. 6 Left: tips of one- and three-sensor probes C1LS18 and C3LS18 (tip diameter 1.80 mm, prismatic shaft diameter 3.0 mm); right: tip of one-sensor pitot probe P1S08 (diameter 0.84 mm)

Sensor Calibration

Introduction. Depending on the time interval considered, different issues are of interest:

- *Static properties:* What is the achievable DC (steady-state) accuracy for pressure and temperature? What are the best time intervals before the sensors have to be recalibrated (long-term properties)?
- *Dynamic properties:* What is the typical dynamic response of the pressure and the temperature reading?

After the probe manufacturing, the sensors require an accurate calibration as a function of temperature, pressure, and time. While the calibration under static conditions takes place prior to and after each measurement campaign for each probe, calibrations under dynamic conditions, i.e., with higher temperature or pressure gradients, are performed for each type of probe only and used as typical data.

Static Sensor Calibration.

Sensor Test Facility. A computer-controlled facility has been developed in which completed probes are calibrated automatically in terms of temperature and pressure. The probe tips are held in an environmental chamber where steady temperature levels are maintained over several hours (level accuracy ± 0.1 K, steadiness within ± 0.02 K). The temperature is cycled according to the temperature range required by the target application. Several successive temperature cycles are necessary to separate drift effects from thermal hysteresis. The reference pressure of the probe inner part is supplied with precision valves in seven steps from 0 to the required maximum pressure (supply fluctuations: 2.5 Pa/min for a range of 1 bar). The reference pressure is measured with ParoScientific "Digi-quartz" transducers. All electric signals are measured with a digital scanner voltmeter built at the Laboratory (maximum absolute error: 50 ppm FS). A steady, low-velocity air flow is blown on the probe tips (or sensor chips, respectively) to minimize heat convection effects in the chamber.

Typical Results for the Pressure Signal. The pressure signal

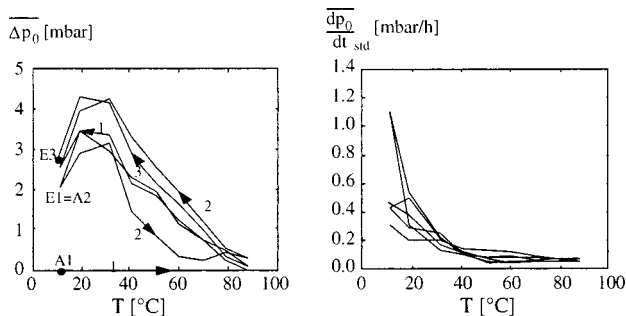


Fig. 7 Pressure signal zero and short-time stability of a typical sensor during three temperature cycles (three-sensor fast-response aerodynamic probe C3S18, $T=12 \dots 92^\circ\text{C}$, $\Delta t=510$ h)

zero changes of a sensor in a three-sensor probe are shown during three temperature cycles between 12 and 92°C and total duration of 510 h in Fig. 7 (left; the lines between the steps are drawn to make the reading easier). At every temperature step, a pressure cycle with seven levels was also applied.

All cycle data are represented as differences to the ascending part of the first temperature cycle and can be interpreted as follows:

- The plots reveal that the sensor's behavior is subject to a "training" effect: The larger differences between the first and the following loops occur not only when the probe is calibrated for the first time, but also after longer stocking periods at ambient temperature. This effect was also observed in medical catheter manufacturing [18], but could not be completely explained yet.
- A small thermal hysteresis occurs between the ascending and the descending cycle part. Apart from the first loop, the hysteresis remains within 2 mbar limits over this temperature range.
- A small drift of the zero can be observed from the end points of the loops and amounts to approximately 0.5 mbar in the second and third cycles.
- The short-term stability is defined herein as the pressure-zero change over a short observation period (in [min] or [h]):

$$\frac{dp_0}{dt} (\Delta p=0, T=\varphi) = \frac{p(t_2) - p(t_1)}{t_2 - t_1} \quad (5)$$

The standard deviation of these gradients at each temperature step during all cycles remains generally below 0.5 mbar/h (Fig. 7, right). The increase of stability of the pressure zeroes above 40°C is of practical interest for turbomachinery applications.

The creep of the pressure reading, i.e., when the probe is submitted to higher pressure levels, amounts to 0.08 percent FS (1 bar), which is an improvement compared to other designs ([8]: 0.3 percent FS). No particular procedures are required in the later

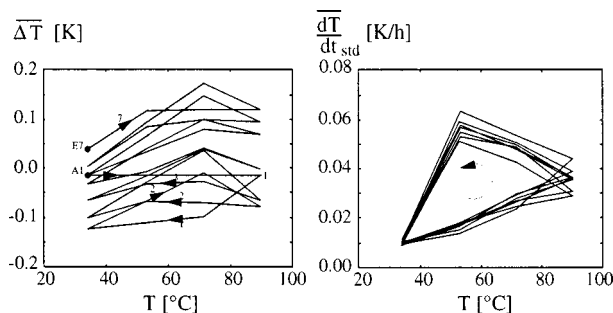


Fig. 8 Long-term stability of the indicated temperature (fast-response aerodynamic probe C1S18#12, four temperature steps of 6 h, $T=35 \dots 92^\circ\text{C}$)

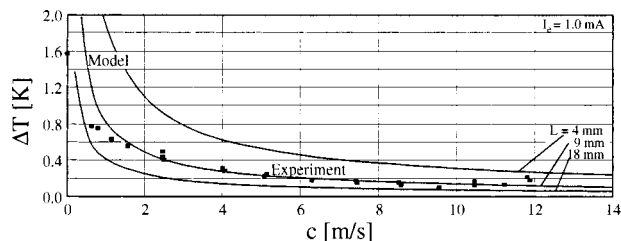


Fig. 9 Overtemperature due to self-heating of a one-sensor fast-response aerodynamic probe C1S18#13 and model results (solid lines)

application, since the fluctuating pressure part (AC) due to the flow remains smaller. The gain of the pressure signal was found to be stable, with changes of only a few per mil per year. Despite the fairly good characteristics of the sensors, the offsets and gains, including the amplifiers and the data acquisition equipment, are routinely readjusted in short time intervals during the measurement process to improve the DC accuracy of the system.

Typical Results for the Temperature Signal. Past experience in several turbomachinery applications revealed the interest for an accurate flow temperature information, besides the time-resolved pressure data. While the offset of each pressure signal can be checked and readjusted during measurements by changing the reference pressure in the probe interior, a temperature offset cannot easily be detected while the probe is inserted in the machine. Therefore, the stability of the temperature signal had to be carefully investigated. The example in Fig. 8 (left) shows the mean indicated temperature of a one-sensor probe for seven temperature cycles, plotted for each step as a difference to the indicated temperature in the ascending part of the first loop.

Compared to the raw sensor chip (i.e., before encapsulation), time-dependent effects can now be noted. However, the mean deviations remain within ± 0.15 K during the observation period of 240 h. These results are typical for this type of sensors and probes, and small in comparison to other errors arising in the flow temperature measurement.

Sensor Self-Heating. Due to the power dissipated in the sensor's resistors, the sensor diaphragms are prone to heat up. Since the heat transfer to the surrounding flow depends on the flow velocity, the measured absolute temperature level as well as the pressure signal stability are affected. Epstein [6] reported about a sensor temperature of $40\text{--}50^\circ\text{C}$ when the probe was in still air at ambient temperature. To reduce such drawbacks, his probes were then equipped with a cooling system.

In the present case, cooling would not only be problematic for the probe design (size), but also prevent the measurement of temperature. Therefore, the governing parameters for self-heating have been investigated. For cylindrical probe tip geometries, the self-heating ΔT can be described as [19]:

$$\Delta T = \frac{n R_e I_e^2}{\lambda \pi L} \frac{1}{0.62(c \cdot D/\nu)^{1/2} \text{Pr}^{1/3} + 0.3 + [1 + (0.4/\text{Pr})^{2/3}]^{1/4}} \quad (6)$$

with n being the number of sensors and D the tip diameter.

Experiments with several probes are in good agreement with Eq. (6). Cases of constant L (tip length involved in the heat exchange) are shown as lines in Fig. 9. The overtemperature of the one-sensor probe type in air at only 2 m/s amounts to 0.5 K.

Dynamic Sensor Calibration

Pressure Calibration. The recessed position of the sensor diaphragm behind the pressure tap (see Fig. 5) defines a pneumatic cavity, which affects the dynamic behavior of the pressure signal. For this reason, several configurations of sensor chips and geom-

eries relevant for this kind of probe have been investigated over a high bandwidth using a shock tube. All cylindrical types of fast-response aerodynamic probe presented herein show amplitude and phase plots with a shape similar to Fig. 10.

The first peak reveals the eigenfrequency of the cavity (90...105 kHz, according to the probe type), and the second sharper peak the sensor diaphragm eigenfrequency (650...850 kHz, depending on sensor type).

An individual calibration of each probe in a frequency range up to 100 kHz can be envisaged for higher requirements in terms of analogue bandwidth, and amplitude and phase accuracy. A numerical correction of the amplitudes and phases can then be applied to the time series in the data evaluation after measurements.

Temperature Calibration. The behavior of the pressure and temperature signals under small and large temperature gradients, e.g., occurring during the run-up of a machine or the sudden immersion in hot flows as encountered under surge conditions, has been tested for each probe type. The typical response of the indicated pressure zero is shown in Fig. 11 (left) during a gentle temperature change (maximum 4 K/min), and in Fig. 11 (right) for a temperature step of 60 K. A closer view of the data shows that a zero offset of 5 mbar is reached after 10 s. The pressure gain was found to be unaffected by dynamic temperature effects.

The response of the indicated temperature has a first-order system behavior (not shown here), with a time constant $\tau_{63\text{ percent}}$ of 13.8 s for the one-sensor fast-response aerodynamic probe C1S18 in low air velocity ($c=1.5$ m/s). The shorter time constant of 7.5 s of the three-sensor type fast-response aerodynamic probe C3S18 is due to the completely different design of the tip interior. The time constants decrease roughly by an order of magnitude if the flow velocity is increased to $M=0.5$ (other conditions unchanged). The pressure zero offset is also more influenced by temperature steps (Fig. 11, right) and might require a correction when applied in blow-down facilities or under surge conditions with larger temperature variations.

Conclusions. The dynamic pressure response has been quantified for different configurations and a bandwidth of over 500 kHz. In the present applications with an analogue bandwidth of 44

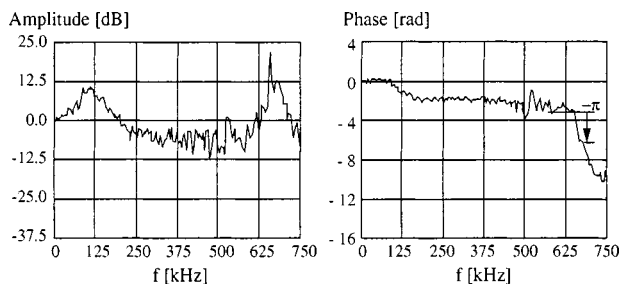


Fig. 10 Dynamic response of a miniature pressure sensor in a recessed cavity [32]

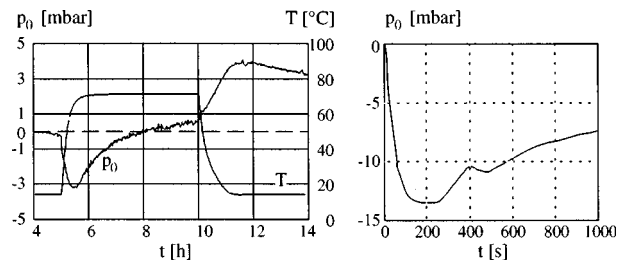


Fig. 11 Indicated pressure zero after temperature changes of ± 60 K and after a step of $+60$ K; fast-response aerodynamic probe C1S18#12

kHz, the signals do not require any corrections. However, the pressure signals could be corrected with the sensor transfer functions for higher requirements regarding the analogue bandwidth or the amplitude and phase accuracy.

The effects of temperature transients on the indicated pressure zero are rather small. A further strong reduction can be achieved by applying adequate operating concepts during the measurements (see below). Depending on the magnitude of the temperature fluctuations occurring during surge, a correction of the measured pressure zero based on experimental data may become necessary. Due to structural integrity of the probe components the flow temperature should not exceed 200°C over time periods longer than 0.5 seconds.

Finally, the time-constant of the indicated temperature (approximately 1 s at $M=0.5$) confines the probes to mean flow temperature measurements. Other techniques such as aspiration or cold wire probes are necessary for time-resolved temperature measurements in turbomachinery (e.g., [20–22]).

Modeling of the Static Sensor Calibration Data

Model-Based Reconstruction. In contrast to most other pressure sensing applications, no external electronic circuitry is used here to compensate temperature effects on the zero offset and the sensitivity of the pressure signal [23]. An active compensation method using a model-based reconstruction is applied [24], to enhance the accuracy and to avoid the larger size due to additional circuits. The sensor characteristics $U_e(T, \Delta p)$ and $U(T, \Delta p)$ are calibrated over the whole pressure and temperature range of the target application. Their integration into a numerical model enhances the accuracy remarkably.

Therefore, the sensor data $U, U_e = F(\Delta p, T)$ collected during the static calibration are used. In particular, the cycle with the lowest drift and hysteresis (see general shape in Fig. 7) will be selected. According to the voltage characteristics of piezoresistive pressure sensors (Fig. 2) and after exchanging the dependent and independent variables, the properties of each sensor can be approximated by a polynomial model:

$$\Delta p(U, U_e) = \sum_{i=0}^m \sum_{j=0}^n k_{pij} U^i U_e^j \quad (7)$$

$$T(U, U_e) = \sum_{i=0}^m \sum_{j=0}^n k_{Tij} U^i U_e^j \quad (8)$$

Model Accuracy. In most cases, the use of polynomials of second degree ($m=n=2$) satisfies the accuracy requirements.

The typical standard deviation of the residuals shown for a one-sensor probe (Fig. 12) amounts to 0.2 mb (FS=1 bar), and 0.04 K (temperature span: 60 K). Using $m=n \geq 2$, the extreme residuals stay below 1 mbar and 0.2 K respectively; see Fig. 12 (right). They contain stochastic as well as systematic measurement errors (partly due to hysteresis and drift) occurring during

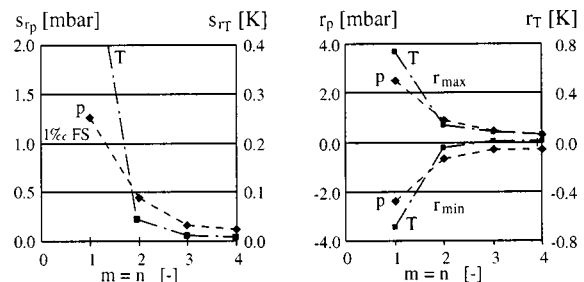


Fig. 12 Reconstructed pressure and temperature signals of fast-response aerodynamic probe C1S18#12: standard deviations of the residuals (left) and minimum and maximum residuals (right)

the calibration. Thus, polynomials of the third degree or above would improve the reconstruction accuracy in special cases only and will not be further considered.

Aerodynamic Calibration of the Probes

Introduction. Although a calibration in controlled dynamic flows would be very valuable, no known facilities can provide such conditions in air for frequencies relevant to turbomachinery. Therefore the time-dependent part of the probe aerodynamics has been investigated with large-scale model experiments in water by Humm et al. [15], and these considerations are taken into account for the real applications. Correction procedures for dynamic effects on the probes are currently investigated [25].

The calibration discussed here is confined to flows under steady-state conditions. The objective to measure also the DC level with good accuracy (i.e., velocity uncertainty <1 percent) requires extensive individual calibration of each fast-response probe in a well-known steady reference flow. Operating conditions such as Mach number must be varied. The angular range is chosen according to the intended application.

Automatic Calibration Facility. The probes are calibrated in a broad Mach number range up to 0.8 in a free jet nozzle (Fig. 13, left). The components of this facility have been designed to achieve data of an accuracy one order of magnitude higher than required in the target application. Since fast-response probes must cover large angular ranges with a fine resolution (see "Design process"), meshes with several hundred points are necessary for each probe at any Mach number level.

To make such time-consuming calibrations feasible, the calibration system is fully computer-controlled. The configuration includes three-axis probe actuators (angular uncertainty: ± 0.03 deg), multichannel pressure monitoring system, voltage scanner for probe sensors signals (absolute uncertainty: ± 50 ppm FS) and thermistors (absolute uncertainty: 0.1 K). A separate control unit is dedicated to the centrifugal compressor air supply. The air flow temperature is controlled within ± 0.05 K (at $0.2 < M < 0.7$) to avoid transient temperature effects on the probe's miniature sensors.

A calibration rate of 800 angular positions per hour can be achieved with fast-response probes. The rate with pneumatic probes is lower (120 positions/h), since pressure-lead transients have to decrease before the measurements are taken (these time delays are controlled by a statistical algorithm based on the standard deviations of the series of pressure samples taken). For example, the calibrated pressure coefficients C_p of a conventional pneumatic probe such as the three-hole probe C3P18 having the same external geometry as the three-sensor probe fast-response aerodynamic probe C3S18 are shown in Fig. 14. The overall repeatability of the C_p is typically better than ± 2 ppm.

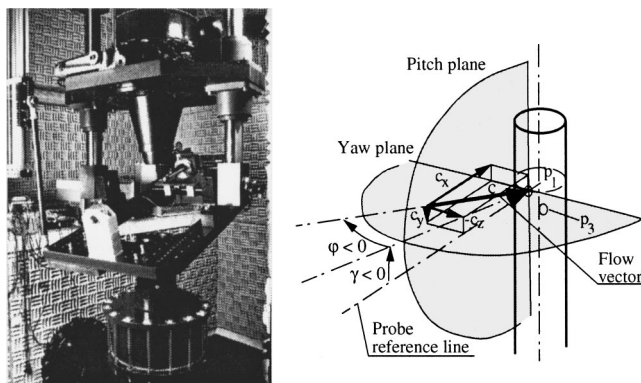


Fig. 13 Vertical-nozzle free jet facility (diameter 100 mm) for the calibration of aerodynamic probes; probe frame of reference: yaw-pitch system (as defined by [33])

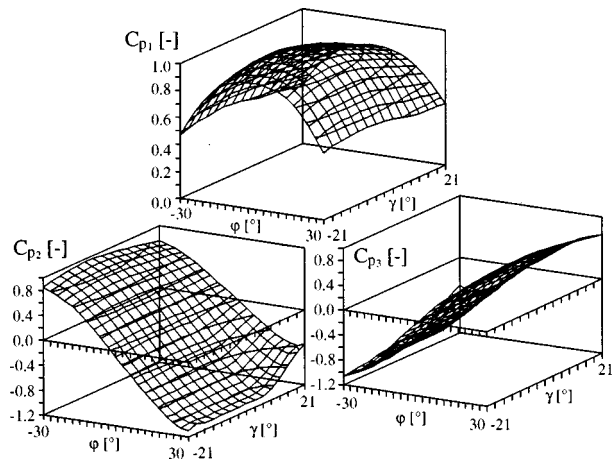


Fig. 14 Aerodynamic coefficients of a three-hole probe (C3S18P, diameter 1.80 mm, $M=0.30$). Each mesh node is a calibration point. The frame of reference of the probe is defined in Fig. 13 (right).

Calibration of the Effective Recovery Factor. To prepare the probes for measuring the (time-averaged) flow temperature additionally to the time-resolved pressure, the effective recovery factor r

$$r = \frac{h_i - h_{stat}}{h_{tot} - h_{stat}} = F(M, T_{stat}) \quad (9)$$

has to be calibrated in the jet nozzle in terms of Mach number and static temperature. The range of temperature is limited by the nozzle facility to $15^\circ\text{C} \leq T_{stat} \leq 70^\circ\text{C}$. The difference between the total flow temperature and the temperature indicated by a one-sensor probe is plotted in Fig. 15 for two typical yaw positions of the probe (stagnation point and angle where the static pressure is approximately measured). The corresponding effective recovery factor can be obtained by using the nozzle velocity c_F and the specific heat c_p as:

$$r = 1 - \frac{2c_p}{c_F^2} \cdot (T_{tot} - T_i) \quad (10)$$

Whereas the dashed line $T_{tot} - T_{stat}$ in Fig. 15 illustrates an (ideal) stagnation-point recovery factor of 1, the effective recovery factor of the one-sensor probe type fast-response aerodynamic probe C1S18 (grey lines in Fig. 15) corresponds to a recovery factor of about 0.6. This much lower value is due to heat conduction in the probe interior. Based on its definition (Eq. (10)), the uncertainty of the recovery factor increases strongly for low velocities where

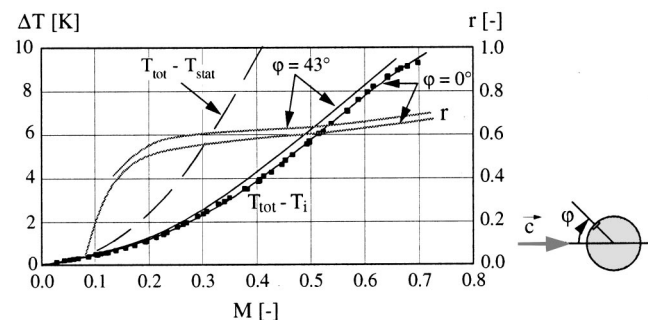


Fig. 15 Difference between flow total temperature and indicated probe temperature; resulting effective recovery factor; fast-response aerodynamic probe C1S18#12

the temperature head $T_{tot} - T_{stat}$ is low. Therefore the range below $M=0.2$ should be disregarded (Smoth [26] even recommends $M=0.3$ as a lower limit).

Modeling of the Static Aerodynamic Probe Calibration Data

Aerodynamic Coefficients. The calibration coefficients C_p obtained for every probe pressure tap are combined into an appropriate set of nondimensional aerodynamic coefficients to allow the evaluation of the physical flow quantities in the application. The choice of these coefficients is depending upon the probe geometry. For the present cylindrical probes, the coefficients have been chosen according to Krause and Dudzinski [27]. The yaw sensitivity is described by:

$$K_\varphi = \frac{p_2 - p_3}{p_1 - p_m} = K_\varphi(\varphi, \gamma, M), \quad \text{with } p_m = \frac{p_2 + p_3}{2} \quad (11)$$

The pitch sensitivity can be obtained by adding a fourth sensor in the three-sensor probe shown above (or by using the four-sensor probe Z4LS2.5 presented in [9]), enabling it to make three-dimensional measurements:

$$K_\gamma = \frac{p_2 - p_3}{p_1 - p_m} = K_\gamma(\varphi, \gamma, M). \quad (12)$$

The total pressure and static dependencies are given by

$$K_{tot} = \frac{p_{tot} - p_1}{p_1 - p_m} = K_{tot}(\varphi, \gamma, M) \quad (13)$$

and

$$K_{stat} = \frac{p_{tot} - p_{stat}}{p_1 - p_m} = K_{stat}(\varphi, \gamma, M). \quad (14)$$

Since all coefficients also depend upon the Mach number, the calibration is performed for several Mach number steps. In the Reynolds number range considered ($Re_s \cong 10^3 \dots 1.2 \times 10^5$), viscosity effects have only a marginal influence for this probe geometry, making a variation of Re unnecessary.

The angular range over which data can be evaluated is limited by the denominator $p_1 - p_m$, which shows numerical poles at yaw angles φ of approximately ± 40 deg for the cylindrical geometry with the given tap locations (Fig. 16). Basically, a data evaluation beyond the poles is possible. However, the solutions become ambiguous and must be identified and treated accordingly [17].

Conditioning of the Calibration Coefficients. To allow the more efficient direct (i.e., noniterative) evaluation of large measurement data sets, the dependent and independent variables in the calibration coefficients defined in Eqs. (11) and (12) are exchanged:

$$\varphi = F(K_\varphi, K_\gamma), \quad \text{and} \quad \gamma = F(K_\varphi, K_\gamma). \quad (15)$$

The functions F are defined by the calibration data. The data of a four-hole probe are shown in Fig. 17 to illustrate also the pitch sensitivity.

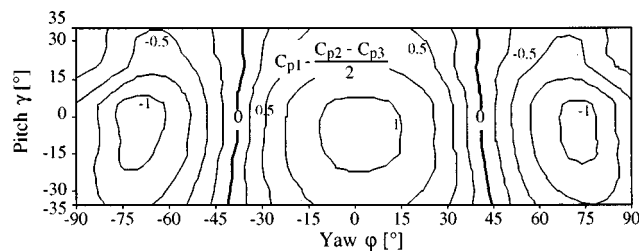


Fig. 16 Angular distribution with poles (zero lines) of the denominator $C_{p1} - (C_{p2} + C_{p3})/2$ of three-hole probe C3P18

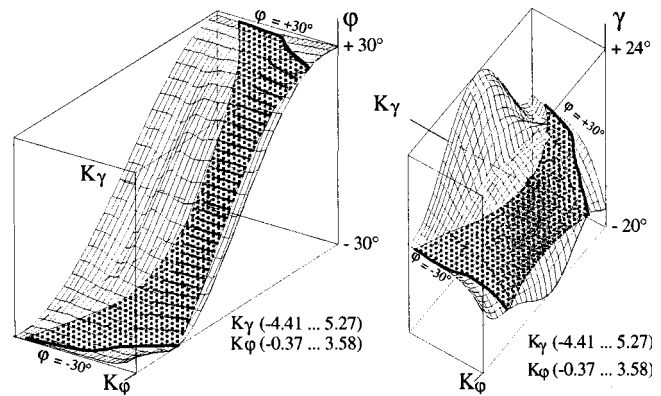


Fig. 17 Calibration surfaces $\varphi(K_\varphi, K_\gamma)$ and $\gamma(K_\varphi, K_\gamma)$ of a cylindrical four-hole probe [34]

Each dot of the “stretched” mesh represents a calibration point. The fine-lined mesh is provided for visualization purposes only and does not affect the further data evaluation.

Modeling and Accuracy. The calibration surfaces represented by Eqs. (13), (14), and (15) are approximated by bivariable polynomials. For accuracy reasons, a third variable containing the Mach number dependency is not implemented; the Mach number is determined using an interpolation between the discretely calibrated Mach number steps. The degree of the polynomial depends on both the required angular range and on the desired accuracy. Practical limits for the degree are set by the CPU time for the later evaluation and by the number of data points available (a high degree of freedom is required for the least-squares approximation to avoid numerical oscillations).

Due to the large angular range required by fast-response measurement, the coefficient surfaces are rather complicated (e.g., Fig. 17, right) making a detailed error analysis necessary. The residuals of the angle evaluation model (Eq. (15)) are shown in Fig. 18 for the cylindrical four-hole probe when the calibration data are modeled to different degrees m, n and within different angular ranges.

For the case considered, polynomial degrees $m=n=6$ are a good compromise: The standard deviation of the yaw residuals remains within 0.1 deg for all three angular ranges. The residuals of the pitch angle are more sensitive to the angular range ($0.05 \text{ deg} < r_\gamma < 0.6 \text{ deg}$). The extreme residuals (Fig. 18, bottom)

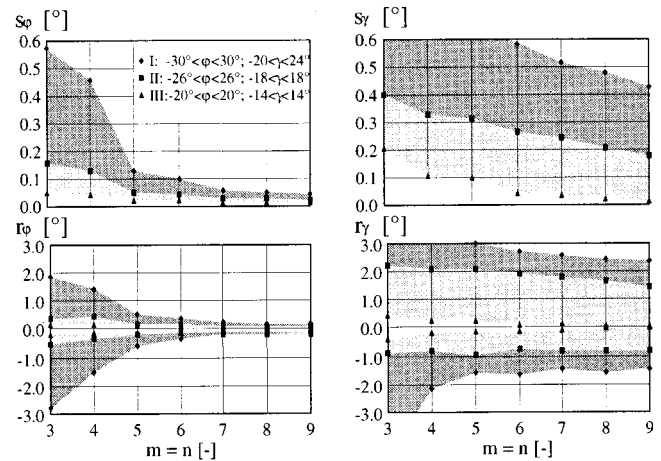


Fig. 18 Accuracy of the yaw and pitch angle evaluation model depending on polynomial degrees (m, n) and angular range

are influenced not only by stochastic calibration errors, but also by systematic differences in some regions of the surfaces.

Operating Concepts and System Configuration

Introduction. In order to achieve a high measurement accuracy with fast-response probes (e.g., velocity uncertainty below 1 percent), the system operating concepts require great attention: They specify the steps necessary in a given turbomachinery application to optimize the measurement system in terms of accuracy, reliability, and gain of information. In the following, some basic operating concepts related to the fast-response aerodynamic probe system are presented. To simplify the discussion, only two-dimensional measurements are considered.

Probe Operation Modes

One-Sensor Probes Operated in the Pseudo-Three-Sensor Mode. In this case, the fluctuating flow is measured time-resolved, at every probe traverse position under three angular positions of the probe shaft (Fig. 19). The time-averaged flow direction is preferably chosen as the center position φ_{FR} , but misalignments within a few degrees are acceptable. At this yaw position, sensor voltage data series $U_1(t)$, $U_{e1}(t)$ are collected over a large number m of rotor revolutions (typically $m = 100 \dots 300$). Then the probe shaft is rotated to the $-\Delta\varphi_{FR}$ position and data acquisition is started at some arbitrary time Δt_I , giving $U_2(t + \Delta t_I)$ and $U_{e2}(t + \Delta t_I)$. The same is done with the probe turned to the $+\Delta\varphi_{FR}$ position, giving U_3' and U_{e3}' from Δt_{II} on. A value of $\Delta\varphi_{FR} = 43$ deg is well adapted to this cylindrical probe geometry, since the pressure tap measures about the (time-averaged) static pressure at this yaw angle position.

Using the sensor calibration data, the voltages are numerically converted into pressure (p_1, p_2', p_3') and temperature (T_1, T_2', T_3') time series, the latter being virtually constant values due to the large time constant of temperature measurement. This conversion concludes the "measurement" part; see Fig. 19.

Each of the time series p_1, p_2', p_3' , typically comprises a steady ("DC") component and fluctuations ("AC") due to deterministic (rotor-position-determined) and stochastic (e.g., turbulence-induced) fluid dynamic events. By ensemble averaging [28] based on a once-per-revolution trigger signal of the turbomachine shaft, all stochastic fluctuations are statistically eliminated and there remain three time series $\tilde{p}_1, \tilde{p}_2', \tilde{p}_3'$, typical of any one rotor revolution $0 < t_N < 1/N$. In terms of shaft synchronized time t_N , these series are simultaneous and may be combined like the signals of a three-sensor probe (with sensors located at $-43, 0, +43$ deg) to give all flow quantities; see Fig. 19.

Thus, the one-sensor probe functions as a pseudo-three-sensor probe. The ensemble-average, marked with " \sim ", is defined as

$$\tilde{p}(t_n) = \frac{1}{m} \cdot \sum_{i=1}^m p_i(t_n), \quad (16)$$

with $p_i(t_n)$ as the value of the pressure sensor i at the rotor-synchronized time t_n . Pressure fluctuations nonsynchronous with the rotor (or its higher harmonics generated, e.g., by blade passing) contribute to the ensemble standard deviation:

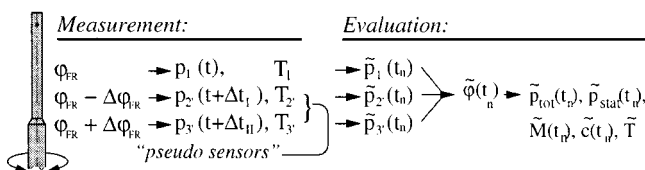


Fig. 19 One-sensor probe used in the pseudo-three-sensor mode

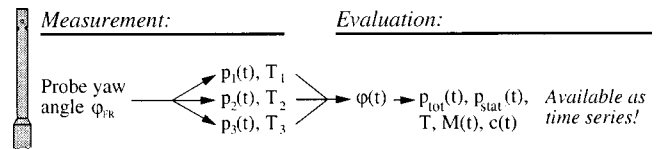


Fig. 20 Description of the three-sensor probe mode

$$\tilde{\sigma}(t_n) = \sqrt{\frac{1}{m} \cdot \sum_{i=1}^m (p_i(t_n) - \tilde{p}(t_n))^2} \quad (17)$$

The data evaluation of these pressure signals provides the time-resolved ensemble-averaged flow quantities $\tilde{\varphi}$, \tilde{p}_{tot} , \tilde{p}_{stat} , \tilde{M} , \tilde{c} and \tilde{T} at a given traverse position for one typical rotor revolution.

Determination of the pitch angle $\tilde{\gamma}$ requires at least one additional sensor or a four-sensor probe. This is not treated here in detail.

The total number m of revolutions to be sampled determines the statistical uncertainty $\tilde{\sigma}_{uea}$ of the ensemble-averaged results:

$$\tilde{\sigma}_{uea} = \frac{\tilde{\sigma}(t_n)}{\sqrt{m}} = \sqrt{\frac{\sum (x_i(t_n) - \tilde{x}(t_n))^2}{m \cdot (m-1)}} \quad (18)$$

Thus the accuracy can only be improved with the square root of the number of revolutions.

Three-Sensor Probe Mode. In this case a time-resolved measurement of the fluctuating flow is carried out at every traverse position under a single angular position φ_{FR} of the probe shaft (Fig. 20), and the signals of these sensors are collected simultaneously. Generally the center sensor tap will face the time-averaged flow direction. A correction of φ_{FR} by repeating the measurement may be necessary if the yaw angle distribution is strongly asymmetric.

The flow information is available as time series, containing also the stochastic parts of the signal, such as turbulence. The drawbacks are the larger data acquisition equipment necessary for the additional sensors and the higher complexity of the data evaluation (e.g., larger angular fluctuations due to the stochastic contents have to be treated).

The experiences with the fast-response aerodynamic probe system applied to several industrial test turbomachines have shown that one-sensor probe systems operated in the pseudo-three-sensor mode cover many demands. They are easier to handle during the calibration, the measurements, and the data processing. However, more specific investigations like stall inception or operations in blow-down test facilities, where cross-correlated time-series are necessary, require the use of multisensor probes to collect the data of each pressure tap simultaneously. Flow direction probes accommodating up to six sensors have been developed for such applications and allow any flow yaw angle around the probe to be determined [29].

Sensor Adjustments. Although the probe's sensors are thoroughly calibrated in terms of temperature and pressure to meet the application's conditions, they are prone to drift and hysteresis effects. To fulfill the accuracy requirements, periodic checks of the sensor pressure-zero $K_z(t)$ and gain $K_g(t)$ drift are necessary in short time intervals, to allow a readjustment of the calibration characteristics in Eq. (7) by applying the correction:

$$\Delta p(U, U_e, t) = K_z(t) + K_g(t) \sum_{i=0}^m \sum_{j=0}^n k_{pij} U^i U_e^j \quad (19)$$

These operations are performed briefly prior and after traversing the flow path by retracting the probe into a recessed tower, where the conditions are monitored. Figure 21 (left) shows a typical evolution of the residuals (standard deviation s_r and extreme

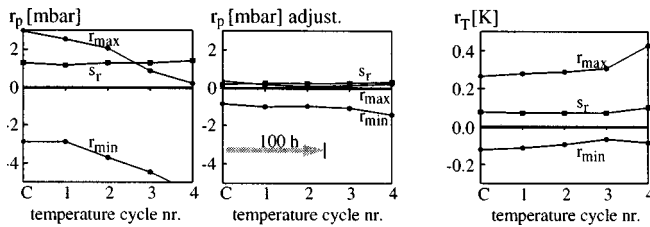


Fig. 21 Residuals of a sensor evaluation: during calibration (C) and four following temperature cycles; fast-response aerodynamic probe C1S18#12

values) of the pressure evaluation using Eq. (7) directly after calibration, and in the following four temperature cycles in the computer-controlled sensor test facility.

The residuals in Fig. 21 (center) illustrate the significant accuracy improvements when the pressure data are readjusted for each temperature cycle using Eq. (19). The temperature readings (Fig. 21, right) are not readjusted, since they were found to be stable over long time intervals.

Measurement System Configuration

Overview. A fully computer-controlled probe control system has been developed (Fig. 22). The automation of all measurement sequences ensures an optimum probe operation for accuracy and timing, and further reduces errors by performing strictly repetitive operations.

Hardware Components of the Fast-Response Aerodynamic Probe System. The system consists of the following components [17]:

- *Probe control system (PCS)* with a LabView™ software application controlling the specific measurement equipment
- *Probe pressure unit (PPU)* providing stable pressure levels to operate the sensors in the most effective pressure range independently of the pressure level in the turbomachinery flow.
- *Instrument amplifiers* in SMD technology mounted into the probe shaft end block to reduce the distance to the sensors.
- *High-speed data acquisition system* with a high gain and phase accuracy over the whole bandwidth. The rotor position reference is set by an optical trigger module.
- *High-precision two-axis probe actuators* with stepping motor controllers used to traverse the probe through the flow passage.
- *Workstation(s) for off-line data evaluation*, connected by Ethernet to the high-speed data acquisition system.

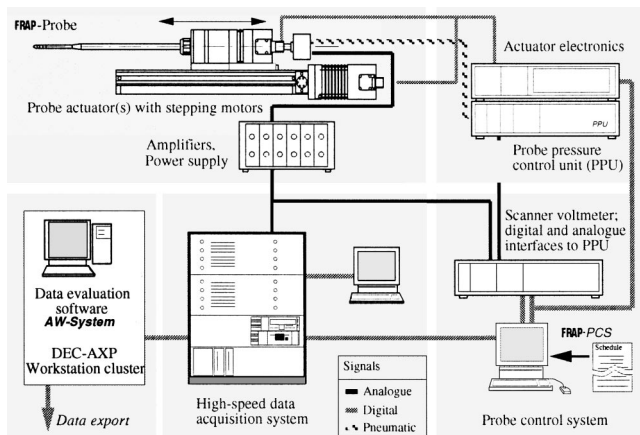


Fig. 22 Configuration of the fast-response aerodynamic probe system for time-resolved measurements in turbomachines

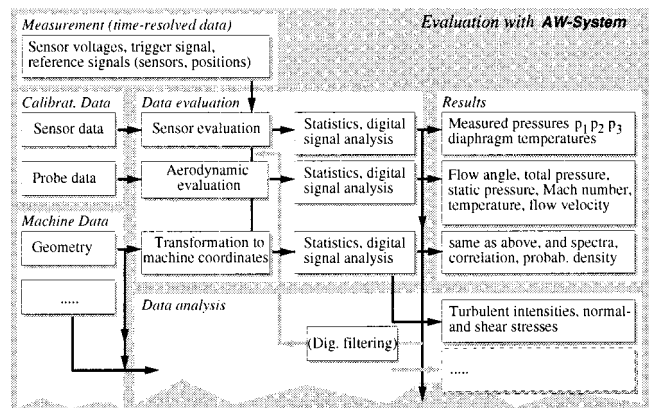


Fig. 23 Flow chart of the standard data evaluation software

System Operation. All sequences for operating automatically the probes and other equipment in the target turbomachine are programmed in a “task file.” Thus, the measurement schedule can be optimized for the task and tested prior to measurement. This way high costs due to missed measurements or even hardware damage can be conveniently avoided.

Measurement Data Evaluation

The numerical evaluation of large time-series of sensor signals, with data acquisition throughputs of typically 3.2 MB/s, to detailed distributions of flow quantities plotted over a traverse requires efficient handling and data processing capabilities. A general overview of the data evaluation is given in Fig. 23. The present software is an evolution of the “AW-System” package developed in-house specifically for large time series [30]. An open user interface provides a good interactivity, in order to monitor and control each evaluation step.

The data analysis, which aims at the detailed fluid dynamic analysis of the results and the feedback to turbomachinery development, is a further step in the data processing.

Applications in Turbomachinery

The fast-response aerodynamic probe system can be used for axial and centrifugal flow turbomachinery applications. Depending on the focus of the investigations, one-sensor probes operated as pseudo-three-sensor probes or more complex three- or four-sensor probes can be used (e.g., if cross-correlated time-series are required such as for turbulence measurements, for stall inception or in blow-down test facilities). The present operating limits are given by the maximum temperature of 140°C, the analogue bandwidth of 45 kHz, the Mach number (0.15 . . . 0.8 under atmospheric conditions, extension planned) and the flow medium (gas). Thanks to the supplied reference pressure, the system can cope with pressure levels up to several bar.

The fast-response aerodynamic probe system has been integrated in several in-house applications such as a turbulent pipe flow [31] or an axial low-speed blower. It is routinely used in the centrifugal compressor test stand “Rigi” (reported in [10], and in Parts 2 and 3 of this paper). The applications in industrial test facilities include measurements in the axial-flow test compressor of a turbojet engine and in an axial-flow research turbine (air). Close contacts with external institutions point toward an increasing interest in the quality data delivered by this technique.

Conclusions and Outlook

The development of fast-response aerodynamic probe measurement equipment at the Turbomachinery Laboratory of the ETH Zurich has resulted in a high-performance system primarily dedicated to turbomachinery applications. All components of this fast-

response aerodynamic probe system, including miniature probes, signal amplifiers, data acquisition electronics, calibration facilities, and data processing, have been individually optimized with respect to the measurement accuracy (AC and DC), to the system flexibility and the operating efficiency. In particular, the one-sensor probes operated as pseudo-three sensor probes have shown a high potential, because they combine the simple application and evaluation methods with a good return of information about the time-resolved flow patterns.

The current improvement of selected components make the fast-response aerodynamic probe system suited for more complex applications, such as detailed two-dimensional flow field measurements or even three-dimensional with four-sensor probes. The system has been successfully used for measurement campaigns in different turbomachines at the ETH and in industrial test facilities. Several new applications are planned in-house and at other institutions.

Nomenclature

| | |
|-----------|---|
| C_p | = nondimensional pressure coefficient |
| c | = flow velocity |
| c_p | = specific heat |
| D | = diameter |
| h | = enthalpy |
| I | = current |
| K | = calibration coefficient |
| L | = length |
| M | = Mach number |
| m | = shaft revolutions during data collection; polynomial exponent |
| N | = shaft revolutions per second |
| n | = number of sensors; polynomial exponent |
| P | = power |
| Pr | = Prandtl number |
| p | = pressure |
| R | = resistance |
| r | = recovery correction factor |
| S | = sensitivity |
| T | = temperature |
| t | = time |
| U | = voltage |
| W | = length |
| α | = heat transfer coefficient |
| γ | = pitch angle |
| λ | = thermal conductivity |
| ν | = kinematic viscosity |
| ξ_D | = dissipation power density |
| φ | = yaw angle |

Subscripts and superscripts

| | |
|--------|--|
| D | = dissipation |
| e | = excitation |
| FR | = fast-response |
| I | = constant current supply |
| N | = shaft synchronized |
| tot | = total |
| s | = sensor |
| stat | = static |
| \sim | = ensemble-averaged (over rotor revolutions) |

References

- [1] Hinze, J. O., 1975, *Turbulence*, 2nd ed., McGraw-Hill, New York.
- [2] Strazisar, A. J., 1993, "Laser Anemometer Applications in Turbomachinery," *Proc. 2nd Intern. Symp. on Experimental and Computational Aerothermodynamics of Internal Flows*, Prague.
- [3] Kerrebrock, J. L., Epstein, A. H., Haines, D., and Thompkins, W. T., 1974, "The MIT Blowdown Compressor Facility," *ASME J. Eng. Power*, **96**, No. 4.
- [4] Kerrebrock, J. L., Thompkins, W. T., and Epstein, A. H., 1980, "A Miniature High Frequency Sphere Probe," in: *Measurement Methods in Rotating Components of Turbomachinery*, Lakshminarayana and Runstadler, eds., ASME, New York.
- [5] Heneka, A., 1983, "Entwicklung und Erprobung einer Keilsonde für instationäre dreidim. Strömungsmessungen in Turbomaschinen," *Mitteilungen des Institutes No. 14*, ITS, University of Stuttgart, Germany [in German].
- [6] Epstein, A. H., 1985, "High Frequency Response Measurements in Turbomachinery," *Measurement Techniques in Turbomachines*, VKI Lecture Series 1985-03, VKI, Rhode-Saint-Genèse, Belgium.
- [7] Larguier, R., 1985, "Experimental Analysis Methods for Unsteady Flows in Turbomachines," ONERA, ISABE 85-7030.
- [8] Cook, S. C. P., 1989, "Development of a High Response Aerodynamic Wedge Probe and Use in a High Speed Research Compressor," *Proc. 9th Int. Symp. on Air Breathing Engines*, ISABE 89-7118, Athens.
- [9] Gossweiler, C., Kupferschmied, P., and Gyarmathy, G., 1995, "On Fast-Response Probes; Part 1—Technology, Calibration and Application to Turbomachinery," *ASME J. Turbomach.*, **117**, pp. 611–617.
- [10] Roduner, C., Köppel, P., Kupferschmied, P., and Gyarmathy, G., 1999, "Comparison of Measured Integral Averages at the Impeller Exit of a Centrifugal Compressor Measured With Both Pneumatic and Fast-Response Probes," *ASME J. Turbomach.*, **121**, pp. 609–618.
- [11] Lisek, Th., Kreutzer, M., and Wagner, B., 1996, "Surface Micromachined Piezoresistive Pressure Sensors With Step-Type Bent and Flat Membrane Structures," *IEEE Trans. on Electron. Devices*, **43**, No. 9.
- [12] Ainsworth, R. W., Allen, J. L., and Batt, J. J. M., 1995, "The Development of Fast Response Aerodynamic Probes for Flow Measurements in Turbomachinery," *ASME J. Turbomach.*, **117**, pp. 625–634.
- [13] Chue, S. H., 1975, "Pressure Probes for Fluid Measurement," *Prog. Aerosp. Sci.*, **16**, No. 2, pp. 147–223.
- [14] Kovaszny, L. S. G., Tani, I., Kawamura, M., and Fujita, H., 1981, "Instantaneous Pressure Distribution Around a Sphere in Unsteady Flow," *ASME J. Fluids Eng.*, **103**, No. 4.
- [15] Humm, H. J., Gossweiler, C., and Gyarmathy, G., 1995, "On Fast-Response Probes, Part 2: Aerodynamic Design Studies," *ASME J. Turbomach.*, **117**, No. 4, pp. 618–624.
- [16] Humm, H. J., 1996, "Optimierung der Sondengestalt für aerodynamische Messungen in hochgradig fluktuierenden Strömungen," Ph.D. Thesis ETH No. 11661, Zurich [in German].
- [17] Kupferschmied, P., 1998, "On the Methodology of Time-Resolved Measurements With Aerodynamic Probes in Compressors and Turbines," Ph.D. thesis ETH No. 12774, Zurich [in German].
- [18] Muntwyler, M., 1997, personal communication, 26. 9. 97, Unisensor AG, Rickenbach-Attikon, Switzerland.
- [19] Kupferschmied, P., Roduner, C., and Gyarmathy, G., 1998, "Some Considerations on Using Miniature Fast-Response Aerodynamic Probes for Flow Temperature Measurements," *Proc. 14th Symp. on Meas. Tech. for Transonic and Supersonic Flows in Cascades and Turbomachines*, Limerick, Ireland.
- [20] Ng, W. F., and Epstein, A. H., 1983, "High-Frequency Temperature and Pressure Probe for Unsteady Compressible Flows," *Rev. Sci. Instrum.*, **54**, No. 12, pp. 1678–1683.
- [21] Van Zante, D. E., Suder, K. L., Strazisar, A. J., and Okiishi, T. H., 1995, "An Improved Aspirating Probe for Total-Temperature and Total-Pressure Measurements in Compressor Flows," *ASME J. Turbomach.*, **117**, pp. 642–649.
- [22] Arts, T., Dénos, R., Brouckaert, J.-F., and Popp, O., 1996, "The Dual Hot Wire Aspirating Probe," *Proc. 13th Symp. on Meas. Tech. for Transonic and Sup. Flows in Cascades and Turbomachines*, Zürich.
- [23] Mallon, J. R., and Bernstein, H., 1983, "Temperature Compensation and Shunt Calibration of Semiconductor Pressure Transducers," *Proc. 12th Transducer Workshop*, Melbourne, FL.
- [24] Gossweiler, C., Humm, H. J., and Kupferschmied, P., 1990a, "The Use of Piezo-Resistive Semi-Conductor Pressure Transducers for Fast-Response Probe Measurements in Turbomachinery," *Proc. 10th Symp. on Meas. Tech. for Transonic and Supersonic Flows in Cascades and Turbomachines*, VKI Brussels.
- [25] Gizzi, W. P., and Gyarmathy, G., 1998, "Correction of Time-Dependent Aerodynamic Measurement Errors of Fast-Response Probes," *Proc. 14th Symp. on Meas. Tech. for Transonic and Supersonic Flows in Cascades and Turbomachines*, Limerick, Ireland.
- [26] Smouth, P. D., 1996, "Probe Installation and Design Criteria," *Temperature Measurements*, VKI Lecture Series 1996-07, von Karman Inst. f. Fluid Dynamics, Rhode-Saint-Genèse, Belgium.
- [27] Krause, L. N., and Dudzinski, T. J., 1969, "Flow-Direction Measurement With Fixed Position Probes in Subsonic Flows Over a Range of Reynolds Numbers," NASA TMX-52576, May.
- [28] Shreeve, R. P., Simmons, J. M., West, J. C., and Winters K. A., 1978, "Determination of Transonic Compressor Flow Field by Synchronised Sampling of Stationary Fast Response Transducers," *Nonsteady Fluid Dynamics*, D. E. Crow and J. A. Miller, eds., ASME, pp. 91–102.
- [29] Riess, W., and Walbaum, M., 1996, "Initiation and Propagation of Flow Instabilities in Multi-Stage Axial Compressor," *AGARD PEP 85th Symposium*, CP-571.
- [30] Herter, D., Chrisander, N. O., and Gossweiler, C., 1992, "AW-System—An Interactive Environment for the Evaluation of Large Time Series," *Proc. 11th Symp. on Meas. Tech. for Transonic and Supersonic Flows in Cascades and Turbomachines*, München.
- [31] Gossweiler, C., Herter, D., and Kupferschmied, P., 1992, "Fast-Response

Probe Measurements in a Turbulent Pipe Flow," *Proc. 11th Symposium on Measuring Techniques for Transonic and Supersonic Flows in Cascades and Turbomachines*, Munich.

- [32] Gossweiler, C., Humm, H. J., and Kupferschmied, P., 1990b, "Dynamic Calibration of Piezoresistive Pressure Transducers in the Frequency Range of Over 500 kHz," *Proc. Micromechanics Europe 1990*, Berlin.

- [33] Treaster, A. L., and Yocum, A. M., 1979, "The Calibration and Application of Five-Hole Probes," *ISA Trans.*, **18**, No. 3.

- [34] Kupferschmied, P., and Gossweiler, C., 1992, "Calibration, Modelling and Data Evaluation Procedures for Aerodynamic Multihole Pressure Probes on the Example of a Four Hole Probe," *Proc. 11th Symp. on Meas. Tech. for Transonic and Supersonic Flows in Cascades and Turbomachines*, Munich.

On the Development and Application of the Fast-Response Aerodynamic Probe System in Turbomachines—Part 2: Flow, Surge, and Stall in a Centrifugal Compressor

Christian Roduner

Peter Kupferschmied

Pascal Köppel

Georg Gyarmathy

Turbomachinery Laboratory,
Institute of Energy Technology,
ETH—Swiss Federal Institute of Technology,
8092 Zurich, Switzerland
e-mail: <http://www.lsm.iet.ethz.ch/lsm/>

The present paper, Part 2 of a trilogy, is primarily focussed on demonstrating the capabilities of a fast-response aerodynamic probe system configuration based on the simplest type of fast-response probe. A single cylindrical probe equipped with a single pressure sensor is used to measure absolute pressure and both velocity components in an essentially two-dimensional flow field. The probe is used in the pseudo-three-sensor mode (see Part 1). It is demonstrated that such a one-sensor probe is able to measure high-frequency rotor-governed systematic fluctuations (like blade-to-blade phenomena) alone or in combination with flow-governed low-frequency fluctuations as rotating stall (RS) and mild surge (MS). However, three-sensor probes would be needed to measure stochastic (turbulence-related) or other aperiodic velocity transients. The data shown refer to the impeller exit and the vaned diffuser of a single-stage high-subsonic centrifugal compressor. Wall-to-wall probe traverses were performed at the impeller exit and different positions along the vaned diffuser for different running conditions. The centrifugal compressor was operated under stable as well as unstable (pulsating or stalled) running conditions. The turbomachinery-oriented interpretation of these unsteady flow data is a second focus of the paper. A refined analysis of the time-resolved data will be performed in Part 3, where different spatial/temporal averaging methods are compared. Two different averaging methods were used for the data evaluation: impeller-based ensemble-averaging for blade-to-blade systematic fluctuations (with constant period length at a constant shaft speed), and flow-based class averaging for the relatively slow MS and RS with slightly variable period length. Due to the ability of fast-response probes to simultaneously measure velocity components and total and static pressure, interesting insights can be obtained into impeller and diffuser channel flow structures as well as into the time behavior of such large-domain phenomena as RS and MS. [S0889-504X(00)01103-X]

Introduction

The highly complex and fluctuating flow field at the exit of centrifugal compressor impellers and within diffuser vane channels [1–4] have been variously investigated by hot-wire techniques [2,4,5] and by optical methods [6–9]. Wall pressure transducers have been included in many rigs [5,10,11] and were crucial in detecting mild surge and rotating stall. Pressure probes equipped with fast-response transducers have been successfully used in axial-flow compressors and turbines [12,13] but were rarely used in centrifugal compressors [3].

All of these methods have strengths and weaknesses. Multiple hot-wire probes give three-dimensional comprehensive unsteady velocity information at low and moderate Mach numbers. Laser techniques are nonintrusive and suited to any Mach number. None of them are capable of yielding static or total pressure data. Fast-response pressure probes are an intrusive technique measuring pressures and the velocity vector. Miniaturization of the probe head is required in order to minimize the intrusion effects (see Part 1 of the present trilogy [14]).

The present paper is aimed at demonstrating the use of ETH's fast-response aerodynamic probe system to measure the high-frequency, high-amplitude flow fluctuations in the very inhomogeneous and turbulent flow field downstream of the impeller in a high speed subsonic centrifugal compressor. The measurements comprised steady-state as well as unstable operating conditions in the centrifugal compressor stage of the Turbomachinery Laboratory of the ETH [15,16].

An overview of compressor instabilities in general is given in [17]. In the compressor presented herein, different instabilities occur along a speedline and their sequence depends on the shaft speed level. They are described in [18] and [19]. Two types of instability are treated here. Mild surge is a system (stage and piping) instability occurring at low flow rate and positive speedline gradients. Rotating stall is an in-stage instability and could be made stationary for the stage configuration presented herein only at a low shaft speed. The probe measurements allow one to investigate the temporal and spatial evolution of large-domain surge and stall processes.

Fast-response measurements deliver large amounts of data that have to be statistically treated, condensed, and critically analyzed. A refined treatment of the data will be made in Part 3 [20] of the present trilogy.

Contributed by the International Gas Turbine Institute and presented at the 44th International Gas Turbine and Aeroengine Congress and Exhibition, Indianapolis, Indiana, June 7–10, 1999. Manuscript received by the International Gas Turbine Institute February 1999. Paper No. 99-GT-153. Review Chair: D. C. Wisler.

Test Stand

The experiments described were performed on a closed loop test rig using air; see Fig. 1. The centrifugal compressor is an unshrouded industrial stage and is driven by a 440 kW DC motor coupled to a two-stage gear box. The flow rate is controlled by a throttle and is measured by a standard orifice [21]. A flow straightener mounted in the suction pipe ensures axial flow at the stage inlet.

During measurements the inlet temperature was held at 24°C and the pressure in the suction pipe was set to 960 mbar.

Figure 2 shows the impeller and diffuser with the casing shroud removed. The configuration seen is used for all measurements described in this paper.

The main data of the impeller were:

| | |
|----------------------------------|------------------|
| Impeller tip diameter ($2r_2$) | 280 mm |
| Full/splitter blades | 11/11 (total 22) |
| Exit blade angle | 30 deg back lean |
| Exit width b | 16.8 mm |

The diffuser configuration used for the measurements consists of two parallel walls and 24 prismatic, circular-arc vanes. The leading edge blade angle $\alpha_{B\text{vane}}$ was set to 25 deg. Additional geometric data of the diffuser are given in Fig. 3.

The radial diffuser is followed by a large-diameter toroidal collecting chamber (Fig. 4, gray parts) providing a virtually uniform

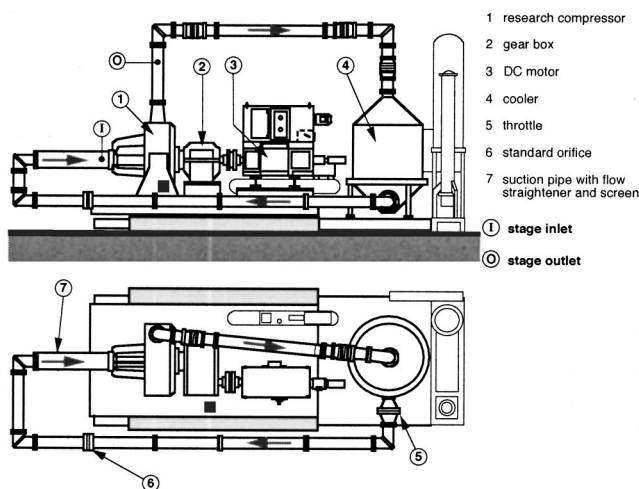


Fig. 1 General view of the centrifugal compressor test rig

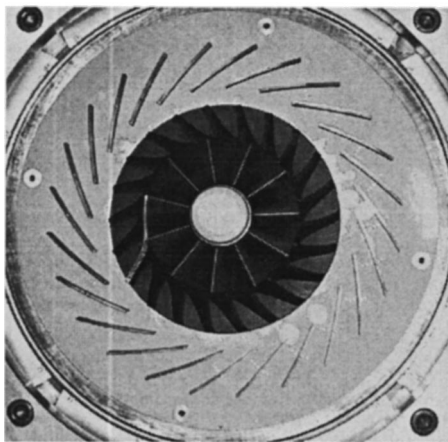


Fig. 2 View of unshrouded impeller and diffuser (configuration: 24 blades, blade angle 25 deg)

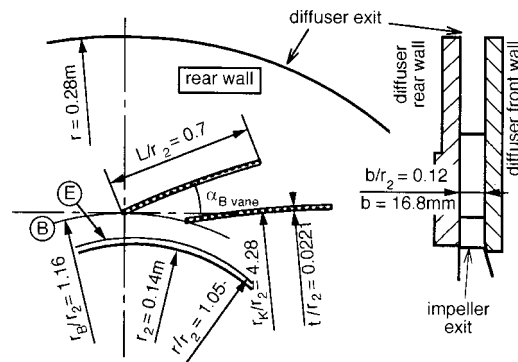


Fig. 3 Geometry of the vaned diffuser

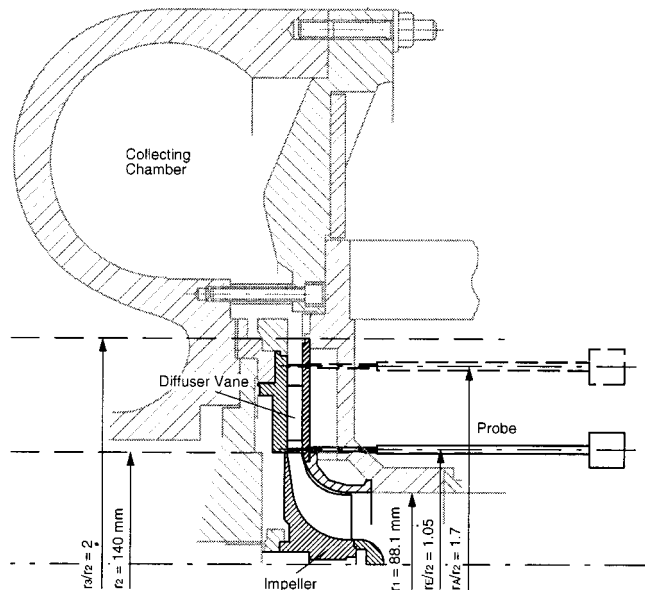


Fig. 4 Cross-sectional view of the centrifugal compressor with probe locations

circumferential pressure distribution at the impeller outlet under all throughflow conditions [15].

The overall performance of the compressor was determined by conventional wall pressure taps and temperature probes in the suction pipe and in the outlet tube. A large number of conventional wall pressure taps are located in the front and the rear diffuser walls. These wall-tap pressure data are measured with a 256-channel pressure data acquisition system. All data were collected by a μ VAX computer.

Measurement System

The probe measurement system used for this campaign is described in detail in Part 1 of this contribution.

Earlier investigations [22] have demonstrated the capabilities of the system to measure absolute flow values in centrifugal compressors like the present one with high accuracy. As a typical example, mass flow calculated from a one-sensor fast-response probe traverse at "best point" ($Mu = 0.75$) compared to the standard orifice measurements showed a difference of only 0.2 percent.

Experimental Setup

The probe actuator can be mounted (Fig. 4) on the front wall of the diffuser at eleven different positions I to XI (Fig. 5). Measure-

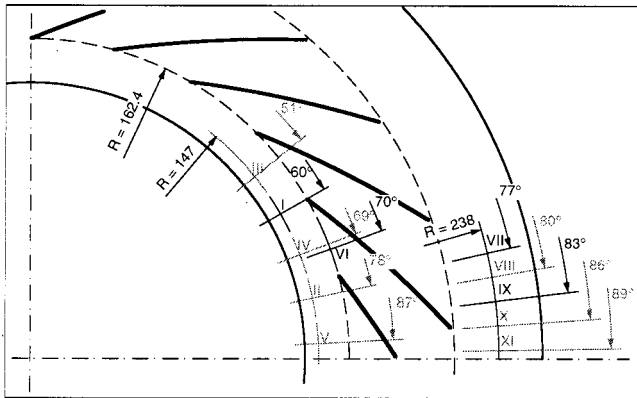


Fig. 5 Top view of the diffuser with probe positions I to XI (gray numbers: positions not discussed herein)

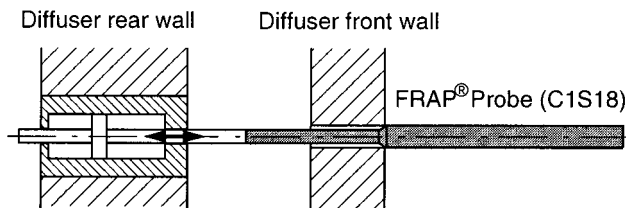


Fig. 6 Sketch of the auxiliary cylinder used to eliminate probe-end effects

ments taken at positions I, VI, VII, and IX (in Fig. 5 indicated with black) are presented and discussed in the following.

The height b of the diffuser channel is 16.8 mm. Three-component LDV measurements performed in this test rig [23] have shown that the axial component of the velocity vector is at least one order of magnitude smaller than the other two components. In the present paper the diffuser flow will be regarded as being two-dimensional.

In order to avoid introducing a three-dimensional disturbance into an otherwise two-dimensional flow field, the free-ending tip of the probe was eliminated by using a cylindrical co-axial device, shown in Fig. 6. A cylinder having the same diameter as the probe is mounted in the rear wall of the diffuser and kept in constant touch with the probe tip by a low-force pneumatic piston. Thus all probe-end effects are eliminated. This arrangement has the great advantage that no mechanical stresses are applied to the probe sensors.

Running Conditions and Performance Map

Measurements taken at four different running conditions of the test rig are presented. Two of them are located in the stable range of the performance map (Fig. 7) and two can be found in the unstable range. The four running conditions are indicated with flags in the performance map (Fig. 7). Measurements taken during stable running conditions are “best point” (BP) and “near surge” (NS). BP is the running condition at a given speed line with the highest efficiency. NS is the operating point with the lowest flow rate for stable operation at the given shaft speed “mild surge” (MS) and “rotating stall” (RS) are located in the unstable range of the performance map. During MS, systematic pressure fluctuations occur in the entire system, resulting in a periodic variation of the flow rate and the pressure rise coefficient of the compressor. A generic description of this phenomenon is given by [17]. For the present compressor MS has been investigated in detail by [24]. RS is an instability of the stage. It is measured and described by many authors [25,26]. A zone with blocked flow is traveling around in

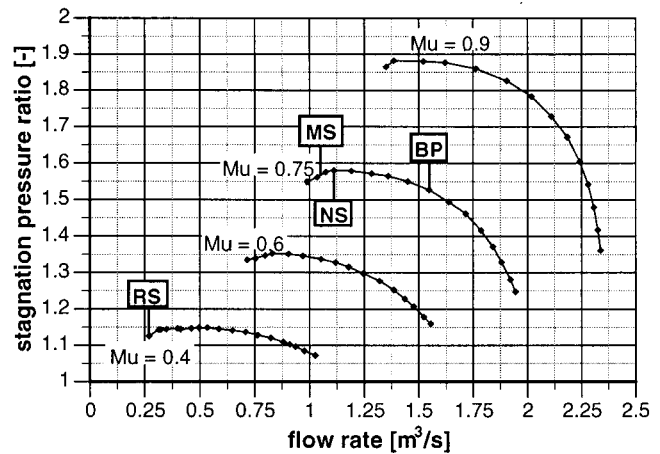


Fig. 7 Performance map of the standard configuration of the centrifugal compressor

Table 1 Overview of the operating points used

| Op. pt. | abbe- viation | \dot{V} [m ³ /s] | \dot{m} [kg/s] | ϕ [-] | rpm |
|-------------------|------------------|----------------------------------|---------------------|------------|-------|
| best point | BP | 1.553 | 1.757 | 0.0768 | 17720 |
| near surge | NS | 1.118 | 1.264 | 0.0553 | 17720 |
| mild surge | MS | 1.052 | 1.192 | 0.0521 | 17720 |
| rotating stall | RS | 0.268 | 0.306 | 0.025 | 9442 |

the circumferential direction with approximately 28 percent of the shaft speed. In the present compressor a single cell full-span rotating stall was found to exist.

For the BP, NS, and MS, points the compressor was operated at 17,720 rpm, i.e., in the high subsonic regime (corresponds to impeller tip Mach number of $Mu=0.75$). Long-time stable RS can only be observed at 9440 rpm (i.e., $Mu=0.4$) in subsonic flow regime. In Table 1 an overview of the corresponding compressor data is given for all measured operating points.

Measurement Procedures and Data Evaluation

All measurements presented herein were performed with a one-sensor fast-response probe (C1S18). In terms of the systematic fluctuations, this probe provides two-dimensional velocity, total and static pressure in steady or periodically unsteady flows. Two alternative measurement procedures were applied. In practical situations the proper procedure has to be selected according to the predominant flow effects to be investigated.

Measurement Procedure for Stable Running Conditions of the Test Rig With the Fast-Response One-Sensor Probe (C1S18). Under stable running conditions of the compressor, the unsteady effects are due to periodic nonuniformities caused by the passage of blades and the stochastic fluctuations caused by turbulence.

The probe was used at every traverse position in a pseudo-three-sensor mode: The fluctuating flow was measured time-resolved under three angular positions of the probe shaft. The middle of the three angle positions was set to the known time-averaged flow direction. For the other two angle positions the

probe was rotated (in yaw) by 43 deg to the left and the right, respectively. In each yaw position the sensor signal was measured and stored for a large number (over 240) of impeller revolutions, starting from a once per revolution trigger signal delivered by an optical trigger on the impeller shaft. By ensemble-averaging over the revolutions, all stochastic fluctuations were canceled and the deterministic ones were obtained over a period equaling one impeller revolution. (This procedure also cancels periodic fluctuations having frequencies alien to the shaft speed if such frequencies are present in the flow.) The ensemble-averaged data chains obtained for the three yaw positions simulate the periodic signals that would be delivered by a three-sensor probe having sensors in the same yaw positions [27].

The aerodynamic calibration-based data evaluation (see Part 1) of the pressure fluctuations thus obtained provides the time-resolved flow values at a given traverse position. By taking these data traverse-point by traverse-point the circumferential systematic flow fluctuations over the diffuser channel height can be plotted. Such plots are shown in Figs. 10–15.

In order to achieve a statistically significant number of events, the sampling rate of the data acquisition system was set to 200 kHz. With a rotation frequency of 295 Hz (17,720 rpm) and a data collection time of 0.82 s at each yaw position, 242 revolutions are measured and averaged. With a rotation frequency of about 295 Hz and a sampling rate of 200 kHz, a resolution of 678 data points per revolution is achieved. This results in angular resolution of about 0.5 deg. Thus each ensemble to be averaged contained $200,000 \times 0.82 / 678 = 242$ events that were considered to be statistically sufficient.

Measurement Procedure for Unstable Running Conditions of the Test Rig With the Fast-Response One-Sensor Probe (C1S18). Under unstable running conditions, a third class of flow fluctuation is superposed on blade passing and turbulence effects. This is typically of much lower frequency and may be caused by mild surge (MS) in the piping system or by rotating stall (RS) in the compressor stage.

Importantly, the period length of MS or RS is subjected to irregular variations. Ensemble averaging with respect to such irregular phenomena requires a subdivision of each period into a constant number of time steps (called classes) rather than keeping the time steps constant. This sort of ensemble averaging will be termed “class-averaging.”

Measurement Procedure During MS. Flow with MS was investigated in two ways: once with the well-known method, where the data are ensemble-averaged with a once per revolution trigger. In this case the impeller revolution is considered to be the dominant effect. Due to ensemble-averaging, turbulence and all non-harmonic flow effects are eliminated and add only noise to the averaged period event.

If MS itself is of interest; however, class-averaging has to be applied. First a trigger event is needed to identify the beginning and the end of a MS period. Here a front-wall-mounted fast-response pressure transducer (at $r^* = 1.05$) was used. The signal of this sensor was measured in parallel to the signals of the fast-response probe. During MS systematic pressure fluctuations in the system (stage, pipes, cooler) can be observed. These fluctuations are typically sinusoidal. The positive gradient zero crossing of the signal was used to determine the end of the previous and the beginning of the following MS period.

The MS frequency was 18 Hz. Therefore, a reduced sampling rate of 50 kHz of the data acquisition system was chosen. The measuring time per point was set to 10.5 s. This resulted in 196 to 197 measured MS periods per yaw position, which was statistically sufficient.

The mean period length over 196 periods is very reproducible (within ± 0.8 ppm), although individual periods may be significantly shorter or longer. Figure 8 shows the variations during 15 consecutive data collection periods.

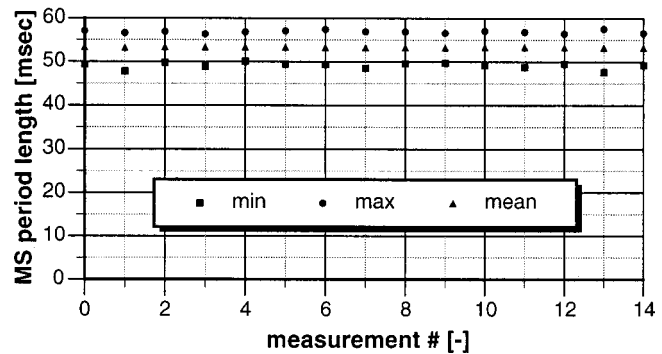


Fig. 8 Variation of the period length during MS, indicating minimum, maximum, and mean lengths of MS periods

For class-averaging, the signals obtained between two trigger events are subdivided into 2500 classes. Data points originating from the 196 different MS periods pertaining to the same class are averaged, resulting in an ensemble-averaged pressure fluctuation for one single “typical” MS period.

After class-averaging, the procedure is analogous to the pseudo-three-sensor mode. The three measured and class-averaged pressure fluctuations at each traverse position are fitted together to simulate a three-sensor probe, giving the time-resolved flow values after performing the aerodynamic evaluation (see Part 1).

Measurement Procedure During RS. The RS frequency of the stage configuration used was 42 Hz as measured by two wall pressure transducers at $r^* = 1.05$ and displaced by 44 deg, which showed a single cell propagating at 28 percent of the shaft speed. The sampling rate of the data acquisition system was set to 50 kHz. The measuring time for one position was set to 6.6 s, resulting in 280 events (rotations of the RS cell) during each measurement.

During one RS period the flow direction is changing in a large angular domain covering up to 80 deg. Since the angular range (in yaw) for an accurate evaluation of three-sensor probes is limited to 60 deg, an appropriate measurement procedure had to be established. In order to cover all potential flow directions in an unknown flow field, the following procedure was chosen. At every traverse position the time-resolved sensor data were collected at 11 yaw positions by rotating the probe in 43 deg steps over one complete revolution of the probe shaft.

For data processing in a first step, all measured sensor signals were class-averaged. Each RS period was divided into 1000 classes. In a second step, triplets of angularly neighboring measurement positions were fitted together to simulate pseudo-three-sensor probes. By this procedure nine yaw positions of a pseudo-three-sensor probe can be simulated per traverse position. The aerodynamic evaluation for all these probes is then performed. As a final step, the probe positioned in the momentary flow direction has to be identified for each phase of the RS period. Finally, the flow quantities for the whole RS can be represented by combining the flow quantities of the selected probes. This data processing mimics a three-sensor probe, which is instantaneously turned into the most appropriate yaw positions during each part of the RS period.

Flow Phenomena at Stable Operating Conditions

Measurements of Impeller-Position Ensemble-Averaged Data Taken During Stable Operation of the Stage. Although the measurements resolved the entire perimeter, only the first three blade periods following the trigger signal will be shown. Figure 9 shows the geometry at the instant the trigger signal is given. As shown, a splitter-blade wake will directly arrive at po-

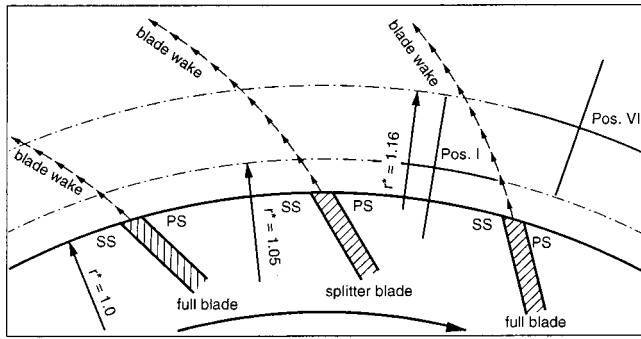


Fig. 9 Impeller blade and wake positions at the instant of triggering

sition I and a full-blade wake at position VI. The essential features of the systematic fluctuations will be discussed by taking the non-dimensional radial velocity ($C_r = c_r/u_2$) measured at positions I, VI, VII, and IX as a reference (see Fig. 5).

Best Point. In Figs. 10–13 the flow is plotted as it develops through the diffuser channel at a given running condition. The

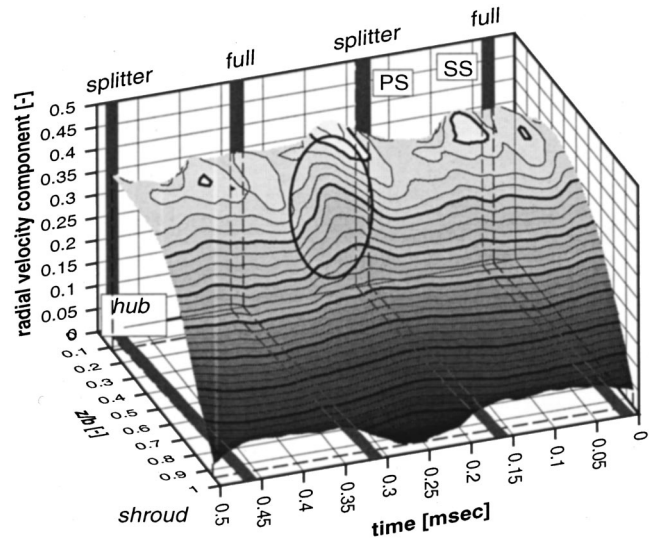


Fig. 11 As in Fig. 10 (top), measured at the leading edge radius ($r^* = 1.16$, position VI) of the diffuser vanes

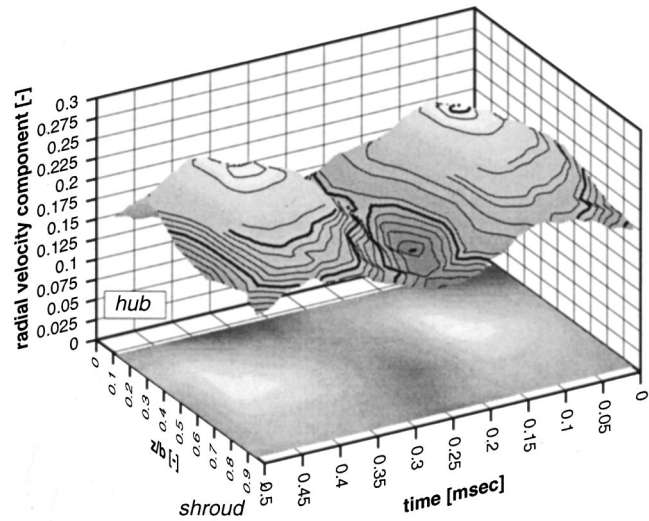
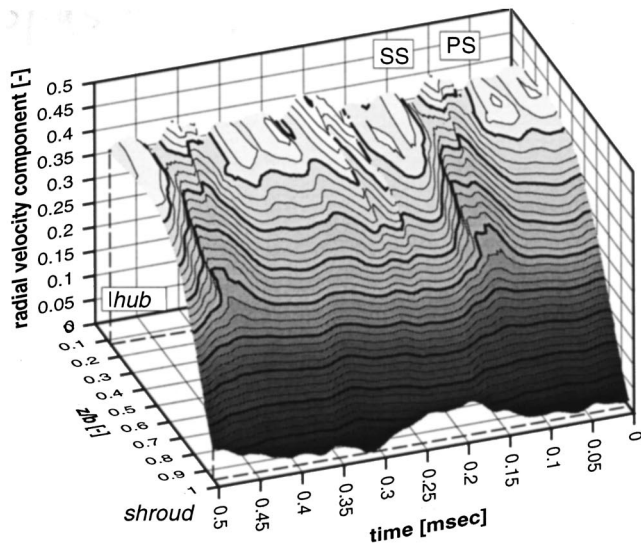


Fig. 12 As in Fig. 10 (top), measured at the diffuser outlet ($r^* = 1.70$, position VII)

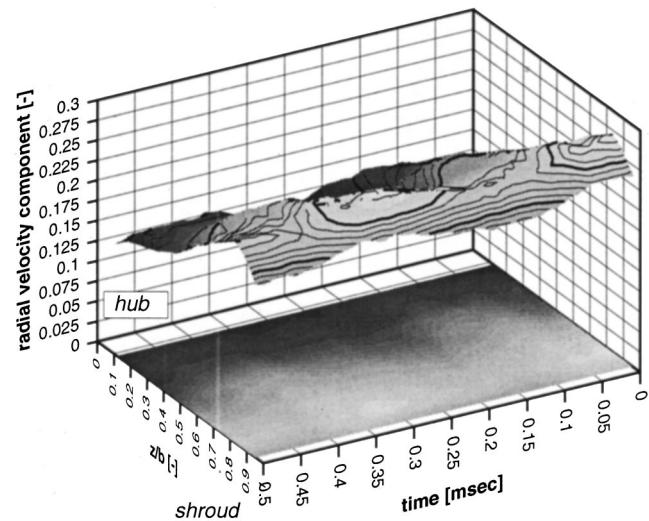
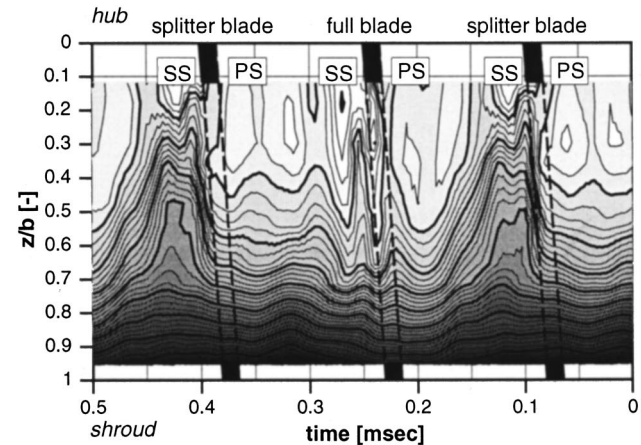


Fig. 13 Same as in Fig. 12, but measured at probe position IX

Fig. 10 Blade-resolved ensemble-averaged distribution of the radial velocity component near the impeller outlet ($r^* = 1.05$, position I). Running conditions: BP, $Mu = 0.75$. Top: three-dimensional view; bottom: top view.

operating point chosen is BP with an impeller tip Mach number of $Mu=0.75$ (see Table I). Figure 10 shows the flow at the impeller exist at a radius ratio $r^*=r_1/r_2=1.05$ in position I. In the top view the impeller blade trailing edges are overlaid on the velocity plot, indicating their instantaneous position projected radially to the radius 1.05. At 0.07 ms a splitter blade will pass, followed by a full blade at 0.22 ms. Since the probe is located at $r^*=1.05$, the wakes of the impeller blades arrive slightly time shifted; see Fig. 9. The time shift is a combined result of impeller blade back-lean and the spiraling character of flow in the relative frame, causing a shift corresponding to about 10 percent of the blade spacing at 105 percent radius.

The most apparent feature of the radial velocity distribution is a flow deficiency near the shroud ($z/b>0.8$), existing even under BP conditions. This is a typical feature of open (unshrouded) impellers of the type used here. In the hub-side half of the flow annulus, the C_r level is consistently high.

The second clear feature is the existence of wakes. They are parallel to the blade trailing edges and show a different topography for the full and the splitter blades. The full blade at the center of Fig. 10 shows a sharp narrow wake crossing the entire midportion of the annulus. This genuine blade wake is displaced leeward (i.e., toward the suction side) by about 10 percent of a blade pitch, as expected in view of the back-lean of 30 deg. Behind the splitter blades, the genuine wake is weaker and can be discerned only near the hub. Another C_r deficiency is seen to occupy about half of the blade channels leeward of the splitter blades. This is the channel wake associated with the secondary flow distribution observed and described by [3] and [2].

In Fig. 11, measurements taken at position VI (see Fig. 5), the leading edge radius of the diffuser vanes ($r^*=r_{VI}/r_2=1.16$), are presented. The impeller blades are again overlaid on the flow distribution. Starting at 0 ms, a full blade, followed by a splitter blade, passes the circumferential position of the probe (position VI, $\vartheta=70$ deg). A rough estimate shows a time delay for the flow to the blades to reach the probe of about 0.08 ms. The blade wakes are almost mixed out whereas the channel wake of the suction side of the splitter blades is still existing (encircled in Fig. 11 by an ellipse).

The characteristics of the time-averaged C_r profiles from hub to shroud are seen to remain unchanged between $r^*=1.05$ and 1.16. We can conclude that over the circumference a mixing out of the blade wakes can be observed. Every second channel wake is mixed out too. In the axial direction the radial velocity distribution remains unchanged. The mean value of the radial velocity decreases from position I to position VI, due to the increase of the area of the flow channel according to continuity.

In Figs. 12 and 13, the radial velocity component distribution at the exit of the diffuser is plotted ($r^*=r_{VII}/r_2=1.70$) as measured at two circumferentially shifted probe positions, position VII ($\vartheta=77$ deg) and position IX ($\vartheta=83$ deg). A circumferentially different behavior of the radial velocity component at $r^*=1.70$ can be seen. There is no uniform distribution at the diffuser exit, neither in the time-resolved nor in the time-mean flow distribution over the diffuser channel. Despite the totally different C_r distributions, the mass flow rate passing at position VII is only 3 percent lower than the mass flow rate passing at position IX.

The channel wakes leeward of the splitter blades are still present and can be seen at both measuring positions. During one impeller revolution, 11 such wakes pass the probe. The amplitude of C_r over time at position VII at $z/b=0.5$ is roughly four times as big as at position IX. Looking at Fig. 5, it can be seen that position VII is located downstream of a diffuser blade, whereas position IX is located downstream of the open diffuser channel. It is possible that at position VII, the flow is alternating between being part of the diffuser vane wake and the sound diffuser channel flow, resulting in high C_r fluctuations.

Comparing the C_r profiles at $r^*=1.16$ (position VI, Fig. 11) and those at $r^*=1.70$ (position IX, Fig. 13), one finds a complete

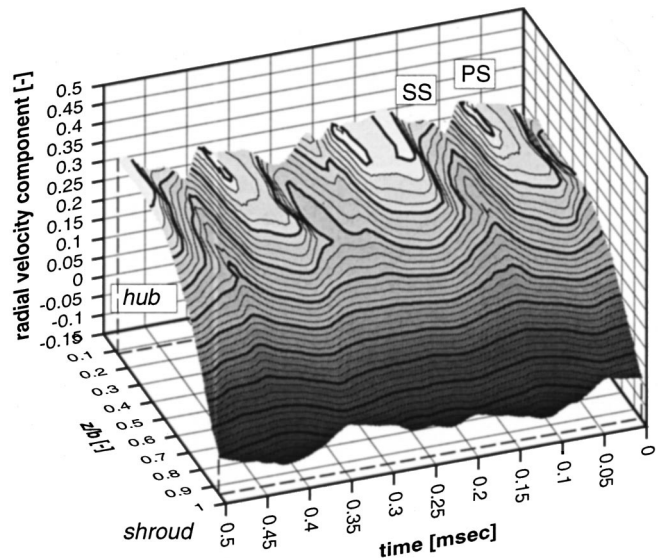


Fig. 14 Blade-resolved ensemble-averaged distribution of the radial velocity component at the impeller outlet ($r^*=1.05$, position I) under steady low-flow running conditions (NS, $Mu=0.75$)

reversal of the hub to shroud distribution. Part of this movement in the axial direction is driven by a diffuser channel vortex measured by Laser Anemometry and shown in [28].

The blade-to-blade velocity vector variation shown in Fig. 10 has been thoroughly compared to Laser-Doppler Velocimetry measurements made for the same operating conditions at the same measurements position [29] showing excellent agreement in both velocity level and flow angle.

Near Surge. Figure 14 shows the radial velocity component distribution at lower flow rate measured in position I. The running condition for this investigations was set to “near surge” NS (see Table I) with the impeller tip Mach number left unchanged at $Mu=0.75$. NS is the running condition with the lowest flow rate in the stable range of operation of this centrifugal compressor.

Compared to the best point (Fig. 10), the C_r level has decreased and a more pronounced jet/wake flow can be observed in the impeller midchannel hub region. The area of low radial momentum at the shroud has increased and close to the shroud a recirculation zone (negative C_r) can be observed. An area equal to 10 percent of the diffuser channel at the impeller exit is blocked due to this recirculation.

Flow Phenomena at Unstable Operating Conditions

Measurements of Impeller Position Ensemble-Averaged Data Taken During Unstable Operation of the Stage. For the measurements plotted in Fig. 15, the flow rate was set to MS (see Table 1). The tip speed Mach number was again $Mu=0.75$. MS is a running condition in the unstable regime of the performance map. During MS, pressure fluctuations of the whole piping system at 18 Hz are present, resulting in fluctuating flow rate and pressure rise of the stage. In Fig. 15, the ensemble-averaged radial velocity distribution over the channel position and time is plotted. For ensemble-averaging, the once per revolution signal of the impeller shaft trigger was used. Since impeller rotation and MS are non-harmonic phenomena, the pressure fluctuations of MS are statistically mixed out in this plot and contribute only to the pressure fluctuation level. The character of the C_r distribution remains unchanged compared to NS075. According to the lower flow rate at MS the C_r mean value is slightly lower.

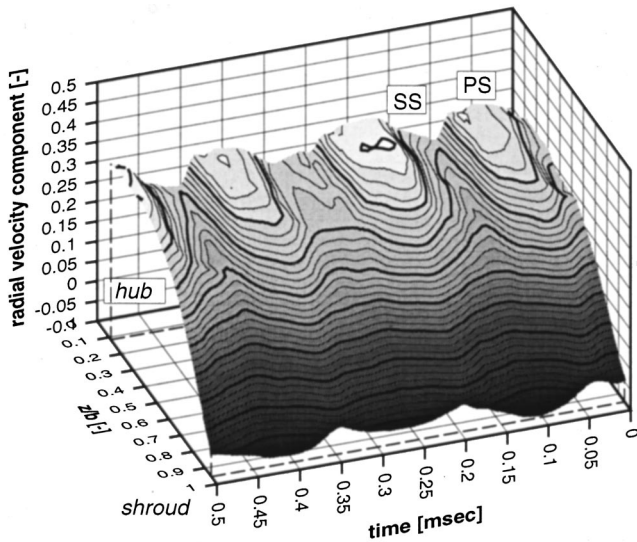


Fig. 15 Blade-resolved ensemble-averaged distribution of the radial velocity component at the impeller outlet ($r^*=1.05$, position I) during mild surge (MS, $Mu=0.75$)

Measurements of Class-Averaged Data During Unstable Running Conditions of the Stage

Measurements During MS. In order to investigate the systematic fluctuations due to mild surge, the above-described class-averaging procedure was applied to the data yielding in Fig. 15. The results are shown in Figs. 16 and 17.

Looking at the performance map (Fig. 7), the range of stable operating points is separated from the unstable range of operation by the vertex of the speedlines. To the right (negative gradients), the compressor operates stable. On the side of the positive gradients, the compressor operates in the unstable range. Here small perturbations of the flow rate lead to an input of energy into the dynamic flow system, resulting in periodic pressure and flow rate fluctuations. For detailed information see [24] and [17].

The C_r data presented in Fig. 16 were taken at midchannel at three different positions of the diffuser, at position I ($r^*=1.05$), at position VI ($r^*=1.16$), and at position IX ($r^*=1.70$). Plotted are class-averaged results for a single MS period. For each MS period about 16 impeller rotations occur according to the MS frequency of 18 Hz.

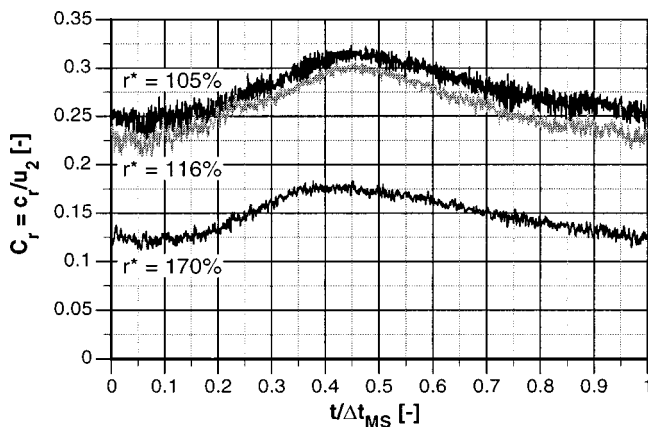


Fig. 16 Class-averaged C_r variation at midchannel, measured at three different diffuser positions plotted over one MS period (MS, $Mu=0.75$, $z/b=0.48$)

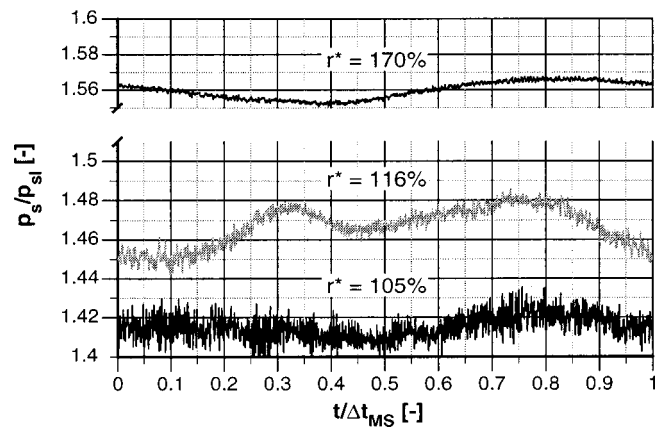


Fig. 17 Class-averaged static pressure variation during mild surge at midchannel, measured at three different diffuser positions, plotted over one MS period (MS, $Mu=0.75$, $z/b=0.48$)

The C_r distributions in Fig. 16 show an approximately harmonic variation of the mass flow during an MS period. Downstream of the diffuser, the amplitude of the C_r fluctuations is smaller due to the lower velocity level. Figure 17 shows the static pressure fluctuations during mild surge. While a sinusoidal variation is seen at diffuser exit ($r^*=1.70$), at the throat ($r^*=1.16$) higher harmonics occur. A discussion of these unsteady phenomena is beyond the scope of the present paper.

Measurements During RS. Since persistent operation in rotating stall cannot be achieved in the present compressor at $Mu=0.75$, the measurements were performed at $Mu=0.4$ where RS occurs as a stable phenomenon. At the measured running conditions (RS04, see Table 1) and the present stage configuration single cell full-span rotating stall is observed.

In Figs. 18–21 class averaged data are presented. In order to show that during RS the entire channel is temporarily blocked, in Fig. 18 the C_r distribution from hub to shroud is plotted. The data presented in Fig. 18 were measured at the impeller exit (position I). Figure 19 shows the same distribution measured at the diffuser exit at position IX. At the impeller exit as well as at the diffuser exit, a zone of blocked or reverse flow covering about 25 percent of the diffuser area can be observed. The phenomenon is seen to

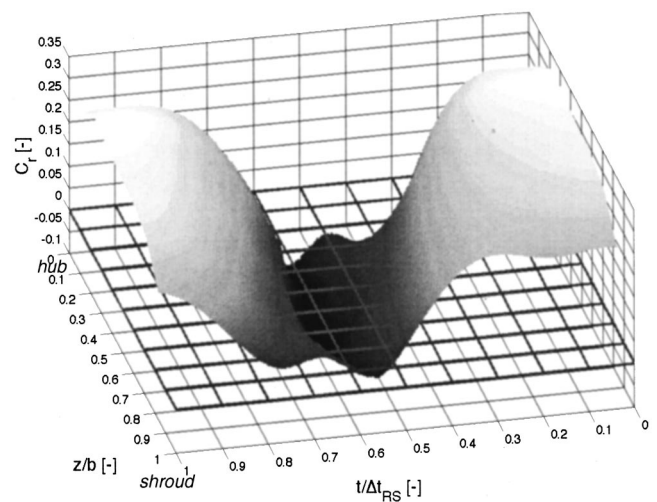


Fig. 18 Class-averaged C_r distribution measured at the impeller exit during rotating stall (position I, $r^*=1.05$) plotted over one RS period (RS, $Mu=0.4$)

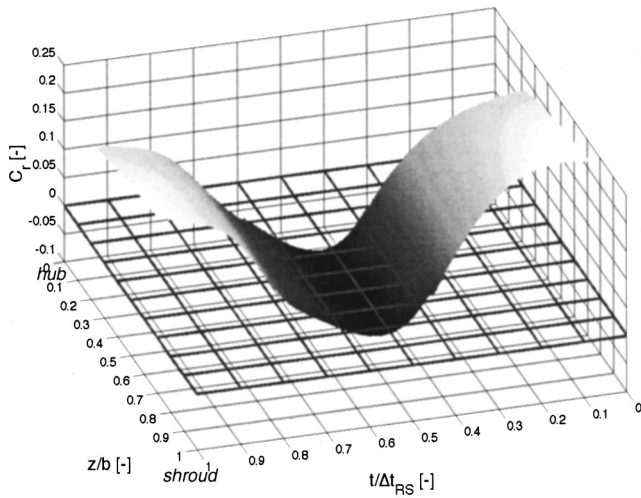


Fig. 19 As in Fig. 18, but measured at the diffuser exit (position IX, $r^* = 1.70$)

be very nearly two dimensional. The stall cell propagates around the circumference at about 28 percent of the impeller speed [19].

Figure 20 shows the midchannel radial velocity component fluctuation during one RS period at the inlet and outlet of the diffuser (probe positions I and IX, $r^* = 1.05$ and 1.70). The impeller rotates approximately three times during one revolution of the RS cell. This results in roughly 70 impeller blade passages during one RS period. In order to check the mass continuity condition, the area-weighted integrals of c_r measured at the diffuser inlet and the diffuser outlet at mid channel ($z/b = 0.48$), over one entire RS period were compared:

$$1.05 \int_0^{\Delta t_{RS}} c_{r105} dt = 1.70 \int_0^{\Delta t_{RS}} c_{r170} dt \quad (1)$$

The difference between the two integrals was found to be only 0.6 percent. This good agreement in terms of the continuity is reassuring, although a conclusive check would require an integration of hub to shroud instead of using the midchannel c_r values.

Another aspect of the curves seen in Fig. 20 is a time shift in the passage of the cell. Both the beginning and the end of reverse flow is registered earlier at the exit of the diffuser than at the inlet, the time shift being 0.06 units for the front and 0.02 units for the

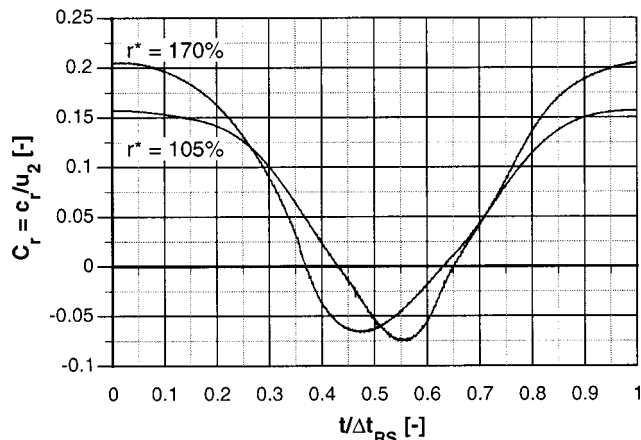


Fig. 20 Class-averaged C_r variation during rotating stall, measured at midchannel at diffuser inlet and outlet, plotted over one RS period (RS, $Mu = 0.4$, $z/b = 0.48$)

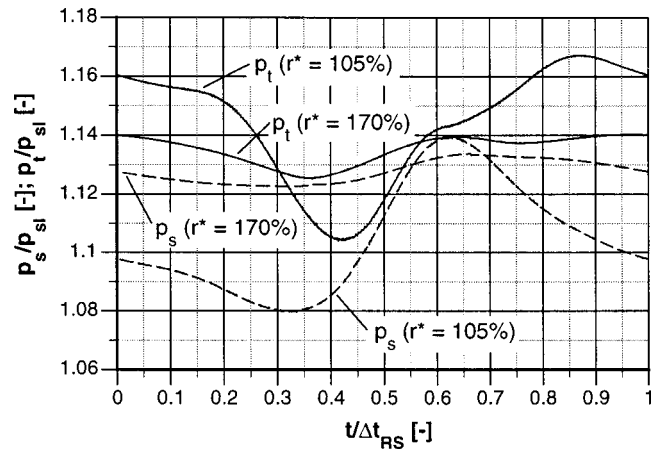


Fig. 21 Same as in Fig. 20, showing the class-averaged total and static pressure variations

rear edge of the cell. As seen in Fig. 5, the probe at position IX is exposed to flow coming from the diffuser channel preceding the channel pertaining to position I. Therefore an earlier probe response to channel blockage events is expected at diffuser exit, the shift being $1/24 = 0.042$. This corresponds well to the shift measured and is another confirmation of mass continuity.

The total and static pressure fluctuations at position I and IX, class-averaged over one RS period, are shown in Fig. 21. While the recirculating zone passes the probe, the difference between total and static pressure is very small due to the very small velocities present in the stall cell.

Seen from the absolute (nonrotating) frame of the probe located at position I ($r^* = 1.05$), the following phenomena during one RS period starting at $t/\Delta t_{RS} = 0$ can be observed. The passage of one RS period, one circumferential rotation of a RS cell, can be divided into four sections:

- Section 1 ($t/\Delta t_{RS} = 0 - 0.2$); the sound flow of nonblocked impeller channels with positive C_r values passes the probe.
- Section 2 ($t/\Delta t_{RS} = 0.2 - 0.4$); the velocity drops and the flow angle α_2 decreases. Total and static pressure decrease and approach each other.
- Section 3 ($t/\Delta t_{RS} = 0.4 - 0.65$); now the probe is downstream of the blocked impeller channels. C_r is low and negative. Dynamic head is small due to the small velocities. The static pressure is increasing.
- Section 4 ($t/\Delta t_{RS} = 0.65 - 1.0$); the stagnant fluid is blown away by sound throughflow coming from the impeller. Velocity and α_2 increase. Due to the acceleration of the flow the static pressure decreases.

In [30], RS is described as impeller–diffuser momentum exchange. This model is in good agreement with the measured pressure traces during one RS period. Stopping and reversing the forward flow is associated with a static pressure minimum in the impeller/diffuser interspace, while its restart requires a pressure maximum. The edges of the cell ($C_r = 0$) closely coincide with the static pressure peaks. The pressure amplitudes are small downstream of the diffuser.

Summary and Conclusions

The fast-response aerodynamic probe system involving a one-sensor probe, as described in Part I [14] of these contributions, has been applied to several types of systematic flow fluctuation occurring in the stable and unstable range of operation of a centrifugal compressor. The time-resolved data were analyzed and interpreted to reveal detailed features of the processes involved.

System Applicability. The probes proved to be rugged and reliable instruments giving accurate high-resolution data in a narrow (16.8 mm) diffuser channel at high shaft speeds with blade passing frequencies of typically 6.5 kHz. Normally, the sampling rate was set to 200 kHz.

A wall-to-wall traverse typically comprised 13 measuring positions with the data collecting time totaling 2.5 seconds per position (0.82 s each in three yaw angle positions), permitting statistical averaging over 242 rotor revolutions for sake of suppressing turbulence effects.

Higher collection times (10.5 s) in each of the three yaw positions were requested during mild surge where the averaging was based on about 200 low-frequency surge cycles (18 Hz), and the sampling rate was reduced to 50 kHz.

During rotating stall (42 Hz) the measurements had to include periods of back flow. Therefore, the number of yaw positions has been increased to eleven, leading to data collection times of $6.6 \times 11 = 72.6$ seconds (at 50 Hz sampling rate) per traverse position. This yielded an ample statistical basis including 280 cell rotations.

The statistically reliable and coherent (pseudo-simultaneous) measurement of velocity vector and pressure data opens up new avenues for the interpretation of unsteady flow phenomena. An example is the phase relationship between pressure and velocity fluctuations during stall and surge processes.

Flow Phenomena Observed. In the stable range, measurements performed at different diffuser positions for two operating points at the same shaft speed (BP075 and NS075) have led to following conclusions with respect to the stage investigated.

- The impeller blade wakes mix out in the vaneless region preceding the diffuser.
- Impeller channel wakes, originating from the “jet/wake” distribution, located near the suction side of the splitter blades are capable of propagating through the vaned diffuser and can still be measured at the diffuser exit while the wakes located at the suction side of the full blades are mixed out. Therefore, half of the impeller blade passing frequency is found to be predominant at the diffuser exit.
- The shroud-side circumferential zone of low radial momentum existing all around the impeller exit is mixed out as the flow passes through the diffuser.

Measurements performed in the unstable range of operation during mild surge have shown that the blade-to-blade radial velocity distributions fluctuate in level but maintain their character in time.

Measurements performed in the unstable range of operation during rotating stall have shown that

- single cell full-span RS occurs
- the measurements are in good agreement with the description of RS as a momentum exchange phenomenon proposed in [30].

It can be concluded: Even a one-sensor fast-response probe is a very valuable tool for investigating time-dependent systematic flow phenomena occurring in turbomachines. A highly detailed insight into blade passing, mild surge, or rotating stall can be achieved not only qualitatively but quantitatively with high accuracy and resolution.

Acknowledgments

The authors would like to thank the Swiss Commission for Technology and Innovation (CTI), ABB Turbo Systems Ltd., and Sulzer Turbo Ltd. for their financial support. They also wish to thank all the technical staff of the laboratory for their support.

Nomenclature

- A = area
 b = diffuser width (axial)

- C = specific speed
 c = velocity
 L = length of diffuser vane
 M = Mach number
 Mu = impeller tip speed Mach number
 m = mass flow
 p = pressure
 R = gas constant
 r = radius
 r^* = radius ratio
 t = diffuser vane thickness, time
 u = circumferential speed
 \dot{V} = flow rate
 z = axial coordinate
 α = flow angle (diffuser coordinates)
 α_{Bvane} = diffuser vane leading edge blade angle
 ϑ = circumferential diffuser position
 φ = specific flow rate = $\dot{V}_1 / (D_2^2 \cdot u_2)$

Subscripts

- 1 = impeller inlet
 2 = impeller outlet
 3 = diffuser outlet
 A = measurement position in the diffuser
 B = diffuser vane leading edge
 E = measurement position in the diffuser
 e = excitation
 I = stage inlet
 K = curvature
 r = radial
 RS = rotating stall
 MS = mild surge
 s = static
 t = total

References

- [1] Traupel, W., 1988, *Thermische Turbomaschinen I*, Springer-Verlag, Berlin, p. 307.
- [2] Dean, Jr., R. C., and Senoo, Y., 1960, “Rotating Wakes in Vaneless Diffusers,” *ASME J. Basic Eng.*, **82**, No. 3, pp. 563–574.
- [3] Eckardt, D., 1975, “Instantaneous Measurements in the Jet-Wake Discharge Flow of a Centrifugal Compressor Impeller,” *ASME J. Eng. Power*, **97**, No. 3, pp. 337–346.
- [4] Inoue, M., and Cumpsty, N. A., 1984, “Experimental Study of Centrifugal Impeller Discharge Flow in Vaneless and Vaned Diffusers,” *ASME J. Eng. Gas Turbines Power*, **106**, No. 2, pp. 455–467.
- [5] Bammert, K., and Rautenberg, M., 1974, “On the Energy Transfer in Centrifugal Compressors,” *ASME Paper No. 74-GT-121*.
- [6] Runstadler, Jr., P. W., and Dolan, F. X., 1975, “Design, Development, and Test of a Laser Velocimeter for High Speed Turbomachinery,” *Proc. LDA-Symposium*, Copenhagen.
- [7] Eckardt, D., 1976, “Detailed Flow Investigations Within a High-Speed Centrifugal Compressor Impeller,” *ASME J. Fluids Eng.*, **98**, No. 3, pp. 390–402.
- [8] Krain, H., 1981, “A Study on Centrifugal Impeller and Diffuser Flow,” *ASME J. Eng. Power*, **103**, No. 4, pp. 688–697.
- [9] Hathaway, M. D., Chriss, R. M., Wood, J. R., and Strazisar, A. J., 1993, “Experimental and Computational Investigation of the NASA Low-Speed Centrifugal Compressor Flow Field,” *ASME J. Turbomach.*, **115**, pp. 527–542.
- [10] Dean, Jr., R. C., and Young, L. R., 1977, “The Time Domain of Centrifugal Compressor and Pump Stability and Surge,” *ASME J. Fluids Eng.*, **99**, No. 1, pp. 53–63.
- [11] Kämmer, N., and Rautenberg, M., 1982, “An Experimental Investigation of Rotating Stall Flow in a Centrifugal Compressor,” *ASME Paper No. 82-GT-82*.
- [12] Ng, W. F., and Epstein, A. H., 1985, “Unsteady Losses in Transonic Compressors,” *ASME J. Eng. Gas Turbines Power*, **107**, No. 2, pp. 345–353.
- [13] Walbaum, M., and Riess, W., 1998, “Einfluss der Leitschaufel-verstellung auf die Entwicklungsformen des Rotating Stall in mehrstufigen Verdichtern,” *VDI Berichte 1425*.
- [14] Kupferschmied, P., Köppel, P., Roduner, C., and Gyarmathy, G., 2000, “On the Development and Application of the Fast-Response Aerodynamic Probe System for Turbomachines—Part 1: The Measurement System,” *ASME J. Turbomach.*, **122**, pp. 505–516.
- [15] Hunziker, R., 1993, “Einfluss der Diffusorgeometrie auf die Instabilitäts-grenze des Radialverdichters,” PhD thesis No. 10252, ETH Zürich, Switzerland.

- [16] Ribi, B., 1996, "Radialverdichter im Instabilitätsbereich," Dissertation ETH No. 11717, ETH Zürich, Switzerland.
- [17] Greitzer, E. M., 1981, "The Stability of Pumping Systems," *ASME J. Fluids Eng.*, **103**, pp. 193–242.
- [18] Hunziker, R., and Gyarmathy, G., 1994, "The Operational Stability of a Centrifugal Compressor and Its Dependence on the Characteristics of the Subcomponents," *ASME J. Turbomach.*, **116**, pp. 250–269.
- [19] Ribi, B., and Gyarmathy, G., 1993, "Impeller Rotating Stall as a Trigger for the Transition From Mild Surge to Deep Surge in a Subsonic Centrifugal Compressor," ASME Paper No. 93-GT-234.
- [20] Köppel, P., Roduner, C., Kupferschmied, P., and Gyarmathy, G., 2000, "On the Development and Application of the Fast-Response Aerodynamic Probe System for Turbomachines—Part 3: Comparison of Averaging Methods Applied to Centrifugal Compressor Measurements," *ASME J. Turbomach.*, **122**, 527–536.
- [21] DIN 1952, 1982, "Durchflussmessung mit Blenden, Düsen und Venturirohren in voll durchströmten Rohren mit Kresisquerschnitt," Beuth Verlag GmbH, Berlin, Germany.
- [22] Roduner, C., Köppel, P., Kupferschmied, P., and Gyarmathy, G., 1999, "Comparison of Measurement Data at the Impeller Exit of a Centrifugal Compressor Measured With Both Pneumatic and Fast-Response Probes," *ASME J. Turbomach.*, **121**, pp. 609–618.
- [23] Stahlecker, D., and Gyarmathy, G., 1998, "Investigations of Turbulent Flow in a Centrifugal Compressor Vaned Diffuser by 3-Component Laser Velocimetry," ASME Paper No. 98-GT-300.
- [24] Ribi, B., and Gyarmathy, G., 1999, "Energy Input of a Centrifugal Stage Into the Attached Piping System During Mild Surge," *ASME J. Eng. Gas Turbines Power*, **121**, pp. 325–334.
- [25] Jansen, W., 1964, "Rotating Stall in a Radial Vaneless Diffuser," *ASME J. Basic Eng.*, **86**, No. 4, pp. 750–758.
- [26] Kämmer, N., and Rautenberg, M., 1982, "An Experimental Investigation of Rotating Stall Flow in a Centrifugal Compressor," ASME Paper No. 82-GT-82.
- [27] Kupferschmied, P., 1998, "Zur Methodik zeitaufgelöster Messungen mit Strömungs sonden in Verdichter und Turbinen," Dissertation ETH No. 12774, ETH Zürich, Switzerland.
- [28] Stahlecker, D., Casartelli, E., and Gyarmathy, G., 1998, "Secondary Flow Field Measurements With a LDV in the Vaned Diffuser of a High-Subsonic Centrifugal Compressor," *9th International Symposium on Application of Laser Techniques to Fluid Mechanics*, Lisbon.
- [29] Gizzi, W., Roduner, C., Stahlecker, D., Köppel, P., and Gyarmathy, G., 1999, "Time Resolved Measurements With Fast-Response Probes and Laser-Doppler-Velocimetry at the Impeller Exit of a Centrifugal Compressor—A Comparison of Two Measurements Techniques," *Proc. 3rd European Conference on Turbomachinery*, London.
- [30] Gyarmathy, G., 1996, "Impeller-Diffuser Momentum Exchange During Rotating Stall," ASME Paper No. 96-WA/PID-6.

On the Development and Application of the Fast-Response Aerodynamic Probe System in Turbomachines—Part 3: Comparison of Averaging Methods Applied to Centrifugal Compressor Measurements

Pascal Köppel

Christian Roduner

Peter Kupferschmied

Georg Gyarmathy

Turbomachinery Laboratory,
Institute of Energy Technology,
ETH—Swiss Federal Institute of Technology,
8092 Zurich, Switzerland
e-mail: <http://www.lsm.iet.ethz.ch/lsm/>

Typically several hundred million data points arise from a comprehensive measurement campaign carried out in a centrifugal compressor test rig with the fast-response aerodynamic probe system (see Part 1). In order to obtain a maximum of information about the unsteady flow at any position in this turbomachine, the time-resolved data processing method has to be optimized. In contrast to the standard time-averaged flow measurements with pneumatic probes, the objective of fast-response aerodynamic probe measurements and of data processing is to extract novel information about crucial unsteady phenomena like turbulence, row-to-row interaction, modal or rotating stall, leakage flow effects, etc. In such cases, the simultaneous measurement of static and total pressures and flow vectors is of particular interest. Novel information means the analysis of averaged and time-resolved (wavelet) spectra, autocorrelations or time averages properly conserving physical fluxes, etc. Different averaging methods are applied to compress the time-dependent data measured by a one-sensor-probe (see Part 2) in a centrifugal compressor. Such results could be used for comparison with pneumatic sensor measurements and CFD calculations. The comparison of averaging methods includes the averaging theories by Traupel and by Dzung, which are compared to simple arithmetic time averaging. From there the specific stage work is calculated. In analyzing the time dependency, several ensemble-averaging procedures for flow pressure and velocity are utilized for separating deterministic from stochastic fluctuations, extracting blade row finger prints or investigating low-frequency surge type fluctuations. With respect to the selection and overall optimization of data processing methods, an overview of generic tools is given and the modularity of the processing procedures is discussed. [S0889-504X(00)01203-4]

Introduction

A measurement campaign using the fast-response aerodynamic probe technology of the ETH (fast-response aerodynamic probe) was performed in a single-stage centrifugal compressor running at two operating points “best point” (BP) and “mild surge” (MS) conditions. The complex and highly fluctuating flow field found close to the outlet of centrifugal impellers [1–3] is suitable for demonstrating the capabilities of the fast-response aerodynamic probe system, for testing measurement concepts and data processing methods, and for confronting different averaging methods.

The huge number of time-resolved data requires an optimization of data processing methods, including the optimization of measurement objectives, measurement concepts, and data evaluation software, and of the data analysis and interpretation procedures. For measurements during MS running conditions, a special triggering and traversing concept and a different ensemble definition had to be established.

Data averaging is one of the key topics in data processing [4–6]. In the first part of this contribution, the ensemble-averaging

methods, including circumferential, blade-to-blade ensemble [7,8] and flow-based averaging methods (see Part 2 [9]) will be compared. Using these, information about deterministic (related, for example to rotor position) and stochastic (related, for example, to turbulence) fluctuations can be gained and the harmonic time-dependent characteristics of the data can be preserved. In the second part, the over-simplified arithmetic averaging is compared with the physically founded averaging methods of [1] and [10,11]. In these methods, the averages of physical conserved flow quantities comply with the conservation equations such as momentum balance, mass balance, moment of momentum balance or energy balance.

Additionally, the influence of different averaging methods on the value of the stage work is presented.

Test Rig, Instrumentation, and Measurement System

The closed-loop test rig where the experiments were carried out is described in more detail in Part 2 [9] of this contribution and in [12]. The centrifugal compressor Fig. 1 is a standard industrial stage. The present measurements were made at a shaft speed of 17,720 rpm at two running conditions given in Table 1. The main data of the impeller were:

Contributed by the International Gas Turbine Institute and presented at the 44th International Gas Turbine and Aeroengine Congress and Exhibition, Indianapolis, Indiana, June 7–10, 1999. Manuscript received by the International Gas Turbine Institute February 1999. Paper No. 99-GT-154. Review Chair: D. C. Wisler.

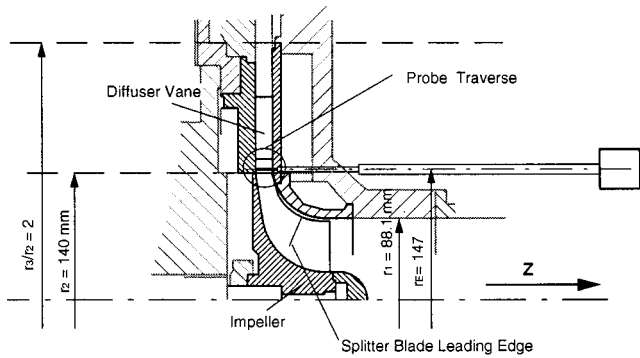


Fig. 1 Cross-sectional view of the centrifugal compressor with fast-response aerodynamic probe

Table 1 Operating points of the centrifugal compressor for the measurements presented

| | „best point“ (BP) | „mild surge“ (MS) |
|-------------------------------|----------------------|----------------------|
| RPM | 17720 | 17720 |
| \dot{V} [m ³ /s] | 1.553 | 1.052 |
| \dot{m} [kg/s] | 1.757 | 1.192 |
| φ [-] | 0.0768 | 0.0521 |

Impeller tip diameter ($2r_2$) 280 mm
 Full/splitter blades 11/11 (total 22)
 Exit blade angle 30 deg back lean
 Exit width b 16.8 mm
 Diffuser vanes 24
 Diffuser vane inlet angle 25 deg from tangential

Every second impeller blade being different (“full” versus “splitter,” see Fig. 1), every second impeller channel will have a noticeably different exit flow. The radial diffuser has parallel plane walls and is followed by a large toroidal collecting chamber (not shown) providing a virtually uniform circumferential pressure distribution at the diffuser outlet [13].

Measurement System

Aerodynamic Probes. The measurements treated herein were carried out by our fast-response aerodynamic probes. More details about the fast-response aerodynamic probe system are given in Part 1 [14] of this contribution and in [15,16].

The straight cylindrical fast-response aerodynamic probe one-sensor probes used here (Fig. 1) have a tip diameter of 1.8 mm with one piezoresistive pressure sensor chip inside the probe. The useful temperature limit of the sensor is about 140°C. The uncertainty of the pressure measurement is typically 0.2 mbar (standard deviation) after adjustment; i.e., about 0.09 percent of the dynamic head in the present case. The sampling frequency of the signals is 200 kHz maximum and the useful frequency bandwidth is 44 kHz after signal filtering with an analog anti-aliasing filter, in contrast to the 6.5 kHz blade passing frequency. The sensor calibration, the aerodynamic probe calibration, and the operating concepts are described in more detail in Part 1 [14] and Kupferschmied [17,18].

Probe Control and Data Acquisition. To be able to measure with the fast-response aerodynamic probe system in special flow conditions (e.g., during MS in the compressor system) complex measurement procedures are necessary. These procedures must

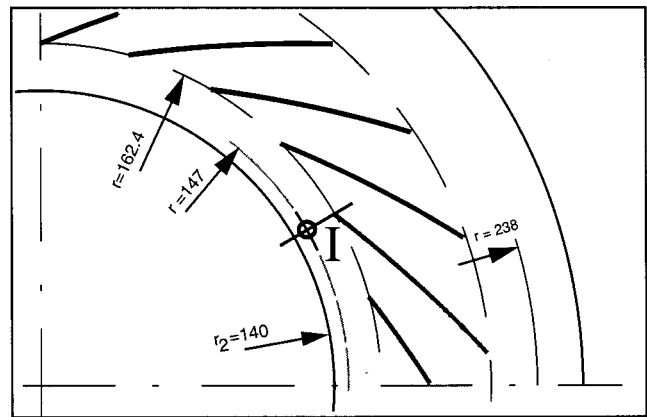


Fig. 2 Top view of the diffuser showing probe position I

comply with the objectives and requirements of the data analysis and are called measurement concepts in the following. To achieve high accuracy and good repeatability, a highly automated operating system is required. The probe control unit, the reference pressure control unit, and all auxiliaries are computer controlled.

Experimental Setup and Measurement Procedure

The probe was mounted at Position I near the exit of the impeller, Fig. 2, for the present measurements. Flow traverses are made by moving the probe in the axial direction with the sensor tap moving from the rear to the front wall in 13 positions, Fig. 1. Only five traverse points were taken for the measurements during MS.

As described in Stahlecker and Gyarmathy [19], high circumferential and radial velocity components exist at position I and the axial component is low (nearly planar flow). This justifies the use of a one-sensor fast-response probe in a pseudo-three-sensor mode (see Parts 1 and 2 [9,14]) to provide the two-dimensional velocity components only.

Data Processing: Conversion and Analysis of Time-Resolved Data

Fast-Response Aerodynamic Probe Data Processing. In this measurement campaign, more than 280 million data points were collected. The processing of these has to consider several requirements, such as handling by suitable software programs, conversion of the signals from voltage to flow quantities, and appropriate presentation of the results. To compare the time-

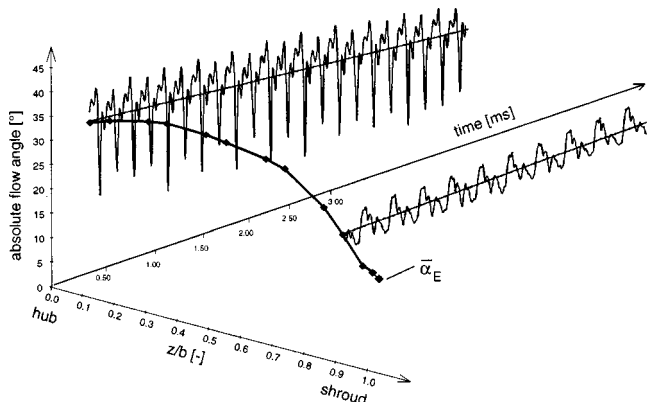


Fig. 3 Example: Compression of the time-resolved absolute flow angle α_E into the time-averaged distribution of α_E over the traverse

resolved flow quantities, such as velocity or flow angle, with time-mean data measured with pneumatic probes data averaging methods are useful to compress the data mound. Figure 3 shows the time-averaged flow angle variation across the flow channel in the foreground. To obtain the time-averaged data point at any one traverse position, nearly a million pressure values were measured, converted into flow angle values, and suitably averaged to give the black dots shown. A short part of the time-resolved value chains (about 0.5 percent) are indicated for two of the dots.

Conceptual Questions. The example in Fig. 3 shows the amount of information contained in the measured fast-response aerodynamic probe data. A lot of questions arise in connection with such large amounts of data. Some questions are more of generic nature:

- What information can be gained from the measured data?
- How to get a maximum of information?
- What can fast-response aerodynamic probe data be used for?

More specific questions are:

- Which flow quantities can be obtained and what are the uncertainties?
- How should the flow quantities be averaged?
- Which quantities of turbulence are measurable?
- Are there unsteady physical phenomena that cannot be detected?

Questions with respect to the organizational procedures are:

- How should a measurement campaign be planned and performed for specific objectives?
- What are the experiences from fast-response aerodynamic probe measurement campaigns?
- How can the costs of a measurement campaign be optimized with appropriate measurement concepts?

Objectives of the Measurement Campaign. The objectives will determine measurement concepts, the data to be obtained, and their refined evaluation. In the present measurement campaign in the centrifugal compressor, two classes of objectives have been set: one concerning the measurement system, and the other the physical flow situation in the machine. Class 1 objectives were:

- To test the in-house developed fast-response aerodynamic probe technology in a high-speed turbomachine.
- To compare different averaging methods for the stage work, the static pressure, and the radial velocity obtained at the impeller outlet.
- To explore flow phenomena such as “mild surge” and rotating stall by means of special measurement concepts and averaging methods. (Only MS data are discussed in Part 3.)

Class 2 objectives were:

- To make detailed time-resolved measurement at the impeller outlet and at different points in a vaned diffuser channel.
- To provide experimental boundary conditions for CFD calculations in the vaned diffuser [20].

Measurement Concepts Used. The measurement concept must define the probe type, and the traverses to be made. It must take into account the key data of the machine, hence determine the characteristic data of the measurement campaign.

Probe Type and Probe Operation Mode. For the objectives defined above, a one-sensor fast-response probe used in a pseudo-three-sensor mode has been chosen. At every traverse position, the fluctuating flow was measured time-resolved under three angular positions of the probe shaft. The middle of the three angle positions was set to the time-averaged flow direction at the local axial position. For the other two angle positions, the probe was rotated (in yaw) by ± 43 deg. A once per revolution signal from

the trigger was used to fit the sensor signals together to a quasi-synchronous pseudo-three-sensor probe (Part 1 [14]).

Traversing. According to the objectives of the measurement campaign, it is necessary to get the time-dependent information over the height of the diffuser channel in axial direction. To resolve gradients in the diffuser channel, the traverse points have to be close to each other. Per traverse, 13 traverse points were taken at each yaw position. The measurements presented in this paper were taken at position I (Fig. 2).

Key Compressor Data and Planning the Measurement Campaign. Table 2 shows the parameter choices associated with the objectives of the measurement campaign and the key data of the compressor.

In the first part of Table 2, the dominant frequencies of the compressor and the resulting setting ranges for the measurement system are listed. In the middle part on the left side, the maximum peaks of the compressor flow quantities are listed. On the right side the resulting resolution of the sensor signals and the calibration ranges are determined. In the bottom part the spatial resolution by the probe and the expected spatial dimension of turbulence are listed.

The following considerations are included in Table 2. The measurement grid is determined by the number of traverse points (13) in the z direction and by m , the number of samples between the passage of two blades, which is defined by the rotational speed of the machine, number of blades and the sampling frequency as $m = f_s / (n \cdot N)$. The averaged magnitude of the dynamic head of 200 mbar leads to signal to noise ratio of 70 dB. This means that the full dynamics of the measurement electronics had to be used. The measuring time span influences the accuracy a of the ensemble-averaged pressure values $p_1(t)$, $p_2(t)$, $p_3(t)$ by way of Eq. (1), where a is the confidential interval. The confidential interval a indicates the statistical certainty of the ensemble-averaged pressure values \bar{p} ,

Table 2 Characteristic data of the measurement campaign at BP with reference to the measurement objectives and the characteristic data of the compressor

| Key data of the machine | | Characteristic data of the measurement campaign | |
|--|---|---|---|
| Impeller RPM | 17720rpm | Number of points per traverses for BP | 13 |
| Number of Blades z_B | 22 | Number of data points between 2 blades | 31 |
| Blade passing frequency: $f_{bp} = z_B \cdot f_{rot}$ | $f_{bp} \approx 6.5$ kHz | Sampling frequency f_s (for „best point“) | 200 kHz |
| Other important frequencies | $f_{MidSurge} = 18$ Hz $f_{RotatingStall} = 42$ Hz | Data length (measuring time) | 163840 points (0.82s) |
| | | Number of revolutions per averaging | 242 |
| | | 95% confidential interval for ensemble averaging | $a = 7.9$ mbar $a/\sigma = 7.9/63 = 0.1$ |
| Dynamic head | ≈ 220 mbar | Accuracy of the sensor (signal/noise ratio) | 220/0.07 = 3142 70dB |
| | | Sensor sensitivity | 6.3 mV/mbar |
| Max. pressure peak | 2200 mbar | Reference pressure in the probe shaft (absolute) | 1700 mbar |
| Averaged pressure | 1510 mbar | Range of the voltage signals from sensor | ± 5 V for U ± 10 V for Ue |
| Max. pressure fluctuation | Max: 814 mbar (peak to peak) | Resolution of the sensor pressure signals for ± 5 V | 0.4 mbar (12 bit) |
| Max. angle fluctuation | $\Delta\varphi = 16.6^\circ$ | Calibration range of the yaw angle | $\varphi = \pm 20^\circ$ |
| Mach number | 0.75 | Calibration range of the Mach number | $0.2 < M < 0.7$ |
| Max. temperature | 62.1 °C | Number of offset and gain adjustments | 2 per traverse |
| | | Spatial resolution of the probe (d_{probe}) | $d_{probe} = 1.2$ mm |
| Spatial dimension of a fluid part ($f_{max} = 44$ kHz) ($c_{max} = 192$ m/s) | $d_{fluid} = 4.4$ mm ($c_{max} = 192$ m/s) | Max. resolution of frequency ($f_{max} = c_{max}/d_{probe}$) | $f_{max} = 160$ kHz ($c_{max} = 192$ m/s) |
| Stability of the machine at the operating point (BP) | 678 ± 1 measuring point per revolution | Minimum resolution of the frequency determined from spectra density | $f_{min} = 100$ Hz |

$$a = \frac{\sigma \cdot C(P, m)}{\sqrt{m}} = \frac{63.3 \text{ mbar} \cdot 1.96}{\sqrt{242}} = 7.9 \text{ mbar} \quad (1)$$

Data Conversion Analysis, and Interpretation. The sensor voltages are converted into pressure and temperature signals by model-based reconstruction using the sensor and aerodynamic calibration data.

A dedicated software package has been developed for the comprehensive task of data processing. This performs the data conversion for an entire traverse and prints the results in a variety of menu-selected diagrams. The program is based on the “AW-System” developed as an interactive environment for the evaluation of large time series [21].

With the present objectives of the measurement campaign and the measurement concepts chosen, data analysis becomes very important for the optimization of the overall data processing. Data analysis involves several topics such as averaging methods, time-resolved spectra, autocorrelations, statistic tools for the investigation of turbulence, and data filtering. The use of averaging methods applied for time-resolved and fluctuating data is discussed in this paper.

Ensemble-Averaged Procedures for Compressing Time-Dependent Information

For the present measurements, a one-sensor probe was operated in the pseudo-three-sensor mode. To link the three nonsynchronous pressure measurements $p_1(t)$, $p_2(t)$, $p_3(t)$, made under constant operating conditions, ensemble averaging has to be utilized. (In nonmodulated flow, e.g., pipes or nozzles, simple time averaging would suffice.) In modulated flow, ensemble averaging has to be based on the time period of the phenomenon to be studied, e.g., the shaft revolution period, or the period of mild surge or rotating stall. In the first case triggering can be done by a geometric signal; in the second case, a flow-dependent signal must be used.

Rotor-Based Ensemble-Averaging Methods. The revolution ensemble-averaging method requires a sharp trigger signal sent at each revolution of the rotor. At one of these signals the time index n is set to zero, and measurement begins. After m shaft revolutions, measurement is stopped.

$$\bar{x}(t_n, z) = \frac{1}{m} \sum_{i=1}^m x_i(t_n, z) \quad (2)$$

Equation (2) quantifies the deterministic rotor-based fluctuation of the pressures $\bar{p}_1(t)$, $\bar{p}_2(t)$, $\bar{p}_3(t)$. In case of blade-to-blade or twin-blade ensemble averaging, Eq. (2) holds, but n and m refer to the trigger signal given after each blade or twin blade passing.

Stochastic fluctuations only appear statistically. They are characterized by the ensemble standard deviation, defined by

$$\bar{\sigma}(t_n, z) = \sqrt{\frac{1}{m} \cdot \sum_{i=1}^m (x_i(t_n, z) - \bar{x}(t_n, z))^2} \quad (3)$$

In case of measurements made at the outlet of the impeller and at BP running conditions (no surge, etc.) the stochastic part of the pressure fluctuations contains the information about the turbulence intensity.

Flow-Based Ensemble-Averaging Methods. These are used for the investigation of periodic flow instabilities like mild surge. In this case the trigger signal is independent of rotor revolutions and is gained from an event-related flow condition. Such trigger signals usually have variable period length and the number of measured data between two trigger events is not constant. A period related “class averaging” method has to be used, as described in Part 2 [9]. The number of classes determines the resolution in time and the statistical accuracy of the averaging process.

The number of classes, 2500 in this measurement campaign for MS, corresponds to a time step of 0.002 ms (frequency=45 kHz) and gives 180–200 data points per class to be averaged.

In case of MS, the trigger period is totally unrelated to the rotor revolution. This means that pressure fluctuations caused by blade passing appear as noise. In the stochastic part of the pressure fluctuations, turbulence and the periodic blade passing are both present, giving a high level of standard deviation.

Comparison of the Ensemble-Averaging Methods. The revolution ensemble-averaged pressure $\bar{p}_1(t)$ gained from the one-sensor-probe determined from preliminary information on the local time averaged flow direction is presented in Fig. 4.

The probe was set at a traverse position $z/b=0.18$. The wakes of the blade trailing edges of the 11 splitter and 11 full blades are visible as peaks. The total pressure rises in the blade wakes from 1510 to 1780 mbar, which is equal to a fluctuation level in the deterministic part of the total pressure of 20 percent from the mean value. In the blade wakes the ensemble standard deviation (stochastic part) in Fig. 4 rises from a low level of 10 mbar to a maximum of 137 mbar. This corresponds to 8 percent of the mean pressure level of $\bar{p}_1(z) = 1587$ mbar. The deterministic and stochastic fluctuations of the pressure $p_1(t)$ are a quantity to characterize the flow in a compressor. There has to be a dissipation process to level out these fluctuations.

In Fig. 5 the standard deviation of the deterministic and stochastic parts of the ensemble-averaged $p_1(t)$ pressure fluctuations are plotted across the channel width, as measured at position I under BP conditions. The curves A represent the standard deviation of the deterministic fluctuation around the time-mean pressure \bar{p}_1 . The curves B represent the standard deviation of the stochastic fluctuations around the instantaneous deterministic value. It is seen that the deterministic p_1 fluctuations dominate at position I over the stochastic events; i.e., the blade wakes are the dominant unsteady effect. Furthermore, both parts of the pressure fluctuation decrease toward the shroud where the flow velocity is very low (see c_r in Fig. 6) and where the wakes are such that the velocity direction (in yaw) fluctuates much less than near the hub. (Yaw fluctuation data are not shown for lack of space.)

During each revolution of the shaft, a sequence of 11 main blades and 11 splitter blades passes the probe. Ensemble averaging can be based on different periods. If the flow period of interest

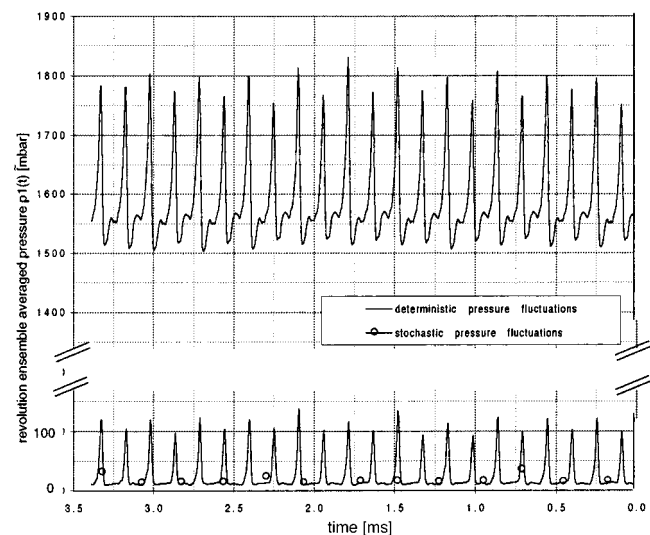


Fig. 4 Revolution ensemble-averaged pressure $\bar{p}_1(t)$ during one impeller revolution (deterministic part of the pressure fluctuation) and the stochastic part represented through the ensemble standard deviation. Running conditions: BP; outlet of impeller, traverse position $z/b=0.18$.

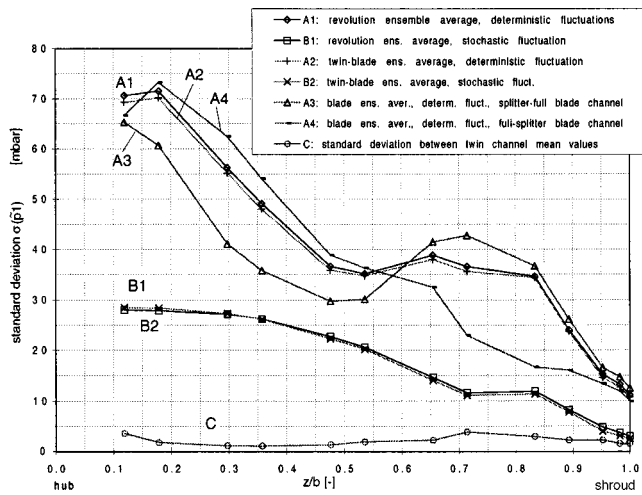


Fig. 5 Averaged deterministic and stochastic pressure fluctuation over traverse position (z/b) obtained from different ensemble-averaging strategies. Running conditions: BP; impeller outlet, position I.

is a complete revolution of the shaft, the time series $p_1(t)$ is compressed to the time duration $\Delta t_R = 1/N$. Another period of interest is $\Delta t_T = 1/11N$, i.e., the passage time of a blade twin. Both types of ensemble averaging have been tested. The revolution ensemble averaging gave curves A1 and B1, while twin-blade averaging gave A2 and B2. It is seen that the methods yield closely identical fluctuations, indicating that all blade pairs of the impeller have closely identical geometry and therefore, there are no low-order (<11) harmonics of N present in the flow.

A further period is $\Delta t_T = 1/22N$; i.e., the passage time of a blade-to-blade section. The deterministic fluctuations are shown separately for the channel between the splitter blade and the pressure side of the full blade versus the channel between the suction side of the full blade and the splitter blade. This ensemble averaging gave curves A3 and A4. The difference between this curve indicates that the flow leaving every second impeller channel is different; see Part 2. The stochastic fluctuations have approximately the same magnitude as curves B1 and B2.

Line C in Fig. 5 shows the standard deviation of the 11 mean values $\bar{p}_1(t)$ obtained for each of the 11 blade channel twins. This variation is a measure for the existence of a “fingerprint” of the impeller. All impeller blade pairs have closely identical geometry and there are no low frequencies in the signal that arise from the interaction of the impeller with the diffuser blades.

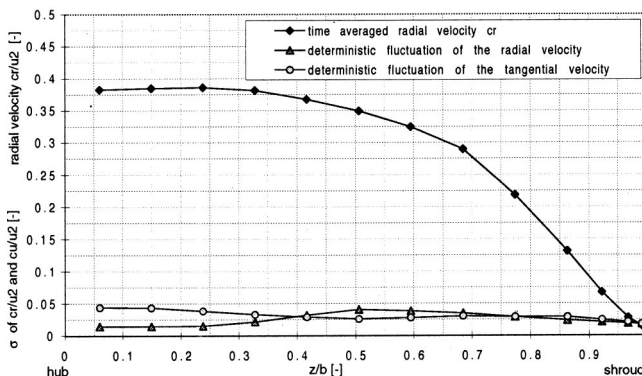


Fig. 6 Time-mean velocity profile and averaged deterministic radial fluctuations over traverse position (z/b). Running conditions: BP.

In Fig. 6, the time-averaged radial velocity c_r (black diamond symbols) and the standard deviation of the deterministic c_r fluctuations (triangle) are presented. The c_r fluctuations are moderate. They are strongest in midchannel and decline toward the shroud (where c_r is low anyway) and toward the hub where c_r is high but fluctuates little. The tangential velocity fluctuations are of similar magnitude (circle symbols). It is important to note that these modest values of the velocity standard deviations do not mean that high instantaneous peaks or dips do not occur. In fact wake-induced deterministic peaks may exceed the standard deviation level by a factor of three or more [22].

Averaging methods have to deal with either or both kinds of nonuniformities, namely the spatial (hub to tip) distribution and the temporal (i.e., circumferential) fluctuations.

Comparison of Averaging Methods

Coordinates. Figure 7 shows the cylindrical coordinates used. Note that the circumferential angle θ is related to measurement time t as

$$d\theta = 2 \cdot \pi \cdot N \cdot dt \quad (4)$$

and the flow area is given by

$$dA = r_E \cdot d\theta \cdot dz = u_E \cdot dt \cdot dz \quad (5)$$

Averaging. Averaging can be done circumferentially only (time averaging, see Eq. (6)), axially only (spanwise averaging, see Eq. (7)) or over the surface area dA (annular averaging, see Eq. (8)).

- Time averaging yields spanwise distributions over the channel width b :

$$\frac{1}{t_0} \cdot \int x(t,z) dt \equiv \bar{x}(z) \quad (6)$$

- Spanwise averaging gives time functions:

$$\frac{1}{b} \cdot \int x(t,z) dz \equiv \bar{x}(t) \quad (7)$$

- Annular averaging yields constant numbers:

$$\frac{1}{b \cdot t_0} \cdot \int x(t,z) dt dz \equiv \bar{x} \quad (8)$$

In the following, averaging theories are formulated for annular averaging. The equations obtained can be easily modified for the timewise or spanwise averaging presented above.

Here $X(t, z)$ may represent any type of flow-dependent quantity or group. Physically meaningful concepts for defining functions X have been established by [1] and [8]. The aim of these

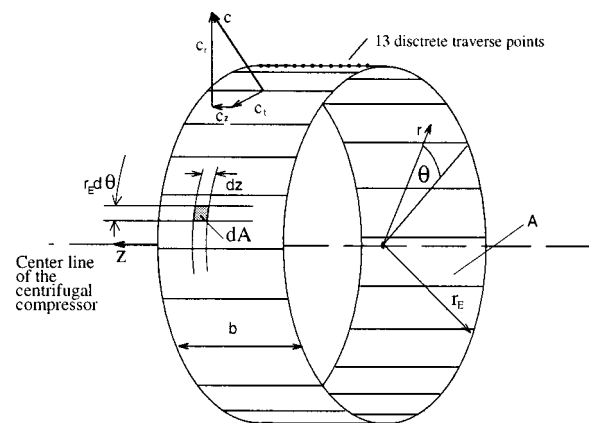


Fig. 7 Coordinate system used

concepts is to provide average values that are relevant from the point of view of turbomachinery theory; i.e., strictly respect the conservation laws of mass, momentum, and energy, and therefore fulfill the mass, force and energy balances. The following flow quantities are measured by a ‘‘pseudo-three-sensor probe.’’

$$\begin{array}{lll} \text{velocity:} & c_r(t,z); & c_t(t,z) \\ \text{pressure:} & p_{\text{tot}}(t,z); & p_{\text{stat}}(t,z) \\ \text{temperature:} & T_{\text{rec}}(z); & \end{array}$$

Due to the thermal inertia of the probe, temperature is not resolved over time, unfortunately.

The probe measures a recovery temperature lying between the time-mean static and total temperature values. With the recovery factor being known from calibration ($r \approx 0.7$, see Part 1 [14]), the time-mean static and total flow temperatures are obtained as

$$T_{\text{stat}}(z) = T_{\text{rec}}(z) - \frac{r}{2c_p} \cdot \overline{c(t,z)^2} \quad (9)$$

$$T_{\text{tot}}(z) = T_{\text{rec}}(z) + \frac{1-r}{2c_p} \cdot \overline{c(t,z)^2} \quad (10)$$

The average of c^2 will be defined below.

The gas equation of state yields local density ρ and enthalpy h as

$$\rho = p/(RT_{\text{stat}}) \quad (11)$$

$$h = c_p(T_{\text{stat}}) \cdot T_{\text{stat}} \quad (12)$$

The velocity components c_r and c_t are equivalent to specifying angle φ and magnitude c . (Note that two-dimensional planar flow is treated here. A third component (c_z) would require the use of four or five sensor probes.)

Averaging Method According to Traupel. The convectively transported flux of a mass-specific flow quantity x through area dA (Fig. 7) in unit time is given by $x\rho c_r dA$. The mass flow rate through an annulus surface A is given by

$$\dot{m} = \int_A \rho(t,z) \cdot c_r(t,z) dA \quad (13)$$

The annulus average of x per unit mass is therefore

$$\bar{x} = \frac{1}{\dot{m}} \cdot \left(\int_A x(t,z) \cdot \rho(t,z) \cdot c_r(t,z) dA \right) \quad (14)$$

The procedure to average annulus flow data with Traupel's method is to determine an annulus-average radial velocity \bar{c}_r from Eq. (14) by setting $x = c_r$, which amounts to averaging the radial momentum flux. Next, a mean tangential momentum flux $\bar{r}c_t$ is determined from Eq. (14) by setting $x = r(z)c_r(t,z)$. The annulus average static enthalpy \bar{h} is obtained by setting $x = h(t,z) \approx c_p T_{\text{stat}}(z)$, and the annular averaged total enthalpy results as

$$\bar{h}_{\text{tot}} = \bar{h} + \overline{(c^2)}/2 \quad (15)$$

(Some error is introduced by the lack of time-resolved temperature data in the present experiments.) The mean kinetic energy flux $\overline{(c^2)}/2$ is obtained by setting $x = [c_r^2(t,z) + c_t^2(t,z)]/2$.

For averaging the static pressure, Traupel recommends a simple (unweighted) area averaging in order to conserve pressure forces in momentum balances. He defines the annulus average pressure as

$$\bar{p} = \frac{1}{A} \cdot \int_A p(t,z) dA \quad (16)$$

With \bar{p} and \bar{h} known, the gas equations are used to calculate a mean density $\bar{\rho}$ as

$$\bar{\rho} = \rho(\bar{p}, \bar{h}) = (c_p/R) \cdot \bar{p}/\bar{h} \quad (17)$$

This momentum-based definition of \bar{c}_r does not satisfy the continuity equation in its simplest form,

$$\dot{m} \neq \bar{\rho} \cdot \bar{c}_r \cdot A \quad (18)$$

because Eq. (13) requires a kind of averaging different from Eq. (14). The correctness of mass flow is restored by Traupel by defining a ‘‘continuity shape factor’’ ε_k for the radial velocity profile as

$$\dot{m} = \bar{\rho} \cdot (1 - \varepsilon_k) \cdot \bar{c}_r \cdot A \quad (19)$$

$$1 - \varepsilon_k = \int_A \frac{\rho(t,z)}{\bar{\rho}} \cdot \frac{c_r(t,z)}{\bar{c}_r} \cdot \frac{dA}{A} \quad (20)$$

Further, the mean tangential momentum flux $\overline{rc_t}$ does not automatically define a mean tangential velocity component \bar{c}_t . For defining \bar{c}_t some reference radius \bar{r}^* has to be specified, as, e.g.,

$$\bar{c}_t = \overline{rc_t/\bar{r}^*} \quad (21)$$

Dzung has called \bar{r}^* the ‘‘Euler radius’’ and conveniently defined it as the radius at which the mean absolute-frame and rotor-frame velocities c_t and w_t are vectorially additive according to $\bar{c}_t = \omega\bar{r}^* + \bar{w}_t$. He found that \bar{r}^* is obtained as

$$\bar{r}^* = \left[\frac{1}{\dot{m}} \cdot \int_A \rho c_r r^2 dA \right]^{1/2} \quad (22)$$

In case of a cylindrical surface, as in the present case, \bar{r}^* equals the cylinder radius.

The specific kinetic energy of the fluid is represented by

$$\frac{\bar{c}^2}{2} = \frac{(\bar{c}_r)^2 + (\bar{c}_t)^2}{2} \quad (23)$$

However, as in the case of mass flux, the kinetic energy flux also requires a correction, because $\bar{c}^2/2$ is not identical to $(\overline{c^2})/2$ defined above. Traupel introduces an ‘‘energy shape factor’’ ε_e to the velocity \bar{c} obtained from momentum averaging as

$$\overline{(c^2)} = [(1 - \varepsilon_e) \cdot \bar{c}]^2 \quad (24)$$

yielding the relation

$$\bar{h}_{\text{tot}} = \bar{h} + [(1 - \varepsilon_e) \cdot \bar{c}]^2/2 \quad (25)$$

In summary, Traupel defines all velocity components by momentum averaging, but needs various shape factors to conserve mass and energy. In case of uniform flow, these become $\varepsilon_k = \varepsilon_e = 0$.

Averaging Method According to Dzung. Dzung's ‘‘consistently’’ averaged values are defined to comply with mass, momentum, and energy conservation and avoid shape factors as described in [8]. For this purpose kinetic energy is defined as

$$\frac{\bar{c}_{Dz}^2}{2} = \frac{\bar{c}_{rDz}^2}{2} + \frac{\bar{c}_t^2}{2} \quad (26)$$

where \bar{c}_t follows from Eq. (21) and \bar{c}_{rDz} is the continuum average of the radial component obtained with Eq. (14) from

$$\dot{m} = \bar{\rho}_{Dz} \cdot \bar{c}_{rDz} \cdot A = \int_A \rho(t,z) \cdot c_r(t,z) dA \quad (27)$$

In order to conserve total enthalpy in adiabatic flow according to the First Law

$$\bar{h}_{\text{tot}} = \bar{h}_{Dz} + \frac{\bar{c}_{Dz}^2}{2} \quad (28)$$

Dzung adapts the definition of static enthalpy as

$$\bar{h}_{Dz} = \frac{1}{\dot{m}} \cdot \int_A h_{\text{tot}}(t,z) \cdot c_r(t,z) \cdot \rho(t,z) dA - \left(\frac{\bar{c}_{rDz}^2}{2} + \frac{\bar{c}_t^2}{2} \right) \quad (29)$$

Compliance with momentum conservation is achieved by adapting the definition of static pressure as

$$\bar{p}_{Dz} = \bar{p} + \frac{1}{A} \cdot \int \rho(t,z) c_r^2(t,z) dA - \frac{\dot{m} \cdot \bar{c}_{rDz}}{A} \quad (30)$$

where \bar{p} is the area averaged pressure determined with Eq. (16). With the static pressure \bar{p}_{Dz} and the enthalpy \bar{h}_{Dz} the density $\bar{\rho}_{Dz}$ can be determined by the gas equation as

$$\bar{\rho}_{Dz} = \rho(\bar{p}_{Dz}, \bar{h}_{Dz}) \quad (31)$$

With the density $\bar{\rho}_{Dz}$ known, the radial velocity \bar{c}_{rDz} can iteratively be calculated again by Eq. (27).

Dzung averaging is formally simple, but flow incidence angles calculated from \bar{c}_{rDz} and \bar{c}_t may be misleading in flows with strongly non-uniform velocity profiles.

Simple Arithmetic Time Averaging. Finally, in order to compare the above averaging methods with simple (i.e., nonphysical) arithmetic timewise and spanwise averaging, we also calculate

$$\bar{x} = \frac{1}{\Delta z \Delta t} \cdot \int_z \int_t x(t,z) (dt) (dz) \quad (32)$$

Comparison of the Averaging Methods. For the comparison of the three averaging methods in the highly fluctuating centrifugal compressor impeller outlet flow field, the stage work is calculated first by inserting the averaged velocity components c_t obtained above into the Euler momentum equation. Due to the straight axial flow at the impeller inlet, c_{t1} is zero and the stage work is

$$\bar{a}_a = \bar{u}_E \cdot \bar{c}_{tE} \quad (33)$$

The differences between the various methods must be viewed in terms of measuring accuracy. The measurement errors of the velocities c_{tE} are about 0.5 percent of the velocity mean value for velocity levels above 50 m/s, 1 percent for levels under 50 m/s. The accuracy of the differential pressure measurement Δp_E is defined with the standard deviation of the residuals having a magnitude of 0.2 mbar for a dynamic head of 250 mbar. The measurement accuracy for the absolute pressure is 0.1 percent correspond-

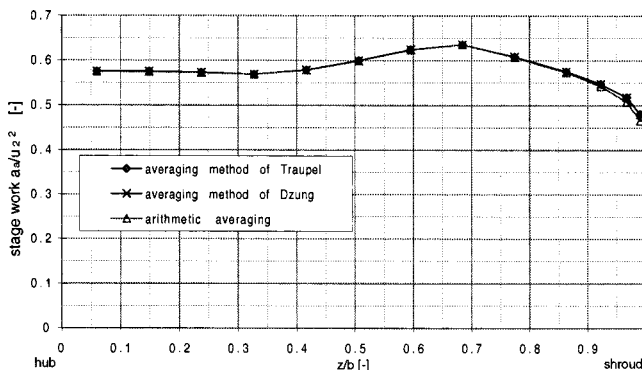


Fig. 8 Stage work a_a across the traverse obtained from different averaging methods. Running conditions: BP.

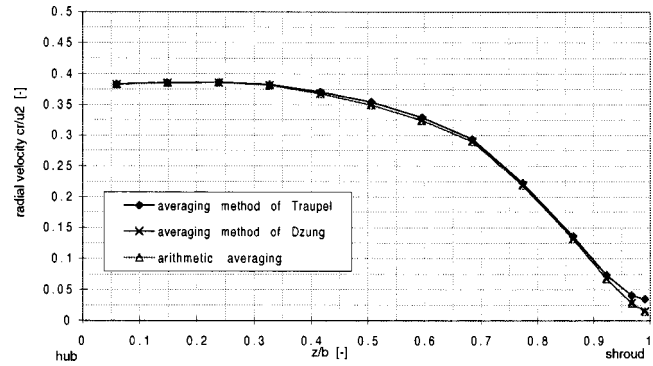


Fig. 9 Radial velocity across the traverse obtained from different averaging methods. Running conditions: BP.

ing to 0.17 mbar for a pressure value of about 1700 mbar (see Part 1 [14]). Dynamic errors of a cylindrical probe are described in [23] and a comparison between fast-response aerodynamic probe and LDA measurements in the present centrifugal compressor is presented in [22].

(a) *Circumferential (Timewise) Averaging:* $\int x(t,z) dt$. The stage work distribution across the diffuser channel (z/b) calculated from Eq. (33), with the circumferential velocity mean gained with different averaging methods is shown in Fig. 8. The three curves virtually coincide.

Due to the shape factor ε_k defined in the averaging method of Traupel as a mass flow correction, the tangential velocity component c_t , calculated with the method of Traupel is identical with the c_t obtained with Dzung. According to Eq. (29), both averaging methods lead to equal stage work values. The difference between the arithmetically time-averaged stage work and the values gained with the thermodynamic averaging methods increases from 0.2 percent at the hub to 2.5 percent at the shroud. The mean difference over the span is a mere 0.4 percent of the work. This is close to the measurement accuracy itself, i.e., negligible.

The radial velocity c_r calculated with the three averaging methods is shown in Fig. 9. The mean differences between the averaging method of Traupel and Dzung across the traverse is 2 percent.

In the averaging model of Traupel, the shape factor ε_k defined by Eq. (20) considers boundary layers and provides an effective area A . Due to the smaller area A , the velocity component c_r has a higher magnitude for the model of Traupel. ε_k is dependent on the fluctuation intensity of c_r .

The static pressure is presented in Fig. 10 and calculated with three averaging methods.

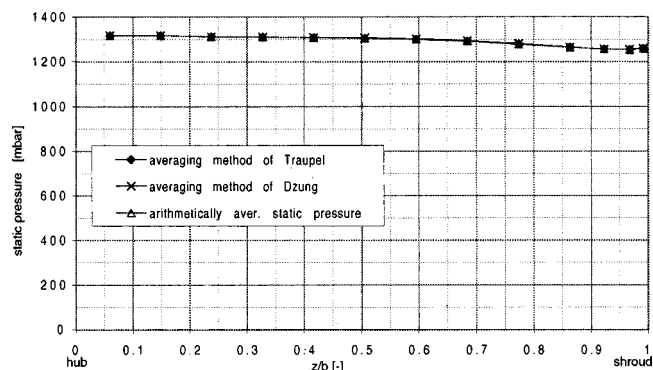


Fig. 10 Static pressure across the traverse obtained from different averaging methods. Running conditions: BP.

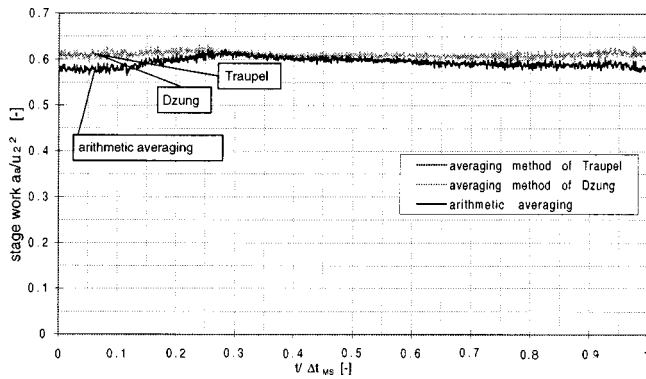


Fig. 11 Stage work during a MS period obtained from different averaging methods. Running conditions: MS.

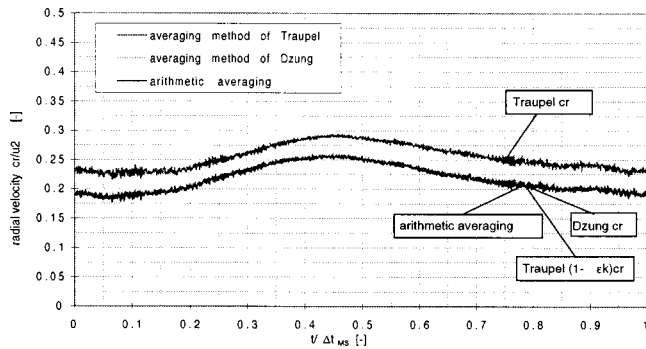


Fig. 12 Radial velocity during a MS period obtained with different averaging methods. Running conditions: MS.

The difference between the static pressure calculated with the averaging method of Dzung and the area averaged pressure from the method of Traupel is less than 0.05 percent across the traverse at position I. This equals 0.3 percent of the mean dynamic head. The measurement error for the pressure is lower than the differences between the averaging methods.

(b) *Spanwise Averaging:* $\int x(t,z)dz$. For the comparison of axially averaged flow quantities based on the three methods, data measured during MS running conditions are used, because the time evolution of such hub-to-shroud averages is mainly of interest during unsteady operating conditions. The averaged data have to be class averaged to get the time-dependent flow quantities $c_r(t,z)$, $c_t(t,z)$, $p_{stat}(t,z)$; see Part 2 [9].

Figure 11 shows the spanwise-averaged momentary stage work during one MS cycle, as calculated with three averaging methods. There is a net difference between the physical averaging methods (Traupel and Dzung) and the physically blind arithmetic average. The mean difference during one “mild surge” period is about 1.26 kJ/kg, or 2.7 percent.

The fluctuation of radial velocity c_r during a MS period is presented in Fig. 12. Due to the high axial nonuniformity of the measured radial velocity c_r the differences between the averaging methods of Traupel and Dzung amount to 16 percent during the whole period. This illustrates the difference between momentum-based (Traupel) and continuity based (Dzung or Traupel $(1 - \epsilon_k)c_r$) averages.

All averages in Figs. 11 and 12 are seen to fluctuate during an MS cycle, the mass flow (c_r) having a much higher amplitude than the stage work. The near constancy of work can be shown to be due to the constancy of the tangential (c_t) component in the

Table 3 Annulus-averaged flow quantities determined with three averaging methods. Running Conditions: BP.

| $\int x(t,z)dt dz$ | averaging method of Traupel | averaging method of Dzung | arithmetic averaging |
|--------------------|-----------------------------|---------------------------|----------------------|
| stage work | 43.68kJ/kg | 43.68kJ/kg | 42.43kJ/kg |
| velocity c_r | 0.345 c_r/u_2 [-] | 0.30 c_r/u_2 [-] | 0.25 c_r/u_2 [-] |
| velocity c_u | 0.59 c_u/u_2 [-] | 0.59 c_u/u_2 [-] | 0.57 c_u/u_2 [-] |
| static pressure | 1296mbar | 1297mbar | 1290mbar |

hub half of the channel where most work transfer occurs.¹ In the coexistence of high mass flow amplitudes with low work (or pressure head) amplitudes is not surprising in an operating point where the head verse flow characteristic of the stage is almost horizontal (see Fig. 7 in Part 2 [9]).

The static pressure differences between the averaging methods of Traupel and Dzung (not shown here) depend on the velocity fluctuation and have a value of 0.5 percent over the entire MS period, while the static pressure amplitude was of the order of 10 percent.

(c) *Annular averaging:* $\int x(t,z)dt dz$. For the comparison of the averaging methods in both scanning directions (t and z), the circumferential ensemble-averaged data for the operation point BP at probe position I have been calculated

In Table 3, the velocity components, the static pressure, and the stage work calculated with the averaging methods of Traupel and Dzung and as simple arithmetic averages are presented for BP running conditions at position I. The flow quantities are first time-wise averaged and then spanwise. The standard deviation of the c_r distribution gets a high level after the first timewise averaging of 56 percent for the method of Dzung and 55 percent for the method of Traupel. This highly inhomogeneous flow across the traverse leads to differences between the averaging methods, especially with respect to the radial velocity component. The differences between the two physically founded methods stem from using different definitions for \bar{c}_r .

Summary and Conclusions

- The comparisons presented in this paper were made for two running conditions of a centrifugal compressor, “best point” and “mild surge,” with the rig operated in the stable and unstable branch of the operating line, respectively.
- The data processing of time-resolved fast-response aerodynamic probe signals comprises data conversion, data analysis, and interpretation using measurement concepts adapted to the individual goals of the measurement campaign.
- The revolution-based and blade-twin-based ensemble averaging methods are discussed. Deterministic pressure fluctuations near the hub reach 35 percent of the averaged dynamic head and 5 percent near the shroud. The differences between the two ensemble-averaging methods are negligible across the diffuser channel. The stochastic fluctuations are much lower than the deterministic ones.
- The averaging methods of Traupel, Dzung, and arithmetic averaging are applied to the time-resolved data. Three averages, namely axial, circumferential, and channel surface, are presented.

¹The arithmetically averaged work is lower than the physical averages because the flow-deficient shroud-side region, where the work transfer is poor, is more heavily weighted.

• Even though the circumferential fluctuations of velocity and pressure in the impeller outlet flow are significant, the circumferential averaging methods yield closely identical axial distributions. However, the spanwise-averaged values differ considerably due to the very low radial through flow existing near the shroud.

Nomenclature

A = area
 ΔA = area for the mass flow calculation
 a = confidential interval
 a_a = specific stage work
 b = diffuser width (axial)
 C = specific speed
 $C(P, m)$ = coefficient of Gauss distribution
 c = velocity
 c_p = specific heat at constant pressure
 f = frequency
 f_A = sampling frequency
 h = enthalpy
 i = summation index
 L = length of diffuser vane
 M = Mach number
 m = number of shaft revolutions or blade twin passing
 Mu = impeller tip speed Mach number
 \dot{m} = mass flow
 n = number of measured data
 N = number of shaft revolution per seconds
 p = pressure
 R = gas constant
 r = radius, recovery factor
 r^* = Euler radius
 s = specific entropy
 T = temperature
 T_{rec} = recovery temperature
 t = time
 t_R = time of one impeller revolution
 t_T = time of a twin blade passing
 t_0 = total measurement time
 u = circumferential speed
 \dot{V} = flow rate
 X = flow quantity
 z = axial coordinate
 α = flow angle (diffuser coordinates)
 $\alpha_{B \text{ vane}}$ = diffuser vane leading edge blade angle
 $\varepsilon_k, \varepsilon_e$ = shape factors of Traupel
 η_{deg} = isentropic efficiency (total-to-total)
 θ = azimuth angle
 ν = specific volume
 ρ = density
 σ = standard deviation
 φ = yaw flow angle (probe coordinates)
 φ = flow coefficient = $\dot{V}_1 / (D_2^2 \cdot u_2)$
 ω = impeller angular velocity

Superscripts

$\bar{\quad}$ = averaged over time, or z , or time and z , Eqs. (6)–(8)
 \sim = ensemble averaged over time

Subscripts

$1, 2, 3$ = sensor yaw positions
 1 = impeller inlet
 2 = impeller outlet ($r_2 = 140$ mm)
 Dz = averaged with the method of Dzung
 E = measurement position ($r_E = 147$ mm)
 i = summation index
 n = ensemble-averaged time index
 r = radial direction

$stat$ = static flow properties
 t = tangential direction
 tot = total flow properties
 z = axial direction

References

- [1] Traupel, W., 1988, *Thermische Turbomaschinen I*, Springer-Verlag, Berlin, p. 307.
- [2] Dean, Jr., R. C., and Senoo, Y., 1960, "Rotating Wakes in Vaneless Diffusers," *ASME J. Basic Eng.*, **82**, No. 3.
- [3] Eckardt, D., 1975, "Instantaneous Measurements in the Jet-Wake Discharge Flow of a Centrifugal Compressor Impeller," *ASME J. Eng. Power*, **97**, No. 3.
- [4] Adamczyk, J. J., Mulac, R. A., and Celestina, M. L., 1986, "A Model for Closing the Inviscid Form of the Average-Passage Equation System," *ASME J. Turbomach.*, **108**, pp. 180–186.
- [5] Gerhard, P. M., 1981, "Averaging Methods for Determining the Performance of Large Fans From Field Measurements," *ASME J. Eng. Power*, **103**, No. 2.
- [6] Kreitmeier, F., and Juvet, P. J., 1997, "Demonstration of a Balance-Based Procedure for Time-Averaging and Modeling of Compressible Three-Dimensional Unsteady Turbulent Flows."
- [7] Ng, W. F., and Epstein, A. H., 1985, "Unsteady Losses in Transonic Compressors," *ASME J. Eng. Gas Turbines Power*, **107**, pp. 345–353.
- [8] Ruck, G., 1989, "Verfahren zur instationären Geschwindigkeits- und Turbulenzmessung mit einer pneumatisch messenden Keilsonde," Mitteilungen des Institutes No. 33, Institut für Thermische Strömungsmaschinen und Maschinenlaboratorium der Universität Stuttgart, Stuttgart, Germany.
- [9] Roduner, C., Kupferschmied, P., Köppel, P., and Gyarmathy, G., 2000, "On the Development and Application of the Fast-Response Aerodynamic Probe System for Turbomachines—Part 2: Flow, Surge, and Stall in a Centrifugal Compressor," *ASME J. Turbomach.*, **122**, pp. 517–526.
- [10] Dzung, L. S., 1967, "Mittelungsverfahren in der Theorie der Schaufelgitter," *Brown Boveri Mitteilungen*.
- [11] Dzung, L. S., 1970, "Flow Research on Blading," *Proc. Symposium of Flow Research on Blading*.
- [12] Roduner, C., Köppel, P., Kupferschmied, P., and Gyarmathy, G., 1998, "Comparison of Measurement Data at the Impeller Exit of a Centrifugal Compressor Measured with both Pneumatic and Fast-Response Probes," *ASME Turbo Expo '98*, 98-GT-241, Stockholm.
- [13] Hunziker, R., 1993, "Einfluss der Diffusorgeometrie auf die Instabilitätsgrenze des Radialverdichters," PhD thesis No. 10252, ETH Zürich, Switzerland.
- [14] Kupferschmied, P., Köppel, P., Roduner, C., and Gyarmathy, G., 2000, "On the Development and Application of the Fast-Response Aerodynamic Probe System for Turbomachines—Part 1: The Measurement System," *ASME J. Turbomach.*, **122**, pp. 505–516.
- [15] Gossweiler, C., Humm, H. J., and Kupferschmied, P., 1992, "Development of a System for Aerodynamic Fast-Response Probe Measurements," *Proc. of the 18th Congress of Int. Council of the Aeronautic Sciences (ICAS)*, Beijing.
- [16] Gossweiler, C., Kupferschmied, P., and Gyarmathy, G., 1995, "On Fast-Response Probes: Part I—Technology, Calibration and Application to Turbomachinery," *ASME J. Turbomach.*, **117**, pp. 611–617.
- [17] Kupferschmied, P., Gossweiler, C., and Gyarmathy, G., 1994, "Aerodynamic Fast-Response Probe Measurement Systems: State of Development, Limitation and Future Trends," *Proc. 12th Symposium on Measuring Techniques for Transonic and Supersonic Flows in Cascades and Turbomachines*, Prague, Czech Republic.
- [18] Kupferschmied, P., 1998, "Zur Methodik zeitaufgelöster Strömungssondenmessungen in Verdichtern und Turbinen," PhD thesis No. 12774, ETH Zürich, Switzerland.
- [19] Stahlecker, D., and Gyarmathy, G., 1998, "Investigations of Turbulent Flow in a Centrifugal Compressor Vaned Diffuser by Three-Component Laser Velocimetry," *ASME Paper No. 98-GT-300*.
- [20] Casartelli, E., Saxer, A. P., and Gyarmathy, G., 1999, "Numerical Flow Analysis in a Subsonic Vaned Radial Diffuser With Leading Edge Redesign," *ASME J. Turbomach.*, **121**, pp. 119–125.
- [21] Herter, D., Chrisander, O., and Gossweiler, C., 1992, "AW-System—An Interactive Environment for the Evaluation of Large Time Series," *Proc. 11th Symposium on Measuring Techniques for Transonic Flows in Cascades and Turbomachines*, Munich, Germany.
- [22] Gizzi, W., Roduner, C., Stahlecker, D., Köppel, P., and Gyarmathy, G., 1999, "Time Resolved Measurements With Fast-Response Probes and Laser-Doppler-Velocimetry at the Impeller Exit of a Centrifugal Compressor—A Comparison of Two Measurement Techniques," *Proc. 3rd European Conference on Turbomachinery*.
- [23] Humm, H. J., Gossweiler, C., and Gyarmathy, G., 1995, "On Fast-Response Probes, Part 2: Aerodynamic Design Studies," *ASME J. Turbomach.*, **117**, pp. 618–624.

Discussion: “On the Development and Application of the Fast-Response Aerodynamic Probe System in Turbomachines—Part 3: Comparison of Averaging Methods Applied to Centrifugal Compressor Measurements” [ASME J. Turbomach., 122, No. 3, pp. 527–535 (2000)]¹

N. A. Cumpsty

Rolls-Royce plc, Derby, United Kingdom

This paper and its two companions (Parts 1&2) describe careful and meticulous work and I therefore hesitate to offer any criticism. Two of my comments refer to form rather than content.

I do wonder whether it is wise to use the term “recovery factor” to describe the temperature ratio in Eq. (9) of Part I. The term is well established in high-speed flow for this same ratio when the cause for its value differing from unity is the conduction of heat across a boundary layer. Here, if I understand correctly, the biggest discrepancy is due to heat transfer inside the probe. Could another term be found?

The last point is an observation about cylindrical probes where the sensing hole is in the side of the cylinder, like the probes described in these papers. Whenever these are used in a flow in which the stagnation pressure is nonuniform in the spanwise direction (i.e., along the axis of the cylinder), an error occurs. Essentially the hole is exposed to, and responds to, a flow that comes from a different spanwise location. The size of the error in pressure is a function of the product of the steepness of the gradient in stagnation pressure and the diameter of the probe; it is normally significant in the boundary layers near endwalls, the hub, and shroud walls for the compressor measured here. Because of the emphasis in the papers to the care given to the construction and calibration of the probes, this inherent source of inaccuracy could be overlooked; a “health warning” is perhaps appropriate.

¹Pascal Köppel, Christian Roduner, Peter Kupferschmied, and Georg Gyarmathy, 2000, “On the Development and Application of the Fast-Response Aerodynamic Probe System for Turbomachines—Part 3: Comparison of Averaging Methods Applied to Centrifugal Compressor Measurements,” ASME JOURNAL OF TURBOMACHINERY, 122, 527–535.

Closure to “Discussion of ‘On the Development and Application of the Fast-Response Aerodynamic Probe System for Turbomachines—Part 3: Comparison of Averaging Methods Applied to Centrifugal Compressor Measurements’ ” [ASME J. Turbomach., 122, No. 3, p. 527–535 (2000)]

Peter Kupferschmied

The point made concerning the flow temperature indicated by probes with internal heat conduction is well taken. The traditional term “recovery factor” used in the pamphlet paper has been replaced by “effective recovery factor.” This, we hope, makes it clear that a parasitic effect (internal conduction) is superimposed on the classic aerodynamic compression/conduction phenomenon, while the definition of the ratio is analogous to the classic recovery factor.

Our trademark FRAP® has been abandoned here in favor of the more general, noncommercial term “fast-response aerodynamic probes.”

The total pressure signal in flow fields with sharp transverse velocity-vector gradients is certainly influenced by the presence of the probe and we agree that the “health warning” made is appropriate indeed. It can be shown that the effect of a given total pressure gradient along the probe axis is reduced by using probes of smaller diameter. This was one of the main driving forces behind the development of the miniaturized fast-response probes described in the papers.

Impact of Film-Cooling Jets on Turbine Aerodynamic Losses

Dibbon K. Walters

James H. Leylek

Department of Mechanical Engineering,
Clemson University,
Clemson, SC 29634

This paper documents a computational investigation of the aerodynamic impact of film cooling on a linear turbine airfoil cascade. The simulations were for single row injection on both the pressure and suction surfaces, downstream of the leading edge region. The cases match experimental efforts previously documented in the open literature. Results were obtained for density ratio equal to 1.0 and 2.0, and a blowing ratio range from 0.91 to 6.6. The domain included the passage flow as well as the film hole and blade interior. The simulation used a dense, high-quality, unstructured hybrid-topology grid, comprised of hexahedra, tetrahedra, prisms, and pyramids. The processing was performed with a pressure-correction solution procedure and a second-order discretization scheme. Turbulence closure was obtained using standard, RNG, and "realizable" $k-\epsilon$ models, as well as a Reynolds stress model. Results were compared to experimental data in terms of total pressure loss downstream of the blade row. Flow mechanisms responsible for the variation of aerodynamic losses due to suction and pressure surface coolant injection are documented. The results demonstrate that computational methods can be used to predict losses accurately on film-cooled airfoils. [S0889-504X(00)01503-8]

1 Introduction and Literature Review

Although film cooling has been used for some time in the hot section of gas turbines, little is known about its impact on the turbine aerodynamics. Coolant gases are injected from a blade or vane surface to provide a layer of relatively cold air between the part and the hot free stream. The coolant air obviously influences and is influenced by the external aerodynamics. In particular, film cooling is expected to decrease aerodynamic performance by increasing the loss through a given blade row. In a modern industrial environment, turbine designers have a need for understanding the complex flow physics associated with losses due to coolant injection. In addition, they require predictive tools that will yield aerodynamic information for new heat transfer designs, without having to resort to expensive full-scale engine experimentation.

The current study is concerned with the effect of film cooling on profile loss, as opposed to endwall or tip leakage loss. A few notable experimental studies have been documented in the open literature that deal with this subject. These studies yield some insight into the nature of loss generation on film-cooled airfoils, but provide little in the way of predictive capability. Only a handful of studies of predictive methods are found in the open literature, and none of these conclusively show that CFD methods can be used to predict the effect of film cooling accurately on losses.

1.1 Experimental Studies. Ito [1] and Ito et al. [2] documented the midspan total pressure loss associated with film cooling by a row of cylindrical holes on the suction and pressure surface of a linear airfoil cascade. Their experiments showed that suction side (SS) injection with low injection rate into a laminar boundary layer increased the loss by initiating transition. Low injection rate into an already tripped boundary layer showed only a small increase in the loss. At higher injection rates, the total pressure loss decreased due to the energizing effect of the coolant. On the pressure side (PS), coolant injection only decreased losses as the injection rate was increased.

Similar work on aerodynamic impact of film cooling on airfoil cascades, but at engine-realistic Mach numbers, can be found in

Haller and Camus [3] and Köllen and Koschel [4]. Both showed variation of loss depending on the axial location of the coolant holes.

Yamamoto et al. [5] and Hong et al. [6] examined loss downstream of a linear airfoil cascade, the former using slots at different axial locations, and the latter using a row of cylindrical film holes on the leading edge, pressure, and suction surfaces. Yamamoto et al. showed the decrease in total pressure loss associated with added coolant momentum for high coolant injection ratios. Hong et al. demonstrated the insensitivity of loss to PS injection, relative to the SS case.

Efficiency measurements for annular nozzle guide vane cascades have been reported by Day et al. [7,8]. Instead of simple mainstream total pressure loss, they measured the overall loss, including within the cooling holes, by considering the total pressure of the coolant in addition to the main flow. Their measurements included the effects of both profile and endwall loss. With regard to the former, it was shown that film cooling resulted in a thickening of the downstream airfoil wake, and thus a decrease in aerodynamic efficiency. The authors argued that momentum flux ratio should be used to scale loss increases due to film cooling.

An examination of profile loss was documented by Osnaghi et al. [9] for a linear nozzle guide vane cascade with shower head, trailing edge, and full coverage coolant injection. The authors concentrated mainly on the so-called thermodynamic loss, which takes into account the total pressure of the injected coolant on the overall losses. Tests were performed for multirow injection, including leading edge, SS and PS, and trailing edge. They found that the thermodynamic loss increased with increasing coolant blowing rate. They also found that losses were equal for different density ratios so long as the momentum flux ratios were equal.

1.2 Analytical/Computational Studies. There are few documented efforts to predict losses associated with film cooling. Some authors have used relatively simple analytical techniques to predict the mixing losses due to injected coolant, though not the overall profile loss of the airfoil. These include Urban et al. [10], whose "TOTLOS" model is based on the assumption of constant pressure mixing within a thin layer near the airfoil surface, and is actually a modification of Hartsel [11]. Their results showed good agreement with experiments for relatively low coolant injection rates, but showed some disagreement at higher injection. Ardey and Fottner [12] found that a simple mixing model could accurately predict losses due to leading edge injection over a wide

Contributed by the International Gas Turbine Institute and presented at the 44th International Gas Turbine and Aeroengine Congress and Exhibition, Indianapolis, Indiana, June 7–10, 1999. Manuscript received by the International Gas Turbine Institute February 1999. Paper No. 99-GT-421. Review Chair: D. C. Wisler.

range of blowing ratios. Other authors [2] have used this simplified approach to predict the losses due to coolant injection with relative success.

These techniques, however, suffer from two important factors. One, they only predict the *increase* of the profile loss due to coolant injection, and not the overall profile loss for a given configuration. Two, they require as input certain measured data. Both of these restrict their applicability in a design environment, and make CFD an attractive possible alternative for loss prediction.

Kubo et al. [13] documented a computational effort for loss prediction of film-cooled airfoils. They modeled film cooling at various axial locations on both the PS and SS of a linear cascade. The approach used two-dimensional slots to model the compound-angled, diffusion-shaped holes, and film-hole exit boundary conditions were applied at the exit plane. Computational studies on the thermal aspects of film-cooling have shown that this practice can introduce considerable error in the jet exit conditions [14,15]. The study used the standard $k-\epsilon$ turbulence model with a modified technique, which effectively bridged the low-Re formulation with wall functions [16]. The computational results for overall profile loss consistently overpredicted the experiments by as much as 30 percent. When only the loss increase due to injection was considered, the predictions showed very good agreement with experiments, except at high blowing or momentum flux ratios. Due to modeling, grid quality, and turbulence modeling issues, the study cannot be used to pass judgment on the ability of CFD to predict losses, although it does represent an important first step.

1.3 Outstanding Issues and Motivation for Present Work

The single outstanding issue motivating this work is the following question: "Can computational fluid dynamics be used consistently and accurately to predict the impact of film cooling on aerodynamic losses?" No documented study to date has answered it. A systematic computational methodology is used that effectively minimizes errors due to computational modeling, geometry and grid generation, and discretization [17]. As a result, the turbulence model performance can be isolated and evaluated.

In addition, the physical mechanisms governing losses due to film cooling are not clearly understood. The physics of loss is examined, and the important contributors are highlighted. The influence of various parameters is discussed in terms of the flow physics; specifically, the role of blowing ratio, density ratio, and momentum flux ratio.

2 Test Case

The test case matches the experimental study of Ito [1] and Ito et al. [2], which documented losses on a linear airfoil cascade for single row film cooling with streamwise-injected, cylindrical holes on both the suction and pressure surface. The experimental setup is shown in Fig. 1. The cooling holes were located 10 percent (SS) and 15 percent (PS) of axial chord (145.3 mm) downstream of the airfoil leading edge. The blade-to-blade pitch of the cascade was 131.1 mm. The film-hole diameter was 2.38 mm, with $L/D=4.4$ and $P/D=3$. The streamwise injection angle was 35 deg.

Total pressure was measured at a location 110 mm downstream (axial direction) of the cascade exit plane. Measurements were taken by traversing a pitot probe at the midspan location across the pitch of one of the blades near the middle of the cascade. Losses presented are therefore only profile losses, and endwall and/or secondary losses are not considered. The reference case was a solid blade with no film cooling. Tests were then performed using different injection rates on both the suction surface and pressure surface. The losses were presented in terms of downstream profiles (SS) and overall pitchwise-averaged total pressure (SS and PS).

For all cases the cascade inlet velocity was 14.1 m/s and the exit velocity was approximately 22.5 m/s. Based on exit velocity and overall blade chord ($L_c=169.1$ mm), the Reynolds number

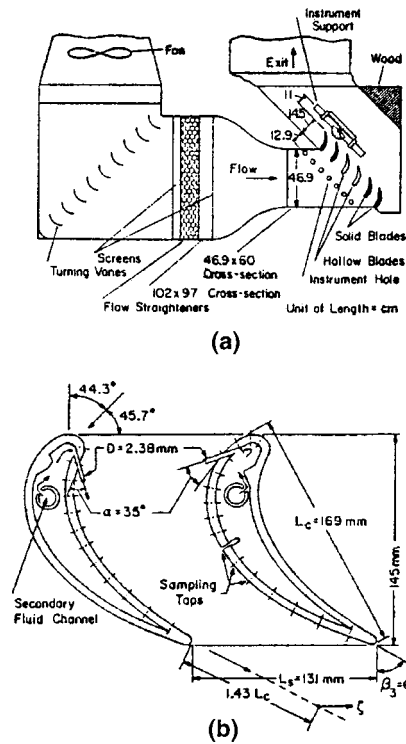


Fig. 1 Geometry of the experimental test case used in this study: (a) overall setup; (b) blading details. Computational domain modeled the experiments (Ito et al., 1980).

was about 2.3×10^5 and the exit Mach number was 0.06. On the suction surface, the approaching airfoil boundary layer displacement thickness was 0.22 mm, and the boundary layer was assumed laminar at the injection location based on Reynolds number. For some experimental cases, the suction surface boundary layer was tripped using a wire and sandpaper near the leading edge. On the pressure surface, the approach boundary layer was assumed turbulent due to an adverse pressure gradient that was present just downstream of the leading edge, although measurements to support this were not reported.

The cases considered in the present study are shown in Table 1. Note that only those cases with $DR=1$ have experimental counterparts. These cases are used for validation of the CFD methodology. The influence of variable coolant density is examined using the cases with $DR=2$. In the experiments, results were given in terms of the mass fraction of coolant flow versus mainstream flow through the passage. Corresponding values for M and I were calculated for the present study as follows. The mainstream mass flow was calculated using the given measured cascade inlet velocity and density. The coolant mass flow for each case was then calculated using the reported mass fraction. The coolant mass flux

Table 1 Summary of computational cases

| Case | Injection Surface | DR | M | I |
|------|-------------------|-----|------|-------|
| REF | Solid Blade | — | — | — |
| S1 | SS | 1.0 | 0.91 | 0.83 |
| S2 | SS | 1.0 | 2.2 | 4.84 |
| S3 | SS | 2.0 | 1.0 | 0.5 |
| S4 | SS | 2.0 | 2.0 | 2.0 |
| P1 | PS | 1.0 | 1.66 | 2.76 |
| P2 | PS | 1.0 | 6.6 | 43.56 |
| P3 | PS | 2.0 | 1.0 | 0.5 |
| P4 | PS | 2.0 | 2.0 | 2.0 |

was obtained by dividing the film-hole cross-sectional area, and coolant density was known. The free-stream velocity was computed based on the static pressure on the blade at the injection location and the inlet total pressure.

3 Numerical Method

3.1 Geometry. The computational domain included the cascade flow, the film-hole, and the supply plenum regions, and was chosen to match as closely as possible the experimental domain shown in Fig. 1. It extended approximately one overall chord length upstream and one chord length downstream of the airfoil. The assumption of periodicity in the blade-to-blade direction was used so that periodic conditions were applied at locations midway between consecutive airfoils. In this way, an infinite cascade was approximated by a single blade-to-blade pitch. Also, the assumption of spanwise periodicity was used along with the fact that the injection is in the streamwise direction, so that only 1/2 of the spanwise film-hole to film-hole pitch was included in the domain, and symmetry planes were applied in the center of the film hole and at the midpitch line between holes. This effectively modeled a cascade with infinite span. The geometry was generated using the *I-DEAS* Solid Modeling and FEA package from SDRC, Inc.

3.2 Grid. A novel grid generation methodology was implemented in order to satisfy all requirements of grid resolution and grid quality on this complex geometry, including the requirement that near-wall cell centers be at approximately $y^+ = 1$ for the two-layer near-wall treatment. The technique used an unstructured, multitopology, super-block approach along with solution-based adaptation to ensure grid independence. Super blocking refers to a technique in which the domain is partitioned into several different subsections in order to achieve maximum control over the grid

quality and density. Each of the subsections was then meshed using an appropriate topology. Hexahedra were placed in near-wall zones in order to achieve high aspect ratios very near the wall and extend the grid through the sublayer. In regions where a Cartesian grid was not feasible, tetrahedra were used in order to maintain high grid quality (minimize cell skewness). Hexahedral and tetrahedral regions were joined using layers of square-based pyramids. In regions far from the jet-crossflow interaction, the flow was assumed to be approximately two-dimensional and so triangular prisms were placed in these regions in order to reduce the overall cell count. Figure 2 shows the grid for the SS cases. Figure 2(a) shows the $z=0$ symmetry plane that exactly divides the film hole in the spanwise direction, and Fig. 2(b) shows the airfoil wall, film-hole wall, and plenum wall. The figure highlights the advantages of the multitopology approach in the current study.

Gridding was performed using a combination of *I-DEAS* and the *T-Grid* package from Fluent, Inc. The background grid contained approximately 600,000 cells, the majority of which were placed in the film-hole and jet-crossflow interaction regions. To check grid independence, the solution for Case *S3* (SS injection, $DR=2$, $M=1$) was refined in high gradient regions and near the wall, with the new grid containing 950,000 cells. This resulted in a negligible change of computed downstream profile loss, and the results on the initial grid were therefore judged to be grid independent. The results from the initial grid are presented here.

3.3 Boundary Conditions. Boundary conditions were chosen to match the experimental test cases as closely as possible. As mentioned above, periodic conditions, or repeating planes, were applied between the blades in order to model an infinite linear cascade. Symmetry conditions were applied on both the plane through the film-hole center and the midpitch plane. Upstream of the cascade, a constant velocity inlet was applied, with magnitude and flow direction (see Fig. 1(b)) of 14.1 m/s and 44.3 deg, respectively. Neither inlet turbulence intensity nor turbulent length scale were documented experimentally, so assumed values of 0.5 percent and 1/100th of the blade-to-blade pitch distance were used. Free-stream inlet temperature was 300 K. At the plenum inlet, constant velocity was applied so that the required blowing ratio was achieved, and turbulence intensity and length scale were assumed 2 percent and 1/100th of the plenum inlet height, respectively. The coolant temperature was 150 K for the $DR=2$ cases. All walls were “no slip” and adiabatic. The use of a two-layer near-wall treatment eliminated the need for wall functions, and this approach is discussed below.

3.4 Solver. The simulations were processed using the Fluent version 5 software from Fluent, Inc. The solver was pressure correction with multigrid acceleration. The discretization was a second-order accurate scheme for use with unstructured grid. The solver is identical to the one used in several recent papers from this research group, and has been validated for problems ranging from laminar two-dimensional flow past a cylinder [18] to three-dimensional flat plate film-cooling problems [17,19].

Convergence was determined three different ways. First, the overall residual level for each of the primary variables was monitored until it was reduced three orders of magnitude and was no longer changing. Second, the overall mass imbalance in the domain was required to be less than 0.01 percent of the passage mass flow rate. Third, different locations in the flowfield were monitored to ensure that no flow variables were changing with increasing iterations, and thus a “steady state” had been achieved.

3.5 Turbulence Modeling. For the present cases, three different variations of the $k-\epsilon$ model were used: the standard $k-\epsilon$ model (SKE) of Launder and Spalding [20], the RNG $k-\epsilon$ (RNG) model [21], and the realizable $k-\epsilon$ (RKE) model [22]. The two-equation approach to turbulence modeling for film-cooling problems is at present considered a “standard” due to ease of implementation and computational economy. However, these models

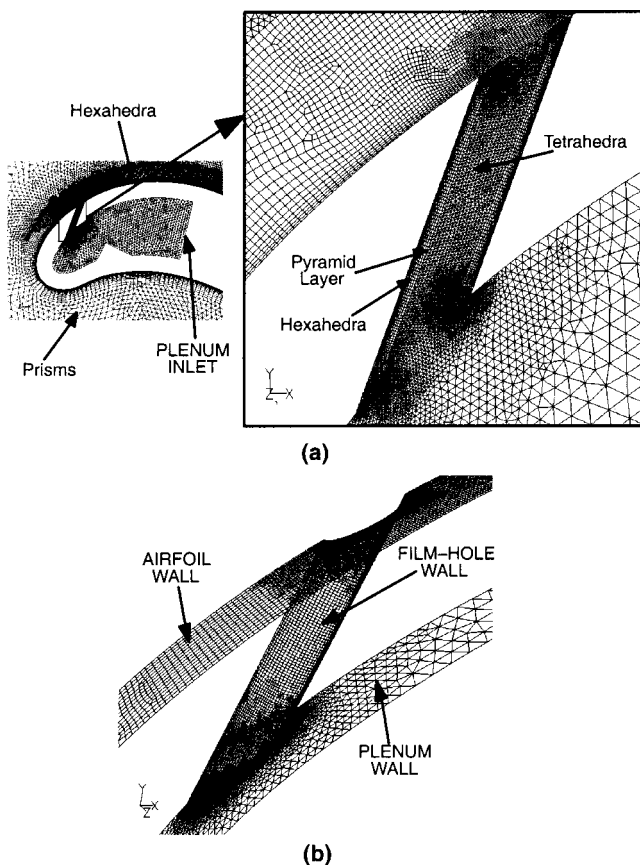


Fig. 2 Details of the SS grid used in the present study: (a) $z=0$ symmetry plane; (b) surface mesh in film-hole region

by their nature suffer from inherent isotropic turbulent viscosity, lack of “history” effects on the individual Reynolds stresses, and inability to represent turbulence at multiple scales. So additionally, results have been obtained for the reference case (REF) using a form of the full Reynolds-Stress (RSM) model (the Basic Model referred to by Launder, [23]). The results from the two-equation models are compared to the RSM case in order to evaluate them more effectively.

The reader is referred to Ferguson et al. [24] for details of the SKE, RNG, and RSM models. The major difference between models is that the first two use an eddy viscosity to relate Reynolds stresses to the mean flow velocity gradients, whereas the RSM model uses a transport equation for each of the Reynolds stresses. The eddy-viscosity for SKE and RNG is calculated from similar relations. For SKE:

$$\mu_T = C_\mu \rho \frac{k^2}{\varepsilon} \quad (1)$$

$$C_\mu = 0.09$$

For RNG:

$$\mu_{\text{eff}} = \mu \left[1 + \sqrt{\frac{C_\mu}{\mu}} \frac{k}{\sqrt{\varepsilon}} \right]^2$$

$$C_\mu = 0.0845$$

The values of turbulent kinetic energy, k , and turbulent dissipation rate, ε , are obtained from their own transport equations. The RNG model contains an extra source term in the transport equation for ε . This extra term has the effect of increasing generation of turbulent dissipation—in comparison to SKE—in regions with high rates of strain.

The realizable $k-\varepsilon$ model (RKE) is also considered in this study, and since this model was not discussed by Ferguson et al. [24], some important points are considered here. The model transport equation for k is identical to the SKE model, and the transport equation for ε is similar, with small differences in the generation and destruction terms. The reader is referred to Shih et al. [22] and Lumley [25] for a thorough discussion.

The “realizability” referred to in the model’s name is the so-called realizability constraint for Reynolds stresses. This constraint requires that Reynolds normal stresses be always positive:

$$\overline{u_i^2} \geq 0$$

and that the Schwarz inequality be satisfied:

$$\frac{\overline{u_i u_j^2}}{\overline{u_i^2} \overline{u_j^2}} \leq 1$$

A concise discussion is available from Durbin [26]. It should be apparent that for the SKE model, these conditions are in general not satisfied, considering both Eq. (1) and the Boussinesq hypothesis:

$$-\overline{\rho u_i u_j} = \mu_T \left(\frac{\partial U_i}{\partial x_j} + \frac{\partial U_j}{\partial x_i} \right) - \frac{2}{3} k \delta_{ij} \quad (2)$$

Specifically, the realizability conditions will be violated in regions of the flowfield with high rates of strain, relative to the inverse turbulent time scale, ε/k . A similar argument holds for the RNG model. The RKE model meets the realizability constraints through the use of a variable parameter C_μ , while using the same Boussinesq relationship for the Reynolds stresses (Eq. (2)), and the same form for the eddy viscosity, μ_T (Eq. (1)):

$$C_\mu = \frac{1}{A_0 + A_s U^{(*)k/\varepsilon}}, \quad U^{(*)} = \sqrt{S_{ij} S_{ij} + \Omega_{ij} \Omega_{ij}}$$

where, for a nonrotating reference frame,

$$\Omega_{ij} = \frac{1}{2} \left(\frac{\partial U_i}{\partial x_j} - \frac{\partial U_j}{\partial x_i} \right)$$

is the mean rotation rate. The parameter A_s is evaluated by:

$$A_s = \sqrt{6} \cos \phi, \quad \phi = \frac{1}{3} \arccos(\sqrt{6}W)$$

$$W = \frac{S_{ij} S_{jk} S_{ki}}{\bar{S}^3}, \quad \bar{S} = \sqrt{S_{ij} S_{ij}}$$

The constant A_0 is set equal to 4.04.

The impact of each of the four turbulence models on loss prediction is discussed in the results section below.

4 Results and Discussion

Comparisons between computed and measured results were made in terms of the loss coefficient, ζ :

$$\zeta = \frac{(P_{t1} - P_{t2})}{(P_{t1} - P_2)} \times \left(\frac{V_2}{V_{2,\text{avg}}} \right) \quad (3)$$

where P_{t1} is the total pressure at the cascade inlet, and P_{t2} , P_2 , V_2 , and $V_{2,\text{avg}}$ are the local total pressure, the local static pressure, the local velocity magnitude, and the pitchwise-averaged velocity magnitude, respectively, at the downstream measuring location. The results, both measured and computed, were obtained at a single spanwise location directly downstream of one of the film-hole centers. For incompressible flow, Eq. (3) is equivalent to a mass-weighted total pressure loss coefficient. Note that some studies use a thermodynamic or kinetic energy loss coefficient, which accounts for the addition of total pressure and/or total temperature to the mainstream by the coolant flow, which typically give a more realistic picture of the aerodynamic penalty incurred by film cooling. However, since the total pressure loss was reported in the experiments, it is the formulation used here. Evaluation of the predictive capability of the current methodology, as well as of the physics of loss, is possible with either form of the loss coefficient, and it is simply noted that a negative loss coefficient in the results does not imply nonphysical behavior. A small adjustment (typically less than 3 percent) was made to the computed loss coefficients in order to more accurately compare them to experiments, and is discussed in the appendix.

4.1 Solid Blade (REF) Results. The solid blade reference case was used as a baseline for film-cooling results and to evaluate turbulence model performance. The loading curve is shown in Fig. 3, which compares measured data and results obtained with the RKE turbulence model. The plot is of free-stream velocity along the airfoil, obtained from the equation:

$$V_\infty = \sqrt{2(P_{t,1} - P)/\rho}$$

and normalized by the average exit velocity, $V_{2,\text{avg}}$. The agreement lends confidence to the current computational approach.

Initially, results were obtained using each of the four turbulence models: standard $k-\varepsilon$ (SKE), RNG $k-\varepsilon$ (RNG), realizable $k-\varepsilon$ (RKE), and a Reynolds stress model (RSM). The profile of loss coefficient, ζ , at the downstream measuring location is shown in Fig. 4 for each of the turbulence models and compared to the experimental results. Both the SKE and RNG models exhibit peculiar behavior, including overprediction of the downstream wake spreading and local regions of negative loss. Both the RSM and RKE models yield reasonable results that show good qualitative agreement with the experiments. Table 2 lists the area-averaged loss coefficient, $\bar{\zeta}$, for each of the cases. The RSM and RKE models show excellent quantitative agreement with measurements, considering likely experimental uncertainty. The RNG model shows improvement over the SKE model, but still overpredicts the profile loss.

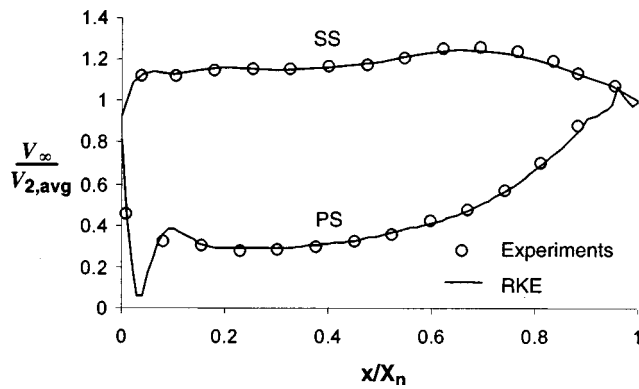


Fig. 3 Solid blade loading curve indicates good agreement between computations and experiments

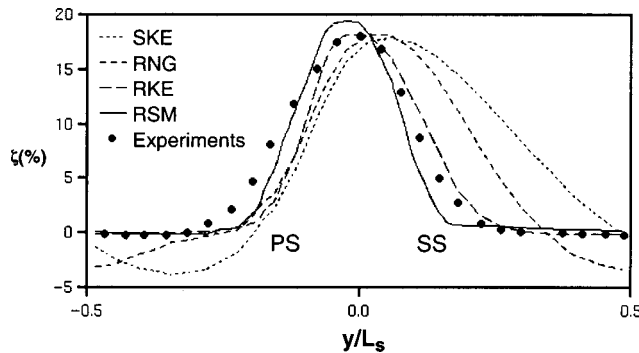


Fig. 4 Profiles of loss coefficient for the solid blade obtained with each of the turbulence models. The RSM and RKE models yield the best agreement with experiments.

Table 2 Pitchwise-averaged loss coefficient (REF case)

| Turbulence Model | $\bar{\xi}$ (%) |
|------------------|-----------------|
| RSM | 4.54 |
| RKE | 4.71 |
| RNG | 5.80 |
| SKE | 7.05 |
| Experiments | 4.58 |

The explanation for these results is seen in Fig. 5, which shows the contours of turbulent kinetic energy normalized by the average exit velocity ($k/V_{2,avg}^2$) over the airfoil for each of the four models. It is evident that both the SKE and RNG models have high turbulence levels in the region near the suction surface of the airfoil. Most of this turbulence is in fact produced in the free-stream region, and not in the airfoil boundary layer. This “excess” turbulence is responsible for overpredicting the growth of the suction side boundary layer and therefore overpredicting the downstream loss coefficient. The reason for this turbulence production can be traced back to the realizability conditions discussed briefly in the section on turbulence modeling. For both the SKE and RNG models, the computed Reynolds normal stresses can be less than zero, violating the realizability condition. (The RNG model is not derived using the concept of Reynolds averaging, but it is a simple matter to determine the “equivalent” Reynolds stresses in the model.)

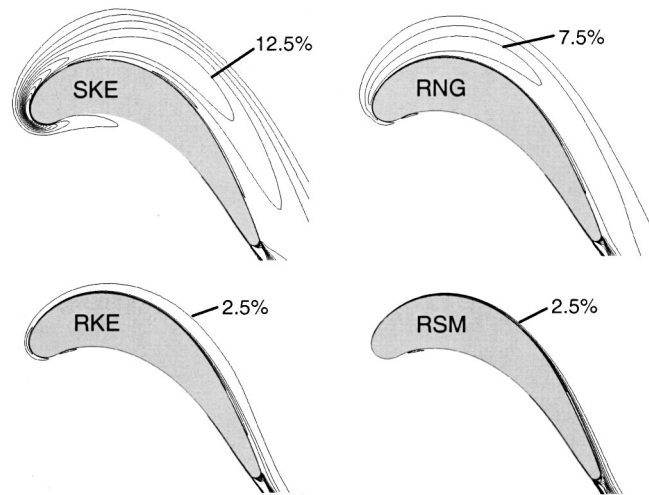


Fig. 5 Contours of turbulent kinetic energy normalized by average exit velocity (k/V_2^2), showing excess turbulence computed with SKE and RNG models

The production term in the k transport equation is derived exactly via Reynolds averaging:

$$G_k = -\overline{\rho u_i' u_j'} \frac{\partial U_j}{\partial x_i}$$

Consider as an example two-dimensional incompressible flow in a coordinate system aligned so that x_1 is in the streamwise direction, and x_2 is in the direction normal to the streamline, at the point of interest. If the flow is rapidly accelerating in the streamwise direction, then $(\partial U_1 / \partial x_1) \gg 0$, and by continuity $(\partial U_2 / \partial x_2) \ll 0$. This situation is similar to what happens when the flow near the suction surface of the airfoil—in the free stream and in the outer region of the boundary layer—is accelerated through the passage. The turbulent production due to normal Reynolds stresses should be the sum of a negative component $(-\overline{\rho u_1'^2} \partial U_1 / \partial x_1)$ and a positive component $(-\overline{\rho u_2'^2} \partial U_2 / \partial x_2)$ if the Reynolds normal stresses are positive, i.e., if they do not violate the realizability constraints. If, however, realizability is violated, then both of the production term components will be positive, and nonphysical turbulence production will result. This physically unrealistic behavior is the source of the “extra” turbulence in the SKE and RNG models. Excess turbulence is also produced in the stagnation region for these two models for the same reasons. This behavior (overprediction of k by the standard $k-\varepsilon$ model in impinging or stagnation regions) has been remarked upon in the literature [26]. The curious negative loss regions in the results obtained with the SKE and RNG models are also due to this excess production of turbulence.

The RNG model suffers less than the SKE model because of the extra source term in the ε transport equation. Obviously, it only mediates the impact of nonphysical behavior, without eliminating it. The RSM model, which uses transport equations for the individual Reynolds stresses, and the RKE model, which uses a formulation for C_μ that forces realizability, do not suffer from the effects of this extra turbulence, and so do a much better job of predicting the downstream loss, as seen in Fig. 4 and Table 2. This deficiency in the SKE model helps to explain the consistent overprediction of airfoil loss by Fukuyama et al. [16] and Kubo et al. [13], even for cases with no coolant injection.

This discussion indicates that accurate prediction of losses with film cooling will only be possible using the RSM or RKE model, out of those considered in the present study. Since the RSM model adds significantly to computational requirements, and since the

two-equation approach for turbulence modeling represents a current standard, the RKE model was chosen for the film-cooling cases discussed below.

4.2 Suction Surface Injection. The pitchwise-averaged downstream loss coefficient is plotted versus blowing ratio in Fig. 6(a) for the computational cases with DR=1 (S1 and S2), and compared to measured data. The experimental results were obtained with a tripwire and sandpaper near the leading edge of the suction surface to ensure a fully turbulent boundary layer, which is matched by the computations. The quantitative agreement between the computed and measured results shown in Fig. 6(a) is quite good. The loss *increase* due to film cooling on the suction surface is shown in Fig. 6(b), and of course looks similar to the overall loss prediction.

Figure 7 shows the profiles of local loss coefficient plotted versus normalized blade-to-blade distance for cases REF, S1, and S2. There is little change between REF and S1 in both the experiments and the computations, but the S2 case shows the energizing effect of the coolant flow, which is exiting the film hole in this case with a higher total pressure than the mainstream. The coolant jet for this case shows less spreading in the computations than in the experiments. This effect is similar to the underprediction by RKE of the airfoil wake spreading evidenced in Fig. 4. Underprediction of coolant spread rate is well documented for computa-

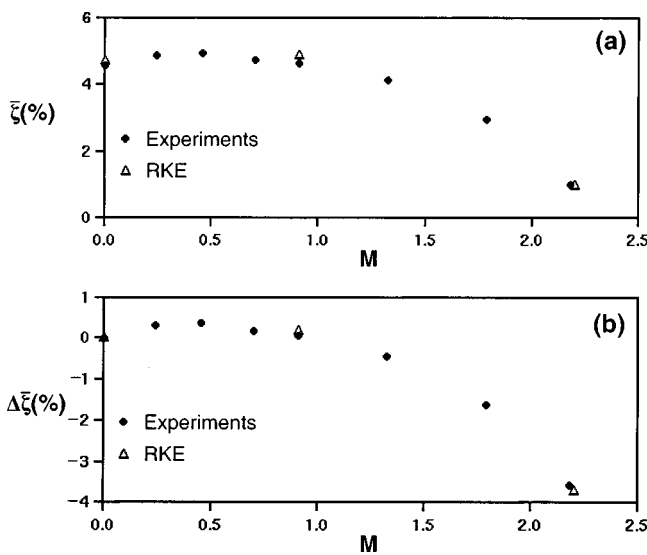


Fig. 6 Pitchwise-averaged downstream loss coefficient for SS injection: (a) overall; (b) increase due to film cooling

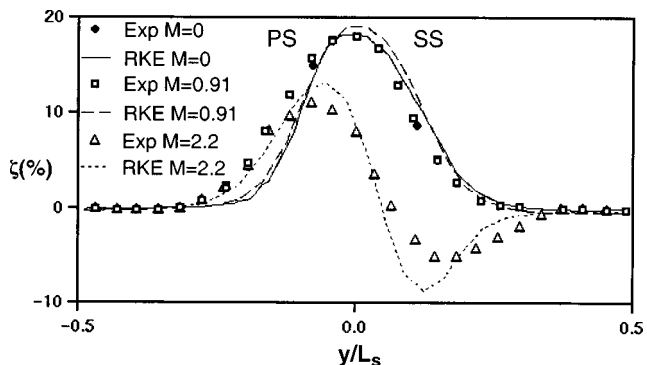


Fig. 7 Profiles of downstream loss coefficient for SS injection

tional film-cooling studies. Note that this underprediction of the spreading has a negligible effect on the area-averaged loss calculations shown in Fig. 6.

4.3 Pressure Surface Injection. Figure 8(a) shows the pitchwise-averaged downstream loss coefficient versus blowing ratio for cases REF, P1, and P2. The results follow the experimental trends, but contain an almost constant positive bias of about 1.25 percent. Better agreement is observed when only the loss *increase* due to coolant injection is considered; Fig. 8(b). The reason for the discrepancy in the overall loss calculation is the state of the *suction surface* boundary layer, which is laminar over most of the airfoil in the experiments, but turbulent over the leading edge onward in the computations. The suction side boundary layer was not tripped for the cases with PS injection, although it was for the cases with SS injection. A proof-of-concept simulation was performed on the solid blade in which the suction side boundary layer was laminar up to a point slightly past the location on the suction surface at which the pressure gradient becomes adverse, and the RKE model was applied downstream of that location. The result was a decrease in overall loss from 4.71 to 3.73 percent, versus an experimental value of 3.42 percent. Of course, the proof-of-concept simulation does not accurately reflect the boundary layer transition region, and so still does not exactly match the experiments. It does, however, highlight the importance of boundary layer state when attempting to predict overall profile losses computationally.

Loss is much less sensitive to injection on the pressure surface than on the suction surface. Note, for example, that at $M=2$, the change of total pressure loss is about -2.5 percent for SS injection and about -0.2 percent for PS injection. This relative insensitivity to pressure side injection has been documented by other researchers [6]. There are two reasons for it: First, because the free-stream velocity at the injection location on the pressure side is low, the coolant injection mass flow ratio (\dot{m}_c/\dot{m}_m) is much lower on the pressure side for equivalent blowing ratios; second, the total pressure mixing loss will depend on the relative difference between the total pressure of the exiting coolant and the total pressure of the free stream. This difference scales with the momentum flux ratio I :

$$\frac{P_{t,c}}{P_{t,\infty}} = \frac{\left(P_{inj} + (I) \left(\frac{1}{2} \rho_{\infty} U_{\infty}^2 \right) \right)}{\left(P_{inj} + \frac{1}{2} \rho_{\infty} U_{\infty}^2 \right)}$$

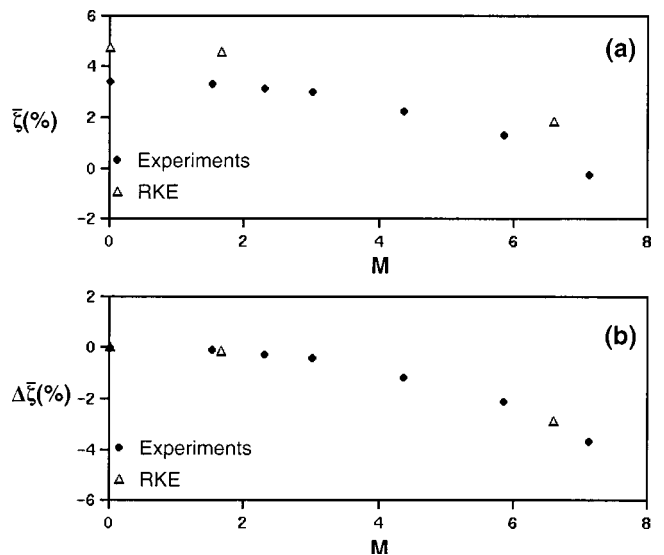


Fig. 8 Pitchwise-averaged downstream loss coefficient for PS injection: (a) overall; (b) increase due to film cooling

For PS injection, where static pressure at the injection location (P_{inj}) is high relative to the suction surface, the total pressure difference is less sensitive to changes in I , and consequently to changes in M . Use of a different loss coefficient, which considers effects of both coolant injection ratio and coolant total pressure, would reduce the sensitivity of results to the injection surface.

4.4 Discussion of Loss Physics. The injection of coolant into the airfoil boundary layer changes the profile loss by two separate mechanisms. One is the mixing loss due to the difference between coolant and mainstream total pressure and/or temperature. The mixing loss at a far downstream location can be determined if the total pressure and temperature of the coolant and mainstream, as well as the final, “mixed-out” condition is known. Typically, the location of interest is far enough downstream that almost all of the mixing has already occurred, and the assumption of a fully mixed flow is applicable. The approach uses a control volume analysis, and does not require knowledge of the details of the mixing process [27]. This approach is the basis for all of the analytical and semi-analytical predictive methods documented in the open literature, and all are generally successful [1,10,12]. Likewise, mixing loss should be relatively easy to predict using computational methods if the downstream location of interest is relatively far from coolant injection.

The second effect of film-cooling on the profile loss concerns its influence on the “wall losses.” Here the term wall losses refers to kinetic energy lost by the flow at the boundaries—the losses that are related to the drag on a turbine airfoil. Injection of a coolant jet will increase the turbulent mixing in the boundary layer, and this can increase the boundary layer loss for the airfoil. The most extreme example of this is when a coolant jet initiates transition in a laminar boundary layer, resulting in a dramatic increase in the wall losses, although film cooling can increase the mixing to some degree even in a turbulent boundary layer. Also, if the coolant jet remains close to the wall (the “film” in film cooling) then it may form a low or high velocity layer near the surface that decreases or increases, respectively, the airfoil wall shear stress. An analogous effect has been documented in experimental measurements of heat transfer coefficient downstream of film holes. For example, Sen et al. [28] showed that the heat transfer decreases just downstream of the film-hole breakout for low I , and increases for high I . Finally, coolant injection can influence the losses at the trailing edge, commonly called the base pressure loss. For the present cases, this influence is felt because of the changes in the boundary layer at the trailing edge as a result of coolant injection. If the boundary layer has been thinned by film cooling because the exiting jet has a high streamwise momentum content, then the separation at the trailing edge is more severe and trailing edge loss increases. The opposite is true for thickening of the boundary layer by a coolant jet with low streamwise momentum content.

The overall loss increase due to film cooling will be a combination of the mixing loss and the increased (or decreased) wall loss. Analytical approaches consider only mixing loss, and yet are known to perform reasonably well for loss increase prediction, especially at low coolant injection rates. This indicates the relative importance of the two loss sources, specifically that mixing loss dominates the loss increase unless film cooling initiates boundary layer transition. As the coolant injection rate is increased, however, the contribution of increased wall loss may become important, even for fully turbulent airfoil boundary layers. Examination of reported analytical approaches shows this behavior. Urban et al. [10] showed that their “TOTLOS” prediction method yielded excellent results for low injection rates, but under-predicted the loss increase at blowing rates above the design point. Similar results were found by Ito et al. [2]. This may be due to the increase in boundary layer loss caused by the injected coolant, which is not accounted for in their models. Ardey and Fottner [12] used an analytical method for their leading edge film cooling study, and showed excellent prediction even at high blowing

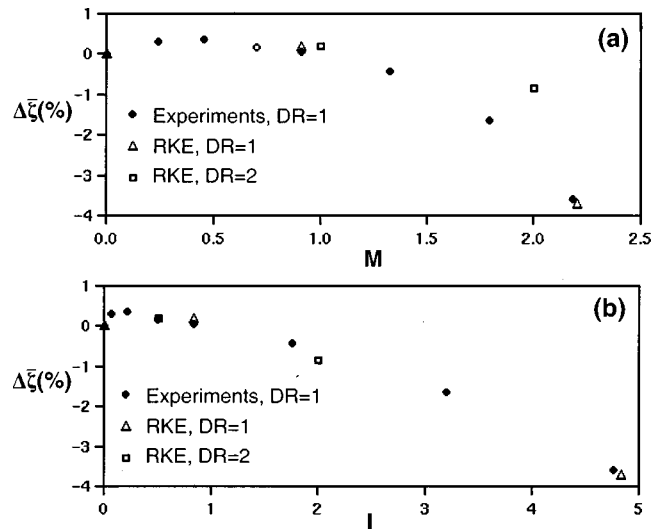


Fig. 9 Effect of density ratio on area-averaged loss coefficient for SS injection. Significant influence is observed when plotted versus M (a), but not when plotted versus I (b).

rates. It is likely that for their case, the increase in boundary layer loss was very small due to the fact that the coolant jets were lifted far away from the surface—shown by their flowfield measurements—and so did not significantly alter the airfoil boundary layer and increase the wall loss.

4.5 Effect of Density Ratio. There is some contradiction in the literature regarding the role of density ratio (DR) in film-cooled airfoil loss. Haller and Camus [3], Day et al. [7], and Osnaghi et al. [9] have reported that DR has negligible effect on the downstream thermodynamic efficiency. However, they first documented the impact of DR changes at constant blowing ratio (M) while the others reported the impact of density changes at constant momentum flux ratio (I). Ito et al. [2] reported significant influence of DR on total pressure loss due to film cooling when comparing results at equivalent M , which contradicts the conclusion of Haller and Camus.

Influence of density ratio for the SS cases is highlighted in Fig. 9. Shown is the increase of the downstream pitchwise-averaged loss coefficient plotted versus M and I , respectively. It is apparent that density ratio exerts a significant influence on loss when results are scaled versus M . The trend shown matches that documented by Ito et al. [2]. When scaled versus I , however, the influence is minimal. For a given momentum flux ratio, an increase in DR appears to result in a very slight decrease in the downstream loss. This small decrease may be due to a reduction in wall loss because of a reduced velocity ratio for the cases with DR=2. On the pressure surface, the effect of density ratio was less obvious, because of the range of blowing ratios considered with DR=2 (see Table 1). The PS trends were similar whether results were plotted versus M or I , in that very little change due to density ratio was noticeable. Overall, however, the current results support the assertion by Day et al. [7] and Osnaghi et al. [9] that downstream loss is best scaled by the film-cooling momentum flux ratio, at least for the current range of operating parameters, and that density ratio has only a slight influence on the loss.

5 Conclusions

To our knowledge, no study exists in the open literature that effectively demonstrates the ability of computational methods to predict profile losses on film-cooled airfoils. A systematic computational approach was used to isolate errors in the turbulence model performance, and to determine what considerations are necessary to predict film-cooling losses accurately. After valida-

tion against experimental results, the computations were used to elucidate loss mechanisms and help explain reported trends in the literature. Specific conclusions are listed:

- CFD methods can consistently yield useful predictions of airfoil loss, at least for the current range of operating parameters, when all sources of error (domain and boundary conditions, grid, discretization, and turbulence modeling) are addressed.
- Proper turbulence modeling is critical to accurate resolution of losses. Particularly, the model must not violate the realizability constraints on the Reynolds stresses. Both the standard form of the $k-\epsilon$ model and the RNG $k-\epsilon$ model were found to violate these constraints and therefore suffer from excess turbulence production. This yielded a consistent overprediction of airfoil profile loss. Use of either a Reynolds stress model, or the realizable form of the $k-\epsilon$ model, resulted in close agreement with measured results.
- The increase in profile loss by coolant injection can be separated into two sources: mixing loss of coolant and mainflow, and changes in the loss at airfoil boundaries because of coolant injection. At lower injection rates, the mixing loss was found to dominate the overall loss increase as long as coolant injection does not initiate boundary layer transition. As injection rate is increased, however, the effect of changes in the wall loss may become significant. Simple analytical or semi-analytical techniques generally only consider the mixing loss, and so are prone to error at these higher injection rates.
- The influence of density ratio on the loss increase was found to be minimal when the results were scaled versus the momentum flux ratio, I . These results support the assertion by Day et al. [7] and Osnaghi et al. [9] that I be used as the pertinent scaling parameter for airfoil loss increase.

Acknowledgments

This work is supported by the U.S. DEPSCoR program. The authors would like to thank Dr. Rick Lounsbury for continuing to give invaluable technical support for Fluent, and to Richard Baldwin for top-notch UNIX support. Thanks to Clemson University DCIT for providing access to high-performance research computing resources, and to Mike Marshall for the technical support.

Appendix

Comparisons between computed and measured results were made in terms of the loss coefficient, ζ :

$$\zeta = \frac{(P_{t1} - P_{t2})}{(P_{t1} - P_2)} \times \left(\frac{V_2}{V_{2,avg}} \right) \quad (3)$$

where P_{t1} is the total pressure at the cascade inlet, and P_{t2} , P_2 , V_2 , and $V_{2,avg}$ are the local total pressure, the local static pressure, the local velocity magnitude, and the area-averaged velocity magnitude, respectively, at the downstream measuring location. For incompressible flow, this is equivalent to a mass-weighted total pressure loss coefficient. Observing Eq. (3), it is apparent that the downstream change in total pressure is scaled by the difference in upstream total and downstream static pressure, $(P_{t1} - P_2)$, as is common practice for presentation of loss results. This formulation can lead to difficulties in comparing computed and measured results, and a discussion of the comparison procedure is in order. The reader is first referred to Fig. 1(a), which shows the experimental setup used by Ito [1]. Downstream of the airfoil cascade, assuming a relatively long extent of the wind tunnel, the flow would at some point be turned approximately 135 deg from its inlet flow angle. In addition, the incompressible flow would approach an average velocity that was equal to the downstream-to-upstream wind tunnel area ratio times the inlet velocity. This would occur regardless of the airfoil cascade, and illustrates the influence of the wind tunnel sidewalls on the downstream flow. In the computations, an infinite cascade was modeled, for which the

effect of wind tunnel walls is zero. If the measurements of interest are far from the walls in the “potential core” of the wind tunnel flow, then the measured change in total pressure should only reflect the impact of the airfoils, so the wall effect would not change that quantity. However, what the wall effect does influence is the scaling term, $(P_{t1} - P_2)$. Consider, for example, a case where the downstream section of the wind tunnel provides extra flow turning and/or decreases in cross-sectional area. Then the core flow would be accelerated, and P_2 would be lower than for a case in which the wall effects were absent. Clearly, scaling total pressure loss by some other, less sensitive value—say inlet dynamic pressure—would ease the comparison between computational and experimental results considerably for these cases.

For the current study, the impact of the wall effect on the scaling term, $(P_{t1} - P_2)$, was difficult to quantify. In order to allow effective comparison between measured and computed results, the following approach was used. First, the experimental value of average velocity at the measuring location (V_2) was calculated based on inlet velocity and reported flow exit angle. It was found to match the reported value. For cases with film cooling, the added mass of the coolant was also considered, and the increase in average velocity was calculated. This assumes that film cooling will have little impact on the turning angle, as has been reported in the literature (e.g., Osnaghi et al. [9]). Second, the difference between the static pressure in the experiments (P_2) and the static pressure in an experiment with an infinite cascade and no wall effects (P_2^*) was estimated based on the velocity differences, using the average velocity obtained in the computations:

$$P_2 - P_2^* = \frac{1}{2} \rho (V_{2,avg}^{*2} - V_{2,avg}^2)$$

where $V_{2,avg}^*$ is taken as the average velocity that would be measured in an infinite cascade, and the computed value is used for this. Substitution of this relation into Eq. (3) yields the loss coefficient modified to account for the wall effects. The obvious assumption is that the calculated average velocity matches the average velocity that would be measured if there were no wall effect in the experiments, or equivalently that the flow turning in the computations equals the flow turning that would be found in an experiment with no wall effects. The validity of this assumption can be checked, at least qualitatively, by considering that the amount of flow turning will depend on the blade loading and on the boundary layer development. If these two characteristics are accurately predicted, then the assumption should be valid. The first can be assessed by Fig. 3, which shows the loading curve for this case, computed versus measured. Agreement is good. The second characteristic can be judged from the downstream wake comparisons in Fig. 4. It was found that this agreement is good as well for the RSM and RKE models, indicating that the present comparison technique is valid. On average, the correction procedure shifted the loss calculation 2.8 percent from its original value.

Nomenclature

- D = film-hole diameter
- DR = density ratio = ρ_c / ρ_∞
- I = momentum flux ratio = $\rho_c V_c^2 / \rho_\infty V_\infty^2$
- L/D = film-hole length-to-diameter ratio
- L_c = overall blade chord = 169.1 mm
- L_s = blade-to-blade pitch distance = 131.1 mm
- M = blowing ratio = $\rho_c V_c / \rho_\infty V_\infty$
- P/D = film-hole spanwise pitch-to-diameter ratio
- P = static pressure
- PS = pressure surface
- P_t = total pressure
- SS = suction surface
- U = mean velocity
- V = velocity magnitude

X_n = axial chord length
 k = turbulence kinetic energy
 \dot{m} = mass flow rate
 u = fluctuating velocity
 x = axial dimension from leading edge
 y = blade-to-blade dimension
 y^+ = nondimensional wall distance
 ε = turbulence dissipation rate
 ζ = total pressure loss coefficient (Eq. (3))
 μ = dynamic viscosity
 ν = kinematic viscosity
 $\bar{\zeta}$ = pitchwise-averaged loss coefficient
 ρ = density

Subscripts

T = turbulent
 avg = area-averaged
 c = coolant
 eff = effective (molecular+turbulent)
 i, j = vector components
 inj = injection location
 m = mainflow (or passage)
 t = total
 ∞ = free stream
 1 = passage inlet
 2 = downstream measuring location

Superscript

* = value assuming an infinite cascade

References

- [1] Ito, S., 1976, "Film Cooling and Aerodynamic Loss in a Gas Turbine Cascade," Ph.D. Thesis, University of Minnesota.
- [2] Ito, S., Eckert, E. R., and Goldstein, R. J., 1980, "Aerodynamic Loss in a Gas Turbine Stage With Film-Cooling," ASME J. Eng. Power, **102**, pp. 964–970.
- [3] Haller, B. R., and Camus, J.-J., 1984, "Aerodynamic Loss Penalty Produced by Film Cooling Transonic Turbine Blades," ASME J. Eng. Gas Turbines Power, **106**, pp. 198–205.
- [4] Köllen, O., and Koschel, W., 1985, "Effect of Film Cooling on the Aerodynamic Performance of a Turbine Cascade," AGARD CP-390.
- [5] Yamamoto, A., Kondo, Y., and Murao, R., 1991, "Cooling-Air Injection Into Secondary Flow and Loss Fields Within a Linear Turbine Cascade," ASME J. Turbomach., **113**, pp. 375–383.
- [6] Hong, Y., Fu, C., Cunzhong, G., and Zhongqi, W., 1997, "Investigation of Cooling-Air Injection on the Flow Field Within a Linear Turbine Cascade," ASME Paper No. 97-GT-520.
- [7] Day, C. R. B., Oldfield, M. L. G., Lock, G. D., and Dancer, S. N., 1998, "Efficiency Measurements of an Annular Nozzle Guide Vane Cascade With Different Film Cooling Geometries," ASME Paper No. 98-GT-538.
- [8] Day, C. R. B., Oldfield, M. L. G., and Lock, G. D., 1999, "The Influence of Film Cooling on the Efficiency of an Annular Nozzle Guide Vane Cascade," ASME J. Turbomach., **121**, pp. 145–151.
- [9] Osnaghi, C., Perdichizzi, A., Savini, M., Harasgama, P., and Lutum, E., 1997, "The Influence of Film-Cooling on the Aerodynamic Performance of a Turbine Nozzle Guide Vane," ASME Paper No. 97-GT-522.
- [10] Urban, M. F., Hermeler, J., and Hosenfeld, H.-G., 1998, "Experimental and Numerical Investigations of Film-Cooling Effects on the Aerodynamic Performance of Transonic Turbine Blades," ASME Paper No. 98-GT-546.
- [11] Hartsel, J. E., 1972, "Predictions of Effects of Mass-Transfer Cooling on the Blade-Row Efficiency of Turbine Airfoils," AIAA Paper No. 72-11.
- [12] Ardey, S., and Fottner, L., 1997, "Flow Field Measurements on a Large Scale Turbine Cascade With Leading Edge Film Cooling by Two Rows of Holes," ASME Paper No. 97-GT-524.
- [13] Kubo, R., Otomo, F., Fukuyama, Y., and Nakata, Y., 1998, "Aerodynamic Loss Increase Due to Individual Film Cooling Injections From Gas Turbine Nozzle Surface," ASME Paper No. 98-GT-497.
- [14] Lylek, J. H., and Zerkle, R. D., 1994, "Discrete-Jet Film Cooling: A Comparison of Computational Results With Experiments," ASME J. Turbomach., **113**, pp. 358–368.
- [15] Garg, V. K., and Gaugler, R. E., 1997, "Effect of Velocity and Temperature Distribution at the Hole Exit on Film Cooling of Turbine Blades," ASME J. Turbomach., **119**, pp. 343–351.
- [16] Fukuyama, Y., Otomo, F., Sato, M., Kobayashi, Y., and Matsuzaki, H., 1995, "Prediction of Vane Surface Film Cooling Effectiveness Using Compressible Navier-Stokes Procedure and $k-\varepsilon$ Turbulence Model With Wall Function," ASME Paper No. 95-GT-25.
- [17] Walters, D. K., and Lylek, J. H., 1997, "A Systematic Computational Methodology Applied to a Three-Dimensional Film-Cooling Flowfield," ASME J. Turbomach., **119**, pp. 777–785.
- [18] Newman, O. M., 1995, "The Development of an Effective Computational Methodology for Complex Flows," Clemson University Undergraduate Honors Thesis.
- [19] Walters, D. K., and Lylek, J. H., 2000, "A Detailed Analysis of Film-Cooling Physics: Part I—Streamwise Injection With Cylindrical Holes," ASME J. Turbomach., **122**, pp. 102–112.
- [20] Launder, B., and Spalding, D., 1974, "The Numerical Computation of Turbulent Flows," Comput. Methods Appl. Mech. Eng., **3**, pp. 269–289.
- [21] Yakhot, V., and Orszag, S. A., 1986, "Renormalization Group Analysis of Turbulence: I. Basic Theory," J. Sci. Comput., **1**, pp. 1–51.
- [22] Shih, T.-H., Liou, W. W., Shabbir, A., and Zhu, J., 1995, "A New $k-\varepsilon$ Eddy-Viscosity Model for High Reynolds Number Turbulent Flows Model Development and Validation," Comput. Fluids, **24**, No. 3, pp. 227–238.
- [23] Launder, B. E., 1989, "Second-Moment Closure: Present . . . and Future?" Int. J. Heat Fluid Flow, **10**, pp. 282–300.
- [24] Ferguson, J. D., Walters, D. K., and Lylek, J. H., 1998, "Performance of Turbulence Models and Near-Wall Treatments in Discrete Jet Film Cooling Simulations," ASME Paper No. 98-GT-438.
- [25] Lumley, J. L., 1992, "Some Comments on Turbulence," Phys. Fluids A, **4**, pp. 203–211.
- [26] Durbin, P., 1996, "On the $k-\varepsilon$ Stagnation Point Anomaly," Int. J. Heat Fluid Flow, **17**, pp. 89–90.
- [27] Denton, J. D., 1993, "Loss Mechanisms in Turbomachines," ASME J. Turbomach., **115**, p. 621.
- [28] Sen, B., Schmidt, D. L., and Bogard, D. G., 1996, "Film Cooling With Compound Angle Holes: Heat Transfer," ASME J. Turbomach., **118**, pp. 800–806.

Transient Heat Transfer Measurements Using a Single Wide-Band Liquid Crystal Test

Dragos N. Licu¹
Matthew J. Findlay²
Ian S. Gartshore
Martha Salcudean

University of British Columbia,
Vancouver, BC, Canada

A technique using a thermochromic liquid crystal coating to measure film cooling effectiveness (η) and heat transfer coefficient (h_f) has been developed so that both of these important parameters can be obtained, as a function of time, from a single transient test. The technique combines a real-time, true color (24 bit) imaging system with the use of a wide-band liquid crystal coating and multiple event sampling for the simultaneous determination of η and h_f from the single test. To illustrate and validate this technique, the flow from compound-angle square jets in a crossflow is examined. The tests, in which the jet air was suddenly heated to about 40°C, lasted 30 seconds. The measured η is compared with measurements made in the same flow under steady-state conditions in a totally different way, using a mass/heat analogy and a flame ionization detector. Good agreement is obtained. Three different blowing ratios (M) of 0.5, 1.0, and 1.5 are investigated with a constant jet Reynolds number of about 5000. Detailed quantitative comparisons of the η measured in both ways are made for all blowing ratios, and plots of η and h_f are presented. [S0889-504X(00)01403-3]

Introduction

Film cooling is a method used to protect surfaces exposed to a high-temperature environment. This technique has numerous engineering applications, of which the most demanding is the cooling of gas turbine components. Film heating, rather than film cooling, is also extensively used in various aircraft applications, such as de-icing of inlets and airfoils. In the case of film cooling, a protective film layer is generated on a surface of interest by injection of a secondary medium through slots or discrete holes into the mainstream boundary layer. Injection through slots typically generates a two-dimensional flow field, while injection through holes generates a more complicated three-dimensional flow field.

Various experimental methods have been developed to measure the film cooling effectiveness and the heat transfer coefficient, which are two parameters required in the design of external cooling systems. Ekkad et al. [1] used a transient liquid crystal technique to measure local η and h_f downstream of one row of compound-angle injection holes. The detailed heat transfer characteristics in the near-hole region provided by Ekkad et al. [1] are based on a transient liquid crystal technique developed initially by Vedula and Metzger [2] in which two similar transient tests are used to obtain two different sets of conditions from the color change of a thermochromic liquid crystal (TLC), for the simultaneous determination of η and h_f . The same technique, also used in a recent study by Yu and Chyu [3] for injection through streamwise inclined holes, requires two transient experiments and does not provide information on the possible variation of η or h_f with time. In principle, both these parameters can vary with time because of deliberate or inherent flow unsteadiness, as illustrated in the results presented in this paper.

Chyu and Hsing [4] have described a new method based on the temperature-sensitive fluorescence of a thermographic phosphor to calculate heat transfer characteristics during a single transient test. Multiple-event sampling was used to minimize the uncer-

tainty of the solution via a least-squares method. The authors state that the technique can be applied for high temperatures and highly unsteady conditions.

The main objective of the present study is to demonstrate the efficacy of a wide-band liquid crystal technique [5], including the comparison between η calculated from the wide-band TLC method and η measured with a completely different technique based on flame ionization detector (FID) sampling in an isothermal mass transfer experiment [6]. Such a direct comparison of results obtained by fundamentally different methods is valuable. The TLC technique presented here shows that accurate results can be obtained with the appropriate imaging system and wide-band liquid crystal using multiple sampling during a single transient test. The film cooling geometry used in the present comparison is a flat plate with compound-angle square holes.

Experimental Apparatus and Methods

The experiments were performed in the Aerodynamics Laboratory at the University of British Columbia using an open-circuit, forced-draft wind tunnel. The maximum tunnel air speed was 12 m/s and was measured by Pitot tube. The test section was 1020 mm \times 405 mm \times 270 mm and was located downstream of a 4:1 area contraction section. The wind tunnel side walls were made of clear plexiglass for observation purposes.

The test section was modified to include a specially designed removable tunnel floor, and a removable nonglare glass tunnel ceiling. The removable floor is basically a flat plate made out of 0.5-in.-thick Plastic G sheet with low thermal conductivity. The physical properties of interest for the Plastic G are density $\rho = 1187.6 \text{ kg/m}^3$, thermal conductivity $k = 0.1872 \text{ W/mK}$, and specific heat $c = 1464 \text{ J/kgK}$.

The removable plate contains a row of five square jets, of size $d = 1/2 \text{ in.}$ (width of the jet with cross-sectional area d^2), angled at 30 deg to the tunnel floor and at 45 deg to the crossflow direction. The row of jets is located 406 mm from the test section entrance. The length of the jet duct is four times its width, so $L/d = 4$. The spacing of the jets in the spanwise direction is $S_j = 3d$ (see Fig. 1).

The jet flow was supplied by a compressor, filtered through multiple oil traps, and metered with the aid of a rotameter such that the jet Reynolds number was kept constant at a value of about $Re_j = 5000$. A honeycomb was inserted in the plenum to prevent a swirling flow pattern inside the plenum.

¹Present address: GE Aircraft Engines, Evendale, OH 45215.

²Present address: GE Power Systems, Greenville, SC 29615.

Contributed by the International Gas Turbine Institute and based on a paper presented at the 44th International Gas Turbine and Aeroengine Congress and Exhibition, Indianapolis, Indiana, June 7–10, 1999. Manuscript received by the International Gas Turbine Institute February 1999. Paper No. 99-GT-167. Review Chair: D. C. Wisler.

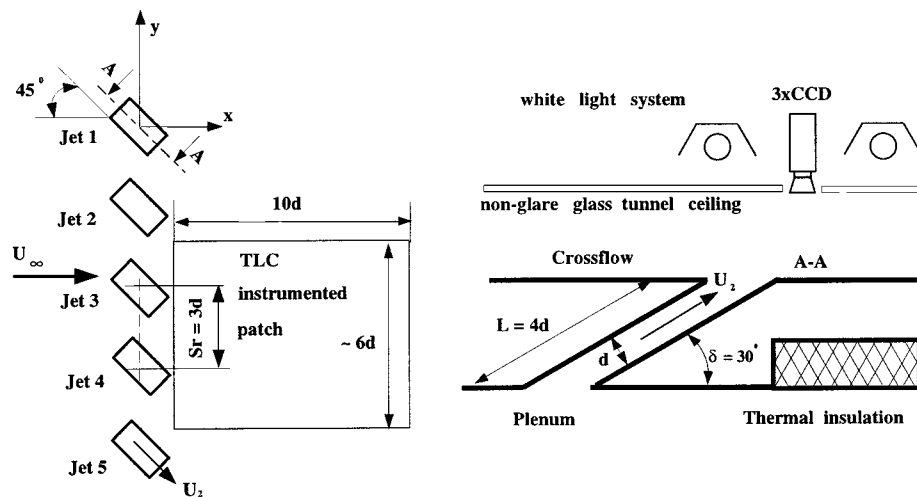


Fig. 1 Jets in crossflow arrangement

A boundary layer trip wire was fixed onto the tunnel floor, just upstream of the test section, to ensure a boundary layer with constant thickness across the span of the tunnel, which was also steady with a fixed transition point. The boundary layer five jet widths upstream ($x/d = -5$) from the center of the row of jets was measured by Findlay [6] and was approximately $2d$ thick for all cases presented here. The momentum thickness Reynolds number at $x/d = -5$ was approximately $Re_{\theta} = 1104, 658, \text{ and } 401$ for $M = 0.5, 1.0, \text{ and } 1.5$ respectively. Further details can be found in Licu [5] and Findlay [6].

Liquid Crystal Thermography Technique. A rectangular patch of dimensions approximately $6d \times 10d$ was covered with a wide-band liquid crystal over the region downstream of the middle jet. The wide-band TLC [7] was sprayed onto the surface by an experienced special coatings technician. The liquid crystal surface was illuminated with the white light system described in [5]. Two Optimarc lamps were symmetrically placed above the tunnel ceiling, and the incident light onto the instrumented liquid crystal surface came uniformly through the tunnel nonglare glass ceiling.

A $3 \times \text{CCD}$ RGB (Red, Green, Blue) color video camera was placed outside the tunnel, perpendicular to the center point of the liquid crystal instrumented patch, such that the camera lens was aligned with the tunnel ceiling and shot through an opening in the nonglare glass ceiling. Details of this arrangement are shown in Fig. 1. Light uniformity is very important and was checked by shooting a white piece of paper placed on the surface within the field of view. The position of the lamps was adjusted until a uniform color signal in the R, G, and B components was achieved across the white subject.

The calibration of the Thermax wide-band TLC was done in the same wind tunnel, and under the same lighting and viewing angle conditions as the actual experiments. A specially designed hollow calibration box was connected in a closed loop to a thermal circulator. The temperature of the bath and the heat input rates were adjusted to obtain a very slow and steady temperature increase of the circulator agent (distilled water). A type K thermocouple, mounted on the surface of the calibration box before the black base paint and the TLC were sprayed, was connected to an OMEGA OMNI-CAL calibrator unit such that the temperature of the TLC instrumented surface was known at all times with an error less than $\pm 0.05^\circ\text{C}$.

Still images were recorded directly on the dedicated imaging system PC's hard drive for each 0.2°C temperature increase of the calibration surface from 18°C to 41°C . The melting point of the TLC was between 19°C and 20°C , and the clearing point was

around 41°C . For the present application, an appropriate relationship must be found between the temperature of the liquid crystal instrumented surface and either the RGB or another similar color space. This function must be easy to compute and must minimize the error in temperature over the entire liquid crystal useful color response.

The double hexcone Hue, Saturation, and Lightness (HSL) color space was used in this study, where the RGB to HSL and HSL to RGB color space conversions can be found in Pitas [8]. The TLC calibration was repeated seven times and the minimum error, which was represented by the standard deviation values from a region 60×40 pixels sampled around the thermocouple leads, corresponded to the Hue component. The absolute error in temperature was calculated based on the absolute error in Hue from all the calibration data sets, and it was as low as $\pm 0.095^\circ\text{C}$ and as high as $\pm 0.247^\circ\text{C}$ for a temperature range between 21.6°C and 30°C . The error in temperature was higher for temperatures below and above this range, so that the useful temperature range was between 21.6°C and 30°C . The average error in temperature for this temperature interval was $\pm 0.155^\circ\text{C}$, and this compares well with the results from Wang et al. [9] where a temperature error of less than 0.3°C was reported for a 15°C band liquid crystal used in a two-temperature situation, where a different Hue, Saturation, Intensity (HSI) color space transformation was implemented.

The jet air was heated in an in-house designed and built in-line heat exchanger, diverted by a system of two-way direct-lift solenoid valves so that it flowed through the plenum, and finally discharged into the mainstream boundary layer through the row of compound-angle ducts. The temperature of the jets was recorded at a sample rate of 200 Hz by two type K thermocouples. The two thermocouples were placed just inside the outer two square ducts so that the flow through the middle jets was not disturbed. The final jet temperature was found by averaging the data recorded from the two thermocouples. During the 30 second transients, the uncompressed RGB images are captured in real time at five frames per second (fps) and stored into the host PC's RAM through a 32-bit color frame grabber. At the end of each run the data are transferred onto hard drives for further processing.

With the system initially in thermal equilibrium at temperature $T_\infty = T_2 = T_i$, transient one-dimensional heat conduction occurs through the plate when a sudden change in temperature is imposed on the jet flow. The semi-infinite solid formulation is then a convenient approach if the thermally affected region is less than the plate thickness. This situation can always be controlled by limiting the duration of the experiment. For the present experiments,

the thermally affected region was less than half of the flat plate thickness. At any time during the transient and at any particular location on the surface of interest, the following expression relates the film heat transfer coefficient h_f and the adiabatic wall temperature T_{ad} with the initial temperature T_i , the temperature of the surface T_w , and physical properties of the wall material α :

$$\frac{T_w(t) - T_i}{T_{ad} - T_i} = 1 - \exp\left(\frac{h_f^2 \alpha t}{k^2}\right) \operatorname{erfc}\left(\frac{h_f \sqrt{\alpha t}}{k}\right) \quad (1)$$

The initial and boundary conditions for Eq. (1) are:

$$T(z, t=0) = T_i \quad (2)$$

$$T(z=\infty, t) = T_i \quad (3)$$

$$-k \left. \frac{\partial T}{\partial z} \right|_{z=0} = h_f (T_{ad} - T_w(t)) \quad (4)$$

where z is taken to be perpendicular to the flat plate surface. Equation (1) was adapted from Carslaw and Jaeger [10] from the solution to the one-dimensional transient heat conduction into a semi-infinite wall with the initial and boundary conditions specified by Eqs. (2), (3), and (4). The film heat transfer coefficient h_f is defined by:

$$h_f = \frac{q_w}{T_w - T_{ad}} \quad (5)$$

where q_w is the heat flux at the wall, T_w is the measured temperature of the wall, and T_{ad} is the adiabatic temperature of the wall or the temperature achieved at the wall when $q_w=0$.

In a film cooling application, the adiabatic wall temperature is unknown and is a function of the location on the surface, cross-flow, and jet flow temperatures, and the degree of mixing between them. For each location on the surface, Eq. (1) has therefore two unknowns, h_f and T_{ad} . The latter can be defined by the use of the film cooling effectiveness η :

$$\eta = \frac{T_{ad} - T_\infty}{T_2 - T_\infty} \quad (6)$$

so that the denominator in the left hand side of Eq. (1) reads:

$$T_{ad} - T_i = \eta(T_2 - T_\infty) + (T_\infty - T_i) \quad (7)$$

The unknowns conveniently become h_f and η . The experiment has to produce only the value of the surface temperature during the transient $T_w(t)$ at all desired locations on the surface of interest. Two equations in the form of Eq. (1) can be written for each point on the surface and at different times during the transient $t = t_a$ and $t = t_b$, to provide the two needed relationships for the simultaneous calculation of h_f and η at that location.

Theoretically, any two time events can be chosen from the transient history during one test, or two separate tests can be conducted with the same flow field but different flow temperatures to calculate a time-independent heat transfer coefficient and film cooling effectiveness. The latter technique has been used in the past in film cooling applications, and can be categorized as a double sampling or double event procedure. A double event procedure provides the minimum required information for calculating h_f and η in a three-temperature situation, while a single event procedure could provide all the necessary information for calculation of the heat transfer coefficient in a two-temperature situation.

In typical jets in crossflow applications, unsteady vortex structures were often observed downstream of the injection sites [11,12]. In such situations, the double sampling techniques, as used in the past, may not lead to an accurate representation of the heat transfer characteristics. Multiple sampling provides further information in these cases and locally time-averaged h_f and η could provide higher accuracy in the representation of the heat transfer process on the surface of interest. Even in a perfectly

steady flow field, the multiple sampling technique can improve the accuracy by noise minimization through the time averaging procedure. The term noise is used here to describe random errors in temperature measurement.

In this study, a multiple sampling technique was used with the advantage that η and h_f were calculated simultaneously during a single transient test. Two separate tests were needed in the past.

A true step change in the temperature of the jet flow could not be achieved in the experiments, so that the temperature of the jets is actually a function of time, $T_2 = T_2(t)$. This information is incorporated in the solution to the transient heat transfer problem, described by Eq. (1) by a method similar to that described by Metzger and Larson [13] where the actual temperature rise was obtained from a superimposed set of incremental steps. A new algorithm was developed in this study to calculate the values of h_f and η . For any arbitrary time event pair, $t = t_a$ and $t = t_b$, a nonlinear equation for the unknown variable h_f can be written in the form:

$$\frac{T_w(t_a) - T_\infty}{T_w(t_b) - T_\infty} = \frac{\sum_{i=1}^{N_a} \left\{ 1 - \exp\left(\frac{h_f^2(t_a - \tau_i)}{\rho c k}\right) \operatorname{erfc}\left(\frac{h_f \sqrt{t_a - \tau_i}}{\sqrt{\rho c k}}\right) \right\} (\Delta T_2)_i}{\sum_{i=1}^{N_b} \left\{ 1 - \exp\left(\frac{h_f^2(t_b - \tau_i)}{\rho c k}\right) \operatorname{erfc}\left(\frac{h_f \sqrt{t_b - \tau_i}}{\sqrt{\rho c k}}\right) \right\} (\Delta T_2)_i} \quad (8)$$

where $(\Delta T_2)_i$ are the finite jet temperature changes corresponding to the discretized time events N_a for $t = t_a$ and N_b for $t = t_b$, respectively. Film cooling effectiveness can be thus calculated from the wall temperature response at either time event, $t = t_a$ or $t = t_b$, for example:

$$\eta = \frac{T_w(t_a) - T_\infty}{\sum_{i=1}^{N_a} \left\{ 1 - \exp\left(\frac{h_f^2(t_a - \tau_i)}{\rho c k}\right) \operatorname{erfc}\left(\frac{h_f \sqrt{t_a - \tau_i}}{\sqrt{\rho c k}}\right) \right\} (\Delta T_2)_i} \quad (9)$$

Equations (8) and (9) are solved numerically for a series of time event pairs. The time-dependent history of η and h_f can then be obtained and mean values can be calculated by averaging through a chosen time interval. The grid cells on the surface where the temperature change is less than the estimated average error in temperature of $\pm 0.155^\circ\text{C}$ are excluded from the calculations. These are mainly regions uncovered by the film cooling jets, so that η is basically zero and the transient heat conduction approach does not apply. Any attempt to solve Eqs. (8) and (9) here would produce an error. The heat transfer coefficient is also assigned a value of zero in these regions so that $h_f=0$ and $\eta=0$; these values are not produced by computations.

As shown by Licu [5] maximum accuracy in the results from the TLC technique is obtained by using time event pairs as far apart as possible. The transient tests used in the TLC measurements were 30 s long; longer tests would have invalidated the assumption of semi-infinite wall, made in formulating Eq. (1). Time event pairs were selected at t_a and t_b where t_a covered the first 8 s of the transient in 0.2 s increments, and $t_b = 30$ s for all cases. As noted earlier, both η and h_f can therefore be obtained for the first 8 s of the test, in 0.2 s intervals.

Although the present application of this method uses a time resolution of 5 Hz, the method is capable of higher frequency resolution. Lower frequency sampling over longer time is preferable in order to obtain a good statistical average. Higher frequency sampling may be useful in other specific circumstances.

Flame Ionization Detector Technique. The flame ionization detector (FID) system used in this study was previously described by Salcudean et al. [14], Findlay [6], and Licu [5]. Propane was

used as a trace gas and was thoroughly mixed with the air jet flow. Measurements of η were made by sampling the mixture of contaminated jet and crossflow air very close to the wall and immediately downstream of the injection sites. Because the temperatures and compositions of the crossflow and coolant gases are essentially the same, the density ratio of the coolant to crossflow gas is essentially one in this method, ensuring similarity with the liquid crystal technique.

The flows for all tests were statistically steady [6], that is, useful mean values of any parameter can be obtained by averaging over time through the unsteadiness due to turbulence (at higher frequencies) and through the large scale or gross unsteadiness (at lower frequencies).

The estimated film cooling effectiveness uncertainty reported by Salcudean et al. [14] accounted for errors in flow rate measurement (less than ± 2 percent) flame ionization detector sensitivity (less than ± 1 percent), sampling at 0.25 mm above the wall (less than ± 3 percent) so that for the present measurements, η was measured with an estimated uncertainty of less than ± 2.5 percent.

Results and Discussion

Three cases were investigated corresponding to the blowing ratios $M=0.5$, 1.0, and 1.5. Identical geometric and flow conditions were established for the two alternative measurement tech-

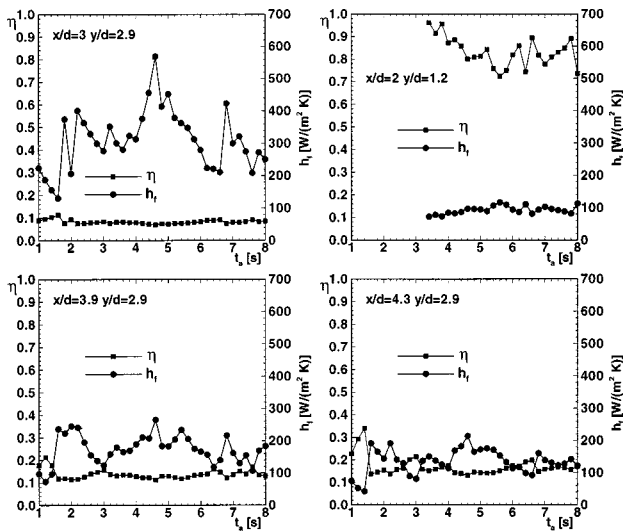


Fig. 2 Time history of h_f and η ; $M=1.0$

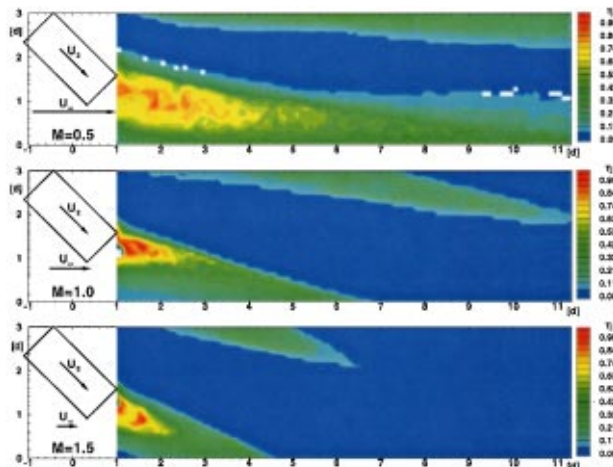


Fig. 3 Film cooling effectiveness contours

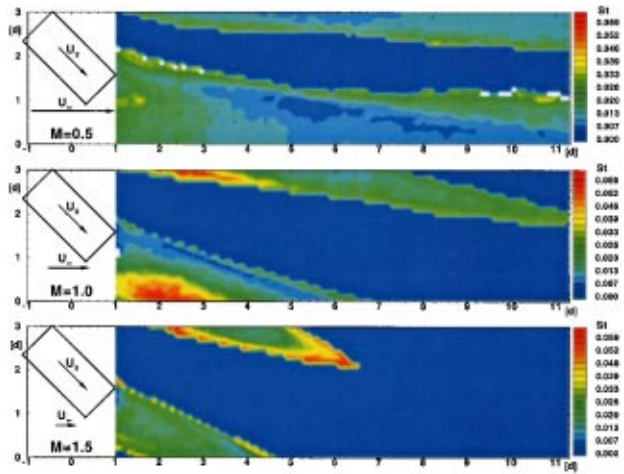


Fig. 4 Stanton number contours

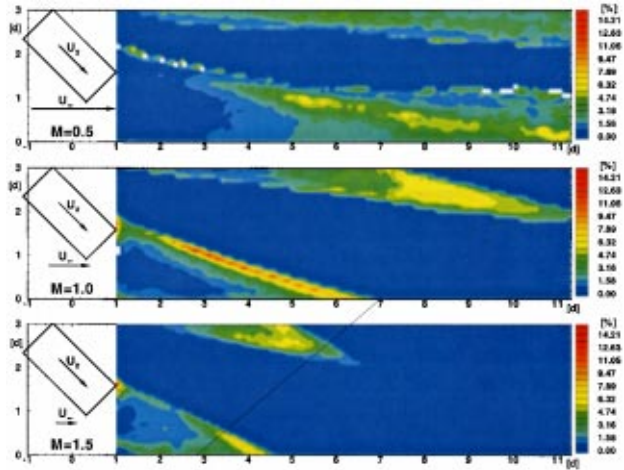


Fig. 5 Contours of uncertainty in the film cooling effectiveness results

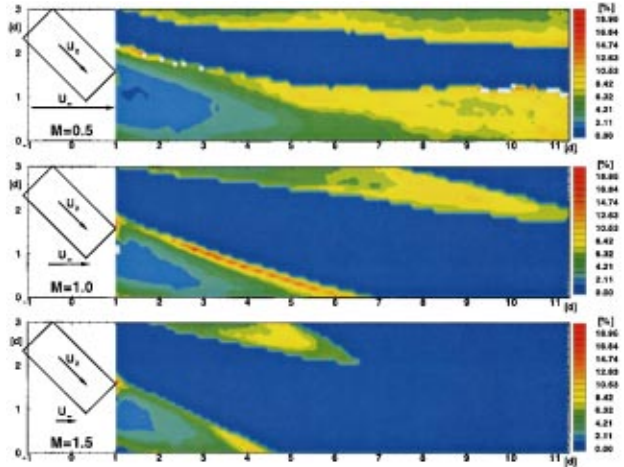


Fig. 6 Contours of uncertainty in the Stanton number results

niques reported here. The FID results provide mean values of η averaged over 15 s of sampling time at 130 Hz. The TLC technique provides the time variation of η and h_f at 5 Hz for an 8 s interval.

Typical transient results for the TLC method are shown in Fig. 2 at a few arbitrarily chosen locations on the surface. It is evident from these plots that the average from all time events can best characterize the complex three-temperature situation. Solutions at any one time could be very misleading. Examination of Fig. 2 shows that there is significant scatter in both η and h_f ; in particular h_f exhibits large variations at the location around the edge of the jet ($x/d=3, y/d=2.9$, see also Fig. 4 for location) while the corresponding η is quite uniform. The largest η variations from these plots is at a location well covered by the jet, $x/d=2$ and $y/d=1.2$ (see also Fig. 3 for location) while the corresponding h_f values are fairly uniform. With the present TLC technique, local transient heat transfer characteristics can be produced at any location on the surface, as needed.

Further data from the TLC technique have been obtained by averaging results over the first 8 s, and over two adjacent holes (jets number 3 and 4 in Fig. 1). This accounts for possible non-uniformities in the TLC layer thickness and large scale unsteadiness of the velocity field.

Figure 3 shows contours of η and Fig. 4 shows contours of h_f in dimensionless form. The axes for all the contour plots presented here are consistent with the representation shown in Fig. 1. Grid cells where a solution was attempted but was not found for at least two time event pairs were discarded, and are shown as blank cells in the contour plots. The contour plots give a very good indication of the area coverage for each of the three blowing ratios. From these plots, it appears that the best coverage is achieved in the $M=0.5$ case, when the jet is strongly deflected toward the floor by the crossflow. The coverage progressively deteriorates for the $M=1.0$ and $M=1.5$ cases, with the poorest coverage in the $M=1.5$ case. The jet seems to separate from the surface at the higher blowing ratio, therefore providing extremely low protec-

tion of the surface. The region with higher η is also significantly larger in the $M=0.5$ case than in the other two cases.

For all cases, h_f is higher around the sides of the jet, consistent with regions of stronger interaction between the jet, crossflow, and the surface. These regions at the sides of the jet are also characterized by the lowest η values. Within the area covered by the jet there are also regions of higher h_f ; such a region, located immediately downstream of the duct exit in the $M=0.5$ case, shifts toward one side of the jet in the other two cases with the highest values of the St number in the $M=1.0$ case. For all cases, regions with lowest h_f are present within the area covered by the jet, rather than on its sides, and at some distance downstream of the injection site, as expected. This trend is more obvious in the $M=0.5$ case, where there is a large central region with lowest values of the St number, starting at about four diameters downstream of the injection site. The heat transfer coefficient is still at high levels as far as 11 diameters downstream around the sides of the jet for the $M=0.5$ and $M=1.0$ cases.

Sun [15] has reported on the level of the St number for an undisturbed (no injection) two-dimensional turbulent flat plate boundary layer with the same fixed transition point and thickness as the boundary layer present in this study. At the location of the present injection sites, the Stanton number was about $St=0.005$ and this value decreased with the streamwise development of the boundary layer to about $St=0.0033$ at $x/d=11$. These values of the St number agree very well with the results from Kays and Crawford [16] for a constant temperature wall boundary condition. It can be seen from Fig. 4 that the presence of the jets has a significant effect on the level and distribution of the Stanton number: values as high as $St=0.03$ are evident for $M=0.5$ and $M=1.0$ at $x/d=11$.

Another important aspect that can be observed from Figs. 3 and

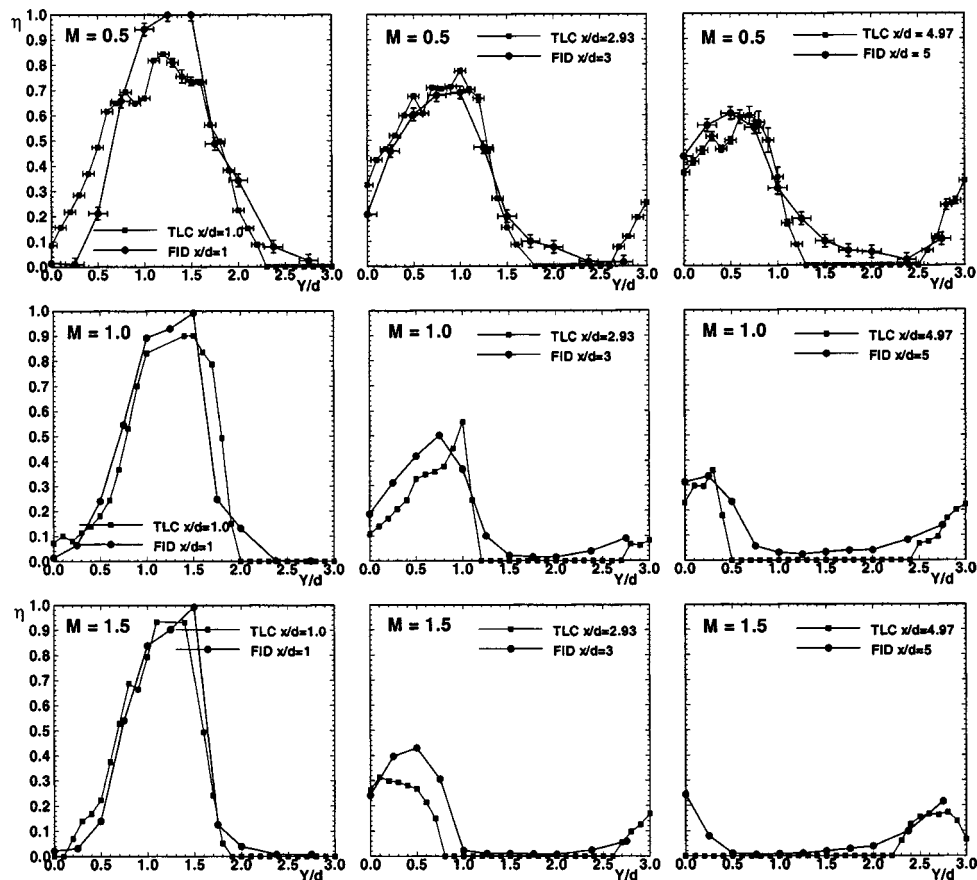


Fig. 7 Spanwise comparison of η for TLC and FID methods

4 is that regions with highest η do not correspond to regions of lowest h_f , and regions with highest h_f do not necessarily correspond to regions of lowest η . This clearly proves the need to determine both η and h_f to specify the film cooling performance on the surface of interest completely.

The uncertainty analysis for the TLC technique was detailed in Licu [5] and follows the methodology outlined in Abernethy et al. [17]. Figures 5 and 6 show the uncertainty maps based on a 95 percent confidence interval. For the $M=0.5$ case, the uncertainty in η is less than 9.55 percent everywhere and is as good as 0.1 percent and the uncertainty in h_f is as high as 20.5 percent and as low as 1 percent with typical values between 2 percent and 10 percent. For the $M=1.0$ case, the uncertainty in η is as high as 15.2 percent toward one side of the jet, and is as low as 0.23 percent with typical values between 1 percent and 7 percent. The uncertainty in h_f is comparable with that in the $M=0.5$ case. For the $M=1.5$ case, the uncertainty in η is less than 7 percent and that in h_f is less than 10 percent everywhere, except for a couple of cells around the downstream duct exit corner where the uncertainty runs as high as 21 percent for η and 27 percent for h_f .

Figure 7 compares spanwise distributions of η from the two methods at different streamwise locations on the surface for all blowing ratios used. Again, all values of $\eta=0$ for the TLC technique are not computed but assigned, being indicative of regions where the change in temperature is less than the calculated experimental error. To help quantify the differences, error bars are shown for each point for the case $M=0.5$ in Fig. 7. The lateral variations are due to positioning error of the FID probes and resolution of the TLC images, respectively, and these values are similar for the other two cases, $M=1.0$ and 1.5 . Although there are some specific regions for which the differences between the two sets of η results are beyond the estimated error bounds, the overall agreement is very good. The presence in the flow of low frequency or gross unsteadiness may lead to differences between the two measurement techniques, arising from their different effective sampling frequencies. This effect has not been considered in the accuracy estimates quoted here. Also, for the statistically steady, fully turbulent boundary layer present here, it is assumed that the values of heat transfer coefficients at any point are essentially independent of the exact upstream wall temperature distribution [18].

In most cases, within the experimental accuracy, the trends are preserved as well as the peak η values. Even at the streamwise location $x/d=1$, in the immediate vicinity of the downstream duct exit, the trends are reproduced by the TLC technique. Except for a few points around the spanwise location $y/d=1.5$, the location of the downstream duct exit corner, the agreement is very good. For the other downstream locations, the peak values of η and their location are well reproduced except for the $M=1.0$ case at $x/d=3$, where a slight shift in the spanwise location of the jet is apparent, and for the $M=1.5$ case at the same downstream location of $x/d=3$. Note that the spanwise distributions of η shown in Fig. 7 represent a detailed test of the measurement techniques. Spanwise averages, commonly used in reporting measured values of η , would show less detail in the TLC and FID results.

Also, based on results from Fig. 7, it appears that the assumption of one-dimensional heat conduction was quite good overall. The region near holes was expected to be affected by multidimensional conduction effects. This is apparent for the case $M=0.5$ where the jets are strongly deflected toward the downstream side of the injection ducts. For all cases, the region on the surface around the lateral and upstream sides of the injection ducts that is influenced by multidimensional conduction effects can be clearly observed from the recorded color images at the end of the 30 second transients. This region is typically less than $d/2$ around the upstream side of the ducts and less than $d/4$ around the lateral sides of the injection ducts.

Conclusions

A complex three-temperature situation is present in compound-angle square jets in crossflow. This particular geometry was used to validate a transient heat transfer technique based on wide-band liquid crystal thermography [5]. The method allows for the simultaneous determination of h_f and η during one transient test using a wide-band liquid crystal and multiple event sampling. Available η data from the FID study of Findlay [6] are used for comparison. The overall record time and the sampling rate for the liquid crystal investigation were different from the FID investigation, and this might account for some of the differences in the reported results. Nevertheless, the film cooling effectiveness data from the two methods are in very good agreement, and this provides confidence in the computed values of the film heat transfer coefficient obtained with the transient liquid crystal technique. The transient results presented in this study indicate that the multiple sampling technique with the time average of the computed results clearly provides a better representation of jets in crossflow, which contain inherent unsteadiness, and also reduces the uncertainty of the solution. A single time event pair sampling, as used in the past, could not possibly capture all the details of the transient experiment.

Acknowledgments

The authors are pleased to acknowledge the support of Pratt & Whitney Canada and the Natural Sciences and Engineering Research Council of Canada (NSERC). The support of Thermographic Measurements Ltd. (Thermax) and the assistance of John Inch from Powertech Labs, Inc., is also gratefully recognized. A preliminary version of this research was presented at the ASME Turbo Expo'99

Nomenclature

| | |
|--------------|---|
| C | = concentration, mass fraction |
| I | = jet-to-crossflow momentum flux ratio = $(\rho U^2)_2 / (\rho U^2)_\infty$ |
| L | = duct length |
| M | = jet-to-crossflow blowing ratio = $(\rho U)_2 / (\rho U)_\infty$ |
| N_a, N_b | = discretized time events |
| Re_2 | = jet Reynolds number = $U_2 d / \nu$ |
| Re_θ | = momentum thickness Reynolds number = $U_\infty \theta / \nu$ |
| S_r | = jet spacing |
| St | = Stanton number = $h_f / \rho c_p U_\infty$ |
| T_∞ | = crossflow temperature |
| T_2 | = jet temperature |
| T_{ad} | = adiabatic wall temperature |
| T_i | = initial temperature |
| T_w | = wall temperature |
| U_2 | = bulk jet velocity |
| U_∞ | = crossflow mean velocity |
| c | = specific heat |
| d | = jet width |
| h_f | = film heat transfer coefficient |
| k | = thermal conductivity, turbulence kinetic energy |
| q_w | = heat flux at the wall |
| t, τ | = time |
| t_a, t_b | = time events |
| x, y, z | = axes of the tunnel coordinate system |
| ΔT_2 | = incremental jet temperature |
| α | = thermal diffusivity |
| η | = adiabatic film cooling effectiveness = $(T_{ad} - T_\infty) / (T_2 - T_\infty) = (C_w - C_\infty) / (C_2 - C_\infty)$ |
| ν | = kinematic viscosity |
| ρ | = density |
| θ | = momentum thickness = $\int_0^\infty u/U(1-u/U)dz$ |

References

- [1] Ekkad, S. V., Zapata, D., and Han, J. C., 1997, "Heat Transfer Coefficients Over a Flat Surface With Air and CO₂ Injection Through Compound Angle Holes Using a Transient Liquid Crystal Image Method," *ASME J. Turbomach.*, **119**, pp. 580–586.
- [2] Vedula, R. J., and Metzger, D. E., 1991, "A Method for the Simultaneous Determination of Local Effectiveness and Heat Transfer Distribution in Three-Temperature Convection Situations," ASME Paper No. 91-GT-345.
- [3] Yu, Y., and Chyu, M. K., 1998, "Influence of Gap Leakage Downstream of the Injection Holes on Film Cooling Performance," *ASME J. Turbomach.*, **120**, pp. 541–548.
- [4] Chyu, M. K., and Hsing Y. C., 1996, "Use of Thermographic Phosphor Fluorescence Imaging System for Simultaneous Measurement of Film Cooling Effectiveness and Heat Transfer Coefficient," ASME Paper No. 96-GT-430.
- [5] Licu, D. N., 1998, "Heat Transfer Characteristics in Film Cooling Applications," Ph.D. thesis, Dept. Mech. Eng., The University of British Columbia, Vancouver, BC, Canada.
- [6] Findlay, M. J., 1998, "Experimental and Computational Investigation of Inclined Jets in a Crossflow," Ph.D. thesis, Dept. Mech. Eng., The University of British Columbia, Vancouver, BC, Canada.
- [7] Thermax—Thermographic Measurements Ltd., 1998, <http://www.thermax.com/>.
- [8] Pitas, I., 1993, *Digital Image Processing*, Prentice Hall, Englewood Cliffs, NJ.
- [9] Wang, Z., Ireland, P. T., Jones, T. V., and Davenport, R., 1996, "A Color Image Processing System for Transient Liquid Crystal Heat Transfer Experiments," *ASME J. Turbomach.*, **118**, pp. 421–427.
- [10] Carslaw, H. S., and Jaeger J. C., 1959, *Conduction of Heat in Solids*, Oxford University Press, New York, 2nd ed.
- [11] Ajersch, P., 1995, "Detailed Measurements on a Row of Jets in a Crossflow—With Applications," M.A.Sc. Thesis, Department of Mechanical Engineering, The University of British Columbia, Vancouver, BC, Canada.
- [12] Haven, B. A., and Kurosaka, M., 1997, "Kidney and Anti-kidney Vortices in Crossflow Jets," *ASME J. Fluid Mech.*, **352**, pp. 27–64.
- [13] Metzger, D. E., and Larson, D. E., 1986, "Use of Melting Point Surface Coatings for Local Convection Heat Transfer Measurements in Rectangular Channel Flows With 90-deg Turns," *ASME J. Heat Transfer*, **108**, pp. 48–54.
- [14] Salcudean, M., Gartshore, I. S., Zhang, K., and McLean, I., 1994, "An Experimental Study of Film Cooling Effectiveness Near the Leading Edge of a Turbine Blade," *ASME J. Turbomach.*, **116**, pp. 71–79.
- [15] Sun, Y., 1995, "An Experimental and Numerical Investigation of Heat Transfer Downstream of a Normal Film Cooling Injection Slot," Ph.D. thesis, Department of Mechanical Engineering, The University of British Columbia, Vancouver, BC, Canada.
- [16] Kays, W. M., and Crawford, M. E., 1980, *Convective Heat and Mass Transfer*, McGraw-Hill, New York, 2nd ed.
- [17] Abernethy, R. B., Benedict, R. P., and Dowdell, R. B., 1985, "ASME Measurement Uncertainty," *ASME J. Fluids Eng.*, **107**, pp. 161–163.
- [18] Eckert, E. R. G., 1984, "Analysis of Film Cooling and Full-Coverage Film Cooling of Gas Turbine Blades," *ASME J. Eng. Gas Turbines Power*, **106**, pp. 206–213.

Film Cooling Effectiveness for Short Film Cooling Holes Fed by a Narrow Plenum

C. A. Hale

M. W. Plesniak

S. Ramadhyani

School of Mechanical Engineering,
Maurice J. Zucrow Laboratories,
Purdue University,
West Lafayette, IN 47907

The adiabatic, steady-state liquid crystal technique was used to measure surface adiabatic film cooling effectiveness values in the near-hole region ($X/D < 10$). A parametric study was conducted for a single row of short holes ($L/D \leq 3$) fed by a narrow plenum ($H/D = 1$). Film cooling effectiveness values are presented and compared for various L/D ratios (0.66 to 3.0), three different blowing ratios (0.5, 1.0, and 1.5), two different plenum feed configurations (co-flow and counterflow), and two different injection angles (35 and 90 deg). Injection hole geometry and plenum feed direction were found to affect short hole film cooling performance significantly. Under certain conditions, similar or improved coverage was achieved with 90 deg holes compared with 35 deg holes. This result has important implications for manufacturing of thin-walled film-cooled blades or vanes. [S0889-504X(00)00603-6]

Introduction

Demands for more power and higher thermal efficiencies have resulted in steadily increasing gas inlet temperatures in modern gas turbines to a level such that aggressive cooling schemes must be implemented. Turbine inlet temperatures of 1900 K are typical of current gas turbines, and there is interest in elevating the temperatures higher. Such temperatures are well above the failure temperature of the blade material. One of the most common methods of protecting the turning vanes and blades in these harsh environments is discrete hole film cooling. Cooler, denser air is bled from the compressor and fed through internal passages in the blade or vane. In the case of advanced first-stage stator designs, coolant flows from the internal passages and impinges on the internal surface of the blade before turning to flow through a narrow plenum. From the supply plenum, the coolant is injected through small holes into the external boundary layer to form a protective film on the surface of the blade and to absorb some of the energy from the hot free-stream fluid. A numerical study by Lylek and Zerkle [1] established that, for short-hole geometries, the plenum and jet flow were strongly coupled with the crossflow in the film cooling hole region. Their results, along with current design interests, necessitate studies of the effects of short discrete film cooling hole and plenum geometries on surface heat transfer and film cooling performance.

Surface heat transfer and flow field measurements have been extensively reported in the literature over the last 35 years. Most studies used injection holes with large length-to-diameter ratios compared to the geometry of interest in the current study (e.g., [2,3]). Goldstein et al. [4] found little difference in film cooling effectiveness for holes with $L/D = 5.2$ and very long injection holes. A more recent study by Lutum and Johnson [5] indicated small to moderate changes in film cooling effectiveness for $5 < L/D < 18$ and concluded that coolant flow characteristics remained unchanged for $L/D > 7$.

Studies by Pietrzyk et al. [6,7], Sinha et al. [8], Sen et al. [9], Schmidt et al. [10], Bons et al. [11], and Kohli and Bogard [12] investigated different aspects of film cooling performance for short injection holes ($L/D \leq 4$). In these cases the plenum was a large, low-speed reservoir, which fed normal to the film cooling hole. These studies have been the standard of comparison for recent short hole numerical studies by Walters and Lylek

[13,14], Berhe and Patankar [15]), and Ferguson et al. [16]. Instantaneous PIV velocity data in the jet-crossflow region was reported by Gogineni et al. [17] for $L/D = 2.4$. Berhe and Patankar [15] also numerically investigated a narrow plenum ($1 < H/D < 4$) configuration in the region of a plenum endwall, where all of the fluid flowing through the plenum exits through the film cooling holes.

The first studies to address a narrow flow channel were conducted by Wittig et al. [18] who presented preliminary results for an experimental and numerical study of a single jet-in-crossflow fed by a narrow channel ($H/D = 2$). The work was extended by Thole et al. [19,20], Gritsch et al. [21], Giebert et al. [22], and Kohli and Thole [23,24]. In this series of studies the authors are careful to differentiate between *channels* feeding the film cooling holes (in which all of the flow through the channel does not flow through the film cooling hole) and the narrow *plenum* introduced by Berhe and Patankar [15]. The implications of these studies are well summarized by Kohli and Thole [24].

Burd et al. [25] reported hydrodynamic measurements comparing 35 deg streamwise injection for injection hole length-to-diameter ratios of 7.0 and 2.3. They found significant differences in the penetration of the jet into the crossflow and the region of influence downstream of the jet. This study was extended by Burd and Simon [26] to investigate plenum geometry. The same L/D ratios were investigated, but in this study a plenum with a height of $2D$ delivered coolant flow cocurrent to the crossflow (co-flow) and countercurrent to the crossflow (counterflow) for some of the $L/D = 2.3$ cases. They reported velocity data, jet-exit velocity profiles, and surface film cooling effectiveness data. Their results showed significant differences for surface film cooling effectiveness values in the near-hole region with the plenum flow direction. This result is contradictory to the numerical results of Berhe and Patankar [15], which indicated the effect of plenum flow direction to be negligible for $H/D = 2$. The study has since been extended to report discharge coefficient data and turbulence spectra and length scale data for the same cases. These studies were the first to report data for the narrow plenum flow geometries introduced in the Berhe and Patankar [15] study, which are of interest in the current study.

The goal of the present study is to measure near-hole surface adiabatic film effectiveness data, while examining the effects of injection angle ($\alpha = 35$ or 90 deg), plenum flow direction (co-flow or counterflow), injection hole length-to-diameter ratio for short holes ($L/D = 0.66$ or 3.0 for 90 deg jets and 1.16 or 2.91 for 35 deg jets), and blowing ratio ($M = 0.5, 1.0, \text{ or } 1.5$) for a narrow plenum ($H/D = 1$). Although effectiveness data have been previ-

Contributed by the International Gas Turbine Institute and presented at the 44th International Gas Turbine and Aeroengine Congress and Exhibition, Indianapolis, Indiana, June 7–10, 1999. Manuscript received by the International Gas Turbine Institute February 1999. Paper No. 99-GT-36. Review Chair: D. C. Wisler.

ously reported for film cooling holes fed by a narrow plenum with $H/D=2$, the current experimental study is the first to explore the effect of the plenum feed direction for a narrow plenum of $H/D=1$.

Experimental Test Facility

The experiments were carried out in an open circuit low-speed wind tunnel with a 122 cm long by 30 cm square, optically clear, polycarbonate test section. A detailed description of the low-speed tunnel is presented in Wolochuk et al. [29,30]. The jet injection region attaches to the floor of the test section, and the boundary layer that encounters the row of jets is conditioned using a 1.3-mm-dia cylindrical trip wire spanning the width of the wind tunnel floor [31]. The trip wire is located 0.66 m upstream of the leading edge of the film cooling holes. A secondary blower supplies the injection air.

Though all cases in the current study are short holes ($L/D \leq 3$) our longest hole geometry will be referred to as "long" from here forward. Four different adiabatic floors, corresponding to the short and long cases for 90 and 35 deg injection, were constructed from polystyrene ($k=0.026$ W/m K). The supply plenum is reversible such that co-flow or counterflow plenum geometries are available. In all cases the plenum height is $1D$ with the plenum end wall $1D$ past the edge of the hole for the 35 deg hole

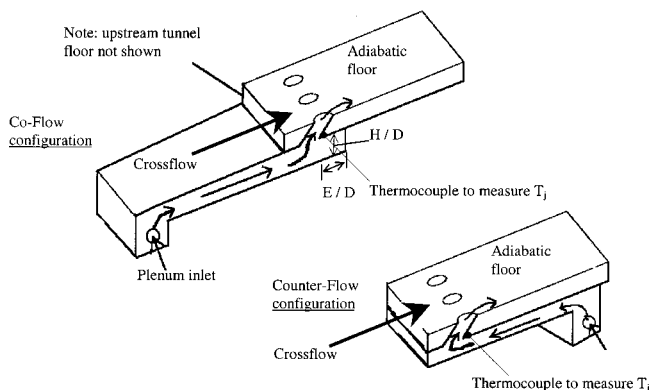


Fig. 1 Schematic of adiabatic test section and plenum

Table 1 Experimental parameters

| | |
|--|---|
| Hole diameter (D) | 19 mm |
| Number of holes | 5 |
| Hole spanwise spacing (P/D) | 3 |
| Density ratio (DR) | 0.90 to 0.94 |
| Free stream velocity (U_∞) | 10 m/s |
| Blowing ratio (M) | 0.5, 1.0, 1.5 |
| Hole length-to-diameter ratio (L/D) | 0.66, 3.0 (90° jets) 1.16, 2.91 (35° jets) |
| Plenum feed direction | co-flow, counter-flow |
| Plenum height (H/D) | 1 |
| Endwall distance (E/D) | 1 (35° jets) 0.66 (90° jets) |
| B.L. Displacement thickness (δ^*/D) | 0.1 to 0.15 |
| B.L. Momentum thickness (θ/D) | 0.09 |
| B.L. Reynolds Numbers (Re_θ) | 1024 |
| | (Re_δ) 10,500 |
| | (Re_{δ^*}) 1428 |
| | (Re_x) 1.4×10^6 |
| Jet Reynolds Number (Re_p) | 12,000 (M = 1.0) |

cases and $0.66D$ past the edge of the hole for the 90 deg hole cases. The plenum attaches directly to the adiabatic floor of the tunnel, as shown in Fig. 1. The experimental parameters of the study are given in Table 1. While the scaled geometric parameters are of interest to the gas turbine industry, the experimental conditions do not replicate density ratios, free-stream turbulence levels, Mach numbers, or surface curvature associated with real engine conditions.

Experimental Procedures

The polystyrene floor was coated with cholesteric liquid crystal paint on a black background. The injection air was heated by three variable-temperature heat guns placed at the inlet of the secondary blower. The mass flow rate of the injection air was monitored by an orifice plate flow meter with an embedded thermocouple to account for changes in air density with temperature. The density ratio of the jet to the free-stream (D.R) varied from 0.90 to 0.94, depending on the set boundary conditions. The corresponding variations in the momentum flux ratio (I) were less than 6 percent, for a fixed value of M . The crossflow free-stream velocity was monitored using a pitot-static tube measuring the dynamic head with a micromanometer with a resolution of 0.025 mm of water. The blowing ratios were calculated based on the plug flow jet-exit velocity associated with the total jet injection mass flow rate.

Heat losses through the plumbing and plenum were irrelevant, since the jet temperature was monitored inside the injection hole. This was accomplished by embedding a thermocouple in the surface of the polystyrene wall within the hole near the plenum-side entrance of the film cooling hole (see Fig. 1). Inasmuch as the thermal conductivity of the test floor was extremely small, this thermocouple measurement was an accurate representation of the gas temperature at the inlet of the injection hole. The tunnel free-stream temperature was also monitored with a thermocouple. The thermocouples were calibrated against each other using the same constant temperature bath at various temperatures and agreed with each other within the readability of the electronic thermocouple reading device (0.2°C). The same thermocouples were used for the *in situ* calibration of the liquid crystal paint. A narrow, 2.8 nm bandwidth optical filter was used in conjunction with a digital camera to record isotherms at 514 nm. The isotherms were measured against the thermocouples in regions of low thermal gradients on the adiabatic floor for calibration purposes. The calibration was repeated for each set of experiments and whenever changes in lighting or camera angle were made.

The tunnel free-stream temperature was monitored and the jet temperature was adjusted to capture the effectiveness value of interest. The free-stream and jet temperatures were monitored over time to ensure that steady-state conditions had been reached (typically 10 to 120 minutes was required to reach steady state). At steady state, photographs of the isotherm were recorded and the jet exit temperature was reset for the next data point. Once the data acquisition was completed, the images were scaled and the data were digitized electronically and plotted. The reported effectiveness (η) is defined by

$$\eta = \frac{T_{aw} - T_\infty}{T_j - T_\infty} \quad (1)$$

where T_{aw} is the adiabatic wall temperature of the isotherm measured by the liquid crystal paint and T_j and T_∞ are the jet and free-stream temperatures measured by the thermocouples, respectively.

A three-dimensional finite-volume heat conduction analysis of the near-hole region was conducted. The domain included the polystyrene floor extending 3 diameters upstream and downstream of the injection hole and spanned from the hole centerline to the plane of symmetry between adjacent holes. The computational domain consisted of a body-fitted hexahedral grid containing 100,000 cells. The numerical model provided corrections for the surface effectiveness measurements in the near hole region and

also indicated that the thermal losses around the injection hole accounted for a drop in the bulk mean temperature of the jet from the measurement point to the jet exit of less than 0.2 percent of the jet-to-free-stream temperature difference. Numerical solutions were obtained for all geometries investigated. The data acquired in the very near-hole region are not presented due to the high corrections required to account for conduction effects. Effectiveness corrections ($\delta\eta$) for the data presented are on the order of 0.01, with the values depending on the geometric configuration considered.

Experimental Uncertainty

The experimental uncertainties for the effectiveness and blowing ratio were calculated using standard uncertainty analysis methods [32]. The uncertainty in the reported values of the effectiveness is 7 to 10 percent, with the highest uncertainty corresponding to the lowest effectiveness value ($\eta=0.1$). The uncertainty in the blowing ratio varied from 4 percent at $M=1.5$ to 8 percent at $M=0.5$. The spatial locations obtained in digitizing the effectiveness data were found to be repeatable within 1 percent.

Experimental Results

Cases and Data. Table 2 lists the cases for which data were obtained.

L/D Effects. For the 90 and 35 deg co-flow, and 35 deg counterflow injection cases, the longer injection holes resulted in greater spanwise spreading of the lines of constant effectiveness than the shorter injection hole cases. These cases also showed higher centerline effectiveness values persisting downstream of the jets and appeared to give better overall coverage (higher effectiveness). As an example, Fig. 2 compares the surface effectiveness values for the 90 deg co-flow geometries at $M=0.5$ with $L/D=0.66$ and 3.0. The longer injection hole data are plotted on the upper half of the figure, while the short injection hole data are plotted on the lower half, so that side by side comparisons can be made. For a given value of η , the downstream persistence of film-cooling coverage along the centerline is greater for the longer injection hole case. For instance, the $\eta=0.29$ contour persists to $X/D \approx 6.8$ for the $L/D=3.0$ case, while it extends only to $X/D \approx 4.9$ in the $L/D=0.66$ case. If the total coverage is examined in the downstream region, the longer holes are more effective (based on more area being covered by higher η values).

Table 2 Test cases

| α | M | plenum flow | |
|----------|---------------|-------------|-----------|
| | | L/D | direction |
| 90° | 0.5, 1.0, 1.5 | 0.66 | CO, CT |
| 90° | 0.5, 1.0, 1.5 | 3.00 | CO, CT |
| 35° | 0.5, 1.0, 1.5 | 1.16 | CO, CT |
| 35° | 0.5, 1.0, 1.5 | 2.91 | CO, CT |

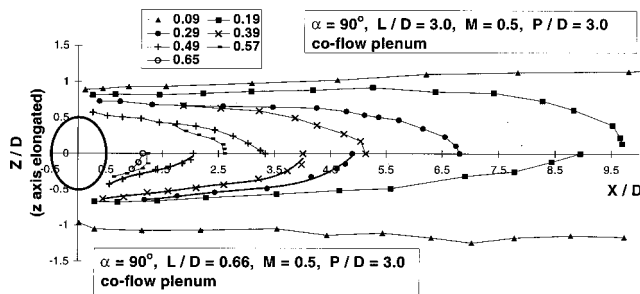


Fig. 2 Effect of L/D on η for co-flow 90 deg injection holes

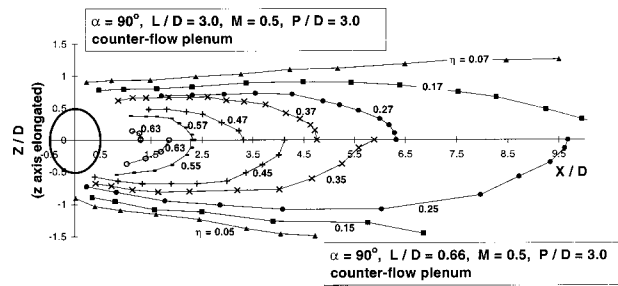


Fig. 3 Effect of L/D on η for counterflow 90 deg injection holes

The opposite trends are observed in Fig. 3 for 90 deg counterflow injection. This figure presents data for $L/D=0.66$ and 3.0 at $M=0.5$. Examination of this figure reveals better coverage of the film-cooled surface with the shorter injection holes than the longer holes. Trends similar to those exhibited in Fig. 3 were found at all blowing ratios investigated for the 90 deg counterflow cases. The trend observed in the 90 deg counterflow cases could be due to the in-hole vortex pairs (as reported by Leylek and Zerkle, [1]; Kohli and Thole [23]; and Brundage et al. [33]) with the opposite sense of rotation to the main counter-rotating vortex pair. The in-hole vortices may persist out of the hole and lower the trajectory of the jet through mutual induction.

In summary it appears that in the cases of the 35 and 90 deg co-flow longer holes, the jet flow is better aligned with the hole and the subsequent jet trajectory is influenced by this alignment. Consequently, better film-cooling coverage is obtained with the longer 35 deg holes than with the shorter 35 deg holes. The anomalous behavior noted with the 90 deg counterflow holes is interesting and worthy of further study.

Plenum Flow Direction Effects. The plenum flow direction had little effect on film cooling effectiveness for the 90 deg long and 35 deg short injection hole cases. Figure 4 shows a comparison of the co-flow and the counterflow plenum situations for the 90 deg short injection holes at $M=0.5$. Higher values of centerline effectiveness, as well as a wider coverage of the surface are observed for the counterflow case. As discussed in the previous section comparing L/D effects, it is believed that in-hole vortex pairs, rotating in the opposite sense to the main counter-rotating "kidney" vortices, are responsible for a lower jet trajectory and higher effectiveness.

Figure 5 displays the influence of the plenum flow direction with 35 deg long injection holes. Although the effects are not very pronounced, a noticeably higher centerline effectiveness is obtained with the co-flow plenum. This may be attributable to a slightly lower jet trajectory with the co-flow plenum compared to the counterflow plenum.

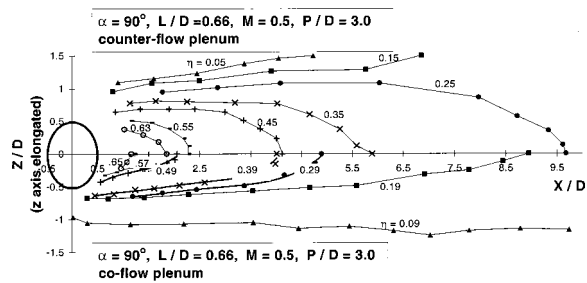


Fig. 4 Effect of plenum flow direction on 90 deg short injection hole effectiveness

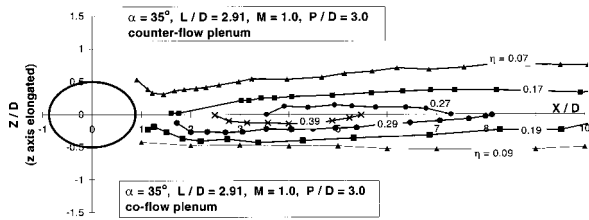


Fig. 5 Effect of plenum flow direction on 35 deg long injection hole effectiveness at $M=1.0$

Injection Angle Effects. Figure 6 compares the film-cooling coverage for the longer normal (lower half of figure) and angled injection (upper half of figure) holes for the counterflow configuration at $M=0.5$. In marked contrast to the 90 deg hole case, the iso-effectiveness lines with the 35 deg holes tend to be more parallel to the x axis in this figure, indicating better downstream protection of the surface. The 90 deg iso-effectiveness lines show slightly greater lateral spreading in the near-hole region. These observations are also true for short holes. However, at $M=1.0$ the coverage provided by the 35 deg angled holes is actually inferior to the 90 deg holes. For a side-by-side comparison attention is directed to Fig. 7, where data are presented for the counterflow plenum with $M=1.0$ and shorter injection holes. The superiority of the 90 deg holes is maintained even with longer injection holes.

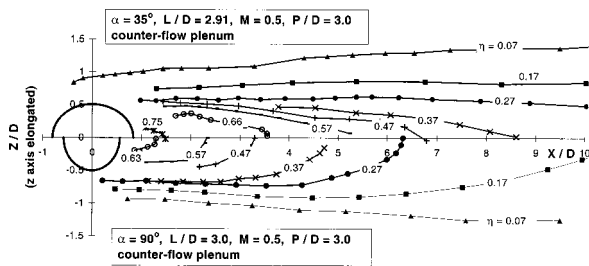


Fig. 6 Injection angle effects for long counterflow injection cases

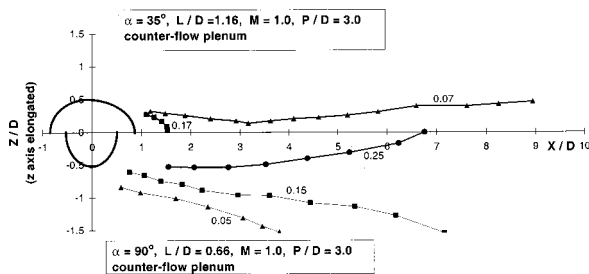


Fig. 7 Injection angle effects for short counterflow cases at higher blowing ratios

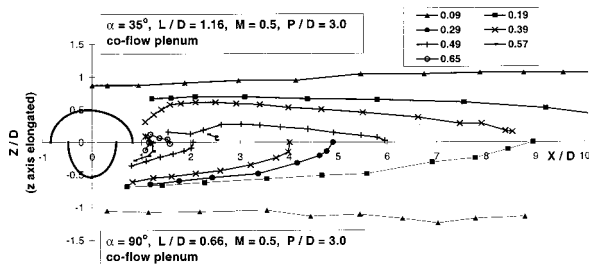


Fig. 8 Injection angle effects for short coflow cases at $M=0.5$

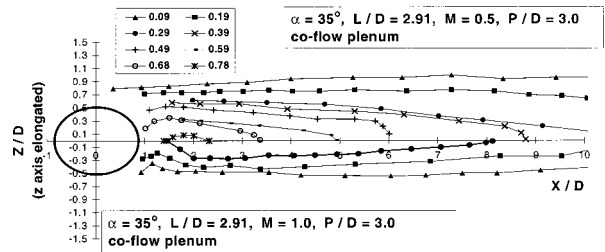


Fig. 9 Effect of jet lift-off on η at higher blowing ratios

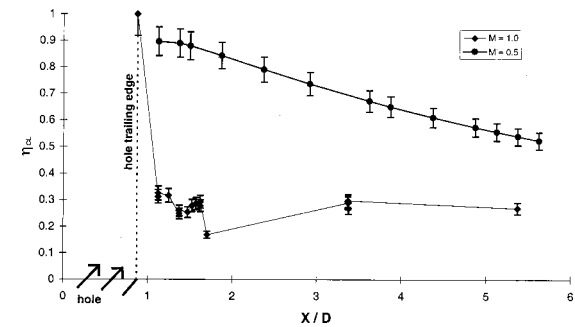


Fig. 10 Centerline effectiveness for 35 deg long counterflow injection

With the co-flow plenum, the effects of the injection angle are less systematic at $M=1.0$. For short holes, both 35 and 90 deg holes offer similar coverage. For longer holes the width of the coverage is greater with 90 deg holes, but the downstream persistence of higher centerline effectiveness is greater with 35 deg holes.

At $M=0.5$ with the co-flow plenum, the shorter 35 deg holes offer substantially greater film cooling effectiveness than the shorter 90 deg holes, as shown in Fig. 8. With longer holes the difference is much smaller.

General Effects. For all the cases studied, the film cooling effectiveness values for blowing ratios of 1.0 and 1.5 were lower than those for a blowing ratio of 0.5. This suggests the need to investigate blowing ratios ranging between zero and one for optimization studies. In some cases, for injection with 35 deg holes, the effectiveness lines were “squeezed inward” and the centerline effectiveness did not follow a monotonic decrease in the streamwise direction. This behavior is likely to be associated with the separation region downstream of the jet. These general effects can be inferred from Fig. 9, which is a plot of the effectiveness data for two different counterflow long 35 deg injection hole cases ($M=0.5$ and 1.0). The “islands” of effectiveness for the $\eta=0.78$ value, plotted on the upper half, and for the $\eta=0.29$ value, plotted on the lower half, imply a centerline effectiveness increase followed by a decrease across the enclosed region. The shape of the lines of iso-effectiveness in the near-hole region plotted on the lower half of the figure result from the acceleration of boundary layer fluid around and underneath the jet and the lift-off of the jet in the near-hole downstream region. Near-hole centerline effectiveness data are shown in Fig. 10 for the 35 deg long injection hole counterflow plenum case. The non-monotonic streamwise variation follows a large initial decrease in the very near-hole region for $M=1.0$; a more gradual monotonic decrease is shown for $M=0.5$.

Concluding Remarks

Film cooling effectiveness data for different L/D ratios, narrow plenum feed configurations, and injection angles in the short-hole regime have been presented. For the narrow plenum studied, the

magnitude of the effect of the plenum geometry on the film cooling effectiveness is dependent on the injection hole length and the streamwise injection hole angle. It was shown that, for short injection holes, the plenum and hole geometry can have significant effects on the flow field in the near-hole region. This is consistent with the findings of Burd and Simon [27,28]. Burd et al. [25] reported that short holes influenced a larger region of the flow field downstream of the jets. The current findings indicate that, for short injection holes investigated ($L/D \leq 3.0$), jets emanating from the longer holes spread more and give better coverage; except in the case of 90 deg counterflow configurations.

For some instances, the 90 deg injection hole resulted in effectiveness comparable to that obtained with angled injection holes and resulted in improved effectiveness at $M = 1.0$ for the counterflow plenum cases. This finding may have implications for easier manufacturing in some thin wall situations. This is consistent with the short-hole findings of Kohli and Bogard [12], where the feasibility of using higher injection angle holes was explored.

Lutum and Johnson [5] reported decreased effectiveness in the short hole regime with shorter holes. The current study draws the same conclusions for 90 deg co-flow, 35 deg counterflow, and 35 deg co-flow cases, but differs for 90 deg counterflow cases. To draw further conclusions, the surface heat transfer coefficients will be obtained and combined in the analysis of the surface heat transfer performance of the different configurations. This work is currently in progress, and the results will be reported in the near future.

Acknowledgments

We gratefully acknowledge the sustained support of Rolls-Royce/Allison Engine Co. during the course of this research.

Nomenclature

| | | |
|---------------|---|--|
| CO | = | co-flow |
| CT | = | counterflow |
| D | = | diameter of the film cooling hole |
| D.R. | = | density ratio = ρ_j / ρ_∞ |
| E | = | distance from edge of hole to plenum end wall |
| H | = | plenum height |
| L | = | length of film cooling hole supply tube |
| M | = | blowing ratio = $\rho_j U_j / \rho_\infty U_\infty$ |
| P | = | spanwise spacing of adjacent jets |
| Re | = | Reynolds number |
| T_{aw} | = | adiabatic wall temperature |
| T_∞ | = | free-stream temperature |
| T_j | = | bulk mean jet temperature |
| U_∞ | = | time averaged free-stream velocity |
| U_j | = | jet cross-sectional average velocity |
| X | = | streamwise distance downstream from center of hole |
| Y | = | distance normal to wall |
| Z | = | spanwise distance from center of hole |
| α | = | streamwise injection angle |
| δ | = | boundary layer 99 percent thickness |
| δ^* | = | boundary layer displacement thickness |
| η | = | effectiveness = $(T_{aw} - T_\infty) / (T_j - T_\infty)$ |
| η_{CL} | = | centerline effectiveness |
| θ | = | boundary layer momentum thickness |
| ρ_j | = | jet air density |
| ρ_∞ | = | free-stream air density |

References

- [1] Leylek, J. H., and Zerkle, R. D., 1994, "Discrete-Jet Film Cooling: A Comparison of Computational Results With Experiments," *ASME J. Turbomach.*, **116**, pp. 358–368.
- [2] Ligrani, P. M., Wigle, J. M., Ciriello, S., and Jackson, S. M., 1994, "Film-Cooling From Holes With Compound Angle Orientations: Part I—Results Downstream of Two Staggered Rows of Holes With $3d$ Spanwise Spacing," *ASME J. Heat Transfer*, **116**, pp. 341–352.
- [3] Ligrani, P. M., Wigle, J. M., and Jackson, S. M., 1994, "Film-Cooling From

- Holes With Compound Angle Orientations: Part 2—Results Downstream of a Single Row of Holes With $6d$ Spanwise Spacing," *ASME J. Heat Transfer*, **116**, pp. 353–362.
- [4] Goldstein, R. J., Eckert, E. R. G., and Burggraf, F., 1974, "Effects of Hole Geometry and Density on Three-Dimensional Film Cooling," *Int. J. Heat Mass Transf.*, **17**, pp. 595–607.
- [5] Lutum, E., and Johnson, B. V., 1999, "Influence of the Hole Length-to-Diameter Ratio on Film Cooling With Cylindrical Holes," *ASME J. Turbomach.*, **121**, pp. 209–216.
- [6] Pietrzyk, J. R., Bogard, D. G., and Crawford, M. E., 1989, "Hydrodynamic Measurements of Jets in Crossflow for Gas Turbine Film Cooling Applications," *ASME J. Turbomach.*, **111**, pp. 139–145.
- [7] Pietrzyk, J. R., Bogard, D. G., and Crawford, M. E., 1990, "Effects of Density Ratio on the Hydrodynamics of Film Cooling," *ASME J. Turbomach.*, **112**, pp. 437–443.
- [8] Sinha, A. K., Bogard, D. G., and Crawford, M. E., 1991, "Film-Cooling Effectiveness Downstream of a Single Row of Holes With Variable Density Ratio," *ASME J. Turbomach.*, **113**, pp. 442–449.
- [9] Sen, B., Schmidt, D. L., and Bogard, D. G., 1996, "Film Cooling With Compound Angle Holes: Heat Transfer," *ASME J. Turbomach.*, **118**, pp. 800–806.
- [10] Schmidt, D. L., Sen, B., and Bogard, D. G., 1996, "Film Cooling With Compound Angle Holes: Adiabatic Effectiveness," *ASME J. Turbomach.*, **118**, pp. 807–813.
- [11] Bons, J. P., MacArthur, C. S., and Rivir, R. B., 1996, "The Effect of High Free-Stream Turbulence on Film Cooling Effectiveness," *ASME J. Turbomach.*, **118**, pp. 814–825.
- [12] Kohli, A., and Bogard, D. G., 1997, "Adiabatic Effectiveness, Thermal Fields, and Velocity Fields for Film Cooling With Large Angle Injection," *ASME J. Turbomach.*, **119**, pp. 352–358.
- [13] Walters, D. K., and Leylek, J. H., 1997, "A Systematic Computational Methodology Applied to a Three-Dimensional Film-Cooling Flowfield," *ASME J. Turbomach.*, **119**, pp. 777–785.
- [14] Walters, D. K., and Leylek, J. H., 2000, "A Detailed Analysis of Film-Cooling Physics: Part I—Streamwise Injection With Cylindrical Holes," *ASME J. Turbomach.*, **122**, pp. 102–112.
- [15] Berhe, M. K., and Patankar, S. V., 1996, "A Numerical Study of Discrete-Hole Film Cooling," *ASME Paper No. 96-WA/HT-8*.
- [16] Ferguson, J. D., Walters, D. K., and Leylek, J. H., 1998, "Performance of Turbulence Models and Near-Wall Treatments in Discrete Jet Film Cooling Simulations," *ASME Paper No. 98-GT-438*.
- [17] Gogineni, S. P., Rivir, R. B., Pestian, D. J., and Goss, L. P., 1996, "PIV Measurements of Flat Plate Film Cooling Flows With High Free Stream Turbulence," *AIAA Paper No. 96-0617*.
- [18] Wittig, S., Schulz, A., Gritsch, M., and Thole, K. A., 1996, "Transonic Film-Cooling Investigations: Effects of Hole Shapes and Orientations," *ASME Paper No. 96-GT-222*.
- [19] Thole, K., Gritsch, M., Schulz, A., and Wittig, S., 1998, "Flowfield Measurements for Film-Cooling Holes With Expanded Exits," *ASME J. Turbomach.*, **120**, pp. 327–336.
- [20] Thole, K. A., Gritsch, M., Schulz, A., and Wittig, S., 1997, "Effect of a Crossflow at the Entrance to a Film-Cooling Hole," *ASME J. Fluids Eng.*, **119**, pp. 533–540.
- [21] Gritsch, M., Schulz, A., and Wittig, S., 1998, "Adiabatic Wall Effectiveness Measurements of Film-Cooling Holes With Expanded Exits," *ASME J. Turbomach.*, **120**, pp. 549–555.
- [22] Giebert, D., Gritsch, M., Schulz, A., and Wittig, S., 1997, "Film-Cooling From Holes With Expanded Exits: A Comparison of Computational Results With Experiments," *ASME Paper No. 97-GT-163*.
- [23] Kohli, A., and Thole, K. A., 1997, "A CFD Investigation on the Effects of Entrance Crossflow Direction to Film-Cooling Holes," *Proc. 32nd National Heat Transfer Conference, ASME HTD-Vol. 12*, pp. 223–232.
- [24] Kohli, A., and Thole, K. A., 1998, "Entrance Effects on Diffused Film Cooling Holes," *ASME Paper No. 98-GT-402*.
- [25] Burd, S. W., Kaszeta, R. W., and Simon, T. W., 1996, "Measurements in Film Cooling Flows: Hole L/D and Turbulence Intensity Effects," *ASME Paper No. 96-WA/HT-7*.
- [26] Burd, S. W., and Simon, T. W., 1997, "The Influence of Film Cooling Supply Geometry on Film Coolant Exit and Surface Adiabatic Effectiveness," *ASME Paper No. 97-GT-25*.
- [27] Burd, S. W., and Simon, T. W., 1999, "Measurements of Discharge Coefficients in Film Cooling," *ASME J. Turbomach.*, **121**, pp. 243–248.
- [28] Burd, S. W., and Simon, T. W., 1999, "Turbulence Spectra and Length Scales Measured in Film Coolant Flows Emerging From Discrete Holes," *ASME J. Turbomach.*, **121**, pp. 551–557.
- [29] Wolochuk, M. C., Plesniak, M. W., and Braun, J. E., 1994, "Evaluation of Vortex Shedding Flow Meters for HVAC Applications," *Purdue University Report ME-TSPC/HERL-TR-94-1*.
- [30] Wolochuk, M. C., Plesniak, M. W., and Braun, J. E., 1996, "The Effects of Turbulence and Unsteadiness on Vortex Shedding from Sharp-Edged Bluff Bodies," *ASME J. Fluids Eng.*, **118**, pp. 18–25.
- [31] White, F. M. 1974, *Viscous Fluid Flow*, McGraw-Hill, New York.
- [32] Kline, S. J., and McClintock, S. J., 1953, "Describing Uncertainties in Single-Sample Experiments," *Mech. Eng., Jan.*, pp. 3–8.
- [33] Brundage, A. L., Plesniak, M. W., and Ramadhyani, S., 1999, "Influence of Coolant Feed Direction and Hole Length on Film Cooling Jet Velocity Profiles," *ASME Paper No. 99-GT-35*.

Predictions of a Film Coolant Jet in Crossflow With Different Turbulence Models

Asif Hoda

Sumanta Acharya

Mechanical Engineering Department,
Louisiana State University,
Baton Rouge, LA 70803

This study investigates the performance of several existing turbulence models for the prediction of film coolant jet in a crossflow. Two-equation models employing $k-\epsilon$ and $k-\omega$ closures, broadly categorized as high-Reynolds-number formulations, low-Reynolds-number formulations, DNS-based formulation, and nonlinear formulations have been used to simulate the flow. In all, seven different turbulence models have been tested. Predictions with different models have been compared with experimental results of Ajersch et al. (1995) and with each other to critically evaluate model performance. The assessment of models has been done keeping in mind that all models have been formulated for wall-bounded flows and may not be well suited for the jet-in-a-crossflow situation. Close agreement with experimental results was obtained at the jet exit and far downstream of the jet injection region, but all models typically overpredicted the magnitude of the velocities in the wake region behind the jet. The present study clearly underscores the deficiencies of the current models, and demonstrates the need for improvements. [S0889-504X(00)03002-6]

Introduction

Film cooling of turbine blades is commonly employed to provide effective blade cooling that is needed to ensure long life of the turbine blades and to permit higher turbine inlet temperatures. The interaction of the coolant jet with the crossflow produces a highly complex, three-dimensional flow field in the vicinity of the jet injection. The flow is characterized by both large-scale coherent structures and small-scale turbulence, and the mixing process is controlled by the dynamics of these structures. The coherent structures of primary importance have been identified in the published literature to be jet shear-layer vortices, which dominate the initial portion of the jet, horseshoe vortices, which wrap around the base of the jet, counter-rotating vortex pair (CRVP), which results from the impulse of the jet on the crossflow, and wake vortices formed in the wake of the jet. Accurate prediction of such structures are necessary to correctly predict the jet penetration and reattachment length that are important for heat transfer calculations and the optimization of film cooling effectiveness.

Several experimental studies [e.g., [1–3]] and numerical investigations [e.g., [4–6]] of a jet-in-crossflow have been reported. In the numerical studies, the primary approach adopted has been to use the Reynolds-averaged Navier–Stokes (RANS) solver, which requires the prescription of a turbulence model. The two-equation turbulence models ($k-\epsilon$ and $k-\omega$) have been used most extensively to simulate a jet-in-crossflow with varying degrees of success. A systematic study of film cooling by Demuren et al. [7] revealed that the very complex flow field established behind the jet was not properly resolved and the turbulent mixing process was crudely simulated with the eddy viscosity model. Demuren [8] also carried out computations using a multigrid method and a second-moment closure model to approximate the Reynolds stresses. Although a fairly good prediction of mean flow trends was reported, there was considerable uncertainty regarding the accuracy of jet penetration height. Multigrid calculations by Claus and Vanka [9] failed to predict the horseshoe vortex even with a highly refined grid. This was attributed partly to the inability of the $k-\epsilon$ model to resolve the complex turbulence field. Findlay

et al. [10] included the plenum in the computational domain for streamwise inclined jets. The computations underpredicted the streamwise injection of fluid from the jet and the flow field was not in good agreement with experimental results for most of the domain. Ajersch et al. [11] conducted an extensive experimental investigation and a companion numerical simulation using a low-Re $k-\epsilon$ model along with a nonisotropic extension to the effective viscosity for near-wall turbulence. The streamwise velocity in the jet wake was overpredicted and the recirculation region behind the jet was found to be smaller and closer to the surface than that observed in the measurements. Noticeable overprediction of shear stresses was observed and the simulation could not capture the local minimum in kinetic energy, which was measured in the wake region of the jet.

The varied and often conflicting investigations carried out so far motivate the present study, where several existing turbulence models and their performance in predicting the film cooling flow behavior are evaluated. The focus of this paper is on the fluid dynamic behavior of the jet, and the ability of the turbulence models to reproduce the expected physical behavior correctly. Therefore, heat transfer predictions are not included in the present paper.

Problem Description

The film cooling configuration chosen corresponds to the experimental study of Ajersch et al. [11] where measurements are presented for normal injection through square holes. The physical domain in Fig. 1 shows a single row of six square jets on a flat plate, which represents the turbine blade surface. The computational domain is chosen to be a periodic module and is shown in Fig. 2 and by the dotted lines in Fig. 1. The experimental investigation for this configuration was carried out for velocity ratios $R=0.5, 1.0,$ and 1.5 . However, the computations have only been carried out for the lowest velocity ratio of $R=0.5$, and the general flow characteristics for this case as predicted by the several models are evaluated by comparison with the measurements.

For the turbulence model to be viable, the main features of the flow are expected to be predicted correctly. In this paper, we evaluate the performance of the models not only by the quantitative comparisons with the measurements reported by Ajersch et al. at a few selected locations (that do not provide a complete

Contributed by the International Gas Turbine Institute and presented at the 44th International Gas Turbine and Aeroengine Congress and Exhibition, Indianapolis, Indiana, June 7–10, 1999. Manuscript received by the International Gas Turbine Institute February 1999. Paper No. 99-GT-124. Review Chair: D. C. Wisler.

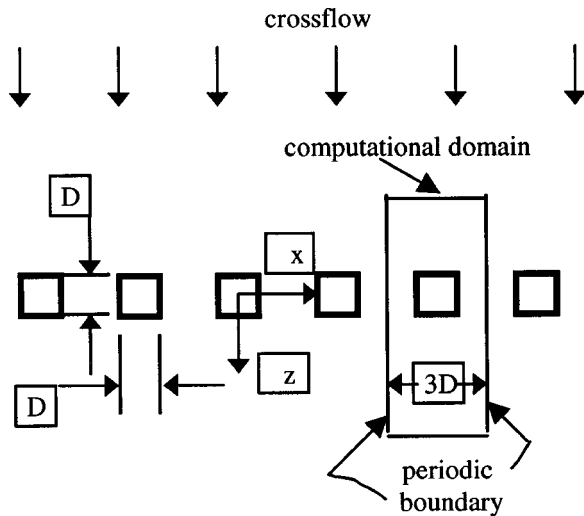


Fig. 1 Schematic of the physical problem

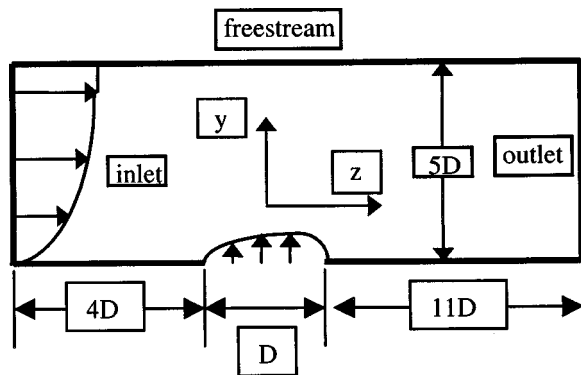


Fig. 2 Side view of the computational domain

description of all the flow features), but also by examining whether the models accurately predict the dominant features of the flow field.

Governing Equations

The steady-state Reynolds-averaged Navier–Stokes equation contains the Reynolds stress tensor $-\rho u'_i u'_j$, which needs to be modeled by a closure approximation. The accuracy of the prediction is based on the adequacy of the closure expressions in capturing the flow physics. The different closure approximations described below include the high-Re models where the near-wall sublayer effects are not resolved, various forms of the low-Re models where the near-wall damping effects are represented by different empirical expressions, and the nonlinear models where turbulence anisotropy is incorporated through nonlinear corrections to the linear stress–strain relations assumed in the linear turbulence models.

Turbulence Models

A number of different models based on the $k-\varepsilon$ and $k-\omega$ closures were used in this study. The various models, under appropriate categories, are listed below:

1 High-Re $k-\varepsilon$ Model. In the standard $k-\varepsilon$ model [12] the Reynolds stress is modeled as

$$-\overline{\rho u'_i u'_j} = -\frac{2}{3} \rho k \delta_{ij} + 2\mu_t \bar{s}_{ij} \quad (1)$$

The eddy viscosity μ_t is related to the turbulent kinetic energy k and to its dissipation rate ε as

$$\mu_t = \rho C_\mu \frac{k^2}{\varepsilon} \quad (2)$$

Note that Eq. (1) represents a linear relationship between the turbulent stress and the rate of strain, and forms the basis for all linear two-equation models.

The distributions of k and ε in the flow field is determined from their modeled transport equations [12]. The source terms in the modeled equations are given by:

$$S_k = P - \varepsilon; \quad S_\varepsilon = C_{\varepsilon 1}(\varepsilon/k)P - C_{\varepsilon 2}(\varepsilon^2/k) \quad (3)$$

where P is the production of turbulence ($= -\rho u'_i u'_j (\partial \bar{U}_i / \partial x_j)$). The high-Re model avoids the need to integrate the modeled equations right down to the wall by making use of the universal behavior of near-wall flows. The standard wall-function approach is thus used to specify the wall boundary conditions for velocity. This is done either in the form of a wall shear stress expression from Couette flow analysis or alternatively by determining the diffusion coefficient on the wall such that the computed shear stress on the wall matches that obtained from the Couette flow analysis.

For the turbulence kinetic energy, a zero value is specified at the wall, while the value of dissipation at a near-wall point is set, using a local equilibrium assumption, as $\varepsilon = C_\mu^{3/4} k^{3/2} / (0.4 \delta y)$.

2 Low-Re Models. The low-Re models resolve the viscous sublayer adjacent to the solid walls and use damping functions that ensure the transition from turbulent stresses to viscous stresses near the wall. The low-Re versions of both $k-\varepsilon$ and $k-\omega$ closure models have been used in this study.

(a) *Low-Re $k-\varepsilon$ Models.* The source terms for k and ε in for the low-Re model take the form:

$$S_k = P - \varepsilon; S_\varepsilon = C_{\varepsilon 1} f_1 \frac{\tilde{\varepsilon}}{k} P - C_{\varepsilon 2} f_2 \frac{\tilde{\varepsilon}^2}{k} + E \quad (4)$$

where

$$\tilde{\varepsilon} = \varepsilon - D \quad \text{and} \quad \mu_t = C_\mu f_\mu \frac{k^2}{\tilde{\varepsilon}} \quad (5)$$

A number of different low Re models [13] have been proposed depending on their use of the functions f_1 , f_2 , and f_μ and the terms D and E . The models used in this study are the Launder–Sharma model [14] and the Lam–Bremhorst model [15]. These two models have been selected due to the asymptotic consistency of their functions in the near wall region as well as in the fully turbulent regime. The Launder–Sharma model uses $\tilde{\varepsilon}$ as the dissipation variable and therefore the term D must asymptote to the nonzero value of ε on the wall and should vanish in the fully turbulent regime where $\tilde{\varepsilon}$ must tend to ε . The term D for the Launder–Sharma model satisfies both the limits, as has been shown by Patel et al. [13]. The asymptotic limits of the damping functions f_2 , f_μ and the term E are also consistent with expectations. The Lam–Bremhorst model, on the other hand, solves for ε itself and therefore the term D is prescribed as zero. The f_μ function for this model shows the correct variation in the near wall region but tends to unity somewhat slowly as compared to the Launder–Sharma model. This model also employs the function f_1 to model the appropriate growth of ε in the region very close to the wall. The f_2 function in this model is modified in order to yield a zero value on the wall. Thus the sink term in the ε equation is damped leading to the expected rapid increase of viscous dissipation as the wall is reached.

(b) *Low-Re $k-\omega$ Model.* The low-Re $k-\varepsilon$ models suffer from the lack of appropriate wall boundary condition for ε , which is specified mostly by ad-hoc empirical functions for the near-wall

flow. The choice of the specific dissipation rate ω is therefore sometimes preferred since the near wall ω behavior is known and therefore the boundary condition at the wall can be specified more accurately. The transport equations for k and ω are given by Wilcox and Traci [16], and have the following source terms:

$$S_k = P - \rho\beta^* \omega k; \quad S_\omega = \alpha \frac{\omega}{k} P - \rho\beta \omega^2 \quad (6)$$

where μ_t is given as $\mu_t = \alpha^* k / \omega$. In implementing this model, all standard functions and constants for the low-Re version of the model, as given by Wilcox and Traci [16], have been used. The functions in this model serve the same purpose as in the low-Re $k-\varepsilon$ models and their asymptotic behavior has also been found to be consistent.

3 DNS-Based Low-Re $k-\varepsilon$ Model. Rodi and Mansour [17] proposed an improved model for the ε equation and a new f_μ function using DNS data for a channel flow. The ε -budget computation for the different terms in the ε equation was used in conjunction with scaling arguments to obtain the following modeled form of the ε equation source term:

$$S_\varepsilon = C_{\varepsilon 1} \frac{\tilde{\varepsilon}}{k} P - C_{\varepsilon 2} f_3 f_2 \frac{\tilde{\varepsilon}^2}{k} + E \quad (7)$$

The constants and expressions as proposed by Rodi and Mansour [17] have been used here with one exception. The expression for f_3 was given as:

$$f_3 = \exp[2(P/\varepsilon)/0.3\text{Re}_t^{1/2}] \quad (8)$$

The choice of 0.3 in this equation is related to the 0.3 value that the structure function ($= -u'v'/k$) assumes in the center of a channel for fully developed turbulence. Since the flow considered here does not represent a fully developed turbulent channel flow, the factor of 0.3 was found to be inappropriate, and empirical adjustment of this constant led to a value of 2.1.

4 Nonlinear Low-Re Models. Experimental studies carried out for the flow situation being considered here have shown that the flow is highly anisotropic due to strong curvature effects and therefore the nonlinear models listed below have been tested to evaluate their performance in this highly complex flow situation.

(a) *Mayong-Kasagi Model.* Mayong and Kasagi [18] proposed an anisotropic extension to the eddy diffusivity model deduced from the interrelationship among the fundamental processes in the kinetic energy budget. Two additional terms containing quadratic velocity gradients and kinetic energy gradients have been added to the standard linear model. The first of these terms has been derived from the interrelationship between production and dissipation terms in the kinetic energy equation, and plays the role of exhibiting anisotropic characteristics for each Reynolds stress component over the whole flow field except for the immediate vicinity of the wall. The second term added has been derived from the balance between the diffusion and dissipation terms so that the wall-limiting condition for the normal Reynolds stresses is satisfied. The second term, however, does not satisfy the general frame invariance necessary for the broadest range of application, because the invariant condition is not generally satisfied in the immediate vicinity of a plane interface where turbulence is quasi-two-dimensional due to the blocking of a normal velocity component. More details of the model are found in Mayong [19].

(b) *Speziale Model.* Speziale [20] derived a nonlinear model by means of an asymptotic expansion, which satisfies both realizability and invariance requirements. This model is expected to incorporate the streamline curvature effects by introducing quadratic velocity gradient terms and is expected to do better in flows where the differences in normal stresses are significant. Although the use of the original Speziale model has been reported primarily in conjunction with wall functions, it has been implemented here

in a low-Re model form with the damping functions in the near-wall region obtained from the Launder-Sharma model.

Computational Details

The modeled transport equations were solved using a three-dimensional CFD code developed by the authors based on the SIMPLER algorithm [21]. A control-volume-based finite difference formulation that uses a second-order accurate central difference scheme for the viscous terms and a power law based scheme for the convective terms has been used. In calculating the source terms in the equations for momentum conservation and turbulence quantities, the first and second-order derivatives were calculated using the Fornberg algorithm [22] employing fourth-order accurate centered differencing scheme for interior points and second-order accurate one-sided differencing for boundary points. A staggered grid arrangement with velocity components stored at the cell faces and all other scalar quantities located at the grid points is employed to avoid checkerboard fields. The system of equations was solved with the Tridiagonal Matrix algorithm employing an underrelaxation procedure to aid convergence.

A nonuniform grid ($59 \times 60 \times 140$) was set up in the computational domain (Fig. 2) with grid points clustered near the bottom wall and around the jet. The jet injection region was resolved with a 19×19 mesh. Inlet profiles for both the crossflow (at $Z/D = -4.5$) and at the exit of the jet hole were provided from the experimental data of Ajersch et al. [11]. The measured data at the crossflow inlet corresponded closely with the 1/7th turbulent boundary layer profile with a boundary layer thickness of $2D$. At the jet-hole exit, all three velocity components plus their rms values were available from the measurements, and these were interpolated to prescribe the numerical boundary conditions for both the mean velocity and the turbulence kinetic energy. A periodic boundary condition was implemented in the spanwise direction representing a transverse row of injection holes while at the outlet the normal gradient of all variables was prescribed as zero. At the top plane, free-stream conditions from the measurements were specified.

The equations were nondimensionalized with the mean jet velocity, V_j , and jet width, D , and computations were carried out at a Reynolds number $V_j D / \nu$ of 4700 for a blowing ratio of 0.5. The mass residual in each cell was determined from the continuity equation and the maximum residual was established as the criterion for assessing the overall convergence of the field. At residual levels of 10^{-6} – 10^{-7} , the solution was found not to change and the solution was considered converged in this range. Grid independence was checked by comparing the $59 \times 60 \times 140$ grid (nearly 0.5 million nodes) solution (using the low-Re $k-\varepsilon$ Launder-Sharma model) with a more refined $71 \times 90 \times 200$ grid (nearly 1.28 million nodes). The difference in the solution on the two grids was found to be minimal, (maximum difference in the velocity values was less than 3 percent) as shown in Fig. 3.

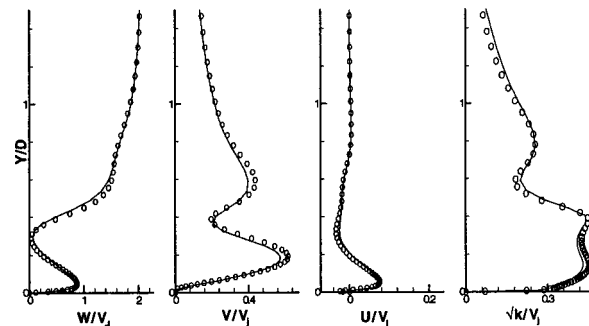


Fig. 3 Grid independence study with the LS model. Velocity and kinetic energy profiles at $X/D=0$, $Z/D=1$; \bullet $71 \times 90 \times 200$ grid; — $59 \times 60 \times 140$ grid.

Results and Discussion

A discussion of the model predictions and comparisons with the measurements of Ajersch et al. [11] will be presented next. The following nomenclature will be followed hereafter while referring to the various models. The high-Re model will be referred to as HRE, the Launder–Sharma model as LS, the Lam–Bremhorst model as LB, the Mansour–Rodi model as MR, the nonlinear Speziale model as SP, the nonlinear Mayong–Kasagi model as MK, and the $k-\omega$ model as KW.

Mean Velocity and Turbulence Statistics. The mean velocity and turbulence kinetic energy profiles are compared with the experimental results of Ajersch et al. [11] at two spanwise locations: $X/D=0$ along the jet center plane in Fig. 4, and $X/D=-0.5$ along the spanwise edge of the jet in Fig. 5. The figures show how the flow varies with distance Y/D from the wall at various downstream locations ($Z/D=0, 1, 3, 5$ and 8). The main flow features, namely the wake of the jet, the counter-rotating vortex pair (CRVP), and the horseshoe vortex are expected to be clearly evident along the $X/D=0$ and 0.5 streamwise planes, and therefore comparison of model predictions with experimental data along these representative planes is likely to reveal how well the models capture the features of the flow. The flow features are also captured in the plots shown in Fig. 7, which present streamwise vorticity component superimposed by velocity vectors along a cross-stream plane.

Figure 4(a) shows the downstream development of the mean streamwise velocity (W/V_j) along the jet center plane ($X/D=0$). At the jet center ($Z/D=0$), where the jet exit plane boundary condition are specified from experimental data, the model predictions compare well with measurements. One hole-diameter downstream of the jet ($Z/D=1$), a reverse flow region close to the wall is observed in the measurements, which is captured well by the HRE model, but all other models predict a much smaller reverse flow region. The differences in the length of the recirculation regions predicted by the various low-Re models and the HRE model is brought out very clearly by the vector plots presented later in Fig. 9. The HRE model behavior very close to the wall is strikingly different from the other models, which typically show three distinct flow regions at this location: a wall-jet-like layer next to the wall with accelerating flow, a wake region above it where low velocities are observed, and a shear layer with strong velocity gradients due to the velocity changing from low values at the top of the wake region to the free-stream value over a very short vertical distance. The wall-jet layer very close to the wall could not be validated as measurements very close to the wall were not available in the data set used in this study. However, several experimental investigations [23] have revealed that a wall-jet structure does exist close to the wall even for low velocity ratio R , although this effect is stronger for the high R cases. At this location ($Z/D=1$), immediately downstream of the jet, the low pressure in the wake of the jet induces laterally inward motion of the surrounding crossflow fluid close to the wall toward the jet center plane. The entrained fluid moves upward, in the vicinity of the jet center plane, toward the jet and it is then swept up by the bent-over jet (Fig. 9). The inward motion of the high momentum fluid toward the jet center plane close to the wall is partly re-oriented in the streamwise direction and leads to the formation of the wall-jet-like structure (seen in Fig. 7).

Evidence of the wall-jet can also be seen from measurements at $Z/D=3$ where there is a peak close to the wall and the velocities then drop to lower values in the wake region. The steep velocity gradient observed close to $Y/D=1$ represents the shear layer where the velocity changes from low values in the wake of the jet to the free-stream value. All models follow the experimental trends appropriately but typically overpredict the streamwise velocity in the wake region. Also the shear layer is closer to the wall which indicates that the wake-height is underpredicted at this center-plane location.

The large deviations of model predictions observed in the vicinity of the jet (Z/D between 1 and 3) indicate that the near field of the jet, influenced significantly by the dynamical behavior of the large-scale structures, is not properly modeled. The effect produced by the damping functions in the low-Re models is therefore not accurate in the immediate vicinity of the jet.

At farther downstream locations, measurements show that the velocity gradients in the wall-jet layer and the shear layer are diminished, and flow recovery toward a boundary layer profile is observed. The velocity gradients are overpredicted in the wall-jet layer at $Z/D=5$ while agreement with experimental results is better at $Z/D=8$. For Z/D greater than 3, the LB model shows the best agreement with experimental data. The LB model is known to give the correct asymptotic behavior $-w'v' \propto y^4$ in the near-wall region due to the appropriate variation of the f_μ functions in the immediate vicinity of the wall. The f_μ function behavior of the LS model has been found to be more consistent in the fully turbulent regime and therefore it does not do as well as the LB model in the near-wall region. The nonlinear SP model does not show any significant improvements in the mean velocity field predictions and its trends are only slightly different from the LS model. This may in part be due to the fact that in the near-wall region both these models employ the same damping functions and also that the nonlinear quadratic terms introduced in the Reynolds stress terms in the SP model do not make any significant contribution. The MK model, at $Z/D=5$ and $Z/D=8$, underpredicts the streamwise velocity gradients in the shear layer and consequently predicts a deeper penetration of the jet into the crossflow. The performance of the nonlinear models cannot however be judged merely on the basis of mean velocity trends and a proper evaluation of the Reynolds stresses will be carried out in a later section in order to get the correct picture on these nonlinear variants of the $k-\varepsilon$ model.

The secondary motions in the cross-stream plane are evaluated by comparing the vertical velocity profiles in Fig. 4(b) and the cross-stream velocity in Fig. 4(c). The vertical velocity distribution at the jet center ($Z/D=0$) once again shows good agreement with experimental data owing to the measured jet inlet conditions specified at the jet-exit plane. The large vertical velocity values (V/V_j greater than 1) are because the crossflow acts as a partial cover over the jet, causing the jet to bend before leaving the jet exit, and leads to the acceleration of the jet toward the downstream edge of the exit hole. In the reverse flow region, at $Z/D=1$, two peaks are recorded, the first peak off the wall is in the wake region where the reversing fluid is lifted up by the deflected jet, while the second peak corresponds to the deflection of the cross stream over the jet. This trend is closely followed by the models, although the peak values are predicted closer to the wall. This is primarily due to the predicted wake region being much closer to the wall and the jet penetration being underpredicted by the models in the jet center plane. Additionally, the models differ in their prediction of the first peak value off the wall while the second peak is the same for all the low-Re models. The LB model predicts the lowest peak value while the MK model records the highest first peak value with the other models lying in between. These differences are related to the behavior of the damping functions for the various models with the LB model functions being asymptotically consistent while the f_μ function of MK model tends to unity somewhat slowly. The dependence on these functions is further emphasized by the observation that the second peak is the same for all the low-Re models since the functions tend to unity at larger distances from the wall.

Further downstream, at $Z/D=3$, measurements suggest that, as for the streamwise velocity, the wake region is not properly predicted with the predictions showing a faster recovery. Measurements between $Z/D=3$ and 8 show a negative velocity at the top of the bent-over jet, which indicates that the crossflow is coming down at this point. The downwash of the crossflow as well as the low-velocity magnitudes in the wake region are not captured by

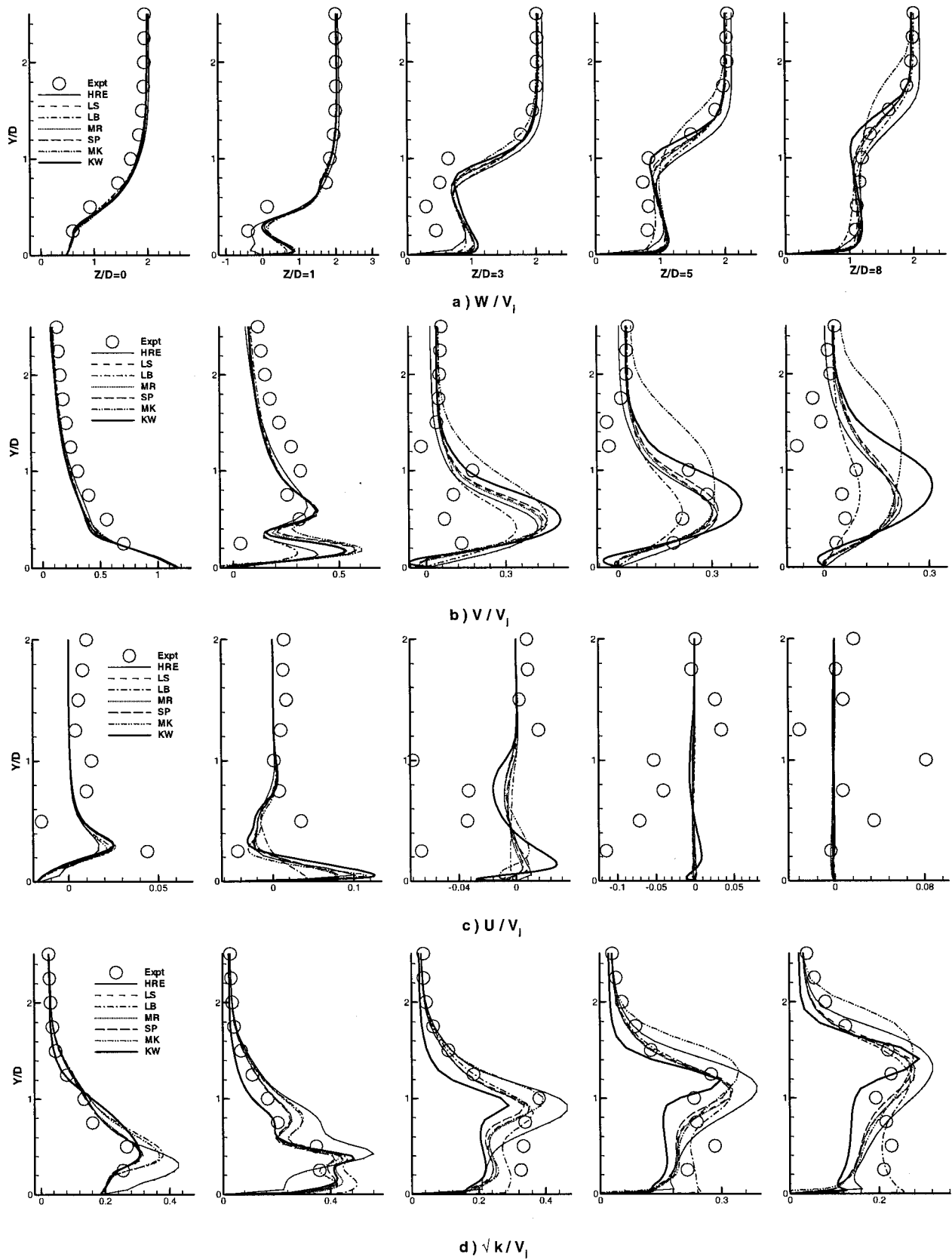


Fig. 4 Velocity and kinetic energy profiles at $X/D=0$ at different Z/D from center of jet

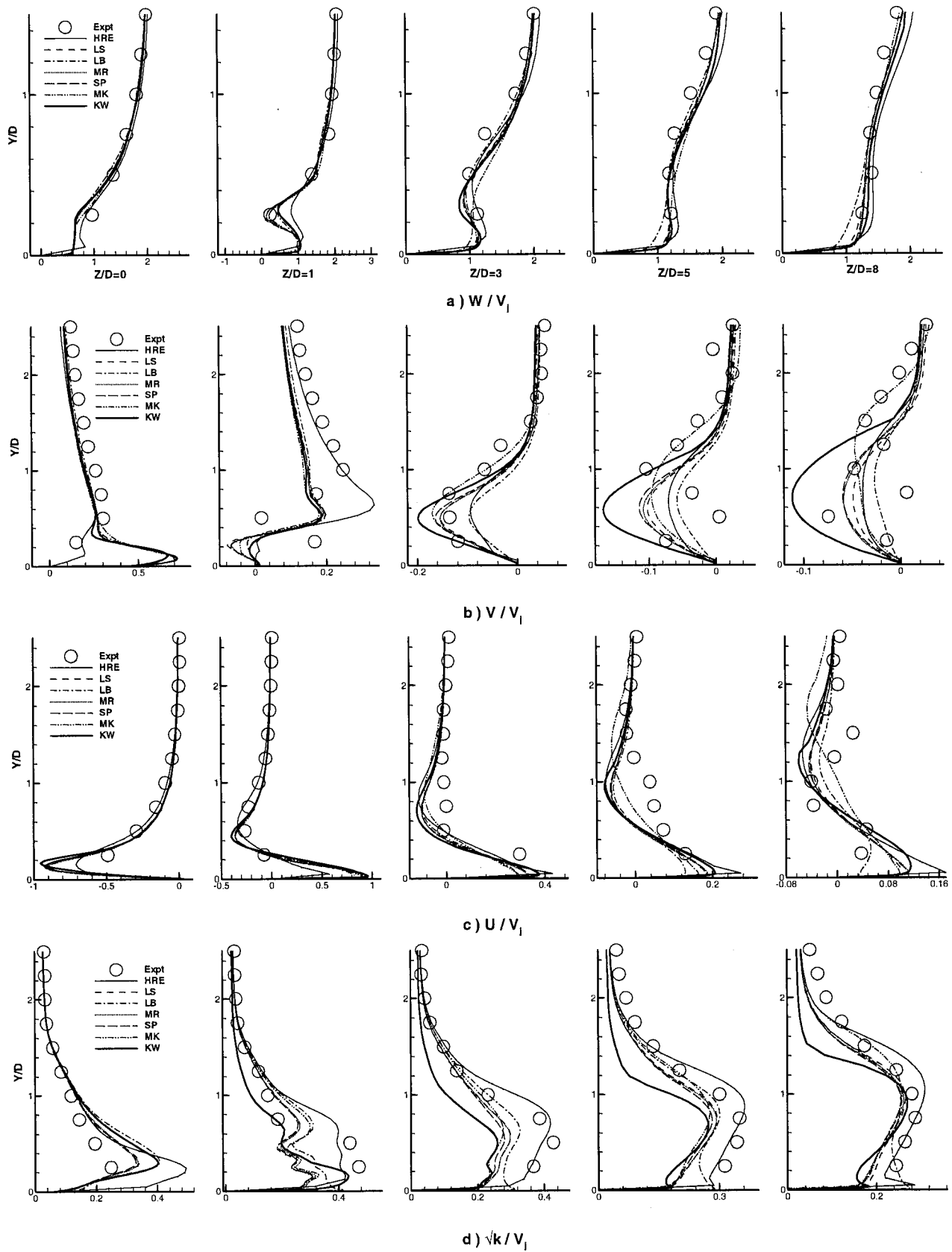


Fig. 5 Velocity and kinetic energy profiles at $X/D = -0.5$ at different Z/D from center of jet

the model predictions. This is probably due to the models' predicting a smaller reverse flow region behind the jet, which implies that the wake effect is not as strong as experimentally observed. The measurements continue to show a dual-peak structure at $Z/D=3$, while the predictions only show a single peak due to the faster flow recovery. The predicted magnitudes at $Z/D=3, 5$, and 8 show the same trends as at $Z/D=1$, with the KW model showing the largest peak values and the LB model showing the smallest magnitudes and the best agreement with the data. The behavior of the MK model at $Z/D=5$ and $Z/D=8$, with the peak shifted upward, is a consequence of the jet penetration being overpredicted at these locations.

The spanwise velocity (U/V_j) presented in Fig. 4(c) should be zero along the jet center plane if the flow at all the inflow planes is symmetric. However, measurements indicate that the inflow at the jet exit plane ($Y/D=0$) is not symmetric with the flow slightly skewed in the lateral direction. This asymmetry in the inlet profile is convected downstream, and is confirmed by the velocity measurements as well as the predictions at the jet exit ($Z/D=0$) and immediately downstream of the jet ($Z/D=1$). As the flow develops downstream, this asymmetry should decrease and the spanwise velocity across the jet-center-plane should become very small. The flow predictions show this trend. However, the measurements show high degree of scatter at downstream locations ($Z/D=5,8$) and therefore cannot be relied upon.

The kinetic energy (KE) profiles along the jet centerline are shown in Fig. 4(d). The KE distribution is governed by a number of factors, the important ones being the interaction of the oncoming boundary layer and the jet, production due to the various velocity gradients $\partial W/\partial Y, \partial V/\partial Z, \partial U/\partial X$ and strong streamline curvature effects especially in the vicinity of the jet. At the jet center plane however, the production due to the gradient $\partial W/\partial X$ seems to be the dominant process as a close correlation between the velocity gradient $\partial W/\partial Y$ (Fig. 4(a)) and the KE (Fig. 4(d)) can be seen. The peak KE values occur at approximately the same locations as the peak velocity gradient positions. The HRE, LB, and MK models overpredict the peak values at the jet center ($Z/D=0$) while the other models show close agreement with measurements. The experimental profile at $Z/D=1$ shows peak values in the wall-jet and lower-wake regions and in the shear layer where strong gradients $\partial W/\partial Y$ occur. Model predictions show three peak values corresponding to the strong gradients in the wall-jet layer, the lower-wake region, and the shear layer. The HRE model overpredicts peak values in the wake region and in the shear layer. Farther downstream at $Z/D=3$ and $Z/D=5$ two distinct peaks are observed in the measurements, which once again correspond to the strong velocity gradient $\partial W/\partial Y$ at these positions. The nonlinear and the low-Re $k-\epsilon$ model predictions in the shear layer are in good agreement with measurements at $Z/D=3$, but the HRE model overpredicts the peak level in this region while the KW model underpredicts the turbulence peak. The models do not behave appropriately in the wake region and are unable to capture the peak value accurately in the wake at $Z/D=3, 5$ and $Z/D=8$. The LB model once again gives better predictions at these locations. However, the KW model significantly underpredicts the KE levels in the wake region. The behavior of the models in the near-wall region is influenced by the dissipation rate ϵ , which forms the sink term in the KE equation. The ϵ level in the near-wall region is controlled by the functions f_1, f_2 and the term E . Both f_1 and E tend to increase the value of ϵ near the wall and thereby reduce the KE levels. The influence of f_1 is confined to a region very close to the wall in case of the LB model, while it is unity for the other models. The term E is therefore dominant in the growth of ϵ near the wall. The LB model has E equal to zero as the model solves for the dissipation rate itself and therefore the KE level in the near wall region is higher as compared to the other models. Clearly, it is more attractive to solve for ϵ from a physical point of view. The KW model greatly underpredicts the KE levels in the wake region. As in the case of

the low-Re $k-\epsilon$ models, the function α multiplying the production term in the ω equation along with the constant β , which tends to decrease the destruction term, lead to very high values of ω in the near-wall region. The combined effect is to reduce the KE levels near the wall. The KE trends in the KW model case suggest that the model functions in the ω equations are not appropriate as they lead to drastic reduction of the kinetic energy. The nonlinear models do not show any significant improvements over their linear counterparts and are unable to predict the correct magnitudes in the wake.

The profiles along the edge of the jet ($X/D=-0.5$) are shown in Fig. 5. The streamwise velocity at different downstream locations is expectedly higher than that along the jet center line (Fig. 4(a)), due to the weaker wake effect, which also results in reduced velocity gradients $\partial W/\partial Y$. The wall-jet layer is also noticed here at $Z/D=1$ with steep gradients in this region and in the shear layer region above the wake. The wake can be seen distinctly at this location, and all the models appear to capture the wake region well except the high-Re model. The wake gradually diminishes with increasing downstream distances, and beyond $Z/D=3$ close agreement with experimental data is shown by all the models.

Vertical velocity comparisons have been shown in Fig. 5(b). As at $Z/D=0$ (Fig. 4(a)), velocities as high as 0.8 times the free-stream velocity are predicted over the jet inlet hole due to the partial cover effect of the crossflow causing the flow to accelerate toward the downstream end. The measurements however do not show this peak at $Z/D=1$, and instead show two peak values; the one closer to the wall is due to the upward motion caused by the CRVP while the other peak at a larger distance from the wall is once again due to the crossflow deflected over the bent-over jet. The predictions show large near-wall deviations from the measured values with negative values close to the wall turning positive around $Y/D=0.3$. The negative values close to the wall represent the outer downward moving parts of the CRVP, while the positive values represent the upper portions of the CRVP and the crossflow regions deflected upward by the jet. Since the measurements do not show negative values close to the wall, it may be concluded that the CRVP in the experiments has a smaller lateral spread relative to the predictions. At Z/D locations farther downstream, the measured and predicted velocities are primarily negative representing the downwash side of the CRVP. The measured behavior is captured well by the models at $Z/D=3$ where the KW model overpredicts the peak downward velocity while the LB model underpredicts it. The experimental measurements shows some scatter in the data at $Z/D=5$ and $Z/D=8$ locations, although the general trend of the jet and the crossflow velocities are downward toward the wall. The downward trend is maintained by the model predictions, but no meaningful comparison can be made with the experimental measurements due to the scatter in the data. In comparing the model predictions with each other, they follow the same trends as observed along the jet center line in Fig. 4 and therefore the arguments extended earlier to account for the model predictions are valid here as well.

Spanwise velocity comparisons in Fig. 5(c) indicate that the model predictions show good agreement with experimental profiles. The spanwise velocities are quite significant at the edge of the jet, and U/V_j reaches values as high as 1 close to the wall. At $Z/D=0$ the spanwise velocity near the lower surface is negative, which indicates that the flow is outward and away from the jet center plane. Close agreement with measurements is observed at this location where the HRE model shows a relatively lower peak value. At $Z/D=1$, the velocities are all positive close to the wall, indicating flow toward the jet centerline. The CRVP entrains the surrounding crossflow fluid close to the wall resulting in positive cross-stream velocity near the wall. The velocity changes sign further away from the wall representing the upper half of the CRVP where the flow is moving away from the centerline. The peak negative value is obtained in the top regions of the CRVP structure and the models are in good agreement with measure-

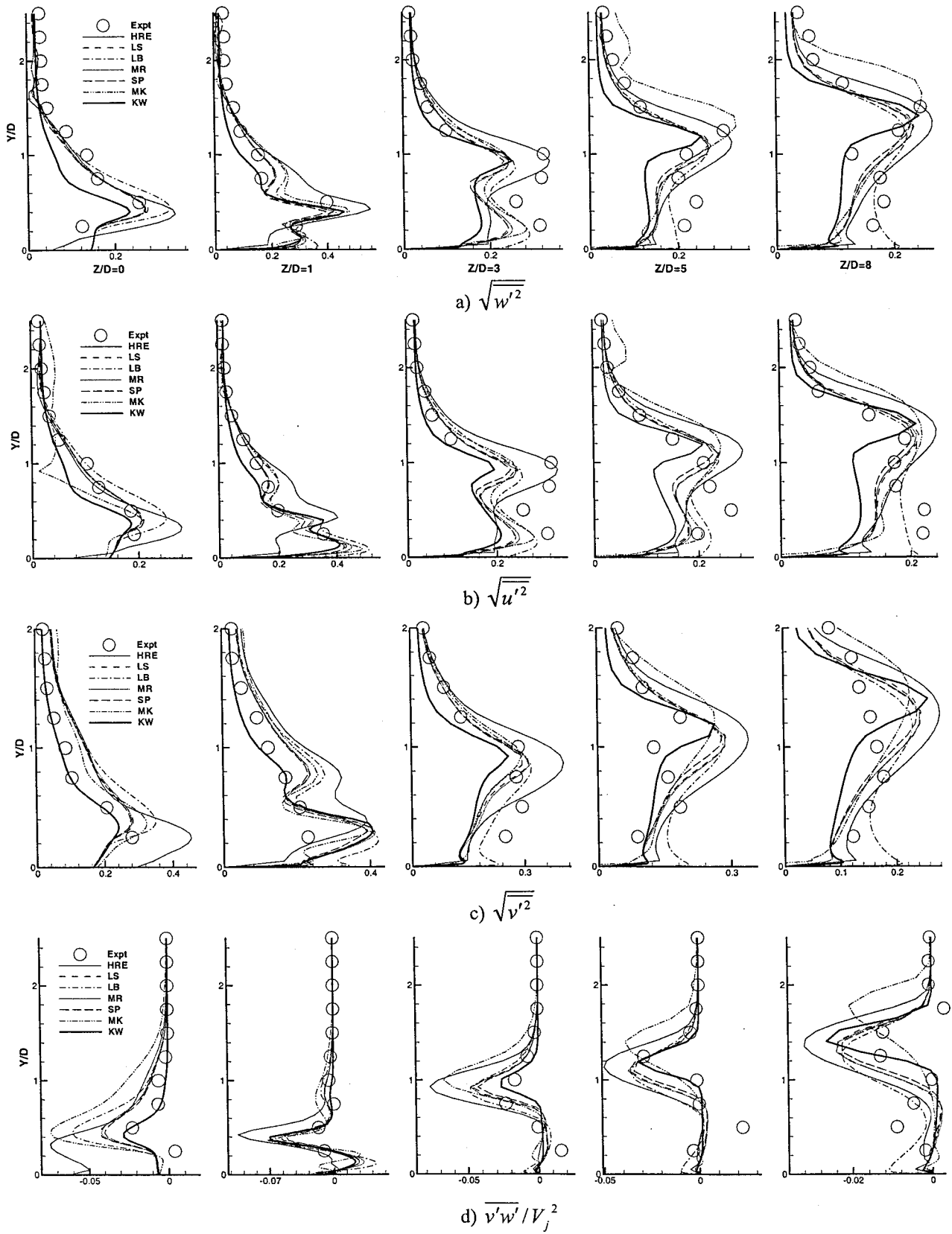


Fig. 6 Stress profiles at $X/D=0$ at different Z/D from center of jet

ments here. As the flow progresses downstream, the CRVP structure diminishes in strength as seen from the experimental profile at $Z/D=3$. Models on the other hand predict a stronger structure at this location. At $Z/D=5$, both the measurements and predictions show a reduction in the strength of the CRVP. However, the measurements do not show any negative values along the top half, indicating a pinched CRVP structure with a wider base and a narrower neck. Predictions, on the other hand, show negative velocities on the top half of the CRVP, both at $Z/D=5$ and 8, indicating a CRVP that is more dispersed in the lateral direction than the experiments. The CRVP cannot be distinctly identified in the measurements at $Z/D=8$ where the scatter in the data indicates that the structure has diminished in strength considerably. The models on the other hand show a distinct structure at this location. The LB model gives better predictions, as before, in the near-wall region at $Z/D=5$ and $Z/D=8$.

Kinetic energy profiles along the edge of the jet correspond to those in a developing boundary layer except in the immediate vicinity of the jet at $Z/D=0$ and $Z/D=1$. At $Z/D=0$ the models follow the experimental trends closely, but overpredict the peak level. Once again, a close correspondence between the velocity gradient $\partial W/\partial Y$ and KE trends is observed at $Z/D=1$ where the peak values correspond to the maximum gradient locations. At this location however, the contribution of the gradient $\partial U/\partial X$ has been found to be significant, largely due to the strong entrainment of the crossflow into the wake region. Model predictions typically show a number of local peak values corresponding to the large spanwise velocity gradients. At downstream locations the experimental profiles are like those in a boundary layer and the models mimic this behavior appropriately, but they underpredict the peak KE levels. The LB and KW models show peak values very close to the wall at $Z/D=5$ and $Z/D=8$, and this is once again related to the steep stream-wise velocity gradients in the near wall region observed at these locations.

The normal stress profiles along the jet center plane ($X/D=0$) are presented in Fig. 6. The experimental w'^2 profiles in Fig. 6(a) shows a correlation to the KE profile and the streamwise normal velocity gradient $\partial W/\partial Y$ in Fig. 5(d). This correlation is particularly strong in the far field ($Z/D>5$) where peak values are obtained in the jet shear-layer region associated with high $\partial W/\partial Y$ and turbulence production. In the near field, peak w'^2 values are observed in the shear layer and in the wall-jet region where large $\partial W/\partial Y$ gradients are found. The correlation between w'^2 and $\partial W/\partial Y$ is not taken into account by the linear eddy viscosity models where the stress w'^2 is assumed to be directly proportional to the gradient $\partial W/\partial Z$ and therefore any simple eddy viscosity model is not expected to do well in this highly complex flow situation.

The measured trends of the stress w'^2 in Fig. 6(b) also show correlation with $\partial W/\partial Y$. In the near field ($Z/D=1$), however, the near-wall behavior also appears to correlate well with $\partial U/\partial X$, which is high close to the surface due to the entrainment of the crossflow boundary layer into the wake region. The anisotropy in the near field of the jet injection close to the wall is clearly evident, and is associated with the dominance of the coherent structures in these regions. However, the low-Re and nonlinear models are found to reproduce this nonisotropic effect in a qualitatively satisfactory manner. At further downstream locations the dependence on the gradient $\partial W/\partial Y$ becomes stronger, especially in the wake of the jet, where the normal stresses w'^2 and u'^2 show trends similar to the KE profiles. Models underpredict the stress levels in the wake region for $Z/D\geq 3$ where the LB model gives better predictions in the near wall region. The anisotropy of the flow in the vicinity of the jet is further demonstrated by the v'^2 profiles at $Z/D=0$ and $Z/D=1$ in Fig. 6(c). In the near field, the v'^2 profiles appear to scale with $\partial V/\partial Y$. At $Z/D=3$ and $Z/D=5$, however, the effect of the gradient $\partial W/\partial Y$ is apparent here

with the peak v'^2 value occurring in the shear-layer region. The profile flattens out as the flow moves farther downstream and at $Z/D=8$ a closer correspondence can be seen with the velocity gradient $\partial W/\partial Y$ rather than with $\partial V/\partial Y$ (see Fig. 4(b)). The normal stresses are therefore not represented appropriately by the models. In the near field, the turbulence exhibits significant anisotropy. The flow field becomes more isotropic farther downstream, but the gradient approximations relating $u_i'^2$ to $\partial U_i/\partial X_i$ do not appear to be valid. Rather all stresses appear to correlate with $\partial W/\partial Y$.

The profiles for the shear stress $w'v'$ is presented in Fig. 6(d). The peak values observed in the measurements and predictions are in the jet-shear-layer regions and is a consequence of the high $\partial W/\partial Y$ in the shear layer region. This dependence is consistent with the fact that the product $v'^2 \partial W/\partial Y$ is the dominant term in the production of $w'v'$. Peak values are overpredicted by the models at $Z/D=0$ location and only the KW model follows the experimental trends closely. The peak values decrease as the flow moves downstream where the streamwise velocity gradients are reduced in the shear layer. At $Z/D=3$ and beyond, the stress values are very small in the wake region, where the velocities are low and fairly uniform. Model predictions in the recirculation region and farther downstream follow the measured trends correctly, largely due to the fact that the eddy viscosity model also incorporates the dependence of $w'v'$ on $\partial W/\partial Y$. The shear stress predicted by the models is found to change sign close to the wall at $Z/D=1$ and is seen to follow the velocity trends reported in Fig. 4(a) where velocity gradients also change sign close to the wall.

In general, the model predictions for the turbulent shear stress $w'v'$ follow the measured trends fairly well in the shear layer and also reflect the appropriate dependence on velocity gradients. In comparing the model predictions, the HRE model shows the greatest level of overprediction in the peak stress levels. This would lead to the greatest levels of turbulent transport, and is consistent with the observation that the HRE model is associated with the highest lateral jet penetration. The failure of the nonlinear models to give better predictions over the linear ones was somewhat unexpected. The introduction of the nonlinear quadratic terms in the stress-strain relationship in order to incorporate the effect of strong streamline curvatures are therefore insufficient and cubic terms must be included in order to obtain the desired stress-strain coupling. The introduction of merely quadratic terms in the SP and MK models do not produce the desired effect of streamline curvatures on the stress levels.

Vector Plots and Vorticity Contours. Attention is now turned toward describing the overall features of the flow field by presenting vorticity contours and vector plots along a typical cross-stream plane. Figure 7 presents the velocity vectors superimposed on the streamwise vorticity contours at $Z/D=3$ cross-stream plane. The predictions for all seven models evaluated are presented, and in each figure the same gray scale is used in order to facilitate a comparison between the different model predictions.

At $Z/D=3$, the CRVP is clearly established and is the dominant feature in the flow field. The HRE model shows the greatest lateral spread, which was also observed in the velocity comparisons shown in Fig. 5, where the spanwise velocities predicted by the HRE model are larger than those predicted by the other models. The MK model shows the greatest vertical spread of the jet, and this was also observed in Fig. 4, where in the MK model predictions, the shear layer region was displaced vertically upward relative to other models and the measurements. The LB model predictions show the weakest CRVP, and the lowest levels of vertical and lateral spread. All the low-Re models show small negative velocities close to the wall between X/D of -1 and -1.5 , and these reflect the manifestation of the horseshoe vortex. It is the strongest, and can be clearly observed in the KW model

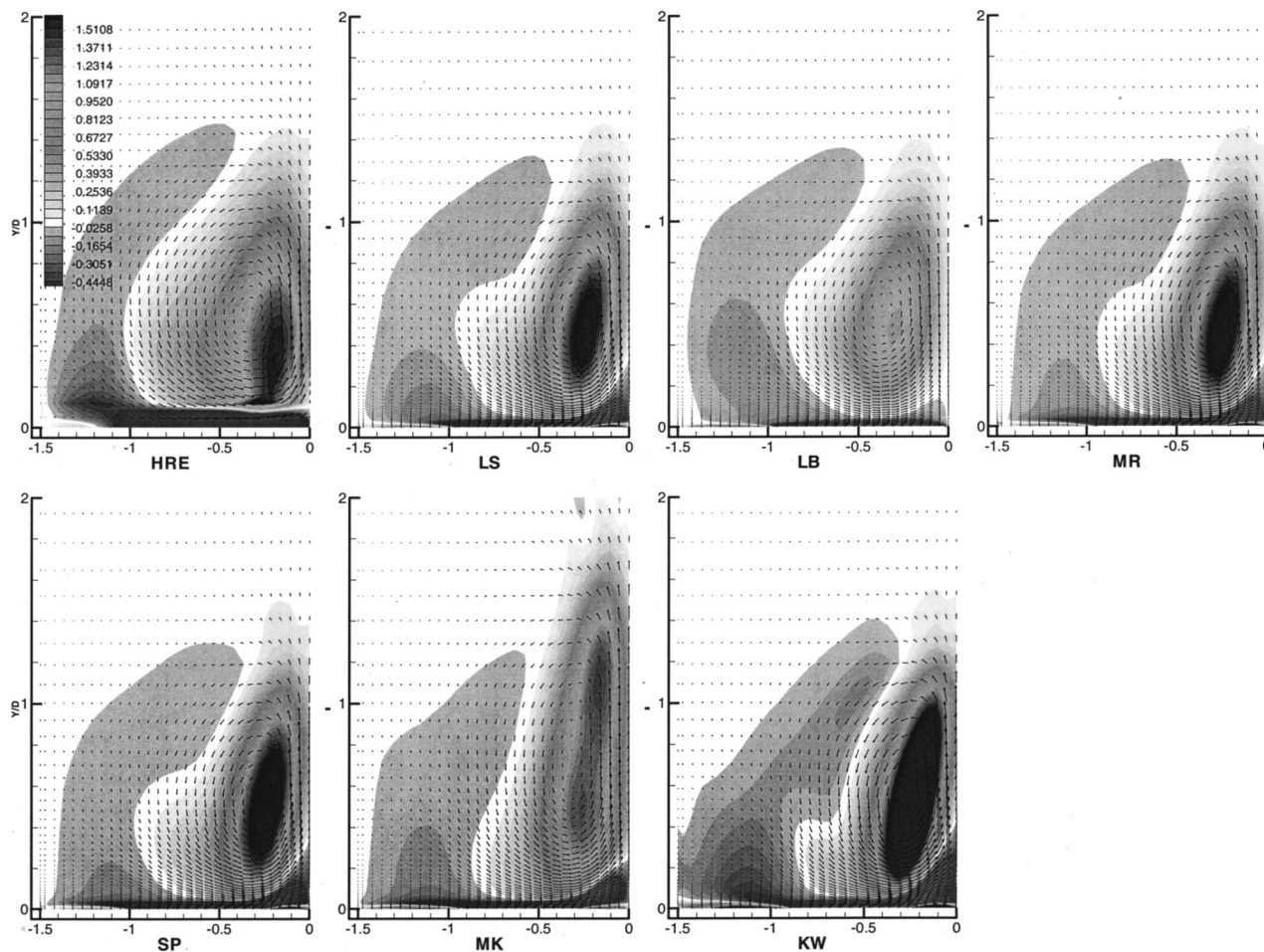


Fig. 7 Z component of vorticity and velocity vectors in X - Y plane at $Z/D=3.0$ for different models

predictions. Also of interest is the clear development of a wall-vortex structure in all the low-Re models. The wall-vortex is a manifestation of the crossflow entrainment into the wake region encountering an adverse pressure gradient in the spanwise direction near the jet centerplane. This adverse pressure gradient leads to flow reversal in the spanwise (XY) plane and the formation of the wall vortex structure close to the surface (as captured by the low-Re models). The vortex is confined between X/D of 0 and -0.5 at this Z/D location. As for the horseshoe, the KW model predicts the strongest wall vortex structure. Note that the HRE model does not predict the wall vortex at all.

Details of the horseshoe vortex predicted at $Z/D=8$ location are shown in an enlarged view in Fig. 8. The horseshoe can be clearly observed in all the model predictions, and show significant differences in size and strength, with the KW model showing the most significant horseshoe structure.

The differences in the recirculation region behind the jet are presented in greater detail in Fig. 9, which shows that the recirculation in all the low-Re models is qualitatively similar, with the reversed flow being entrained upward into the jet and then carried forward along its trajectory. The HRE model shows a much larger region of negative streamwise velocity, with strong crossflow entrainment into the wake. The recirculation region in the HRE model extends all the way to $Z/D=1.5$, while in the other models the recirculation region is less than $1D$ from the center of the jet-exit.

The region upstream of the jet marks the inception of the horseshoe vortex. An exploded view of this region is shown in Fig. 10, where the KW model, the SP model, and the MR model all show the inception of the horseshoe at this $X/D=0$ centerplane. Since all models show the horseshoe vortex at constant- Z/D planes further downstream (see Figs. 7 and 8), this implies that for the

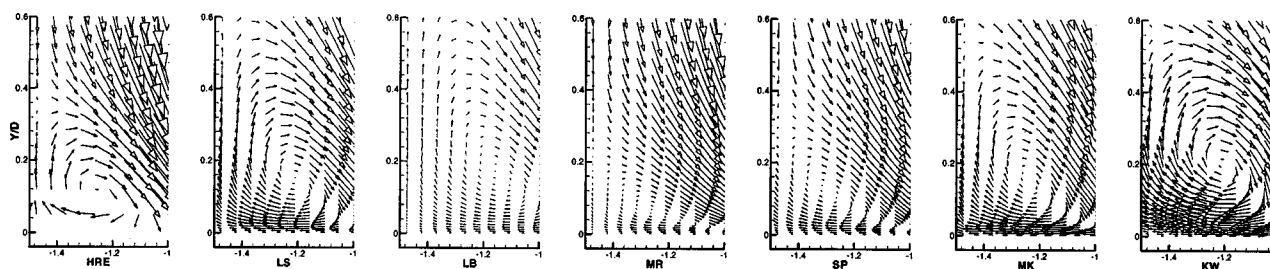


Fig. 8 Velocity vectors in X - Y plane at $Z/D=8$

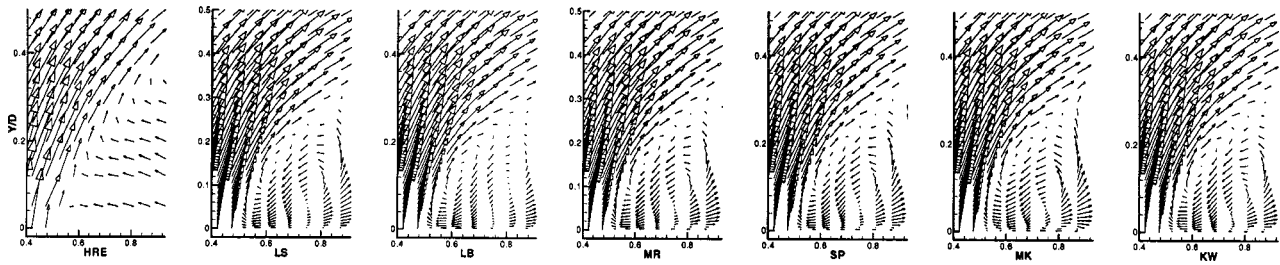


Fig. 9 Velocity vectors in $Y-Z$ plane at $X/D=0$

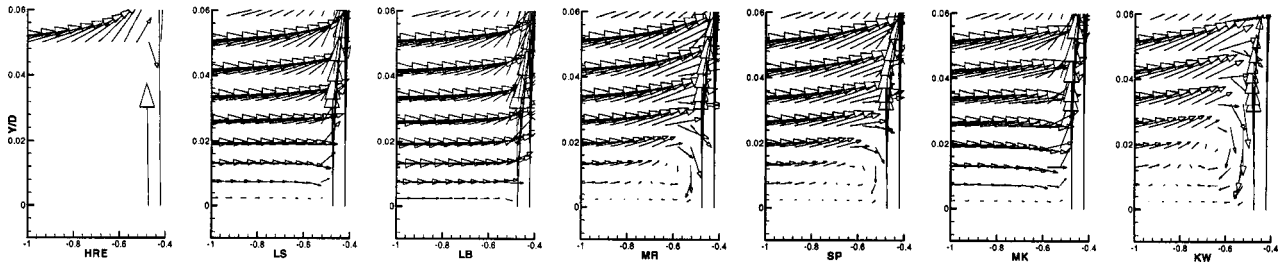


Fig. 10 Velocity vectors in $Y-Z$ plane at $X/D=0$

models where the horseshoe is not observed at $X/D=0$ in Fig. 10, the inception may occur at other X/D planes. Evidence of this is seen in streamwise and spanwise vorticity contours (not shown here) at a constant Y/D plane ($=0.05$) very close to the wall.

Concluding Remarks

Numerical predictions for film cooling jet in a crossflow have been carried out in this study using seven different turbulence models: a high-Re model (HRE), low-Re models (LS, LB, KW), nonlinear models (SP, MK), and a DNS based low-Re model (MR). The mean flow velocity and turbulent statistic profiles in general agree fairly well with experimental trends. The CRVP is distinctly predicted by all the models, but only a few models manage to capture the horseshoe structure correctly for the low blowing ratio case considered in this paper. The HRE model is not very well suited for the specific flow situation as it does not resolve the near-wall region properly. Although the mean flow profiles are predicted well, the turbulence levels are overpredicted and the HRE model is also unable to capture the recirculation in front of the jet. The HRE model predicts the largest levels of spanwise-jet-penetration, and substantially overpredicts the measured values of the spanwise and vertical velocities. The use of this model in such a complex flow situation is therefore not recommended. The LS model, which resolves the near-wall region, follows the experimental trends correctly, but fails to predict the correct trends in the wake of the jet, and does not represent the turbulent mixing taking place in this region appropriately. The near-wall region behavior of the LB model is consistently good, and this model, in general, seems to provide the best agreement with measurements. Compared to the other models, the LB model shows the smallest levels of vertical and spanwise spread. However, predictions in the jet region do not follow the experimental trends correctly, and the model is also unable to capture the recirculation in front of the jet. This structure is distinctly captured by the MR model. In this region the gradients in the vertical direction are of primary importance and the scaling arguments used for deriving the correlation terms in the ε -budget [17] hold good. In the jet and its vicinity, however, the gradients in the other directions cannot be neglected, and therefore the simplified ε budget is inadequate in the jet and its wake region. Clearly, the ε budget needs to be optimized for the present flow situation using DNS

data on lines similar to the MR model. The SP model predicts the turbulent characteristics trends correctly, but like the other models it is unable to resolve the variations observed in the wake of the jet. The MK nonlinear model significantly overpredicts the vertical jet penetration. The inability of the SP and MK nonlinear models to give better predictions compared to the linear models is thought to be a consequence of the fact that the nonlinear model coefficients were obtained through curve fitting of experimental data for simple wall bounded flows [18,20] and may not be well suited for the jet in a crossflow situation. The improved predictions of the near-wall structures obtained with the KW model can be attributed in part to the fact that the boundary conditions specified for ω are more accurate than those for ε . This problem related to the ε behavior near the wall has been pointed out by a number of researchers.

It is therefore clear from the present study that the models in their present form give overly simplistic predictions for the highly complex flow field being considered here. A comparison of the model predictions clearly reveals the need for better resolution of the near-wall region, asymptotic consistency of model coefficients, and damping functions in the jet and wall-bounded regions, respectively, and an appropriate representation of the ε budget. Also required is a suitable nonlinear formulation to predict the nonisotropic nature of the flow accurately. An effort along these directions using DNS predictions for jet in a crossflow [24,25] to guide the model development is being made by the authors and is to be reported shortly.

Acknowledgments

This work was done with support from NASA-Lewis (Grant No. NAG3-1641). Dr. Chi Wang and Dr. Ray Gaugler served as contract monitors. Their support is gratefully acknowledged.

Nomenclature

- $C_\mu, C_{\varepsilon 1}, C_{\varepsilon 2}$ = empirical constants appearing in $k-\varepsilon$ turbulence models
- D = function used in the low-Reynolds-number $k-\varepsilon$ model; also jet diameter (=jet width)
- E = function used in the low-Reynolds-number $k-\varepsilon$ model

f_1, f_2, f_μ = empirical functions of turbulent Reynolds number in low-Re $k-\varepsilon$ models
 f_3 = empirical function used in the Mansour–Rodi $k-\varepsilon$ model
 k = turbulent kinetic energy
 P = turbulence production term
 R = jet-to-crossflow velocity ratio
 Re_t = turbulent Reynolds number
 U, V, W = mean velocity components in $x, y,$ and z directions, respectively
 V_j = mean jet velocity
 $\overline{u'_i u'_j}$ = Reynolds stresses
 $\overline{u'^2}, \overline{v'^2}, \overline{w'^2}$ = normal stresses with respect to x, y, z axes
 $\overline{u'v'}, \overline{v'w'}, \overline{u'w'}$ = shear stresses
 x = coordinate in the cross-stream direction
 y = coordinate normal to the wall
 z = coordinate in the streamwise direction
 $\alpha, \alpha^*, \beta^*$ = empirical functions in the $k-\omega$ model
 β = empirical constant in the $k-\omega$ model
 ε = rate of dissipation of kinetic energy
 $\bar{\varepsilon}$ = modified dissipation rate
 μ, μ_t = dynamic and turbulent viscosity
 ν, ν_t = kinematic and turbulent kinematic viscosity
 ρ = density
 σ = Prandtl number
 ω = specific dissipation rate = ε/k

References

- [1] Fric, T. F., and Roshko, A., 1994, "Vortical Structures in the Wake of a Transverse Jet," *J. Fluid Mech.*, **279**, pp. 1–47.
- [2] Lee, S. W., Lee, J. S., and Ro, S. T., 1994, "Experimental Study on the Flow Characteristics of Streamwise Inclined Jets in Crossflow on Flat Plate," *ASME J. Turbomach.*, **116**, pp. 97–105.
- [3] Kelso, R. M., Lim, T. T., and Perry, A. E., 1996, "An Experimental Study of Round Jets in Crossflow," *J. Fluid Mech.*, **306**, pp. 111–144.
- [4] Garg, V. K., and Gaugler, R. E., 1997, "Effect of Coolant Temperature and Mass Flow on Film Cooling of Turbine Blade," *Int. J. Heat Mass Transf.*, **40**, No. 2, pp. 435–445.
- [5] Kim, S. W., and Benson, T. J., 1993, "Fluid Flow of a Row of Jets in Crossflow—A Numerical Study," *AIAA J.*, **31**, No. 5, pp. 806–811.
- [6] Walters, D. K., and Lylek, J. H., 2000, "A Detailed Analysis of Film-Cooling Physics: Part I—Streamwise Injection With Cylindrical Holes," *ASME J. Turbomach.*, **122**, pp. 102–112.
- [7] Demuren, D. K., Rodi, W., and Schonung, B., 1986, "Systematic Study of Film Cooling With a Three-Dimensional Calculation Procedure," *ASME J. Turbomach.*, **108**, pp. 124–130.
- [8] Demuren, A. O., 1993, "Characteristics of Three-Dimensional Turbulent Jets in Crossflow," *Int. J. Eng. Sci.*, **31**, No. 6, pp. 899–913.
- [9] Clauss, R. W., and Vanka, S. P., 1990, "Multigrid Calculations of Jet in Crossflow," *AIAA Paper No. 90-0444*.
- [10] Findlay, M. J., He, P., Salcudean, M., and Gartshore, L. S., 1996, "A Row of Streamwise-Inclined Jets in Crossflow: Measurements and Calculations," *ASME Paper No. 96-GT-167*.
- [11] Ajersch, P., Ketter, S., Zhou, J. M., Gartshore, L., and Salcudean, M., 1997, "Multiple Jets in a Crossflow: Detailed Measurements and Numerical Simulations," *ASME J. Turbomach.*, **119**, pp. 330–342.
- [12] Launder, B. E., and Spalding, D. B., 1974, "The Numerical Computation of Turbulent Flows," *Comput. Methods Appl. Mech. Eng.*, **3**, No. 2, pp. 269–289.
- [13] Patel, V. C., Rodi, W., and Scheuerer, G., 1985, "Turbulence Models for Near-Wall and Low-Reynolds Number Flows: A Review," *AIAA J.*, **33**, pp. 1308–1318.
- [14] Launder, B. E., and Sharma, B. I., 1974, "Application of the Energy Dissipation Model of Turbulence to the Calculation of Flow Near a Spinning Disc," *Lett. Heat Mass Transfer*, **1**, pp. 131–138.
- [15] Lam, C. K. G., and Bremhorst, K. A., 1981, "Modified Form of the $k-\varepsilon$ Model for Predicting Wall Turbulence," *ASME J. Fluids Eng.*, **103**, pp. 456–460.
- [16] Wilcox, D. C., and Traci, R. M., 1976, "A Complete Model of Turbulence," *AIAA Paper No. 76-351*.
- [17] Rodi, W., and Mansour, N. N., 1993, "Low Reynolds Number $k-\varepsilon$ Modelling With the Aid of Direct Simulation Data," *J. Fluid Mech.*, **250**, pp. 509–529.
- [18] Mayong, H. K., and Kasagi, N., 1990, "Prediction of Anisotropy of the Near-Wall Turbulence With an Anisotropic Low-Reynolds-Number $k-\varepsilon$ Turbulence Model," *ASME J. Fluids Eng.*, **112**, pp. 521–524.
- [19] Mayong, H. K., 1988, "Fundamental Studies on Two-Equation Turbulence Models for Numerical Prediction of Wall-Bounded Shear Flows and Heat Transfer," *Dr. Eng. Thesis, The University of Tokyo*.
- [20] Speziale, C. G., 1987, "On Nonlinear $k-l$ and $k-\varepsilon$ Models of Turbulence," *J. Fluid Mech.*, **178**, pp. 459–475.
- [21] Patankar, S. V., 1980, "Generation of Finite Difference Formulas on Arbitrarily Spaced Grids," *Math. Comput.*, **31**, No. 184, pp. 699–706.
- [22] Fornberg, B. G., 1988, "Generation of Finite Difference Formulas on Arbitrarily Spaced Grids," *Math. Comput.*, **31**, No. 184, pp. 699–706.
- [23] Andreopoulos, J., and Rodi, W., 1984, "Experimental Investigation of Jets in a Crossflow," *J. Fluid Mech.*, **138**, pp. 93–127.
- [24] Muldoon, F., and Acharya, S., 1999, "Dynamics of Large-Scale Structures for Jets in a Crossflow," *ASME J. Turbomach.*, **121**, pp. 577–488.
- [25] Sharma, C., and Acharya, S., 1998, "Direct Numerical Simulation of a Coolant Jet in a Periodic Crossflow," *Heat Transfer in Turbomachinery*, ASME HTD-Vol. 361-3/PID-Vol. 3, p. 363.

Continuous Monitoring of Binary Gas Mixture Concentration With Application to Turbine Blade Cooling Experiments

Tomas Strilka

Graduate Student.
e-mail: tstrilka@scotty.ase.uc.edu

Miklos Sajben

Professor.
Mem. ASME
e-mail: m.sajben@uc.edu

Peter Nagy

Associate Professor.
Mem. ASME
e-mail: pnagy@uceng.uc.edu

Department of Aerospace Engineering and
Engineering Sciences,
University of Cincinnati,
Cincinnati, OH 45221-0070

Turbine blade cooling experiments often use mixtures of air and a heavy gas (CO_2 , SF_6) to simulate coolant/mainstream density ratios. If the mixing of the mainstream with the coolant ejected from the blade is of interest, then it may be necessary to determine the spatial distribution of the heavy gas concentration in the flowfield. Commercial analyzers are too slow and have other disadvantages when used for this purpose. To meet this special need, a device has been developed to monitor the heavy gas concentration continuously in a small sample stream by determining the speed of sound in the sample. Together with the temperature of the sample, the information is sufficient to determine the concentration. The device measures the time of propagation for an ultrasonic burst transverse to the stream. The temperature of the gas contained in the device is controlled and measured. Calibration with several gas mixtures (air and CO_2 , SF_6 , He) has shown an uncertainty ($C_{meas} - C_{true}$) of 2 percent over the full concentration range of 0–100 percent for CO_2 and SF_6 . The device is operable in the pressure range from –50 to 100 kPa gage and in the temperature range from 0°C to 40°C. The instrument is rugged and will survive in noisy, turbulent environments. [S0889-504X(00)01202-2]

Introduction

Gas turbine technology often has to deal with situations where two gas streams having unequal temperatures are mixed. Coolant gases injected into combustors and coolant gas exhausting into the mainstream from cooled turbine blades or from interdisk cavities are just a few examples. The duplication of the temperature distributions of these flows in developmental tests or detailed experimental studies is generally quite costly. In many situations a partial simulation may be acceptable in which the hot (or cold) stream is simulated by some inert gas that has the same temperature as the test air, but its molecular weight (i.e., density) is different. Coolant streams may be simulated with a heavy gas, such as CO_2 or SF_6 , while helium is an appropriate substitute for hot gases. For the purposes of the present paper, we shall refer to such a gas as a “ballast” gas. A wide range of density ratios may be realized by mixing ballast gases with air in various controlled proportions.

The thermodynamic state of a binary gas mixture of known constituents is characterized by three variables, e.g., pressure, temperature, and mass fraction of ballast gas. The mass fraction affects all thermodynamic properties. If the constituent gases are thermally and calorically perfect gases with known properties, then the computation of the speed of sound is a simple matter (see appendix).

If the test in question requires the determination of spatial flow property distributions, i.e., local measurements have to be made, then the knowledge of mass fraction is necessary to compute the local Mach numbers from pressure probe data. The dependence of Mach number on mass fraction (for a given value of the static/total pressure ratio) is significant, especially at low speeds. If the local mass fraction is not known, then this variation becomes a measurement error.

The focus of the present work lies in the measurement of time

mean flowfield properties in turbulent, adverse environments. Turbulence property measurements and optical methods are not considered. The paper relates to measurements that involve the withdrawal of a sample gas stream through a small sampling probe that offers good spatial resolution. Since ballast gases are inert, the mass fraction is unaffected by any pressure or temperature change that might occur in the sample stream after ingestion.

The desired characteristics of the method are dictated by the nature of experiments simulating propulsion devices. The method has to be fast, because test times may have to be short. Short run duration may be mandated by the cost of the ballast gas, and/or by a requirement that measurements be made at many locations throughout the flow in a single run. Purging times of the sampling flow system have to be short, which generally implies that the system must have very low volume. The system must work at the wide range of pressure levels usually found in propulsion experiments.

Commercially available systems are generally highly accurate. There are systems based on gas chromatography, thermal conductivity, paramagnetic resonance, or a variety of other principles. These systems are generally too slow, require too large a sample or discrete, stationary samples. Most have limitations on the operating pressure that make them poorly suited for the type of experiments considered here. Most commercial systems represent an overkill in terms of analytical capability and precision. In our case, the ability to detect minute mass fractions of unknown elements is not required. The species present in the gas are known and true analysis is not needed: only the mass fraction of a known gas is to be determined. For the purposes considered here, a modest 1–2 percent uncertainty in concentration is entirely adequate.

The best known technique that approaches these requirements has been developed by Brown and Rebollo [1]. Their method uses a hot wire placed behind a choked sampling orifice, and has a fine spatial resolution and an excellent time response, suitable for the determination of turbulence properties. On the other hand, the device is not robust, its fabrication requires high skill levels, and

Contributed by the International Gas Turbine Institute and presented at the 44th International Gas Turbine and Aeroengine Congress and Exhibition, Indianapolis, Indiana, June 7–10, 1999. Manuscript received by the International Gas Turbine Institute February 1999. Paper No. 99-GT-365. Review Chair: D. C. Wisler.

the operation relies on extensive calibrations. For the purposes of time mean property measurements, the extremely fast response of the Brown and Rebollo scheme is not required.

This paper describes a device for the measurement of heavy gas concentration, with characteristics that make it suitable for research applications involving cooling problems.

Acoustic Measurement of Concentration. The measurement concept is based on the fact that the molecular weights of ballast gases are significantly different from those of air for the very reason they are being employed. All gases considered here are assumed to be thermally and calorically perfect, such that R and c_p are constants. The values of these constants differ significantly from the values applicable to air (Table 1). The gas properties of the mixture depend on the mass fraction of the ballast gas, C_b (details in appendix).

In particular, the speed of sound for a mixture of thermally perfect gases is given [2] as

$$\bar{a} = \sqrt{\gamma \bar{R}(C_b) T} \quad (1)$$

If the temperature is known from an independent measurement, then Eq. (1) establishes a relation between the mass fraction of the ballast gas and the speed of sound. Figure 1 illustrates that the connection between \bar{a} and C_b is unique for a given mixture and it is also monotonic. It is evident that a basis exists for the measurement of the ballast gas mass fraction by measuring the speed of sound of the mixture. One important advantage of the method is that calibration is not required, at least not in principle. Practical considerations or a need for the highest possible accuracy may make calibration advisable, but the corrections are expected to be minor.

The authors arrived at this concept independently, but discovered later that similar methods have been proposed and at least partially developed by others earlier [3]. However, the details of implementation described here are new.

Table 1 Gas properties

| Property | Molecular weight | Gas constant | Ratio of spec. heats | Sound speed* |
|-----------------|------------------|--------------|----------------------|--------------|
| Unit → | kg/kmol | J/kg/K | | m/s |
| Species ↓ | | | | |
| Helium | 4.003 | 2,077.0 | 1.67 | 999.7 |
| Air | 28.967 | 287.0 | 1.40 | 340.3 |
| CO ₂ | 44.009 | 188.9 | 1.30 | 266.0 |
| SF ₆ | 146.054 | 56.92 | 1.102 | 134.3 |

*Evaluated at standard sea level condition (288.15°K)

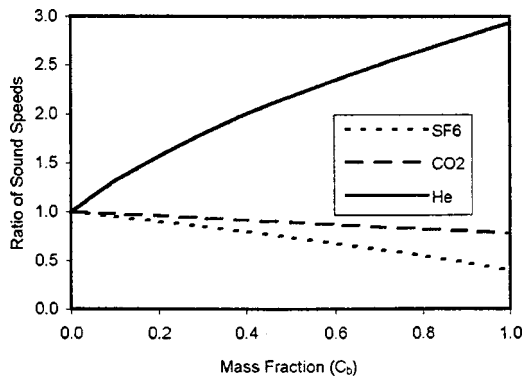


Fig. 1 Acoustic speed in binary gas mixtures of air and other gases; values normalized by the acoustic speed of air

Sampling. The sample to be analyzed is withdrawn from a turbulent stream using a small tube facing the flow. In the application that motivated this work, the mean Mach number of the stream is in the range 0.8–1.4 and the static pressure varies from 80 to 140 kPa absolute. The frontal open area of the probe is 0.21 mm², which is 52 percent of the total frontal area including the wall thickness. The volumetric flow rate of the sample flow is 1–4 L/min. The local mean velocity, total pressure, and temperature are determined simultaneously by independent means and are available in real time to assist the concentration measurement.

The intent is to sample the flow in such a way that the disturbance to the flow is minimized and thereby spatial resolution is maximized. It is assumed that this condition is best approximated if the mean velocity of the sample (at the entrance opening of the aspirating tube) is equal to the time mean velocity of the undisturbed flow at the same location (“isokinetic sampling”). Provisions are included in the design to achieve this condition.

Sampling a turbulent stream of variable density is a complex process (especially in supersonic flow). The relation of the mixed-out sample concentration to the mean and turbulent properties of the stream is an important issue, but outside the scope of this paper. The paper is focused on the determination of concentration in the sample flow.

Transverse Transmission of Sound

There are probably many ways to determine acoustic speed in a sample flow. Sajben and Crafton [4] describe several concepts that have been tested using audio frequencies, with limited success. The acoustic methods were handicapped by turbulence noise in the audio range and were replaced by concepts involving ultrasonic signals. Devices using streamwise propagation have been tried, but were unworkable with SF₆, due to a combination of (a) large distance between the transducers and (b) high level of absorption in SF₆ at ultrasonic frequencies (which was unexpected). Eventually, a concept using transverse propagation of ultrasound evolved. This device has been fully developed and the rest of this paper is devoted to its detailed description.

Concept. Figure 2 shows two views of the device and Fig. 3 shows details of the ultrasonic transducer installation. The principal element of the device is a flat, rectangular cross-sectional channel, with two transducers facing each other on opposite sides. Transmission occurs in a direction normal to the flow, in one direction only. The travel time of the signal does not depend on the flow speed.

Previous work provided ample warning that precise temperature control will be an essential part of the final configuration, in

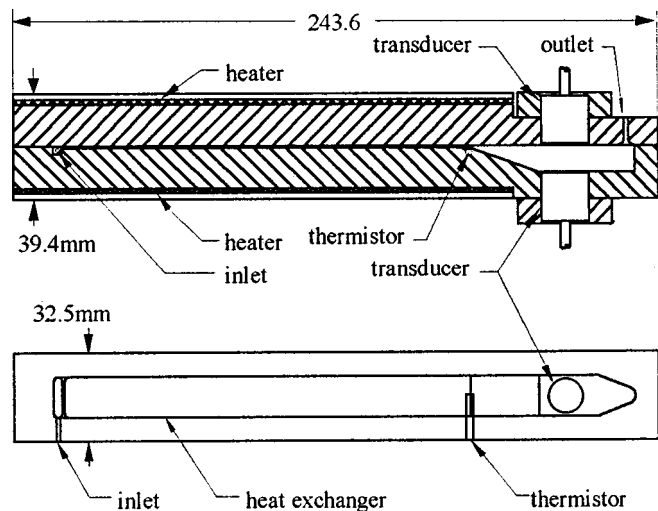


Fig. 2 Assembled device

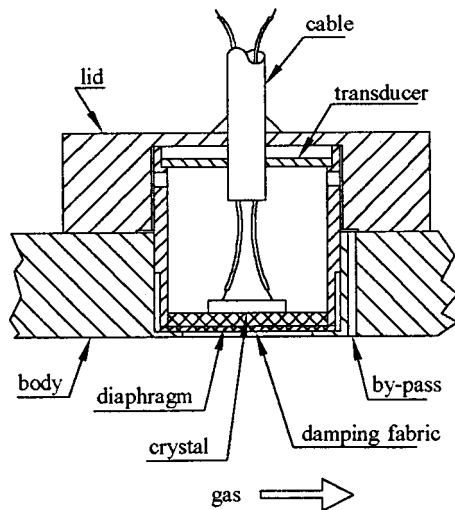


Fig. 3 Mounting of ultrasonic transducers

part to allow the calculation of the speed of sound, and in part because the transducers are temperature dependent and minor temperature drifts were seen to cause major changes in output.

The configuration of the device was dictated to a large extent by the requirements of thermal control. All flow passages are contained within an aluminum block that is kept at a constant temperature by a ribbon heater surrounding it. The block is split in the middle to allow installation and inspection of the transducers and other internal components. The heater is driven by a controller using the output from a thermistor located very near to the end of the narrow channel. The flow first enters a small plenum chamber, then passes into a very high aspect ratio, flat channel ($0.8 \times 15.2 \times 152$ mm). The small channel height allows the stream to reach thermal equilibrium with the walls before reaching the transducers. The channel entry is slightly constricted to improve the spanwise flow distribution.

The channel widens greatly just upstream of the transducers, to provide the separation required for a reasonable travel time and thereby for an acceptable accuracy. Since large area ratio diffusers are known to have distorted exit flows, fine screens are placed both upstream and downstream of the actual measurement section to force an even flow distribution.

Description of System Components. A schematic diagram of the entire system is shown in Fig. 4. The sample of a gas mixture is taken at the location of interest in a stream of unknown concentration. The sample enters the device; it is thermally stabilized in the flat channel and enters the sensor part where the speed of sound of the sample is detected. After leaving the device, the gas sample passes through a flowmeter and a flow controller, a damping volume, and eventually a vacuum pump. The flowmeter monitors and the controller adjusts the actual mass flowrate. The vacuum pump ensures that the pressure differential required to drive the sample stream is available, even at relatively low test section pressures.

The concentration measurement requires its own PC, designated as CMPC. The CMPC is in communication with the computer controlling the entire experiment (designated as EXPC).

The aluminum block and the components contained within it will be referred to as the "concentration meter" or CM for short. The CM and all the associated additional components taken together will be called the "concentration measurement system," or CMS.

The following subsections provide detailed descriptions of the system components.

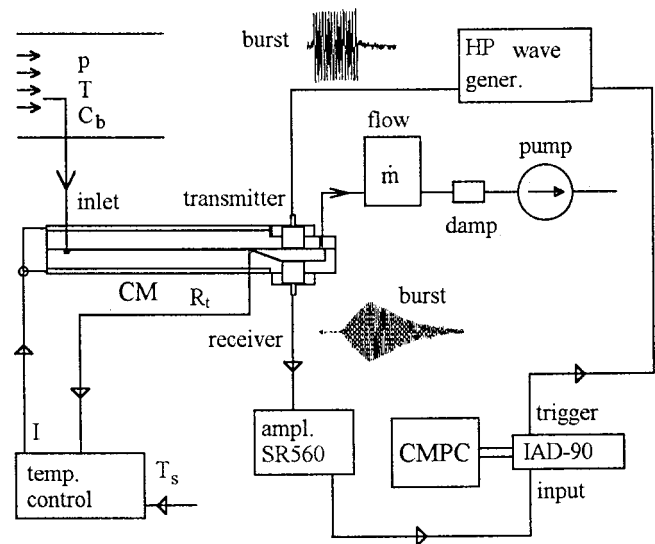


Fig. 4 Overall scheme of the measurement system (CMS), including the means for the withdrawal of the sample gas

Transducers. We selected a resonant ultrasonic transducer with a resonant frequency of 150 kHz (International Transducers Corp., Model ITC-9072). The interior of the transducer (Fig. 3) contains a cylindrical cavity bounded on one side with a piezoelectric crystal, to the outer side of which a silicon diaphragm (diameter=16 mm) is attached. The gas environment is on the outside of the silicon membrane. Since the distance between the two sensors is only 12 mm, a pressure pattern of multiple reflections is created in the space separating them, after sending a sine burst of 15 cycles. In order to minimize the disturbing effects of these reflections, a fabric layer is attached to both transducers to damp the reflections coming off them. While the fabric also attenuates the initial signal, this loss is more than balanced by the fact that the multiple reflection pattern essentially vanishes.

The sensor must be operational at pressures significantly higher (or lower) than atmospheric (from -50 to $+100$ kPa gage). This is a nontrivial requirement and received special attention. External overpressures of this magnitude could deflect the diaphragms and increase the distance between them such that the propagation time would increase. Transducer characteristics could also change with the deformation. To avoid these problems, a small bypass passage was machined into the bore holding the transducer (Fig. 3). The passage equalizes the static pressures on the two sides of diaphragm and the diaphragm deformation does not occur.

Thermal Control. The speed of sound depends on the gas temperature [Eq. (1)], hence temperature measurement errors translate into inaccuracies of the concentration measurement. Furthermore, the resonant-type ultrasonic transducer responded by large phase shifts to even moderate temperature changes.

An effective solution of this problem is a temperature regulation of the aluminum block that contains the entire CM. The temperature of the gas sample is controlled by keeping the wall temperature constant in a narrow passage through which the gas flows just before entering the sensor section. The block also provides a constant temperature environment for the ultrasonic transducers, minimizing drifts in their outputs.

Figure 5 shows the configuration of the thermal controls. The core of the system is a $32 \times 39 \times 244$ mm aluminum block (Fig. 2), equipped with two flexible ribbon heaters attached to the block surface. Silicon paste is used to reduce contact resistance to heat conduction. The heaters are connected in parallel, for a total resistance of 4Ω . The maximum power produced by the heaters is 16 W.

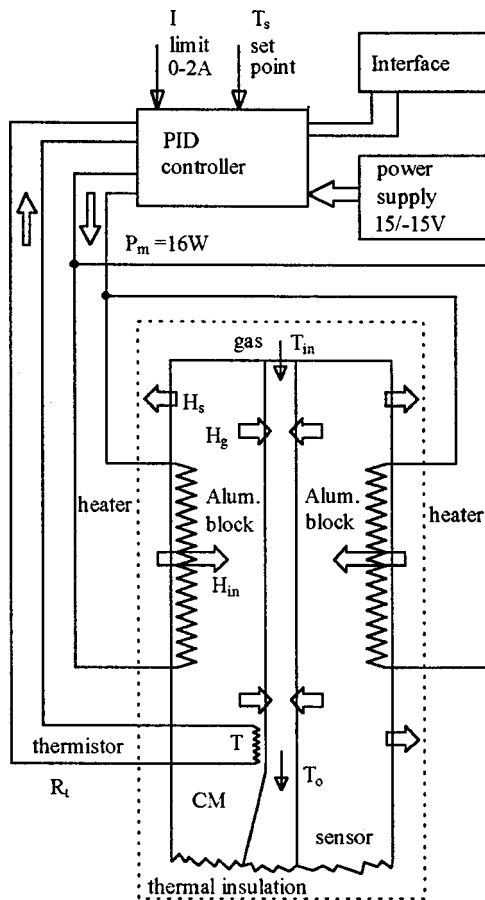


Fig. 5 Thermal control of the CM and the gas sample

The gas sample is heated as the gas flows through a rectangular channel inside the aluminum block. The dimensions of the channel were chosen to produce less than 0.1 K deviation from the set temperature in the gas stream at the outlet of the slot (i.e., just before entering the sensor section), provided the input temperature of the gas is within 10 K of the set point temperature of the regulator. The design calculations assumed the flow rate to be 3 L/min for both air and SF₆.

To obtain a high level of temperature stability, a commercial PID controller has been chosen, in combination with a sensitive thermistor as temperature sensor. The output of the controller is constant voltage while the heater current varies as needed. The performance of the temperature controller is monitored and its functions can be commanded by the operator through the controller/EXPC interface. The aluminum block is enclosed in a thermally insulated lucite capsule to minimize the effects of temperature variations in the surrounding air.

Tests of the heat exchanger and the control system showed that the design conditions were met. Typically, when the inlet air temperature was 10°C, then a set point temperature of 30°C resulted in outlet stream temperatures within 0.2°C of the set value.

The exit temperature of the sample was measured by an uncalibrated thermocouple located 5 mm downstream of the heat exchanger outlet. The thermistor used to measure the channel wall temperature was calibrated against a (commercially calibrated) T-type thermocouple. Since temperature drift is of more concern than a precise knowledge of absolute temperature, these sensors were considered adequate. (Note that 1 K temperature error causes only 0.17 percent error in the speed of sound.)

Control and Measurement of Flow Rate. Isokinetic sampling requires the measurement and control of the gas sample

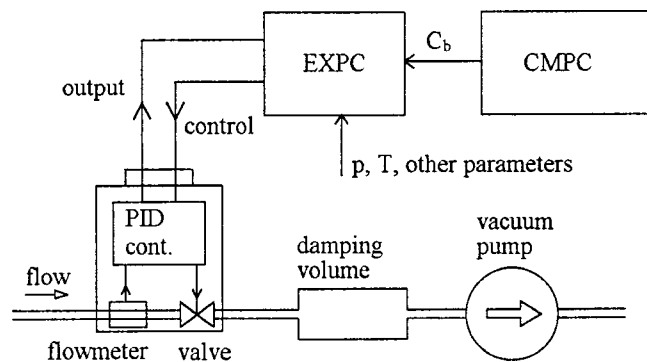


Fig. 6 Flowrate measurement and pumping system

flow. This is accomplished by a thermal mass flowmeter/controller (Datametrics Model 825). This unit is a combination of a mass flowmeter and a control system (Fig. 6).

Since pressure, temperature, and mixture mass fraction can all change during the experiment, the measurement of flow rate is a nontrivial problem for most flowmeters. A thermal mass flowmeter was selected mostly because it has the advantage of having a high tolerance for pressure and temperature variations. Once calibrated, a simple relation exists between the output signal, the actual mass flowrate, and the specific heat (c_p) of the mixture. The specific heat depends on the mass fraction, but since the latter is continuously measured, the variation of c_p can be readily accounted for in the data reduction procedure.

The Datametrics unit has a built-in control system and control valve that regulates the flowrate according to an externally input set-point signal and to the flowmeter readout representing the actual flowrate. The readout and control signals are handled by the computer (EXPC). All data needed to calculate the isokinetic condition are available to the EXPC, such that the necessary flowrate in the sampling system using the flow controller can be set.

Since the pressure at the sampling probe may drop below atmospheric under some conditions, a vacuum pump is provided near the downstream end of the flow system. A damping volume is also inserted between the pump and the flowmeter to attenuate pressure oscillations caused by the vacuum pump. If the total pressure at the sampling probe is sufficiently high, then the vacuum pump is not needed. For simplicity, the pump is left in place at all times, since its presence has no adverse effects on the operation of the system.

Measurement of Propagation Time. The CMPC is equipped with a Physical Acoustics data acquisition card (model IAD-90) capable of a maximum sampling frequency of 32 MHz. This card has one eight-bit channel operated in the range of ± 10 V. Before a data sample is taken, the data card sends out a trigger signal. This signal is received by the digital wave generator (Hewlett Packard HP33120A), which then sends a 15-cycle sine burst at a frequency of 150 kHz to one of the ultrasonic transducers. This transducer emits an ultrasonic wave, which propagates through the gas sample in the transverse direction and is received by the second sensor. This sensor converts the arriving burst into an electronic signal, which is filtered and amplified (Stanford Research amplifier SR560). The conditioned output signal is then read by the data acquisition card and is analyzed by the software.

Software and Data Acquisition Procedures. The basic approach of the software is an adaptation of the scheme developed by Nagy and Blaho [5]. Other options are available, but this method offered the best combination of accuracy and reliability. The software is Windows-based and is convenient to use.

The method is based on selecting a particular single period (a "reference wave") from the received ultrasonic burst and track-

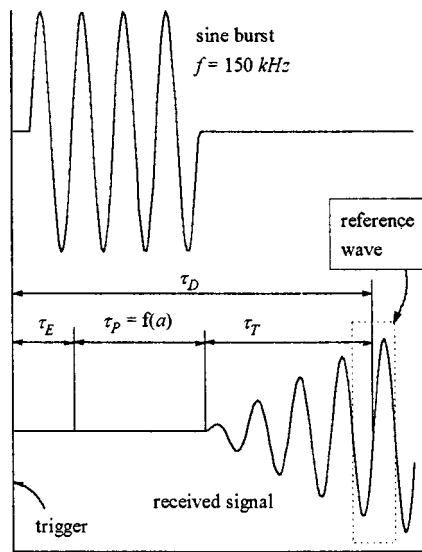


Fig. 7 Detection of propagation time

ing the zero-crossing point of this wave as the concentration changes. When a pure “reference gas” of known properties (i.e., air) is blown through the sensor, then the reference wave is located in the received burst (Fig. 7) at the start of the measurement. If the gas is changed into a mixture, then the wave pattern will drift, i.e. the time interval τ_D between the trigger signal and the reference wave will change. Only a small drift is expected between two consequent measurements since the burst rate is a fast 200 Hz. The location of the new zero crossing is expected to be between the minimum on the left and maximum on the right side of the previous zero crossing. The interval between one of the extrema and the zero crossing corresponds to a quarter cycle, or $1.67 \mu\text{s}$. A new zero crossing is found in the new data and taken as a new reference point for the next measurement.

A sudden change of concentration or other errors could cause the system to loose track of the wave, causing a large error in concentration measurement. If this occurs, the reference wave has to be reestablished by blowing the reference gas through the device again. The tests of the system show that the 200 Hz data rate is sufficient to capture rapid changes in the concentration of the sample gas. The largest drift measured in calibrations corresponded to a phase shift about 50° of the burst signal ($0.93 \mu\text{s}$).

The time delay, τ_D , contains two parts, a constant, τ_C , and a variable part, τ_P . The constant part, τ_C , can be further broken down into two contributions: τ_E , that is caused by the electronic circuits and the mechanical properties of the ultrasonic transducers, plus the time, τ_T , the time elapsed between the beginning of the first wave of the burst and the actual reference point. The variable part, τ_P , is the burst propagation time in the sample gas. We have

$$\tau_D = \tau_C + \tau_P = (\tau_E + \tau_T) + \tau_P \quad (3)$$

In order to illustrate the importance of these intervals, consider that at a driving frequency of $f = 150 \text{ kHz}$, the wave period is $T_W = 6.67 \mu\text{s}$. For a spacing of 1 cm between the transducers, the propagation times vary from $\tau_P = 33 \mu\text{s}$ (pure air) to $\tau_P = 83 \mu\text{s}$ (pure SF_6). The difference is $50 \mu\text{s}$, or 7.5 periods. This means that the identification of the intended reference wave is of paramount importance.

The propagation time τ_P calculation is based on the comparison of the measured time delays (τ_D) of the reference gas and of the mixture. The speed of sound of the reference gas is calculated using the temperature of the set point. The propagation time of this reference gas is calculated from the speed of sound and the distance between the transducers ($L = 0.0123 \text{ m}$). The propagation

time of the mixture is then calculated as the difference between the time delays (τ_D) of the mixture and the reference gas, plus the propagation time of the reference gas. The speed of sound of the mixture is a function of the propagation time of the mixture and the distance L . Once the speed of sound is known, the concentration calculation is just a matter of using the equations in the appendix.

The CMPC software continuously sends the information about the actual concentration to the EXPC through a serial connection.

Temporal Characteristics. The ultrasonic system is capable of acquiring concentration data at rates up to 200 values per second. However, the response time to concentration changes is limited by the purging time of the system, which is governed by the internal volume of the CM and by the volumetric flow rate (7.6 cm^3 and $1\text{--}4 \text{ L/min}$). The corresponding ratios of volume to volumetric flow rates range from 0.11 to 0.45 s. The system is thus estimated to be capable of acquiring 2–8 valid data points per second, each data point being the average of approximately 10–20 bursts.

This time limitation is rooted in the size of the ultrasonic transducers, which dictated the dimensions of the duct segment that contain them. This duct segment is the largest contributor to the total internal volume. A search is under way for alternate configurations that could minimize the transducer-related volumes.

The CM also has a response time to pressure changes, due to the finite time required to equalize the pressures on the two sides of the ultrasonic transducer diaphragm (Fig. 3). The time is controlled largely by the cross-sectional area of the equalizing passage. This response time was found to be approximately 1 s. Enlargement of the passage size would reduce this time.

The sampling probe will generally experience turbulent fluctuations that might induce pressure fluctuations inside the system. However, these fluctuations occur at frequencies well below the 150 kHz frequency of the ultrasonic signal and they are completely filtered out before the signal is processed. In any case, the sample flow system has a high resistance to flow, which implies a high level of viscous damping, such that even the low-frequency oscillation amplitudes are likely to be low.

Calibration of Flowmeters

As stated in the beginning, the CMS should not require calibration. However, such a claim is unlikely to be accepted by potential users without a demonstration of its capabilities, and a comparison to another, independent method was made.

Accurate flow metering is required for two different purposes: (a) calibration of the flowmeter to be used for the routine, operational measurement of the sample stream flow rate, and (b) one-time creation of a sample stream with precisely known concentration, for the purpose of validating the ultrasonic concentration measurement method.

While the primary purpose of this work was to create a reliable device and method for measuring concentration, the achievement of accurate flow metering required a large part of the total effort.

Thermal Mass Flowmeter. As stated before, a thermal flowmeter was chosen for the routine measurement of the mass flow of the sample stream. This type of flowmeter is based on measuring the temperature change in the gas flowing through a bypass thermal element where a constant heat flux is applied into the gas. The mass flow rate is then obtained from an equation of the form

$$\dot{m}_o = \frac{f(\Delta T)}{c_p} \quad (4)$$

The function f is (in principle) independent of the gas being measured: The gas properties enter only through the specific heat. The specific heat (c_p) can be calculated, in our application, from the speed of sound measurement, and the expectation was that no additional data would be necessary.

The Datametrics 825 thermal mass flowmeter was calibrated with various gases, against a precision volume flow device (SKC Accuflow Film Calibrator 715) in a range of 0–5 L/min. These calibrations showed that the simple relation given as Eq. (4) is in error by a few percent. To account for the discrepancy, a correction factor was calculated from the calibration data for each gas. The correction factors for various gases, when plotted against c_p , showed a systematic variation and could be fitted by an algebraic expression. This expression was assumed to apply to all mixtures and was used to determine flow rates in all cases. Since the correction factor depended only on c_p , the procedure may be viewed as using an “effective” or “corrected” specific heat for the gas.

Rotameters. An experimental setup was assembled that created continuous streams of two different gases, measured both flowrates, mixed them, and fed the mixture to the ultrasonic meter. The gases were of commercial purity obtained from standard high-pressure bottles. The pure gas flowrates were measured by rotameters (Gilmont GE700).

The rotameters were calibrated against the Datametrics thermal mass flow meter (which was previously calibrated against the Accuflow device). Since the pressures and temperatures of the gases during the rotameter calibrations were not identical to those during the Datametrics calibration against the Accuflow unit, nor were they the same during actual CMS operation, the rotameters require corrections. The test conditions are different because of a large pressure drop across the CM, its associated small tubing, and also the exhaust tubing to a vent (up to 50 kPa). These pressure differentials were not present during the calibrations.

The need for corrections implied that static pressure and temperature had to be monitored at each rotameter. The relevant conditions are those prevailing at the floats and these were best approximated by the condition downstream of the rotameter. The pressure upstream of the rotameter was generally very different from that near the float, due to a precision flow control valve built into the rotameters on the upstream side, which created a large pressure drop. The static pressure was measured by using a pressure transducer (Meriam Instrument, Model DN0010PG) attached to a tap in a tube fitting, and the temperature by a thermocouple inserted into the stream.

Since the rotameters are volumetric flow devices, the pressure and temperature were also needed to make the conversions to mass flow units.

The data showed that the standard density corrections recommended by the manufacturers were inadequate to account for the condition changes in a rotameter. A correction procedure has been developed that represented the aerodynamic forces on the spherical float as a drag force [6]. According to this analysis, the actual flow rate and the flow rate under standard conditions are related by the following expression:

$$\frac{\dot{m}}{\dot{m}_{SC}} = \sqrt{\left(\frac{\rho}{\rho_{SC}}\right) \left(\frac{c_D(Re_{SC})}{c_D(Re)}\right)} \quad (5)$$

where the dependence of the drag coefficient on Reynolds number. [i.e., the $c_D(Re)$ relation] is specific to the float geometry. In our case we used the drag coefficient relation for a sphere in an infinite stream. While this procedure neglects the influence of the surrounding tube on the sphere drag, the viscous trends are likely to be the same.

Correction (5) was found to work quite well in relating different measurement conditions for a single gas. As illustrated in Fig. 8, accounting for the Reynolds number dependence in the above-described fashion reduced the errors to less than half in comparison to those associated with a simple density ratio correction.

Unfortunately, large errors were found when we attempted to use Eq. (5) to relate calibrations performed in air to measuring flow rates of other gases. This finding prompted the separate calibration of the rotameters against the Datametrics unit for each gas.

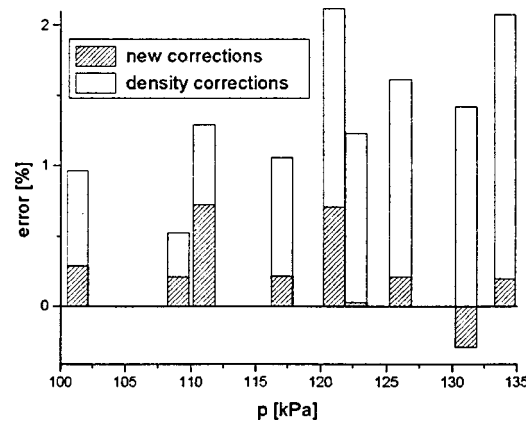


Fig. 8 Comparison of the improved and standard corrections for flowrate measurements of air by a rotameter

Results of Comparison Tests

The CMS was tested extensively using test streams of known concentration. Figure 9 shows the configuration of the system in the comparison test. Two streams of pure gases are obtained from high-pressure bottles and mixed to create the test gas mixture. The flowrate of each pure gas stream is regulated manually with a valve and measured with a calibrated rotameter. The mass flowrates were calculated after applying corrections to each flowmeter, as appropriate for the gas and for the measured pressure/temperature. The actual mass fraction of the mixture downstream of the mixing point was then obtained. The temperature of the ultrasonic CM (and thereby that of the gas mixture) was set on the temperature controller and kept constant at 30°C for all tests.

Data were obtained for mixtures of air with He, air with CO₂, and air with SF₆. Information from the flowrate measurement (“actual” values) and from the ultrasonic technique (“indicated” values) is compared in Figs. 10–15. It is important to realize that data from the conventional measurement methods (which we opted to label “actual” quantities) are subject to errors that are marginally smaller or perhaps even larger than those we are attempting to validate (and call “indicated” values). Regardless of the relative accuracies, a good agreement justifies confidence in both.

Two types of figures are presented for each mixture. The first type of graph represents the relation between the actual speed of sound and the propagation times (both actual and indicated). The actual propagation time was calculated from the mass fraction, known from the measured mass flow rates. For this mass fraction

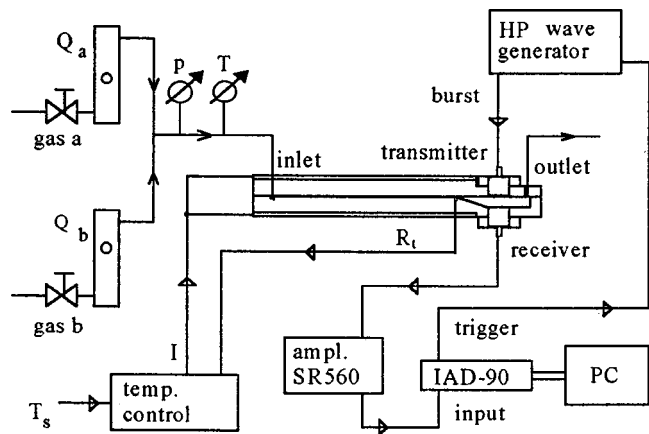


Fig. 9 Configuration of the comparison test

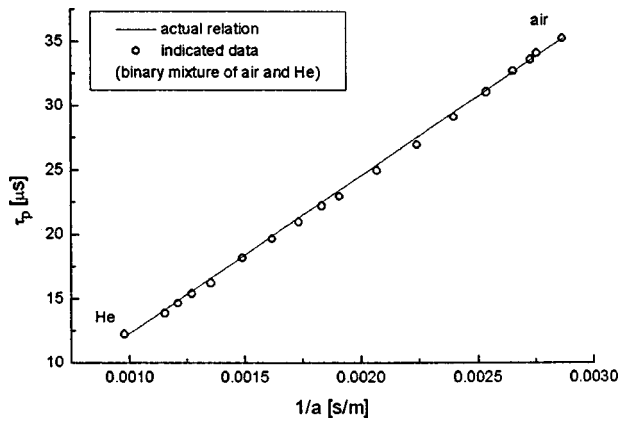


Fig. 10 Travel time in a mixture of He and air

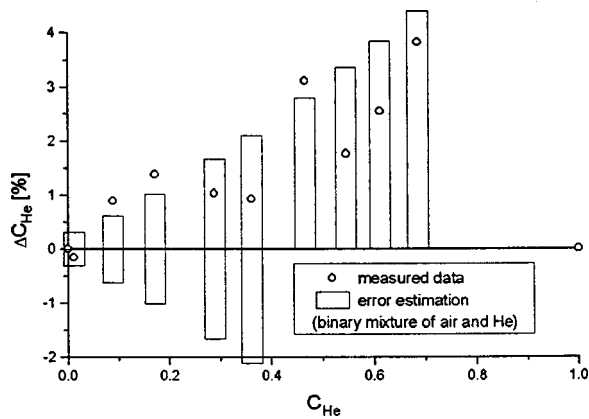


Fig. 11 Comparison of two methods in a mixture of He and air

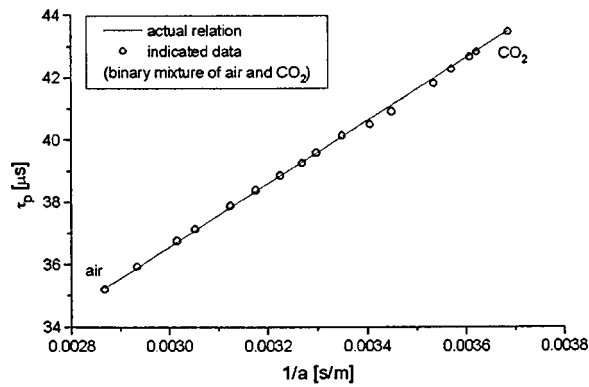


Fig. 12 Travel time in a mixture of CO₂ and air

the actual speed of sound was calculated using the relations of the appendix. The actual travel time τ_p was calculated from this speed of sound and the distance between the transducers. The indicated travel time was obtained from the ultrasonic measurement.

The second type of graph illustrates the difference between actual and indicated concentrations as the function of the actual concentration. The actual concentration of the ballast gas was calculated from the mass flow rates. The indicated speed of sound was evaluated from the measured travel time τ_p and the distance between the transducers. Using the relations of the appendix, the

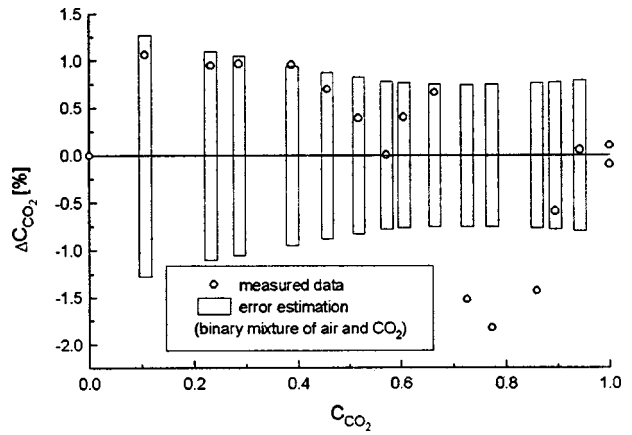


Fig. 13 Comparison of two methods in a mixture of CO₂ and air

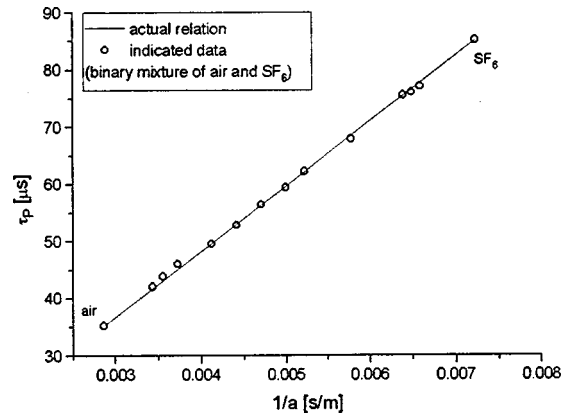


Fig. 14 Travel time in a mixture of SF₆ and air

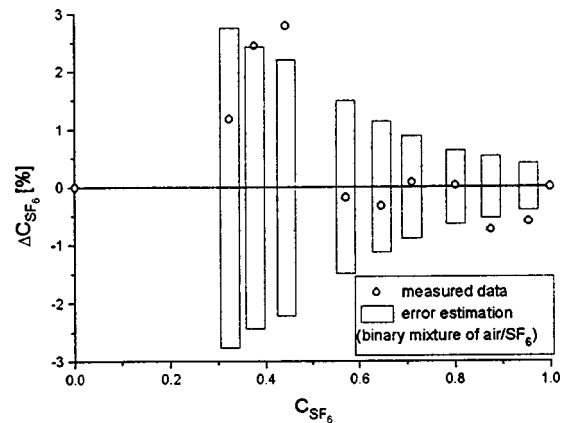


Fig. 15 Comparison of two methods in a mixture of SF₆ and air

indicated mass fraction could be calculated from this speed. The difference between the actual and indicated concentrations (ΔC_b) is plotted in the graph against the actual concentration. The difference ΔC_b is multiplied by 100 to obtain the result in percentages.¹ Clearly, the differences shown represent the combined uncertainty of the rotameter and ultrasonic measurements.

¹If desired, the relative concentration error ($\Delta C_b/C_b$) can be immediately computed from the presented information. The quantity ΔC_b varies over a much narrower range and was preferred here.

Figures 10 and 11 are for He/air mixtures. The travel time is shorter for He than for air because the speed of sound is much higher in He (Table 1). Figure 11 shows that ΔC_b between the two concentration measurement methods is within 2 percent until the He concentration reaches 0.4, beyond which the difference goes up to 4 percent. The reason for the trend is that at high He concentrations the rotameter used for air mass flow rate measurement operates at the very low end of its range and the associated flowrate error is likely to be a major contribution to the total.

Figures 12 and 13 show the results for CO₂/air mixtures. The properties of these gases are very close to each other, so that no difficulties were observed with the rotameter measurements over any portion of the mass fraction range. The difference ΔC_b is in the range of 2 percent.

Figures 14 and 15 show the data for SF₆/air mixtures. The densities and acoustic speeds of these two gases are very different. This fact led to problems very similar to those found with the He/air mixtures, except in this case the inaccuracies were related to using the low range of the rotameter for the heavy gas. The comparison graph for ΔC_b (Fig. 15) shows that large errors occur when the SF₆ concentrations are less than 0.5.

Relatively large combined errors were thus found at conditions where the densities of the component species were very different. However, the ultrasonic method operates most accurately under such conditions, because large differences in the speeds of sound help the resolution of the travel time measurement. It is thus highly probable that the large apparent errors at very high (or very low) concentrations are due to errors in determining the "actual" values of the concentration, and not to errors associated with the "indicated" values produced by the ultrasonic new method.

Uncertainty Estimates

As mentioned before, the comparison of the two methods yields discrepancies that have contributions from each method.

Uncertainty in the indicated data may be due to errors in determining (a) the burst propagation time or (b) the gas temperature, or else they may be caused by (c) temperature or/and (d) pressure effects on the ultrasonic transducers. It is noted that the high digitization rate (32 MHz) allows an accurate measurement of time intervals such that errors due to time measurements are on the order of 0.1 percent in the time of propagation and 0.2 percent in the concentration measurements for pure air. Estimating the accuracy of the basic measurements, the resultant uncertainty of the concentration figures can be determined [7]. A detailed analysis of this type was carried out. The study is reported elsewhere [6] and only some of results are summarized here.

For an air/SF₆ mixture and for a worst-case operating pressure of 100 kPa gage the resultant uncertainty was computed to be 0.18 percent (at $C_{SF_6}=100$ percent) and 2.0 percent (at $C_{SF_6}=0$ percent). The numbers represent uncertainties of the absolute concentration (i.e., ΔC_b , not $\Delta C_b/C_b$) and correspond to two standard deviations (implying that the confidence for obtaining results within the error bars on any of the plots is 96 percent). The largest error contribution is due to pressure effects on the ultrasonic transducers, amounting to 83 percent of the uncertainty figures given above.

The combined uncertainties (including those related to both the actual and the indicated data), are shown in Figs. 11, 13, and 15 with error bars. The error bars are given for 96 percent confidence. The trends clearly show that the errors are due to using the low range on one of the two rotameters, as explained in the previous section.

Summary

A measurement system was developed for the measurement of mass fraction in very low flow rate sample flows of binary gas mixtures. The system measures the speed of sound by ultrasonic methods and calculates the mixture concentration by using the

connection between concentration and acoustic speed. The operational features of the system make it suitable for use in experiments relevant to cooling where the coolant/mainstream density ratios are simulated by the use of air/heavy gas mixtures. The accuracy of the system (difference between indicated and actual concentration) was demonstrated to be better than 2 percent for mixtures of air and He, CO₂, and SF₆. The system may be used for any pair of gases without a need for calibration, provided their densities are unequal. Time response is limited by the purge time of the system, and is equal to approximately 0.1–0.5 s, depending on flowrate. Optical access to the site of sampling is not required by the technique. The system is rugged and may be used in noisy, turbulent environments.

Acknowledgments

The authors wish to express their thanks to Dr. David Davis of NASA Lewis Research Center for his advice and for loaning a thermal flowmeter. The assistance of Russell G. DiMicco and Curtis Fox in various aspects of the laboratory work was invaluable. The Windows-based software developed for a similar application (and adapted for the present one) by Dr. Gabor Blaha is a large and critical part of the system.

Nomenclature

| | |
|------------|---|
| a | = local speed of sound |
| c_D | = drag coefficient |
| c_p, c_v | = specific heat capacity at constant pressure and volume |
| C | = mass fraction |
| f | = frequency |
| H | = heat flux |
| I | = electric current |
| L | = distance between two transducers |
| \dot{m} | = mass flow rate |
| p | = static pressure |
| P | = power |
| Q | = volumetric flow rate |
| R | = gas constant |
| Re | = Reynolds number |
| R_t | = thermistor resistance |
| T | = static temperature |
| T_s | = temperature set point at controller |
| T_w | = wave period |
| ΔC | = difference between actual and indicated concentrations |
| ΔT | = temperature difference |
| γ | = ratio of the specific heat capacities |
| ρ | = gas density |
| τ_C | = constant part of the time delay |
| τ_D | = total time delay obtained |
| τ_E | = constant time delay caused by electronics and mechanics |
| τ_P | = propagation time |
| τ_T | = time delay between the first and the reference wave |
| φ | = ratio of molecular weights |

Subscripts

| | |
|-------------------|--------------------------------|
| a, b | = component species |
| g | = into gas |
| in | = input |
| m | = maximum |
| o | = output |
| s | = into surrounding environment |
| SC | = at standard conditions |
| ($\bar{\quad}$) | = mixture property |

Appendix

Speed of Sound in Binary Gas Mixtures. The properties of mixtures of perfect gases are available in many texts [2]. In the following, expressions relevant to the calculation of the speed of sound are reviewed.

The mass fraction of species i is defined as

$$C_i = \frac{\rho_i}{\rho} \quad (A-1)$$

where ρ_i is the density of the component species i . For our binary mixture $i = a$ or b , and the two mass fractions are simply related:

$$C_a + C_b = 1 \quad (A-2)$$

The gas constant of the mixture is given by

$$\bar{R} = C_a R_a + C_b R_b, \quad \text{or} \quad (A-3)$$

$$\frac{\bar{R}}{R_a} = 1 - \left(\frac{\varphi - 1}{\varphi} \right) C_b \quad (A-4)$$

where $\varphi = m_b/m_a$ is the ratio of the molecular weights of the component species. The specific heats of the mixture are obtained from the specific heats of the constituents by using the expressions

$$\bar{c}_p = C_a c_{pa} + C_b c_{pb}, \quad \bar{c}_v = C_a c_{va} + C_b c_{vb} \quad (A-5)$$

The ratio of the specific heats for the mixture, $\bar{\gamma}$, is defined as \bar{c}_p/\bar{c}_v . Using the previously introduced notations, $\bar{\gamma}$ can be expressed as

$$\frac{\bar{\gamma}}{\gamma_a} = \frac{1 - \left(1 - \frac{1}{\varphi} \frac{\gamma_b (\gamma_a - 1)}{\gamma_a (\gamma_b - 1)} \right) C_b}{1 - \left(1 - \frac{1}{\varphi} \frac{(\gamma_a - 1)}{(\gamma_b - 1)} \right) C_b} \quad (A-6)$$

The acoustic speed of the mixture, normalized by the acoustic speed of species a , is given by the relation

$$\frac{\bar{a}}{a_a} = \sqrt{\left(\frac{\bar{\gamma}}{\gamma_a} \right) \left(\frac{\bar{R}}{R_a} \right)} \quad (A-7)$$

where the ratios inside the square root sign can be calculated from Eqs. (A-4) and (A-7). Equation (A-7) includes the assumption that the reference gas (air) is at the same temperature as the mixture.

References

- [1] Brown, G. L., and Rebollo, M. R., 1972, "A Small, Fast-Response Probe to Measure Composition of a Binary Gas Mixture," *AIAA J.*, **10**, No. 5, pp. 649–652.
- [2] Zucrow, M. J., and Hoffman, J. D., 1976, "Gas Dynamics," Vol. I, Ch. 1–15, Wiley, New York.
- [3] Jena, A., Magori, V., and Russwurm, W., 1993, "Ultrasound Gas-Flow Meter for Household Application," *Sens. Actuators A*, **37–38**, pp. 135–140.
- [4] Sajben, M., and Crafton, D. A., 1997, "Low-Cost Measurement of Mass Fraction in Binary Gas Mixtures," *AIAA Paper No. 97-0602*.
- [5] Nagy, P. B., and Blaho, G., 1994, "Experimental Measurement of Surface Stiffness on Water-Saturated Porous Solids," *J. Acoust. Soc. Am.*, **95**, No. 2, pp. 828–835.
- [6] Strilka, T., 1999, "A Development of an Ultrasonic Method for Mass Fraction Measurement in Binary Gas Mixtures," MS thesis, The University of Cincinnati, Department of Aerospace Engineering and Engineering Mechanics.
- [7] Coleman, H. W., and Steele, W. G., 1989, *Experimentation and Uncertainty Analysis for Engineers*, Wiley, New York.

Local Heat/Mass Transfer Measurements in a Rectangular Duct With Discrete Ribs

H. H. Cho

e-mail: hhcho@yonsei.ac.kr

S. J. Wu

H. J. Kwon

Department of Mechanical Engineering,
Yonsei University,
Seoul 120-749, Korea

The influence of arrangement and length of discrete ribs on heat/mass transfer and friction loss is investigated. Mass transfer experiments are conducted to obtain the detailed local heat/mass transfer information on the ribbed wall. The aspect ratio (width/height) of the duct is 2.04 and the rib height is one tenth of the duct height, such that the ratio of the rib height to hydraulic diameter is 0.0743. The ratio of rib-to-rib distance to rib height is 10. The discrete ribs were made by dividing each continuous rib into two, three, or five pieces, which were attached periodically to the top and bottom walls of the duct with a parallel orientation. The combined effects of rib angle and length of the discrete ribs on heat/mass transfer are considered for the rib angles (α) of 90 and 45 deg. As the number of the discrete ribs increases, the uniformity of the heat/mass transfer distributions increases. For $\alpha=90$ deg, the heat/mass transfer enhancement with the discrete ribs is remarkable, while the heat/mass transfer performances are slightly higher than that of the transverse continuous ribs due to the accompanied high friction loss penalty. For $\alpha=45$ deg, the average heat/mass transfer coefficients and the heat/mass transfer performances decrease slightly with the discrete ribs compared to the case of the angled continuous ribs. [S0889-504X(00)00103-3]

Introduction

Rib turbulators are used to augment heat transfer in internal cooling passages of modern gas turbine blades that must be protected from hot gas streams. Heat transfer in ducts roughened with ribs is augmented remarkably because the ribs disturb flows, promote flow mixing and turbulence, and induce diverse secondary flows. Various rib conditions, such as rib height (e), rib angle of attack (α), rib-to-rib pitch (p), rib shape and arrangement, have great effects on heat transfer and friction, and a number of studies have been performed [1–5]. One of the recent subjects of the investigations on heat transfer augmentation in rib roughened ducts lies in separating ribs in pieces and rearranging them. Lau et al. [6–8] examined the effects of rib angle of attack on the average heat transfer enhancement for a wide range of Reynolds numbers with a square duct roughened with discrete ribs. They used two or five pieces of the discrete ribs per one pitch, and concluded that the largest average heat transfer coefficient was obtained at $\alpha=60$ deg for the five-piece-discrete ribs, and $\alpha=90$ deg for the two-piece-discrete ribs. Taslim et al. [9] and Ekkad and Han [10] performed the experiments using the liquid crystal technique and measured the local distribution in a duct with discrete ribs. There are other interesting studies on the different experimental conditions, such as a very narrow duct with two-piece-discrete ribs by Chyu and Natarajan [11] and a converging passage with seven-piece-discrete ribs by Hu and Shen [12].

It can be inferred from the results of the previous studies that properly arranged discrete ribs would cause higher heat transfer on the duct wall than continuous ribs. Han and Zhang [13] presupposed that broken or discrete ribs might create more secondary flow cells and produce more local turbulence and could perform better than continuous ribs. However, studies on the number of discrete ribs into which each continuous rib should be separated to obtain better heat transfer performance have not been carried out systematically. In addition, it is expected that arrangement of dis-

crete ribs has a strong influence on secondary flows and local turbulence. Therefore, in the present study, the combined effects of the number of discrete ribs (i.e., the rib length-to-height ratio) and rib angle are investigated.

For the purpose of designing rib turbulators, it is important to understand flow patterns and find out the link to the local heat transfer; e.g., to find thermally weak regions such as hot spots. Thus, numerical analysis of the flow field and mass transfer experiments using the naphthalene sublimation method is conducted to obtain the detailed local heat/mass transfer information. It is taken for the main focus in the present study to provide insight into the heat/mass transfer augmentation by discrete rib turbulators through the local investigation, while the previous studies on rib turbulators mainly focused on the average heat transfer, except for some notable works on the local heat transfer [14–18]. For two rib angles of 90 and 45 deg, numerical analysis is performed with two-piece-discrete ribs and mass transfer experiments are conducted with two-, three-, and five-piece-discrete ribs. In addition to the detailed local data, the area-weighted average heat/mass transfer coefficients are presented to compare the overall heat/mass transfer enhancements. Rib turbulators not only enhance heat/mass transfer on the duct walls, but also increase pressure drop through the duct, and in general, the maximum heat/mass transfer is accompanied by the largest pressure drop. Thus, the friction factors are presented and the heat/mass transfer performances for the constant pumping power are considered to evaluate the heat/mass transfer augmentation and the friction loss penalty simultaneously.

Numerical Analysis Conditions

Numerical analysis of flow field in a duct with two-piece-discrete ribs is performed using a commercial code, FLUENT version 4.3. The calculated geometry is almost the same as the experimental one. Thus, the square-rib height is one tenth of the duct height ($e/H=0.1$) with $\alpha=90$ and 45 deg, and the rib pitch-to-height ratio is ten ($p/e=10$). The calculation domain represents one rib-to-rib pitch region and a cyclic condition is applied, so that the flow field results are obtained in the hydrodynamically fully developed state. Considering a symmetry condition, grids of $102 \times 32 \times 82$ (267,648 total) cells and $94 \times 42 \times 82$ (323,736 total)

Contributed by the International Gas Turbine Institute and presented at the 44th International Gas Turbine and Aeroengine Congress and Exhibition, Indianapolis, Indiana, June 7–10, 1999. Manuscript received by the International Gas Turbine Institute February 1999. Paper No. 99-GT-121. Review Chair: D. C. Wisler.

cells are generated for $\alpha=90$ and 45 deg, respectively, in the one-pitch half-duct domain. The working fluid is air at a system pressure of 1 atm and the Reynolds number is 30,000. The RNG $k-\varepsilon$ turbulence model is used to calculate the turbulent separation flows over the ribs and standard wall function is applied for the near-wall treatment.

Experimental Apparatus

A schematic view of the test duct is illustrated in Fig. 1. The cross-sectional area ($W \times H$) is $102 \text{ mm} \times 50 \text{ mm}$ and thus the duct aspect ratio (AR) is 2.04. The hydraulic diameter (D_h) of the duct is 67.3 mm and the length of the roughened region is 1000 mm ($15D_h$). The area ratio of the inlet contraction is 6:1. Airflow entering the inlet contraction passes through the test duct and the plenum, and is discharged out of the room by the blower. The orifice flowmeter between the plenum and the blower is used to measure the mass flow rates of the airflow. The nominal mean velocity through the test duct is 7 m/s in the mass transfer experiments, so that Reynolds number based on the hydraulic diameter (D_h) is 30,000.

The ribs are made of brass and Plexiglas and have a square cross section. The rib height is 5 mm , which is $1/10$ of the duct height and the rib height-to-hydraulic diameter ratio (e/D_h) is 0.0743. The ribs are glued onto the bottom and top walls of the duct by double-sided tape with an in-line orientation. The rib-to-rib pitch is 50 mm so that $p/e=10$. Two rib angles of attack of 90 and 45 deg are selected for the discrete-rib tests based on the results of the continuous-rib tests of our previous work [18]. Three types of discrete ribs are tested in length: a half, a third, and a fifth of the continuous rib length. The types of rib arrangement are shown in Fig. 2. Some rows of the discrete ribs are shifted by a half rib-to-rib pitch in the flow direction so that each row and its neighboring row(s) are staggered. With these arrangements, the total areas covered by the ribs with the same rib angle on the walls are identical for all types of rib length. The numerals, A90 and A45, represent the rib angles of attack. Similarly, N2, N3 and N5 indicate the number of discrete ribs made out of each continuous rib; for example, N3 corresponds to the three-piece-discrete ribs. Thus, N1 is assigned to the continuous ribs. Since the positioning templates are used for rib installation, rib-positioning error is less than $\pm 1 \text{ mm}$ ($0.2e$) and rib-to-rib pitch (p) varies within 2 percent.

The mass transfer experiments are performed by using the naphthalene sublimation method instead of heat transfer experiments in the present study. The naphthalene-coated surface starts from a position $7.6D_h$ downstream from the first rib in the duct and extends over $4.5D_h$ downstream. Since the mainstream passes over eight to ten ribs before reaching the naphthalene-coated surface, the boundary layer of mass transfer starts to develop in the hydrodynamically fully developed turbulence regime. The bound-

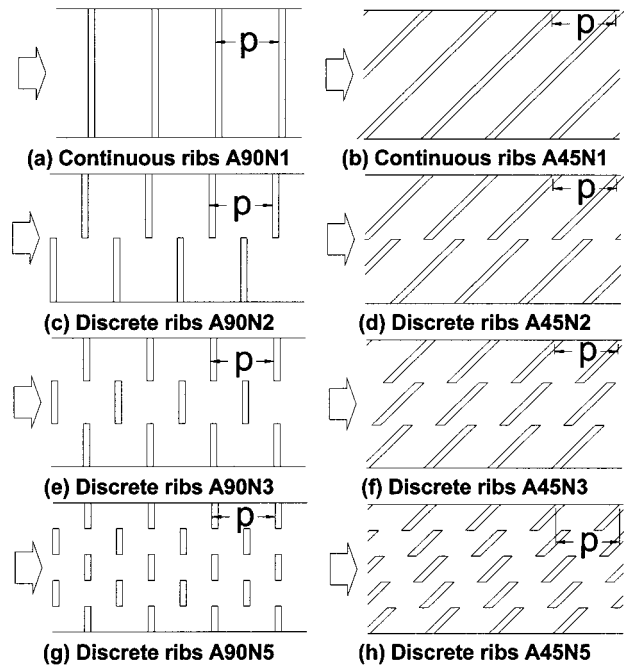


Fig. 2 Types of rib arrangement

ary condition of the naphthalene-coated surface corresponds to the constant temperature condition of heat transfer experiments. The mass transfer inactive ribs attached to the naphthalene-coated surface result in distortion of the boundary condition to some extent. However, many study groups have concluded that this distortion of the boundary condition doesn't make a significant difference in the experimental results. Taslim and Spring [19] noted that the heat transfer coefficients were not sensitive to the choice of wall thermal boundary conditions in their inactive rib study. Liou and Hwang [20] showed that the average heat transfer coefficients from the smooth surfaces of the inter-rib regions (exclusive of the heat transfer inactive ribs) were not significantly different from those from the total heat transfer surfaces (inclusive of the heat transfer active ribs). The deviations between the average heat transfer coefficients from the inactive rib and the active rib experiments were less than 10 percent according to the comparisons by Han et al. [21], Chandra et al. [14], and Ekkad and Han [10]. Moreover, since the main focus of the present study is to provide insight into the heat/mass transfer augmentation by rib turbulators through the local heat/mass transfer measurements in detail, the present experimental method is well-suited to the objective of the study. A large number of local heat/mass transfer coefficients are obtained in the present experiments and the number of data obtained from an inter-rib region reaches approximately 1000.

The coordinate system of the duct takes the mainstream, lateral, and vertical directions as x , z and y , respectively, and the middle point of the start line of the naphthalene-coated area for its origin. Therefore, the domain of the mass transfer measurement covers $0 \leq x/e \leq 60$ in the mainstream direction and $-10.2 \leq z/e \leq 10.2$ in the lateral direction. The ribbed region of $15D_h$ is divided into three sections: the middle section coated with naphthalene ($4.5D_h$ long), the upstream section ($7.6D_h$ long), and the downstream section ($2.9D_h$ long).

The mass transfer active surface is cast with naphthalene using a set of mold composed of the test plate and the molding plate with the highly polished smooth surface. To obtain the local mass transfer rates, the sublimation depths of the naphthalene surface are measured at the numerous positions using the automated positioning table and LVDT (Linear Variable Differential Transformer) of which the resolution is $0.025 \mu\text{m}$ and the diameter of

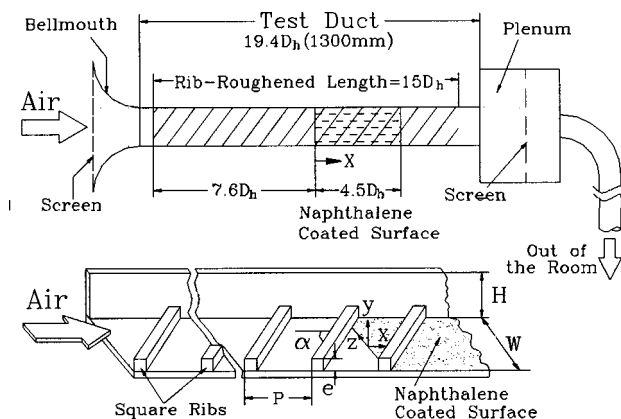


Fig. 1 Schematic diagram of the experimental setup

the measuring tip is 1.588 mm. The error caused by the measurement is less than 1 percent of the average sublimation depth, 0.0762 mm (3 mil). Since the vapor density of naphthalene is very sensitive to temperature and varies 10 percent per 1 °C temperature change, the iron–constantan thermocouple is installed in the test plate to measure the temperature at the naphthalene surface accurately.

The 25 pressure taps with 1.3 mm hole diameter are drilled at $y = H/2$ on the one of the side walls to measure pressure drop through the duct. The pressure tap spacing is 50 mm, which is the same as the rib-to-rib pitch. The micromanometer, with resolution 0.01 mmH₂O, is used to measure the static pressure differences between the taps over the Reynolds number range of 25,000 to 70,000.

Data Reduction

The local depths of the naphthalene-coated surface are measured before and after the run of the duct experiment. The local mass transfer coefficient is calculated from the difference of the local surface depth, i.e., the naphthalene sublimation depth with the correction of the sublimation due to the natural convection during the measuring and the test plate installing/uninstalling, and it is expressed as

$$h_m = \frac{\dot{m}}{\rho_{v,w} - \rho_{v,b}} = \frac{\rho_s(dy/d\tau)}{\rho_{v,w}} \quad (1)$$

where \dot{m} is the local mass transfer rate of naphthalene per unit area and $\rho_{v,w}$ and $\rho_{v,b}$ are the vapor density at the naphthalene surface and the bulk vapor density of naphthalene, respectively. Since the bulk vapor density of naphthalene, $\rho_{v,b}$, at the exit of the duct is at most 0.9 percent of $\rho_{v,w}$, the denominator of Eq. (1), $\rho_{v,w} - \rho_{v,b}$, can be reduced to $\rho_{v,w}$. Therefore, the local mass transfer coefficient is determined from the local naphthalene sublimation depth (dy), the run time ($d\tau$), the density of solid naphthalene (ρ_s) and the vapor density on the naphthalene surface ($\rho_{v,w}$). From the local mass transfer coefficient, the Sherwood number is calculated as

$$\text{Sh} = h_m D_h / D_{\text{naph}} \quad (2)$$

where D_{naph} is the diffusion coefficient of naphthalene in air. The uncertainty in the Sherwood number is estimated within 7.1 percent at the 95 percent confidence level by using Kline and McClintock's uncertainty estimation method [22]. The uncertainty of the naphthalene properties [23,24], such as the vapor density with 4.7 percent error and the diffusion coefficient with 5.1 percent error, are dominant in this error. Nusselt numbers can be obtained from Sherwood numbers by the heat and mass transfer analogy correlated as $\text{Nu}/\text{Sh} = (\text{Pr}/\text{Sc})^{0.4}$ for turbulent flows. The mass transfer results are presented as the Sherwood number ratios, Sh/Sh_0 , to estimate the heat/mass transfer augmentation effectively, where Sh_0 is the Sherwood number for a fully developed turbulent flow in a smooth circular tube correlated by McAdams [25] as $\text{Sh}_0 = 0.023 \text{Re}^{0.8} \text{Pr}^{0.4} (\text{Sc}/\text{Pr})^{0.4}$. In the present study, Sherwood numbers in the smooth duct decrease rapidly from the start position of the naphthalene-coated surface, $x/e = 0$, and remain almost a constant value after $x/e = 25$. This baseline Sherwood number is proportional to $\text{Re}^{0.8}$ but it is approximately 12 percent higher than Sh_0 calculated from McAdams' correlation, which may be due to the differences in geometry and boundary condition. Nevertheless, Sh_0 in McAdams' correlation is chosen as the reference Sherwood number in normalizing the measured data, because the measured baseline Sherwood numbers change a little with positions in the flow direction.

The average Sherwood number ($\overline{\text{Sh}}$) is obtained by the integration of the local Sherwood numbers weighted by area. The streamwise distributions of the mass transfer coefficients between the ribs are repeated with the nearly same values after

$x/e = 10$. Therefore, the region of $35 \leq x/e \leq 55$ is selected to calculate the average Sherwood numbers, where the measuring point distant is $0.2e$.

The average pressure drop is obtained from the slope calculated by a linear curve-fitting of the local pressure difference data in the middle region of the duct ($\Delta P/\Delta L = dP/dx$) where the static pressure decreases linearly. The friction factor is calculated with the average pressure drop as

$$f = \Delta P / [4(\Delta L/D_h)(1/2)\rho V^2]. \quad (3)$$

The uncertainty of the friction factor is within 4.4 percent. The friction loss results are presented as the friction factor ratios, f/f_0 , where f_0 represents the friction factor for a fully developed turbulent flow in a smooth circular tube. The empirical equation that closely fits the Kármán-Nikuradse equation over the range $10^4 < \text{Re} < 5 \times 10^6$ proposed by Petukhov [26] is employed as $f_0 = 2(2.236 \ln \text{Re} - 4.639)^{-2}$. The deviations between the experimentally obtained friction factors in the smooth duct and f_0 calculated from the correlation given above are within 5 percent for the range $25,000 < \text{Re} < 70,000$.

The heat/mass transfer performance, η , obtained by considering both the heat/mass transfer augmentation and the friction loss increase is presented based on the constant pumping power condition and it is expressed as the following equation:

$$\eta = (\overline{\text{Sh}}/\text{Sh}_0)/(f/f_0)^{1/3} \quad (4)$$

Results and Discussion

1 A Review of Continuous Rib Cases and Baseline Check.

The effects of the rib length-to-height ratio of the discrete ribs are taken into account with the combined effects of rib angle. As the first step, the effects of rib angle of continuous ribs are reviewed briefly based on our previous work [18]. The Sherwood number ratio distributions for the continuous ribs are plotted in Fig. 3. For $\alpha = 90$ deg, the high Sherwood number ratios of $\text{Sh}/\text{Sh}_0 \geq 2.6$ are distributed widely over central inter-rib regions of the rib-roughened surface due to the reattachments of the flows passing over the ribs, as shown in Fig. 3(a). The lateral distributions are uniform except for the regions near the side walls. The mass transfer coefficients are enhanced slightly over the regions behind the ribs because the recirculation flows are formed. Detailed local streamwise distributions of the mass transfer coefficients are presented in Fig. 3(c) at a couple of lateral positions where the dotted lines are plotted in Fig. 3(a), and the nearly identical pattern of the distribution is repeated at most lateral positions. For $\alpha = 45$ deg, the secondary flows moving along the angled ribs near the ribbed wall have a great influence on the mass transfer distribution. The secondary flows move up near the one side wall at $z/e = 10.2$ and thus downward flows are induced near the other side wall at the opposite position, $z/e = -10.2$. The secondary flows are induced near the opposite ribbed wall, which results in the creation of pairs of the counterrotating secondary flow cells. Since the downward flows lead the almost naphthalene-free fluid from the core of the duct and impinge onto the ribbed wall, the regions where mass transfer is augmented highly are observed near the side wall at $z/e = -10.2$ [Fig. 3(b)]. As the secondary flows move along the ribs, the flows contain more naphthalene vapor with the developing mass boundary layers, and thus mass transfer decreases. Since the downward/upward flows reinforce or weaken (or even vanish) the reattachments of the flows passing over the ribs, the mass transfer distributions are quite different at the different lateral positions, as shown in Fig. 3(d). More detailed results of the rib angle effects are found in the works of Wu et al. [27] and Cho et al. [18]. For other angled ribs, $\alpha < 90$ deg, mass transfer distributions are basically similar to the case of $\alpha = 45$ deg. Therefore, the transverse rib with $\alpha = 90$ deg and the representative angled rib with $\alpha = 45$ deg are chosen in the investigation of the discrete ribs, and the results for other rib angles can be interpolated or extrapolated.

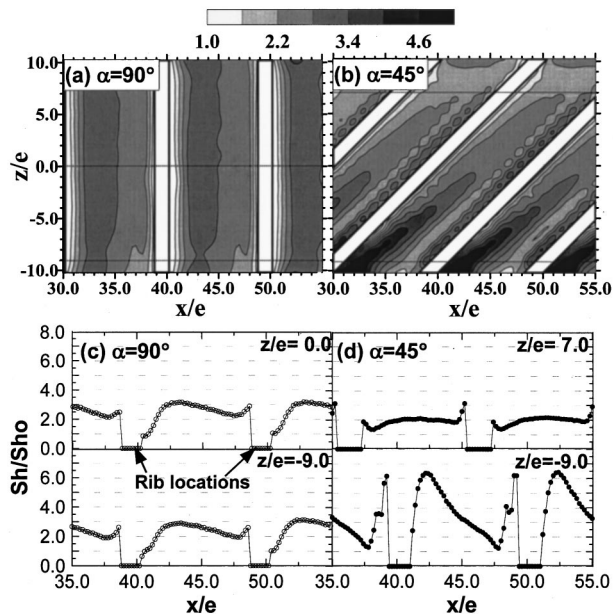


Fig. 3 $\overline{Sh}/\overline{Sh}_0$ distributions for the continuous ribs [18]: A90N1 for (a) and (c); A45N1 for (b) and (d)

The comparison of the average heat/mass transfer results with other references is presented in Fig. 4. It is noted that the experimental investigations using the ducts with $AR=0.5, 1, 2$ and 4 by Han and Park [28] and Han et al. [2] showed that the effect of rib angle on the heat transfer enhancement is significantly influenced by the duct aspect ratio. The reason may be that the ratio of the actual area blocked by ribs to the whole duct cross section changes with the duct aspect ratio even though the rib height to

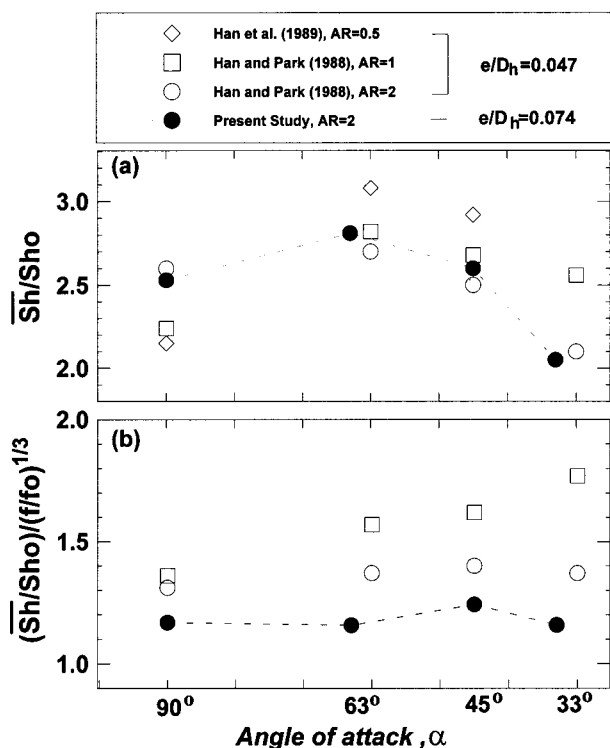


Fig. 4 Average Sherwood number ratios, $\overline{Sh}/\overline{Sh}_0$ and heat/mass transfer performances, η , for continuous ribs with various angles of attack at $Re=30,000$

hydraulic diameter ratios, e/D_h , are identical. In addition, the different duct aspect ratio results in the different flow patterns in ribbed ducts, which include the changes of the rotating secondary flow cells induced by angled ribs. Considering the difference in e/D_h , the average heat/mass transfer coefficients of the present study agree fairly well with those of Han and Park [28] for the same duct aspect ratio, $AR=2$. The performance results are consistent qualitatively with Han and Park's results but the differences in values amount up to 15 percent due to the higher friction factors resulting from the higher blockage ratio, e/D_h , in the present study. It must be noted that the angled ribs perform better in the square duct ($AR=1$) or the narrow duct ($AR=0.5$) than the wide ducts ($AR=2$).

2 Numerical Analysis Results of Flow Field. For the discrete ribs A90N2 and A45N2, velocity vectors in the vicinity of the surface at $y/e=0.1$ and in the duct cross section parallel to the ribs are presented in Fig. 5 with a plot of the angled continuous ribs A90N1 for comparison. For $\alpha=90$ deg, the flow in the vicinity of the ribbed wall turns to be accelerated, passing through the gap between the rib tips due to the existence of the low static pressure region behind the rib marked with LP as shown in Fig. 5(a). Thus, the flow stagnates at the upstream face of the rib around the rib tip and creates the high static pressure region in front of the rib marked with HP. Therefore, the flow near the rib tip goes another way and produces a secondary flow moving from the central region of the ribbed surface to the side wall along the upstream face of the rib. In the case of the continuous rib, this secondary flow is very weak and induced by the nonuniform static pressure distribution near the side wall [29]. Turbulence intensity is high over the wide area around the rib tips due to the flow disturbance and the additional flow separations at the rib tips.

For $\alpha=45$ deg, even though discrete ribs are used, the strong rotating secondary flows are also induced along the ribs, as in the case of the continuous ribs (Fig. 5(c); [18]), which is clearly de-

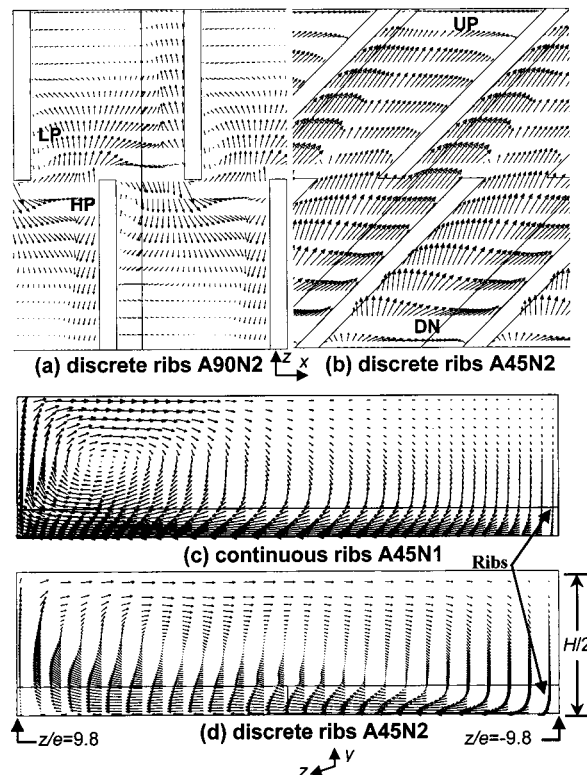


Fig. 5 Calculated velocity vectors (not to scale): (a) and (b) $x-z$ plane at $y/e=0.1$; (c) and (d) the rotating secondary flows in the cross section parallel to the ribs

picted in Fig. 5(d). Due to these secondary flows, the flow impingement and the reinforced reattachment of the flow passing over the rib provide high static pressure and high turbulence intensity over the downward flow region marked with DN in Fig. 5(b). On the other hand, static pressure and turbulence intensity are relatively low in the upward flow region marked with UP in Fig. 5(b). Although the secondary flows are accelerated as they move along the ribs because of the difference in static pressure, there are no remarkable local accelerations of the flows passing through the gap between the rib tips. The reason is that the secondary flows have no abrupt pass changes. Therefore, the discrete-rib tips don't disturb the flows much.

3 Local Heat/Mass Transfer. The distributions of the local Sherwood number ratios are presented in Figs. 6 and 7. For $\alpha = 90$ deg, Sherwood numbers change very rapidly around the tips of the discrete ribs, resulting in the complicated distributions shown in Fig. 6. However, far from the tips, e.g., at $z/e = -9.0$,

the distributions of the mass transfer coefficients are similar to those for the continuous ribs presented in Figs. 3(a) and 3(c). For the discrete ribs A90N2 and A90N3, high mass transfer coefficients are observed over the wide regions around the rib tips as shown in Figs. 6(a), 6(b), 6(d), and 6(e). The reason is that the flows are accelerated between the rib tips, and the additional disturbances by the rib tips promote flow mixing and local turbulence as discussed in the section of the numerical analysis results. For the discrete ribs A90N5, Sherwood numbers have the relatively moderate values around the rib tips, as shown in Figs. 6(c) and 6(f). It is due to the fact that the rib length-to-height ratio (l/e) of the discrete ribs A90N5 is relatively low compared to the other discrete ribs. Thus the low static pressure regions behind the ribs become small, resulting in a moderate flow acceleration: The length-to-height ratios (l/e) are 10.2 and 6.8 for the discrete ribs A90N2 and A90N3, respectively, while $l/e = 4.1$ for A90N5. The width of the flow paths between the rib tips is $4e$ (i.e., the tip-to-

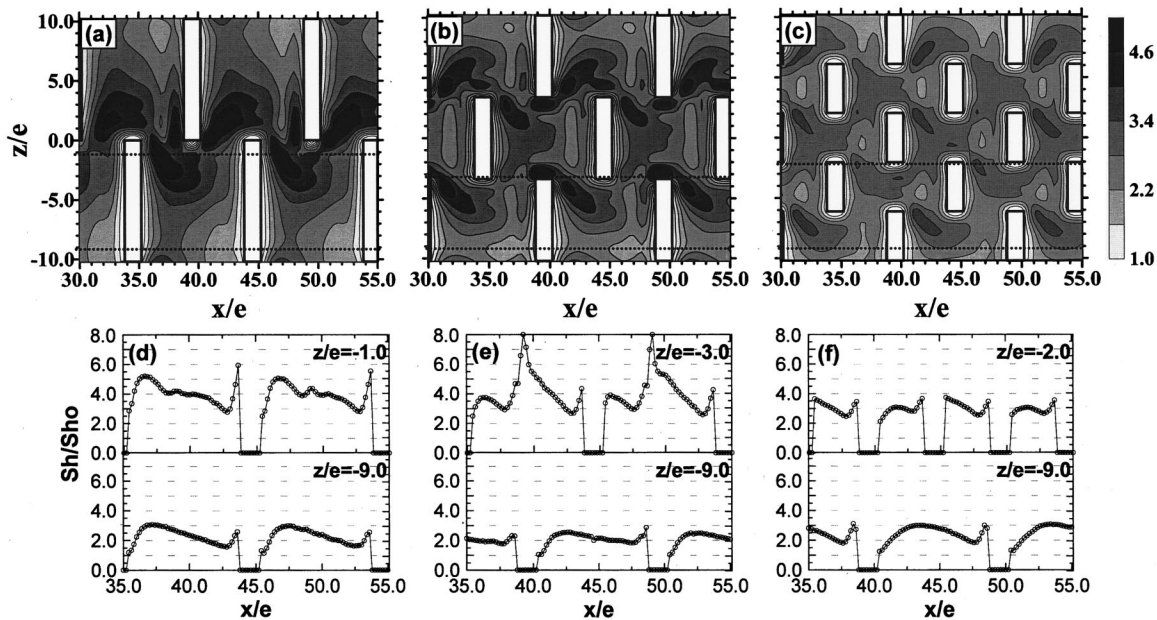


Fig. 6 Sh/Sh_0 distributions for the discrete ribs with $\alpha=90$ deg: (a) and (d) A90N2; (b) and (e) A90N3; (c) and (f) A90N5

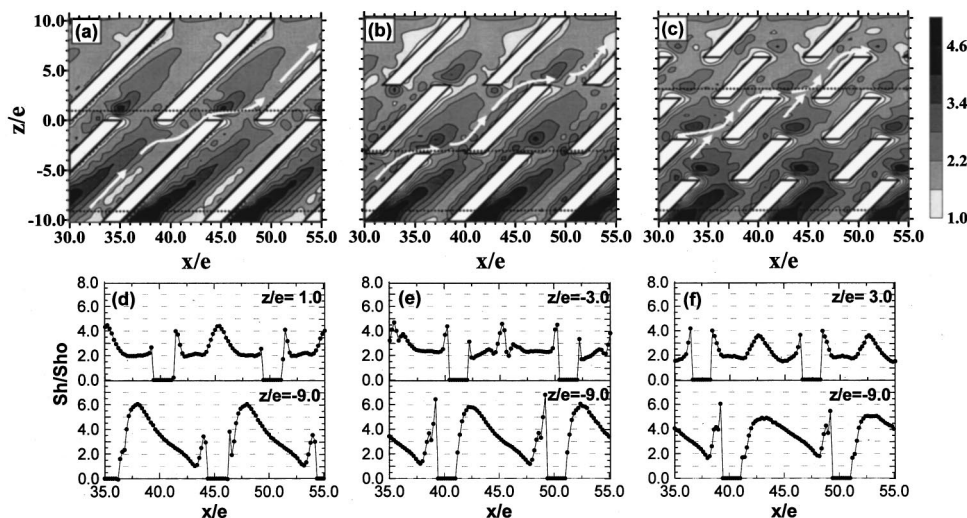


Fig. 7 Sh/Sh_0 distributions for the discrete ribs with $\alpha=45$ deg: (a) and (d) A45N2; (b) and (e) A45N3; (c) and (f) A45N5

tip pitch is $5e$), which is similar to the rib length of the discrete ribs A90N5. Thus, the flow near the surface roughened with the discrete ribs A90N5 doesn't undergo abrupt path changes. As a result, the flow would be neither disturbed nor accelerated largely around the rib tips. Although mass transfer isn't enhanced notably with the discrete ribs A90N5, a fairly uniform distribution of the mass transfer coefficients is obtained with the low mass transfer regions narrowed behind the ribs where the flow recirculations exist. It is expected that potential hot spots and thermal stresses in ribbed ducts be reduced with the discrete ribs A90N5.

Figure 7 shows the results for $\alpha=45$ deg. As the number of discrete ribs increases, the distributions of the mass transfer coefficients become more uniform in the same manner as the case of $\alpha=90$ deg. However, it must be noted that the regions of large Sherwood number increase around the rib tips are confined to very small areas. The reason is that the secondary flows move along the angled ribs, as discussed in the section of the numerical analysis results. The flows near the ribbed walls do not experience either sudden path changes or remarkable local acceleration by being led to the inclined direction along the angled ribs, as depicted in Fig. 5(b). According to the flow visualizations and the flow pattern sketch on the rough wall with angled discrete ribs performed by Hu and Shen [12], the separated flows cause circulation in front of the ribs, which produce vortices along the angled ribs. These vortices separate only at the downstream tips of the discrete ribs. Hence, Sherwood numbers are high in the vicinity of the downstream tips of the discrete ribs, not around the upstream tips. The wide regions where mass transfer is augmented notably by the downward secondary flows are observed even for the short angled discrete ribs A45N5, as well as the other angled discrete ribs. These regions have also been observed for the angled continuous ribs as shown in Fig. 3(b). It is interesting that, for $\alpha=45$ deg, the contour plot patterns of the mass transfer coefficients do not change largely even with the short discrete ribs A45N5. Consequently, the main common characteristics of the local mass transfer for the angled discrete ribs are that the mass transfer coefficients are very high in the regions near the side wall at $z/e = -10.2$ and decrease with the increasing z/e value, and that mass transfer is enhanced highly in the small areas only in the vicinity of the downstream tips of the discrete ribs. These are caused by the fact that the effects of the secondary flows moving along the angled discrete ribs are strong enough to dominate the flow fields near the ribbed walls regardless of the length of the angled discrete ribs tested in the present study.

4 Friction Loss. Figure 8 shows the results of the pressure drop experiments in the form of the friction factor ratios, f/f_0 . The friction losses in the ribbed duct are at least eight times

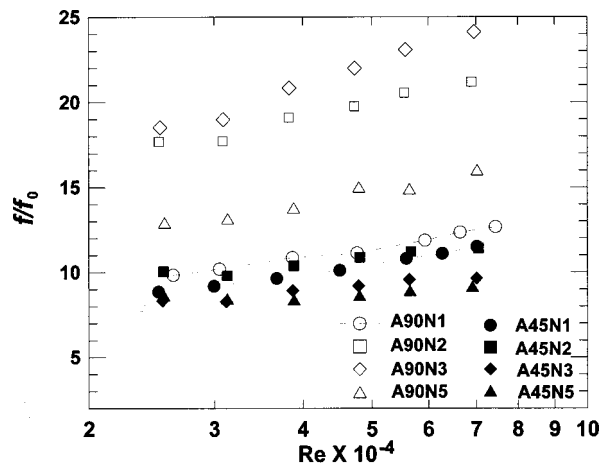


Fig. 8 Friction factor ratios, f/f_0 , for continuous and discrete ribs

greater than that in a smooth duct for the Reynolds number range tested. Friction factors for $\alpha=90$ deg are higher than those for $\alpha=45$ deg in all cases of continuous and discrete ribs. For $\alpha=90$ deg, the discrete ribs A90N2 and A90N3, which enhance mass transfer remarkably, cause great increases in friction loss. These losses are about twice as large as those of the continuous ribs. The discrete rib A90N3 has the largest friction loss. The friction loss of the discrete ribs A90N5 is relatively small as the mass transfer augmentation is also lower than those of the other discrete ribs with $\alpha=90$ deg. The friction factors of the discrete ribs with $\alpha=45$ deg are lower than those of the angled continuous ribs A45N1 except for the discrete ribs A45N2, while those of the discrete ribs with $\alpha=90$ deg are much higher than those of the transverse continuous ribs A90N1. Although the friction factors have almost constant values or decrease slightly in ribbed ducts as the Reynolds number increases, the friction factor ratios increase with Reynolds number. These increasing rates of the friction factor ratios of the discrete ribs A90N2 and A90N3 are somewhat higher than those of the other ribs.

5 Average Heat/Mass Transfer and Performance. For $\alpha=90$ deg, as shown in Fig. 9(a), mass transfer is highly augmented with the discrete ribs A90N2 and A90N3, so that the average Sherwood number ratios amount to 3.2, which is 27 percent higher than that of the continuous ribs A90N1. On the other hand, the average Sherwood number for the discrete ribs A90N5 is similar to that of the continuous ribs A90N1. However, the mass transfer performances for the discrete ribs A90N2 and A90N3 are only 3–5 percent higher than those of the continuous ribs A90N1, as shown in Fig. 9(b), because the great friction losses are also accompanied for the discrete ribs A90N2 and A90N3.

For $\alpha=45$ deg, the average Sherwood numbers are similar in all the angled rib cases of A45N1–A45N5, as expected from the local mass transfer results, and the highest value is observed for the continuous ribs A45N1. The present results for the angled discrete ribs are different from the results presented by Lau et al. [6,7] and Han and Zhang [13], while the results for the discrete ribs with $\alpha=90$ deg are qualitatively consistent with those of other studies, such as the works of Chandra et al. [14] and Taslim et al. [9], as well as the references mentioned above. Lau et al.

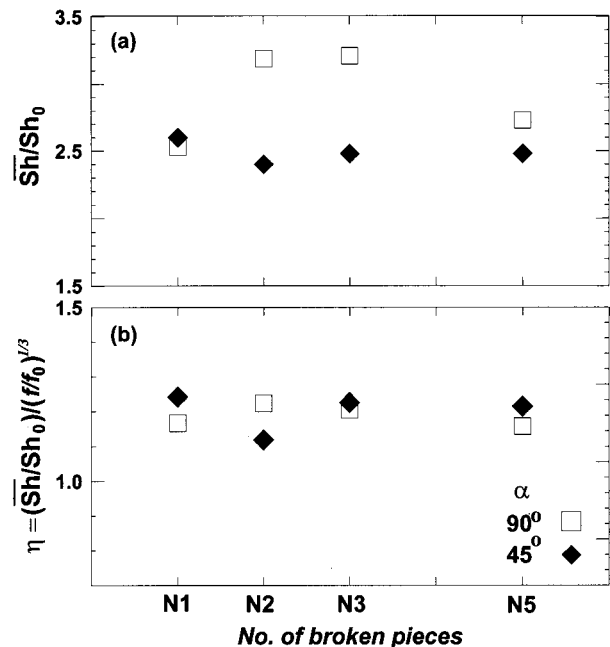


Fig. 9 Average Sherwood number ratios, \bar{Sh}/Sh_0 , and heat/mass transfer performances, η , at $Re=30,000$

[6,7] and Han and Zhang [13] concluded that the three-piece-discrete ribs or the five-piece-discrete ribs with $\alpha=45$ deg enhanced more heat transfer compared to the cases of $\alpha=90$ deg. The rib height-to-hydraulic diameter ratio (e/D_h) in their experiments is 0.0625, which is similar to that of the present study, $e/D_h=0.0743$, with the same rib-to-rib pitch, $p/e=10$. However, they used a square duct, while a rectangular duct with an aspect ratio of 2.04 is used in the present study. Hence, the rib height-to-duct height ratio, e/H , is 0.1 in the present study, which is about 60 percent larger than that in their investigations. As a result, stronger rotating secondary flows moving along the angled ribs are induced in the duct of the present study. As the secondary flows become stronger, the effect of "discretization" of the angled ribs on heat/mass transfer becomes weaker, as discussed in the section on local heat/mass transfer. In addition, since duct aspect ratios affect heat transfer significantly, as shown in Fig. 4, this discrepancy can be caused by the difference of the duct aspect ratios. Chyu and Natarajan [11] also obtained the different results for two-piece-discrete ribs with $\alpha=90$ deg from the other references, because they conducted experiments with a very wide duct, that is, one with a high aspect ratio.

The mass transfer performance of the angled continuous ribs A45N1 is similar to those of all the angled discrete ribs, except for the discrete ribs A45N2, which has the lowest value. In considering rib angle of attack, the average Sherwood number for $\alpha=45$ deg is slightly higher than that for $\alpha=90$ deg in the case of the continuous ribs, but, in all the cases of the discrete ribs, the values for $\alpha=90$ deg are much higher than those for $\alpha=45$ deg. However, the mass transfer performances for $\alpha=45$ deg are slightly higher than that for $\alpha=90$ deg in all the cases except the case of the discrete ribs A45N2.

Conclusions

Heat/mass transfer and friction loss in a duct roughened with the various discrete ribs were investigated and compared with the results of the continuous ribs. The main conclusions are described as follows:

1 For $\alpha=90$ deg, the discrete ribs A90N2 and A90N3 enhance heat/mass transfer highly around the discrete-rib tips, while the discrete ribs A90N5 enhance slightly. The reason is that the rib length is relatively short, so that it is nearly the same length as the width of the flow paths between the rib tips.

2 For $\alpha=45$ deg, the Sherwood number distributions for the discrete ribs are similar to those for the angled continuous ribs due to the dominant effects of the rotating secondary flows along the angled ribs on the flow fields in the vicinity of the ribbed walls.

3 The friction factors of the discrete ribs A90N2 and A90N3 are almost twice as high as those of the continuous ribs in the cases of $\alpha=90$ deg. For $\alpha=45$ deg, a small friction loss is observed as the number of the discrete ribs increases. The friction factors for $\alpha=90$ deg are always higher than those for $\alpha=45$ deg.

4 The discrete ribs A90N2 and A90N3 provide the highest average Sherwood numbers, while have slightly higher heat/mass transfer performances than the transverse continuous ribs A90N1 due to the large friction losses. The average heat/mass transfer and the heat/mass transfer performances of the angled ribs affected slightly by the "discretization" of the ribs with the high e/H of the present study.

Nomenclature

AR = duct aspect ratio = W/H
 D_h = duct hydraulic diameter
 D_{naph} = mass diffusion coefficient of naphthalene vapor in air
 $d\tau$ = run time
 dy = sublimation depth of the naphthalene surface
 e = rib height
 f = friction factor

f_0 = friction factor of a fully developed turbulent flow in a smooth pipe
 H = duct height
 h = heat transfer coefficient
 h_m = mass transfer coefficient
 l = discrete rib length
 \dot{m} = local naphthalene mass transfer rate per unit area
 Nu = Nusselt number = hD_h/k
 Pr = Prandtl number
 p = rib-to-rib pitch
 Re = Reynolds number = $D_h V/\nu$
 Sc = Schmidt number
 Sh = Sherwood number = $h_m D_h/D_{\text{naph}}$
 Sh_0 = Sherwood number of a fully developed turbulent flow in a smooth pipe
 \overline{Sh} = average Sherwood number
 V = mean velocity
 W = duct width
 x = streamwise distance from the starting line of the naphthalene-coated region
 y = vertical distance from the ribbed wall
 z = lateral distance from the center of the duct
 α = rib angle of attack
 ΔP = pressure drop
 η = heat/mass transfer performance = $(\overline{Sh}/Sh_0)/(f/f_0)^{1/3}$
 $\rho_{v,b}$ = bulk vapor density of naphthalene
 $\rho_{v,w}$ = vapor density of naphthalene on the surface

References

- [1] Han, J. C., Glicksman, L. R., and Rohsenow, W. M., 1978, "An Investigation of Heat Transfer and Friction for Rib-Roughened Surfaces," *Int. J. Heat Mass Transf.*, **21**, pp. 1143–1156.
- [2] Han, J. C., Ou, S., Park, J. S., and Lei, C. K., 1989, "Augmented Heat Transfer in Rectangular Channels of Narrow Aspect Ratios With Rib Turbulators," *Int. J. Heat Mass Transf.*, **32**, No. 9, pp. 1619–1630.
- [3] Taslim, M. E., Rahman, A., and Spring, S. D., 1991, "An Experimental Investigation of Heat Transfer Coefficients in a Spanwise Rotation Channel With Two Opposite Rib-Roughened Walls," *ASME J. Turbomach.*, **113**, pp. 75–82.
- [4] Lau, S. C., Kukreja, R. T., and McMillin, R. D., 1991, "Effects of V-Shaped Rib Arrays on Turbulent Heat Transfer and Friction of Fully Developed Flow in a Square Channel," *Int. J. Heat Mass Transf.*, **34**, No. 7, pp. 1605–1616.
- [5] Mochizuki, S., Murata, A., and Fukunaga, M., 1997, "Effects of Rib Arrangements on Pressure Drop and Heat Transfer in a Rib-Roughened Channel With a Sharp 180 Turn," *ASME J. Turbomach.*, **119**, pp. 610–616.
- [6] Lau, S. C., McMillin, R. D., and Han, J. C., 1991, "Turbulent Heat Transfer and Friction in a Square Channel With Discrete Rib Turbulators," *ASME J. Turbomach.*, **113**, pp. 360–366.
- [7] Lau, S. C., McMillin, R. D., and Han, J. C., 1991, "Heat Transfer Characteristics of Turbulent Flow in a Square Channel With Angled Discrete Ribs," *ASME J. Turbomach.*, **113**, pp. 367–374.
- [8] Lau, S. C., Kukreja, R. T., and McMillin, R. D., 1992, "Turbulent Heat Transfer in a Square Channel With Staggered Discrete Ribs," *J. Thermophys. Heat Transfer*, **6**, No. 1, pp. 171–173.
- [9] Taslim, M. E., Li, T., and Kercher, D. M., 1996, "Experimental Heat Transfer and Friction in Channels Roughened With Angled, V-Shaped, and Discrete Ribs on Two Opposite Walls," *ASME J. Turbomach.*, **118**, pp. 20–28.
- [10] Ekkad, S. V., and Han, J. C., 1997, "Detailed Heat Transfer Distributions in Two-Pass Square Channels With Rib Turbulators," *Int. J. Heat Mass Transf.*, **40**, No. 11, pp. 2525–2537.
- [11] Chyu, M. K., and Natarajan, V., 1989, "Local Heat Transfer on a Flat Surface Roughened With Broken Ribs," *ASME HTD-Vol. XXX*, pp. 25–31.
- [12] Hu, Z., and Shen, J., 1996, "Heat Transfer Enhancement in a Converging Passage With Discrete Ribs," *Int. J. Heat Mass Transf.*, **39**, No. 8, pp. 1719–1727.
- [13] Han, J. C., and Zhang, Y. M., 1992, "High Performance Heat Transfer Ducts With Parallel Broken and V-Shaped Broken Ribs," *Int. J. Heat Mass Transf.*, **35**, pp. 513–523.
- [14] Chandra, P. R., Han, J. C., and Lau, S. C., 1988, "Effect of Rib Angle on Local Heat/Mass Transfer Distribution in a Two-Pass Rib-Roughened Channel," *ASME J. Turbomach.*, **110**, pp. 233–241.
- [15] Chyu, M. K., and Wu, L. X., 1989, "Combined Effects of Rib Angle-of-Attack and Pitch-to-Height Ratio on Mass Transfer From a Surface With Transverse Ribs," *Exp. Heat Transfer*, **3**, pp. 291–308.
- [16] Kukreja, R. T., Lau, S. C., and McMillin, R. D., 1993, "Local Heat/Mass Transfer Distribution in a Square Channel With Full and V-Shaped Ribs," *Int. J. Heat Mass Transf.*, **36**, pp. 2013–2020.
- [17] Acharya, S., Myrum, T., Qiu, X., and Sinha, S., 1997, "Developing and Periodically Developed Flow, Temperature and Heat Transfer in a Ribbed Duct," *Int. J. Heat Mass Transf.*, **40**, pp. 461–479.

- [18] Cho, H. H., Wu, S. J., and Kim, W. S., 1998, "A Study on Heat Transfer Characteristics in a Rib-Roughened Rectangular Duct," *Proc. 11th International Symposium on Transport Phenomena*, Hsinchu, Taiwan, pp. 364–369.
- [19] Taslim, M. E., and Spring, S. D., 1994, "Effects of Turbulator Profile and Spacing on Heat Transfer and Friction in a Channel," *J. Thermophys. Heat Transfer*, **8**, No. 3, pp. 555–562.
- [20] Liou, T. M., and Hwang, J. J., 1993, "Effect of Ridge Shapes on Turbulent Heat Transfer and Friction in a Rectangular Channel," *Int. J. Heat Mass Transf.*, **36**, No. 4, pp. 931–940.
- [21] Han, J. C., Chandra, P. R., and Lau, S. C., 1988, "Local Heat/Mass Transfer Distributions Around Sharp 180 deg. Turns in Two-Pass Smooth and Rib-Roughened Channels," *ASME J. Heat Transfer*, **110**, pp. 91–98.
- [22] Kline, S. J., and McClintock, F. A., 1953, "Describing Uncertainty in Single-Sample Experiments," *Mech. Eng.*, Jan., pp. 3–8.
- [23] Ambrose, D., Lawrenson, I. J., and Sparke, C. H. S., 1975, "The Vapor Pressure of Naphthalene," *J. Chem. Thermodyn.*, **7**, pp. 1173–1176.
- [24] Goldstein, R. J., and Cho, H. H., 1995, "A Review of Mass Transfer Measurement Using Naphthalene Sublimation," *Exp. Therm. Fluid Sci.*, **10**, pp. 416–434.
- [25] McAdams, W. H., 1942, *Heat Transmission*, 2nd ed., McGraw-Hill, New York.
- [26] Petukhov, B. S., 1970, *Advances in Heat Transfer*, **6**, pp. 503–504, Academic Press, New York.
- [27] Wu, S. J., Kim, W. S., and Cho, H. H., 1998, "Augmented Heat Transfer in a Rectangular Duct With Angled Ribs," *J. KSME (Korean Society of Mechanical Engineers) B*, **22**, No. 4, pp. 530–541.
- [28] Han, J. C., and Park, J. S., 1988, "Developing Heat Transfer in Rectangular Channels With Rib Turbulators," *Int. J. Heat Mass Transf.*, **31**, No. 1, pp. 183–195.
- [29] Wu, S. J., 1998, "A Study on Heat Transfer and Pressure Drop Characteristics in a Rib-Roughened Rectangular Duct," M.S. Thesis, Department of Mechanical Engineering, Yonsei Univ., Seoul, Korea.

**On the Momentum Balance
in Linear-Combination Models
for the Transition Zone**

J. Dey

Department of Aerospace Engineering, Indian Institute of Science, Bangalore 560012, India

The momentum balance of the linear-combination integral model for the transition zone is investigated for constant pressure flows. The imbalance is found to be small enough to be negligible for all practical purposes. [S0889-504X(00)00703-0]

1 Introduction

The laminar-turbulent transition zone modeling in viscous flows for technological applications is significant [1]. As Mayle [2] points out, accuracy in modeling is also of importance. Although a variety of transition zone models are now available [3], including the Navier-Stokes solutions being attempted by various investigators, a simple linear-combination integral boundary layer calculation is still useful in the interactive design of turbomachine blades. One such simple model is the linear-combination integral model of Dhawan and Narasimha [4] for two-dimensional incompressible flows. This model takes the mean velocity and, consequently, the skin-friction coefficient in the transition zone as a linear combination of the laminar boundary layer (LBL) and the turbulent boundary layer (TBL) values, weighted by the flow intermittency (γ). This model, in spite of being very successful in predicting various transitional boundary layer parameters (e.g., [5-8]), is open to the criticism that the linear combination of the velocity distribution does not ensure momentum balance in the transition zone. This is not a serious one, as many effective approximate methods do not satisfy momentum balance exactly, e.g., the famous Thwaites [9] integral method. However, a closer examination of this issue seems worthwhile, as reported in this paper.

2 Evaluation of the Momentum Imbalance

The mean velocity (U) distribution, and the skin friction coefficient (C_f) in the linear-combination model of Dhawan and Narasimha [4] are:

$$U_{lc} = (1 - \gamma)U_L + \gamma U_T, \quad C_{f_{lc}} = (1 - \gamma)C_{f_L} + \gamma C_{f_T}, \quad (1)$$

respectively. Here the subscripts lc , L , and T denote the linear-combination quantity, the laminar value, and the turbulent value,

respectively; the velocity is nondimensionalized with respect to the free-stream velocity (U_∞). The momentum thickness (θ) for this velocity distribution is:

$$\begin{aligned} \theta_{lc} &= \int_0^\delta U_{lc}(1 - U_{lc})dy \\ &= [\dots] = (1 - \gamma)\theta_L + \gamma\theta_T + \gamma(1 - \gamma) \\ &\quad \times \int_0^\delta (U_L - U_T)^2 dy. \end{aligned} \quad (2)$$

Here δ is the boundary layer thickness. This expression for θ_{lc} is obtained by adding and subtracting the quantities $(1 - \gamma)\int_0^\delta U_L^2 dy$ and $\gamma\int_0^\delta U_T^2 dy$ in $[\dots]$. We may note that this expression for θ_{lc} is different from:

$$\begin{aligned} \theta_{lc} &= \gamma(1 - \gamma) \int_0^\delta [U_L(1 - U_T) + U_T(1 - U_L)]dy \\ &\quad + (1 - \gamma)^2\theta_L + \gamma^2\theta_T, \end{aligned} \quad (3)$$

used by Dhawan and Narasimha [4]. This artificial difference is only because of the re-grouping of various terms in Eqs. (2) and (3). The streamwise (x) derivative (denoted by a prime) of θ_{lc} is:

$$\theta'_{lc} = (1 - \gamma)\theta'_L + \gamma\theta'_T + I_1 + I_2'; \quad (4)$$

$$I_1 \equiv \gamma'(\theta_T - \theta_L), \quad I_2 \equiv \gamma(1 - \gamma) \int_0^\delta (U_L - U_T)^2 dy.$$

The constant pressure momentum integral equations for laminar and turbulent boundary layers and $C_{f_{lc}}$ in Eq. (1) give:

$$2\theta'_{lc} - C_{f_{lc}} = 2(I_1 + I_2'). \quad (5)$$

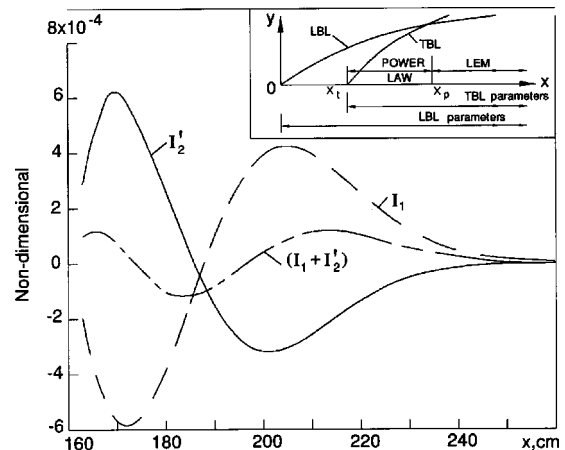


Fig. 1 Variation of I_1, I_2' , and momentum residual for the velocity distribution (1)

Contributed by the International Gas Turbine Institute of THE AMERICAN SOCIETY OF MECHANICAL ENGINEERS. Manuscript received by the International Gas Turbine Institute October 1997. Associate Technical Editor: T. H. Okiishi.

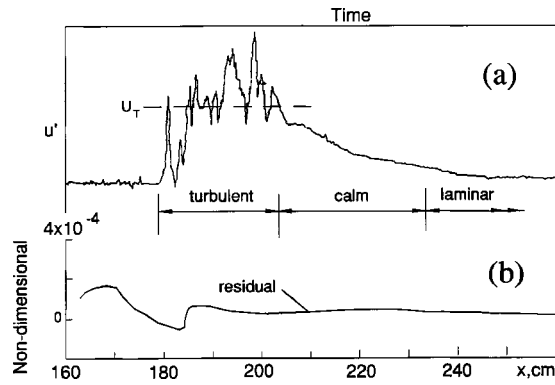


Fig. 2 (a) Idealized velocity fluctuations due to a turbulent spot; (b) momentum residual for the velocity distribution (7)

It can easily be recognized that the right-hand side represents the momentum integral residual arising due to the choice of the velocity distribution, Eq. (1). An anonymous referee has suggested that the constant pressure momentum integral equation and C_f in Eq. (1) require that $\theta'_{lc} = (1 - \gamma)\theta'_L + \gamma\theta'_T$. We do not attempt to solve this equation here. Instead, we evaluate the momentum imbalance in Eq. (5) due to the velocity distribution, Eq. (1). J. E. Green (private communication), from a local momentum balance consideration, suggests that $\theta_{lcG} = (1 - \gamma)\theta_L + \gamma\theta_T$ may be more appropriate than the expression in Eq. (3) for θ_{lc} used by Dhawan and Narasimha [4]. It is, however, clear here that θ_{lc} in Eq. (2) has a part identical with Green's proposal.

An estimate of the momentum residual ($I_1 + I_2$) is made for the constant pressure data of Schubauer and Klebanoff [10] as a test case. The computational scheme used is that of Dey and Narasimha [5], which is based on the linear-combination model, Eq. (1), and the intermittency distribution, $\gamma = 1 - \exp(-0.41[(x - x_t)/\lambda]^2)$, of Narasimha [11]; here x_t is the transition onset location, and λ is a measure of the transition zone length. Various computational domains in this scheme are shown in the inset in Fig. 1; x_t also corresponds to the origin of the TBL; a power-law profile is assumed between x_t and x_p to initiate the lag-entrainment method (LEM) of Green et al. [12] for the TBL; for the present estimation, δ_T at x_p is taken as 85 percent of the power-law value for a smooth variation of I_2 at x_p , although this causes a slight kink in the variation of δ_T at x_p [13]; for the data considered here, $x_t = 161$ cm, $\lambda = 21.3$ cm and $(x_p - x_t) = 3$ cm [5]. As shown in Fig. 1, the terms I_1 and I_2 are of opposite signs and tend to cancel each other. The momentum residual, however, is not exactly zero everywhere in the transition zone, but small in comparison with θ'_{lc} [13]. Noting the oscillating nature of the residual, it is expected that the error in drag estimation will be insignificant; for the data of Schubauer and Klebanoff considered here, it is only 2.5 percent.

An improvement upon the linear-combination model, Eq. (1), is suggested here by considering the "calm" region following the passage of a turbulent spot. As shown in Fig. 2(a) for an idealized velocity fluctuation (u') due to an artificial turbulent spot, the velocity in the calm region is neither turbulent nor laminar, but a combination of these two end states. It can therefore be assumed (Narasimha, private communication) as:

$$U = \gamma U_T + [a_1 \gamma(1 - \gamma) + a_2 \gamma^2(1 - \gamma)^2 + \dots](c_1 U_L + c_2 U_T) - [(1 - \gamma) - (a_1 \gamma(1 - \gamma) + a_2 \gamma^2(1 - \gamma)^2 + \dots)]U_L, \quad (6)$$

where a_1 , a_2 , c_1 , and c_2 are constants. To a first approximation, the mean velocity that follows from Eq. (6), is

$$U = \gamma U_T + (1 - \gamma)U_L + A \gamma(1 - \gamma)(U_L + B U_T), \quad (7)$$

where A and B are constants. Compared to Eq. (1), the additional term in Eq. (7) accounts for the calm region; due to space limitations, the expressions for θ and C_f are not discussed here. The resulting momentum residual for this velocity distribution shown in Fig. 2(b) is seen to be very small over a large extent in the transition zone; here $A = -0.015$ and $B = 1$ are found by trial and error, as these constants are unknown.

3 Conclusion

To sum up, the linear-combination transition zone model of Dhawan and Narasimha [4] has a small momentum imbalance. This fact and the associated simplicity of the model, however, render it an attractive one. A simple means toward a better momentum balance is also suggested.

Acknowledgments

This work is an outcome of Prof. R. Narasimha's concern that this problem be taken up by the author. The author wishes to thank him for various suggestions during the course of this work.

Nomenclature

| | |
|------------|---|
| C_f | = skin-friction coefficient |
| U | = boundary layer streamwise velocity |
| U_∞ | = free-stream velocity |
| I_1 | = $(\theta_T - \theta_L)d\gamma/dx$ |
| I_2 | = $\gamma(1 - \gamma)\int_0^\delta (U_L - U_T)^2 dy$ |
| x | = streamwise distance |
| x_t | = transition onset location |
| x_p | = x location at the end of power law for turbulent flow |
| y | = coordinate normal to flow |
| γ | = flow intermittency |
| δ | = boundary layer thickness |
| θ | = momentum thickness |

Subscripts

| | |
|------|----------------------------|
| L | = laminar value |
| T | = turbulent value |
| lc | = linear combination value |

References

- [1] Cebeci, T., ed., 1983, *Proc. Numerical Physical Aspects of Aerodynamic Flows II*, Springer-Verlag, New York.
- [2] Mayle, R. W., 1991, "The Role of Laminar-Turbulent Transition in Gas Turbine Engines," *ASME J. Turbomach.*, **113**, pp. 509-537.
- [3] Narasimha, R., and Dey, J., 1989, "Transition Zone Models for 2-Dimensional Boundary Layers: A Review," *Sadhana*, **14**, pp. 93-120.
- [4] Dhawan, S., and Narasimha, R., 1958, "Some Properties of Boundary Layer During Transition From Laminar to Turbulent Motion," *J. Fluid Mech.*, **3**, pp. 418-437.
- [5] Dey, J., and Narasimha, R., 1988, "An Integral Method for the Calculation of 2D Transitional Boundary Layers," Dept. Aerospace Engg., Report 88FM7, Indian Institute of Science, Bangalore.
- [6] Dey, J., and Narasimha, R., 1990, "Integral Method for the Calculation of Incompressible Two-Dimensional Transitional Boundary Layer," *J. Aircr.*, **27**, pp. 859-865.
- [7] Singer, B. A., and Dinavahi, S. P., 1991, "Testing of Transition Region Models: Test Cases and Data," NASA CR 4371.
- [8] Gostelow, J. P., Hong, G., Walker, G. J., and Dey, J., 1994, "Modelling of Boundary Layer Transition in Turbulent Flow by Linear Combination Integral Method," ASME Paper No. 94-GT-358.
- [9] Thwaites, B., 1949, "Approximate Calculation of the Laminar Boundary Layer," *Aeronaut. Quart.*, **1**, pp. 245-280.
- [10] Schubauer, G. B., and Klebanoff, P. S., 1955, "Contributions on the Mechanics of Boundary Layer Transition," NACA TN 3489.
- [11] Narasimha, R., 1957, "On the Distribution of Intermittency in the Transition Region of a Boundary Layer," *J. Aeronaut. Sci.*, **24**, pp. 711-712.
- [12] Green, J. E., Weeks, D. J., and Brooman, J. W. F., 1973, "Prediction of Turbulent Boundary Layers and Wakes in Compressible Flow by Lag-Entrainment Method," Royal Aircraft Establishment, Tech. Report 72231, Farnborough, UK.
- [13] Dey, J., 1998, "On the Momentum Balance in Linear Combination Models for the Transition Zone," Dept. Aerospace Engg., Report 98FM7, Indian Institute of Science, Bangalore.